

# Characterization of Minerals, Metals, and Materials

Edited by

Jiann-Yang Hwang

S.N. Monteiro

Chen-Guang Bai

John Carpenter

Mingdong Cai

Donato Firrao

Byoung-Gon Kim

 WILEY

TMS

# **Characterization of Minerals, Metals, and Materials**

# TMS 2012

**141<sup>st</sup> Annual Meeting & Exhibition**

*Check out these new proceedings volumes from the  
TMS2012 Annual Meeting,  
available from publisher John Wiley & Sons:*

3rd International Symposium on  
High Temperature Metallurgical Processing

CFD Modeling and Simulation in Materials Processing

Characterization of Minerals, Metals, and Materials

Electrometallurgy 2012

Energy Technology 2012: CO2 Management and Other Technologies

EPD Congress 2012

International Smelting Technology Symposium  
(Incorporating the 6th Advances in Sulfide Smelting Symposium)

Light Metals 2012

Magnesium Technology 2012

Supplemental Proceedings: Volume 1:

Materials Processing and Interfaces

Supplemental Proceedings: Volume 2:

Materials Properties, Characterization, and Modeling

T.T. Chen Honorary Symposium on Hydrometallurgy, Electrometallurgy  
and Materials Characterization

To purchase any of these books, please visit **[www.wiley.com](http://www.wiley.com)**.

*TMS members should visit [www.tms.org](http://www.tms.org) to learn how to get discounts on  
these or other books through Wiley.*

# **Characterization of Minerals, Metals, and Materials**

Proceedings of a symposium sponsored by  
the Materials Characterization Committee of  
the Extraction and Processing Division of  
TMS (The Minerals, Metals & Materials Society)

Held during the  
TMS 2012 Annual Meeting & Exhibition  
Orlando, Florida, USA  
March 11-15, 2012

*Edited by*

**Jiann-Yang Hwang**

**S.N. Monteiro**

**Chen-Guang Bai**

**John Carpenter**

**Mingdong Cai**

**Donato Firrao**

**Byoung-Gon Kim**



**WILEY**

A John Wiley & Sons, Inc., Publication

**TMS**

**Copyright © 2012 by The Minerals, Metals, & Materials Society.  
All rights reserved.**

**Published by John Wiley & Sons, Inc., Hoboken, New Jersey.  
Published simultaneously in Canada.**

---

No part of this publication may be reproduced, stored in a retrieval system, or transmitted in any form or by any means, electronic, mechanical, photocopying, recording, scanning, or otherwise, except as permitted under Section 107 or 108 of the 1976 United States Copyright Act, without either the prior written permission of The Minerals, Metals, & Materials Society, or authorization through payment of the appropriate per-copy fee to the Copyright Clearance Center, Inc., 222 Rosewood Drive, Danvers, MA 01923, (978) 750-8400, fax (978) 750-4470, or on the web at [www.copyright.com](http://www.copyright.com). Requests to the Publisher for permission should be addressed to the Permissions Department, John Wiley & Sons, Inc., 111 River Street, Hoboken, NJ 07030, (201) 748-6011, fax (201) 748-6008, or online at <http://www.wiley.com/go/permission>.

---

**Limit of Liability/Disclaimer of Warranty:** While the publisher and author have used their best efforts in preparing this book, they make no representations or warranties with respect to the accuracy or completeness of the contents of this book and specifically disclaim any implied warranties of merchantability or fitness for a particular purpose. No warranty may be created or extended by sales representatives or written sales materials. The advice and strategies contained herein may not be suitable for your situation. You should consult with a professional where appropriate. Neither the publisher nor author shall be liable for any loss of profit or any other commercial damages, including but not limited to special, incidental, consequential, or other damages.

---

Wiley also publishes books in a variety of electronic formats. Some content that appears in print may not be available in electronic formats. For more information about Wiley products, visit the web site at [www.wiley.com](http://www.wiley.com). For general information on other Wiley products and services or for technical support, please contact the Wiley Customer Care Department within the United States at (800) 762-2974, outside the United States at (317) 572-3993 or fax (317) 572-4002.

---

Library of Congress Cataloging-in-Publication Data is available.

**ISBN 978-1-11829-122-1**

Printed in the United States of America.

10 9 8 7 6 5 4 3 2 1



**WILEY**

A John Wiley & Sons, Inc., Publication

**TMS**

# TABLE OF CONTENTS

## Characterization of Minerals, Metals, and Materials

Preface .....	xiii
Editors.....	xv

### Characterization of Minerals, Metals, and Materials

#### Characterization of Ferrous Metals I

Characterization of the Microstructure of Compacted Graphite Cast Iron .....	3
<i>V. Rastegar</i>	
EBSD Analysis of Complex Microstructures of CSP <sup>®</sup> Processed Low Carbon Micro-Alloyed Steels .....	11
<i>C. Reip, R. Flender, and M. Frommert</i>	
Empirical Models of Cold Working Effect in Steel Tube Production .....	19
<i>R. Batson, and J. Zhang</i>	
Microstructural Investigation of Carbon Steel after Hot Rolling to Optimize Complex Hot Forming of Thick Plates .....	27
<i>G. Tober, O. Anopuo, and P. Maier</i>	
Microstructural Characterization of Fe-Mn-C Ternary Alloy under Near-Rapid Solidification .....	35
<i>W. Xia, R. Yang, C. Song, and Q. Zhai</i>	
Effects of Surface Modifications on SCW Corrosion Resistance .....	43
<i>J. Li, S. Penttilä, and W. Zheng</i>	
Interface Mass Transfer during the Tribofinishing Process .....	49
<i>I. Hilerio, D. Medina, V. Cortes, and J. Muñoz</i>	

## **Characterization of Non-Ferrous Materials**

- Improvement of Mechanical Properties in Severely Plastically Deformed Ni-Cr Alloy .....61  
*K. Song, H. Kim, H. Son, and W. Kim*
- Processing and Microstructural Control of Copper Foams for Thermal Wick Material Systems .....69  
*K. Ledford, S. Lin, and J. Nadler*

## **Characterization of Minerals and Ceramics**

- A Novel Low-Energy Route for the Extraction of Copper And Cobalt Metals/Alloys from the Zambian Sulphide Concentrates .....79  
*Y. Hara, and A. Jha*
- Structural and Chemical Modification of Sulfide Mineral Surfaces by High-Power Nanosecond Pulses .....89  
*I. Bunin, V. Chanturiya, A. Kovalev, I. Khabarova, and E. Koporulina*
- Characterization of Magnetic and Non-Magnetic Iron Oxide Nanoparticles Synthesized by Different Routes .....99  
*A. Maich, E. Erdem, and F. Doyle*
- Characterization of Concentrate, Pellet and DRI Samples for Trace Elements .....107  
*M. Zhang*
- The Dielectric and the Temperature-rising Characteristics of Ore Fines Materials in Microwave Field .....115  
*H. Zhu, L. Dai, J. Peng, W. Liang, Z. Wei, Z. Weng, Q. Ye, and J. Chen*
- Characterization on the Roughness of the Iron Ore Particles .....123  
*X. Lv, X. Huang, R. Zhang, and M. Zhou*
- Synthesis and Characterization of Al, Ag, Ti, Cu, and B Substituted Hydroxylapatite .....131  
*C. Ergun, T. Webster, G. Gunes, A. Bahadir, H. Liu, and I. Erden*
- Electric Resistivity of Fine Chromite Ore.....139  
*C. Pan, X. Lv, C. Bai, X. Liu, and D. Li*

Melting and Reduction of Manganese Sinter with Fluxes .....	147
<i>T. Brynjulfssen, and M. Tangstad</i>	
Ceramic Pigments with Spinel Structure Obtained by Low Temperature Methods .....	155
<i>O. Restrepo, E. Chavarriaga, and L. Jaramillo</i>	
Mechanical Characterization of Cellular Ceramic Materials .....	163
<i>W. Acchar, F. Barcelos, and L. Pereira</i>	
Study of Attapulgit for Human Health .....	169
<i>W. Acchar, T. Moura, A. Costa, and L. Barreto</i>	

### **Characterization Technologies**

3D Metallography of Multiphase Steels .....	177
<i>M. Fischer, P. Lutomski, A. Stieben, and W. Bleck</i>	
Characterization of Open-Pored Metals Using Image Processing .....	185
<i>B. Hinze, and J. Roesler</i>	
Thermography Assisted Fatigue Testing .....	193
<i>A. Saigal, R. Gu, C. San Marchi, and D. Matson</i>	

### **Characterization of Environmental and Construction Materials**

Tile Production Using Wastes from Mining Industry of the Mining District Pachuca and Real Del Monte.....	203
<i>J. Hernandez, E. Salinas, F. Patiño, I. Rivera, J. Flores, N. Trápala, M. Pérez, M. Flores, and I. Reyes</i>	
Concrete with Cementitious Steel Slag Composites and Its Applications .....	211
<i>H. Fang, J. Hwang, G. Xue, and L. Lu</i>	
Characterization of Dust Generated in the BOF Converter .....	221
<i>E. Junca, J. Oliveira, D. Espinosa, and J. Tenório</i>	
Experimental Research to Improve the Soundness of Cementitious Material Blended with Cycled Fluidized Bed Ash.....	229
<i>S. Zhu, and X. He</i>	

Production of Apatitic Material Using Turkish Colemanite Mineral.....	239
<i>Ç. Moral, T. Başargan, and G. Nasun-Saygılı</i>	
Setting Time of Concrete Material; Laboratory Measurements Versus Field Applications.....	251
<i>M. Riad, S. Shoukry, and G. William</i>	
Gas Emission and Structural Changes in the Firing of Red Clay Ceramics with Addition of Sanitary Ware Mass Wastes .....	259
<i>R. Faria, V. Souza, S. Cosin, R. Toledo, and H. Vargas</i>	

## **Characterization of Energy, Electronic and Optical Materials**

Influence of La <sub>2</sub> O <sub>3</sub> Additive Content on the Phase Stability, Sintering and Microstructure of 8 MOL% Y <sub>2</sub> O <sub>3</sub> Stabilized Cubic Zirconia (8YSZ) Ceramic Used for Solid Oxide Fuel Cell Applications .....	269
<i>S. Tekeli, B. Aktas, and S. Salman</i>	
Development and Characterization of Carbonaceous Materials Incorporated with Metal (Ti, V and Zn )-Organic Compounds for Hydrogen Storage.....	277
<i>M. Nath, A. Kumar, and A. Mallick</i>	
Characterization of Nickel Oxide Nanoparticles for Hydrogen Adsorption with External Electric Field .....	285
<i>Z. Zhang, X. Sun, Z. Peng, and J. Hwang</i>	
Nanocrystalline CdS Thin Films Prepared by Vacuum Evaporation.....	293
<i>S. Ikhmayies</i>	
Structure-Property Correlation of xPb(Ni <sub>0.33</sub> Nb <sub>0.67</sub> )O <sub>3</sub> -(1-x)Pb(Zr <sub>0.31</sub> Ti <sub>0.69</sub> )O <sub>3</sub> Based Relaxor-Ferroelectric Ceramics Synthesized Via Columbite Precursor Method.....	303
<i>B. Malleham, T. Jayaraman, A. James, and D. Das</i>	
The Characteristics of Optical Recording Media Affected by the Accelerating Aging Test .....	311
<i>D. Huang, J. Lin, T. Lin, J. Chen, M. Lin, and J. Tsai</i>	
A Comparison between the Properties of Spray-Pyrolyzed SnO <sub>2</sub> :F/CdS:In Structures Prepared by Using NH <sub>4</sub> F and HF as a Source of Fluorine.....	319
<i>S. Ikhmayies, and R. Ahmad-Bitar</i>	

Characterization and Preparation of Anti-Reflection Coatings in the RANGE of 3-5 $\mu\text{m}$ for Si Optical Window .....	327
<i>K. Iqbal, A. Maqsood, M. Mujahid, and M. Asghar</i>	

## **Characterization of Carbon and Soft Materials**

Thermal Properties of Polyester Composites Incorporated with Coir Fiber .....	341
<i>H. Santafé Júnior, N. Simonassi, and S. Monteiro</i>	
Investigating the Rheology of LCPs through Different Die Geometries .....	349
<i>A. Ahmadzadegan, M. Zimmerman, and A. Saigal</i>	
Effect of the Fiber Equivalent Diameter on the Elastic Modulus and Density of Sisal Fibers .....	357
<i>A. Camposo Pereira, W. Pereira Inácio, F. Muylaert Margem, and S. Neves Monteiro</i>	
Correlation between the Density and the Diameter of Buriti Fibers .....	365
<i>A. de Paula Barbosa, M. Picanço Oliveira, A. da Silva Crespo, N. Suely Silva Santos, F. Muylaert Margem, and S. Neves Monteiro</i>	
Thermal and Morphological Behavior of EVOH/Piassava Fiber Composites ..	373
<i>B. Nogueira, A. Chinellato, A. Ortiz, A. Parveen, V. Rangari, and E. Moura</i>	
Thermal Behavior of Banana Fiber .....	381
<i>F. Muylaert Margem, L. Barbosa de Souza Martins, N. Carneiro Garcia Rosa, and S. Neves Monteiro</i>	
Comparative Studies of Crushing Behavior of Various Fiber Reinforced Skin Polyurethane Foam Cored Composite Sandwich Structures .....	387
<i>K. Sharma, and M. Sripathy</i>	
Elastic Modulus Variation with Diameter for Ramie Fibers .....	395
<i>A. Barreto Bevitori, I. Leão Amaral da Silva, R. Sapeletto Carreiro, F. Muylaert Margem, and S. Neves Monteiro</i>	
Comparative Study of the Sugarcane Bagasse Fiber/HDPE Composite Properties Using Electron-Beam and Gamma Radiation Treatments .....	403
<i>A. Pereira, A. Soria, A. Abreu, A. Chinellato, N. del Mastro, and E. Moura</i>	

## **Characterization of Light Metals**

Influence of Deformation on the Properties of Carbon-Fiber Reinforced 2024 Alloy Matrix Composites.....	413
<i>L. Wu, and G. Yao</i>	
Microstructure and Deformation Behavior of Mg-Zn-Al-Re Magnesium Alloy.....	421
<i>J. Zhang, F. Pan, and C. Bai</i>	
Microstructures and Tensile Mechanical Properties of Mg-9Zn-0.6Zr-2Er Magnesium Alloy.....	427
<i>J. Zhang, and B. Zhang</i>	
Nanobond - The Perfect Refractory Choice for Quick Lining and Repairing of Aluminium Melting Furnaces.....	435
<i>T. Schemmel, H. Jansen, B. Kesselheim, and U. Kremer</i>	
Characterization of Grit Blasted Metallic Biomaterials by Thermoelectric Power Measurements.....	443
<i>H. Carreon, S. Barriuso, J. González-Carrasco, F. Garcia-Caballero, and M. Lieblich</i>	
Characterization of the Torsional Response of As-cast A359-SiCp-30% at Elevated Temperatures.....	451
<i>J. DeMarco, J. Karl, Y. Sohn, and A. Gordon</i>	

## **Characterization of Ferrous Metals II**

Comparison of Creep Life Assessment between Tin-Based Lead-Free Solders and Lead Solders.....	479
<i>K. Monden</i>	
Correlation between $J_{IC}$ and Equivalent Fracture Strain Determined by Small-Punch Test in JN1, JJ1 and JK2 Austenitic Stainless Steels.....	487
<i>V. Lopez-Hirata, M. Saucedo-Muñoz, and T. Hashida</i>	
Effect of Heat Treatment on the Surface Characteristics of AISI D2 Steel Machined by Wire EDM.....	495
<i>M. Dhobe, I. Chopde, and C. Gogte</i>	

Hot Deformation Study by Processing Maps of N Containing Microalloyed Steel .....	503
<i>M. Dikovits, C. Poletti, F. Warchomicka, G. Chaudhari, and V. Pancholi</i>	
Influence of Annealing Treatment on Microstructure and Mechanical Properties of Cold-Rolled Sheet of Fe-36Ni Invar Alloy .....	511
<i>X. Jiang, L. Li, X. Xia, J. Huang, and Q. Zhai</i>	
Mechanical Properties of Friction Stir Welded Inconel 600/SS 400 Lap Joints.....	519
<i>K. Song, W. Kim, and K. Nakata</i>	
Author Index .....	527
Subject Index .....	531

## Preface

This volume collects selected papers presented at the Symposium on Characterization of Minerals, Metals and Materials organized in conjunction with the 2012 TMS Annual Meeting in Orlando, FL, USA.

To process minerals, metals and materials, it is always necessary to understand the chemistries, physical properties, forms, structures, occurrences, functions, relations, etc., of the associated materials prior, during, and after the processing of materials. This type of work, which is broadly understood as characterization, is usually the first step taken to define and solve the industrial processing problems. Various characterization technologies have been developed and applied to meet the needs. In many cases, characterization has served as the brain for the processing of materials.

The Materials Characterization Committee of TMS sponsors this symposium annually as a major event of its activities. The committee is under the Extraction & Processing Division and has extended its focus from the Process Mineralogy for the mineral processing industry in the early days to the downstream metals and materials processing fields. Characterization is the common theme for all these areas.

This symposium received more than 150 abstracts from all over the world. Among them, 105 were selected for presentations on the symposium and 60 papers were accepted for publication in this book after a peer review process.

The book is divided into nine sections and each section has different focus. They include Characterization Technologies, Minerals and Ceramics, Ferrous Metals, Nonferrous Metals, Light Metals, Environmental and Construction Materials, Carbon and Soft Materials, and Energy, Electronic and Optical Materials. In each section, the characterization technologies developed and applied for the specific material are discussed with various examples.

There are very few books published with focus on characterization. We hope this book will serve as a good reference book in this area. We understand the breadth of characterization and materials processing. This book will by no means be able to fill all the needs. But it will provide the up to date information on the current and newly developed characterization technologies with examples on how they have been applied for the processing of various materials. This can be handy and stimulative for people trying to solve problems in the material industries.

We are very grateful to the authors of the included papers for their knowledge contributions, the reviewers for their time and effort dedicated to the manuscripts during the review process, and the publisher for their assistance on the final details. We are also thankful to TMS for giving us the platform to carry out this task. Finally, we would like to express our gratitude to all the previous chairs and members of the Characterization Committee. Their vision and work have made this field prosperous.

*Jiann-Yang Hwang, Sergio Neves Monteiro, Chengguang Bai, John Carpenter, Mingdong Cai, Donato Firrao, Buoung-Gon Kim*

*December 2011*

## Editors

**Jiann-Yang (Jim) Hwang** is a Professor in the Department of Materials Science and Engineering at Michigan Technological University. He is also the Chief Energy and Environment Advisor of the Wuhan Iron and Steel Group Company. He has been the Editor-in-Chief of the Journal of Minerals and Materials Characterization and Engineering since 2002. Several universities have honored him as a Guest Professor, including the Central South University, University of Science and Technology Beijing, Chongqing University, Kunming University of Science and Technology, etc.



Dr. Hwang received his B.S. degree from National Cheng Kung University 1974, M.S. in 1980 and PhD in 1982, both from Purdue University. He joined Michigan Technological University in 1984 and has served as its Director of the Institute of Materials Processing from 1992 to 2011. He has been a TMS member since 1985. His research interests include the characterization and processing of materials and their applications. He has been actively involved in the areas of separation technologies, pyrometallurgy, microwaves, hydrogen storages, ceramics, recycling, water treatment, environmental protection, biomaterials, and energy and fuels. He has more than 20 patents, published more than 200 papers, and founded several companies. He has chaired the Materials Characterization committee and the Pyrometallurgy committee in TMS and has organized several symposiums.

**S.N. Monteiro** (June 24, 1943) graduated as Metallurgical engineer (1966) at the Federal University of Rio de Janeiro (UFRJ). Received his MSc (1967) and PhD (1972) from the University of Florida, followed by a course 1975 in Energy at the Brazilian War College and Post-doctorate (1976) at the University of Stuttgart. Joined (1968) the Metallurgy Department and was appointed (1977) full professor of post-graduation program in engineering (COPPE) of the UFRJ. Elected head of department (1978), coordinator of COPPE (1982) and Under-Rector for Research (1983). Invited as Under-Secretary of Science for the State of Rio de Janeiro (1985) and Under-Secretary of College Education for the Federal Government (1989). Retired in 1993 and joined the State University of North Rio de Janeiro (UENF). Published over 900 articles in journals and conference proceedings. Has been honored with several awards including the ASM Fellowship. Is presently top researcher (1A) of the Brazilian Council for Scientific and Technological Development (CNPq), vice-president of the Superior Council of the State of Rio de Janeiro Research Foundation (FAPERJ), consultant for the main Brazilian R&D agencies and member of the Editorial board of 3 international journals.



**Chen-Guang Bai** is a Professor in the Department of Materials Science and Engineering at Chongqing University, China. He is also the Vice Chairman of Chongqing University Committee, Director of Chinese Society for Metals.

Prof. Chen-Guang Bai graduated from Chongqing University in 1982. After graduating from University he began his teaching and research career. His research interests include the iron-making with V-Ti-magnetite and some characterization related with raw materials pretreatment processes. Recently he has interesting in iron ore sintering, microwaves application in metals extraction, energy saving and CO<sub>2</sub> deducing processes. He has published more than 160 papers and about 10 patents.



**John Carpenter** is a postdoctoral researcher in the Materials Science and Technology Division at the Los Alamos National Laboratory. Dr. Carpenter received his Ph.D. in Materials Science and Engineering from the Ohio State University in 2010 after performing his undergraduate studies at Virginia Tech.

His research interests include the characterization, processing, fabrication, and mechanical testing of nanocomposites. Currently his work focuses on understanding the relationship between plastic strain, texture, and the mechanical properties of Cu/Nb bimetallic nanocomposites fabricated via accumulative roll bonding. This research involves the use of several characterization techniques including neutron scattering, x-ray synchrotron, TEM, EBSD, and SEM. Mechanical testing for this work includes methods such as micropillar compression, microtension, and nanoindentation.

Dr. Carpenter serves as the JOM editor for the Materials Characterization committee and is also a member of the Mechanical Behavior of Materials and Nanomechanical Behavior committees of TMS.



**Mingdong Cai** received his BS degree in Metallurgical Engineering and MS degree in Materials Processing from Southeast University (formerly known as Nanjing Institute of Technology, China) in 1996 and 1999, respectively. Mingdong earned his Ph.D. degree in Materials Science and Engineering from the University of Manchester (U.K.) in 2004. Dr. Cai then worked at Washington State University for three years as Postdoctoral Research Associate and then at University of Houston as Visiting Assistant Professor before joined industry in 2008. Dr. Cai has been an active researcher in academia and have published over 50 technical papers and gave more than 40 conference presentations in the area of physical metallurgy of aluminum alloys, thermal-mechanical processing, surface science and engineering, laser-materials interactions, thin film functional materials, and solidification, etc.

Dr. Cai holds Research Engineer position at Schlumberger Inc. His current research interest includes fracture mechanics, alloy development, powder metallurgy with emphasis on Oil and Gas applications. He is also an adjunct Professor of Southeast University (China).



Dr. Cai serves on the Editorial Board for the *China Foundry Journal* and recently co-edited an issue of *Journal of Materials Engineering and Performance* (in Vol.20 of 2011). Dr. Cai has been an active member of TMS since he joined in 2004. As a member in the TMS EPD Materials Characterization and TMS EPD Shaping and Forming Committees, he currently serves as Technical Advisor to JOM and co-Chair of the TMS Materials Characterization Committee.

**Prof. Donato Firrao**, born in Bari, Italy in 1944, got his Laurea in Chemical Engineering at the Politecnico di Torino, Italy in 1968 and his M.Sc. in Metallurgical Engineering at the Ohio State University, Columbus, OH, USA in 1970. Assistant Prof. at the Politecnico di Torino since 1968 and Associate Prof. there since 1983, he became Full Prof. of Technology of Metallic Materials in the same university in 1986. He has also been visiting fellow at the O.S.U. in 1978-79. Author of more than 180 papers in the fields of Mechanical Metallurgy and Surface Heat Treatments, he is a member of AIM, ASM, TMS-AIME. Having been the President of the Federation of European Materials Societies, he is now President of the Collegio Universitario di Torino as well as Dean of Engineering at the Politecnico di Torino. He was recently nominated Fellow of the American Society for Materials International and Honorary member of the Italian Group on Fracture.



**Byoung-Gon Kim** is a Senior Researcher in the Department of Mineral Processing at Korea Institute of Geoscience & Mineral Resources (KIGAM) and a Professor in the Department of Resources Recycling Engineering at University of Science & Technology.

Dr. Kim received his PhD degree from Kangwon National University in 2000. His research interests include the mineral processing, coal preparation, fine particle processing and their applications. He has been actively involved in the areas of separation technologies, beneficiation of minerals, artificial soil, carbon (graphite) materials, resources recycling. He has more than 30 patents, published more than 50 papers. He has been managing Coal Preparation Project in Korea.



*Characterization of Minerals, Metals, and Materials*  
Edited by: Jiann-Yang Hwang, Sergio Neves Monteiro, Chengguang Bai,  
John Carpenter, Mingdong Cai, Donato Firrao, and Buoung-Gon Kim  
TMS (The Minerals, Metals & Materials Society), 2012

# **Characterization of Minerals, Metals, and Materials**

## **Characterization of Ferrous Metals I**

Session Chairs:

**Jian Li**

**Donato Firrao**

## **CHARACTERIZATION OF THE MICROSTRUCTURE OF THE COMPACTED GRAPHITE CAST IRON**

Vahid Rastegar

Dalarna University; Röda Vägen 3; Borlänge, Dalarna, 781 70, Sweden

Keywords: Compacted graphite cast iron, Color metallography, Dendrites arm spacing

### **Abstract**

Characterization of the microstructure and revealing dendrites in the microstructure and also measuring the dendrites arm spacing and the distribution of silicon were studied in various pieces of compacted graphite cast irons with 0.17, 0.185, 0.2, 0.22 and 0.24 percent of mischmetal. Black-white and color metallography (quantitative and qualitative) were carried out on the various steps of the cast samples. Distribution of silicon was studied quantitatively using spot analysis with scanning electron microscopy. Furthermore, effects of two variables (cooling rate and mischmetal percentage) on dendrites arm spacing were investigated.

In order to color metallography, the samples were plunged into a boiling solution of 18% KOH, 9% NaOH and 9% picric acid in distilled water. It was inferred that the microstructure coloration varies according to the sequence: green→red→yellow→blue→dark brown→light brown as the silicon content decreases. After observing dendrites, dendrites arm spacing was measured. In this method, it seems to be possible to predict the mechanical properties of compacted graphite cast irons by knowing dendrites arm spacing and without any destructive testing. After studying the two variables, it was concluded that dendrites arm spacing decreases as the amount of mischmetal increases and it increases as the cooling rate increases.

### **Introduction**

In general, detecting of primary austenite dendrites is not possible in cast irons due to their solidification system. Observing the dendrites in the room temperature is possible only in those gray cast irons that contain type D graphite. With collecting data of dendrites arm spacing (DAS) measurements, it could be possible to achieve the mechanical properties of cast irons without any destructive testing. In this research by applying a particular method, primary austenite dendrites and also distribution of silicon in the microstructure has been observed.

### **Experimental Procedure**

In order to provide the basic melt, ductile iron ingot was used. Rare-earth elements were added to five step block patterns. Graphite compaction process was done by adding the mischmetal alloy to the melt. After hot mounting, the samples were ground on water-lubricated paper down to 1500 grade, and finally polished using diamond. In order to color metallography, the specimens were plunged into a boiling solution of 18% KOH, 9% NaOH and 9% picric acid in distilled water. 2% Nital etchant was used for black-white metallography. Remelted test pieces were analyzed by quantometer before pouring. In order to study the effect of cooling rate on quantitative distribution of silicon, EDX spot analysis of samples was performed on samples. DAS was measured in five regions of some samples with ocular counting the number of arms in a particular length and finally using the following formula [1].  $DAS = L / [M(n-1)]$

Hardness testing was carried out by Vickers hardness testing, 30kgf was selected as force.

## Results and Discussion

### Spot Analysis

According to Radzikowska [2], the highest amount of Si usually can be found inside the eutectic cell while the intercell regions are almost silicon free. By matching the analysis results of Si with metallographic images, it became evident that the microstructure color changes as the Si percentage varies. The microstructure coloration varies according to the sequence: green →red →yellow →blue → dark brown→ light brown as the silicon content decreases. The same sequence of colors corresponds to the stage of austenite formation from the liquid: the earliest stage is close to the graphite nodules while the latest one is at the cell boundaries.

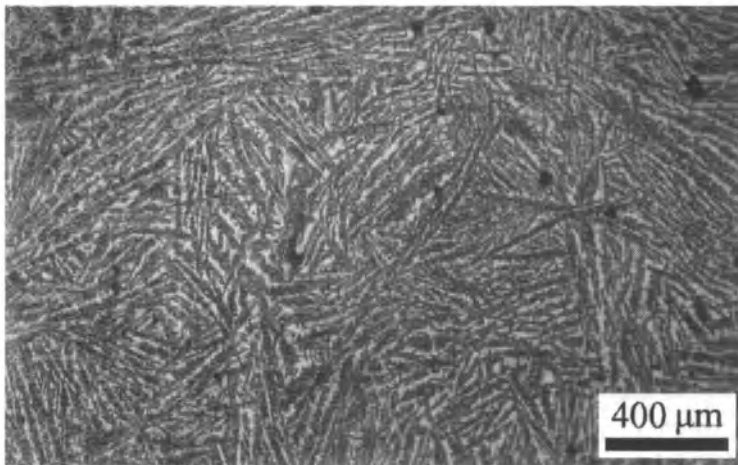


Fig. 1. The microstructure of the sample with 0.22 mischmetal and 3mm thickness, after etching by boiling solution of KOH+NaOH+Picric acid.

### Graphite Morphology

Formation of different graphite morphology is due to possibility of growth on (1010) or (0001) planes [3]. Application of rare-earth elements in varying graphite morphology is due to decrease in concentration of impurities such as oxygen and sulfur which are dissolved in the molten metal.

Table 1. Estimation of compacted graphite amount in different steps (%)

Added mischmetal (wt.%)	Thickness of Step (mm)					
	3	6	12	25	37	50
0.17	0	35 ± 5	70 ± 5	90 ± 5	95 ± 5	95 ± 5
0.185	0	30 ± 5	65 ± 5	85 ± 5	90 ± 5	90 ± 5
0.2	0	25 ± 5	50 ± 5	80 ± 5	90 ± 5	90 ± 5
0.22	0	20 ± 5	45 ± 5	75 ± 5	90 ± 5	85 ± 5
0.24	0	5 ± 5	35 ± 5	70 ± 5	85 ± 5	80 ± 5

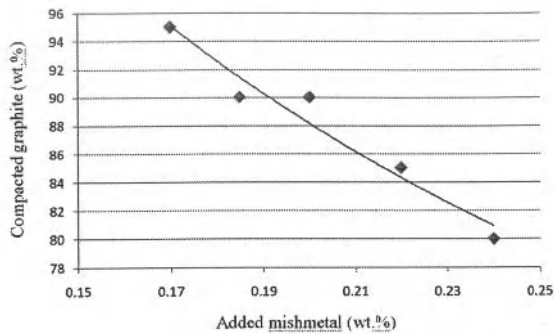


Fig. 2. Effect of changes in added mischmetal percentage on the compacted graphite formation in the sixth step of the samples.

The exact control over the amount of the rare-earth elements in the molten metal provide the possibility of graphite growth based on both mechanism, the spiral growth and the growth in the presence of impurities. The formation and the growth of the compacted graphite are due to growth on (1010) and (0001) planes simultaneously. Being fined down the structure of flake graphites, and the formation of structure type D in the least thickness of the samples are resulted from increasing in the cooling rate. It could be justified by the role of the cooling rate in determination of predominant mechanism of growth. Changes in the cooling rate could result in predominance of spiral growth mechanism or graphite growth in presence of rare-earth element, which are dependent on driving force. Due to possibility of impurities absorption in the (1010) planes of graphite crystal which results in forming the rough interface, these planes have a high intrinsic mobility. Therefore, growth on these planes needs less driving force in comparison with (0001) planes. However, Subramanian et al. [3] in dynamic modeling of crystal growth reported that growth mechanism based on the presence of impurities on the (1010) planes of graphite have a linear dependence on the driving force. While growth rate of spiral mechanism on the (0001) planes are affected by the driving force parabolically [3]. Thus, despite the predominance of impurity mechanism in low cooling rates, spiral growth mechanism in the presence of high driving forces can overcome the growth mechanism based on the presence of impurities, which results in increasing the formation of the spheroidal graphite in the microstructure of CGI. In Fig. 3 with a decrease in the cooling rate, possibility of the compacted graphite formation has been provided based on the simultaneous presence of the spiral growth mechanism and the growth based on the impurities presence, and the compacted graphite amount has decreased.

#### The Effect of the Rare-Earth Elements Content on the Microstructure

Based on the results, an increase in the rare-earth elements amount has associated with increasing the formation of cementite. Fear of forming cementite phase in the CGI microstructure is the most important restriction on the use of rare-earth elements in the graphite compaction process. Graphite compaction with rare-earth elements results in increasing the formation of cementite in comparison with Mg [4]. The present research also approves the effect of increasing the rare-earth elements amount on the formation of cementite. This effect is due to the role of these elements in reducing the space between stable and metastable eutectic lines. These elements cause likely crossing the stable eutectic line in the solidification process.

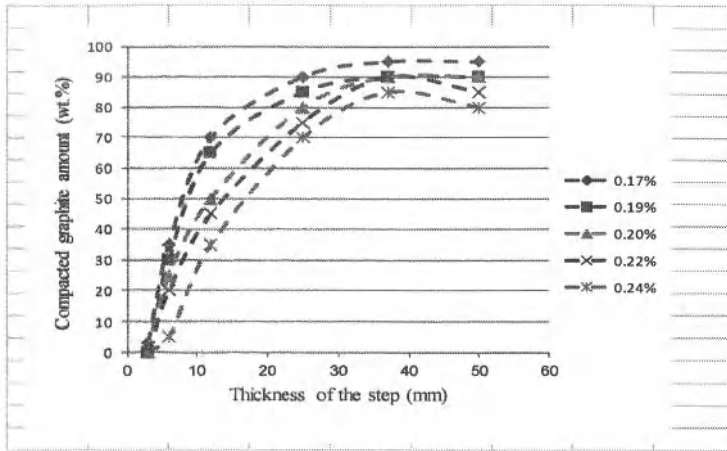


Fig. 3. Effect of changes in samples thickness on the amount of compacted graphite formation.

Table II. Microstructure survey in different samples steps (Carbide + Pearlite + Ferrite(wt. %)).

Added mish metal (wt.%)	Thickness of the step (mm)					
	3	6	12	25	37	50
0	0+44+56	0+64+36	0+28+72	0+21+79	0+5+95	0+9+91
0.17	33+64+3	0+35+65	2+25+73	0+22+78	0+15+85	0+11+89
0.185	42+58+0	0+40+60	0+29+71	0+25+75	0+13+87	0+16+84
0.20	51+49+0	0+42+58	5+35+60	0+27+73	0+22+78	0+20+80
0.22	53+47+0	7+50+43	5+45+50	4+33+63	0+25+75	1+23+76
0.24	55+45+0	40+52+8	21+47+32	8+35+57	1+28+71	3+31+66

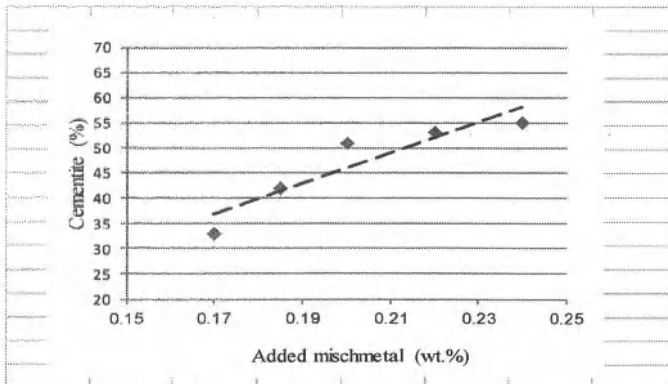


Fig. 4. Cementite formation trend line in the matrix structure of 3 mm step, as a result of variation in rare-earth elements amount.

Lack of access to a structure without any cementite in the sections less than 4 mm which have compacted by rare-earth elements can be justified by simultaneous effect of rare-earth elements presence and high cooling rate, which prevent the graphitization and persuade the formation of cementite. In the sections less than 4 mm, provision of essential supercooling for graphite growth is not possible without crossing the metastable eutectic line. While Stefanescu et al. [5] with simultaneous use of 0.024% Mg and 0.13% Ti in the compaction process achieved a structure without any cementite in sections with 4 mm thickness. An increase in the cementite formation in the samples has associated with a decrease in the pearlite presence in the microstructure. Another point in the samples with 3 mm thickness is that ferrite phase was formed only in very narrow margin adjacent to the graphites. In fact, formation of 3% ferrite was possible only in the step with 0.17% added mischmetal. However, with an increase in the rare-earth elements amount in the other samples with 3 mm thickness, the amount of ferrite phase dropped to 1%. An increase in the amount of rare-earth elements in the thicker samples also leads in persuading the formation of cementite in the structure. Nevertheless, due to a decrease in the cooling rate, a tremendous drop in the tendency to the formation of cementite can be observed as compared with the samples with 3 mm thickness. As an example, in the step with 6 mm thickness the formation of cementite only is limited to the samples with the maximum amount of rare-earth elements. Reducing from the formation of ferrite phase in the structure is the main influence of increasing the amount of rare-earth elements in the thicker samples. 26% average reduction of ferrite formation in the structure of the sample steps with 0.17% added mischmetal as compared with the same steps in the sample with 0.24% mischmetal approves this theory.

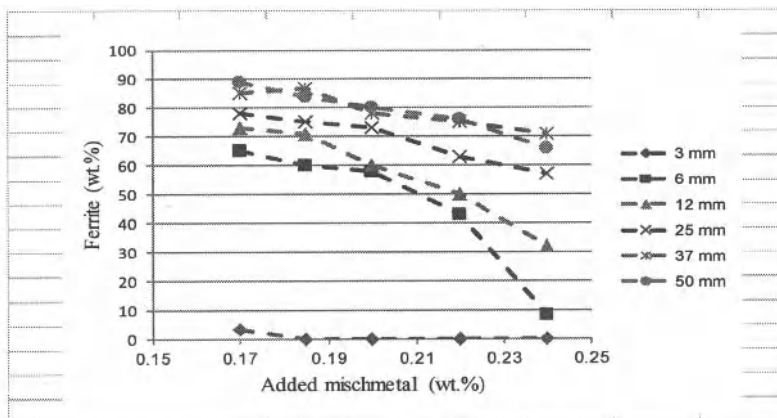


Fig. 5. Ferrite presence trend line in the matrix structure of different steps, as a result of the variation of the rare-earth elements amount.

#### The Effect of Cooling Rate on the Microstructure

Function of the cooling rate in changing the microstructure of CGI is due to different nature of interfaces in austenite, cementite and graphite phases. The cooling rate associated with sufficient driving force plays an important role in the growth of graphite, austenite and cementite phases. The formation of ferrite phase in the microstructure increases as the cooling rate decreases. Fig. 7 shows similar trend line of ferrite formation which can be justified by: (a) available extensive

surface of the compacted graphites, and (b) partly absence of obstacles to the diffusion of carbon atoms toward the formed compacted graphites in the structure.

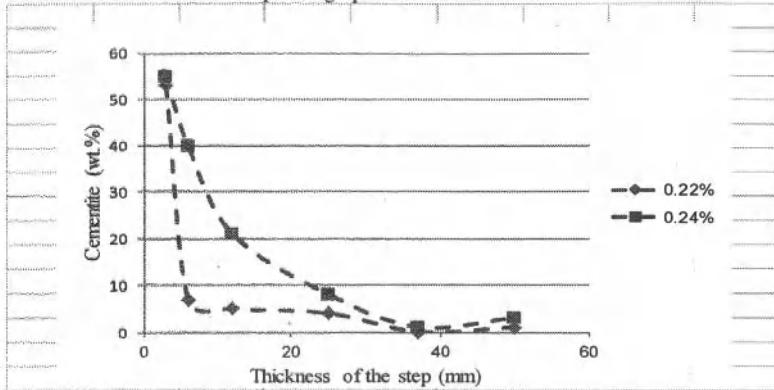


Fig. 6. Cementite formation in the samples with 0.22% and 0.24% added mischmetal.

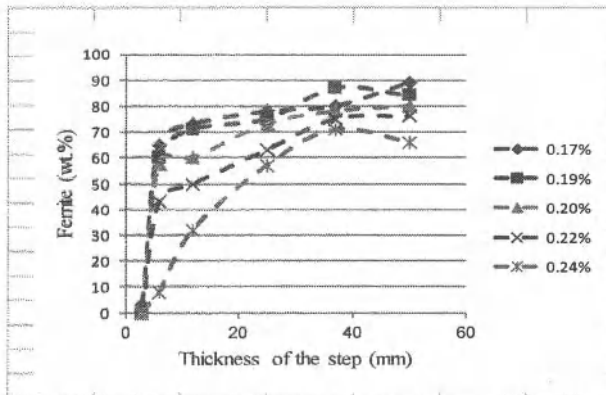


Fig. 7. Ferrite presence, as a result of thickness variation of the steps.

#### Dendrite Arm Spacing (DAS)

According to Table III, it can be concluded that DAS increases as the cooling rate decreases. Also by increasing the mischmetal amount, DAS decreases and it can be anticipated that the mechanical strength would increase.

In alloys with low melting point such as aluminum, predicting the mechanical properties of parts is possible easily with assistance of non-destructive testing such as measuring the DAS by revealing the dendrites. But it has not been possible for cast irons and has not been done so far, and just destructive methods have been applied for measuring the mechanical properties of cast irons. In this study, using color metallography by the special etchant, the dendrites were revealed in CGI for the first time, and thus a method for predicting the mechanical properties of CGI was

provided. Consequently, no more destruction of CGI parts is needed in order to measure the mechanical properties, and thus a new economical method can be introduced to the industry.

Table III. The comparison of calculated DAS between the samples

Thickness of sample	Added mischmetal (wt.%)	DAS ( $\mu\text{m}$ )
3	185.0	67.166
3	24.0	82.58
50	185.0	62.384
50	24.0	49.169

### Results of Hardness Test

In CGI series, the hardness is mainly affected by the matrix structure. An increase in the presence of nodular graphites also leads in increasing the hardness. Fig. 28 shows an increase in the hardness of steps with same thickness as a result of increase in the rare-earth elements amount. Increase in the rare-earth elements amount in the graphite compaction process leads in formation of cementite. Also in low cooling rates, despite the cementite absence, increase in the amount of rare-earth elements leads in formation of pearlite. Extensive formation of cementite also causes a major difference between hardness test results in the steps with 3 mm thickness. Nevertheless, hardness decreasing trend varies similar to changes in the matrix microstructure and amount of compacted graphite formation in the steps with 37 mm and 50 mm thickness.

Table V. Vickers hardness test results in different steps of the samples.

Added mish metal (wt.%)	Thickness of the step (mm)					
	3	6	12	25	37	50
0	-	136	131	118	103	105
0.17	534	219	193	175	169	167
0.185	590	240	197	181	166	170
0.20	675	243	223	187	180	178
0.22	687	334	275	205	192	194
0.24	690	564	351	242	195	196

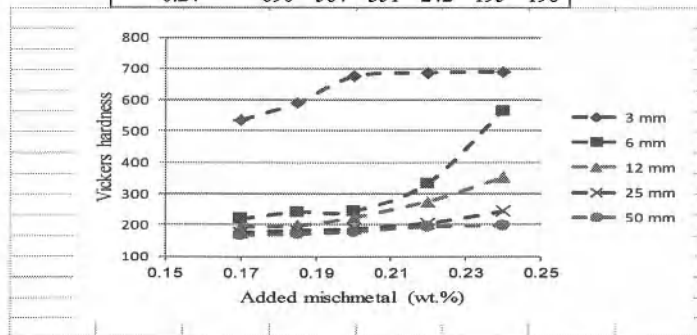


Fig. 8. Hardness variation in the steps, as a result of variation in the rare-earth elements amount

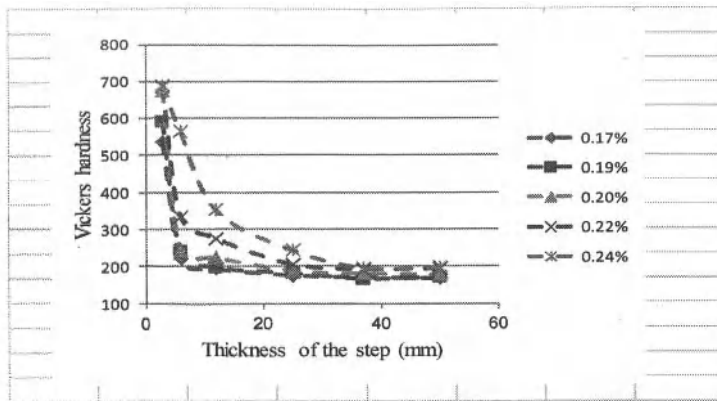


Fig. 9. Hardness variation, as a result of thickness variation of different steps of the samples.

These results approve the theory of predicting the mechanical properties by measuring DAS. It can be seen from Fig. 8 that the hardness of the samples increases as the amount of added mischmetal increases, and it was predicted before by section 3.6. Also according to Fig. 9, it can be seen that the hardness of the samples decreases as the thickness of them increases, and it was predicted before by section 3.6 too.

### Conclusions

Becoming more rounded is the most important effect of increasing the rare-earth elements amount in the graphite compaction process. It can be justified by predominance of spiral growth mechanism in the growth process. Furthermore, increase in the amount of rare-earth elements in the compaction process leads in persuading formation of spheroidal graphites in the structure. Weakness of graphite compaction process using rare-earth elements could result in local formation of cementite in the microstructure of CGI. In other words, if complete distribution of rare-earth elements is not provided before pouring in the molten metal, cementite will be formed in the structure locally. By decreasing the cooling rate or the amount of mischmetal, DAS increases and the hardness decreases and also the formation of compacted graphite and ferrite phases increases and the formation of cementite and pearlite phases decreases

### References

1. "Quantitative Metallography", Metals Handbook, 9th edition, 1986.
2. Janina M. Radzikowska, "Effect of specimen preparation on evaluation of cast iron microstructures", Materials Characterization, pp 287–304, 2005.
3. S. V. Subramanian, D. A. R. Kay, G. R. Purdy, "Compacted graphite morphology control", AFS Transaction, Vol. 90, pp 589-603, 1981.
4. H. H. Cornell, C. R. Loper, E. N. Pan, K. Ogi, "Some aspects of the inoculation and fading of rare earth-treated compacted/vermicular graphite cast iron", AFS Transaction, Vol. 92, pp 401-408, 1984.
5. S. Charoenvilaisiri, D. M. Stefanescu, R. Ruxanda, "Thin Wall Compacted Graphite Iron Castings", AFS Transaction, Vol. 110, code 02-176, 2002.

## **EBSD ANALYSIS OF COMPLEX MICROSTRUCTURES OF CSP® PROCESSED LOW CARBON MICRO-ALLOYED STEELS**

Carl-Peter Reip<sup>1</sup>, Reinhard Flender<sup>2</sup> and Matthias Frommert<sup>2</sup>

<sup>1</sup>SMS Siemag Aktiengesellschaft, Eduard-Schloemann-Strasse 4, 40237 Düsseldorf, Germany

<sup>2</sup>Salzgitter Mannesmann Forschung GmbH, Ehinger Strasse 200, 47259 Duisburg, Germany

Keywords: EBSD, microstructure, micro-alloyed steels, toughness, CSP

### **Abstract**

Today there is a growing demand for strip of superior steels with specifically tailored technological properties. Especially strips of high-strength, micro-alloyed steel grades applied to manufacture longitudinally and spiral-welded pipes are a growth market. Tubes are generally required to have high strength and sufficient toughness values and thus favour specific hot strip microstructures. The correlation of chemical analysis, process parameters and mechanical properties with microstructural features is still a challenging task. During the last decades, scanning electron microscopy (SEM) and electron backscatter diffraction (EBSD) have become useful tools for the characterization of complex microstructures. The EBSD data provides an immense variety of post-processing possibilities, e.g. related to grains, grain boundaries, misorientations or texture. This paper highlights the results of an advanced analysis of microstructures representing industrial produced hot-rolled strips and presents an approach to define and quantify some essential microstructural parameters.

### **Introduction**

High-strength microalloyed steels have been used for the production of welded pipes for more than 30 years. However, the alloy design of pipeline grades is being continuously modified and the process technology optimized because of the increasing high strength-toughness combination requirement for pipeline steels. Compact strip production (CSP®) technology is an upcoming promising route for the production of high-quality pipeline steel grades [1].

One of the development projects concentrated on the production of near-net-shape hot strip from pipe steel, with strength levels ranging between 500 and 700 MPa and ample toughness even at temperatures of down to -60°C. The toughness levels are mainly determined by the microstructure existing in the coiled hot strip. Therefore, a significant metallurgical challenge was the definition, as a function of the required hot-strip thickness and considering the limited overall degree of deformation, of an optimal pass schedule design and cooling strategy to achieve sufficiently fine-grained and homogenous microstructures especially for a hot-strip thickness of more than 6 mm.

Generally, resulting microstructures are quite complex and not easily quantifiable by conventional methods such as light optical microscopy. Therefore, high-resolution scanning electron microscopy (SEM) using the EBSD technique was applied with the aim to correlate variations of chemical analysis, process parameters and mechanical properties with microstructural features.

## CSP<sup>®</sup> Processed Low Carbon Micro-Alloyed Steels

### Steel Composition and Processing Methods

The chemical composition of the investigated micro-alloyed steels is presented in Table I. As a basis, a low carbon content of ~0.06 % was preferred from the viewpoint of segregation and slab surface conditions as well as toughness and weldability. The sulfur, phosphorus and nitrogen contents were controlled at ~0.0015%, 0.012% and values between 0.0050 and 0.0079%, respectively, through the selection of feedstock and secondary metallurgical measures. As microalloy additives, vanadium, niobium and titanium were used. The alloy CMnMoNi(VNbTi) which is additionally alloyed with 0.182% nickel and the alloy CMnMo(VNbTi) contain 0.187% and 0.222% molybdenum, respectively.

Table I. Chemical composition of micro-alloyed steels (weight %).

Steel	C	Mn	Mo	Ni	V	Nb	Ti	N
CMn(VNbTi)-1	0.07	1.34			0.051	0.051	0.017	0.0073
CMn(VNbTi)-2	0.05	1.62			0.019	0.076	0.014	0.0079
CMnMoNi(VNbTi)	0.05	1.30	0.187	0.182	0.051	0.044	0.013	0.0063
CMnMo(VNbTi)	0.06	1.32	0.222		0.053	0.042	0.013	0.0050

The hot strips were produced with the CSP<sup>®</sup> technology. In the process, both the 52mm and the 65mm thick thin slabs that were up to 1,900mm wide, were first cast in the CSP<sup>®</sup> caster, then homogenized in the tunnel furnace at temperatures of around 1,130°C and finally rolled to 12.7mm thick hot strip in the finishing mill, Table II.

Table II. Thin slab and strip dimensions as well as tensile properties of hot-rolled strips.

Steel	Slab-thickness in mm	Strip-thickness in mm	Ratio $t_{slab}/t_{strip}$	Yield strength in MPa	Tensile strength in MPa	Ratio YS/TS
CMn(VNbTi)-1	52	12.7	4.1	478	580	0.82
CMn(VNbTi)-2a	65	12.7	5.1	537	640	0.84
CMn(VNbTi)-2b	65	12.7	5.1	578	655	0.88
CMnMoNi(VNbTi)	52	12.7	4.1	529	626	0.85
CMnMo(VNbTi)	52	12.7	4.1	542	654	0.83

For the thermomechanical treatment, pass schedules with different reduction distributions in the various millstands and different temperature controls were considered as a function of the slab thickness. To avoid rolling in the temperature range of partial static recrystallization, the corresponding millstands were opened.

### Hot-strip properties

On account of the differences in chemical composition and the process parameters selected for the thermomechanical treatment, the hot strip produced has different technological properties. The yield-point levels established and the tensile strength are shown in Table II. The toughness properties were identified in the Charpy impact test with V-notch standard samples. The resulting temperature dependencies of the shear area are shown in Figure 1 for the various alloys. The transient temperatures established therefrom for a shear fracture component of 50% and the relating yield points are shown in Figure 2. It becomes clear that the three variants CMn(VNbTi)-1, CMnMoNi(VNbTi) and CMn(VNbTi)-2b, despite their obvious differences in strength levels, have similar toughness levels. Increasing the starting slab thickness with the

option of optimizing the reduction distribution especially in the front and rear millstands will, as a function of the relating yield point values, lead to an improvement of the toughness levels.

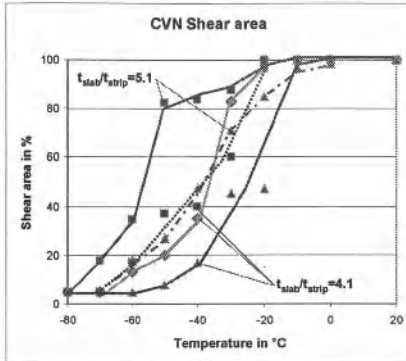


Figure 1. Charpy-V notch toughness properties of 12.7 mm hot-rolled strip.

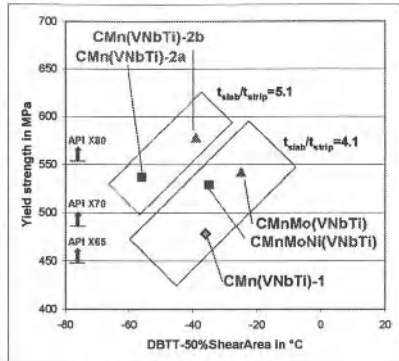


Figure 2. Yield strength vs. toughness of 12.7 mm hot-rolled strip.

The lightmicroscopic,  $\text{HNO}_3$  etched microstructures that pertain to the various hot strips are shown in Figure 3. The relating microsections were removed in the immediate vicinity of the notched-bar test pieces and thus reflect the microstructures that each pertain to the respective technological properties each. The following paragraphs include a more detailed analysis of the microstructures.

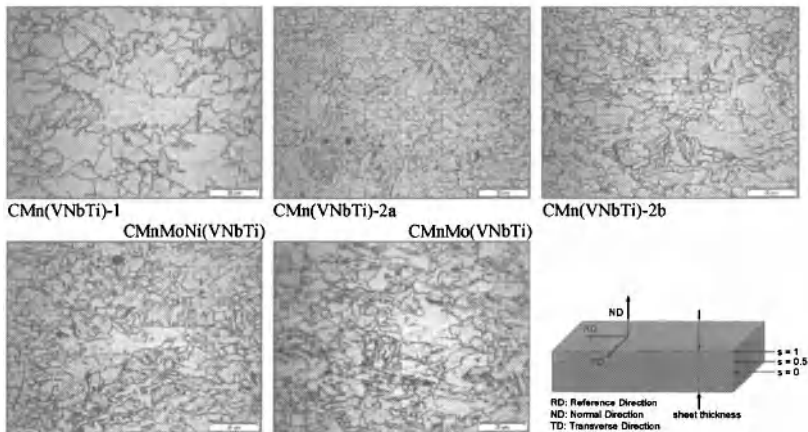


Figure 3.  $\text{HNO}_3$ -etched microstructures of hot-rolled strip at a quarter of sheet thickness ( $s=0.5$ ).

### Method of Microstructural Analysis: Electron Backscatter Diffraction (EBSD)

EBSD allows the measurement of local crystallographic orientations. For EBSD, a perfectly polished sample surface is necessary, as any deformation due to mechanical grinding or polishing has to be avoided since it directly influences the pattern quality. Figure 4 shows the EBSD setup in a standard scanning electron microscope (SEM). The sample is tilted to  $70^\circ$  toward a phosphorus screen. A CCD camera collects the Kikuchi patterns which are formed when a stationary electron beam interacts with a crystalline lattice in a highly tilted sample in the SEM. The geometrical relationships of the bands hold information about the crystal lattice in the diffracting volume. Sophisticated image analysis routines analyze these relationships to automatically determine the crystallographic phase and orientation of the lattice. The EBSD data are collected by moving the electron beam to points on a regular grid, i.e. "scanning" the area of interest of the sample.

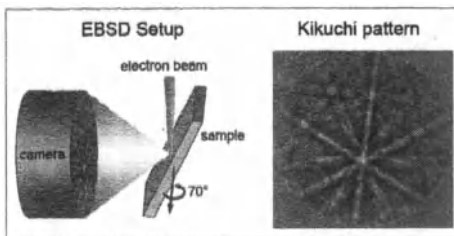


Figure 4. Schematic SEM set up for EBSD measurement and example of a Kikuchi pattern.

The EBSD data provides a wide variety of post-processing possibilities, e.g. related to grains, grain boundaries, and misorientations. The EBSD software can also be used to visualize the orientation aspects of microstructures and gather statistical information on preferred orientations of the material. Some of the analysis techniques used in this investigations are explained in more detail in the following section.

For the current investigation, the EBSD maps were acquired with a step size of 400 nm. For each map, an area of  $400 \times 400 \mu\text{m}^2$  was analyzed. The measurement areas were selected at a quarter of the sheet thickness ( $s = 0.5$ , see Figure 3). In some cases, a supplementary measurement was performed at  $s = 0$ .

### Analysis of hot-strip microstructures

The inverse pole figure (IPF) describes the position of the sample coordinate system with reference to the crystal coordinate system. The IPF map is a reconstruction of the grain structure achieved by colouring the crystallographic orientations with regard to a certain colour code based on the inverse pole figure. By definition, it shows the arrangement of grains as well as orientation changes within grains. It is possible to superimpose different types of grain boundaries defined, for example, by their misorientation angles as lines (grain boundary misorientation (GBM) maps).

Figure 5a shows the resulting IPF maps for the hot strips made of CMn(VNbTi)-1, CMnMoNi(VNbTi) and CMn(VNbTi)-2a. Moreover, Figure 5b shows the grain boundaries for different misorientation angle intervals. For the Mo-alloyed variant and the variant with a higher Nb alloy, a clear increase in the amount of grain boundaries with misorientations of less than  $15^\circ$  has been found. These small-angle grain boundaries are assigned to substructures, of which some can be seen in Figures 3 and 5a. CMn(VNbTi)-1, in contrast, reveals large areas of grain boundaries with misorientations between  $15^\circ$  and  $45^\circ$  (see also Figure 5c), in which the micro-

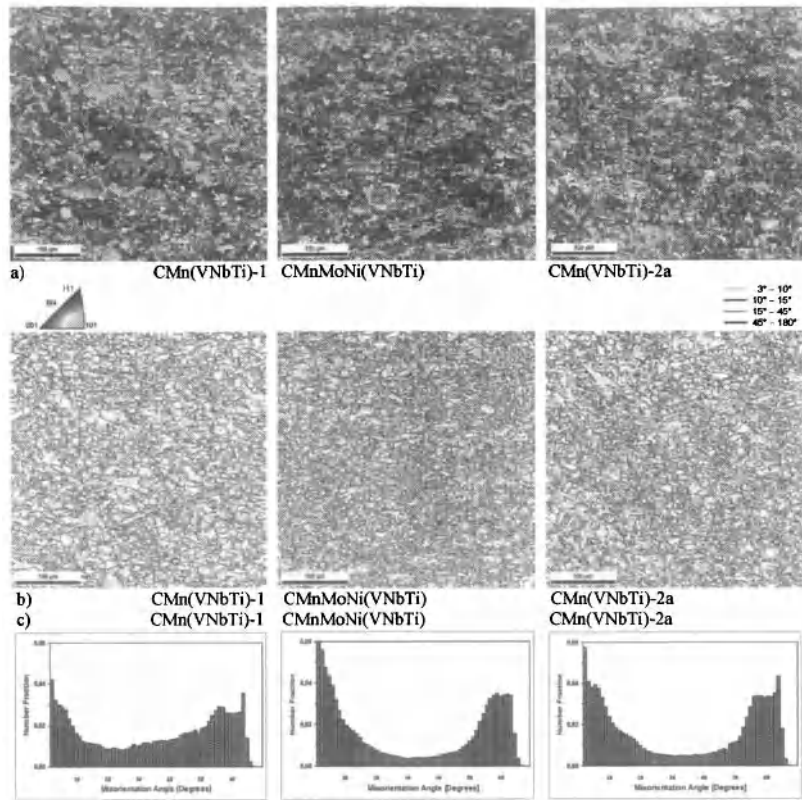


Figure 5. Microstructural details of hot-rolled strips ( $s=0.5$ ): a) Inverse pole figure maps; b) Grain boundary misorientation maps; c) Misorientation angle distribution.

structure constituents dominated by small-angle grain boundaries are embedded. The resulting grain boundary fractions for the five alloys considered and for different areas of misorientations are compiled in Table III. As shown by the example of alloy CMn(VNbTi)-2a, the differences between the quarter position and strip center are small.

Table III. Fraction of grain boundaries (in %) with a certain misorientation.

Steel	s	< 5°	5° - 10°	10° - 15°	15° - 45°	> 45°
CMn(VNbTi)-1	0.5	7	13	7	34	39
CMn(VNbTi)-2a	0.5	10	18	10	20	42
CMn(VNbTi)-2a	0	11	19	10	19	41
CMn(VNbTi)-2b	0.5	8	11	7	34	41
CMnMoNi(VNbTi)	0.5	14	19	9	18	40
CMnMo(VNbTi)	0.5	14	19	9	19	39

Certain microstructural components like martensite, upper bainite, lower bainite, and granular bainite show characteristic misorientation distributions due to their displacive formation mechanism. The transformed variants of bainite roughly follow the crystallographic relationship postulated by Kurdjumow and Sachs. In contrast, a diffusion controlled ferritic transformation reveals a more random distribution with a maximum at  $45^\circ$  misorientation. Therefore, the shape of the histogram theoretically should be an indicator for the type of microstructure [2]. However, a quantification of phase fractions on the basis of the misorientation is of high uncertainty [3].

The kernel average misorientation (KAM) indicates the local misorientation of a single point with regard to its neighbors. Based on the assumption that local misorientation gradients are generated by dislocations, the KAM is, therefore, a measure of the stored energy in terms of dislocation density in the microstructure. This allows us to use the measure of kernel average misorientation as a quantitative value to characterize the distribution of the dislocation density. It has been shown that the different types of ferrite e.g. polygonal ferrite, non-polygonal ferrite or bainitic ferrite differ in their own particular dislocation density, which increases with falling transformation temperature [4]. Thus, kernel average misorientation maps should also indicate the distribution of the various types of ferrite. For calculation it is necessary to define a threshold value above which neighboring points are considered to belong to neighboring grains and are thus not considered in the calculation.

Kernel average misorientation maps are shown Figure 6. Blue areas correspond to regions showing a lower KAM misorientation and are assumed to correlate with polygonal ferrite. Green and yellow regions represent components with higher misorientation thus reflecting non-polygo-

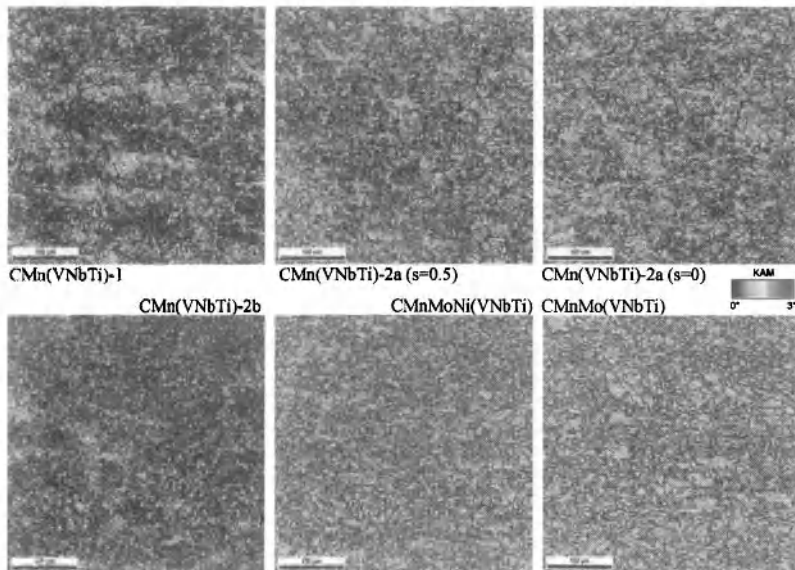


Figure 6. Kernel average misorientation (KAM) maps; threshold misorientation  $3^\circ$ ,  $3^{\text{rd}}$  neighbor.

Table IV. Kernal average misorientation: Number fraction with a certain local misorientation (in %) and Kernal average misorientation value (in degrees).

Steel	s	< 1°	1° - 2°	2° - 3°	Average KAM
CMn(VNbTi)-1	0.5	68	30	2	0.8
CMn(VNbTi)-2a	0.5	39	53	8	1.2
CMn(VNbTi)-2a	0	35	57	8	1.3
CMn(VNbTi)-2b	0.5	62	32	5	0.9
CMnMoNi(VNbTi)	0.5	12	71	17	1.6
CMnMo(VNbTi)	0.5	10	73	17	1.6

nal and bainitic ferrite portions. KAM maps of CMn(VNbTi)-1 and -2 reveal a mixture of polygonal ferrite and in dependence of niobium content and chosen thermomechanical processing higher portions of non-polygonal and bainitic ferrite components. Mo-alloyed strips display highest number fractions of local misorientation in the range of 2° to 3° and consequently increased average KAM values (Table IV). Thus, high portions of bainitic ferrite are assumed.

For the determination of the grain size, two methods were applied. Firstly, the average grain size  $d_{av}$  was calculated directly from the EBSD maps with a variation of both the threshold value of misorientation (grain tolerance angle GTA) and the minimum number of measurement points (NP) considered. Two combinations were tested: GTA 5° / NP2 and GTA 15° / NP20. A careful data post-processing was performed to reveal misindexed data points which may influence data analysis [5]. Secondly, a procedure following previously published studies was applied which focuses on microstructural heterogeneities, i.e. the presence of coarse grain fraction. A parameter denoted as  $d_{20}$  was suggested which describes the grain size, for which 20% of the area fraction of grains have a size larger than this value [6].

The corresponding data are collected in Table V. While the average grain sizes based on high-angle boundaries with a misorientation of 15° are similar, the  $d_{20}$ -values differ considerably. However, neither average grain size nor  $d_{20}$ -value could be clearly correlated with the corresponding toughness here expressed by the Charpy impact transition temperature. Other factors like distribution of dislocations as well as precipitates and homogeneity of microstructural components may also affect ductile-brittle behavior. A qualitative method to describe grain size heterogeneities is presented in Figure 7. Large grains with grain size  $d > d_{20}$  are highlighted in the image quality (IQ) map and grain size distribution. However, a part of the grains contains a higher fraction of small angle grain boundaries. Reduced threshold values of misorientation i.e. GTA 5° in combination with adapted values of considered measuring points i.e. NP 2 lead, as expected, to lower grain sizes. For hot strips with similar yield strength and

Table V. Comparison of grain size  $d_{20}$  and average grain size (in  $\mu\text{m}$ ) determined from EBSD maps for different GTA and NP values.

Steel	GTA 5° / NP 2		GTA 15° / NP 20	
	$d_{20}$	$d_{av}$	$d_{20}$	$d_{av}$
CMn(VNbTi)-1	15.7	5.6	24.8	6.5
CMn(VNbTi)-2a	15.2	3.3	30.5	6.0
CMn(VNbTi)-2b	12.4	3.4	21.5	5.8
CMnMoNi(VNbTi)	14.1	4.5	28.5	5.7
CMnMo(VNbTi)	16.9	4.8	30.5	5.8

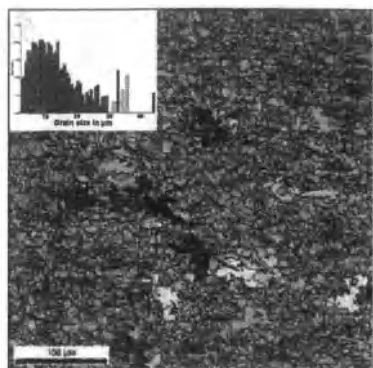


Figure 7. CMnMo(VNbTi) grain size distribution and IQ map with highlighted grains with  $d > d_{20}$  (GTA 15° / NP 20).

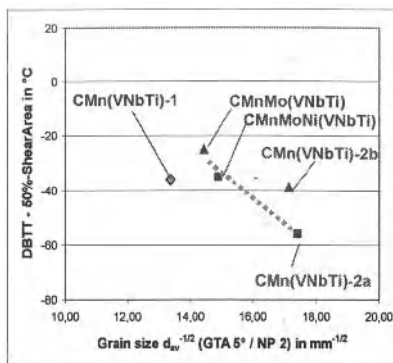


Figure 8. Charpy impact transition temperature as a function of the inverse average grain size estimated for a tolerance angle of 5°.

higher fraction of small-angle grain boundaries, Charpy impact transition temperature is shifted to lower values with decreasing average grain size based on 5° misorientation, Figure 8.

### Summary

Five samples of CSP<sup>®</sup> processed hot-strip material with variations in chemistry and mechanical properties were characterized using EBSD. The task of this study was to advance the methods of EBSD data analysis for this type of complex microstructures and to explore the potential and constraints of EBSD. Systematic variations of grain definition parameters, misorientation relationships and grain boundary settings were performed to understand their influence on the microstructural features like grain size, grain boundary fractions and local misorientations and to define relevant microstructural parameters. Future work will be addressed to the identification of damaging features.

### References

1. Reip, C.P.; Kempken, J.; Schiüter, J.: *Metallurgical Aspects of High-Strength Steel Grades and their Processing through CSP<sup>®</sup> Technology*. International Conference on New Developments on Metallurgy and Application of High-Strength Steels (2008) Buenos Aires (Argentina).
2. Zajac, S.; Schwinn, V.; Tacke, K.-H.: *Characterization and Quantification of Complex Bainitic Microstructures in High and Ultra-High strength Linepipe Steels*. Mat.Sci.Forum 50 (2005) p.387-394.
3. Konrad, J.; Stallybrass, C.; Schneider, A.; Meuser, H.; Meimeth, S.; Grimpe, F.: *Characterisation of the Microstructure of X80 Heavy Plate for Pipeline Applications using the EBSD Method*. 3<sup>rd</sup> International Conference on Thermomechanical Processing of Steels (2008), Padua (Italy).
4. Smith, W.F.: *Structure and Properties of Engineering Alloys*. 1981, New York, McGraw-Hill.
5. Wright, S.I.: *A Parametric Study of Electron Backscatter Diffraction based Grain Size Measurements*. Prakt. Metallogr. 47 (2010) p.16-33.
6. Olasolo, M.; Uranga, P.; Rodrigues-Ibabe, J.M.; López, B.: *Effect of austenite microstructure and cooling rate on transformation characteristics in a low carbon Nb-V microalloyed steel*. Mater.Sci.Eng. A528 (2011) p.2559-2569.

## **EMPIRICAL MODELS OF COLD WORKING EFFECT IN STEEL TUBE PRODUCTION**

Robert G. Batson and Jing Zhang

University of Alabama, Construction Engineering Program, Tuscaloosa, AL 35487-0205, USA

Keywords: Steel tube production, cold working of steel, physical properties of steel, multiple regression analysis

### **Abstract**

Carbon steel is purchased in coils, slit to width, and fed into electrical resistance welding mills that convert it into round, square, or rectangular structural tubing. The objective of this project was to establish relationships between certain properties (yield, tensile, elongation) of the tube after cold working and those of the flat coil before cold working, and build empirical predictive models from a data base of before-and-after properties provided to us by a tube manufacturer. Using multiple regression analysis, a set of three regression models was built with tube geometry and flat steel properties as the independent variables, and tube physical properties as the dependent variables. These regression models can be used by the manufacturer for both prediction of results when coil properties are known, and the computation of ideal coil steel specifications. We provide a sample solution of the latter "inverse problem" using the three equations and Excel Solver.

### **Introduction**

The authors cooperated with a tube manufacturer which produces square, rectangular, and round tubing in a wide range of sizes and gages. Their tubing capabilities range from 1/2" square  $\times$  1/16" gage through 10" square  $\times$  1/2" gage with comparable rectangular sizes, and from 3/4" through 7" diameter round tubes, primarily ASTM-A500 Carbon Steel Grade B and C Structural Tubing. The manufacturer's Quality Assurance (QA) Department handles all raw material and product quality specifications and parameters. The QA laboratory testing includes microhardness, Rockwell hardness, tensile, flare, compression, Charpy impact, and metallographic tests. Dimensional measurements are made during production operations — at the slitter, during the tubing mill runs, and on samples of finished product. Assuring their customers that their purchased tubing meets all dimensional and physical properties specifications is a key service of the QA Department. Another (internal) service is directing purchasing as to what quality steel coils to buy, for a given application.

### **Background of Steel Tube Manufacturing**

Steel tubular products refer to all hollow steel products in round, square, rectangular, oval, or other symmetrical shapes. The most common applications of such products are as conveyors of fluids and as structural members. Steel tubing can be divided into three named use groups: pressure tubes, structural tubing, and mechanical tubing [1]. The tube mills at the manufacturer are examples of Electric Resistance Welding (ERW) tube mills. ERW utilizes a series of operations, in which the flat-rolled steel is cold shaped into tubular form, and the tube is then

joined at the longitudinal seam by welding [1]. The welding method is a special type of ERW known by the trade name “*Thermatool*”, described in Liu and Batson [2].

Problem Background

As mentioned above, steel tubes are made from flat coil by processes that include cold working [3] which deforms a metal at temperatures below the annealing temperature, usually at ambient temperature. Changes in both dimensional and physical properties take place due to cold working. Thus, it is important for a manufacturer to have a better understanding of cold working effects of its various mills on the physical properties in steel tube making, that is, quantitative relationships between the properties of the tubes after cold working and those of flat coil before cold working. Furthermore, QA wants to know how to specify flat coil physical properties from suppliers, in order to ensure their customer’s specified tube dimensions and physical properties.

Problem Definition and Research Approach

The objective of this project is to investigate relationships between the properties of the tube after cold working and those of the flat coil before cold working. The objective is achieved by developing a series of multiple regression models which predict the physical properties of steel tubing based on the tube dimensional characteristics and the flat steel physical properties. Some properties of steel tubes and coils, with their corresponding notation, are listed in Table I.

Table I. Some Properties of Steel Tube and Input Flat Coil

	Steel Tube	Flat Coil
Dimensional Properties	Size	Slit Width
	Shape (square, rectangular, round)	
	Gage	Gage
Physical Properties	Yield — $Y_T$	Yield — $Y_F$
	Tensile — $T_T$	Tensile — $T_F$
	Elongation — $E_T$	Elongation — $E_F$

To achieve the objectives of this project, the following research approach was followed:

1. Understand the tube manufacturing processes at the manufacturer.
2. Collect data.
3. Construct various scatter diagrams from historical data, and interpret these graphs in order to discern qualitative patterns.
4. Build regression models.
5. Validate regression models.
6. Provide report to the manufacturer.

## Literature Review

This research focuses on prediction of the physical properties of ERW steel tubing based on the tube dimensional characteristics and the flat steel physical properties. Rather than theoretical models of the phenomenon under study, the primary objective is to build empirical models from actual production data supplied by a steel tube manufacturer. Though not a primary objective, optimization of steel coil purchasing decisions proved feasible by applying the fitted equations in an “inverse problem” optimization routine. As explained in Hunter [4], the inverse problem “has the desired output known, while it is the system input that is to be determined.” In order to support these objectives and to gain a suitable understanding of the ERW production process and previous related work, a thorough literature search has been conducted mainly in four subjects: electrical resistance welding to produce steel tubing; physical properties of steel; changes in physical and dimensional properties of metals under cold working; and previous application of regression to model cold working effect.

### Changes in Physical and Dimensional Properties of Metals under Cold Working

Cold working indicates the application of plastic deformation to a material at relatively low temperatures (compared with the melting point of the material), when the effect of strain hardening is not relieved. It has long been utilized as an important industrial process to harden metals or alloys in the absence of heat treatment [5]. Changes in dimension can be achieved via various cold working processes. One or two dimensions of metal are reduced at the expense of an increase in the other dimension(s). In addition, cold working leads to changes in the physical properties of a metal. Yield strength, tensile strength and hardness increase, whereas elongation (or ductility) decreases, with increasing amount of cold working [5], [6]. Figure 1 is the variation of tensile properties with amount of cold work.

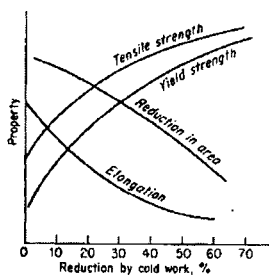


Figure 1. Variation of Tensile Properties with Amount of Cold Work [5]

### Previous Application of Regression to Model Cold Working Effect

No books and papers on applications of regression modeling in the cold working have been found in our literature research. A project completed by a former University of Alabama MSIE graduate student, Song Liu, and the first author has related research. In that project, a

regression model was developed to estimate the gage growth after cold working of flat steel of known gage into a tube of specified size and shape [2]. They found that gage growth was a function of shape and gage, but did not depend on physical properties of the flat coil. Our research will show that physical properties of tubing depend on both dimensional specification of the tubing and physical properties of the flat steel.

### Regression Model Building

The process of building a regression model involves four phases: data collection and preparation; reduction of predictor variables; model refinement and selection; and model validation [7].

#### Data Collection and Preparation

Collected information on dimensional and physical properties of tube and flat coil include *Tube Gage*, *Tube Size*, *Yield in Tube*, *Tensile in Tube*, *Elongation in Tube*, *Yield in Flat Coil*, *Tensile in Flat Coil*, and *Elongation in Flat Coil*. *Tube Gage* is measured by nominal thickness of a tube in inches. *Tube Size* is coded as specific item code by the manufacturer according to tube shape, i.e., round, square and rectangle, as well as the tube length, tube width or tube diameter. Since information on *Tube Size* cannot be used in regression models, two new variables are introduced to substitute for it and defined as follows:

$$\text{ShapeRatio} = \begin{matrix} 0 & \text{if tube shape is round} \\ 1 & \text{if tube shape is square} \\ \text{Tube Width} / \text{Tube Length} & \text{if tube shape is rectangular} \end{matrix}$$

$$\text{SlitWidth} = \text{Tube perimeter.}$$

Variables *Yield in Tube*, *Tensile in Tube* and *Elongation in Tube* represent the physical properties of tube, whereas *Yield in Flat Coil*, *Tensile in Flat Coil* and *Elongation in Flat Coil* represent that of raw material flat coil. Because in tube manufacturing, the process converts flat coil into tube, variable *Yield in Tube*, *Tensile in Tube* and *Elongation in Tube* are chosen to be response variables. Table II summarizes the three response variables and six predictor variables that will be used in our regression analysis.

Table II. Response Variables and Potential Predictor Variables

Response Variables	Yield in Tube ( 10 <sup>3</sup> psi )
	Tensile in Tube ( 10 <sup>3</sup> psi )
	Elongation in Tube ( % )
Potential Predictor Variables	Gage (inches)
	Shape Ratio
	Slit Width (inches)
	Yield in Flat Coil ( 10 <sup>3</sup> psi )
	Tensile in Flat Coil ( 10 <sup>3</sup> psi )
	Elongation in Flat Coil ( % )

The data set is then checked for error. Box plots for each variable are prepared (not shown) to detect extreme outliers. After deleting those extreme outliers, 1748 observations of the original data are used in our Minitab regression model study. A general rule of thumb to decide whether the number of cases is large enough states that there should be at least 6 to 10 cases for every variable in the pool of potentially useful explanatory variables [7]. According to this rule, the data set provided has sufficient observations for regression study. Our strategy is to divide the data into two subsets with half of the cases picked up randomly to build regression models, whereas the other half is used for model validation. The first and the second data set are also referred to as model building data set and validation data set, respectively.

### Reduction of Predictor Variables

Traditional methods of scatter plots, correlation matrices, and best subsets regression were used to narrow the search for predictor variables, for each of the three steel tube properties to be modeled. The Minitab best subsets algorithm identifies a group of “best subsets” according to specified criteria without requiring the fitting of all of the possible subset regression models. The output of best subsets regression for response *YieldT* showed that for response *YieldT*, the four variable subset (*Gage*, *ShapeRatio*, *SlitWidth*, *TensileF*) and the five variable subset (*Gage*, *ShapeRatio*, *SlitWidth*, *YieldF*, *TensileF*) are “good” since their  $R^2$  and  $R_a^2$  is maximum, and their  $C_p$  are small and close to  $p$ . Because variable *YieldF* should in theory be important to *YieldT*, the five-variable subset, in which *YieldF* is included, is chosen. The fitted model is obtained and the output of regression analysis is:

$$\text{YieldT} = 35.9 + 8.18 \text{ Gage} + 2.44 \text{ ShapeRatio} - 0.203 \text{ SlitWidth} + 0.0353 \text{ YieldF} + 0.398 \text{ TensileF} \quad (2)$$

### Model Refinement and Selection of YieldT Model

At the model refinement stage, further studies of curvature and interaction effects, influential observations, and collinearity for current “good” regression models are performed by using residual analysis and other diagnostic tools. Necessary remedial measures are then taken to improve present models.

It was seen from analysis of the regression output for the above model that the coefficient of *YieldF* is not significant. Because *YieldF* and *TensileF* are correlated, we could delete either of them. After deleting *TensileF*, the coefficient of *YieldF* became significant in the refitted model. Next we focus on examining the adequacy of function form, i.e., whether the high order and interaction terms need to be included in the model. Plots of residuals against each of the two-variable interaction terms not included in the model (not shown here) do not exhibit any pattern, thus there are no interaction terms required in the model. Residuals against all the predictor variables are also plotted to examine whether a pattern exists. It was found that the residual plots against *ShapeRatio* and *SlitWidth* suggest possible curvature effect. A remedy is to add the square term of *ShapeRatio* and *SlitWidth* to the model. In order to reduce collinearity between the first-order term and the second-order term, variable *ShapeRatio* and *SlitWidth* need to be centered. The centered variable can be expressed as:  $x_i = X - \bar{X}$ . After the two square terms  $(\text{ShapeRatio} - 0.82)^2$  and  $(\text{SlitWidth} - 17.96)^2$  are added in the model, the following revised regression model ( $R^2 = 28.4\%$ ) is obtained:

$$\text{YieldT} = 53.8 + 12.7 \text{ Gage} - 0.645 \text{ ShapeRatio} - 0.322 \text{ SlitWidth} + 0.222 \text{ YieldF} - 7.64 (\text{SR}-0.82)^2 + 0.0132 (\text{SW}-17.96)^2 \quad (1)$$

### Validation of YieldT Model

The final step of model building process is the validation of the selected model, involving appropriateness of the variables selected, the magnitude of regression coefficient, as well as the predictive of the model. The second half of the data set, obtained by data splitting, is used for validation. One validation method is to fit the selected model to the validation data. The re-estimated coefficients and various characteristics are then compared for consistency to those obtained from model building data set [7]. In addition, residuals analysis of the fitted model is performed to check the model adequacy for the validation data set.

Table III. Regression Results of Model *YieldT* Based on Model Building and Validation Data Set

Statistic	Model Building Data Set		Validation Data Set	
	Coef	SE Coef	Coef	SE Coef
Constant	53.772	2.089	54.719	2.082
Gage	12.711	2.529	14.708	2.633
ShapeRatio	-0.6447	0.7716	-0.188	0.8038
SlitWidth	-0.32200	0.02048	-0.37285	0.02165
YieldF	0.22205	0.03742	0.19681	0.03841
(SR-mean) <sup>2</sup>	-7.640	2.174	-5.413	2.422
(SW-mean) <sup>2</sup>	0.013166	0.001512	0.016401	0.001540
MSE	14.33		14.93	
R-Sq	28.4%		30.4%	

The estimated regression coefficient, the estimated standard deviation, and R-square based on the model building and validation data set are compared in Table III. Note that the magnitude and sign of each regression statistic is consistent, across the two modeling efforts.

### Tensile and Elongation Models

Similar detailed regression studies resulted in the following regression models for tensile strength ( $R^2 = 30.4\%$ ) and elongation ( $R^2 = 12.8\%$ ):

$$\text{TensileT} = 35.5 + 16.8 \text{ Gage} - 0.169 \text{ ShapeRatio} + 35.5 (1/\text{SW}) + 0.423 \text{ TensileF} - 5.07 (\text{SR}-0.82)^2 + 723 (1/\text{SW}-0.070)^2 + 0.0525 (\text{TensileF}-59.74)^2 \quad (3)$$

$$\text{ElongT} = 23.8 - 4.33 \text{ Gage} - 1.97 \text{ ShapeRatio} + 0.126 \text{ SlitWidth} + 0.138 \text{ ElongF} - 0.00651 (\text{SW}-17.96)^2 \quad (4)$$

### **Optimization**

In previous sections, we have built three regression models, i.e. three properties prediction models for a given steel coil supplier. At this point, relationships between the properties of tube and those of flat coil have been established. In practice, these equations can be used on coil steel already in stock or offered to the manufacturer by this supplier. QA can quickly assess whether

the product they have to produce will have acceptable tube physical properties if made from the proposed coil(s). More generally, these regression models can help QA to specify the properties of flat coil according to customer's requirements of tubes, as explained below.

Given tube information: *Gage*, *ShapeRatio*, *SlitWidth* and specified properties (YieldS, TensileS, ElongS), we need to find the optimal value ( $YieldF^*$ ,  $TensileF^*$ ,  $ElongF^*$ ) to minimize the deviation from tube properties specifications. The objective function and constraints are:

$$Min \quad d = (Y_i - Y_s)^2 + (T_i - T_s)^2 + (E_i - E_s)^2$$

S.T.  $Y_i = f(Gage, ShapeRatio, SlitWidth, Y_F, T_F, E_F)$   
 $T_i = g(Gage, ShapeRatio, SlitWidth, Y_F, T_F, E_F)$   
 $E_i = h(Gage, ShapeRatio, SlitWidth, Y_F, T_F, E_F)$   
 $YieldF \geq 40$   
 $TensileF \geq 54$   
 $ElongF \geq 27$

Where function *f*, *g*, *h* are models derived from the data as described above, and the lower limits of variable *YieldF*, *TensileF*, *ElongF* are set according to the minimum value of the range of the data on which our regression models are built.

Excel solver can be used to solve for the optimal solution of this problem, a type of "inverse problem" often encountered in engineering. Figures 2 shows how to use Excel solver to get optimal value of  $Y_F^*$ ,  $T_F^*$  and  $E_F^*$ , following the below steps:

Step 1: Input the known conditions: *Gage*, *ShapeRatio*, *SlitWidth*, YieldS, TensileS and ElongS in the Shaded areas.

Step 2: Click value of *d* (Cell A11). On the **Tool** menu, click **Solver**. In the **Solver Parameters** dialog box, **Set Target Cell** A11 equal to **Min**. Set value of *YieldF*, *TensileF*, *ElongF* (Cell D4, E4, F4) as **By Changing Cell**. Then click **Solve**.

Step 3: In the **Solver Result** dialog box, click **Keep Solver Solution**, then click **OK**.

The particular example shown used input of:

Gage:	0.25	SlitWidth:	16	TensileS:	65
ShapeRatio:	1	YieldS:	60	ElongS:	30.

The Excel Solver solution tells the manufacturer to order coils with properties:

YieldF:	40.63
TensileF:	55.71
ElongF:	52.6,

with the resulting tube having expected value (average) of YieldT and ElongT exactly on specification and TensileT = 66.04 *kpsi*, whereas TensileT was specified to be 65 *kpsi*.

### Conclusions

Relationships between the properties of a welded steel tube after cold working and those of the input flat coil were established. The results only apply within the range of the observations used for model building. For another supplier with a different steel-making and rolling process, we

confirmed in related work that *new* models would have to be fit. That is, the empirical models constructed as described in this paper are *supplier-specific*.

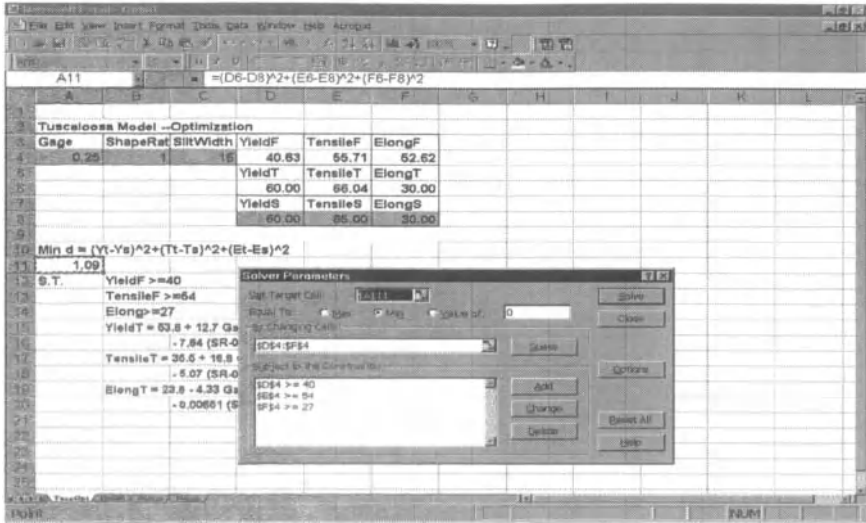


Figure 2. Using Excel Solver to Get Optimal Solution ( $YieldF^*$ ,  $TensileF^*$ ,  $ElongF^*$ )

## References

1. Rudolph Steiner, *Properties and Selection: irons, steels, and high performance alloys*, Vol. 1, ASM Handbook, 10<sup>th</sup> Ed. (Materials Park, Ohio: ASM International, 1990).
2. Song Liu and Robert G. Batson, "A Nested Experimental Design for Gauge Gain in Steel Tube Manufacturing," *Quality Engineering* 16 (2) (2003) 269-282.
3. George E. Dieter, *Forming and Forging*, Vol. 14, ASM Handbook, 9<sup>th</sup> Ed. (Metals Park, Ohio: ASM International, 1988).
4. J. Stuart Hunter, "Discussion," *Journal of Quality Technology* 31 (1) (1999) 54-57.
5. George E. Dieter, *Mechanical Metallurgy (SI Metric edition)* (London: McGraw-Hill, 1988).
6. M. Macdonald et al., "The Effect of Cold Forming on the Yield Strength of Thin Gauge Steel--Hardness Test Approach," *Thin-Walled Structures* 29 (1997) 243-256.
7. John Neter, *Applied Linear Regression Models*, 3<sup>rd</sup> Ed. (New York: McGraw-Hill, 1996).

## **MICROSTRUCTURAL INVESTIGATION OF CARBON STEEL AFTER HOT ROLLING TO OPTIMIZE COMPLEX HOT FORMING OF THICK PLATES**

Gerhard Tober, Okechukwu Anopuo, Petra Maier

University of Applied Sciences Stralsund, Mechanical Engineering,  
Zur Schwedenschanze 15, 18435 Stralsund, Germany

Keywords: Hot rolling, thick plates, complex hot forming

### **Abstract**

In this study, an investigation on the microstructure of hot rolled steel S355J2+N was conducted to optimize process parameters of complex forming, which combines rolling and bending. The best sets of parameters are worked out based on homogeneous mechanical properties and microstructure within the varied deformation degree with maximum at  $\varphi = 1.14$  on a 25 mm thick plates. Mechanical properties, especially of heavy plates, are strongly influenced by the local deformation degree, strain rate and temperature. Detailed microstructural analyses showed that the ferrite-pearlite band structure changes near the surface, while maintaining homogeneous microstructure within the deformed work piece. Surface decarburization was also observed and this leads to decrease in hardness. To minimize iron oxide formation which could lead to side cracking, reduction in exposure time to temperature was suggested. On the other hand, temperature reduction below a critical value would risk the accurate forming process.

### **Introduction**

This work presents the preliminary results of research to develop a new complex deformation process of thick steel plates. Complexity is given because the forming process combines rolling to reduce thickness and profiling by bending. The work piece will experience a thickness reduction from 25mm to 8 mm and is double curved. To explain and understand forming of thick plates basics of sheet forming as well as massive forming need to be used. At the moment there is no forming process established to produce double curved plates including reducing thickness in one process step. Technologies nowadays consist of two process steps: flat rolling and pressing in shape. Due to good weldability and formability the final product will be made of steel S355J2+N. This low-carbon steel is well understood and has a low strengthening exponent, which is expected to keep the forming forces down. Reduction of thickness from 25 mm to 8 mm gives furthermore a high deformation degree. Thus, hot forming has to be applied. The determination of process parameters is the main aim of overall research project; temperatures above 1000°C are expected. Flow curves in literature are given at various temperatures and strain rates [1]. However, experiments with data close to the industrial application are rarely found, especially at low strain rates and high deformation degrees. Pre-test were done by flat rolling, being aware that the influence of bending is eliminated. The microstructure evolution were characterised in relationship to material formability with special attention to grain size change and recrystallization. Representative samples should be selected from specific locations in the deformation zone according to the knowledge about the metal forming process [2]. Due to no further alloying elements in S355, no precipitation hardening is expected to take place during hot

forming, which keeps the mechanisms simple and the concentration on the feasibility of the complex forming process is given.

### Experimental

In this study, various experiments were carried out to determine the forming-relevant properties of S355J2+N. These include tension, compression and flat rolling tests and their respective structural examinations. The strength parameters were determined for tension and compression load. From the data of the compression tests flow curves were determined. They are the basis for the ascertainment of the needed deformation force and therefore deformation energy. Material tests have been carried out with two test machines, MTS 813.2 (250 kN) for tests at room temperature and TIRAtest 28100 (100 kN) for tests at elevated temperatures. Tensile tests were carried out according to DIN EN 10002-1:2001. The experiments were performed at testing speed of 0.04 mm/s. For the compression test, flow curves were determined for true strain rates  $\dot{\varphi}$  of  $-0.01 \text{ s}^{-1}$ ,  $-0.1 \text{ s}^{-1}$  and  $-0.5 \text{ s}^{-1}$ . The diameter/height ratio was 1.5 with a diameter of 10 mm. For the strain rate of  $0.1 \text{ s}^{-1}$  the diameter was 8 mm and the final true strain was set to 1. However, due to limitations of the testing machine the test stopped when the load limit of 10 kN was reached.

A rolling machine from Binder and Weichert with maximal compressive force of 500 kN was used for the flat rolling tests. The radius of the plain rolls is 100 mm and rollings were carried out using 2 and 6 revolutions per minute (rpm). The geometry of the samples for the rolling tests is as follows: length of 150 mm, width of 30 mm and thickness of 25 mm, according to the industrial application. Specimens were rolled to 15 mm and 8 mm thickness at  $650^\circ\text{C}$  which translates to total true strain of  $\varphi = -0.51$  and  $\varphi = -1.14$ , respectively. In a second rolling test the sample geometry was  $l = 150 \text{ mm}$ ,  $w = 30 \text{ mm}$  and  $t = 12 \text{ mm}$ . They were rolled to 8 mm ( $\varphi = -0.405$ ) at  $400^\circ\text{C}$  and  $650^\circ\text{C}$ . On one hand the rolling temperature is limited by the rolling machine used, and therefore strain hardening will occur. On the other hand, low forming temperatures allow a better handling of the work pieces. Hot corrosion was not observed (steel plates have a primer coating) and the forming process is expected to be less energy consuming. Due to strain hardening during forming at  $600^\circ\text{C}$  and below, heat treatment was applied to relieve stresses in the work piece or even initiate a recrystallization process, all under supervision of surface decarburization leading in hardness loss.

Optical micrographs and the micro-hardness were done using Neophot 2 from the company Carl Zeiss Jena. Preparation process for structural examination was according to reference [3]. A line intercept method was used to measure the grain size of the steel samples according to EN ISO 643. For the determination of the grain sizes, a total of three different measurements were taken for one grain size and the mean and standard deviation were calculated.

### Result and Discussion

Starting with the flow curves at elevated temperatures, they have been determined from compression tests. Figure 1 shows flow curves for S355J2+N at  $1000^\circ\text{C}$  at three different strain rates. The maximum flow stress  $k_{f,max}$  for a deformation rate of  $\dot{\varphi} = -0.01 \text{ s}^{-1}$  is approximately 62 MPa, for  $\dot{\varphi} = -0.1 \text{ s}^{-1}$   $k_{f,max} = 85 \text{ MPa}$  and for  $\dot{\varphi} = -0.5 \text{ s}^{-1}$  the maximum could not be determined because of the load limit of the testing machine. The flow curves show that increasing deformation speed increases the flow stresses and thus the maximum stress  $k_{f,max}$  as well as the true strain at the maximum stress. For  $\dot{\varphi} = -0.01 \text{ s}^{-1}$  it is obvious that recrystallization

occurs in an oscillating way, which has also been found in literature for other deformation parameters [3]. The material recrystallizes dynamically faster than the increasing of dislocation density by increasing forming strain. That behaviour becomes weaker with increasing true strain. For forming higher strain rates (here  $\dot{\varphi} = -0.1 \text{ s}^{-1}$ ) dynamic recrystallization has also been observed. However, overlapping hardening and softening mechanisms keep the flow stress  $k_f$  (76 MPa) at a constant value for strains, where steady-state stress takes place. Determined data are furthermore the basics for numerical simulation of the complex forming process, which will not be presented in this paper. These numerical simulations will provide deformation forces for the real forming process taking various work piece geometries into account.

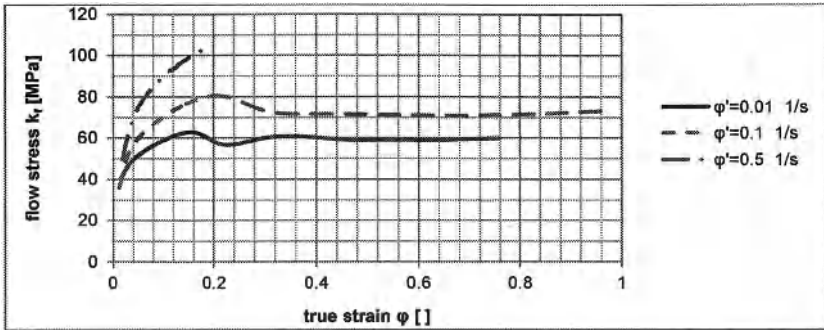


Figure 1: Flow curves for S355J2+N at 1000°C, for deformation rates  $-0.01 \text{ s}^{-1}$ ,  $-0.1 \text{ s}^{-1}$  and  $-0.5 \text{ s}^{-1}$  (absolute values)

Flow curves for S355 at 600°C, see also in literature [1], do not show any dynamic recrystallization. At this temperature, the hardening effects act very strongly, leading to an increase in flow stress with reduced elongation to fracture. Due to the flow stress increase, annealing needs to be applied after the rolling tests, to guaranty a work piece with sufficient ductility. Here the time and temperature of the heat treatment has to be determined.

The rolling parameters deformation degree ( $\varphi_E$ ) and mean compressive force ( $F_m$ ) with their standard deviation of sample ST3 are illustrated in table 1 as a representative example for rolling at 600 °C. The original sample thickness was 25.26 mm. Due to the limit of compressive force of the rolling machine (500 kN) the rolling process has been done in 5 steps to reach the final deformation degree of  $\varphi = -1.06$ . However, by applying 5 passes work hardening can be seen looking at the mean compressive force values, which increases with increasing deformation degree.

Table 1: Rolling parameters of sample ST3 for rolling in 5 passes at 600°C

rolling	$\varphi_E$ [ ]	$F_m$ [kN]	standard deviation [kN]
pass 1	-0.14	230	18.285
pass 2	-0.34	281	19.609
pass 3	-0.49	290	21.354
pass 4	-0.83	407	6.473
pass 5	-1.06	417	24.251

Between two rolling passes a very short heat exposure period of 5 minutes has been applied to ensure an equal starting temperature for the flat rolling process. The time was chosen as short as possible to minimize static structural changes in the test execution. An increase in mean values of the compressive force ( $F_m$ ) at each pass indicates work hardening by rolling. The rather high standard deviation of  $F_m$  can be explained by temperature decrease of the sample during rolling, which takes approximately 10 seconds. Grain size measurements were also carried out using line intercept method to observe if recrystallization or grain growth has already taken place at temperature of 600°C. In table 2 further parameters of the rolling sequence of sample ST3 are given. For two chosen true strains ( $\phi_E$ ) of -0.49 and -1.06 the effect of short heat treatment, annealing at 650°C for 20 min, was investigated by structural examinations in longitudinal (LK) and transversal (QW) rolling direction. The principle idea of applying heat treatment to the material is to find out the influence of the annealing process on the ability to reduce the dislocation density after deformation. After increasing material ductility and brittle fracture resistance, additional stepwise deformation by rolling is possible in case higher deformation degrees are needed.

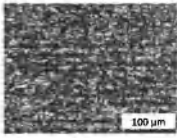
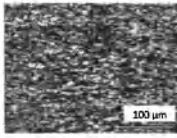
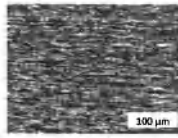
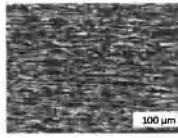
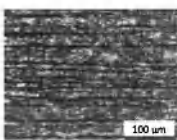
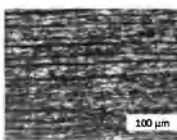
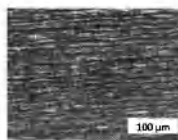
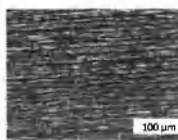
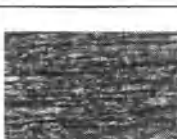
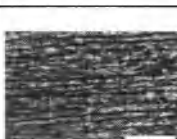
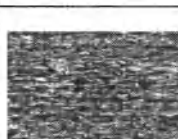
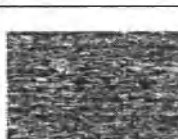
Table 2: Rolling and heat treatment parameters of sample ST3 for rolling in 3 passes (ST3-15) and 5 passes (ST3-8) plus giving information on direction of microstructural analysis: longitudinal (LK) and transversal (QK) rolling direction

sample	direction	$\phi_E$	heat treatment
ST3-8 LK	longitudinal	-1.06	---
ST3-8 QK	transversal	-1.06	---
ST3-8 LW	longitudinal	-1.06	20 min at 650 °C
ST3-8 QW	transversal	-1.06	20 min at 650 °C
ST3-15 LK	longitudinal	-0.49	---
ST3-15 QK	transversal	-0.49	---
ST3-15 LW	longitudinal	-0.49	20 min at 650 °C
ST3-15 QW	transversal	-0.49	20 min at 650 °C

Microstructural analyses of the samples according to Table 2 are shown in table 3. The effect of microstructural change as a result of rolling at elevated temperatures is expected to be higher in rolling direction. Thus the longitudinal rolling direction is presented. Two major results are observable: the microstructure is not homogeneous over the thickness of the sample and secondly the heat treatment enforces less banded pearlite regions at the upper and lower sections near the surface. A re-arrangement of the pearlite bands near the surface region of the rolled specimens in comparison to the centre section can be clearly seen. This phenomenon is associated with the decarburization on the surface of the rolled sample due to diffusion activation of carbon in cementite during heat treatment. The degree of decarburization decreases moving closer to the centre of the specimen, as shown in table 3. Generally, it is expected that the rate of heat exchange is relatively higher at the surface than at the centre of the specimen due to contact with the colder rolling plates and the environment. On the other hand these regions are more stressed compared to the centre of the rolling work piece. Furthermore, influences such as oxidation during rolling or heating are also expected to play a significant role in this.

The microstructural images shown in table 3 do not give straight away any information whether the higher deformation degree due to surface friction or the decarburization is responsible for the re-arrangement of the pearlite region. On the other hand decarburization is known to have a negative effect, especially on the surface hardness.

Table 3: Microstructure of ST3-L before (K) and after annealing at 650 °C (W), longitudinal rolling direction, upper surface, centre and lower surface, magnification of 200x

	ST3-15LW	ST3-15LK	ST3-8LW	ST3-8LK
upper				
centre				
lower				

It is well known that the microstructure also affects mechanical properties. Therefore grain size has been determined and is presented in figure 2. A significant change in grain size in dependence of the region measured can not be seen. However, the influence of the thermo-mechanical treatment on the grain size is given and will be discussed below.

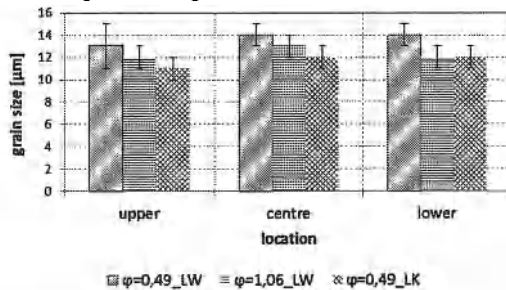


Figure 2: Grain size in dependence on location and thermo-mechanical treatment, ST3-15LW - 0,49\_LW, ST3-8LW - 1,06\_LW: rolling plus 20 min annealing at 650°C, ST3-15LK - 0,49\_LK: rolling

The indication of increase in mean compressive stress during rolling tests, shown in table 1, proves that there is no evidence of dynamic or static recrystallization taking place within the temperature range investigated (650°C), even at higher deformation degrees. The grain size values of rolling (LW) and rolling plus tempering 20min at 650°C (LK), presented in figure 2, do not differ significantly. However, grains are strongly stretched in rolling direction at a deformation degree of 1.06 (ST3-8). From the deformation mechanism map of pure iron as documented by Ashby and Frost [4], dynamic recrystallization is expected at a higher homologous temperature of up to 0.7, which is in the range of 995°C. Static recrystallization could however start in pure iron already at 450°C to 550°C depending on the deformation degree and possible heat treatment. Grain nuclei could appear due to thermodynamic potential differences on the ferrite - iron carbide interfaces and the duration of heat treatment [5]. Alloying elements also lowers the stacking faults energy and by extension the recrystallization temperature of pure iron. From this work, 650°C is approximately 0.5 T/T<sub>M</sub>. No dynamic or static recrystallization was observed; rather recovery is the rate controlling deformation mechanism during rolling at 650°C.

In order to investigate the heat treatment effect, hardness test was carried out on the rolled material. Measurements were carried out at the upper, centre and lower sections of the specimens. Three measurements were made for each data group, out of these the mean value and standard deviation was calculated. In table 4 the hardness values HV0.1 are given. It can be seen that heat treatment lowers the hardness significantly.

Table 4: Micro-hardness HV0.1 in dependence of the location over the thickness with respect to the heat treatment after rolling

sample	upper	centre	lower
St3LK8	285 ± 6.2	246 ± 17.2	258 ± 3.5
St3QK8	274 ± 7.8	242 ± 16.2	267 ± 4.2
St3LW8	198 ± 10.0	219 ± 9.6	211 ± 5.3
St3QW8	197 ± 6.8	211 ± 6.5	209 ± 3.9

This decrease in hardness is a result of the annealing process at 650°C. The increase in hardness with increasing deformation degree is expected. Theoretically, as the deformation degree increases, the dislocation density increases and the material strain hardens. For high stacking fault energy material such as the bcc S355, dynamic recovery is more favourable at the temperature of interest in this investigation. Annealing at 650°C for 20 minutes will simply initiate glide of dislocations on the preferred glide planes thereby lowering the energy within the microstructure and makes the rolled specimens deformable by lowering the dislocation density. The hardness values show that in the decarburized sections the hardness decreases after annealing because the dislocation density decreases. With those results further rolling tests were done to investigate the influence of the temperature on the homogeneity of the rolled samples. Figure 3 shows the expected behaviour, that the needed forming force decreases with increasing temperature. The peak of the force (F<sub>R</sub>) also shows that after the intermediate annealing the hardening effect is still present. However, rolling forces only increase to a smaller extent at rolling and annealing at 650°C. Thus softening mechanisms are present and during annealing static recovery and static recrystallization are possible. Due to longer annealing times, decarburization was more obvious in the microstructure. These are shown in table 5. Here annealing has been applied for one and two hours at 400°C and 650°C, respectively.

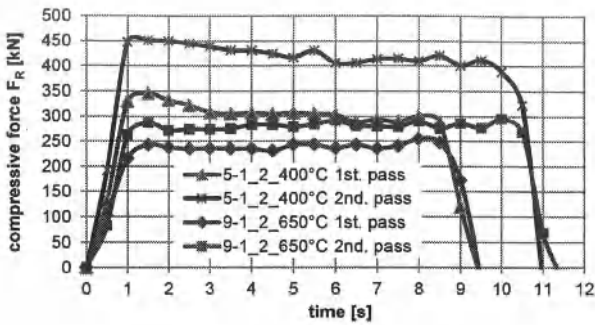


Figure 3: Compressive force with respect to time for different intermediate annealing temperatures for  $n_w = 2 \text{ rev/min}$

Table 5 Microstructure for different annealing times depending on the local region

Magnification: 200x	3-1_2_650°C_1h (longitudinal)	9-1_2_650°C_2h (longitudinal)
upper surface		
centre		
lower surface		

After annealing for two hours, almost all banded ferrite-pearlite structure disappeared. Comparing it with the microstructural images in table 3 it can be observed that the differences between 20 min annealing and 60 min annealing are not very strong. Two hours annealing is more effective in homogenizing the microstructure regarding the ferrite-pearlite bands.

## Summary

This research study gives a small overview about the deformation properties of S355J2+N to provide data for numerical simulations of complete complex forming of thick plates, which are rarely described in the literature. Microstructural analyses showed that the ferrite-pearlite band structure disappears near the surfaces in contact with the rolls, while maintaining homogeneous microstructure within the deformed work piece. Surface decarburization was also observed at annealing for two hours at 650°C. However, even having less local pearlite fraction in the microstructure of the upper and lower section, no hardness decrease was observed. It seems that due to the surface friction work hardening overlaps the expected hardness decrease. Further investigations will focus on the influence of rolling at higher temperature. Here, recrystallization effects will appear to a stronger extent and thus the influence of the decarburization on the hardness, strength and homogeneity of S355J2+N could be influenced significantly.

## Acknowledgements

The work presented in this paper has been fully supported by the Mecklenburg-Vorpommern's Ministry of Economics, Labour and Tourism and the European Union. Authors acknowledge the financial support of the project "Process Development for the Three-Dimensional Complex Forming of Heavy Plates".

## References

1. Spittel, M., Spittel, T.: Steel symbol/number: S355J2G3/1.0570. Warlimont, H. (ed.). SpringerMaterials - The Landolt-Börnstein Database (<http://www.springermaterials.com>). (Springer-Verlag Berlin Heidelberg, 2009). DOI: 10.1007/978-3-540-44760-3\_30
2. W. Z. Misiólek, "Modelling of Microstructure Response to Deformation Parameters in Selected Metal Forming Processes", in G. Hirt (ed.), A. E. Tekkaya (ed.): Special Edition: 10th International Conference on Technology of Plasticity, ICTP 2011 - Plenary Keynotes, (Weinheim, Wiley-VCH Verlag GmbH & Co. KGaA, 2011), 56-62.
3. M. Spittel, T. Spittel: Ver- und Entfestigung bei Warmumformung, in: Freiburger Forschungshefte edited by the rector of the Bergakademie Freiberg, Vol. B 235, (Leipzig 1982), 12-21.
3. STRUERS GmbH: Generic methods - Struers Preparation Methods → Ferrous Metals, [http://www.struers.com/modules/emetalog/generic\\_list\\_sub.asp?category=Ferrous Metals](http://www.struers.com/modules/emetalog/generic_list_sub.asp?category=Ferrous+Metals).
4. H.J. Frost and M.F. Ashby; Deformation-Mechanism Maps for Metals and Alloys, Cambridge University, CUED/C/MATS/TR. 87 Nov. 1981.
5. I.A. Borisov: Recrystallization of steel in a coarse-grain state in heating, Metal Science and Heat Treatment vol. 37. Nos. 7-8, 1995.

## **MICROSTRUCTURAL CHARACTERIZATION OF Fe-Mn-C TERNARY ALLOY UNDER NEAR-RAPID SOLIDIFICATION**

Wenbin Xia, Rong Yang, Changjiang Song, Qijie Zhai\*

Shanghai Key Laboratory of Modern Metallurgy & Materials Processing, Shanghai University,  
Shanghai 200072, China, Email: [qjzhai@shu.edu.cn](mailto:qjzhai@shu.edu.cn)

Keywords: Fe-Mn-C, Near-rapid Solidification, Carbide, Stacking Fault

### **Abstract**

This paper focus on the influence of carbon content and cooling rate on the microstructure and phase formation of Fe-Mn-C alloys under near-rapid solidification. When manganese content is about 11wt.%, more  $\epsilon$ -martensite can be obtained with cooling rate increasing when carbon content is 0.14wt.%, the formed phase changed from  $\alpha$  phase to  $\gamma$  phase when 0.74wt.% carbon is added to the samples, and when carbon content up to 2.1wt.%, carbide can be obtained in the sample. A host of stacking fault, which attributes to the strain-induced martensite, can be observed in the sample. The microhardness increased with cooling rate increasing, and under the same cooling rate, the microhardness of samples with 0.14wt.% carbon is highest.

### **Introduction**

To obtain high performance materials is eternal pursuit of material science research. Material scientists have explored many new ways to obtain high performance materials from long time ago. Rapid solidification is one of most popular ways to produce advanced materials by obtaining metastable phases, because it is widely known that the solidification of metals in metastable phases gives access to a whole range of materials with novel properties [1]. Furthermore, nowadays metastable materials have been extensively used in many fields, for example, many of our modern high performance materials such as steel products or aluminum alloys for aeronautical applications are in the form of metastable rather than stable phases [1].

Fe-Mn-C is one of hadfield steel which is extensively used in automobile, and also a class of metastable material, which is well known for its "transformation induced plasticity" (TRIP) and "twinning induced plasticity" (TWIP) effects [2]. And, Fe-Mn alloys also show a good damping capacity which is caused by  $\epsilon$ -martensite formed on cooling [3,4]. So, many researches have been carried out for the  $\gamma \rightarrow \alpha$  or  $\gamma \rightarrow \epsilon$  martensitic transformation of Fe-Mn-C both theoretically and experimentally [5-7]. I.R. Sare revealed that  $\epsilon$ -phase retained upon splatcooling was found to increase with cooling rate and carbon content within the restricted range [8]. In this paper, Fe-Mn-C system was selected to investigate its microstructure evolution and phase formation during near-rapid solidification.

## Experiment

A series of Fe-Mn-C ingots were prepared from high purity iron (99.99 %), manganese (99.9 %) and Fe-C master alloy (containing about 4wt.% carbon), by electric arc melting in a water-cooled copper crucible under argon protective atmosphere. The Fe-Mn-C ingots have a nominal manganese concentration of 11wt.% Mn, with carbon contents of 0, 0.14, 0.74, and 2.1wt.%, respectively. The results of elemental analysis indicate that Mn content are 10.0, 10.06, 10.01 and 9.90wt.% for the ingots of 0, 0.14, 0.74, and 2.1wt.% carbon, respectively.

The Fe-Mn-C ingots were cut into small blocks with weighing about 5g, and then these two or three pieces of block in quartz glass tube were melted by induction coil. After that, the melt was sprayed, under argon protective atmosphere, into the copper mould whose cavity was designed into the width of 30mm, height of 35mm and thicknesses of 1mm and 1.5mm, respectively (as shown in Figure 1). The strips solidified at different cooling rates can be obtained.

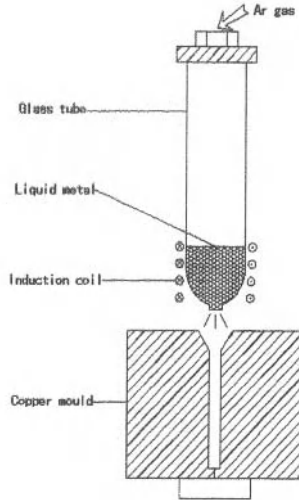


Figure 1. Schematic illustration of spray casting

The strips were analyzed by means of X-ray diffractometry (D<sub>max</sub>-2200X) with Cu K $\alpha$ -radiation. Thin strips for transmission electron microscopy (TEM) were prepared using 10 pct HClO<sub>4</sub> in alcohol by double-jet polishing apparatus. TEM observations were conducted on a (JEOL) JSM-2010.

## Results and Discussion

The cooling rates for strips with thickness of 1mm and 1.5mm calculated by simulation were  $2.0 \times 10^4$  K/s,  $8.8 \times 10^3$  K/s, respectively.

### XRD Analysis

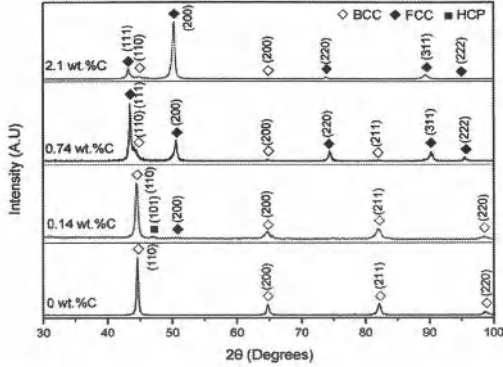


Figure 2. X-ray diffractograms of Fe-11wt.%Mn-Xwt.%C strips with thickness of 1mm

**Effect of Carbon Content:** Figure 2 shows the XRD patterns of strips with 0, 0.14, 0.74 and 2.1wt. % carbon under the same cooling rate, respectively. It can be seen that only BCC phase was observed in the strip without carbon element, all of FCC, BCC and HCP phases in the strip

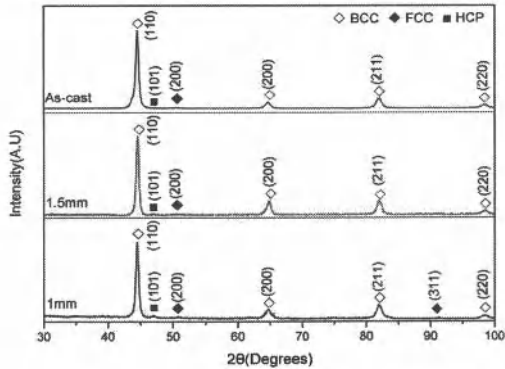


Figure 3. X-ray diffractograms of Fe-11wt.%Mn-0.14wt.%C strips with thickness of 1mm, 1.5mm, and the as-cast sample

with 0.14wt.% carbon and FCC, BCC phases in the strips with 0.74wt.%, 2.1wt.% carbon. The  $\epsilon$ -martensite (HCP structure) peak can be only detected when the carbon content is 0.14wt.%. Peak height of FCC crystalline structure phase are much more distinguishable than BCC crystalline structure phase's when carbon contents are 0wt.% and 0.14wt.%, but when carbon contents are 0.74 wt.% and 2.1wt.%, the results are reverse. So, the formation of austenite can be strongly promoted by addition of carbon, and a little carbon addition can promote the formation of  $\epsilon$ -martensite.

**Effect of Cooling Rate:** X-ray diffractograms of Fe-11wt.%Mn-0.14wt.%C strips with thickness of 1mm, 1.5mm, and the as-cast sample are shown in Figure 3. The coexistence of BCC, FCC and HCP crystalline structure phase in three strips can be confirmed from their XRD patterns. The  $\{101\}$  martensite peak is more and more distinguishable with cooling rate increasing. Thus, increasing cooling rate is likely to induce  $\gamma_{fcc} \rightarrow \epsilon_{hcp}$  martensitic transformation.

#### TEM Analysis

Transmission electron micrographs of three alloys with different carbon contents are shown in Figure 4 and 5. A host of typical lath martensite in matrix, which is identified as BCC structure

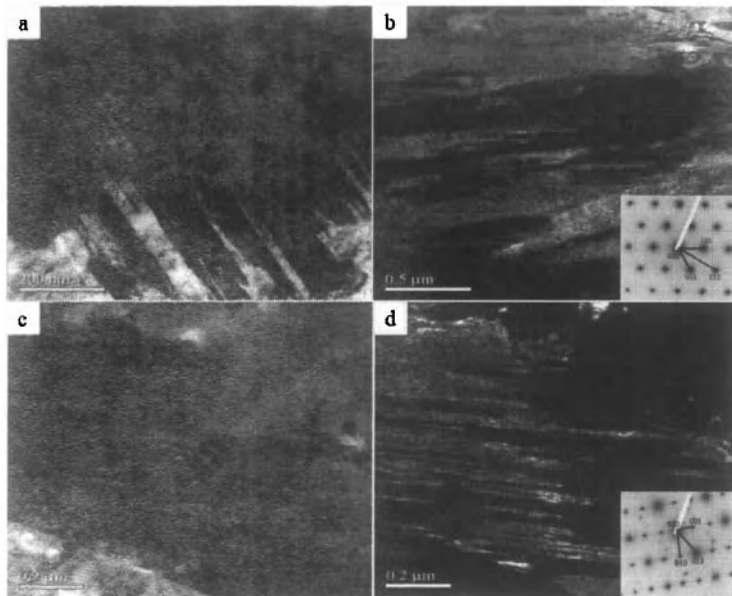


Figure 4. Transmission electron micrographs of Fe-11wt.%Mn-0.14wt.%C strip with thickness of 1mm. (a) and (b) a'-martensite; (c) BF morphology of  $\epsilon$ -martensite; (d) DF morphology of  $\epsilon$ -martensite.

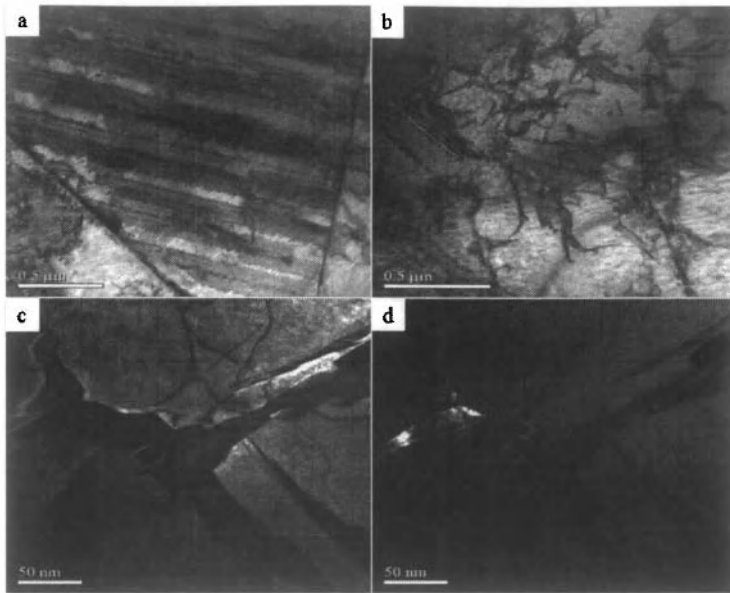


Figure 5. (a) and (b) Transmission electron micrographs of Fe-11wt.%Mn-0.74wt.%C strip with thickness of 1.5mm. (c) and (d) TEM BF and DF micrograph of Fe-11wt.%Mn-2.1wt.%C strip with thickness of 1mm.

by the corresponding diffraction pattern, can be observed in Fe-11wt.%Mn- 0.14wt.%C strip with thickness of 1mm, as shown in Figure 4 (a) and (b), and the martensite's lath width is about 60nm. Moreover, it can be seen from Figure 4 (c) and (d) that a little amount of different phase, which contain much narrow twins, all lying in the one direction in a given grain, exist between martensite lath in this alloy, and the phase is identified as HCP structure by the diffraction pattern, which demonstrates the  $\epsilon$ -martensite. The presence of  $a'$ -martensite and  $\epsilon$ -martensite is confirmed by results of TEM and XRD.

Figure 5 (a) and (b) show that only numerous stacking fault and dislocation piled up at  $\gamma$  (FCC structure) grain boundary, no evidence of  $a'$ -martensite or  $\epsilon$ -martensite was found. And when carbon content is up to 2.1wt.%, carbide precipitated along grain boundary, and tiny dislocation can be also observed near grain boundary, as shown in Figure 5 (c) and (d). So, TEM results reveal that  $a'$ -martensite (BCC structure) and  $\epsilon$ -martensite (HCP structure) only exist in Fe-11wt.%Mn-0.14wt.%C under near-rapid solidification.

The reason of occurrence of  $a'$ -martensite or  $\epsilon$ -martensite in Fe-11wt.%Mn-0.14wt.%C under near-rapid solidification is probably increase of stacking fault induced by the presence of

moderate carbon in solution, so that  $\gamma_{fcc} \rightarrow \epsilon_{hcp}$  martensitic transformation was promoted. However, too much carbon would stabilize  $\gamma$  phase, pin dislocation and stacking fault, and increase stacking fault energy, so martensitic transformation will be suppressed [9]. And when carbon content increases furthermore, carbide is easy to precipitate.

#### Microhardness Measurements

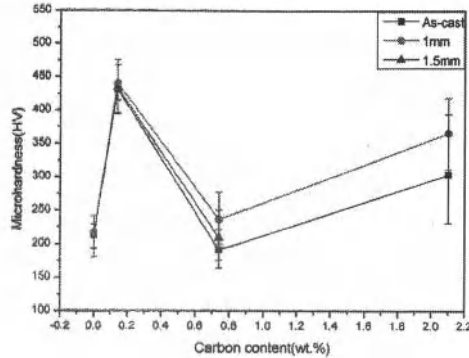


Figure 6. Microhardness of Fe-11wt.%Mn-Xwt.%C alloys

Figure 6 shows the microhardness of Fe-Mn-C alloys with different carbon content and cooling rate. Since the microstructure affects the microhardness measurements, these measurements provide a tool for evaluating the formed microstructures [10]. For the samples with same carbon content, their microhardness increased with cooling rate increasing. The higher hardness of the sample at higher cooling rate is probably a result of smaller grain caused by increasing cooling rate.

Likewise, when under the same cooling rate, microhardness of the alloy with 0.14wt.% carbon is highest. The highest hardness at 0.14wt.% carbon content results from the presence of  $\alpha'$ -martensite or  $\epsilon$ -martensite which is considerably hard. A 190-250 HV hardness value of the alloy with 0wt.% or 0.74wt.% corresponds to that of the ferrite or austenite phase (XRD result in Figure 2 can support this interpretation). Carbide precipitates (the phase can be observed in Figure 5 (c) and (d)) along grain boundary are attributed to the second highest hardness of alloy with 2.1wt.% carbon.

#### **Conclusions**

- (1) Moderate carbon is found to promote  $\gamma_{fcc} \rightarrow \epsilon_{hcp}$  martensitic transformation, and too much carbon will make carbide precipitated along grain boundary in Fe-Mn-C alloy;
- (2) Increasing cooling rate can promote  $\gamma_{fcc} \rightarrow \epsilon_{hcp}$  martensitic transformation, so that increase volume fraction of  $\epsilon$ -martensite;
- (3) Carbon content range from 0wt.% to 0.14wt.%, BCC structure phase is formed, and carbon

content above 0.74wt.%, FCC structure phase is formed, and metastable HCP phase can be detected in Fe-11wt.%-0.14wt.%C alloy strips under near-rapid solidification;

(4) The microhardness increases with cooling rate, and the microhardness of alloy with 0.14wt.% carbon is highest under the same cooling rate.

#### Acknowledgements

The authors wish to express their grateful thanks to National Natural Science Foundation of China (No.51074104 ) and National Basic Research Program of China (No.2010CB630802) for the financial support of this work and Instrumental Analysis & Research Center of Shanghai University for providing analysis and testing of samples.

#### References

- [1] B. Feuerbacher, "Phase Formation in Metastable Solidification of Metals," *Materials Science Reports*, 42 (6) (1988), 1-4.
- [2] P. Sahu, A.S. Hamada, R.N. Ghosh et al., "X-ray Diffraction Study on Cooling-Rate-Induced  $\gamma_{\text{fcc}} \rightarrow \epsilon_{\text{hcp}}$  Martensitic Transformation in Cast-Homogenized Fe-26Mn-0.14C Austenitic Steel," *Metallurgical and Materials Transactions A*, 38 (A) (2007), 1991-1994.
- [3] C.S. Choi, J.D. Kim, T.H. Cho et al., "Damping Capacities in Fe-X%Mn Martensitic Alloys," (Paper presented at Proceedings of the 7<sup>th</sup> International Conference on Martensitic Transformations, Monterey, California, 20-24 July 1992), 509-512.
- [4] C.S. Choi, Woojin OSK Corp., US Patent No. 5290372, 1994.
- [5] J. Agren, "Computer Simulations of the Austenite/Ferrite Diffusional Transformations in Low Alloyed Steels," *Acta Metallurgica*, 30 (8) (1982), 841-851.
- [6] Z.K. Liu, J. Agren, "On the Transition from Local Equilibrium to Paraequilibrium during the Growth of Ferrite in Fe-Mn-C Austenite," *Acta Metallurgica*, 37 (12) (1989), 3157-3163.
- [7] X. Lu, Z.X. Qin, Y.S. Zhang et al., "Study of the Paramagnetic-Antiferromagnetic Transition and the  $\gamma \rightarrow \epsilon$  Martensitic Transformation in Fe-Mn Alloys," *Journal of Materials Science*, 35 (2000), 5597-5603.
- [8] I.R. Sare, "The  $\epsilon$ -phase in Rapidly Solidified Ferrous Alloys," *Journal of Material and Science*, 16 (1981), 3470-3478.
- [9] K. Chen, X.J. Jin, "The Influence of C and N Elements on Stacking Fault Energy of Fe-Mn-Si Alloy," *Functional Materials*, 38 (2007), 3236-3238.
- [10] N.H. Pryds, X. Huang, "The Effect of Cooling Rate on the Microstructures Formed during Solidification of Ferritic Steel," *Metallurgical and Materials Transactions A*, 31 (A) (2000), 3156-3157.

## **Effects of Surface Modifications on SCW Corrosion Resistance**

Jian Li<sup>1</sup>, S. Penttilä<sup>2</sup> and W. Zheng<sup>1</sup>

<sup>1</sup>CANMET - Materials Technology Laboratory, 183 Longwood Rd. S., Hamilton, ON, Canada

<sup>2</sup>VTT Technical Research Center of Finland, Materials for Power Engineering, P.O. Box 1000,  
FI-02044 VTT, Finland

### **Abstract**

Materials selection for Gen IV supercritical water reactor in-core components faces major challenges due to severe operating condition. Beside high-temperature mechanical properties, SCC and general corrosion resistance of commercially available materials are also major focuses in recent research. Recent reports suggest that certain types of surface modifications are beneficial to SCW corrosion resistance. In this study, the effects of surface modifications are investigated, and possible mechanisms for improved corrosion performance are discussed.

**Keywords:** SCW, corrosion, surface modification

### **Introduction**

The current Canadian pressure-tube supercritical water reactor (SCW) design specifies a core outlet temperature of 625 °C under 25 MPa of pressure, with peak cladding temperature as high as 850 °C. Challenges in materials selection include high-temperature mechanical properties, corrosion resistance, SCC resistance and radiation damage. Most of the SCW corrosion test results available are below 730 °C. Early work by Allen [1] summarized the corrosion resistance of alloy groups including Ni-based super alloys, stainless and ferritic/martensitic (F/M) steels that can potentially be used for SCW reactors. F/M steels can only be used at low temperature sites (e.g. down stream piping). At 500 °C and 25 MPa, F/M steels develop a thick but mechanically stable oxide layer. However, the long term stability of the surface oxide layer is largely unknown. Ni-based alloys appear to form very thin surface oxide, however pitting was observed in the vicinity of some intermetallic precipitates [2-5], and dissolution of major alloying components could pose significant problems for down stream piping [6]. In addition, concerns of Helium formation due to Ni transmutation prevented this alloy group to be used as fuel cladding. The corrosion resistant austenitic stainless steels (e.g. 316L) are found to be susceptible to localized corrosion such as pitting, intergranular attack and stress corrosion cracking (SCC) [7].

Some early studies suggest the surface modification and surface roughness significantly reduced SCC failure rate of steam generator tubes [8, 9]. The effect of surface modification was also reported in recent literature [10-12]. Most of these reports are based on weight change measurement and/or statistical analysis. In contrast, Arioka [13] suggested that plastic strain will promote SCC propagation due to increased density of cavities ahead of crack tip. Staehle also described that machined surface of 316NG taken from recirculating line of a BWR with surface nano structure is prone to SCC problem [14]. These controversial conclusions mainly arise from the confusion of different surface conditions in their tests. From severely deformed, nano-crystalline to fully recrystallized fine grained structure, the surfaces could have very different characteristics, thus behaving very differently in terms of corrosion and SCC resistance. In this

study, we do not attempt to resolve this complex issue, but rather we focus on investigating a specific case of surface modification using advanced microscopy techniques.

### **Experimental Details**

316L stainless steel tubes were used in this study. The outer surfaces of the test specimens were prepared to give various starting surface finishes. The “as-machined” specimen represents a rough surface which presumably gives substantial subsurface mechanical damage. The “polished” surfaces (polished with 600 grit and 1200 grit SiC paper) provide smooth surface with little subsurface mechanical deformation. The test coupons were subjected to SCW corrosion test in an autoclave at 650°C and 25 MPa of pressure for 3000 hours at VTT. The dissolved oxygen content was 150 ppb. After testing, the specimens were studied using microscopy techniques including SEM, FIB and TEM.

### **Results and Discussion**

After SCW exposure, weight changes were recorded. The coupon with the “as-machined” surface was found to have the least weight change [12]. As shown in Figure 1, the machined surface appear to be smooth and shiny, while coupons with other surface finishes appear to be severely oxidized after SCW exposure.

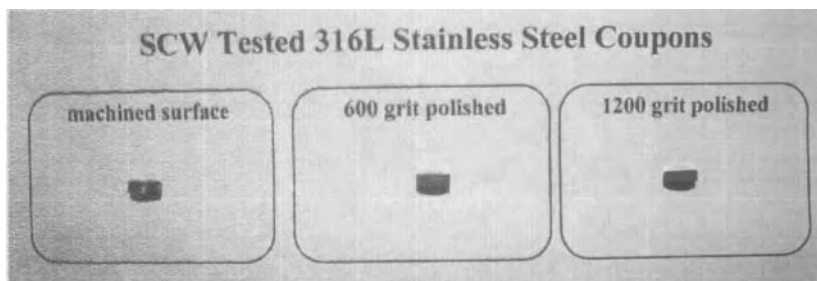


Figure 1. Digital photograph of tested tube samples

SEM images taken from the surfaces indicated that little corrosion took place on the machined surface (Figure 2a). The machining marks are well preserved. The polished surfaces were covered with thick oxide layer (Figure 2b).

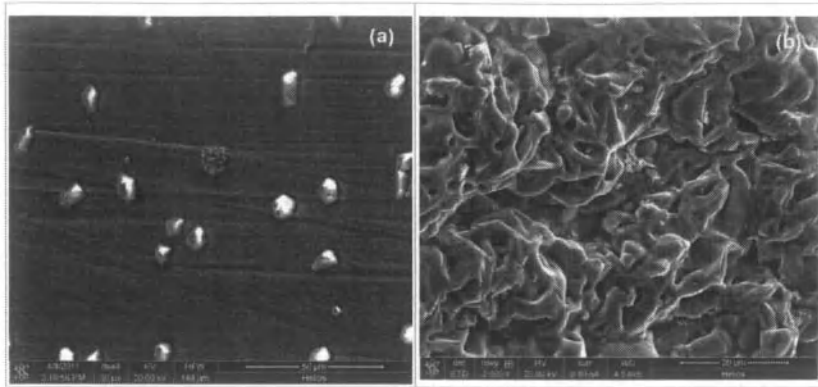


Figure 2. SEM images of surface morphology after SCW exposure (a) machined surface, (b) 600- grit polished.

A dual-beam FIB microscope was used to perform ion beam cross-sections on two tested specimens (machined and 600-grit polished). Details of FIB techniques can be found in literature [15]. As shown in Figure 3, there are substantial differences in the morphology of the two samples.

#### 1) Surface oxide layer

The SCW exposure resulted in a very thin surface oxide layer on the machined surface. This thin oxide layer is represented by the dark line indicated in Figure 3a. One of the occasional surface oxide islands was intentionally included in the FIB cross section. It appears that this oxide particle did not penetrate into the substrate. The specimen with an initially polished surface formed a relative thick surface oxide layer, which is composed of magnetite polycrystal as later confirmed by our TEM analysis (Figure 3b). Detailed TEM analysis results will be presented elsewhere.

#### 2) Subsurface microstructure

As shown in Figure 3a, a layer of fine-grained microstructure can be found immediately beneath the thin oxide layer followed by a zone of deformed microstructure. The deformed microstructure is featured by micro shear bands and mottled grains [16].

The 600 grit polished sample appear to be severely oxidized during SCW exposure. Internal oxidation associated with grain boundary voids are found on random FIB sections (Figure 3b). This will no doubt deteriorate its mechanical properties. The oxidation could have penetrated quite deep into the substrate, i.e. beyond this FIB cross section range.

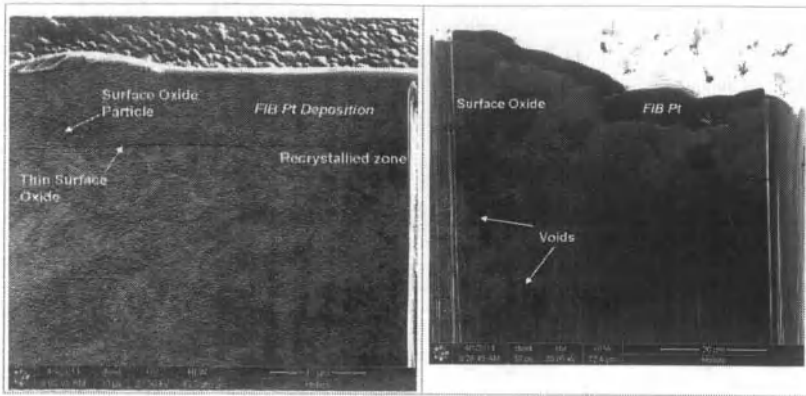


Figure 3. FIB cross section of the SCW tested 316L samples (a) machined surface, (b) 600-grit polished

### 3) Contributing factors

Mechanism of such significant difference between the machined and polished samples can be complex. However, it is widely accepted that maintaining a dense, continuous and coherent passive film is the key in corrosion prevention for stainless steels.

Prior to SCW exposure, the machined surface exhibited significant residual strain near the surface. The deformed zone is depicted as a severely disturbed layer shown in Figure 4 (sand blasted 316L alloy). During the subsequent SCW exposure at 650°C, the severely deformed zone becomes recrystallized, forming a fine-grained microstructure near the surface (Figure 3a). The test temperature in this experiment is not high enough to cause grain growth. The increased grain boundaries area in the fine grained layer could act as short circuits for outward diffusion of Cr. This helps to provide sufficient Cr near the surface to maintain a continuous  $\text{Cr}_2\text{O}_3$  passive layer during SCW exposure. Study by Tsuchiya et al. [17] on corrosion and SCC resistance of normal-size and fine-grained stainless steels in SCW support our explanation. In case of the formation of nano structure as that shown by Staehle [14], the surface layer will have significantly reduced strength, which could lead to SCC initiation.

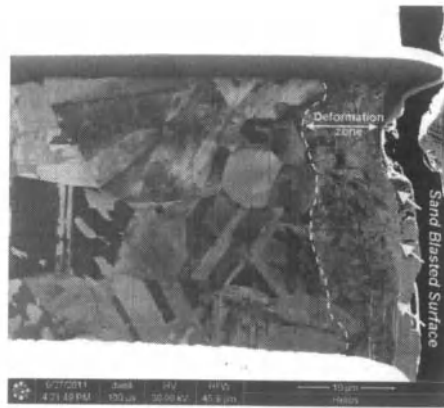


Figure 4. FIB section of sand blasted 316L stainless steel

On the other hand, SCW exposure of polished surface that had coarse grain structure oxidized severely. The rate of corrosion is affected by both the outward diffusion of Fe to form  $\text{Fe}_3\text{O}_4$  crystals on the surface, and inward diffusion of oxygen to form the interfacial Cr-rich complex oxide. Because of the limited densities of grain-boundaries that can act as “short-cut” pathway for Cr diffusion, the high integrity of passive chromium oxide layer could not be maintained during SCW exposure.

### **Summary**

Surface treatment could improve corrosion resistance of stainless steels under certain conditions, as seen in the 316L samples that were tested in the as-machined conditions. The machining introduced significant sub-surface plastic deformation, which led to recrystallization and grain-refining. There was much less oxide formed on the as-machined samples than on the polished samples. Grain refinement although improves corrosion resistance, bulk fine-grained materials should not be used as cladding due to their poor creep resistance. In combination with various coating effort, surface treatment that lead to fine-grained surfaces could provide a solution for materials solution for Gen-IV reactor cladding.

### **Acknowledgement**

The authors would like to thank financial support from PERD and from NSERC/NRCan/AECL Generation IV Technologies Program. High-quality FIB images taken by Mrs. Pei Liu at CANMET-MTL are highly appreciated.

### **References**

- [1] T.R. Allen, K. Sridharan, Y. Chen, L.Tan, X. Ren and A. Druizenga, 16th Pacific Basin Nuclear Conference, Aomori, Japan, Oct 13-18, 2008, Paper ID: P16P1032.
- [2] G.T. Hong, D.W. Ordway and V.A. Ziberstein, First Int. Workshop on Supercritical Water Oxidation, Jacksonville, Florida, Feb 6-9, 1995.

- [3] P. Kritzer, N. Boukis and E. Dinjus, *Corrosion* 98, Paper No. 415, NACE, Houston, TX (1998).
- [4] L.B. Kriksunov and D.D. Macdonald, *Journal of Electrochem. Soc.*, 4069, (1995).
- [5] S. Huang, et. al., ACS Symposium Series, 406, 287, ACS, Washington, DC (1998).
- [6] Jian Li, D. Guzonas, J. Wills, H. Dole, J. Michael, W. Zheng, O-T. Woo and W. Cook, Property of Passive Films Formed on Alloys Tested in SCW, paper #56, 4<sup>th</sup> International Symposium on Supercritical Water-cooled Reactors, March 8-11, 2009, Heidelberg, Germany.
- [7] D.B. Mitton, N. Eliaz, J.A. Cline and R.M. Latanision., *Corrosion* 2001, Paper No. 01352, NACE, Houston, TX, (2001).
- [8] P. Berge, Influence of Surface Treatment on Various Types of Stainless Steels Corrosion", Proc. 3<sup>rd</sup> International Conference on Metallic Corrosion, May 16-25, 1966 (Moscow, USSR), MIR (1969; p. 405
- [9] G. Slama, Shot Peening Experience After Nine Years, Proc. SFEN International Symp. On Environmental Degradation of Materials in Nuclear Power Systems – Water Reactors, August 7-10, 1995 (Breckenridge, Colorado), vol. 1, p.281-299.
- [10] L. Tan, X. Ren, K. Sridharan and T.R. Allen, *Corrosion Science*, 50, 2040-2046, 2008.
- [11] J. Kaneda, S. Kasahara, F. Kano, N.Saito, T.Shikama and M. Matsui, 5<sup>th</sup> International Conference on SCWR (ISSCWR-5), Vancouver, BC, Canada, March 13-16, 2011.
- [12] S. Penttilä, A. Horvath, A. Toivonen and Z. Zolnai, 5<sup>th</sup> Int. Symposium on Supercritical Water-cooled Reactors (ISSCWR-5), Vancouver, BC, Canada, March 13-16, 2011.
- [13] K. Arioka, T. Yamoto, T. Yamada, T. Terachi, "Formation of Cavities Prior to Crack Initiation and Growth on Cold-Worked Carbon Steel in High-Temperature Water," *Corrosion*, Vol. 66 No. 1, 2010.
- [14] X. Ru and R.W. Stachlie, Predicting Corrosion and SCC of Fe-Cr-Ni Alloys in Supercritical Water Based on Historical Experience, presented in Materials and Chemistry for Supercritical Water Cooled Reactors, July 18 to 22, 2011, at the Institute of Energy, Joint Research Centre of European Commission (IE-JRC-EC), Petten, the Netherlands
- [15] Jian Li, Focused Ion Beam Microscope, *Journal of Metal*, Vol. 58, No.3, 27-31, 2006
- [16] Jian Li, The Detection of Local Plastic Strain in Microscopic Scale, *Materials Letters*, vol. 62. issu.6-7, 804-807, 2008.
- [17] Y. Tsuchiya, F. Kano, N. Saito, M. Ookawa, J. Kaneda, N. Hara, *Corrosion and SCC Properties of Fine Grain Stainless Steel in Subcritical and Supercritical Pure Water*", Paper 07415, *CORROSION* 2007, March 11 - 15, 2007, Nashville, Tennessee, USA.

## **INTERFACE MASS TRANSFER DURING THE TRIBOFINISHING PROCESS**

I. Hilerio, D.Y. Medina, V. J. Cortés J.D. Muñoz  
Universidad Autónoma Metropolitana, Distrito Federal

**Keywords:** Mass transfers, tribofinishing, wear, abrasive wear.

### **Abstract**

The process of Tribofinishing is investigated as a means to reach a state of quality for the surface treated. During the said process there occurs mass transfer at the interface of the piece to be treated and the abrasive charge (abrasive plus additives). This situation is studied for Titanium as a possibility for application in prosthesis. With these results is intended to produce a model of the mass transfer that would allow having further control of the process.

### **Introduction**

Tribofinishing is a process to improve the surface state of a given component that includes: elimination of rough edges, chips, seams, scales, burrs, offshoots, sprues, flashes, cast seams, featheredges and other defects, also to round off angles, to polish selectively, with a technology that uses unguided cutting tools which work under conditions of soft wear [1].

The basic concepts for tribofinishing are comprised in the area of study which deals with the laws that control fretting and wear: tribology. This is the science that studies the problems associated to interacting surfaces which are in movements relative to each other, making emphasis in the mechanisms that control the overall process and on modelling the degradation observed. Tribology is influenced by two dissipative phenomena: fretting and wear.

Fretting is associated with the existence of a resistance to relative movement due to the interaction between solids, on their actual contacting surfaces. Namely the consumption of energy. Wear describes the processes of destruction of the surfaces as a consequence of the relative movement of two bodies. That is consumption of matter. Amidst the wear phenomena, the most aggressive types are the adhesive and the abrasive [2].

The signs of such types of wear are scratches, furrows, tearing of very small and, after, of larger chips of the material under the action of abrasive particles in movement or of hard protuberances from one of the surfaces involved.

Hard asperities or the abrasive grains can be considered as cutting tools.

A theoretical approach would consist in modelling one abrasive particle that can be considered as a cone of half angle  $\theta$  at the vertex, under a differential load  $dP$ . The particle penetrates the surface with a depth  $z$ . (see Fig. 1).

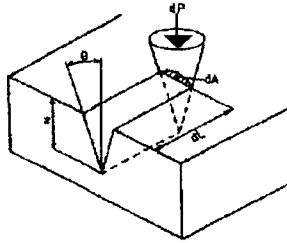


Fig. 1. Wear model for the contribution abrasive.

Using as a definition the Meyer hardness  $H$  as:

$$H = \frac{dP}{dA} \quad (1)$$

where  $dA$  is the projected surface within the plane of the indent, we can make the following considerations. The contribution of the abrasive particle to the load is:

$$dP = dA \times H \quad (2)$$

In other words:

$$dP = \frac{1}{2} \pi z^2 \tan^2 \theta \quad (3)$$

The factor  $\frac{1}{2}$  comes from the geometry of the indent.

The volume of material  $dV$  from a sliding distance  $dL$ , as given by geometry is:

$$dV = \frac{1}{2} \pi z^2 \tan \theta \times dL \quad (4)$$

Then:

$$\frac{dV}{dL} = \frac{2 \cot \theta}{\pi} \times \frac{dP}{H} \quad (5)$$

For all abrasive particles a wear percent is obtained that is expressed as:

$$\frac{V}{L} = k \left[ \frac{2 \cot \theta}{\pi} \right] \times \frac{P}{H} = K \frac{P}{H} \quad (6)$$

Where:

$$K = k \left[ \frac{2 \cot \theta}{\pi} \right]$$

is obtained experimentally and generally is of the order  $10^{-2}$ .

It is important to realise at this point that eq.(6) expresses the wear percent ( $V/L$ ) in terms of the load  $P$  and of the Meyer hardness  $H$  of the material, regardless of the wear mechanism: be it adhesive, surface fatigue, tribofinishing, etc. From this point of view, the value of  $K$  appears as a measure of the severity of the wear process [3].

It is the interest of the present work as a first approach to the problem, to propose a general law of behaviour.

### General Basis for Tribofinishing

Tribofinishing is related to:

- The action of rubbing between the load for work given by the different kinds of abrasives and the work pieces to be treated.
- The work load is generally kept within a wet environment by means of an aqueous solution that controls the physico-chemical conditions for fretting.

Thus there are three variables that have influence on the process:

1. - A machine that imparts relative movement and the energy associated.
2. - The work load which carries out the work during the process
3. - The liquid solution which acts as an agent with defined surface properties.

The mechanical aspect of the process rests upon control of the multiple collisions between the load of particles and the work piece [4].

### The Machines

These can be classified in terms of the movement produced:

- Alternative lineal movement
- Simple rotating movement
- Vibratory movement
- Centrifugal rotating movement.

Regardless of the type of machine selected, the constituents of the work load, work piece-abrasive, are subjected to a permanent internal fretting action, which gives rise to wear.

Whichever kind of movement imposed, there are three classes of principal interactions between the piece and the abrasive: shearing, impact or percussion and abrasion. (see Figure 2).

It is necessary to look for an optimal movement of the machine that permits the best interaction in the relative contact between the treated material (pieces) and the charge abrasive.

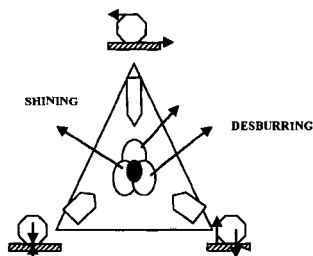


Fig. 2. Ternary diagram showing the mechanisms of tribofinishing.

## The Workload

This action is made up by the abrasives and the work pieces. By abrasive it is understood the material that produces wear by fretting: it can be a mineral, metal or an agglomerate.

The selection of a given abrasive depends on the following:

- The relative proportion of abrasion, impact or shearing.
- The shape of the work piece
- The type of machine to be used [5].

From a general point of view, if the piece to be treated is a soft metal, a polymer abrasive will give the best result. On the contrary if the piece is hard, it should be best to use a ceramic abrasive, which due to its significant chemical inertness there should be no effects upon the system considered. The main parameters for the selection of the abrasive are given as follows:

- Characteristic weight: this is related to the structural nature of the material, which determines its density.

- Cutting capacity: the amount of material cut by means of a tribological action  $Q$  is determined by the following expression:

$$Q = \sum_{n=1}^n A_n (V_M - V_m) \quad (7)$$

where:

$Z_1$  = number of abrasive cutting grains

$A_n$  = area of one cut obtained

$V_m$  = velocity of the work piece during contact

$V_M$  = velocity of the abrasive during contact

- Reliability of the abrasive: this is related to the structural homogeneity, to cohesion, fragility, ...

## The Environment

Generally, the tribological actions occur in an aqueous medium that contains additives. Among the most common additives, the surfactants are preferred, because they favour machining the surface, very likely because they affect favourably the local cutting conditions.

The HLB theory (Hydrophile Lipophile Balance) permits to reach the best condition to obtain an adequate surface. The theory establishes that an HLB=11 is correct for a non ferrous material [6].

## Experimental Procedure

There exists a correlation between the quantity of material that has been cut away and the relative variation of elements in the workload. In order to analyze the problem, it is of interest to use this kinematic approach. The work principle for barrel turning is schematised in Figure 3.

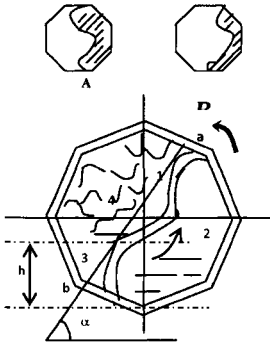


Fig. 3. Important characteristics for barrel turning. (1 rubbing circuit, 2 return circuit, 3 aqueous solution, 4 foam solution, h level solution, A cascade very high velocity, B cascade charge insufficient).

For a better understanding of the problem in hand, it has been carried out a kinematic study of the movement of a workload within the barrel. The cylindrical symmetry of the barrel of radius R is considered and the workload is assumed to be distributed in the internal periphery of the barrel at a given point M. The latter is defined in the X-Y plane in relation to angle  $\theta$ . (see Fig. 4).

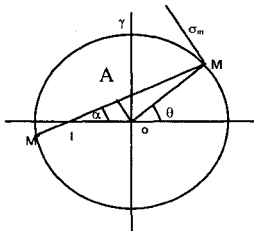


Fig. 4. Kinematic study for the tribological process in the barrel.

The point M is associated with an interface  $MM'$  that cuts across the X axis at position I, which is responsible for the change of movement in the workload. (see Fig. 4).

There is a second reference fixed  $X_1-Y_1$  (see fig. 5), where point M with coordinates  $(X, Y)$  has new coordinates  $(X_1, Y_1)$ . This is to say:

$$\overline{OM} = R \cos \theta \cdot \overline{X} + R \sin \theta \cdot \overline{Y} \quad (8)$$

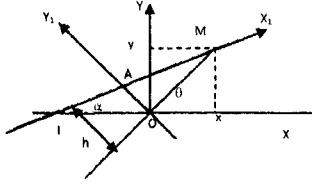


Fig. 5. New reference axis to study the kinematics of movement.

$$\overline{OM} = h(-\text{sen } \alpha \cdot \overline{X} + \text{cos } \alpha \cdot \overline{Y}) + AM(\text{cos } \alpha \cdot \overline{X} + \text{sen } \alpha \cdot \overline{Y}) \quad (9)$$

From the expressions (8) y (9) we have:

$$\begin{aligned} R \text{cos } \theta &= AM \text{cos } \alpha - h \text{sen } \alpha \\ R \text{sen } \theta &= AM \text{sen } \alpha + h \text{cos } \alpha \end{aligned} \quad (10)$$

Which gives:

$$\tan \theta = \frac{AM \text{sen } \alpha + h \text{cos } \alpha}{AM \text{cos } \alpha - h \text{sen } \alpha} \quad (11)$$

The last expression permits to relate both parameters h and  $\theta$ . Besides, it is seen that (see fig. 5) is fulfilled:

$$AM = (R^2 - h^2)^{1/2} \quad (12)$$

From the defined coordinates, it is possible to define the instantaneous velocity at point M:

$$\overline{V}_M = \frac{d\overline{OM}}{dt} = -R\theta' \text{sen } \theta \cdot \overline{X} + R\theta' \text{cos } \theta \cdot \overline{Y} \quad (13)$$

Taking into consideration the change of reference system, we have:

$$\begin{aligned} \overline{X} &= \overline{X}_1 \text{cos } \alpha - \overline{Y}_1 \text{sen } \alpha \\ \overline{Y} &= \overline{X}_1 \text{sen } \alpha + \overline{Y}_1 \text{cos } \alpha \end{aligned} \quad (14)$$

Expression (13) may be written as:

$$\overline{V}_M = -R\theta' \text{sen}(\theta - \alpha) \overline{X}_1 + R\theta' \text{cos}(\theta - \alpha) \overline{Y}_1 \quad (15)$$

$$\overline{V}_M = -R\omega \text{sen}(\theta - \alpha) \overline{X}_1 + R\omega \text{cos}(\theta - \alpha) \overline{Y}_1$$

Where the angle  $\alpha$  physically represents the sliding slope.

With the same reasoning, the acceleration at point M is given by:

$$\overline{\gamma}_M = \frac{d\overline{V}_M}{dt} = R\omega^2 \text{cos}(\alpha - \theta) \overline{X}_1 + R\omega^2 \text{sen}(\alpha - \theta) \overline{Y}_1$$

(16)

The last expression has been numerically calculated for different values of the angles  $\alpha$  and  $\theta$ .

It is important to emphasize that point M is a particular point, where one particle that is initially in contact with the wall of the barrel, which is not involved in the uniform rotation movement around the OZ axis and it is sliding suddenly toward the inner part of the barrel following the sliding slope, in accordance to the reference:  $OX_1 - OY_1$ .

If the value of the  $\alpha$  is fixed (since it depends on the adherence between the particle and the wall of the barrel) then it is possible to study the evolution of the sliding speed  $V$  as a function of the workload level (see Fig. 6).

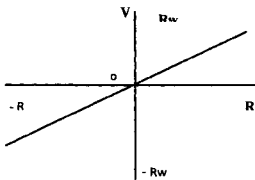


Fig. 6. Evolution of the sliding speed as a function of the workload for  $\alpha=45^\circ$ .

It can be observed from Fig. 6 a linear relationship, but most important that the initial sliding speed is positive for a workload level higher than half the barrel.

It is very important to seek to determine which are the parameters that permit an optimization of the abrasive action. Therefore, the sliding speed increment should accelerate the process.

The normal speed component calculated as a function of the height of the workload at point M produces a positive circular profile. This does not permit to obtain an interesting practical conclusion. The evolution of the components of acceleration as a function of the sliding angle for different workload levels, is found to be constant. (see Fig. 7).

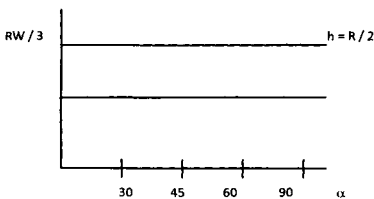


Fig. 7. Evolution of the sliding speed as a function of the angle for different workload levels.

Therefore, the sliding angle is not an important factor for the sliding speed, whereas the workload level will influence more. The sliding height can be defined as the projection of the sliding length on the vertical axis.

It is observed that the sliding height or sliding potential is maximum when  $h = 0$ , regardless the sliding angle (see Fig. 8).

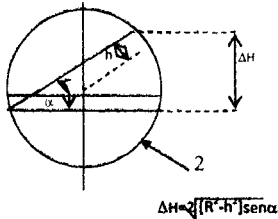


Fig.8 Variation of the aliding height with the diameter of the barrel

It is observed that sliding height or sliding potential is maximum when  $h = 0$ , regardless the sliding angle (see Fig.9).

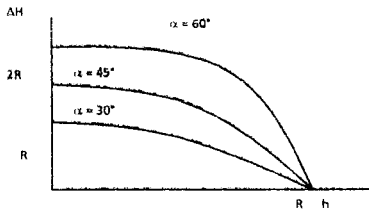


Fig. 9. Evolution of the sliding height of  $\Delta H$ , as a function of the workload for different sliding angles.

To increase the  $\alpha$  angle will increase the maximum value for  $\Delta H$ .

### Conclusions

It is evident that the workload of the barrel at half height has two important characteristics, maximum length and a sliding potential; however, the sliding speed is initially null.

The best compromise appears to be a workload level equivalent to  $\frac{3}{4}$  the capacity of the barrel. As a matter of fact this permits to obtain a non negligible initial sliding speed, which in turn minimizes the influence of the other factors.

### Acknowledgements

The author wishes to acknowledge Professor C. Roques-Carnes, director of L. M. S. (Laboratory for Surface Microanalysis) of the E. N. S. M. M. at Besançon, France, where this work was produced. Also he is grateful to T. Leclerc for his help during the work.

### References

- [1]. B. Lamy, Contribution à l'étude phenomenologique de l'enlèvement de matière et de la déformation des surfaces antagonistes dans le processus d'abrasion. Thèse de Doctorat d'État . Université de Haute Alsace. (2002).
- [2]. Bengtsson, A. Rönnerberg, Proc. 3rd. Int. Conf. on Metrology and properties of engineering surfaces. Teeside Polytechnic, Teeside. (1985). Wear, 109, (2005).
- [3]. T.R. Thomas, Rough surfaces. Longman, London, 2002.
- [4]. A.Niku Lari, Traitements mécaniques de surface. Vol. I (pp. 17-205), et Vol.II (pp.183-228). Ed. Dunod. 2005.
- [5]. P. Kunz, Introduction à une étude fondamentale de la Tribofinition. M.écanique, Matériaux, Electricité. 362,(2000), pp. 59-66.
- [6]. W.C. Griffin, The hidrophile-Lipophile Balance system, J. Soc. Cosmet. Chem. I. 2009

*Characterization of Minerals, Metals, and Materials*  
Edited by: Jiann-Yang Hwang, Sergio Neves Monteiro, Chengguang Bai,  
John Carpenter, Mingdong Cai, Donato Firrao, and Buoung-Gon Kim  
TMS (The Minerals, Metals & Materials Society), 2012

# **Characterization of Minerals, Metals, and Materials**

## **Characterization of Non-Ferrous Materials**

Session Chairs:  
**Igor Z. Bunin**  
**Byoung-Gon Kim**

## **IMPROVEMENT OF MECHANICAL PROPERTIES IN SEVERELY PLASTICALLY DEFORMED Ni-Cr ALLOY**

K.H. Song<sup>1</sup>, H.T. Son<sup>1</sup>, H.S. Kim<sup>1</sup>, W.Y. Kim<sup>1</sup>

<sup>1</sup>KITECH (Korea Institute of Industrial Technology); 7-47, Songdo-Dong, Yeonsu-gu, Incheon, 406-840, Korea

**Keywords:** Cross-roll rolling, Ni-20Cr alloy, Electron back-scattered diffraction, Grain refinement, Mechanical properties.

### **Abstract**

In order to evaluate the grain refining and mechanical properties due to severe plastic deformation (SPD), this work was carried out. Conventional rolling (CR) and cross roll rolling (CRR) as a SPD method were introduced, and Ni-20Cr alloy as an experimental material was chosen. The materials were cold rolled to 90% in thickness reduction and subsequently annealed at 700oC for 30 min to obtain the fully recrystallized microstructure. For annealed materials after cold rolling, electron back-scattered diffraction (EBSD) analysis was carried out to investigate the grain boundary characteristic distributions (GBCDs). CRR process was more effective to develop the grain refinement relative to CR process, as a result, grain size was refined from 70  $\mu\text{m}$  in initial material to 4.2  $\mu\text{m}$  (CR) and 2.4  $\mu\text{m}$  (CRR), respectively. These grain refinements directly affect the mechanical properties improvement, in which microhardness and yield and tensile strengths were significantly increased than those of initial material.

### **Introduction**

Cross-roll rolling (CRR), i.e., a new rolling process in which roll axes are tilted against the transverse direction (TD) in the rolling direction (RD) – TD plane, was proposed by Chino et al. [1]. This new rolling process can impose a higher effective strain than that of conventional rolling (CR), resulted mainly from shear deformation of  $\epsilon_{23}$  [2]. Generally, the effective strain imposed in material during deformation directly affects the resulting grain size through heat treatment, in other words, a higher effective strain can obtain the more refined grain size [2]. Ni base alloy used in this study has an intermediate stacking fault energy (SFE), ranging between Cu and Al alloys, however, an increase in Cr content on Ni matrix led to the gradual decrease in SFE [3, 4]. As known theoretically, the lower SFE materials are more easy to acquire the refined grain size than that of the higher SFE materials through SPD and subsequent annealing process, resulted from the more nuclei sites [3, 4]. Therefore, CRR process with a higher effective strain than that of CR process could be obtained the notably refined grain size and accompanying the increased mechanical properties. Lately, SPD processes, such as equal channel angular pressing (ECAP), high pressure torsion (HPT) and high speed ratio differential speed rolling (HRDSR), have been studied with regard to obtaining of high strength, resulted from refined grain size [5-7]. However, the research of CRR process on Ni-Cr alloys has not been carried out thus far.

In the present study, we evaluated the microstructural and mechanical properties enhancement on severely plastic deformed Ni-20Cr by using CRR, comparing with CR processed material, and discussed the effect of effective strain on grain refinement and accompanying the mechanical properties development.

## Experimental Procedures

The material used in this study was Ni-20Cr alloy with size of 30 mm × 50 mm × 8 mm. Solution treatment was carried out at 1000°C for 1 h to remove the cast structure and obtain the homogenized microstructure. Specimen was mechanically ground to remove the surface oxidation and cold rolled to 90% thickness reduction, without lubricant to maximize the shear strain. In particular, CRR was carried out with retaining the roll mill condition in which roll axes were tilted by 5° from the transverse direction (TD) in RD-TD plane. In order to observe the microstructures of cold rolled materials by CR and CRR, transmission electron microscopy (TEM) was employed, and cold rolled sheets were then cut to 3 mm disc, mechanically ground to 80 μm and jet-polished to 10 μm by using the solution of 10 ml perchloric acid and 90 ml methanol at -30°C. TEM analysis on thinned specimens was carried out at 200 kV.

For annealing on cold rolled material, specimens were prepared by 5 mm × 5 mm in size and annealed at 700 °C for 30 min to obtain the fully recrystallized microstructure. To analysis the grain size, grain boundary characteristic distributions (GBCD) and textures on annealed materials, electron back-scattered diffraction (EBSD) was introduced. For this work, specimens were additionally polished by vibratory polisher, and the specimen surfaces were then analyzed using orientation image mapping incorporated in scanning electron microscopy (SEM). To evaluate the mechanical properties, Vickers microhardness and tensile test were employed. The former test was carried out on cross sections of the specimens, with a load of 9.8 N and dwell time of 15 s. Tensile test specimens were used to evaluate the transverse tensile strength of the cold rolled and recrystallized materials, as shown in Fig. 1.

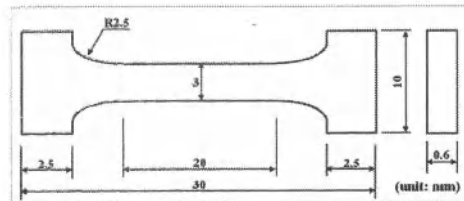


Figure 1. Configuration of transverse tensile specimen used in this study.

## Results and Discussion

The grain boundary map, grain size distribution and grain boundary misorientation angle distribution, acquired by EBSD analysis, of initial material is shown in Fig. 2. Initial material was composed of equiaxed grains, including a large amount of annealing twins in the grains, as shown in Fig. 2(a). At this state, grains ranging between 2.4 and 130 μm in size were heterogeneously distributed, with average size of 70 μm, as shown in Fig. 2(b). In addition, the high-angle grain boundary at all fraction occupied more than 90%, in which 60° distribution showed the highest fraction of the misorientation angle distribution, as shown in Fig. 2(c). This was identified as annealing twin boundary, which is well performed at materials with lower stacking fault energy in fcc metals.

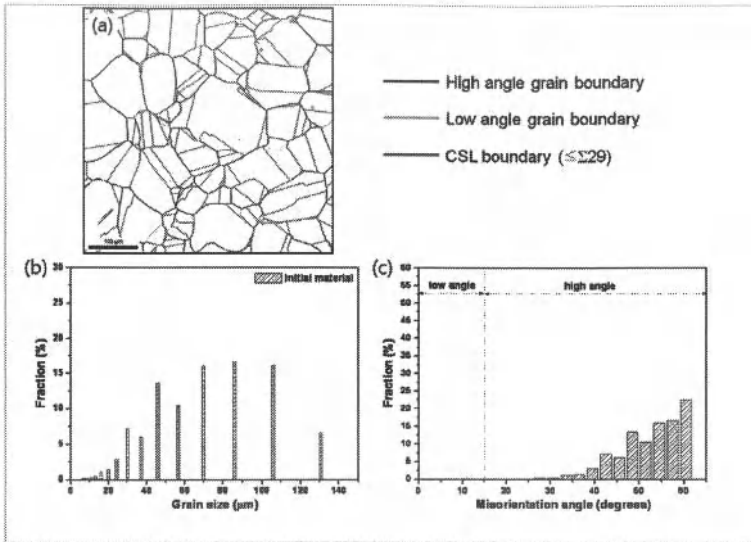


Figure 2. (a) Grain boundary map, (b) grain size and (c) misorientation angle distributions of initial material. Black, gray and red lines in the grain boundary map indicate high angle, low angle and CSL boundaries ( $\leq \Sigma 29$ ), respectively.

Grain boundary maps and grain boundary misorientation angle distribution of cold rolled and annealed materials are shown in Fig. 3. Application of cold rolling was effective to improve the grain refinement through heat treatment. As a result, CR processed and annealed material consisted of grains ranging between 0.2 and 12.2  $\mu\text{m}$  with average size of 4.2  $\mu\text{m}$ , which is significantly refined size than that of initial material, as shown in Fig. 3(a). CRR material showed the more effect in grain refining, consequently, the grains were ranged from 0.2 to 9  $\mu\text{m}$  with average size of 2.4  $\mu\text{m}$ , as shown in Fig. 3(b). For misorientation angle distribution, high angle grain boundary occupied more than 95% at all conditions, as shown in Fig. 3(c-d). In addition, 60o distribution showed the highest fraction at all conditions, which was identified as annealing twin boundaries similar to that at initial material, as mentioned above.

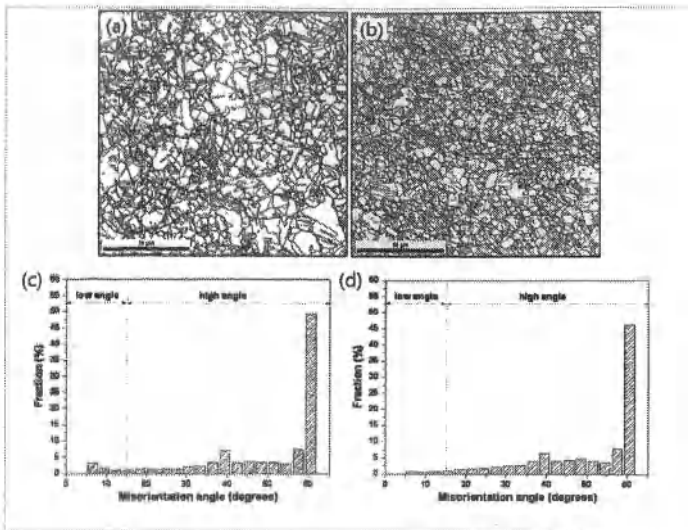


Figure 3. Grain boundary maps and misorientation angle distributions of recrystallized material after cold rolling. Grain boundary maps; (a) conventionally rolled and annealed material and (b) cross-roll rolled and annealed material. Misorientation angle distributions; (a) conventionally rolled and annealed material and (b) cross-roll rolled and annealed material. Black, gray and red lines in the grain boundary maps indicate high angle, low angle and CSL boundaries ( $\leq \Sigma 29$ ), respectively.

Change in Vickers microhardness due to the application of cold rolling and annealing is shown in Fig. 4. Application of cold rolling led to an increase in microhardness, as a result, microhardness increased from 116 Hv in initial material to 348 and 427 Hv in CR and CRR, respectively, showing notably higher value in CRR. In case of annealed materials, microhardness exhibited 200 Hv in CR and 266 Hv in CRR, respectively, which also showed a higher value in CRR material, similar to that at cold rolled materials.

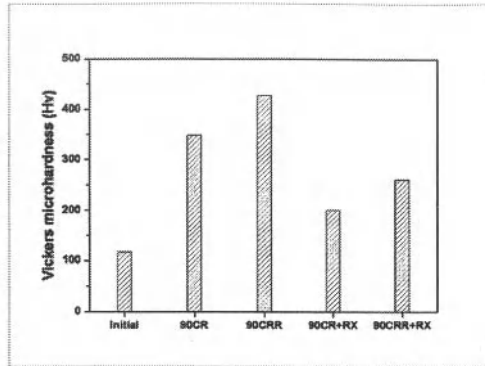


Figure 4. Changes in Vickers microhardness distributions during deformation and annealing.

Tensile properties of initial, cold rolled, and annealed materials are shown in Fig. 5. Initial material exhibited 42 and 418 MPa in yield and tensile strengths, respectively, with elongation of 50%. Application of cold rolling led to the notable increase in yield and tensile strengths, consequently, CR and CRR processed materials showed 848 and 963 MPa in yield strength and 1054 and 1067 MPa in tensile strength, respectively. However, their elongation decreased to 6.8 (CR) and 5.6% (CRR), respectively. At annealed materials, yield and tensile strengths of CR material were 189 and 494 MPa, with elongation of 34%. CRR material showed 340 and 566 MPa in yield and tensile strengths with elongation of 32%, significantly increased yield strength without remarkable decrease in elongation when compared to CR material.

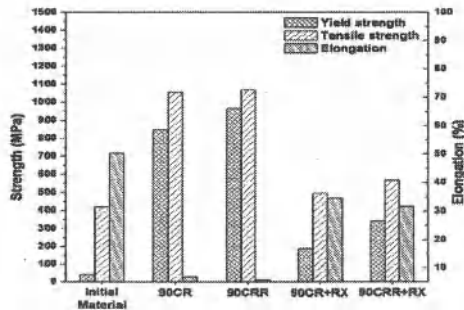


Figure 5. Tensile properties of cold rolled and annealed materials.

Change in texture distributions of initial material, and cold rolled and subsequently annealed materials is shown in Fig. 6. At initial material, the grains were densely distributed at  $\langle 001 \rangle // ND$ , showing the highest intensity, as shown in Fig. 6(a). CR processed and annealed material also showed the densely distributed grains at  $\langle 001 \rangle // ND$ , similar to that at initial material, as shown in Fig. 6(b). However, the grains in CRR processed and annealed material were densely distributed at  $\langle 111 \rangle // ND$ , as shown in Fig. 6(c).

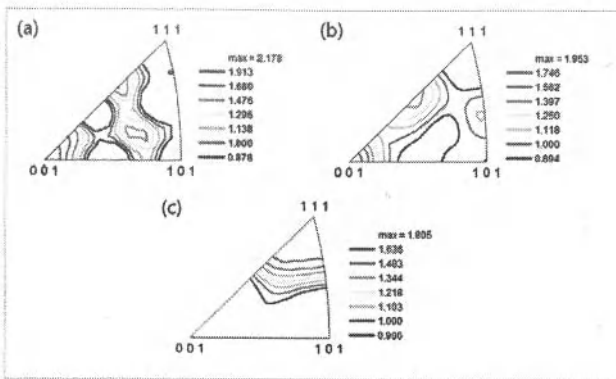


Figure 6. ND inverse pole figures of the initial material, and cold rolled and annealed materials. (a) initial material, (b) CR and (c) CRR materials.

Application of SPD process such as CR and CRR led to the notable grain refinement, as a result, average grain size was significantly refined from 70  $\mu\text{m}$  in initial material to 4.2 and 2.4  $\mu\text{m}$  in CR and CRR, respectively, as shown in Fig. 2 and 3. In particular, CRR processed material showed the more refined size than that of CR processed material. This can be explained in terms of the effective strain which imposed during deformation. Generally, a larger effective strain imposed in material can lead to the more refined grains through heat treatment. CRR process applied in this study has a larger effective strain than that of CR process due to shear deformation of  $\approx \epsilon_{23}$  [8]. As known by theoretically, CR mainly impose the deformation with  $\epsilon_{11} = \epsilon_{33}$  and  $\epsilon_{22} = \epsilon_{12} = \epsilon_{13} = \epsilon_{23} = 0$ , whereas in the practical rolling process  $\epsilon_{13}$  is not zero. However, CRR process can expect the shear deformation with  $\epsilon_{12}$ ,  $\epsilon_{13}$  and  $\epsilon_{23}$ , without expecting at CR, which results in change in grain shape during the deformation [8]. Therefore, these shear deformation due to CRR process, resulting in a higher effective strain, can lead to the more large grain refinement after heat treatment.

Grain refinement led to an increase in mechanical properties, such as Vickers microhardness and yield and tensile strength. At Vickers microhardness, its values were significantly increased from 116 Hv in initial material to 200 Hv in CR and 266 Hv in CRR materials, respectively, 30% higher value in CRR than that of CR, as shown in Fig. 4. In case of yield and tensile strengths, its values in both processes showed outstanding increase, however, CRR processed and subsequently annealed material exhibited the more increased values than that of CR, as a result, they were increased from 42 MPa and 418 MPa in initial material to 340 MPa and 566 MPa in CRR material, respectively, as shown in Fig. 5. These increases in mechanical properties can be explained in terms of grain refinement. In other words, smaller grain size mainly attributed to their strength enhancement.

The relationship between yield strength and grain size in CR processed material was satisfied with Hall-Petch relationship. The following relation was derived,  $\sigma = -5.6 + 399d^{-1/2}$ , however, CRR processed specimen showed 37% higher value than that of CR processed material, consequently, which was distributed at upper side of Hall-Petch straight line of CR. Therefore, we conclude that CRR caused greater enhancement of the mechanical properties. This conclusion is also supported by the finer grain size and texture distribution of the CRR processed

specimen. Particularly, different texture distributions in CR (001//ND) and CRR (111//ND), as shown in Fig. 6, could be considered for reason of increase in mechanical properties. These findings suggest that CRR can lead materials to smaller grain size and improved mechanical properties after recrystallization by subsequent annealing.

### Conclusions

Application of cold rolling on Ni-20Cr alloy was effective to develop the grain refinement. As a result, average grain size was refined from 70  $\mu\text{m}$  in initial material to 4.2  $\mu\text{m}$  in CR and 2.4  $\mu\text{m}$  in CRR, respectively, showing a higher refinement in CRR. These grain refinements led to the increase in mechanical properties such as microhardness, and yield and tensile strengths. In particular, the yield strength in CRR processed and annealed material increased to 800% relative to the initial material and 180% relative to the CR processed and annealed material, respectively. Notable increase in yield strength of CRR material is caused by a higher effective strain relative to CR material, mainly resulted from  $\epsilon_{23}$ , as well as the texture development of  $\langle 111 \rangle // \text{ND}$ . Therefore, CRR process imposed a higher effective strain can enhance the grain refinement and accompanying the mechanical properties, more effectively.

### References

- [1] Y. Chino et al., "Enhanced formability at elevated temperature of a cross-rolled magnesium alloy sheet." *Materials Science and Engineering A*, 441 (2006) 349-356.
- [2] Y. Chino et al., "Stretch formability at elevated temperature of a cross-rolled AZ31 Mg alloy sheet with different rolling routes." *Materials Science and Engineering A*, 473 (2007) 195-200.
- [3] K. Neishi, Z. Horita, and T.G. Langdon. "Grain refinement of pure nickel using equal-channel angular pressing." *Materials Science and Engineering A*, 325 (2002) 54-58.
- [4] S. Komura et al., "Influence of stacking fault energy on microstructural development in equal-channel angular pressing." *Journal of Materials Research*, 14 (1999) 4044-4050.
- [5] K. Sitarama Raju et al., "Grain size and grain boundary character distribution in ultra-fine grained (ECAP) nickel." *Materials Science and Engineering A*, 491 (2008) 1-7.
- [6] A.P Zhilyaev et al., "Microhardness and microstructural evolution in pure nickel during high-pressure torsion." *Scripta Materialia*, 44 (2001) 2753-2758.
- [7] W.J. Kim, K.E. Lee, and S.H Choi, "Mechanical properties and microstructure of ultra fine-grained copper prepared by a high-speed-ratio differential speed rolling." *Materials Science and Engineering A*, 506 (2009) 71-79.
- [8] J.J. Nah et al., "Effect of strain states during cold rolling on the recrystallized grain size in an aluminum alloy." *Scripta Materialia*, 58 (2008) 500-503.

## **PROCESSING AND MICROSTRUCTURAL CONTROL OF COPPER FOAMS FOR THERMAL WICK MATERIAL SYSTEMS**

Keri Ledford<sup>1</sup>, Stephanie Lin<sup>2</sup>, Jason Nadler<sup>1</sup>

<sup>1</sup>Georgia Tech Research Institute Electro-Optical Systems Laboratory;  
939 Dalney Street NW, Atlanta, GA 30332-0245, USA

<sup>2</sup>Georgia Institute of Technology School of Materials Science and Engineering;  
771 Ferst Drive, Atlanta, GA 30332-0245

Keywords: Copper, Thermal wick, Microstructure, Processing

### **Abstract**

Novel processes are being developed to fabricate thin copper thermal wick samples of a targeted porous microstructure. Structures of desired porosity, thickness and pore size and distribution are achieved by tailoring the incorporation of sacrificial polymer beads into slurry precursors. The thickness of the final structure is dictated by precisely controllable slurry application methods, such as spin coating. In a subsequent heat treatment, the polymer components thermally decompose and the remaining copper particles sinter to form a reticulated foam. The resulting microstructures are characterized in terms of porosity, permeability and specific surface area.

### **Introduction**

Thermal wick systems composed of open celled, microporous copper foams have proven to show efficient performance capabilities in passive cooling devices, such as heat pipes or in vapor chambers. These foams are comprised of a solid copper phase that confines a network of interconnected pores. This pore network is responsible for the fluid transport properties through the wick, the copper foams are therefore able to function as cooling systems by wicking fluid from a condenser region within the device, to an evaporative region [1, 2]. There are a number of methods utilized to fabricate cellular metallic foams: including foaming liquid metal precursors, use of metal powders and metal ion precursor solutions [3]. The copper foams being analyzed in this article are fabricated from sintered copper powder, and the fabrication process employs a sacrificial templating method of using space-holding filler materials to affect the characteristic porosity. [4]

One issue that arises with systems of open celled porous structures is the occurrence of overheating and/or dry-out, in which the heat transfer from the application exceeds the capabilities of the vapor chamber, and the fluid evaporates faster than it can be wicked through the system. In such cases, the fluid no longer returns to the condenser region from the evaporative region and the vapor chamber ceases to function as a cooling device [1]. The ability to determine the performance parameters and critical characteristics of the thermal wicks prior to their implementation in application situations would decrease the chances of the wick overheating. Knowing the limits of the thermal wick would allow the prevention of placing the wick in an application that function outside the range of the thermal wick's capabilities. It would also be favorable to have the ability to reliably produce devices with the same critical characteristics and performance parameters.

Critical characteristics that thermal wicks must demonstrate are a high thermal conductivity, efficient capillary transport and evaporative transport over the porous region of the device. Performance of the thermal wick, particularly the capillary flow and transport, can be

characterized by the microporous structure of the foam [2]. This structure can be controllably tailored to optimize these characteristics and the overall performance of the thermal wick. The capillary transport will be dependent on the radii of the pores, and the permeability is largely determined by the porosity of the foam [2].

This study aims to develop a method that will reliably produce thermal wick specimens with predictable critical features. This fabrication process will include the production of the slurry precursor, application by spin coating or doctor-blading and a heat treatment. This will be done by determining a set of precursor slurry formulations that will give a predictable final structure when submitted to a specified fabrication process. The processes being developed in this study will be adaptable, as to obtain certain desired features within the resultant structures. For example, thin foams are predicted to be better fabricated by applying the slurry suspension via a spin coating method, whereas thicker foams are predicted to be more easily achieved by employing the doctor-blade technique. Changing the viscosity of the solvent will also allow for control over the thickness of the slurry layer and final structure; less viscous slurries are expected to give thinner foams and more viscous slurries are expected to give thicker foams. The size of the pores within the structure can be controlled by using space-filling sacrificial polymer beads of differing sizes. The amount of template polymer beads added to the precursor slurry suspension should directly affect the porosity of the final structure, with higher volume percentages of template resulting in higher porosities. Combining the two parameters, polymer bead size and volume, should lead to control over the effective surface area of the foam.

The structural parameters this study is seeking to optimize through an adaptive process are the effective pore size, effective surface area, tortuosity and porosity of the cellular metallic foams. As the critical parameters are difficult to determine experimentally, the porous structures will be subsequently characterized by subjecting scanning electron microscopy images of the foams to previously established image analysis methods [2, 5]. Through calculation and analysis of these parameters, the theoretical permeability of the foams can be determined to establish the performance capabilities of the microporous copper foam as a thermal wick.

## Experimental

### Development of Formulations

Six distinct slurry formulations were created to fabricate a series of samples to be structurally analyzed. Two different sizes of poly(methyl methacrylate) spheres were utilized for sample fabrication, one type with an average diameter of 40 $\mu$ m (Scientific Polymer Products, Inc) and another with an average diameter of 15 $\mu$ m (Arkema, Inc). Three different volume percentages of the polymer pore templates were utilized to effect differing levels of porosity, 53% template by volume, 65% and 73%. The different formulations were developed by first determining the ratio of copper powder to polymer template necessary to create dry mixtures of poly(methyl methacrylate) and copper powder that were 53%, 65% and 73% template by volume. The copper powder used to fabricate the foams was derived in the laboratory from 3-5 $\mu$ m copper (II) oxide powder (American Chemet). The liquid portion of the slurry was a solution of 25% 8000 molecular weight poly(ethylene glycol) (Carbowax™) in water. The poly(ethylene glycol) served as a binder to keep the foam layer from cracking when the solvent was evaporated after the slurry was applied to the substrate.

The smallest volume of solvent required to fully solvate the slurry was determined by performing solids loading experiments with the individual and combined solid components. The solids loading experiments were executed by weighing a known amount of the solid onto a watch glass, and adding the solvent drop wise until the mixture formed a cohesive paste.

The precursor slurries were created by weighing the required masses of copper powder and polymer beads into a small beaker, then dispensing the required volume of solvent into the

beaker via syringe. The components were mechanically blended into a cohesive mixture. After application to the substrate, the thermal wick samples underwent a heat treatment to thermally decompose the space-filling template and sinter the copper powder.

#### Application Methods

Two application methods were implemented to effect thin, uniform layers of the slurry on the substrates: spin coating and doctor blading. To create a sample by the spin coating method, the substrate was attached to the chuck of the spin coater by a vacuum mechanism and an amount of slurry sufficient to coat the entire substrate surface was dispensed onto the substrate via pipette. The samples were spun at velocities ranging between 500 revolutions per minute (rpm) and 1150rpm, with a constant acceleration for 10 seconds. The water in the solvent was allowed to evaporate from the slurry, leaving behind the binder, and the thickness of the slurry layer of the substrate was measured via micrometer. The doctor bladed samples were prepared by placing the substrate between two spacers of known thickness. The slurry was applied to the substrate to the level of the spacer, allowing exact control over the height of the slurry layer being applied.

#### Microstructural Analysis

Microstructural analysis of the open celled foam samples was achieved by capturing representative cross-sectional images of each formulation with a Hitachi S-4700 scanning electron microscope. The samples were prepared by infiltrating the foam with a conductive epoxy (Epoxy Technology, Inc) prior to cross-sectioning the sample. The surface to be imaged was then ground and polished by standard metallurgical procedures. The images were obtained using a backscatter detector at magnifications that allow the entire cross-section of the structure to be shown in the image. The thicknesses of the structures to be analyzed were within a 100 $\mu$ m to 400 $\mu$ m range. The image preparation- cropping and conversion to a binary image from an 8-bit image by Otsu thresholding- was executed with Fiji image processing and analysis software and the porosity, perimeter density, tortuosity and effective pore diameter calculations were completed by use of a previously established numerical method code in a MATLAB<sup>®</sup>-based computation [2, 5]. The porosity was measured by converting the images to binary and determining the percentage of the image that was the pore, the number of white pixels in the image, compared to the total number of pixels. The perimeter density was determined by an edge detection algorithm measuring the distance of the boundary lines of the foam-pore interfaces [5]. Tortuosity values were determined by generating a random starting point within the image, and measuring the distance that must be traveled to escape the image relative to the actual distance between the starting point and the image boundary. This measurement was repeated 1000 times to generate an average value. Due to its suitability for calculating the permeability of the porous foams, the Kozeny-Carman equation (1),

$$k = \frac{\phi^3}{\tau s^2} \quad (1)$$

was employed where  $k$  is the permeability,  $\phi$  is the porosity,  $\tau$  is the average tortuosity and  $s$  is the perimeter density [6, 7]. The equation was modified to better detail the data gained from the highly porous and anisotropic structures; the modification being that a specific area term was utilized rather than a particle diameter [5]. The efficiency of the capillary transport was determined by the equation (2)

$$K = \frac{k}{r^2} \quad (2)$$

where  $K$  is the normalized permeability,  $k$  is the permeability and  $r$  is the pore radius. The effective pore diameter was calculated by quantifying the size distribution of the pores using a marker controlled watershed algorithm and particle analysis.

## Results and Discussion

### Formulations

The results of the solids loading tests for each component of the slurries were instrumental in determining the amount of solvent needed for each formulation. This is important, as the thickness of the layers to be produced is dependent on the thickness of the slurry, which is in turn dependent on the amount of solvent present in the mixture. A larger volume of solvent was required for samples using the same volume fraction of the 15 $\mu\text{m}$  average diameter polymer spheres than was required for the 40 $\mu\text{m}$  average diameter polymer spheres. The average diameter of the polymer spheres utilized in this experiment was obtained by particle size analysis [8]. Similarly, as the polymer template volume percentage increased, the amount of solvent required also increased.

Varying the size of the sacrificial template spheres resulted in a vast difference in the resulting microstructures. As displayed in Figure 1, the 40 $\mu\text{m}$  average diameter template (Figure 1a) affected an open celled foam structure with much larger pores than the foam created with the 15 $\mu\text{m}$  average diameter template (Figure 1b). The 15 $\mu\text{m}$  average diameter template foam image suggests that the surface area between the foam and the pore is greater than that of the 40 $\mu\text{m}$  average diameter template foam. The differences between the structures affected by varying the template size are significant, as the different structures will have different critical properties that will allow them to be tailored to specific applications based upon their performance capabilities. The larger pore size foams show a higher level of interconnection within the solid phase, however the uniformity of the inter-particle pore network is more uniform in the foams created from smaller pore templates.

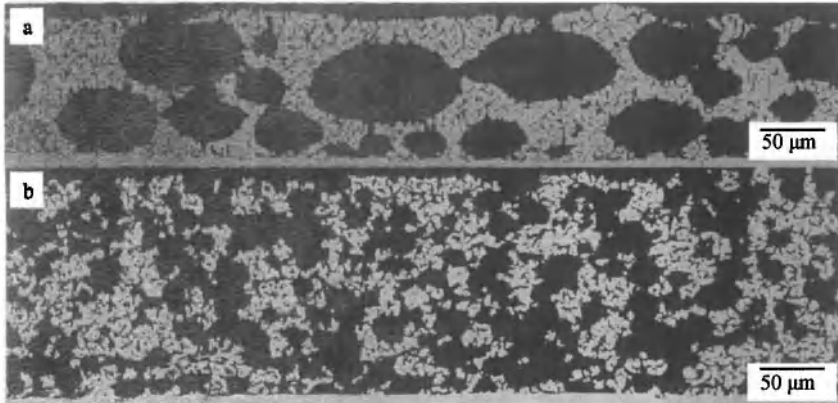


Figure 1. a) Scanning electron microscopy cross-sectional image of a section of foam from a 53% by volume 40 $\mu\text{m}$  average diameter template precursor slurry. b) Scanning electron microscopy cross-sectional image of a section of foam from a 53% by volume 15 $\mu\text{m}$  average diameter template precursor slurry.

### Application Methods

It was observed that as the spin coating velocity increased, the thickness of the resulting slurry layer decreased. An example of this is outlined in Figure 2, which displays the results of spinning a slurry mixture that is 53% by volume 40 $\mu\text{m}$  average diameter template beads over a range of velocities between 400 revolutions per minute (rpm) and 1150rpm. It was experimentally determined that changing the acceleration rate had no considerable effect on the final thickness. The thickness of the slurry layer was determined by subtracting the height of the substrate from the height of the sample measured after the slurry was applied and spun. The data suggests that there exists a velocity threshold that must be overcome to exact a significant change in the resultant slurry layer thickness. There is a 120 $\mu\text{m}$  difference between the slurry layer formed by spinning at 500rpm and 625rpm, but past 625rpm the difference between consecutive velocities is greatly decreased. As demonstrated in Figure 2, the spin coating method is ideal for reliably and easily producing uniform slurry coatings of less than 400 $\mu\text{m}$ .

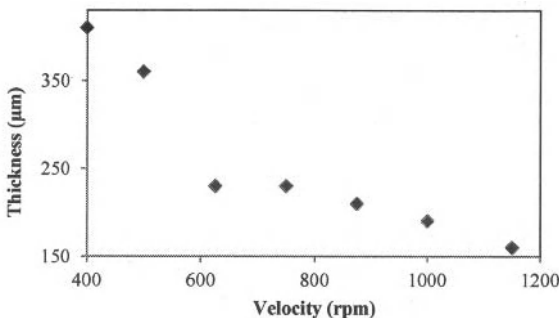


Figure 2. Plot of spin speed velocity versus slurry thickness for 53% by volume 40 $\mu\text{m}$  average diameter template material slurry

The thicknesses of the samples that were doctor-bladed were dependent on the thickness of the spacer utilized for that sample. Use of this technique led to the creation of layers of foam structures ranging from several millimeters thick to several hundred microns thick. These results conclude that this method is capable of producing a wide thickness range of slurry, and therefore wick, layers. It is worth noting that although the doctor-blading method is capable of producing thin layers within the same thickness range as those produced by spin coating; the spin coated samples were shown to have more even, uniform layers than the doctor-bladed samples.

### Microstructure Analysis

The results of this study demonstrate that tailoring the formulation of the slurry precursor by polymer sphere size and content can directly affect the porosity, effective pore diameter and the permeability of the porous structures as is expected. This is significant as these characteristics are influential in the performance of the thermal wick. By enabling control over these characteristics, the performance capabilities of the structure can be predicted by the composition of the precursor. As shown in Table I, increasing the volume fraction of the 40 $\mu\text{m}$  average diameter template actually decreased the porosity of the samples. These samples also demonstrated a decrease in theoretical permeability with an increase in the template volume

fraction, which shows a direct relationship between the porosity and the permeability as dictated by the Kozeny-Carman equation (1). Although there is no distinct correlation between the effective pore diameter and the amount of template, the normalized permeability of the foams increased with decreasing amounts of template. The effective pore size of these foams is smaller than the average size of the associated polymer sphere templates due to numerous micron and submicron-scale pores in the material surrounding them. These smaller pores, shown in Figure 1a, are a result of incomplete inter-particle sintering of the micron scale copper particles, and are the main contributor to this significant decrease in effective pore diameter. It was observed experimentally that as the target thickness of the foam approaches the size of the template, changes to the formulation to affect the porosity show increasingly negligible results. This observation infers that the achievable level of porosity is dependent on a correlation between the size of the template and the targeted thickness of the foam.

The foams created with the 15 $\mu$ m average diameter template displayed an increase in the area fraction of pore in the final structure between the 53% template and 65% template samples, but the difference in porosity between the 65% template and 73% template samples was negligible. This suggests that for this template size, there is a threshold in which increasing the volume fraction of template in the precursor slurry no longer appreciably changes the resultant porosity. This same trend was also found in the effective pore diameter and permeability data; increasing the template volume percentage past 65% did not show any real change in either parameter. It is interesting to note that increasing the volume fraction of the 40 $\mu$ m average diameter template spheres decreased the theoretical permeability; however increasing the volume fraction of the 15 $\mu$ m average diameter template beads increased the theoretical permeability. This phenomenon is likely due to the larger surface area of the foams fabricated with the smaller polymer spheres. The normalized permeability of the 15 $\mu$ m average diameter template bead samples increased with the volume fraction of pore material, which corresponds to similar increases in permeability and pore diameter.

Table I. Permeability

Average Template Diameter ( $\mu$ m)	40			15		
Template Volume Fraction	0.53	0.65	0.73	0.53	0.65	0.73
Area Fraction of Pores	0.654	0.599	0.559	0.613	0.698	0.696
Effective Pore Diameter ( $\mu$ m)	21.6	17.0	21.8	10.4	11.9	11.5
Permeability ( $\mu$ m <sup>2</sup> )	15.7	9.41	7.63	6.03	14.1	15.0
Normalized Permeability	0.135	0.130	0.0642	0.223	0.398	0.454

Comparison of the data sets from both template sizes lead to the conclusion that the template size is influential in dictating the trends that the structural characteristics follow. There is a larger discrepancy between the template size and the effective pore diameter seen with the 40 $\mu$ m average diameter template, as the large space holder template increases the inter-particle spaces within the sintered powder. The effective pore diameter of the 15 $\mu$ m average diameter template was not as drastically affected, likely due to the decreased amount of space within the inter-particle sintering, and also that the size distribution between the inter-particle spacing and the template size is much narrower. It is interesting to note that the permeability and normalized permeability values for the larger template size foams decreases with increasing amounts of template, but the opposite is true for the smaller template size foams. This observation suggests that in these size regimes, pore size has a greater effect on permeability than overall porosity.

### Conclusions

This study successfully demonstrated that by creating an adaptable process, thermal wick samples possessing a set of desirable structural features can be consistently and easily produced. The process involved the creation of a set of distinct precursor slurry formulations that could easily be altered to affect microstructural changes. By changing the formulation of the precursor slurry suspension, the pore size and pore content of thermal wick structures could be predicted and achieved. Variable application processes allowed for the formation of a precise slurry thickness over a wide range of measurement. A non-destructive method of quantifying key structural features was successfully implemented to predict the performance parameters of the open celled copper foam. Future work can be done to improve this process by evaluating the structural characteristics of the produced copper thermal wick systems by other, non-two-dimensional methods, such as tomography. Statistical data detailing the spatial distribution of the pores would greatly assist in further characterizing the permeability of the thermal wicks, as well as leading to a method to dictate how thick a formulation must be made to achieve a certain porosity, as was described previously. Data correlating the structural parameters determined by this process to actual thermal processing is necessary to validate the trends of the different formulations with respect to the evaporative cooling efficiency and overall thermal performance.

### Acknowledgements

The authors gratefully acknowledge the support of this work by the Defense Advanced Research Projects Agency (DARPA).

### References

- [1] R. Ranjan, J.Y. Murthy and S.V. Garimella, *Analysis of the Wicking and Thin-Film Evaporation Characteristics of Microstructures* (Journal of Heat Transfer, 2009),
- [2] S.J. Lin and J.H. Nadler, *Parametric Studies of a Thermal Wicking Material Using Image Analysis* (Mater. Res. Soc. Symp. Proc. Vol. 1188, 2009)
- [3] J. Banhart, *Manufacture, Characterisation and Application of Cellular Metals and Metal Foams* (Progress in Materials Science, 2001), 559
- [4] A.R. Studart et al., *Processing Routes to Macroporous Ceramics: A Review* (Jour. Am. Chem. Soc., 2006), 1771
- [5] S.J. Lin and J.H. Nadler, *Structural Characterization of Micron-scaled Reticulated Copper Foams*
- [6] J.G. Berryman and S.C. Blair, *Kozeny-Carman Relations and Image Processing Methods for estimating Darcy's Constant* (1987), 2221
- [7] S. Torquato and D. Pham, *Optimal Bounds on the Trapping Constant and Permeability of Porous Media* (Phys Rev Lett, 2004) 255505

*Characterization of Minerals, Metals, and Materials*  
Edited by: Jiann-Yang Hwang, Sergio Neves Monteiro, Chengguang Bai,  
John Carpenter, Mingdong Cai, Donato Firrao, and Buoung-Gon Kim  
TMS (The Minerals, Metals & Materials Society), 2012

# **Characterization of Minerals, Metals, and Materials**

## **Characterization of Minerals and Ceramics**

Session Chairs:  
**Doyle M. Fiona**  
**Chen-Guang Bai**

## **A NOVEL LOW-ENERGY ROUTE FOR THE EXTRACTION OF COPPER AND COBALT METALS/ALLOYS FROM THE ZAMBIAN SULPHIDE CONCENTRATES**

Yotamu Stephen Rainford Hara and Animesh Jha

The Institute for Materials Research, Houldsworth Building  
Clarendon Road, The University of Leeds, Leeds LS2 9JT (UK), England

### **Abstract**

Conventional smelting of copper – cobalt – iron sulphide concentrates result in the oxidation of cobalt and iron, which are subsequently lost into the slag. The emission of SO<sub>2</sub> bearing gas from smelting causes serious health and environmental problems. In this investigation, three different types of copper–cobalt–iron sulphide concentrates, derived from froth flotation, were investigated., the concentrates, each containing more than 40 wt % percent gangue material, were directly reduced in the presence of lime and carbon in the temperature range of 1073 K – 1573 K, for the production of an alloy containing copper, cobalt and iron. We demonstrate the basic principles of process physical chemistry for the recovery of alloy by carrying out a detailed process analysis utilising the predictions from thermodynamic equilibrium and the results from the kinetics of reduction reaction. The effect of temperature on the reduction kinetics and alloy formation were determined and analyzed in detail.

**Key words:** CoFe alloy, reduction, SO<sub>2</sub>, process chemistry

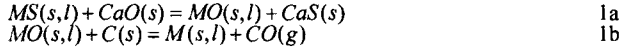
### **Introduction**

Nearly 80 % of the copper produced in the world originates from the sulphide mineral concentrates [1], roasting and smelting are the common methods employed during metal recovery from such concentrates. In Zambia, copper sulphides minerals are predominately associated with cobalt and iron sulphide minerals. Most pyrite minerals contain significant amount of cobalt as the ionic radius of Fe<sup>2+</sup> (0.076 nm) and Co<sup>2+</sup> (0.074 nm) are very close to each other [2], which may permit solid solubility in sulphide mineral matrix.

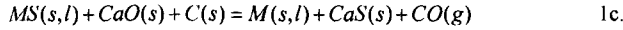
Smelting of copper - cobalt - iron sulphide concentrates result in sulphur dioxide emission and the loss of cobalt and iron into the slag via oxidation. Most of the smelting slag in Zambia contains up to 1.5 weight % and 25 weight % cobalt and iron, respectively. Cobalt is a valuable metal which is used in high temperature applications, lithium batteries, and high-temperature magnets. According to London Metal Exchange, the spot price of cobalt was \$30,000 per tonne, compared with the \$7130 per tonne price for copper and \$555/tonne for steel. Most copper-cobalt smelter slag is processed in Zambia for metal recovery at great cost by remelting the quenched smelter slag and reprocessing.

In Zambia, the Cu /Co ~10, since cobalt is nearly 5 times dearer than copper, losing significant quantities of cobalt into slag is equivalent to the loss of 50 weight % of copper into the slag phase. Froth flotation concentrates containing up to 2 weight % cobalt are treated by roasting, leaching, and electro-winning of copper and cobalt. The major disadvantage of roasting of sulphide concentrates with high gangue concentration is that the SO<sub>2</sub> bearing gas produced is too dilute for economic acid or elemental sulphur production. Release of such dilute gases into the atmosphere is unacceptable for environment and detrimental for animal and plant life. The SO<sub>2</sub> is also a green house gas with 3-4 times more radiation absorption properties than CO<sub>2</sub>.

Mineral sulphides can be directly reduced in the presence of a basic oxide and reducing agent [3-9]. The presence of a basic oxide; e.g. lime is essential as it acts as an exchange medium for S<sup>2-</sup> ions in the mineral concentrates, shown by MS, in equation 1a. Once the exchange reaction 1a, transforms a sulphide into an oxide, the reduction reaction 1b may then yield metal and CO gas, depending on the magnitude of kinetic barriers.



The overall reaction 1c is the sum of reactions 1a and 1b:



### Experimental Procedure

Nchanga, Nkana and Baluba froth flotation concentrates from Zambia were used in this investigation and mineralogical composition is shown in table 1. The reduction experiments were carried out isothermally in order to analyse the overall kinetics of reduction reaction 1c as a function of temperature. The generic experimental set up is discussed in detail elsewhere [3], which was adopted in this study, except in this investigation the thermogravimetric balance was a commercial Sartorius microbalance with the sensitivity in the sub milligram range. The reaction tube was purged with argon gas at 0.5 litres (minute)<sup>-1</sup> through out the experiment for maintaining an inert atmosphere and sweeping off the product gas mixture, so that the equilibrium in eq. 1c can be shifted in the forward direction.

Table 1 – Mineralogical composition of froth flotation concentrates in weight %

	Cu <sub>2</sub> S	CuFeS <sub>2</sub>	Cu <sub>5</sub> FeS <sub>4</sub>	CuCo <sub>2</sub> S <sub>4</sub>	FeS <sub>2</sub>	SiO <sub>2</sub>	Other
Nchanga	28.29	5.80	11.08	0.2	4.93	34.53	17.84
Nkana	0.7	8.60	5.00	2.20	10.10	19.00	54.4
Baluba	0.5	54.80	0.6	1.94	15.49	9.13	17.54

The froth flotation concentrates were mixed in stoichiometric ratios with lime and carbon by following equation 1(c). Since the Zambian concentrates contain up to 2 weight % cobalt, in order to fully understand the behaviour of cobalt during carbothermic reduction, we also designed experiments in which we mixed an additional 10 weight % CoO in the concentrate/lime/carbon mixture for tracking the elemental distribution between the slag forming gangue and the alloy phase during the course of reduction reaction. This is an important approach for the overall analysis of loss of cobalt into the gangue minerals, under reducing condition.

All reacted samples were analysed by optical microscopy, and X-ray powder diffraction and scanning electron microscopy techniques. A portion of the reacted material was ground in a mortar and pestle for X-ray powder diffraction which was carried out using the Philips X'pert machine with Cu K $\alpha$  (0.15417 nm) radiation, at an acceleration voltage of 40 KV. For microscopic analysis, a portion of the pellet was mounted in resin and left for 12 hours to cure, followed by grinding and polishing to 1  $\mu$ m, for cross-sectional examination of phases present using optical and scanning electron microscopic (SEM) analysis. For SEM, the polished surface was coated with 5 nm of platinum for minimizing the charging of the prepared surface during analysis; without a platinum coating the surface may charge and adversely affect the image quality. The energy dispersive X-ray (EDX) was carried out on several areas for obtaining a semi-quantitative chemical analysis of phases, which can be then utilized to supplement the phase analysis data from X-ray powder diffraction. The EDX data can also be transformed into an elemental map of compositions, showing the dissemination of each element over the cross-section under examination.

### Results and Discussion

The percent reduction (%R) was calculated by taking the ratio of the apparent or observed reduction in weight at time "t" due to the loss of CO gas, with stoichiometric weight loss via reaction 1c and the resulting equation is given in equation 2(a)

$$\% \text{Reduction at any time} = \frac{\text{Weight loss at any time}}{\text{Theoretical weight loss}} \times 100 \dots\dots\dots 2(a); \text{ and}$$

$$\text{Theoretical weight loss} = \frac{\%S}{100\%} \times \frac{28(\text{RMM of CO})}{32(\text{RMM S})} \times \text{Weight of Concentrate} \dots\dots\dots 2(b)$$

**Low Temperature Reduction**

Thermal gravimetric analysis (TGA) was carried out between 1073 K and 1323 K in order to study the kinetics of carbothermic reduction. The weight losses were recorded every 10 seconds at the reduction temperature. The X-ray diffraction analysis reveals that metallization was achieved by determining and comparing the relative intensities of diffraction peaks for copper, cobalt and iron metallic phases. No peaks for starting mineral sulphide concentrates were identified in the fully reacted samples, which was characterized by defining the cessation of weight loss due to reaction 1c. The completion of reaction 1c was characterized by examining the X-ray diffraction peaks for three different types of mineral concentrates reduced at 1273 K. In the powder diffraction patterns in Figures 3a to 3c, intense peaks for CaS, pure SiO<sub>2</sub> and metallic phases, and unreacted lime were observed.

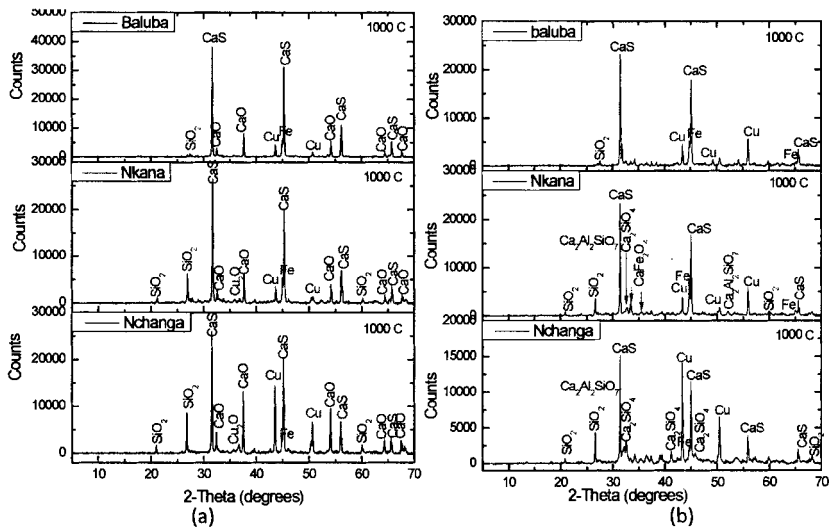


Figure 1 – The XRD powder pattern for the Nchanga, Nkana and Baluba concentrates reduced in the presence of lime and carbon at 1273 K (a) S:CaO:C = 1:2:2 (b) S:CaO:C = 1:2:1

**Effect of Temperature, Lime (CaO) and Carbon Concentration**

The carbothermic reduction of mineral concentrates in the presence of lime, is an endothermic process and is therefore dependent on the temperature. For a fixed S/CaO/C = 1:1.5:4, the reduction reactions completed within 30 minutes at 1323 K, however by comparison the reduction reactions did not reach completion even after 3 hours at 1073 K. The total percentage reduction (%R) was higher at 1273 K than at 1173 K or 1073 K, as shown in figure 2(a). As the temperature increases, the rate of carbon monoxide evolution increases due to the reaction between metal oxide and carbon, according to equation 1(c). The

unreacted mineral sulphides were not identified in the XRD pattern for the mineral concentrates reacted at and above 1223 K. However, unreacted mineral sulphides ( $\text{Cu}_2\text{S}$ ,  $\text{Cu}_5\text{FeS}_4$ ) were identified for the experiments carried out for 3 hours at 1073 K.

In order to understand the effect of lime during carbothermic reduction of mineral concentrates, the carbon to mineral concentrate ratio was fixed. The weight losses at any time were higher with increase in lime concentration, as shown in figure 2(b). Since the exchange reaction depends on the contact surface area of lime with the sulphide mineral, by increasing the ratio of CaO/sulphide the apparent rate of exchange reaction might increase, allowing a larger proportion of oxides of Cu, Fe, and Co to form. The Cu, Fe and Co oxides react with carbon and produces carbon monoxide, according to equation 1b. When the mineral sulphide concentrates were mixed with lime and carbon in ratios of S:CaO:C=1:1.5:4, 1:2:4 and 1:3:4, no unreacted mineral sulphides were identified in the powder diffraction patterns of the reaction products after 2 hours of reaction at 1273 K. However, when the reduction temperature was lowerer to 1173K and for a mixture containing S:CaO:C=1:1.5:4, the  $\text{Cu}_2\text{S}$  and  $\text{Cu}_5\text{FeS}_4$  were identified as unreacted phases, which were found to be absent at S:CaO:C=1:3:4 mixture. This comparative observation suggests that both the ratios of lime:sulphide and carbon:sulphide concentrates are critical for controlling the overall yield of metal values at a given temperature. These observations might be consistent with the chemically controlled and diffusion controlled rate steps, reported elsewhere [10]. Mineral concentrates contain gangue materials, as shown in table 1, which reduces the contact area between lime and mineral sulphides. It is therefore important to add lime at least 50 % in excess of the stoichiometric requirement for achieving near completion reaction 1c.

The percent reduction (%R) was higher for stoichiometric addition of carbon, S:CaO:C = 1:2:1 than at mixtures of S:CaO:C = 1:2:2 and S:CaO:C = 1:2:4. At lower stoichiometric ratio of C: CaO both the  $\text{SO}_2$  and  $\text{CO}_2$  gases may contribute to overall weight loss, which may then exaggerate the maximum expected reduction via reaction 1c. The XRD analysis in figure 1(b) shows that metallization was not complete due to the presence of calcium ferrite in the reacted sample. At lower concentrations of carbon, the propensity for  $\text{SO}_2$  formation increases according to equations 3. Any calcium sulphate which may form will decompose to yield lime and  $\text{SO}_2$  through reduction calcination [11].  $\text{SO}_2$  is heavier than CO causing higher weight loss.



The overall % reduction were similar at 1273 K for S:CaO:C = 1:2:2 or = 1:2:4, as shown in figure 3(a). However, the % reduction at S:CaO:C=1:2:4 were higher than at S:CaO:C = 1:2:2 at 1173 K as can be seen in figure 3(b). In order to achieve near 100% conversion of metal sulphide into metal, it is essential to increase the contact surface area for carbon reduction which means the ratio of carbon to metal sulphide must be optimised.

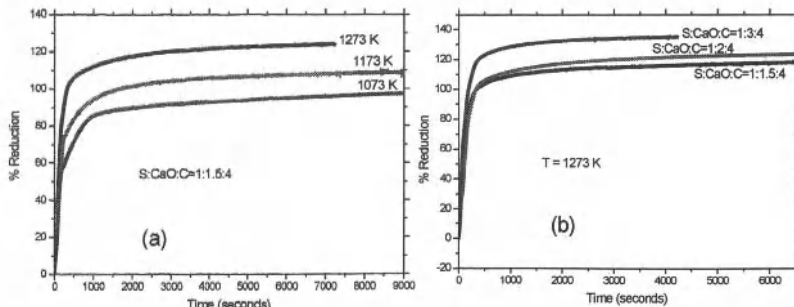


Figure 2- (a) Effect of temperature at S:CaO:C=1:1.5:4 and (b) Effect of changing CaO concentration at 1273 K and during carbothermic reduction of Nchanga mineral concentrate

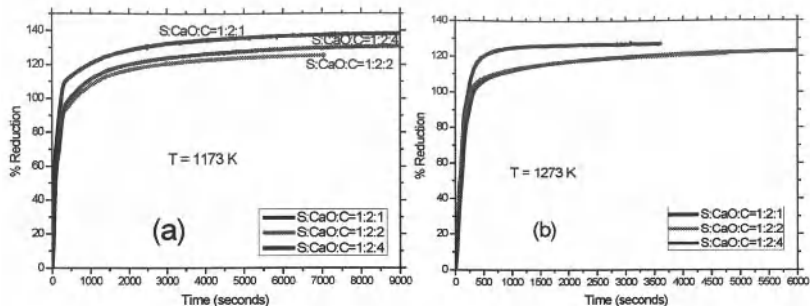


Figure 3 - Effect of changing carbon concentrations during carbothermic reduction of Nchanga mineral concentrates (a) at 1173 K and (b) at 1273 K

### High Temperature Reduction at 1573 K

Thermal gravimetric analysis was not carried out at high temperatures due to the limitation on the thermogravimetric balance. For the analysis of reduction reactions at 1573K, the mineral concentrates mixed with lime and carbon, were heated at 1573 K in an elevating hearth furnace. The initial and final weights of the samples were taken before and after the experiment, in order to determine the overall weight loss. Mineral concentrates mixed with lime and carbon were heated from room temperature to 1573 K and held at this temperature for 3 hours, after which the furnace was turned off and the crucible containing the sample was taken out of the furnace and cooled in air. In another experiment, the mineral concentrates were first isothermally reduced at 1273 K for 2 hour, followed by reheating at 1573 K for 3 hours in order to see further phase changes which may occur above the melting point of copper rich alloy.

When Nchanga, Nkana and Baluba mineral concentrates were reduced for 2 hours at 1273 K, a portion of the reacted sample was analysed by X-ray diffraction, cobalt and excess lime were identified from XRD patterns, as shown in figure 4a. When the remaining samples which were reduced at 1273 K, were heated and held at 1573 K for 3 hours, cobalt was not identified in the XRD patterns in all samples. In addition, the excess lime was completely absent from the samples after heating at 1573 K. This was due to the formation of calcium silicate compounds, as shown in figure 4b. The absence of cobalt metal peaks from the XRD patterns can be explained as a result of the formation of CoFe alloy phase in figure 4b. Formation of CoFe phase is possible because of the mutual solubilities of elemental metals increase with temperature. Iron and cobalt have high melting points, but they exhibit extensive solid solubility in each other [12, 13].

Copper and cobalt sulphides in figure 4(b) were identified in the Nchanga and Nkana samples after reheating the sample at 1573 K. The reason that residual copper/cobalt sulphides are present in Figures 4b, might appear to be a product of internal sulphide phase formation via metallic copper and cobalt in the presence of a dicalcium silicate slag. The  $\text{Ca}_2\text{SiO}_4$  forms as a result of CaS reaction with the  $\text{CaO}\cdot\text{SiO}_2$  which then releases the  $\text{S}^{2-}$  ions leading to matte formation ( $\text{Co}_9\text{S}_8$  and  $\text{Cu}_2\text{S}$ ). In the presence of more than the stoichiometric amount of lime and carbon, the sulphide matte formation does not occur because the excess lime participates in calcium silicate formation as well as in the sulphide exchange reaction 1a.

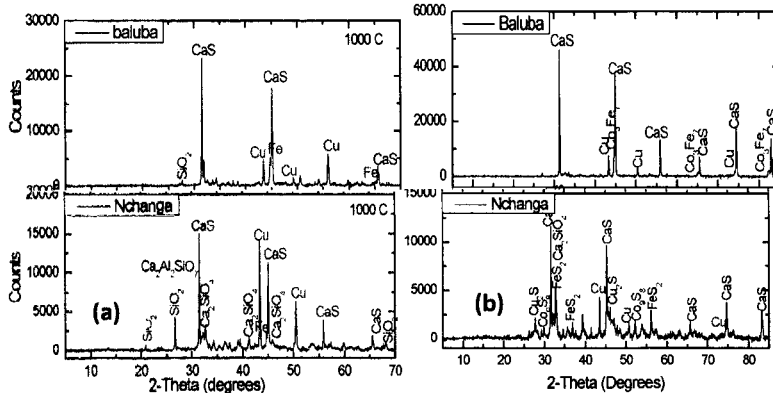


Figure 4 - Carbothermic reduction of mineral concentrates (a) reduced at 1273 K, (b) reduced samples reheated to 1573 K for 2 hours (S:CaO:C= 1:1.8:2.2)

#### Metal / Alloy Formation during Carbothermic Reduction

The SEM - EDX analysis was carried out in order to confirm the presence of phases obtained during XRD analysis and the results are shown in table 2. Since the unit cell dimensions of  $\gamma$ -iron [0.3647 nm] is comparable with that of the high-temperature allotrope of cobalt [0.3544 nm], we expect extensive mutual solubility in liquid and the solid solutions, which is why the alloys of Fe and Co form CoFe. The metallic copper similarly shows reasonably high solubility in both in  $\gamma$ -iron and cobalt. The EDX analysis confirms the presence of this alloy as shown in table 2.

The metallic phases in the back-scattered electron image in SEM appear bright. Semi quantitative results in all analysed areas of the reacted samples are compared in table 2, which correspond well with the predictions from the binary Co-Fe, Cu-Fe, and Co-Cu phase diagrams. The maximum solubility of copper in cobalt is about 20 weight % at 1643 K, whereas that of cobalt in copper is nearly 10 weight % at 1385 K [12-14]. Maximum solubility of iron in copper and copper in iron is 4.1 % and 15 weight %, respectively [14]. The results in table 2 show the maximum solubility of iron in copper and copper and iron are 1.79 weight % and 5.13 weight %, respectively. From the semi quantitative analysis data in table 2, it is possible to produce copper over 96 weight % purity in a single step. Elemental mapping in figure 5 further shows that the reduced metals (copper, cobalt and iron) have limited solubility in each other at 1273 K. Figure 5 also shows that sulphur was tied up with calcium which was identified as CaS during X-ray diffraction analysis. Mass balance in spectrum 2 of table 2 further shows that there is no sulphur loss during metal / alloy production.

The EDX analysis of the sample, reduced at 1273 K and then reheated at 1573 K, showed the areas with 43.78 weight % Fe, 38.44% Co and 12.58 weight % Cu. Elemental mapping in figure 6 shows that Co distributed with Fe because of higher solubility between these elements.

Table 2- EDX Semi quantitative results for some selected areas, Nchanga  
(S:CaO:C=1:1.8:1.8) reduced at 1273 K

Area	Cu	Co	Fe	Ca	S	O	Si
A	11.49	81.66	2.77	0.9	0.86	1.63	
B	7.01	89.94	-	0.9	0.66	1.63	
C	5.16	57	22.49	4.09	3.49	3.781	
D	5.13	-	93.46	1.38	0.74		
E	0.52	-	0.39	-	-	54.91	44.32
F	93.49	0.32	2.49	-	0.44	3.49	-
G	0.26	-	0.63	-	-	56.63	44.40
H*( Ni = 2.25 %)	91.78	-	1.68	0.16	0.53	1.82	1.18
J	96.36	0.95	1.79	0.26	0.44	-	-
Spectrum 1	13.62	2.41	4.56	20.48	13.62	31.65	10.21

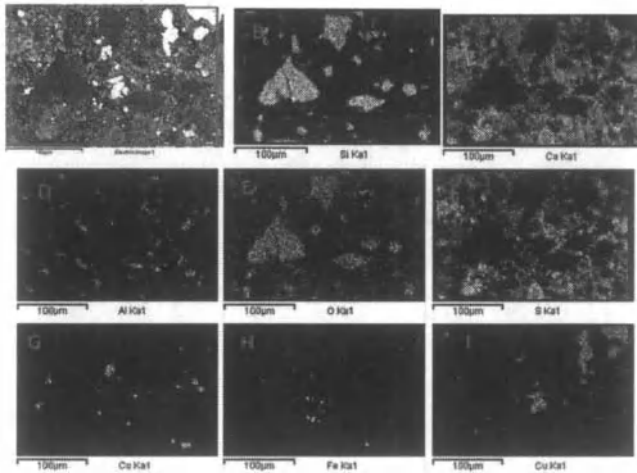


Figure 5 – Backscattered elections (BSE) image for the Nchanga concentrate which was reduced at 1273 K with 10% CoO added to the mineral concentrates before reduction in the mixture (S:CaO:C=1:1.8:1.8). (A) sample area investigated, (B) Ca distribution, (C) C distribution, (D) Co distribution, (E) Fe distribution, (F) Cu distribution.

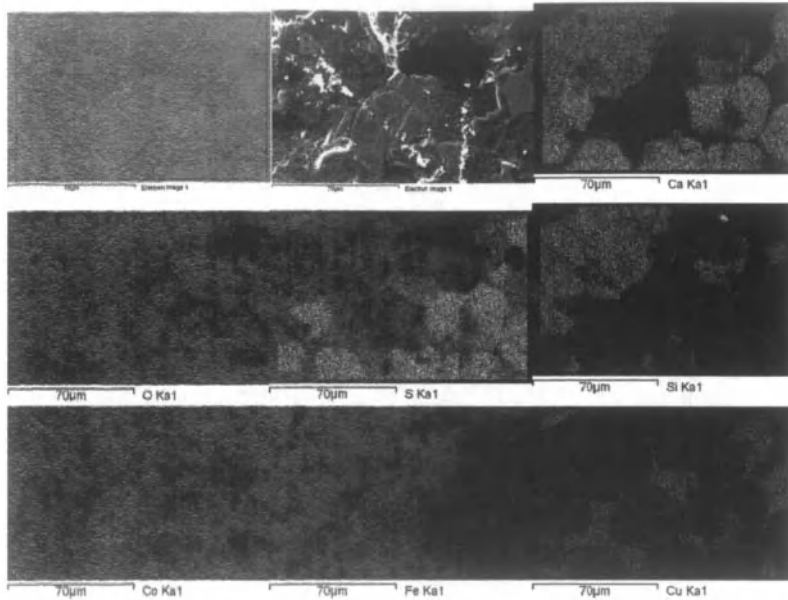


Figure 6 – Elemental mapping showing distribution of elements for Nchanga concentrate (S:CaO:C=1:1.8:1.8), reduced at 1273 K and reheated at 1573 K, with 10% CoO added to the mineral concentrates before reduction in the mixture (A) sample area investigated under (A) BSE imaging, (B) SEM imaging.

### Conclusions

- The carbothermic reduction of sulphide mineral concentrates in the presence of lime at different S:CaO:C ratios were investigated in the temperature range 1073 K – 1573 K. The percentage reductions from 1073 K to 1323 K were found to be dependent on temperature. Metallization was incomplete even after 3 hours at 1073 K which reached completion at 1323K within 30 minutes.
- The process of metallization depends on S:CaO and S:C ratios, the percentage reduction was higher at S:CaO:C = 1:3:4 than at S:CaO:C=1:1.5:4, as shown in figure 2(b). The metallization was incomplete at stoichiometric addition of carbon (S:CaO:C=1:2:1) due to formation calcium ferrite, as shown in figures 1(a) and 1(b).
- Pure silica and excess lime were found in all samples reacted at temperatures below 1323 K but the presence of excess lime yielded complex calcium silicate for the experiments carried out at 1573 K.
- Both the XRD and EDX analyses confirmed the presence of Cu, Co and Fe phases at temperatures below 1323 K, while the Cu-rich and Co-Fe phases formed at 1573 K, as shown in the elemental maps in figures 5 and 6.
- The EDX analysis shows that the composition of alloys formed during carbothermic reduction of mineral concentrates agrees well with the binary metallic phase equilibria. Some analysed areas using EDX analysis shows that the copper with a purity of over 96 weight % was produced in a single step during carbothermic reduction of mineral concentrates in the presence of lime.

### Acknowledgements

The authors would like to thank the Institute of Materials, Minerals and Mining (IOM<sup>3</sup>), and the Copperbelt University in Zambia for the financial support

### References

1. Davenport, W.G.L., et al., *Extractive Metallurgy of Copper (4th Edition)*. Chemical, Petrochemical & Process. 2002: Elsevier. 1-452.
2. Jha, A., S. Tang, and A. Chrysanthou, *Phase equilibria in the metal-sulfur-oxygen system and selective reduction of metal oxides and sulfides: Part I. The carbothermic reduction and calcination of complex mineral sulfides*. Metallurgical and Materials Transactions B: Process Metallurgy and Materials Processing Science, 1996. **27**(Compendex): p. 829-840.
3. Jha, A., P. Grieveson, and J.H.E. Jeffes, *Investigation on the carbothermic reduction of copper sulfide minerals: Kinetics and thermodynamic considerations*. Scandinavian Journal of Metallurgy, 1989. **18**(Compendex): p. 31-45.
4. Igiehon, U.O., *Carbothermic reduction of complex sulphides*, in *Department of materials*. 1990, Imperial College of Science: London.
5. Jha, A., U.O. Igiehon, and P. Grieveson, *Carbothermic reduction of pyrrhotite in the presence of lime for production of metallic iron. Part I. Phase equilibria in the Fe-Ca-S-O system*. Scandinavian Journal of Metallurgy, 1991. **20**(Compendex): p. 270-278.
6. Jha, A., B.S. Terry, and P. Grieveson. *Physical chemistry of carbothermic reduction of sulphide minerals: 'a novel metal production route'*. in *Proceedings of the International Conference on Extractive Metallurgy of Gold and Base Metals, October 26, 1992 - October 28, 1992*. 1992. Kalgoorlie, Aust: Publ by Australasian Inst of Mining & Metallurgy.
7. Jha, A. and P. Grieveson, *Carbothermic reduction of chalcopyrite in the presence of lime. Part III. Production of iron and copper*. Scandinavian Journal of Metallurgy, 1992. **21**(Compendex): p. 127-137.
8. Jha, A. and P. Grieveson, *Carbothermic reduction of pyrrhotite in the presence of lime for the production of metallic iron*. Scandinavian Journal of Metallurgy, 1992. **21**(Compendex): p. 50-62.
9. Rankin, W.J. and T.P. Hall, *LIME-ENHANCED CARBOTHERMIC REDUCTION OF CHALCOPYRITE*, in *Epd Congress 2009, Proceedings*, S.M. Howard, Editor. 2009. p. 817-827.
10. Habashi, F., ed. *Kinetics of metallurgical processes*. 1999, Quebec : Métallurgie Extractive.
11. E.T, T., *Physical chemistry of high temperature technology* 1980: Academic Press 290 - 302.
12. Anon, *Cobalt monograph*. Cobalt Monograph. 1960, Brussels, Belgium: Centre d'Information du Cobalt. 515.
13. Betteridge, W., ed. *Cobalt and its alloys*. 1 ed. Industrial metals 1982, Ellis Horwood: Chichester. 43 - 48.
14. Hasebe, M. and T. Nishizawa, *Calculation of phase diagrams of the iron-copper and cobalt-copper systems*. CALPHAD: Computer Coupling of Phase Diagrams and Thermochemistry, 1980. **4**(2): p. 83.

## **STRUCTURAL AND CHEMICAL MODIFICATION OF SULFIDE MINERAL SURFACES BY HIGH-POWER NANOSECOND PULSES**

Igor Zh. Bunin, Valentine A. Chanturiya, Alexey T. Kovalev,  
Irina A. Khabarova, Elizaveta V. Koporulina

Research Institute of Comprehensive Exploitation of Mineral Resources RAS;  
Russian Academy of Sciences, 4 Kryukovsky Tupik, IPKON RAS; Moscow, 111020, Russia

Keywords: Sulfide mineral, High-power nanosecond pulses, Electric breakdown channels,  
Electric breakdown channels, Micro- and Nanophases, Sorption, Electrode potential

### **Abstract**

This paper presents new theoretical and experimental data on possible mechanisms for the formation of micro- and nanophases on the surfaces of sulfide minerals under the effect of high-power nanosecond electromagnetic pulses (HPEMP). The gas outflow from nanosecond breakdown channels of sulfide minerals under the effect of HPEMP is considered, with allowance for the condensation of iron vapors. The condensation of matter in an outflowing jet is shown to be an effective mechanism for structural and chemical transformations of sulfide surfaces. It is established that electrode potential of pyrrhotite is moved together in the negative party owing to formation of iron oxides (hydroxides) and iron sulfates by HPEMP, that provides decrease of xanthate sorption and reduction flotation extraction of this sulfide, whereas electrode potential of pentlandite gets more positive values at the expense of additional formation of element sulfur, that causes increase of xanthate sorption and, as a consequence, increase of nickel sulfide extraction.

### **Introduction**

The prospects for applying pulsed power technologies in the mineral processing in order to increase the contrast between the floatation properties of raw minerals dictates the need to perform special studies of the effect of high-power nanosecond electromagnetic pulses on the structural state, phase composition, and physicochemical properties of surfaces of sulfide minerals as the principle carriers of precious metals [1–3].

X-ray analysis of pyrite specimens on a Rigaku D/MAX 2200 - diffractometer showed that weak peaks of hematite  $\text{Fe}_2\text{O}_3$  ( $d = 2.69$  and  $2.52$  Å) are formed on X-ray photographs of specimens under the nonthermal [4, 5] action of HPEMP [6]. This indicates a substantial local temperature rise at the points of contact between mineral particles and in regions of inhomogeneity on their surfaces [7–9]. Such an effect was observed during the radiation–thermal processing of pyrite in [10]: the phase transition of  $\text{FeS}_2$  pyrite into  $\text{Fe}_2\text{O}_3$  magnetic hematite occurred under the effect of an accelerated electron flow.

The morphology, sizes, and elemental composition of neoformations on sulfide surfaces have been studied by scanning electron microscopy (SEM, LEO 1420 VP), X-ray spectral microanalysis (XRMA, EDS, INCA Oxford 350 X-ray microanalysis system), and scanning probe microscopy (AFM, INTEGRA Prima, NT-MDT). The results of SEM–XRMA investigations of the surface structure of pyrite, arsenopyrite, pyrotine, and pentlandite indicate the formation of defects (breakdown channels and microcracks) and the forced formation of new

micro- and nanophases on sulfide surfaces, due to electric pulse processing. In addition to intensity peaks corresponding to Fe, Ni, As, and S, a pronounced peak corresponding to oxygen has been traced in the X-ray spectrum of a surface from the region of localization of neoformations, possibly indicating the formation of autonomous and nonautonomous phases, presumably oxides (hydroxides) of iron and anhydrous sulfides of iron (II/III) [1–3, 6].

This work presents new theoretical and experimental data on possible mechanisms for the formation of micro- and nanophases on the surfaces of sulfide minerals under the effect of high-voltage nanosecond pulses. A model of heated gas outflow from the nanosecond breakdown channels of sulfide minerals (pyrite) under the action of HPEMP was considered in [11]. It was shown that the gas outflow from such a channel can be an additional damaging factor in the electric pulse disintegration of finely dispersed mineral complexes. The possible condensation of vapors of matter flowing out of a breakdown channel was not, however, taken into account in considering an outflow of evaporated matter from a breakdown channel in pyrite. At the same time, when a jet flows out of a breakdown channel into air of normal density, it expands, cools, and the conditions for vapor condensation are met.

#### Condensation of Matter during Gas Outflow from Nanosecond Breakdown Channels of Sulfide Minerals

This work considers gas outflow from a channel with allowance for iron vapor condensation. Calculating the complete set of equations for the nonequilibrium kinetics of formation and growth of iron clusters and estimating the condensed iron particle distribution over size in the process of jet expansion require substantial computational resources [11]. The concentration of nuclei of critical size was therefore calculated using the classical evaporation–condensation model [12]. According to [12], the rate of formation of these particles is

$$\frac{dn_{cr}}{dt} = I_0 n^2 \exp\left\{-\frac{4\pi\sigma r_{cr}^2}{3kT}\right\}, \quad (1)$$

$$I_0 = \sqrt{\frac{2\sigma}{\pi m}} n_b^{-1},$$

where  $n_{cr}$  is the concentration of particle of critical size,  $r_{cr} = \frac{2\sigma}{kTn_b \ln S}$  is the critical radius,  $n$  is the concentration of iron atoms in a gas phase,  $n_b$  is the concentration of iron atoms in a gas phase,  $m$  is the iron atom mass,  $\sigma$  is the surface energy of the condensed phase,  $S = n/n_0$  is the oversaturation at the given temperature,  $n_0 = n_b \exp(-H/kT)$  is the equilibrium vapor concentration, and  $H$  is the sublimation energy per one atom. The energy released during condensation is transferred to the ambient gas. The particles of condensed matter are transported together with the gas flow. The thermodynamic properties of iron are taken from [13]. As for the rest, the problem of gas outflow was solved according to the scheme we used in [11].

Evaporation produces an outflow of gas from the breakdown channel, the gas being a mixture of monoatomic iron and sulfur. The radius of the breakdown channel is 4  $\mu\text{m}$ , and its length is 160  $\mu\text{m}$ ; the initial gas density is  $0.3 \times 10^3 \text{ kg/m}^3$ , and the initial density of the gas energy in the channel is  $10^7 \text{ J/kg}$ . The dimensions of the calculation region are  $41 \times 160$  points for the breakdown channel (the analytical grid) and  $205 \times 321$  points beyond the channel (a grid that

narrows as it approaches the channel opening). Under normal conditions, the outflow is into the air. The density of the condensed matter in each cell was calculated as  $n_{cr}m/V$ , where  $V = 2\pi r\Delta r\Delta z$  is the cell volume.

The jet flowing out of the channel first expands toward the low-density region, carrying and dispersing the air in front of it. During  $\sim 100$  ns, the profiles of the channel matter density and those of the total density (including the air involved in the motion) are almost identical. The jet then starts to decelerate and a shock wave of air is formed in front of it. At  $t = 300$  ns, all of the channel matter is behind the jet front, as can be seen from a comparison of the total density profile and the profile of the channel matter density (Figure 1).

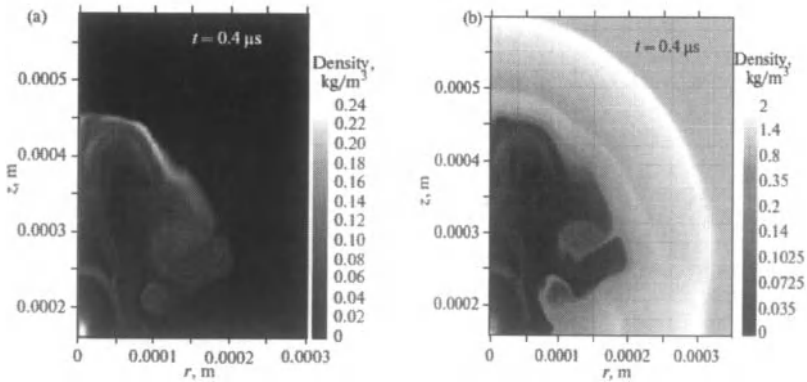


Figure 1. Density of the matter flowing out of a breakdown channel (a) and the total density with allowance for air (b). A shock wave propagates in the air while the gas flowing out of the channel remains behind its front. The coordinate of the channel opening is  $z = 0.00016$  m (as measured from the back channel wall). Here and below, only a part of the calculation region beyond the breakdown channel is shown.

Condensation begins predominantly in the rarefaction region behind the jet front. When all of the channel matter is behind the front and the jets starts to defragment, the process of condensation then covers the entire jet. It can be seen from the temperature distribution (Figure 2a; maximum temperature  $>5000$  K) and density of the condensed matter (Figure 2b) in the jet region at  $t = 0.8$   $\mu$ s that condensation is maximum in the minimum temperature range. In the region where the temperature is less than 1000 K, almost all of the iron vapors are condensed. The heavy white line limits the region with the channel matter.

As the jet disintegrates, it undergoes defragmentation due to local vortices. In Figure 3, which presents the distribution of the condensed vapor density, we can see the motion of the fragments left within the calculation region at  $t = 2-8$   $\mu$ s. The degree of condensation at this stage approaches 1 everywhere except the near-axis region, which the residual gas flowing out of the breakdown channel continues to enter. The characteristic size of the fragments is 0.01–0.1 mm, and the characteristic density of the condensed vapors in these fragments is 0.01–0.02  $\text{kg m}^{-3}$ . The sizes of the condensed particles can be determined as follows: if each fragment condenses

into an isolated drop, the characteristic size of these drops has to be  $0.1\text{--}3\ \mu\text{m}$ . The radius of the positioning of the iron condensate left near the mineral surface is no larger than  $0.3\ \mu\text{m}$  (Figure 3). This value can be considered an estimate of the size of the region around the breakdown channel opening where condensed iron particles precipitate. Since the calculations were performed in a two-dimensional axisymmetric geometry rather than in a three-dimensional geometry, the obtained estimates are qualitative. We should nevertheless note that they are in agreement with the experimental studies.

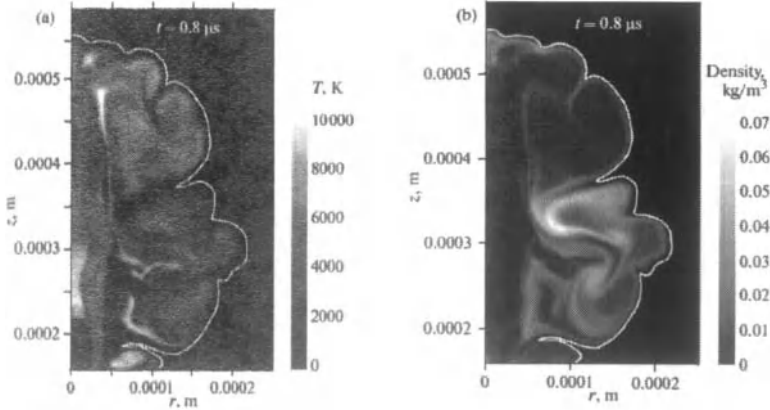


Figure 2. Temperature distribution (a) and density of the condensed matter (b). The high-temperature region ( $>12000\ \text{K}$ ) near the channel opening is not shown.

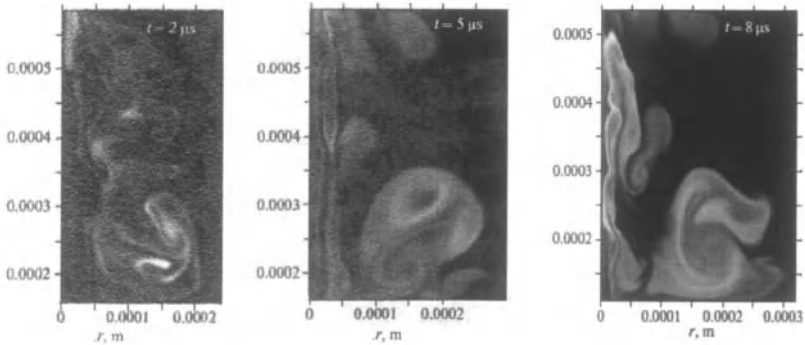


Figure 3. Distribution of condensed matter at the late stage of outflow from the channel. The color scale is the same as in Figure 2. For the sake of qualitative comparison, the density corresponding to the maximum brightness (on the order of  $0.02\ \text{kg m}^{-3}$ ) is slightly different for these images.

## Experimental

### Structural and Chemical Transformations of the Sulfide Mineral Surfaces

Three types of neoformations corresponding to the processes of structural and chemical transformations of the sulfide mineral surfaces due to the HEMP effect were revealed on the sulfide surfaces by means of analytical electron microscopy (Figure 4).

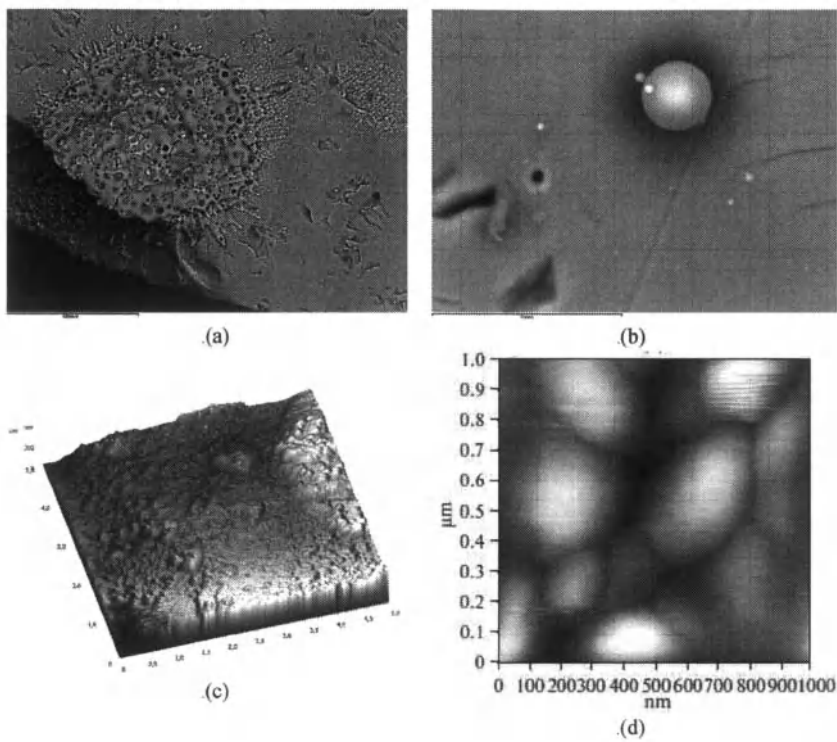


Figure 4. Neoformations on the surface of chalcopyrite (a), (b) and pyrrotine (c), (d), formed under the effect of nanosecond HPEMP: (a) extended ( $\sim 100 \mu\text{m}$ ) coatings and (b) spherical formation (white ball); (c) thin film with a thickness of less than 100 nm. Scale bars are  $100 \mu\text{m}$  (a),  $10 \mu\text{m}$  (b); scanning fields are  $5 \times 5 \mu\text{m}$  (c) and  $1 \times 1 \mu\text{m}$  (d); height  $Z < 100 \text{ nm}$ ; SEM (a), (b), AFM (c), (d)

The first of these form dense, extended ( $\sim 100 \mu\text{m}$ ) coatings that are fractured and porous, with local swells of beadlike and irregular spherical shapes that, in some cases, decorate the breakdown channel openings (Figure 4a). The second phase, represented by spherical formations with sizes of  $3 \mu\text{m}$  and lower (Figure 4b), is found mainly near the breakdown regions, though in some cases it is observed at some distance from the destructive zones. Superthin (low dimensional) films of the third phase (Figure 4c and 4d), which hypothetically consist of

anhydrous sulfides of iron (II/III) and can be diagnosed by scanning probe microscopy (SPM–AFM), uniformly cover the sulfide surface mainly in the regions where the craters and erosion holes of breakdown channels and microcracks are localized.

#### Electrochemical and Flotation Properties of Pentlandite and Pyrrhotite

Investigations of change of physical-chemical properties of sulfide minerals, depending on conditions and parameters of electromagnetic pulse processing, have been conducted on samples of pyrrhotite  $Fe_{1-x}S$  and pentlandite  $(Fe,Ni)_9S_8$  extracted from copper-nickel pyrrhotite-bearing ore of Norilsk Industrial Area.

Electrode potential of minerals has been determined by method of potentiometric titration with the simultaneous control of mineral potential and pH. Working electrodes have been made of clean pyrrhotite and pentlandite. A comparison electrode was silver-chloride sated electrode. pH-value has been changed by submission of a lime solution, interval of pH was 5.5-11.0. pH has been determined through the pH-meter (Multitest IPL-103). The dependence of electrode minerals potential from pH has been investigated previously for the raw pyrrhotite and pentlandite samples, then the minerals have been subjected to electromagnetic pulse processing and the measurements have been spent repeatedly. The root-mean-square mistake of measurements was 1.5-2 %.

In Figure 5 the experimental data about the effect by HPEMP on electrochemical properties (electrode potential) of pyrrhotite and pentlandite are submitted, according to which electrode potential of pyrrhotite is moved together in the negative party at pulse processing ( $10^3$  pulses) (Figure 5a). The maximal difference of electrode potential meanings before and under processing ( $\Delta\varphi_{max}$ ) equal to 73 mV in alkaline environment at pH 10. Electrode potential of pentlandite gets more positive values at processing ( $10^3$  pulses) at pH 5.5-8.7 (Figure 5b). In a range pH from 8.7 to 11 electrode potential of pentlandite processed HPEMP is a little bit reduced (on 10 mV).

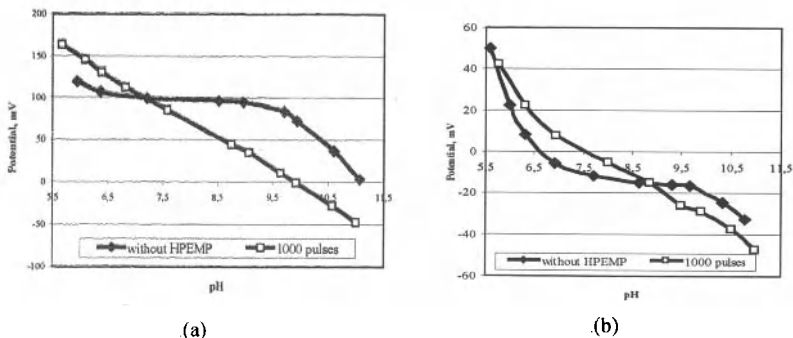


Figure 5. The effect of HPEMP on electrode potential of pyrrhotite (a) and pentlandite (b), white points – HPEMP-treatment; black points – without treatment

As electrode potential of a mineral surface determines substantially an energetic state of a surface and its sorption properties, so the effect by HPEMP on potassium butyl xanthate (BX) sorption on the surface of researched minerals has been investigated. Minimal sorption of BX

(decrease on 17 %) on pyrrhotite surface has been found out at  $10^3$  pulses (Figure 6a). It will be coordinated to the data about the effect by HPEMP on electrode potential of pyrrhotite: sharp shift of electrode potential of pyrrhotite in negative meanings area (the Figure 5a) results in decrease of anionic collector sorption on a mineral. The maximum of BX sorption on pentlandite has been found out at  $10^3$  pulses (Figure 6b).

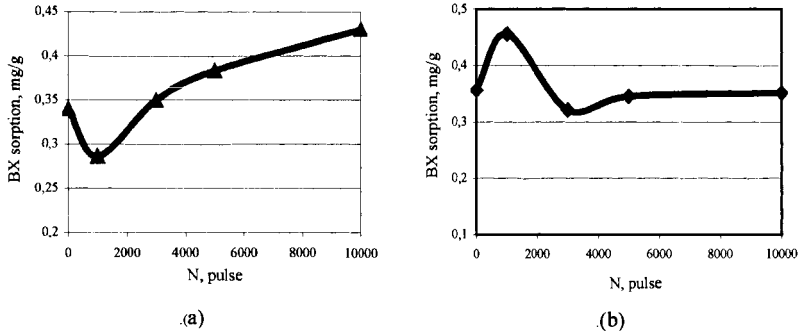


Figure 6. The effect of HPEMP-treatment on BX sorption on pyrrhotite (a) and pentlandite (b)

Thus, it is established, that electrode potential of pyrrhotite is moved together in the negative party owing to formation of iron oxides (hydroxides) and iron sulfates by HPEMP ( $10^3$  pulses), that provides decrease of xanthate sorption and reduction flotation extraction of this sulfide (Figure 6), whereas electrode potential of pentlandite gets more positive values at the expense of additional formation of element sulfur, that causes increase of xanthate sorption and, as a consequence, increase of nickel sulfide extraction.

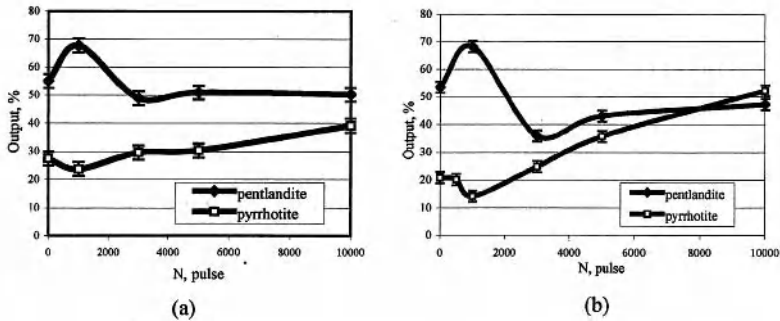


Figure 7. The effect of HPEMP on floatability of pentlandite and pyrrhotite with BX alone (a) and with DMDC + BX combination (b) at pH 10.5

Flotation activity of pyrrhotite with BX changes nonlinearly at increase of pulses number. In the field of low intensity of the pulse effect ( $10^3$  pulses), decrease of mineral floatability is observing (Figure 7a). Floatability of pyrrhotite rises with increase of number of impulses, owing to

elevation of amount of elementary sulfur on its surface. The maximal output of pentlandite is reached at  $10^3$  pulses (Figure 7a) owing to elevation of amount of elementary sulfur on its surface and increases of electrode sulfide potential. The preliminary electropulse treatment of pyrrhotite and pentlandite and introduction sodium dimethyldithiocarbamate (DMDC) at flotation (Figure 7b) results in increase of selectivity of flotation separation of minerals ( $\Delta\epsilon = 35\%$  without processing by HPEMP,  $\Delta\epsilon = 55\%$  at  $10^3$  pulses).

### Summary

This work considers only the process of iron condensation, while that of sulfur was not analyzed. In the rarefaction region where density and temperature decline drastically, sulfur condensation is also possible. In addition, reactions between sulfur and iron are also possible in both the gaseous and the condensed state, this being accompanied by the formation of different compounds (equilibrium and nonequilibrium), along with the physical condensation (precipitation) of sulfur on iron particles. Iron particles can interact with atmospheric oxygen only at the outer boundary of the jet or after the jet decelerates, disintegrates, and mixes with the air, i.e., at  $t > 1 \mu\text{s}$ . Taking the extreme thermodynamic nonequilibrium of the conditions of the electric pulse action into account, a great number of intermediate oxide phases with different compositions (and probably chalcogenide semiconductor glasses as well [14]) can be formed during the oxidation of iron-containing sulfides [1–3].

The effect of consecutive oxidation of pyrrhotite surface with formation of iron oxides (hydroxides) and iron sulfates has been established by the electromagnetic pulse effect, whereas the formation of element sulfur has been observed on pentlandite, that provides contrast of electrochemical, sorption and flotation properties of minerals.

### Acknowledgements

The authors acknowledge the financial supports from the RFBR (Grant no 11-05-00434-a) and the Program of the Scientific School of Russian Federation (Grant no NSh-3184.2010.5).

### References

1. V.A. Chanturiya, T.A. Ivanova, I.A. Khabarova, and M.V. Ryazantseva, "Effect of ozone on physical-chemical and flotation properties of surface of pyrrhotite under nanosecond electromagnetic pulse treatment," *Journal of Mining Science*, 43 (1), (2007), 83-90.
2. T.A. Ivanova, I.Zh. Bunin, I.A. Khabarova, "On the characteristic properties of oxidation of sulfide minerals exposed to nanosecond electromagnetic pulses," *Bulletin of the Russian Academy of Sciences: Physics. Allerton Press, Inc.*, 72 (10), (2008), 1326-1329.
3. V.A. Chanturiya, et al., "Effect of powerful nanosecond electromagnetic impulses on surface and flotation properties of carbonate-bearing pyrite and arsenopyrite," *Journal of Mining Science*, 44 (5), (2008), 518-530.
4. V.A. Cherepenin, "Relativistic multiwave oscillators and their possible applications," *Phys-Usp*, 49 (10), (2006), 1097-1102.
5. I.Zh. Bunin, N.S. Bunina, V.A. Vdovin, et al., "Experimental Studies of Non-Thermal Action of High-Power Electromagnetic Pulses on Resistant Gold-Containing Mineral Products,"

*Bulletin of the Russian Academy of Science: Physics (Izvestiya RAS: Ser. Phys.)*, 65, (12), (2001), 1788-1792.

6. I.Zh. Bunin, A.T. Kovalev, and E.V. Koporulina, "On theory of disintegration of fine-disseminated mineral complexes under high-power nanosecond pulses," *Phase transition, ordered state and new materials*, 2 (3), (2010). Available from: <http://ptosnm.ru>.

7. V.A. Chanturiya, I.Zh. Bunin, A.T. Kovalev, "Field-Emission Properties of Sulfide Minerals under High-Power Nanosecond Pulses," TMS2008 137<sup>th</sup> Annual Meeting & Exhibition Supplemental Proceedings, Vol. 2: Characterization of Minerals, Metals, and Materials, USA: TMS, (2008), 27-32.

8. V.A. Chanturiya, I.Zh. Bunin, A.T. Kovalev, "Energy Concentration in Electrical Discharges between Semiconducting Sulfide Mineral Particles under High-Power Nanosecond Pulses," TMS2009 138<sup>th</sup> Annual Meeting & Exhibition Proceedings, EPD Congress 2009, Characterization of Minerals, Metals, and Materials, Part: Characterization of Processing, USA: TMS, (2009), 41-46.

9. V.A. Chanturiya, I.Zh. Bunin, A.T. Kovalev, "Nanosecond Electrical Discharge between Semiconducting Sulfide Mineral Particles in Water," TMS2010 139<sup>th</sup> Annual Meeting & Exhibition Proceedings, EPD Congress 2010, Characterization of Minerals, Metals, and Materials, Part: Characterization of Micro-, Nano-, and Thin Films, USA: TMS, (2010), 257-264.

10. G.R. Bochkarev, Yu.P. Veigelt, and V.I. Rostovtsev, "Phase conversion in sulfide ores on combined irradiation and heating," *Journal of Mining Science*, 36 (1), (2000), 81-86.

11. I.Zh. Bunin, V.A. Chanturiya, A.T. Kovalev, I.A. Khabarova, and E.V. Koporulina, "Application of High-Power Nanosecond Pulses to Flotation Separation of Sulfide Minerals," TMS2011 140<sup>th</sup> Annual Meeting & Exhibition Proceedings, EPD Congress 2011, Characterization of Minerals, Metals, and Materials, Part: Mineral Processing and Analysis, USA: TMS, (2011), 47-54.

12. Ya.I. Frenkel, "Kineticheskaya teoriya zhidkostei (Kinetic Theory of Liquids)," Leningrad: Nauka, (1975).

13. "Termodinamicheskie svoystva individual'nykh veshchestv: Spravochnik v 4 tomakh (Thermodynamic Properties of Individual Matters: Handbook in 4 Volumes), Editor: V.P. Glushko, Moscow: Nauka, (1978-1982), available from: <http://www.chem.msu.su/rus/tsiv/Fe/welcome.html>.

14. Yu.L. Mikhlin, "Nonequilibrium nonstoichiometric surface layer in the reactions of metal sulfides," *Zh. Ros. Khim. Obshch. im. D.I. Mendeleeva (Journal of Russian D.I. Mendeleev Chemical Society)*, 45, (3), (2001), 80-85.

## **CHARACTERIZATION OF MAGNETIC AND NON-MAGNETIC IRON OXIDE NANOPARTICLES SYNTHESIZED BY DIFFERENT ROUTES**

Alyssa A. Maich<sup>1</sup>, E. Yegan Erdem<sup>2</sup>, Fiona M. Doyle<sup>1</sup>

<sup>1</sup>University of California at Berkeley; Department of Materials Science and Engineering  
210 Hearst Mining Building; Berkeley, CA, 94720-1760, United States

<sup>2</sup>University of California at Berkeley; Department of Mechanical Engineering  
5101 Etcheverry Hall; Berkeley, CA, 94720-1740, United States

Keywords: Iron oxide, Nanoparticle synthesis, Thermal decomposition, Aqueous synthesis, Microreactor

### **Abstract**

There is an expanding interest in synthesizing high quality magnetic nanoparticles, most notably for biomedical applications. Different processing routes have been reported for the synthesis of magnetite and maghemite. However, some ambiguity remains on their precise chemistry, intermediates, and final products, due to the structural similarity of maghemite and magnetite, and the relative ease of redox transitions during synthesis. Here we present the results of TEM, x-ray and electron diffraction, and SQUID studies aimed at characterizing the products from two different reaction systems, thereby clarifying the reaction chemistry. The first system hydrolyzed aqueous FeCl<sub>2</sub> and FeCl<sub>3</sub> chlorides with ammonia in a microfluidic reactor at ambient temperature; although the reaction product displayed a uniform distribution, it included non-magnetic goethite and lepidocrocite. If the aqueous solutions contained dissolved oxygen, there appeared to be extensive oxidation of Fe(II). The second system thermally decomposed iron (III) acetylacetonate in ether. In prior studies, oleylamine has been reported to serve as both a reducing agent and capping ligand to control particle characteristics; however, our studies revealed little reduction, with maghemite dominating the reaction products.

### **Introduction**

Magnetite and maghemite nanoparticles are commonly used in ferrofluids, in medical applications, and in drug delivery. Superparamagnetic properties, along with low cytotoxicity, colloid stability and bioactive molecule conjugation capability, make these nanomagnets ideal for both in-vitro and in-vivo biomedical applications [1]. One of the major constraints on widespread adoption of nanoparticles for these applications is the amount needed. Typical batch synthesis methods produce polydispersed nanoparticles, which require further size selection procedures to isolate the monodisperse nanoparticle population needed for many applications. In order to maximize the yield of usable particles from a synthesis operation, the reaction conditions must be closely controlled. This requires full knowledge of how the reaction conditions control the various aspects of nanoparticle growth. Many methods have been used to synthesize iron oxides, including sonochemical reactions, mechanochemical synthesis, hydrolysis and thermal decomposition. This work examines the latter two methods, focusing on oxidation and reduction of iron.

Fe(III) ions are hydrolyzed by water to form hydroxo- polymers whose structures and growth are affected by the ligands present. These eventually nucleate hydroxides, oxyhydroxides and oxides. Fe(II) is less susceptible to hydrolysis, but is easily oxidized to Fe(III), and will also co-

precipitate with Fe(III). Magnetite can be synthesized relatively easily by increasing the pH of acidic aqueous solutions containing Fe(II) and Fe(III) salts, but this approach has not generally produced high quality nanoparticles in batch processes. Microfluidic reactors have been used to produce high quality nanoparticles, because they can provide a more controlled synthesis environment. Here we investigate both the size distribution of iron oxide nanoparticles synthesized in a microfluidic reactor, and the ability of dissolved oxygen to oxidize Fe(II) and hence affect the nature of the final product.

Magnetite has also been precipitated by thermal decomposition of iron-containing organometallics or organic salts. Although this approach has been widely reported in the literature, some ambiguity remains on the precise chemical processes involved. Ferric acetylacetonate is frequently used as the starting material. Thermal decomposition at temperatures of about 200°C releases acetone and carbon dioxide, in amounts that are sensitive to the precise temperature and treatment time [2]. Because of the tendency of many iron oxide nanoparticles to aggregate magnetically, long chain or chelating ligands are needed to stabilize the nanoparticles [3]. Reaction parameters such as the nature, ratios and concentrations of capping ligands, along with reaction times, have been reported by various research groups. Many synthesis methods have used a combination of oleylamine and oleic acid as capping ligands, although some have used only oleylamine. Oleylamine has also been reported to reduce Fe(III) to Fe(II), although amines are not generally strong reducing agents. Here we present TEM, x-ray and electron diffraction, and magnetic studies on nanoparticles produced using exclusively oleylamine or oleic acid, to characterize the nature of the products and assess whether oleylamine is serving as a reducing agent.

## Experimental Methods

### Nanoparticle Synthesis Inside a Microfluidic Reactor from Aqueous Iron Chloride Solutions

Two slightly different methods were used to synthesize iron oxide nanoparticles in a microfluidic reactor. The first used 2 mol/L aqueous ammonia to hydrolyze a de-aerated aqueous solution containing 0.48 mol/L FeCl<sub>3</sub>, 0.24 mol/L FeCl<sub>2</sub> and 0.5 mol/L HCl following the method of Frenz et al. [4], which has been reported to follow the reaction:



The iron oxide formed in reaction 1 is magnetite, a cubic spinel ferrite. Both solutions were prepared with deionized water de-aerated under argon to minimize oxidation of Fe(II) during reaction. Hydrolysis was carried out at ambient temperature under argon. The ammonia solution and iron chloride solution were introduced into the reactor from separate channels, briefly mixed and then formed a droplet in a third channel containing mineral oil as a carrier fluid. Nanoparticles formed as the two aqueous solutions continued to mix within the droplet.

The second aqueous synthesis route used 12.1 mol/L aqueous ammonia to hydrolyze an aqueous solution containing 0.15 mol/L FeCl<sub>3</sub> and 0.1 mol/L FeCl<sub>2</sub> following the method of Karaağaç et al. [5]. The same microfluidic reactor described above was used. No steps were taken to de-aerate the solutions. The flow rates of the ammonia and iron chloride solutions were equal. Although the initial Fe(II) to Fe(III) ratio was higher than that in magnetite, at least some of the Fe(II) present initially would be expected to undergo oxidation by dissolved oxygen. One would only expect Fe<sub>3</sub>O<sub>4</sub> to appear if some of the Fe(II) remained unoxidized.

### Nanoparticles Synthesis by Thermal Decomposition of Iron Acetylacetonate

Iron oxide nanoparticles were also synthesized batchwise following the method of Xu et al. [6]. 3 mmol of iron (III) acetylacetonate ( $\text{Fe}(\text{acac})_3$ ) was dissolved in a solution of 4 ml of oleylamine and 4 ml of benzyl ether. The solution was dehydrated at  $110^\circ\text{C}$  for 1 hour under a nitrogen atmosphere, then cooled. A solution of 11 ml oleylamine and 11 ml benzyl ether was then heated to approximately  $210^\circ\text{C}$  in a round-bottomed flask under reflux. The  $\text{Fe}(\text{acac})_3$  solution was injected into the hot solution, causing the temperature of the mixture to decrease to approximately  $180^\circ\text{C}$ . The mixture was held under reflux at  $180^\circ\text{C}$  for 60 minutes. A variant on this synthesis method substituted oleic acid for oleylamine, keeping all other conditions unchanged.

### **Results and Discussion**

#### Nanoparticles Synthesized Inside Microfluidic Reactor from Aqueous Iron Chloride Solutions

Nanoparticles synthesized from the aqueous chloride solution with a 1:2 stoichiometric ratio of  $\text{Fe}(\text{II}):\text{Fe}(\text{III})$  under argon were characterized by x-ray diffraction (XRD) and transmission electron microscopy (TEM). Magnetic nanoparticles formed when the flow rate of the ammonia solution was twice that of the iron chloride solution, providing excess base. These particles were  $5\text{nm} \pm 0.5\text{nm}$  in diameter, representing a 10% standard deviation in size. This size distribution is an improvement over batch synthesis techniques using similar aqueous chemistries. Figures 1 and 2 show a TEM image and the XRD pattern of the particles. As noted in Figure 2, only the (311) peak of magnetite appears. The largest peak, at  $2\theta$  of about  $22^\circ$   $\alpha\text{-FeOOH}$  corresponds to

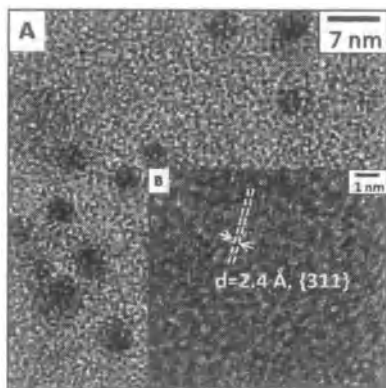


Figure 1. TEM image of nanoparticles synthesized in a microreactor by hydrolysis of an aqueous  $\text{Fe}(\text{II})\text{-Fe}(\text{III})$  chloride solution under argon. The d spacing (inset) corresponds to the {311} plane of magnetite.

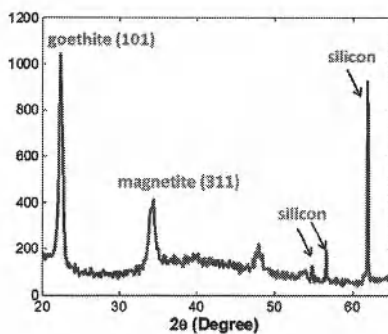


Figure 2. X-ray diffraction pattern of nanoparticles synthesized in a microreactor under argon gas. Only the (311) peak of magnetite,  $\text{Fe}_3\text{O}_4$ , appears.

goethite,  $\alpha$ -FeOOH. The peak at about  $62^\circ$  and smaller peaks at about  $55^\circ$  and  $57^\circ$  were matched directly with the pattern of the silicon substrate on which the particles were mounted (which would be oxidized at the surface). In addition to the distinctive peaks, there is a very broad peak with a maximum at about  $40^\circ$ . This peak could be the (111) peak of goethite. When the flow rates of the ammonia and iron chloride solutions were equal, which did not provide enough base to neutralize the acid and hydrolyze all the iron, the synthesized particles were non-magnetic. Since Fe(II) is less readily hydrolyzed than Fe(III), it seems likely that this product would contain only Fe(III) and is probably goethite.

Nanoparticles synthesized in the microfluidic reactor using the more dilute chloride solution, with dissolved oxygen available to oxidize Fe(II) to Fe(III), were also characterized by X-ray diffraction and TEM. The particles were  $4.6\text{nm} \pm 0.7\text{nm}$  in diameter, representing a 15% standard deviation in size. As with the more concentrated solution in which Fe(II) could not oxidize, the size distribution was narrower than for nanoparticles synthesized in batch processes employing similar aqueous chemistries [5]. Figures 3 and 4 show TEM images and the XRD pattern of the particles. Figure 4 is distinctly different from Figure 2, indicating that the dissolved oxygen did, indeed, affect the nature of the product. Four of the major peaks in Figure 4 appeared to correspond to maghemite,  $\gamma\text{Fe}_2\text{O}_3$ . This would suggest that all of the Fe(II) had been oxidized to Fe(III) before precipitation. As in Figure 2, two additional peaks were seen, at  $2\theta$  values of  $22^\circ$  and  $48^\circ$ ; as before, the former probably corresponding to goethite,  $\alpha$ -FeOOH. The precipitate was largely magnetic.

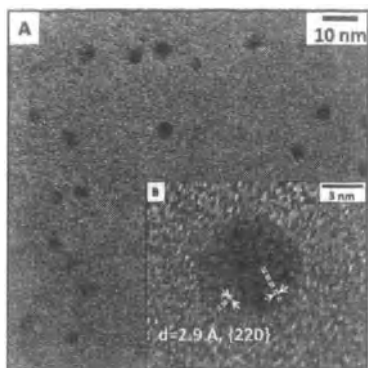


Figure 3. TEM image of nanoparticles synthesized in a microreactor by hydrolysis of an aqueous Fe(II)-Fe(III) chloride solution containing dissolved oxygen. The d spacings (inset) correspond to the {220} and {313} planes of maghemite.

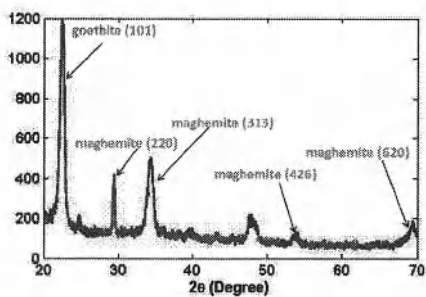


Figure 4. X-ray diffraction pattern of nanoparticles synthesized in a microreactor from aqueous solutions containing dissolved oxygen. Four peaks correspond to maghemite,  $\gamma\text{Fe}_2\text{O}_3$ .

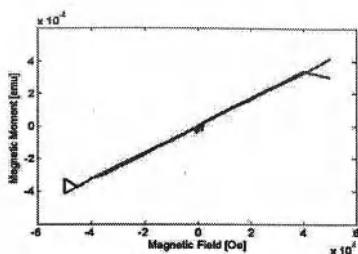


Figure 5. Magnetization curve of maghemite nanoparticles synthesized in a microreactor by hydrolysis of an aqueous Fe(II)-Fe(III) chloride solution containing dissolved oxygen. Particles show paramagnetic behavior.

The magnetic behavior of the synthesized particles was analyzed using a super conducting quantum interference device (SQUID). Figure 5 shows the magnetization curve of the maghemite nanoparticles synthesized in the microreactor from the more dilute iron chloride solution containing dissolved oxygen. The magnetization of the particles increases linearly with the applied magnetic field with no hysteresis, characteristic of a paramagnetic material. Bulk maghemite is ferrimagnetic; however, in the nanoparticulate form each nanoparticle acts as a single magnetic domain whose internal field aligns with the applied magnetic field; consequently a collection of maghemite nanoparticles displays paramagnetic characteristics.

#### Nanoparticles Synthesized by Thermal Decomposition of Iron Acetylacetonate

Figures 6 and 7 show a TEM image and the XRD pattern of nanoparticles produced by the batch-wise thermal decomposition of iron acetylacetonate in oleylamine and benzyl ether. The particles were  $5.5 \pm 1.2$  nm, corresponding to a 22% standard deviation in size; this is a broader

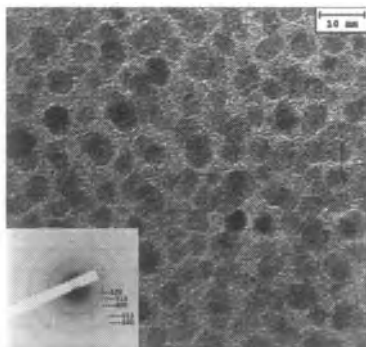


Figure 6. TEM image and diffraction patterns of nanoparticles synthesized by thermal decomposition of iron acetylacetonate in oleylamine and benzyl ether

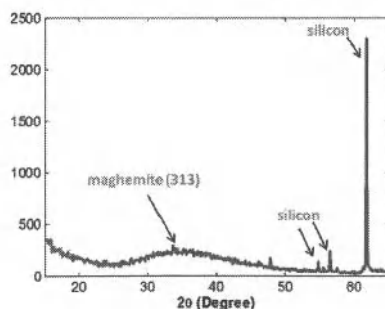


Figure 7. X-ray diffraction pattern of nanoparticles synthesized by thermal decomposition of iron acetylacetonate in oleylamine and benzyl ether

size distribution than obtained from the microfluidic reactor, even though the former operated at ambient temperature, which is generally considered sub-optimal. Figure 7 is clearly significantly different from the XRD patterns of the samples synthesized in the microreactor using aqueous iron chloride solutions. There was a very broad peak with a maximum at around  $35^\circ$ , and no peak at  $22^\circ$  corresponding to goethite. Indeed, there were no sharp peaks below about  $55^\circ$ . The 3 main peaks correspond to the silicon substrate, as discussed for Figure 2. Rings in the TEM diffraction pattern for the sample grown in oleylamine (inset of Figure 6), were assigned to the (220), (313), (400), (513), and (440) reflections of the inverse spinel structure of maghemite (high intensity peaks). When comparing to the diffraction pattern for magnetite, a medium intensity ring (the ring labeled 400) could not be matched to a reflection in magnetite.

Figure 8 shows the magnetization data of the particles synthesized in oleylamine. Comparing with Figure 5, it is seen that the magnetic moment saturates at a relatively modest magnetic field, with a value over an order of magnitude higher than the maximum obtained for the maghemite sample synthesized in the aqueous solution. There is no hysteresis. Hence this appears to be a superparamagnetic material.

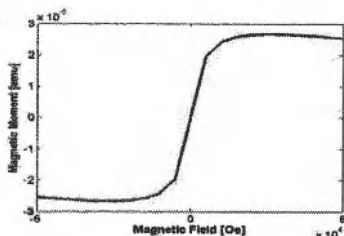


Figure 8. Magnetization curve of nanoparticles synthesized by thermal decomposition of iron acetylacetonate in oleylamine and benzyl ether. Particles show superparamagnetic behavior

Figures 9 and 10 show a TEM image and the XRD pattern of nanoparticles produced by the batch-wise thermal decomposition of iron acetylacetonate in oleic acid and benzyl ether. The XRD pattern in Figure 10 is extremely similar to that in Figure 7. However, the TEM image shows two distinctive types of particle, small equiaxed ones, and much larger, acicular particles. The rings in the TEM diffraction pattern, for the sample grown in oleic acid (inset of Figure 9), were assigned to the (210), (101) (also the 220 peak in magnetite and maghemite), (020), (610), and (511) reflections of the orthorhombic structure of lepidocrocite [7]. One of the weaker peaks coincides with the 513 peak in maghemite but not to a lepidocrocite peak. No 301 reflection of lepidocrocite (expected to be a medium intensity peak) was seen in the pattern shown, but was visible elsewhere on the sample. This sample has multiple diffraction rings that did not match reflections for goethite, hematite, akaganeite, schwertmannite, wustite, or  $\epsilon$ - $\text{Fe}_2\text{O}_3$ . In contrast to the similar XRD patterns, the magnetic behavior of the precipitate synthesized by thermal decomposition of iron acetylacetonate in oleic acid (Figure 11) was different from that of the superparamagnetic particles synthesized in oleylamine (Figure 8). Although the magnetization curve was also sigmoidal, with little hysteresis, the material saturated at a very low magnetic field, with a saturated magnetic moment about two orders of magnitude lower than for the material prepared in the presence of oleylamine. This suggests that the magnetic phase accounts for only about 1% of all material in the sample. From visual inspection of Figure 9, this would

be consistent with the small, equiaxed particles being maghemite and the larger, acicular particles being lepidocrocite.

Oleic acid has been reported to be a less labile capping agent than oleylamine, presumably due to oleate being able to give bidentate chelation of iron. This appears to interfere with the growth of the cubic maghemite, instead promoting the formation of the orthorhombic lepidocrocite.

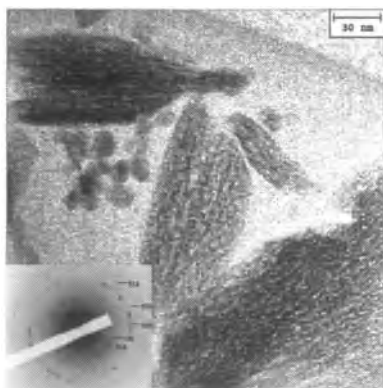


Figure 9. TEM image of particles synthesized by thermal decomposition of iron acetylacetonate in oleic acid and benzyl ether. Inset: diffraction pattern of large, acicular particle

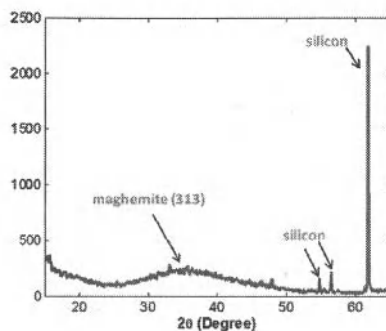


Figure 10. X-ray diffraction pattern of nanoparticles synthesized by thermal decomposition of iron acetylacetonate in oleic acid and benzyl ether

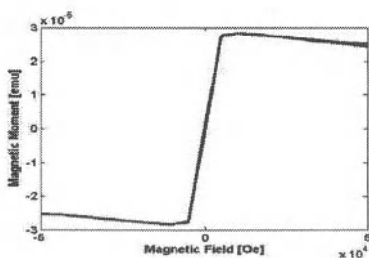


Figure 11. Magnetization curve of particles synthesized by thermal decomposition of iron acetylacetonate in oleic acid and benzyl ether with silicon substrate contribution removed.

## Conclusions

Hydrolysis of an acidic aqueous solution of Fe(II) and Fe(III) chloride in a 1:2 molar ratio in a microreactor under argon produced paramagnetic magnetite nanoparticles, along with  $\alpha$ -FeOOH, with a narrow size distribution of  $5\text{nm} \pm 0.5\text{nm}$  in diameter, corresponding to a 10% standard

deviation in size. Hydrolysis of an aqueous solution with a 1:1.5 molar ratio of Fe(II) and Fe(III) containing dissolved oxygen produced paramagnetic maghemite nanoparticles along with what appears to be  $\alpha$ -FeOOH. Given the dominance of Fe(III) in the products, there was clearly extensive oxidation by dissolved oxygen of the Fe(II) originally present in the solution.

Thermal decomposition of iron acetylacetonate in oleylamine and benzyl ether produced a superparamagnetic product with a broader size distribution than seen in the particles synthesized from aqueous solutions in a microfluidic reactor. The XRD pattern of this product was quite different from that of either product formed in aqueous solution; the pattern was dominated by a low, broad peak that probably corresponded to maghemite. There appeared to be little reduction of Fe(III) by oleylamine, despite reports of oleylamine behaving as a reducing agent [6]. Thermal decomposition of iron acetylacetonate in oleic acid and benzyl ether produced a mixture of particle morphologies, including acicular particles of lepidocrocite. Although the XRD pattern was nearly identical to that of product generated in the presence of oleylamine, the saturation magnetic moment was two orders of magnitude lower, consistent with much of the product being lepidocrocite. It seems likely that oleate ligands from oleic acid interfere with the formation of cubic maghemite, instead promoting the formation of orthogonal lepidocrocite.

#### Acknowledgements

This work was supported in part by the National Science Foundation, under award DMI-0555921, and by the University of California, Berkeley through a Jane Lewis Fellowship Award. The authors thank Prof. Albert Pisano for technical discussions, Dr. Jim Cheng for help with TEM measurements, Dr. Gabriele Vigevani for help with XRD measurements, and Mr. John Heron for assistance with SQUID measurements.

#### References

- 1 M. Mohapatra and S. Anand, "Synthesis and Applications of Nano-Structured Iron Oxides/Hydroxides – A Review," *Int. J. Engineering Sci. Technol.*, 2 (8) (2010), 127-146.
- 2 J. Von Hoene, R.G. Charles, and W.M. Hickman, "Thermal decomposition of metal acetylacetonates; mass spectrometer studies," *J. Physical Chemistry*, 62 (1959), 1098-1101.
- 3 S. Wan, J. Huang, H. Yan, and K. Liu, "Size-controlled Preparation of Magnetite Nanoparticles in the Presence of Graft Copolymers", *J. Mater. Chem.*, 16 (2006), 298-303.
- 4 L. Frenz, A. El Harrak, M. Pauly, S. Bégin-Colin, A. D. Griffiths, and J.-C. Baret, "Droplet-Based Microreactors for the Synthesis of Magnetic Iron Oxide Nanoparticles", *Angew. Chem. Int. Ed.*, 47 (2008), 6817-6820.
- 5 Ö. Karaağaç, H. Koçkar, S. Beyaz, and T. Tanrisever, "A Simple Way to Synthesize Superparamagnetic Iron Oxide Nanoparticles in Air Atmosphere: Iron Ion Concentration Effect", *IEEE Trans. On Magnetics*, 46 (2010), 3978.
- 6 Z. Xu, C. Shen, Y. Hou, H. Gao, and S. Sun, "Oleylamine as Both Reducing Agent and Stabilizer in a Facile Synthesis of Magnetite Nanoparticles", *Chem. Mater.*, 21 (9) (2009), 1778-1780.
- 7 Rochelle M. Cornell and Udo Schwertmann, *The Iron Oxides: Structure, Properties, Reactions, Occurrences, and Uses* (Darmstadt, Germany: Wiley-VCH, 2003).

## **CHARACTERIZATION OF CONCENTRATE, PELLET AND DRI SAMPLES FOR TRACE ELEMENTS**

Mingming Zhang

ArcelorMittal Global R&D, 3001 E. Columbus Dr., East Chicago, IN 46312, USA

Keywords: Mineralogical, Characterization, Iron Ore, Phosphorus, Sulfur, Trace Elements

### **Abstract**

Three samples received from the EAF shop have been characterized by chemical, X-ray diffraction (XRD), optical microscopy (OM) and scanning electron microscopy (SEM) methods. The objective of this characterization work is to investigate the occurrence of nickel, copper, zinc, sulfur and phosphorus in these samples and identify their origin and associations with iron minerals in the concentrate samples that are from mines.

The samples were identified as Mineral, Pellet, and HRD. The latter is the DRI product. All three samples were received as fine powders. The results indicate that, in the mineral sample, magnetite is the major iron oxide mineral with hematite as a second phase based on the OM and XRD studies. Pyrite [FeS<sub>2</sub>], chalcopyrite [CuFeS<sub>2</sub>] and bravoite [(Fe,Ni)S<sub>2</sub>] are major sulfide minerals. Trace amounts of apatite [Ca<sub>5</sub>(PO<sub>4</sub>)<sub>3</sub>(F,Cl,OH)], wardite [Na<sub>4</sub>CaAl<sub>12</sub>(PO<sub>4</sub>)<sub>8</sub>(OH)<sub>8</sub>·6H<sub>2</sub>O], giniite [Fe<sub>5</sub>(PO<sub>4</sub>)<sub>4</sub>(OH)<sub>3</sub>·2H<sub>2</sub>O] and vivianite [Fe<sub>3</sub>(PO<sub>4</sub>)<sub>2</sub>·8H<sub>2</sub>O] were identified by SEM and XRD. Microscopic studies also indicated that most of the sulfide grains in the mineral sample are present either as liberated fine particles (about 10 microns) or as inclusions within the magnetite and hematite grains. XRD studies revealed magnetite as the major mineral with subordinate amounts of hematite and pyrite confirming the microscopic findings. Copper, nickel, and zinc are mainly present as chalcopyrite, bravoite, and franklinite [(Zn,Mn,Fe)(Fe,Mn)<sub>2</sub>O<sub>4</sub>] in trace amount in the mineral samples, respectively. Impurities carry over to the Pellet and HRD samples.

Chemical analyses of the three iron-bearing samples indicate that sulfur and phosphorus in the Pellet sample exceeded the specification. Since liberated pyrite and chalcopyrite particles were observed both in mineral and pellet samples, magnetic and flotation processing routes for this ore should be effective for sulfide removal but at the cost of iron losses. The high phosphorus content of all three samples indicates that there are phosphates which are difficult to remove by the current concentrating process (magnetic separation and flotation)

### **Introduction**

Begin typing remainder of paper... As high-grade ore resources that have been the core of the iron-making industry diminish and tend to be controlled by a few mining entities, the industry is turning to lower-grade and alternative ores to meet future market demand [1].

In order to further expand the source of iron ores and achieve more self-sufficiency in iron ore supply, it is necessary to carry out fundamental research work with the aim of studying economical ways of producing high grade steel from phosphorus contaminated ores. A review of available processing methods indicates that upgrading of low grade iron ore can be achieved by a combination of physical, thermal, and chemical methods depending upon the mineralogical

association of the phosphorus minerals and the degree of liberation attained in processing [2], [3]. However, removal of phosphorus from the iron ore becomes more challenging at low levels of phosphorus, and processing may lead to an increase in iron loss, or require the production of several grades of products. A mineralogical analysis of contaminant elements in raw materials versus the cost of removal in steelmaking will be required when suitable technology is identified.

This study was carried out as requested by pelletizing plant and EAF shop to investigate the origin of trace contaminant elements in concentrates from mine. The mine has a capacity of 2 Mt iron ore concentrate per year. Pre-concentrated iron ore is shipped from the mine by truck to the upgrading Plant where it is processed into a high-grade concentrate. After upgrading, the concentrate is transported by rail cars to the Port and shipped to the steel-making plant. Table 1 and Table 2 show the ROM from mine and pellet product specifications at the pelletizing plant where DRI-grade pellets are made. The steelmaking facilities have a pelletizing plant for DRI-grade pellets, two direct reduced iron plants, and an electric arc furnace-based steel-making plant with continuous casting facilities.

### Experimental and Discussions

The iron concentrate from mines is used as raw material for DRI pellets. However, because of a relatively high content of sulfur and phosphorus, the iron concentrate cannot be used alone as a raw material for pellets but can be used as an auxiliary material for blending with other higher grade concentrates. Thus, the production of the iron concentrate from the mine has been limited and the sulfur and phosphorus contents are concerns in the steelmaking process. For this reason, a detailed mineralogical characterization and elemental analysis of process relevant minerals and their conversion were performed using chemical, optical microscopy, XRD, and SEM with EDS techniques.

Table 1. Mine ROM quality

Contents	Unit	Mine
Cut-off grade	% Fe	15.0
Average grade	% Fe	50.0
Product quality	Natural	Fines
Fe total	%	63.4
Fe mag	%	63.1
SiO <sub>2</sub>	%	3.8
Al <sub>2</sub> O <sub>3</sub>	%	0.4
P	%	0.7
S	%	1.38
CaO	%	3.83

Table 2. Specifications for DR pellet product

	Fe Total	Fe <sup>72</sup>	SiO <sub>2</sub>	S	P	CaO	Al <sub>2</sub> O <sub>3</sub>
Upper	-	0.95	4.00	0.007	0.04	1.07	1.10
Lower	66.1	-	-	-	-	-	-

### Chemical Analysis

Three samples including concentrate (MINERAL), DRI-grade oxide pellet (PELET), and DRI reduced pellet (HRD) were received in powdered form. Portions of these three samples were sent

to two laboratories (Lab 1 and Lab 2) for chemical analysis. Lab 1 uses an X-ray fluorescence (XRF) spectrometer and Lab 2 uses an Inductively Coupled Plasma (ICP) spectrometer. The results are summarized in Table 3. Fe is the dominant element in all three samples with weight percentage ranging from 66.37 to 91.42. Copper, Nickel, Zinc, Sulfur, and Phosphorus are present as trace elements ranging from 0.003 to 0.179 percent.

Table 3. Chemical analysis results of three samples.

Element	Mineral		Pellet		DRI	
	Lab 1	Lab 2	Lab 1	Lab 2	Lab 1	Lab 2
Cu	0.015	0.003	0.005	0.004	0.004	0.004
Ni	0.019	0.042	0.008	0.038	0.021	0.051
Zn	0.007	0.010	0.004	0.010	0.006	0.013
Fe	67.08	69.99	66.37	67.29	79	91.42
Al <sub>2</sub> O <sub>3</sub>	0.33	-	0.54	-	0.47	-
CaO	0.74	-	0.80	-	0.77	-
SiO <sub>2</sub>	2.39	-	2.97	-	2.90	-
S	0.167	0.100	<0.005	0.02	<0.005	0.01
P	0.07	0.140	0.11	0.124	0.13	0.179

According to the chemical analyses, the DRI pellet product is high in iron content, but acid gangue (SiO<sub>2</sub> and Al<sub>2</sub>O<sub>3</sub>), sulfur and phosphorus contents exceed normal specifications. It should be noted that Ni is much higher than Cu or Zn. Lab 2 analyses seem to be closer to reality. From concentrate to fired pellet, there is a slight decrease in iron content, decrease in sulfur, and increase in gangue content due to binder addition, flux addition and oxidation of sulfides and magnetite. Iron content increases and sulfur content decreases in the DRI reduced sample (HRD) due to removal of oxygen and sulfur.

#### X-ray Diffraction (XRD) Analysis

The powdered samples to be analyzed by XRD were placed on a flat glass plate without further grinding since they are very fine in size already. The diffraction patterns were obtained employing an X'pert Pro Diffractometer by PANalytical using Ni filtered Cu K $\alpha$  radiation at 35kV and 50 mA. The samples were scanned at room temperature from 20 to 120 degree at a step size of 0.10°, with a recording time of 4 s for each step.

XRD analysis of the Mineral sample revealed (Table 4) that the major iron bearing mineral is magnetite followed by hematite. The sulfide minerals identified are pyrite, chalcopyrite, arsenopyrite and bravoite. The phosphorus minerals are wardite, giniite and vivianite. Trace amount of nickel is present as bravoite, which is closely related to pyrite. Bravoite is a nickel or cobalt bearing variety of pyrite, with substitution of Ni<sup>2+</sup> for some of the Fe<sup>2+</sup>. Zinc is also present in trace amounts and is mainly present as zinc oxides such as franklinite and zincite. Franklinite is a mineral much resembling magnetite in form, color, and general appearance and is weakly magnetic. Compositionally, it is a variety of iron spinels, containing both zinc and manganese.

XRD analysis of the Pellet sample showed most of the phases present in the Mineral sample. New phases identified are calcium oxide and hydrated iron phosphate, which could be introduced by the flux addition and other concentrate during the blending and pelletizing process. There is also a trend of phase transformation from magnetite to hematite due to oxidation. Sulfide and

phosphate contents decrease in the Pellet sample which is consistent with chemical analysis results.

XRD analysis of the HRD sample did not show the hematite phase as a result of complete reduction to magnetite, wustite and metallic Fe. There is no occurrence of pyrite, chalcopyrite, arsenopyrite, franklinite or phosphate minerals in the sample. Only trace amount of bravoite and zincite were detected which are minerals associated with nickel and zinc. Phosphates were likely reduced to metallic phosphorus and dissolved in the iron phase.

Table 4. Phase identification of XRD peaks

Mineral (concentrate)		Pellet		HRD (DRI)	
Score	Phases	Score	Phases	Score	Phases
82	Magnetite, Fe <sub>3</sub> O <sub>4</sub>	23	Magnetite	2	Magnetite
55	α-hematite, Fe <sub>2</sub> O <sub>3</sub>	89	α-hematite		
46	Hematite, Fe <sub>2</sub> O <sub>3</sub>	72	Hematite		
50	Franklinite, ZnFe <sub>2</sub> O <sub>4</sub>	10	Franklinite		
* 26	Zincite, ZnO	* 3	Zincite	* 1	Zincite
33	Pyrite, FeS <sub>2</sub>	12, 16	Pyrite		
* 17	Bravoite, (Fe, Ni)S <sub>2</sub>	* 10	Bravoite	* 8	Bravoite
* 18	Chalcopyrite, CuFeS <sub>2</sub>	* 11	Chalcopyrite		
				29	Wustite
26	Wardite, NaAl <sub>3</sub> (PO <sub>4</sub> ) <sub>2</sub> (OH) <sub>4</sub> 2H <sub>2</sub> O				
23	Giniite, Fe <sub>3</sub> (PO <sub>4</sub> ) <sub>4</sub> (OH) <sub>3</sub> 2H <sub>2</sub> O	12	Giniite		
		11	Vivianite, Fe <sub>3</sub> (PO <sub>4</sub> ) <sub>2</sub> 8H <sub>2</sub> O		
				49	Bainite, ferrite, Fe

\* A higher score indicates a better match between reference pattern lines and the scan/peak features.

#### Microscopic Study

Samples for optical microscopy were cast in a cold-mounting epoxy resin mould under vacuum. The mounted samples were ground and polished using standard techniques. The polished samples were observed using a Zeiss Observer Z1m optical microscope up to 1600X.

Optical microscopic observation revealed that the Mineral sample contain magnetite and hematite as the major minerals with pyrite and chalcopyrite as minor minerals. Phosphorus minerals were also observed in the Mineral sample. Microspecular hematite was rarely noticed in the Mineral sample. Sulfides appear as minute grains of different sizes either as liberated particles or fine inclusions (Figure 1). Such fine inclusions might pose a problem for liberation since most of them are in ultra-fine sizes (a few microns).



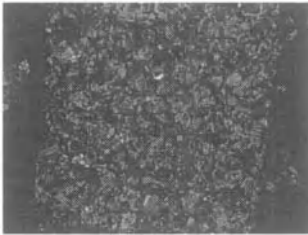
(a) Plane polarized light (X1600)



(b) Plane polarized light (X1600)

Figure 1. Optical microscopy of concentrate sample (MINERAL) with liberated pyrite grain and magnetite grains with fine pyrite inclusion.

The major contents of the concentrate sample (Mineral) are magnetite and hematite in aggregate or in mixed particles. The principal phases are magnetite with hematite. This observation is consistent with XRD analysis. Magnetite is often porous and is found free or interspersed among other iron oxide crystals and may show microspecular texture (shown in Figure 2). Quartz is mostly free of inclusions. Occasionally, quartz occurs within aggregates and shows a brighter coloration due to internal reflection.



(a) Plane-polarized light (X1000)



(b) Cross-polarized light (X1000)

Figure 2. Porous magnetite with recrystallized hematite observed in Mineral sample under plane and cross-polarized lenses.

From the three samples in different processing stages, it is obvious that iron minerals in the samples undergo transformation from Magnetite and Primary Hematite -> Primary, Secondary Hematite and Wustite -> Ferrite and Wustite. Figure 3 shows an optical micrograph of pellet fines particle containing portions of magnetite (dark grey) along with hematite (light grey).



Figure 3. Microstructure of Pellet sample - residual magnetite (grey) with recrystallized hematite (white) under plane polarized light (X1600).

#### SEM/EDS Analysis

The same samples used for optical microscopic observation were used for Scanning Electron Microscopy analysis. The molded specimens were fixed on an aluminum mount and coated with a thin layer of gold using a Denton Vacuum sputter coater (Desk IV). The coated specimens were examined under a JEOL-6060 scanning electron microscope. The Energy Dispersive X-ray Spectrometry (EDS) was also done on the sample to obtain chemical mapping of the sample.

Figures 4 and 5 show typical grains of magnetite and pyrite with EDS point analyses (analyses performed on micros with gold coatings). The EDS elemental analysis of the magnetite and pyrite grains confirmed their chemical compositions and observation by optical microscopy method. Efforts were also made to identify nickel, copper and zinc mineral grains in all samples. However, only a few pyrite grains containing nickel were found under the microscope since they contain only trace amounts by chemical analyses.

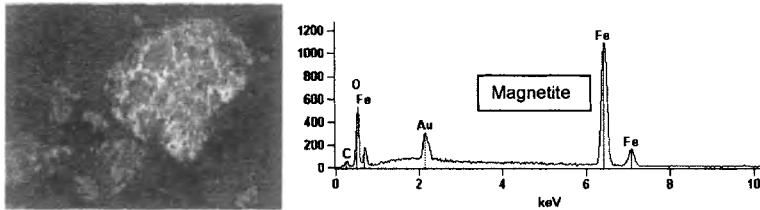


Figure 4. SEM micrograph of magnetite grains with recrystallized hematite in Mineral sample (with gold coating).

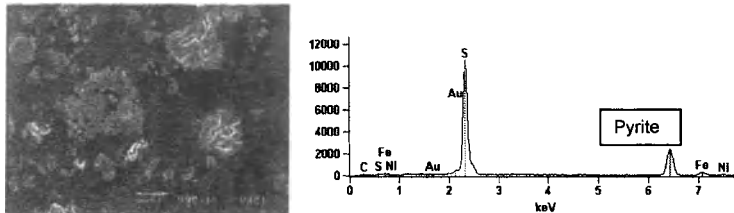


Figure 5. SEM micrograph of pyrite grain in Mineral sample showing trace of Ni (with gold coating).

Figure 6 and 7 show a backscattered electron micrograph (BSE) with EDS analyses of iron phosphate (giniite or vivianite), iron oxide (magnetite), calcium phosphate (apatite) and quartz in the Mineral sample. It can be seen the phosphate grains (point 1 and 4) are intergrown with iron minerals and those grains are in the fine size range (10 to 100 microns). This is an indication that further grinding may help to liberate phosphate further in the mineral samples.

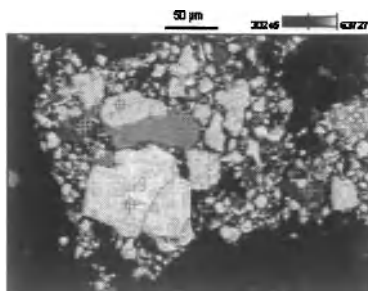


Figure 6. Backscattered Electron micrograph and EDS point analyses of Mineral sample.

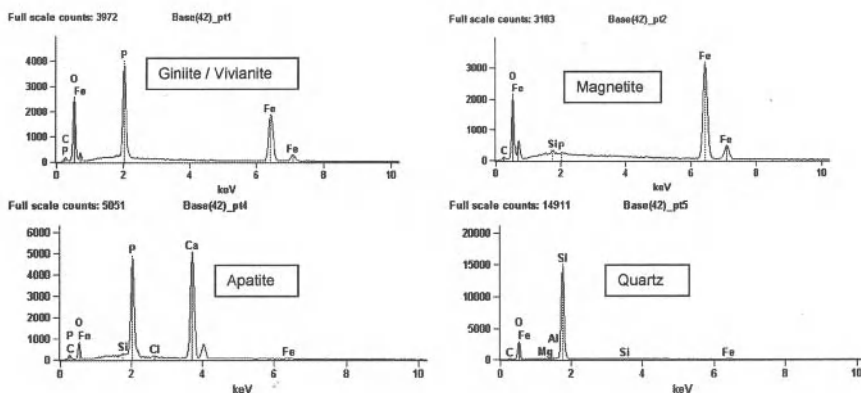


Figure 7. EDS point analyses of giniite/vivianite (point 1), magnetite (point 2), chloroapatite (point 4), and quartz (point 5) grains in Mineral sample.

### Conclusions

Mineralogical studies on the Mineral sample by optical microscopy and SEM indicated that magnetite and hematite are the major iron oxide minerals with minor amounts of pyrite, and chalcopyrite as sulfide minerals. XRD studies revealed magnetite as the major mineral with smaller amounts of hematite, franklinite, pyrite, and apatite confirming the microscopic findings.

Phosphorus is present in apatite, wardite, giniite and vivianite. Wardite disappeared in the Pellet sample after treatment at high temperature.

Optical microscopic studies indicated that most of the sulfide and phosphate grains are present as liberated particles with a few inclusions in both the magnetite and hematite grains in the size range of 10 to 100 microns. The high phosphorus content of all three samples indicates that there are phosphates which are difficult to remove by the present concentrating process (magnetic separation and flotation). Detailed examination of the concentrating process flowsheet combined with mineralogy studies would be needed to determine the potential to improve the grade of the concentrate.

XRD analyses revealed that nickel and copper are mainly present as bravoite and chalcopyrite respectively in trace amounts in the Mineral sample. Chemical analysis also showed that these elements are present as trace elements ranging from 0.003 to 0.051 percent. Since bravoite and chalcopyrite are closely related to pyrite, an enhanced sulfide flotation method would be required to further reduce the contamination of nickel and copper in the concentrate. Zinc is mainly present as franklinite and zincite. Because franklinite is feebly magnetic and is compositionally a variety of magnetite, magnetic separation is not likely to be effective to obtain good removal efficiency of zinc. Selective flotation for franklinite and zincite along with gangue might be an option to further reduce zinc contamination in the concentrate, but would require additional study.

#### References

- [1]. D. S. Rao, T. V. Kumar, S. S. Rao, S. Prabhakar and G. B. Raju, Mineralogy and Geochemistry of A Low Grade Iron Ore Sample from Bellary-Hospet Sector, India and Their Implications on Beneficiation, Journal of Minerals & Materials Characterization & Engineering, Vol. 8, No.2, pp 115-132, 2009.
- [2]. M. Zhang, Review of Technologies for Beneficiating High Phosphorus Iron Ore, ArcelorMittal Internal Technical Report, 2009.
- [3]. H. Kokal, "The Origin of Phosphorus in Ironmaking Raw Materials and Methods of Removal - A Review," 63<sup>rd</sup> Annual Meeting Minnesota section AIME, (1990), pp 225-257.

## **The Dielectric and The Temperature-rising Characteristics of Ore Fines Materials in Microwave Field**

Hongbo Zhu<sup>1,2,3</sup>, Linqing Dai<sup>1,2,3</sup>, Jinhui Peng<sup>1,2,3</sup>, Qianxu Ye<sup>1,2,3</sup>,  
Jian Chen<sup>1,2,3</sup> Wei Liang<sup>1</sup>, Zheng Wei<sup>1</sup>, Zhenliang Weng<sup>1</sup>

(1. Faculty of Metallurgy and Energy Engineering, Kunming University of Science  
and Technology, Kunming Yunnan 650093;

2. Key Laboratory of Unconventional metallurgy, Ministry of Education,  
Kunming Yunnan 650093;

3. Engineering Laboratory of Microwave Energy Application and Equipment  
Technology, Yunnan Province, Kunming Yunnan 650093)

**Keywords:** iron ore fine, microwave fields, dielectric constant, temperature-rising  
characteristics, direct reduced iron

### **Abstract**

By testing the dielectric constant and the dielectric loss factor of concentrated Dahongshan, millscale, anthracite and light-burned dolomite in different frequency and temperature, and by studying the temperature-rising characteristics of the materials in the microwave field of 2.45GHz in frequency, the research in the paper shows that to reach at 1250°C under the same condition – 2KW the microwave power and 30g the mass -- the time concentrated Dahongshan takes is 330s, whereas the millscale is 855s and the anthracite is 820s. About the last one, the higher the temperature is, the stronger the absorptivity is. After the temperature has rose to 400°C, the anthracite's absorptivity increases dramatically. The result of the research would serve as the foundation of the further study on making direct reduced iron by microwave heating.

### **1. Introduction**

Under the microwave fields, materials' dissipation of dielectric bodies would generate thermal effect. Therefore, the dielectric constant and the dielectric loss factor are closely related to materials' ability of absorbing microwave energy—the larger the dielectric constant and the dielectric loss factor are, the stronger the material's ability of absorbing microwave energy is, and the better the thermal effect would be[1-2]. In order to research how to make reduced iron from iron ore fines by microwave heating deeply and systematically, the test of raw materials' dielectric constants and dielectric loss factors are of the essence. What's more, because a mineral' conductivity is influenced by its components and crystal structure[3], it is necessary to study different materials' different temperature-rising characteristics; hence such studies would

## 2. Experimental

### 2.1 Equipments and measures

The precise anti-resistance analyzer(Agilent 4294A) is introduced to test the dielectric constant of samples of iron ore fines. First, researchers weigh 30g material into a crucible covered by thermal insulation material and then heat it by a box-looked microwave(frequency:2450 MHz; power: 2KW). Do not stop heating until the temperature has reached the required one; meanwhile researchers should record the temperature per 30 second during heating. Thus, a time versus frequency curve can be made by recorded statistics. Its changing tendency reflects the material's temperature-rising characteristic.

### 2.2 The chemical composition of iron ore fines

There two types of iron ore fines used in this research: concentrated Dahongshan and millscale. The diagram below shows their chemical composition.

Table 1 The chemical composition of different types of iron ore fines (%)

iron ore fine	TFe	FeO	SiO <sub>2</sub>	CaO	MgO	Al <sub>2</sub> O <sub>3</sub>	MnO	S
concentrated Dahongshan	62.98	24.86	6.86	0.43	0.81	1.36	0.04	0.024
millscale	69.18	53.60	2.84	1.44	0.62	0.64	0.63	0.020

Continou Table 1

iron ore fine	P	TiO <sub>2</sub>	Pb	Zn	K <sub>2</sub> O	Na <sub>2</sub> O	loss	Moisture
concentrated Dahongshan	0.033	0.58	0.004	0.009	0.056	0.260	-1.54	5.80
millscale	0.070	0.15	0.006	0.016	0.020	0.085	--	1.40

Anthracite is the reducing agent in this research. Table 2 shows anthracite's industrial analysis and the content of S and P.

Table 2 Anthracite's industrial analysis, chemical composition and other characteristics

Fixed carbon /%	Ash /%	Volatile /%	S /%	P /%	Moisture /%	Calorification /MJ·kg <sup>-1</sup>	Characteristic of char slag/1~8
70.42	22.40	9.25	0.9	0.014	1.69	26.93	1

The desulfurizing agent used in this research is light-burned dolomite. Table 3 shows its chemical composition.

Table 3 The chemical composition of light-burned dolomite (%)

CaO	MgO	SiO <sub>2</sub>	Al <sub>2</sub> O <sub>3</sub>	S	P
41.10	26.39	<0.5	0.038	0.016	<0.005

### 3. Result and Analysis

#### 3.1 Iron ore fines' dielectric constants and dielectric loss factors

Fig.1 shows the changing tendency of concentrated Dahongshan's, millscale's and anthracite's dielectric constant respectively:

(1)With the same frequency, millscale's dielectric constant is the largest, and the concentrated Dahongshan's is the second largest, and the anthracite's is the smallest.

(2)The concentrated Dahongshan's and millscale's dielectric constant reduce as the frequency increases.

(3)The faster the frequency is, the smaller the reducing range of concentrated Dahongshan's and millscale's dielectric constant would be.

(4)With the same condition, the reducing range of concentrated Dahongshan's dielectric constant is smaller than millscale.

(5)When the frequency has reached 110MHz, concentrated Dahongshan's and millscale's dielectric constant are comparatively larger(56.14 and 144.46 respectively).

(6)Anthracite's dielectric constant changes little as the frequency increases, and it has a tendency that first decreases then increases. For example, when the frequency has reached 104492133.612Hz, anthracite's dielectric constant reduces to the lowest point 5.68; when the frequency has increased to 110MHz, it augments to 5.81.

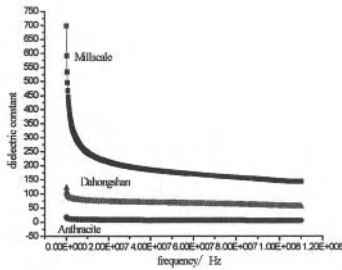


Fig.1 The changing tendency of concentrated Dahongshan's, millscale's and anthracite's dielectric constant

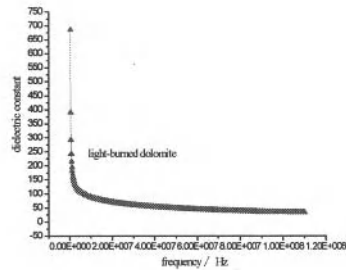


Fig.2 The changing tendency of light-burned dolomite's dielectric constant

Fig.2 is the changing tendency of desulfurizing agent's dielectric constant. According to Fig 2, desulfurizing agent's dielectric constant reduces as the frequency increases, and the faster the frequency is, the smaller the changing range of the dielectric constant is.

The following formula shows how dielectric's microwave power dissipates under the alternating electric field[2]:

$$P = 2\pi f \epsilon_0 \epsilon'' E^2 \quad (1)$$

In this formula(1), P is microwave power(the unite is W); f is the frequency(the unite is Hz);  $\epsilon_0$  is a mineral's vacuum dielectric constant,  $\epsilon_0 = 8.85 \times 10^{-12} \text{ F/m}$ ;  $\epsilon''$  is

complex dielectric constant, reflecting the degree of dissipation of dielectric; E is the electric field intensity (the unite is V/m).

Formula (2) represents dielectric's  $\epsilon$

$$\epsilon = \epsilon' - i\epsilon'' \quad (2)$$

In formula (2),  $\epsilon'$  is the real part of complex dielectric constant, reflecting dielectric's ability to bound charge.

dielectric's complex dielectric constant  $\epsilon$  can be represented by dissipation angle  $\tan \delta$

$$\epsilon = \tan \delta = \frac{\epsilon''}{\epsilon'}$$

If both of a material's dielectric constant and dielectric loss factors are comparatively larger, the material's ability to absorbing microwave will be stronger[4-7].

Fig.3, 4, 5, 6 show the changing tendency of concentrated Dahongshan's, millscale's, anthracite's and desulfurizing agent's dielectric loss factors as the frequency changes.

In Fig.3, concentrated Dahongshan's dielectric loss factor reduces as the frequency increases. When the frequency is 98512164.4Hz, concentrated Dahongshan's dielectric loss factor reaches its positive minimum value. As the frequency continues increasing, the dielectric loss factor becomes negative. When the frequency has reached 110MHz, the dielectric loss factor is -5.53. In another word, when the frequency is less than 98512164.4Hz, the absolute value of concentrated Dahongshan's dielectric loss factor increases as the frequency decreases; when the frequency is greater than 98512164.4Hz, the dielectric loss factor increases as it augments.

According to Fig.4, millsacle's dielectric loss factor reduces as the frequency increases, and the faster the frequency is, the smaller the changing range is. When the frequency is 110MHz, the dielectric loss factor is 18.34.

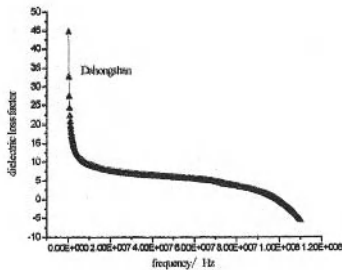


Fig.3 Changing tendency of concentrated Dahongshan's dielectric loss factor

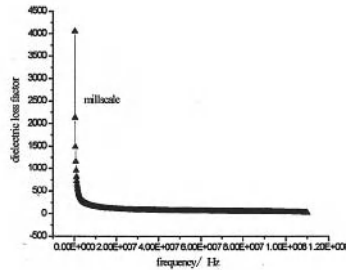


Fig.4 Changing tendency of millsacle's dielectric loss factor

In Fig.5, anthracite's dielectric loss factor reduces as the frequency increases. When the frequency has reached 102918457.5Hz, its dielectric loss factor is 0. If the frequency continues to increase, the dielectric loss factor's value becomes negative. When the frequency is 110MHz, the value is -0.46, which means that with the frequency increasing, the absolute value of anthracite's dielectric loss factor reduces when the frequency is less than 102918457.5Hz while it increases when the frequency is greater than 102918457.5Hz.

According to Fig.6, desulfurizing agent's dielectric loss factor reduces as the frequency increases. When the frequency has reached 102288987.1Hz, the dielectric loss factor is 0. As the frequency continues to increase, the dielectric loss factor becomes negative. When the frequency has reached 110MHz, the dielectric loss factor is -0.58. In a word, with the frequency increasing, the absolute value of desulfurizing agent's dielectric loss factor reduces when the frequency is less than 102288987.1Hz while it increases when the frequency is greater than 102288987.1Hz.

Materials' ability of absorbing microwave energy is related to the absolute value of dielectric loss factor—the larger the absolute value is, the better the ability would be. Combining materials' changing tendency of dielectric constants and dielectric loss factors with the frequency increasing, the absolute value of concentrated Dahongshan's dielectric loss factor changes most, then is anthracite's and millscale's, and the light-burned dolomite's is the least.

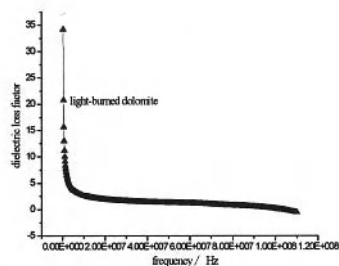
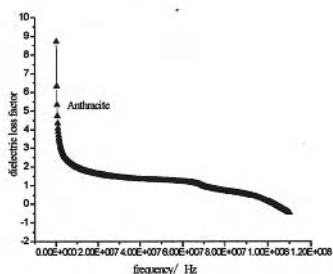


Fig.5 The changing tendency of anthracite's dielectric loss factor

Fig.6 The changing tendency of light-burned dolomite's dielectric loss factor

Under the same electric field intensity and the same microwave frequency, the larger a mineral's dielectric constant, the more energy dissipation is when converting microwave energy to heat, and the better the ability of absorbing microwave is. Therefore, concentrated Dahongshan's ability of absorbing microwave is the best.

### 3.2 The temperature rising characteristic of materials in microwave field

Fig.7 shows concentrated Dahongshan's and millscale's temperature rising curve. According to the graph, heated by microwave radiation, concentrated Dahongshan and millscale have different points of inflection. After being radiated for 60 seconds,

the temperature of concentrated Dahongshan reaches to 610°C. When the temperature has rose to 800°C, the temperature rising speed slowed down. It takes 330 seconds to rise to 1250°C, while millscale takes 855 seconds to reach the same temperature. As a result, under the microwave field, both of concentrated Dahongshan and millscale have good abilities of absorbing microwave, and the former one's is comparatively better.

Fig.8 shows anthracite's temperature rising curve. According to the graph, the curve's point of inflection is patent. Below 400°C, anthracite's temperature rising speed is slow. This results from the influence of anthracite's Volatile matter and ash content [8-9]. When above 400°C, it takes only 160 seconds for anthracite's temperature to rise from 400°C to 1250°C. So anthracite is a kind of microwave-absorbed materials. After being radiated for a while, anthracite's absorptivity becomes stronger gradually, especially when the temperature is above 400°C.

The formula below shows samples' temperature rising speed when considering the heat's radiation dissipation.

$$\frac{dT}{dt} \approx \frac{1}{\rho C_p} (2\pi\epsilon_0\epsilon''fE^2 - \frac{\epsilon\alpha A}{V}T^4) \quad (3)$$

In formula (3), T is temperature(the unite is K); t is time(the unite is s);  $\epsilon_0$  is permittivity of vacuum;  $\epsilon''$  is dielectric loss factor; f is microwave frequency; E is electric field intensity;  $\epsilon$  is a sample's thermal radiation coefficient;  $\alpha$  is Stefan Boltzman constant; A is a sample's surface area; V is a sample's volume.

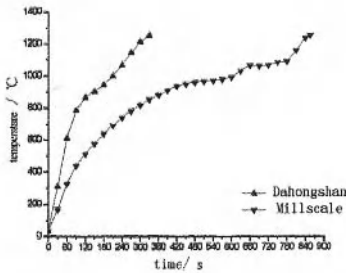


Fig. 7 The temperature rising curve of concentrated Dahongshan and millscale

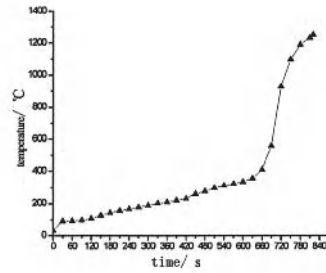


Fig. 8 the temperature rising curve of anthracite

#### 4. Conclusion

1. By testing sample minerals' dielectric constants and dielectric loss factors, the research proves that concentrated Dahongshan, millscale and anthracite have good absorptivity.

2. Under the microwave field, there are differences between iron ore fines' and anthracite in temperature-rising characteristic.

The research also shows that rising to a temperature of 1250°C, concentrated Dahongshan takes 330 second; millscale takes 855 second; anthracite takes 820

second. What's more, anthracite's temperature-rising characteristic becomes stronger as the temperature increases, and its absorptivity become stronger dramatically after the temperature has rose to 400°C.

3. By understanding concentrated Dahongshan's, millscale's and anthracite's temperature-rising characteristics under microwave field can lay a foundation for further research on how to make reduced iron by microwave heating.

### References

- [1] Shaolin Wang. Questions and answers of microwave knowledge [M]. Machinery industry press. 1998.
- [2] Qinhan Jin, Shushan Dai, Kama Huang. Microwave chemistry [M]. Technology press.1999.
- [3] Jinkai Xiao. The composition and structure of minerals and their influences on dielectric constant [J]. Minerals. 1985.5(4). 331-337.
- [4] Bingguo Liu, Jinhui Peng, Libo Zhang. The study of absorptivity and temperature-rising characteristics of Cobaltous carbonate,basic under microwave field [J]. Inorganic salt industry. 2010, 42(3). 11-13
- [5] Wenbo Bu, Jie Xu, Tai Qiu. The basic study on microwave absorbing materials and the mechanism of microwave dissipation [J]. Materials newspaper. 2001,15(5). 14-17.
- [6] Kesheng Zhou, Kelong Huang, Deming Kong. The mechanism and design of microwave absorbing materials [J]. Journal of Central South University of Technology. 2001,32(6). 617-621.
- [7] Yan-Hong Zou, Hong-Bo Liu, Li Yang. The influence of temperature on magnetic and microwave absorption properties of Fe/graphite oxide nanocomposites[J].Journal of Magnetism and Magnetic Materials, 2006, (302):343~347.
- [8] Xiumei Feng, Jin Chen, Ning Li. The study of electromagnetic characteristics of anthracite and bituminous coal [J]. Journal of Taiyuan science and technology univeisity. 2007,38(5). 405-407.
- [9] Hongwu Xu. The test and study of coal's electric parameters [J]. Geology and exploration of coalfield. 1996,24(2). 53-56.

## **CHARACTERIZATION ON THE ROUGHNESS OF THE IRON ORE PARTICLES**

Xuwei Lv<sup>1</sup>, Xiaobo Huang<sup>1</sup>, Rende Zhang<sup>1</sup>, Maojun Zhou<sup>2</sup>

<sup>1</sup>College of Materials Science and Engineering ,  
Chongqing University , China

<sup>2</sup>Ironmaking plant , Baoshan Iron & Steel Co., Ltd., Shanghai, China

Keywords: Iron Ore, Roughness, Specific surface area

### **Abstract**

The characterization of the surface roughness of the mineral particles is of vital importance for the studies of the mineral processing. In this study, an evaluation of the roughness of the iron ore particles, with the measurements of size distribution and the measurements of specific surface area with the liquid nitrogen absorption, was developed. The main theory of this method is the fact that the roughness of the particle influences the specific surface area apparently. The specific surface area of the particles can be measured with the laser diffraction method and the liquid nitrogen absorption method. The influence of the surface roughness of the particle can be measured with the nitrogen absorption and cannot be measured with the laser diffraction. Therefore, the roughness can be got by comparing the specific surface area with two measurement methods.

### **Introduction**

The characterization of the surface roughness of the mineral particles is of vital importance for the studies of the mineral processing. There are three main methods for measuring the size distribution of mineral particles: sieving, laser diffraction, and sedimentation<sup>1</sup>). Many techniques involve sedimentation such as the Horiba<sup>2, 3</sup>) and the Cyclo-sizer<sup>1</sup>). In the mineral industry, size distribution is usually determined by sieving because it can be carried out accurately for all particle sizes larger than 45 . The preferred method to obtain the size distribution of finer particles is laser diffractometry. The technique has several advantages: it produces measurements in a few minutes with considerably less labor compared with the cyclo-sizer and for a range of sizes considerably wider in comparison with the sedigraph<sup>4</sup>). The equivalent-sphere size distribution reported by laser diffractometry is valid for metallurgical calculations and can be routinely used in mineral processing plants. The surface area of the particles can be measured by the BET method of nitrogen adsorption, or it can be calculated from the size distribution. However, the latter calculation requires the size distribution to be accurately known across the whole size

range, and assumptions have to be made about the shapes and surface roughness of the particles and presence or absence of pores (see below). The BET method is based on the physical adsorption of gas over the whole exposed surface area and measures the surface area stemming from the roughness and open pores on the surface of the particle<sup>5</sup>). The calculation of the surface area from the size distribution is usually based on the assumption that all the particles are smooth spheres, without considering the shape and/or roughness of the particles. Determining the surface roughness of the particle with these methods, is the objective of this study.

### Experimental

The sieve-sizing method and the laser diffraction method were used to measure the particle size. The series of screens used in the sieve sizing are 0.038, 0.2, 0.7, 1, 3, 5, 8, and 10 mm. The laser diffractometer used in this study is MS 2000 (Malvern Instruments). The measuring range is from 0.02–2000  $\mu\text{m}$ . The specific surface areas of the particle samples were measured by ASAP 2020 (Micromeritics). The principle of the ASAP 2020 is to adsorb nitrogen at low temperature. The mass of nitrogen absorbed is measured; thus, the surface area can be calculated with these data based on the theoretical absorption model, such as the BET model and the Langmuir model.

### Results and Discussion

In the current study, samples of eight different iron ores were selected for the measurements. Size distribution was measured by dry screening without prior wet screening; data are shown in Table 1. In 5 of the 8 cases, more than 50% of the materials were smaller than 0.2 mm. The particle size distribution of the samples under 0.2 mm and their surface area were measured using the laser diffractometer. The results are shown in Table 2. Measurements by the laser diffraction analyzer show that the 99% of the particles, which are sized down to 0.2 mm by the screen, are scarcely bigger than 0.2 mm. In the particles under 0.2 mm in the eight samples, ore C has the smallest average size at about 4.63  $\mu\text{m}$ . Ore F has the largest average size at about 50.4  $\mu\text{m}$ .

Table 1 Size distribution (mm) of iron ores, mass%

Ore	>10	8-10	5-8	3-5	1-3	0.7-1	0.2-0.7	0.038-0.2	<0.038
A	1.5	0.3	4.6	9.3	3.8	1.8	10.9	49.7	18.2
B	4.0	3.2	10.0	11.6	11.1	7.1	26.3	17.8	8.9
C	1.6	5.1	30.1	37.0	15.9	3.6	3.4	1.1	2.3
D	0.0	0.7	1.0	0.8	0.9	1.1	13.8	51.6	30.1
E	0.0	0.0	2.3	0.7	0.4	0.1	4.7	65.1	26.6
F	3.9	1.6	11.1	12.5	11.6	5.8	15.7	28.4	9.4
G	0.0	0.4	0.2	0.2	0.4	0.4	3.9	55.1	39.4
H	0.0	0.0	0.0	0.0	0.0	0.0	0.3	61.5	38.1

Table 2 Surface area and equivalent diameter of the particles below 0.2mm

Iron ores	A	B	C	D	E	F	G	H
Surface area m <sup>2</sup> /g	0.25	0.25	2.81	0.27	0.43	0.31	0.44	0.44
D(0.1) μm	11.09	14.87	0.79	10.45	6.90	12.90	7.59	6.66
D(0.5) μm	48.25	41.95	4.63	43.53	34.50	50.40	38.90	36.48
D(0.9) μm	113.98	95.61	50.37	102.70	87.10	109.40	95.50	109.50
D(3,2) μm	23.59	23.44	2.14	22.30	13.90	19.20	13.50	13.56
D(4,3) μm	62.76	49.28	16.32	57.40	46.30	56.60	45.86	60.20

D(x): defined as diameter where the x of the particles are smaller than D(x), x is the mass fraction. D(3,2): surface median diameter, D(4,3): volume median diameter.

Based on Tables 1 and 2, the cumulative size distribution of the eight iron ore samples are plotted in Fig.1, where samples D, E, G, and H are fine ores, sample C is a very coarse ore, and samples A, B, and F are medium. The surface area of the iron ore samples of a unit mass is calculated by Eq. [1]:

$$S = 4\pi \cdot \sum n_i \cdot r_i^2 \quad (1)$$

where S is the total surface area of all particles of a unit mass, and r<sub>i</sub> is the radius of the particles with different sizes. The number of particles with size r<sub>i</sub> can be calculated by

$$n_i = \frac{m_i}{\rho} \cdot \frac{3}{4\pi r_i^3} \quad (2)$$

where m<sub>i</sub> is the mass fraction of particles with size r<sub>i</sub> in 100 g of raw materials. Replacing n<sub>i</sub> in Eq. [1] by Eq. [2] gives the following:

$$S = \sum \frac{m_i}{\rho} \cdot \frac{3}{r_i} \quad (3)$$

The bulk and real density of the iron ore samples are shown in Table 3. The surface area can be calculated according to Eqs. [2]–[4]. The results are shown in Table 4, where the medium particle size in the fixed size range is used. For particles <0.2 mm and >10 mm, D (0.5) from the laser diffraction measurements and 15 mm are used as the medium diameter in the calculations. Based on the calculations, ores E, G, and H have a great specific surface area caused by the high fraction of small particles.

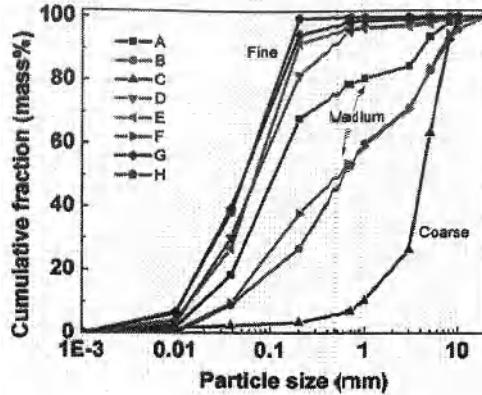


Fig.1 Cumulative size distributions of the eight iron ore samples

Table 3 Bulk density and true density of iron ore  $g/cm^3$

Iron ores	A	B	C	D	E	F	G	H
Bulk density	2.03	2.06	2.29	2.11	2.12	2.49	2.15	2.04
True density	4.14	4.09	4.62	4.17	4.65	4.54	4.15	4.02

Table 4 Surface area of the samples calculated with the size distribution

$d_{min} \sim d_{max}$	$d_M$	A	B	C	D	E	F	G	H
$10^{-3} m$		$cm^2/100g$							
<0.2	D(0.5)	20787.7	9409.5	9958.6	27743.7	39284.6	11069.1	35908.7	40344.7
0.2~0.7	0.45	356.3	851.8	98.7	437.0	148.1	421.4	121.2	10.8
0.7~1	0.85	31.3	120.8	54.7	18.4	2.2	81.8	6.4	0.5
1~3	2	28.2	81.0	104.4	6.7	2.8	69.8	2.6	0.0
3~5	4	34.5	42.4	121.0	2.7	2.6	37.7	0.8	0.1
5~8	6.5	10.4	22.4	60.6	2.1	5.1	20.6	0.5	0.0
8~10	9	0.5	5.1	7.5	1.1	0.0	2.2	0.6	0.0
>10	15	1.4	3.9	1.4	0.0	0.0	3.1	0.0	0.0
Total		21250.2	10536.8	10406.9	28211.7	39445.4	11705.7	36040.7	40356.1

D(0.5) from Table 4

The surface area and features of the pores in the particles of the samples measured by the ASAP 2020 are shown in Table 5. Comparing the results of the surface area by different methods, which are classified as (a) a mathematical model for the calculation of size distribution (sieving or laser diffraction) and (b) measurement by nitrogen absorption, the results are shown in Table 6. The surface area measured by the ASAP 2020 is much larger than that by combining the size distribution measured by laser diffraction and the mathematical model calculation. Note that the surface area measured by nitrogen adsorption should be close to the real value of the particle surface area according to the theory of adsorption. The mathematical model used to calculate

the surface area from the size sieving and laser diffraction methods is based on the important assumption that all particles are fully dense smooth spheres. However, real iron ore particles are never smooth spheres but are rather very irregularly shaped with great roughness; both characteristics can increase the surface area of the particle. In the size-sieving method, very fine particles can (a) agglomerate or (b) adhere to the large particles, resulting in some errors in measuring the size distribution. However, in the laser diffraction method, all the particles should be fully dispersed in the medium used to obtain a suspension of the particles. The previous discussion explains why the surface area measured by nitrogen adsorption is larger than that calculated from the size distribution measured by laser diffraction.

Table 5 Measurements of the iron ore by ASAP2020

Surface area (m <sup>2</sup> /g)	A	B	C	D	E	F	G	H
BET model	3.005	16.460	1.182	3.405	1.729	9.948	1.611	2.915
Langmuir model	4.186	22.928	1.654	4.686	2.404	13.719	2.260	4.102
Micropore area	0.181	0.699	0.086	0.657	0.123	2.399	0.065	0.287
External area	2.824	15.762	1.096	2.749	1.608	7.549	1.545	2.627
Pore volume cm <sup>3</sup> /g	0.005	0.026	0.005	0.005	0.006	0.014	0.005	0.005
Pore size Å	67.05	66.15	173.72	68.27	127.34	60.75	125.08	65.68

Table 6 Shape factors of the sample

Factors	A	B	C	D	E	F	G	H
all particles (N.A./Cal.)	134.5	1432.9	109.6	98.2	41.2	629.1	42.9	65.7
all particles (N.A./L.D. <0.2mm)	11.1	61.6	0.4	10.2	3.7	24.1	3.5	5.9
<0.2mm (L.D./Cal.)	8.2	7.3	8.8	7.9	10.0	10.8	11.7	10.8
<0.038mm (L.D./Cal.)	6.4	5.4	7.0	6.6	8.1	8.1	9.1	8.9

The roughness of the surface of the particle and the presence of open pores greatly influence the surface area of the particle. The relationship between roughness and the specific surface area is deduced as follows.

The ratio between the measurements by nitrogen absorption and the laser diffraction gives the information on the shape and roughness of the particle, as shown in Table 6. The ratio varies greatly among the samples. In samples B and F, the surface area measured by ASAP is as high as 1432 and 629 times of that calculated by the model. In the other samples, such as E and G, the measurements by ASAP are as high as about 42 times of the calculations. In the others, the value varies from 60–130 times.

To study the reason why the values change so greatly, the particles were observed under the SEM machines; the morphology of the samples are shown in Fig. 2. The surface of the particle in samples B and F is much rougher than that of other samples. There are many humps on the surface of the particle. Sample C is different from others because its particle size is much smaller than that of the others. In the other samples, the smooth

surface, which forms during the crash, is clear.

If the average value of the specific area increase is assumed 6.5 times  $((3+10)/2=6.5)$ , then the effect of the roughness on the increase in specific surface area can be calculated roughly as 9.47 for sample B  $(61.6/6.5=9.47)$  from Table 10) and 3.70 for sample F  $(24.1/6.5=3.70)$  from Table 10). According to the mathematical models, such as Eq. [8], there are about 1–3 layer humps on the particles.

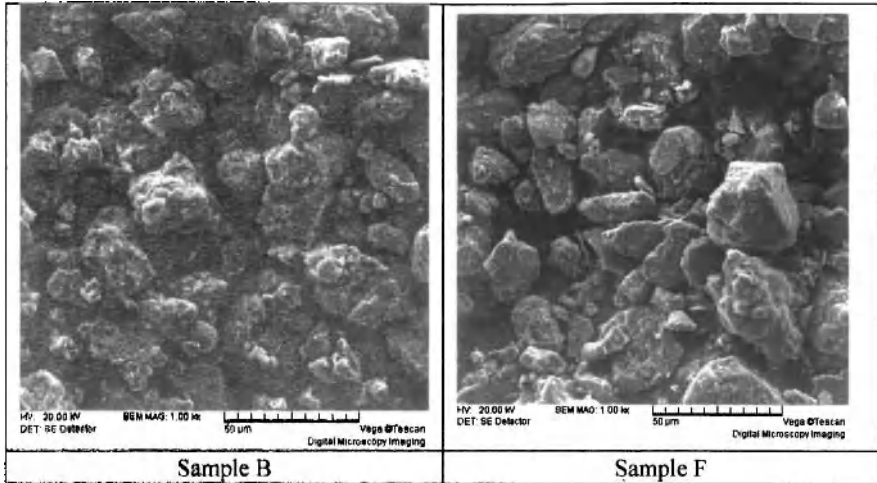


Fig.2 Morphology pattern of the particles

### Conclusions

The characterization of roughness of the particle was discussed in the current study. The conclusions are summarized as follows:

The roughness of the particle apparently influenced the specific surface area. The effects were roughly evaluated by the model. The shape of the particle can enlarge the surface area by 3–10 times for the samples used, and roughness can enlarge the surface area 4–10 times on average.

### Acknowledgments

This study was Supported by National Natural Science Foundation of China (Grant No. 51104192).

### References

- 1) D. F. Kelsall, C. J. Restarick, P. S. B. Stewart: *Proc. Australas. Inst. Min. Metall. No.251*, (1974), 9-10.

- 2) D. Goossens: *Sedimentology*, **55**(2008), 65.
- 3) M. Staiger, P. Bowen, J. Ketterer *et. al.*: *Journal of Dispersion Science and Technology*, **23**(2002), 619.
- 4) C. L. Schneider, R. Neumann, A. S. Souza: *International Journal of Mineral Processing*, **82**(2007), 30.
- 5) S. Kondo, T. Ishikawa, I. Abe: *Adsorption Science (In Japanese)*, ed., eds., Maruzen Co. Ltd., Tokyo, (1991).

## **Synthesis and Characterization of Al, Ag, Ti, Cu, and B Substituted Hydroxylapatite**

**Celaletdin Ergun<sup>1</sup>; Thomas J. Webster<sup>2</sup>; Gurbuz Gunes<sup>1</sup>;  
Abdurrahman Bahadır<sup>3</sup>; Huinan Liu<sup>4</sup>; Ibrahim Erden<sup>5</sup>;**

<sup>1</sup>Istanbul Technical University; <sup>2</sup>Brown University;  
<sup>3</sup>MSTU; <sup>4</sup>University of California, Riverside; <sup>5</sup>Yildiz Technical University;

Keywords: hydroxylapatite, doping, biocompatibility.

### **Abstract:**

B, Ti, Ag, Al and Cu substituted hydroxylapatites were synthesized via precipitation method. Then the samples were air-sintered at 1300°C for 2 hrs and characterized with XRD, SEM, FTIR, and cell adhesion behaviors.

### **Introduction**

Synthetic hydroxylapatite (HA,  $\text{Ca}_{10}(\text{PO}_4)_6(\text{OH})_2$ ) has a similar composition and structure to biological apatite. Therefore, it has been safely and extensively used as an implant material for bone substitute. However, synthetic HA has been used for a various applications including medical or non-medical applications, such as matrices for drug release control, bone cements, tooth paste additive, blood purification agent, monolithic implants or coatings on metallic implants, packing media for column chromatography, gas sensors, catalysis and host materials for lasers and luminescent materials, etc. [1–9].

The major factors affecting the performance of HA on these applications are crystal morphology, density, porosity, pore size and distribution, chemical composition, and surface structure. As provided by the high flexibility of the apatite structure a great variety of cationic and anionic species can be substituted into HA structure which is specifically considered as an effective method to modify the properties of HA [10,11].

The objective of the current study is to develop a better understanding on the structure and behavior of the B, Ti, Ag, Al, Cu substituted HA. In order to do this, samples were synthesized by precipitation method, and sintered in air at 1300°C. Subsequently, the materials were characterized by X-ray diffraction (XRD), Fourier transform-infrared spectroscopy (FT-IR), scanning electron microscopy (SEM).

### **Experimental Procedures**

#### **Synthesis of titanium-substituted apatites**

Pure HA and Ag, Cu, Al, Ti-doped HA were synthesized with precipitation method [10]. Briefly, for pure HA synthesis, solutions of 1M  $\text{Ca}(\text{NO}_3)_2 \cdot 4\text{H}_2\text{O}$  and 0.6M  $(\text{NH}_4)\text{H}_2\text{P}_2\text{O}_7$  were separately brought to pH 11–12 with concentrated  $\text{NH}_4\text{OH}$ . The calcium nitrate solution was stirred vigorously at room temperature (RT), and the ammonium phosphate solution was added dropwise into this calcium nitrate solution to produce a gelatinous precipitate. The precipitated solution was stirred for 24 h at RT to form nano-grained HA.

Reagent grade tetraethyl orthotitanate (Fulka), Aluminum Nitrate, Acid Boric, Silver Nitrate, Copper Nitrate (Merck) were added into the calcium nitrate solution in appropriate proportion to synthesis the substituted HAs. Dopant molar incorporation ratios for Ca ions were chosen as 2 mol%. The stoichiometric value of 1.67 for (Ca + Dopant)/ ratio was aimed to achieve in the HA after incorporation of dopant ions into Ca sites. Therefore, molar ratios of Ca ions deliberately added 2 mol% less than that of required for pure HA into the precursor solutions in order to compensate the difference with dopant ions. In other words, for 2 mol% dopant substitution into Ca positions, solutions of 0.98M  $\text{Ca}(\text{NO}_3)_2 \cdot 4\text{H}_2\text{O}$  were used. The reaction mixture was centrifuged and washed repeatedly to remove the unreacted ammonia. Next, the sludge was filtered using a 0.2- $\mu\text{m}$  filter paper to form a sticky cake, which was then dried for at least 48h at 60°C. Dried cakes were crushed and passed through a 200-mesh screen to obtain a powder with particle sizes <75 $\mu\text{m}$  in diameter.

The powders of apatites were cold-pressed into cylindrical pellets under 150MPa pressure. Resulting pellets were about 1 cm in diameter and 3mm in thickness. Subsequently, the pellets were sintered in air at 1300°C for 2 h depending on the experimental protocol. After sintering, one surface of each pellet was polished with SiC paper and then with diamond powder. The surfaces were finished with a 0–1  $\mu\text{m}$  diamond solution.

### **Materials characterization**

Lattice parameters (a and c) and phases present in the HA were determined with X-ray diffraction (using a Philips type PW2273/20 diffractometer). The structure of HA is usually considered to be hexagonal, with space group P63/m. However, there is evidence for a variant HA structure that is monoclinic, with atomic positions that are close to those of the hexagonal structure. For our present purpose, we will consider the structure of HA to be hexagonal for lattice parameter measurements. Cu K $\alpha$  radiation ( $\lambda = 1.5406 \text{ nm}$ ) produced at 40 kV and 35mA scanned the diffraction angles ( $2\theta$ ) between 20 and 70° at every 0.02° for 20 s. Diffraction signal intensity throughout the scan was monitored and processed with JADE software. Changes were calculated by subtracting the values of lattice parameters a and c of undoped from doped HA formulations. FTIR spectra of sample powders were recorded at room temperature on a PerkinElmer Fourier transform-infrared spectrometer using an ATR attachment. Grain size and porosity of the pure and substituted hydroxylapatite samples of this study were determined by SEM (Philips/FEI XL30FEG SEM Electron Microscope system). For the examination of the HA under SEM, it was etched in a 0.1-M lactic acid (Sigma) and coated with gold at RT. Samples were examined at 20 kV. Linear intercept method was used to determine the average grain size. Chemical analyses were performed on the samples sintered at 110°C for 2 h with the same SEM system in conjunction with the energy dispersive spectrometer.

### **Cytocompatibility tests;**

#### **Cell culture**

Human osteoblasts (bone-forming cells; CRL-11372 American Type Culture Collection) were cultured in Dulbecco's modified Eagle's medium (DMEM; GIBCO, Grand Island, NY) supplemented with 10% fetal bovine serum (FBS; Hyclone) and 1% penicillin/streptomycin (P/S; Hyclone) under standard cell culture conditions, that is, a sterile, 37°C, humidified, 5% CO<sub>2</sub>/95% air environment. Cells at population numbers 6–9 were used in the experiments.

#### **Osteoblast adhesion**

All sterilized substrates listed in Table 1 were placed in 12-well tissue culture plates (Corning, New York) and were rinsed three times with sterilized phosphate buffered saline (PBS; a solution containing 8 g NaCl, 0.2 g KCl, 1.5 g Na<sub>2</sub>HPO<sub>4</sub>, and 0.2 g KH<sub>2</sub>PO<sub>4</sub> in 1000 mL DI water adjusted to a pH of 7.4; all chemicals were from Sigma). Osteoblasts were then seeded at a concentration of 2500 cells/cm<sup>2</sup> onto the compacts of interest in 2 mL of DMEM supplemented with 10% FBS and 1% P/S and were then incubated under standard cell culture conditions for 4 h. After that time period, non-adherent cells were removed by rinsing with PBS and adherent cells were then fixed with formaldehyde (Fisher Scientific, Pittsburgh, PA) and stained with Hoechst 33258 dye (Sigma); the cell nuclei were, thus, visualized and counted under a fluorescence microscope (Leica, excitation wavelength 365 nm and emission wavelength 400 nm). Cell counts were expressed as the average number of cells on eight random fields per substrate. Typical osteoblast morphologies were also digitally acquired. All experiments were run in triplicate and cell adhesion was evaluated based on the mean number of adherent cells. Numerical data were analyzed using standard analysis of variance techniques; statistical significance was considered at  $p < 0.05$ .

## Results

XRD patterns of the samples are presented in Fig. 1. X-ray peaks of as precipitated phase show similarities to the JCPDS standard peaks of pure hydroxylapatite. The well defined peaks of all samples are also the indication of their crystalline structures. However, the wider peaks of Ag doped samples should be due to very small size of the precipitates and/or partial disorderness in the precipitates. The second wider peaks were belonged to B doped samples. No second phases observed in any of the samples.

The hexagonal lattice parameters were calculated based on these two superimposed XRD patterns (Table 2). In all substituted apatites, both lattice parameters *a* in hexagonal structures for both superimposed data were larger than in pure HA, however, *c* were smaller in samples coded as Al, Al-Ti, Al-Cu, Ag-Cu, and B, and larger in Ag, Ag-Ti. On the other hand a decrease in the volume of unit cells of Al, Al-Cu, Ag, Ag-Ti was observe while an increase of those of Al-Ti, Ag-Cu and B was observed.

The SEM photographs of the samples are given in Fig. 3. The average grain sizes of Al, Al-Ti, Al-Cu, Ag, Ag-Ti, Ag-Cu, and B were 1.8, 3.6, 9.1, 2.7, 4.1, 3.6, 4.1  $\mu\text{m}$ , respectively.

The FT-IR spectrum of the doped are presented in Fig. 3. The bands at 1090  $\text{cm}^{-1}$ , 1041  $\text{cm}^{-1}$ , and 960  $\text{cm}^{-1}$  were assigned to PO<sub>4</sub><sup>3-</sup> stretching [X-X]. There was a broadening of these in sample B, which may be a crystallinity compared to other samples.

## Cytocompatibility properties

Osteoblast adhesion results are given in Table 2. It was found that all samples except Al doped one showed better osteoblast adhesion behavior than pure HA. The best result was observed on sample B.

## Discussion

XRD results showed that all doped samples had similar crystalline structures as pure HA. All doped samples showed a different lattice parameters and lattice volumes than that of pure HA. The largest change in lattice volume was in Ag-Ti doped sample in the form of contraction. On the other hand the second largest volume change was observed in B doped sample in the

form of expansion. The grain sizes of the doped samples showed a spread but all are in the order of micrometer. The largest grain size was observed in samples Al-Cu while the smallest grain size was in sample Al. Osteoblast adhesion tests showed that sample Al has lower response than pure HA, however all other doped samples showed better performance than pure HA. The best result was on sample B.

#### References

- [1]. De Groot, K., Bioceramics consisting of calcium-phosphate salts. *Biomaterials*, 1980, 1, 47.
- [2]. Jarcho, M., Calcium phosphate ceramics as hard tissue replacements. *Clin. Orthop.*, 1981, 157, 259.
- [3]. LeGeros, R. Z., Calcium phosphate materials in restorative dentistry: a review. *Adv. Dent. Res.*, 1988, 2, 164.
- [4]. Daculsi, G., Passuti, N. and Martin, S., Macroporous calcium phosphate ceramic for long bone surgery in human and dogs: clinical and histological study. *J. Biomed. Mater. Res.*, 1990, 24, 379.
- [5]. LeGeros, R. Z., Apatite in biological systems. *Prog. Cryst. Growth Charact.*, 1981, 4, 1.
- [6]. Narasaraaju, T. S. B. and Phebe, D. E., Some physiochemical aspects of hydroxylapatite. *J. Mater. Sci.*, 1996, 31, 1.
- [7]. Itokazu, M., Yang, W., Aoki, T. and Kato, N., Synthesis of antibiotic-loaded interporous hydroxyapatite blocks by vacuum method and in vitro drug release testing. *Biomaterials*, 1998, 19, 817.
- [8]. Kenny, S. M. and Buggy, M., Bone cements and fillers: a review. *J. Mater. Sci.: Mater. Med.*, 2003, 14, 923.
- [9]. Niwa, M., Sato, T., Li, W., Aoki, H., Aoki, H. and Daisaku, T., Polishing and whitening properties of toothpaste containing hydroxylapatite. *J. Mater. Sci.: Mater. Med.*, 2001, 12, 277.
- [10]. Ergun, C., Webster, T. J., Bizios, R. and Doremus, R. H., Hydroxylapatite with substituted magnesium, zinc, cadmium, and yttrium. Part I. Mechanisms of osteoblast adhesion. *J. Biomed. Mater. Res.*, 2002, 59, 305.
- [11]. Ergun, C., Effect of Ti ion substitution on the structure of hydroxylapatite. *J. Eur. Cer. Soc.*, 2008, 28, 2137-2149.
- [12]. Ribeiro, C. C., Gibson, I. and Barbosa, M. A., The uptake of titanium ions by hydroxyapatite particles—structural changes and possible mechanisms. *Biomaterials*, 2006, 27, 1749.

**Table 1:** Abbreviation and composition of the compacts tested in the present study

Sample reference	Ca (Mol.%)	P (Mol.%)	Al (Mol.%)	Ag (Mol.%)	Ti (Mol.%)	Cu (Mol.%)	B (Mol.%)
HA	10	6					
Al	9.98	6	0.02				
Al-Ti	9.98	6	0.01		0.01		
Al-Cu	9.98	6	0.01			0.01	
Ag	9.92	6		0.02			
Ag-Ti	9.98	6		0.01	0.01		
Ag-Cu	9.98	6		0.01		0.01	
B	9.98	6					0.02

**Table 2:** Lattice parameters, grain sizes, cell adhesion results and bacterial test results of the samples

Sample reference	a	$\Delta a$	c	$\Delta c$	$\Delta V$ (%)	Grain Size ( $\mu m$ )	Cell Adhesion (cell/cm <sup>2</sup> )
HA	9,418	-	6,884	-		2	1490
Al	9,4091	0,0089	6,8881	-0,0041	-0,1332	1,8	1395
Al-Ti	9,4163	0,0017	6,9018	-0,0178	0,2183	3,6	2027
Al-Cu	9,4091	0,0089	6,8949	-0,0109	-0,0345	9,1	2591
Ag	9,4049	0,0131	6,8785	0,0055	-0,3617	2,7	2730
Ag-Ti	9,3946	0,0234	6,8813	0,0027	-0,5374	4,1	2068
Ag-Cu	9,3946	0,0234	6,9361	-0,0521	0,2545	3,6	2487
B	9,4163	0,0017	6,9223	-0,0383	0,5170	4,1	3311

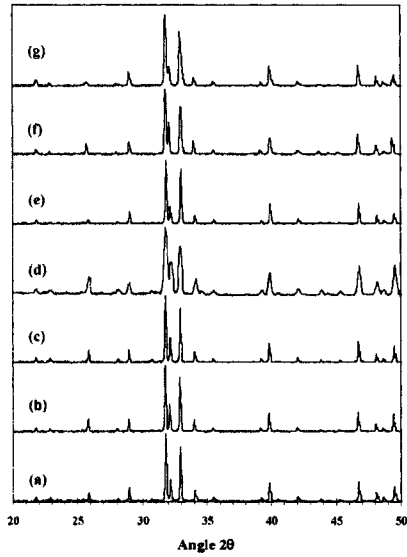


Figure 1: XRD patterns of doped HAs: (a) Al, (b) Al-Ti, (c) Al-Cu, (d) Ag, (e) Ag-Ti, (f) Ag-Cu, (g) B

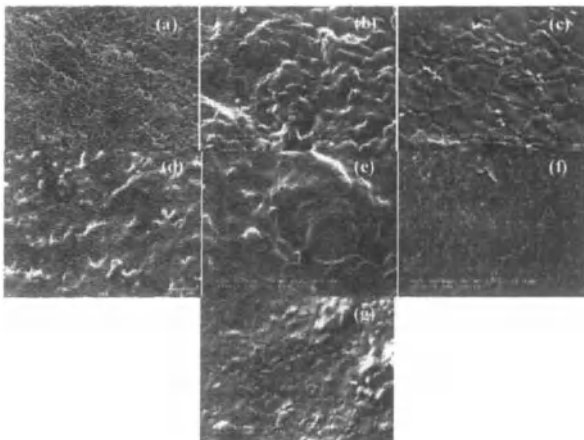


Figure 2: SEM patterns of doped samples: (a) Al, (b) Al-Ti, (c) Al-Cu, (d) Ag, (e) Ag-Ti, (f) Ag-Cu, (g) B

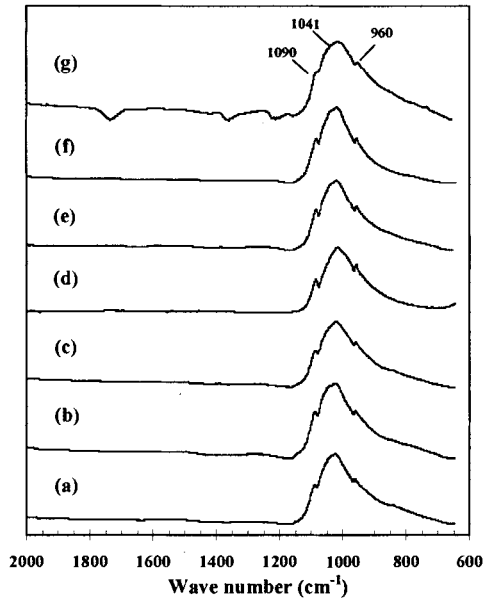


Figure 3: FTIR patterns of doped samples: (a) Al, (b) Al-Ti, (c) Al-Cu, (d) Ag, (e) Ag-Ti, (f) Ag-Cu, (g) B

## **Electric Resistivity of Fine Chromite Ore**

Cheng Pan, Xuewei Lv, Chengguang Bai, Xuyang Liu, Donghai Li  
College of Materials Science & Engineering, Chongqing University,  
Chongqing 400044, China  
Emails: panchengcq@163.com. lvxuewei@cqu.edu.cn

Keywords: Chromite, Electric resistivity, Particle size

### **Abstract**

Fine chromite ore is the common raw material to produce ferrochrome alloy through the submerged electric furnace process. The electric resistivity of fine chromite ore plays an important role in the operation efficiency because it determines the current distribution. The effect of particle size and the contact area of the particles on electric resistivity for several of chromite were investigated at room temperature, and the relationship between the electric resistivity of mixed particles and the volume fraction of lump ore to fine ore was also studied. The results shown that the electric resistivity increases with the increase of particle size, and the electric resistivity of mixture decreases with the increase of volume ratio of fine ore.

### **Introduction**

Chromium is one of the most important alloying elements in manufacturing of stainless steel that used at high temperature and corrosive environment applications [1, 2]. As the raw materials to be charged into the steel, ferrochromium alloys and charge chromium are produced directly by smelting of chromite ore with the reducing agent in submerged electric arc furnace (SAF). During the process, the oxides of chromium and iron were reduced by carbon and meanwhile the electrical energy were consumed [3, 4]. The ideal industrial process is to achieve high recovery level of Cr and Fe with minimal power consumption. In SAF process, the electric resistivity of charge stock has significant effect on the current distribution, which determines the heat distribution, molten bath structure and chemical reactions in the furnace. High resistance of the charge is desired to reduce the current distribution through the charge stock, thus the electrodes may insert into the charge stock with proper depth to form a high temperature arc heat source, and proper smelting can be realized[5].

China is lack of chromite resources, many companies have to import kinds of fine chromite from other countries all over the world. The electric resistivity of chromite changes a lot with the mineral constituents, chemical composition and particle size, etc. In this study, the effect of particle size and the specific contact area of the particles on the electric resistivity were investigated at room temperature. Furthermore, the relationship between the electric resistivity of the mixed particles and the volume fraction of lump ore to fine ore was also studied.

## Experimental

### Conduct Mechanism

Minerals and oxides are considered as semi-conductors. The electrical conductivity,  $\delta$  ( $S.m^{-1}$ ) is due to the diffusion of charge-carrying species, and can be expressed with the Nerst–Einstein equation[6],

$$\delta = Dz^2e^2n / KT \quad (1)$$

Where  $D$  ( $m^2.s^{-1}$ ) is the diffusion coefficient,  $z$  is the valence of the conducting species,  $e$  is the charge of the electron,  $n$  is the concentration of the conducting species,  $K$  ( $J.K^{-1}$ ) is Boltzmann constant and  $T$  ( $K$ ) is temperature. Since diffusion is a thermally activated process, the electrical conductivity of minerals is classically expressed as [6-8]:

$$\delta = \frac{\delta_0}{T} e^{-\frac{E}{KT}} \quad (2)$$

In equation (2)  $\delta_0$  is the preexponential constant and  $E$  ( $J.mol^{-1}$ ) is the activation energy. In practice, the  $1/T$  factor in the preexponential term is often omitted when direct measurements of electrical conductivities are performed[6].

### Experimental Materials and Scheme

The composition and mineral phase of the four kinds of chromites used in this study are shown in Table 1 and Fig.1. The main mineral phases in the chromites are similar, these mineral include  $MgCr_2O_4$ ,  $Fe_3O_4$ ,  $MgFeAlO_4$ ,  $(Mg,Fe)(Al,Cr)_2O_4$ ,  $(Mg,Al)(Si,Fe)_4O_{10}(OH)_8$ . In order to study the effect of particle size on electric resistivity, the chromite was screened to different size range. In this study, four kinds of chromites were investigated.

Table 1 The composition of the chromite ore

Composition/%	TFe	Cr <sub>2</sub> O <sub>3</sub>	MgO	CaO	SiO <sub>2</sub>	Al <sub>2</sub> O <sub>3</sub>	Cr <sub>2</sub> O <sub>3</sub> /FeO
Ore A	10.6	42.8	17.5	0.63	8.0	10.6	3.1
Ore B	11.0	38.6	20.1	0.61	8.8	10.4	2.7
Ore C	17.9	37.8	10.3	0.74	8.1	15.2	1.6
Ore D	9.4	41.5	21.2	0.74	10.0	6.2	3.4

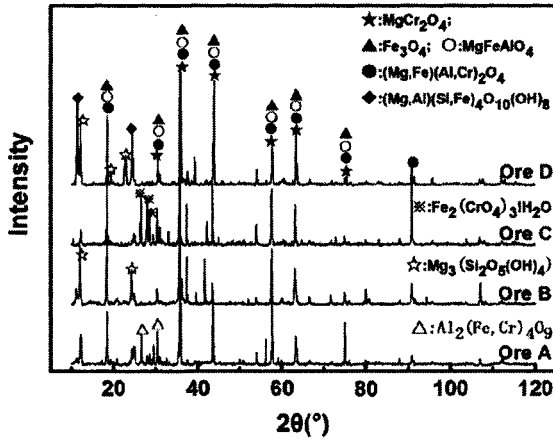


Fig.1 The XRD pattern for the chromite ore

Sample C has the highest total Fe among the four samples while the other three are barely the same. The ratio of  $\text{Cr}_2\text{O}_3/\text{FeO}$  of sample D is maximum, and that of sample C is minimal. For the mineral phases in the samples, sample A and sample C are similar; while sample B and sample D are similar. The sample A and C contains a little  $\text{Al}_2(\text{Fe,Cr})_4\text{O}_9$ ,  $\text{Fe}_2(\text{CrO}_4)_3 \cdot \text{H}_2\text{O}$ , respectively; and sample C and D has a little  $\text{Mg}_3(\text{Si}_2\text{O}_5(\text{OH})_4)$ .

### Experimental Apparatus

The experimental apparatus is shown in Fig.2. In the experimental process, the samples were loaded in the organic glass tub. The upper and lower surface of the stock column was contacted with the graphite brick, and the electric resistance of the stock column was measured by the multimeter, and the height of the stock column was measured by ruler. The electric resistance was frustrated in the beginning, 30 minutes was necessary for stabilizing the values measured. Once the reading on the multimeter was stable, the electric resistance and the height of the stock column were recorded. In order to eliminate system error, the dependency of the electric resistance on the height stock column was measured for each chromite, which is expressed as:

$$R = \rho L/S \quad (3)$$

where  $R$  ( $\Omega$ ) is electric resistance,  $\rho$  ( $\Omega \text{ m}$ ) is electric resistivity,  $L$  (m) is height of the stock column,  $S$  ( $\text{m}^2$ ) is the cross-sectional area of the stock column. So the slope of the fit line of  $R$  and  $L/S$  is  $\rho$ .

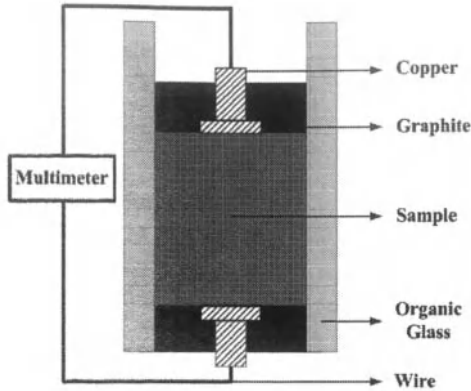


Fig.2 Apparatus for the measurement of electric resistivity of minerals

### Results and Discussions

#### Effect of Particle Size on Electric Resistivity

Fig.3 shows the relationship between electric resistance and the height of stock column. The electric resistivity was obtained based on Equation (3).

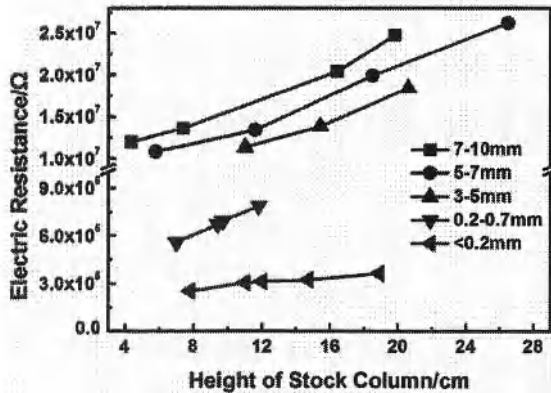


Fig.3 The relationship between electric resistance and height of stock column

Fig.4 shows the relationship between the electric resistivity and particle size of chromite. The electric resistivity of four kinds of chromites are different in the case of particle size is in the same range. For instance, when the particle size is less than 0.2mm, the electric resistivity of ore A is the minimum while ore D's is the maximum, the electric resistivity of ore D is two orders of magnitude higher than ore A. The electric resistivity decreases with the decrease of particle size for each sample though the amplitude is different. There are abrupt decrease for the electric resistivity

of ore A and ore C when the particle size is less than 0.5mm and 0.2mm respectively. The electric resistivity of ore B and ore D change smooth with the change of particle size.

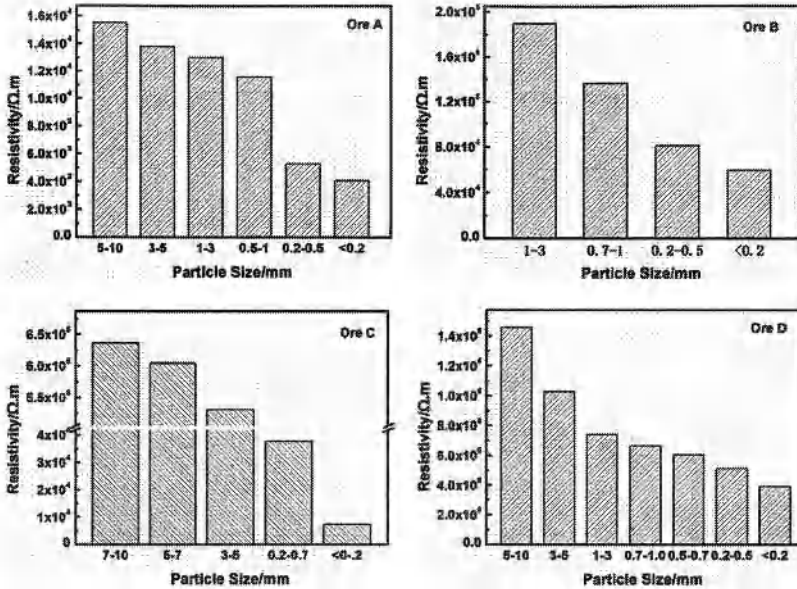


Fig.4 The relationship between electric resistivity and particle size

The effect of particle size on electric resistivity owes to the contact resistance, which in turn is determined by the contact area between the particles. Thus, it is essential to investigate the influence of the contact area between particles on the electric resistivity. In this study, total specific surface area of chromite particles for unit volume was defined to characterize the contact area. The average particle size was used to calculate the specific surface area of chromite in unit volume. The shape of the particles was considered as spherical.

It can be obtained From Fig.5 that the electric resistivity decreases with the increase of superficial area. The influence of contact area between particles on electric resistivity is obvious. The relationship between electric resistivity and superficial area of unit volume chromite can be expressed as follow,

$$y = A \times \exp(-x / t) + y_0 \quad (4)$$

In equation (4)  $A$ ,  $t$ ,  $y_0$  are constant,  $y$  is electric resistivity,  $x$  is superficial area.

Equation (4) can be written as Equation (5) based on Equation (2):

$$\rho = \rho_1 \times \exp(-x / t) + \rho_0 \quad (5)$$

In Equation (5),  $\rho$ ,  $\rho_1$ ,  $\rho_0$  may be interpreted as total electric resistivity, maximum contact resistivity and mineral characteristic electric resistivity respectively. The results show that  $\rho_1$  and  $\rho_0$  are different for the different chromites, this is due to the contact resistivity depends on surface microstructure of particles and mineral characteristic electric resistivity depends on chemical composition and material phase, etc.

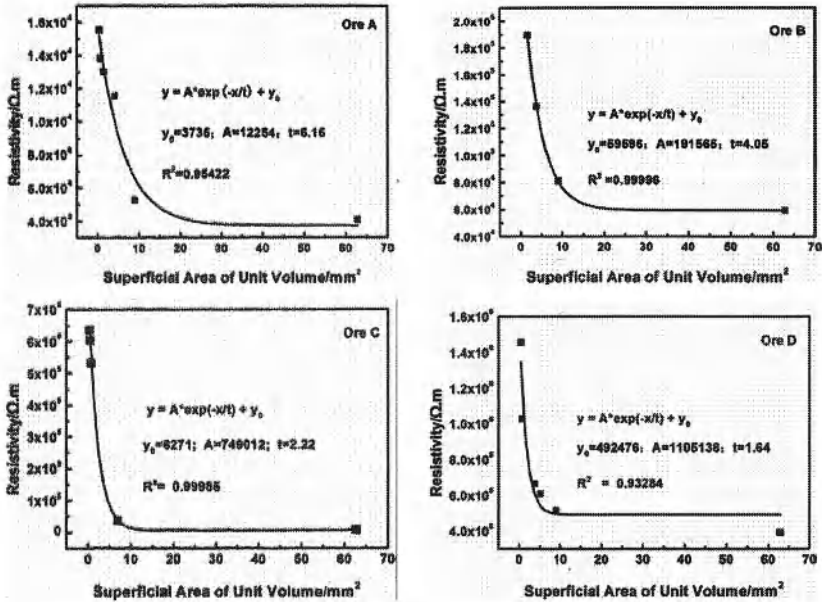


Fig.5 The relationship between electric resistivity and superficial area

To interpret the relationship between electric resistivity and superficial area can be explained by Fig.6, which shows the equivalent circuit of different particle size chromite. From Fig.6, it can be obtained that the total electric resistance is composed of  $R_m$ (chromite characteristic resistance) and  $R_c$ (contact resistance). The contact resistance depends on contact area between particles in the cross-section of the stock column. The contact area is significantly influenced by the number of contact points between particles, while the contact points in a cross-section depend on particles size. As an illustration, as shown in Fig.6, the number of contact points changes with the decrease of particle size from one to infinitely great in cross-section A. For another, that the total electric resistivity equal to mineral characteristic electric resistivity when superficial area is infinite based on Equation(5), that meet the above analysis well. So the particle size of chromite has a significant effect on the electric resistivity of fine chromite.

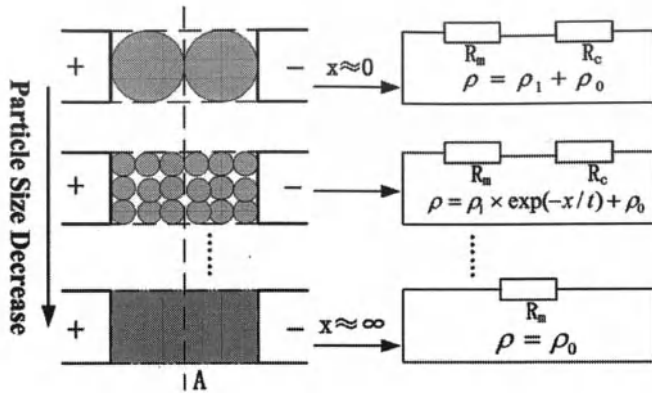


Fig.6 Equivalent circuit of different particle size chromite ( $R_m$ : chromite characteristic electric resistance;  $R_c$ : contact resistance;  $x$ :superficial area)

### Effect of Volume Fraction of Lump and Fine

A high electric resistance is beneficial in the SAF process, and small particle chromite has lower electric resistivity. Therefore, it is necessary to study the effect of volume ratio of small particle on the electric resistivity of mixture stock. In this study, the ore D was screened into fine ore and lump ore, where, the particle size is less than 0.2mm and in the range of 5-10mm respectively. Fig.7 shows the dependency of the electric resistivity on the volume ratio between the fine ore and lump ore. It is obvious that the electric resistivity of the mixture decreases with the increase of fine ore, and the relationship agree with equation (5) well too. It indicates that the electric resistance of the burden can be improved by changing the distribution of the particle size.

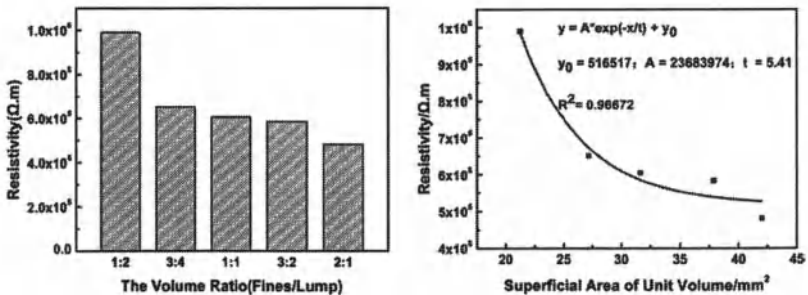


Fig.7 Effect of volume ratio of fine ore and lump ore on electric resistivity

### Conclusions

1. The electric resistivity of chromite decreases with the decrease of particle size and with the increase of the contact area.

2. The electric resistivity of the mixture of fine ore and lump ore decrease with the increase of volume ratio of fine ore.

### Acknowledgements

The authors are especially grateful to Major Program of National Natural Science Foundation of China (Grant No. 51090383) and Chongqing University Postgraduates' Science and Innovation Fund (Grant No. CDJZR11 13 00 27).

### Reference

1. Atasoy, A. and F.R. Sale. An investigation on the solid state reduction of chromite concentrate. in *Mechatronic Systems and Materials III*. 2009. Laubisrutistr.24, Stafa-Zuerich, CH-8712, Switzerland: Trans Tech Publications Ltd.
2. Weber, P. and R.H. Eric, The reduction of chromite in the presence of silica flux. *Minerals Engineering*, 2006. 19(3): p. 318-324.
3. Chakraborty, D., S. Ranganathan, and S.N. Sinha, Carbothermic reduction of chromite ore under different flow rates of inert gas. *Metallurgical and Materials Transactions B: Process Metallurgy and Materials Processing Science*, 2010. 41(Compendex): p. 10-18.
4. Li, J.-C., G.-H. Bai, and G.-H. Li, Solid-state reduction properties of carbon-bearing chromite pellets. *Zhongguo Youse Jinshu Xuebao/Chinese Journal of Nonferrous Metals*, 2011. 21(Compendex): p. 1159-1164.
5. Chu, S.-J., et al., Simulation on the conductivity of charging stock with percolation structure in the submerged arc furnace. *Guocheng Gongcheng Xuebao/The Chinese Journal of Process Engineering*, 2003. 3(Compendex): p. 413-413.
6. Vacher, P. and O. Verhoeven, Modelling the electrical conductivity of iron-rich minerals for planetary applications. *Planetary and Space Science*, 2007. 55(4): p. 455-466.
7. Dobson, D.P., N.C. Richmond, and J.P. Brodholt, A high-temperature electrical conduction mechanism in the lower mantle phase (Mg,Fe)<sub>0.1-x</sub>O. *Science*, 1997. 275(5307): p. 1779-1781.
8. Yoshino, T., et al., The effect of water on the electrical conductivity of olivine aggregates and its implications for the electrical structure of the upper mantle. *Earth and Planetary Science Letters*, 2009. 288(1-2): p. 291-300.

## MELTING AND REDUCTION OF MANGANESE SINTER WITH FLUXES

Thomas Brynjulfsen<sup>1</sup>, Merete Tangstad<sup>1</sup>,

<sup>1</sup> Norwegian university of science and technology, Department of Materials science and technology

Keywords: Manganese, Agglomerates, Sinter, Smelting, Reduction, Fluxes

### Abstract

Manganese ore fines, generated during mining and transportation, can not be added to the submerged arc furnace directly as they will prevent even gas flow through the burden. Low gas permeability in the burden will lower the degree of pre-reduction of ore and subsequently increase the carbon and energy consumption of the process. In order to utilize manganese ore fines in the furnace they are agglomerated into sinter, pellet or briquettes. The agglomeration process will however change the reduction properties of the ore. In this work the melting and reduction properties of sinter has been investigated.

The melting temperature and melting mechanisms has been studied. The mineralogy of the raw ores and agglomerated has been found using XRD, and the composition established using EPMA(WDS). The effect of adding fluxes such as dolomite and quartz has also been investigated.

### Introduction

Manganese metal is produced in a submerged electric arc furnace or in blast furnaces. The reduction of manganese oxide in blast furnace has in the recent years become more unusual due to the high consumption of reducing carbon material[5]. Manganese metal for alloying in steel usually contains silicon and iron, and are therefore called ferro manganese and silicomanganese.

During mining, transportation and handling the manganese ore is broken up into different size fractions. The larger lump are used directly in the electric arc furnace, but the finer materials can not be added without treatment. The fine ore can disrupt the flow of CO and CO<sub>2</sub> gas through the burden, subsequently reducing the degree of pre-reduction. The fine fractions must therefore be agglomerated into larger lumps, in order to promote gas flow. This can be achieved through a number of different processes. The agglomerate used in this work has been sintered, which means that it has been partly molten and reduced, in order to create bigger lumps.

### Experiments

#### XRD

X-ray diffraction was performed on samples of the ore and sinter in order to determine the phase compositions of the unreduced materials.

### Induction Furnace Experiments

To investigate the melting and reduction of Gabonese sinter under more industrial like conditions a 50 kW induction furnace was used. A carbon crucible was used to contain the sample mix. The carbon crucible also acts as a heating element in the induction furnace. A coke layer in the bottom will work as the coke-bed in the industrial furnace. The charge mixture itself is a mixture of Gabonese sinter, dolomite/quartz and coke. A coke layer on the top works as insulation, and ensures that the charge is not re oxidized. An s-type thermocouple was placed inside a carbon tube which rested on top of the coke bed. Another thermocouple was placed on top of the charge mix. The thermocouple on top of the coke bed was used as a reference when controlling the temperature of the furnace.

The composition of the charge mixture is given in table1. In each experiment around 1 kg of charge mixture were used. The size of the coke particles was 5-10 mm and the sinter and flux particles were sieved to 8-18 mm.

Table 1: Charge composition in addition to 100g of sinter and final temperature of experiments

Sample	coke*	Quartz*	dolomite*	Temperature
D1	25	0	25	1370
D2	25	0	25	1450
D3	25	0	25	1510
D4	25	0	25	1570
Q1	25	35	0	1300
Q2	25	35	0	1390
Q3	25	35	0	1460
Q4	25	35	0	1500

\*Per 100g of sinter

The crucible was heated up to 1200°C where it was held for 30 minutes. This was done to ensure that the ore was completely pre-reduced before the last heating step. After the pre-reduction step the crucible temperature was increased 20°C per minute until the target temperature was reached. The furnace is then shut down and the melting and reduction reaction stops instantly due to the endothermic nature of the reaction. The experiments were repeated with different target temperatures in order to investigate the temperature dependence of the reduction and melting. There will be a temperature between the top and bottom of the coke bed. The difference in temperature is around 200°C during the holding time, and it decreases below 50°C when the whole charge is melted or reduced. After cooling the crucibles were filled with epoxy. A two cm thick vertical slice was cut out from the middle of crucible. These slices was used as a basis to determine the fraction of melted and reduced sinter. Cores were drilled out from selected areas of each crucible, and further studied using EPMA.

## Results

### XRD

The Gabonese ore contained around 30% nsutite ( $MnO_{2-x}OH_x$ ) and 53 % cryptomelan ( $K_xMn_8O_{16}$ ) in addition to 12% of pyrolusite ( $MnO_2$ ). The same composition was reported by [2]. The sinter consisted of around 45% of distorted hausmannite ( $Mn_3O_4$ ), 22% of tephroite ( $Mn_2SiO_4$ ) and 10% of manganosite (MnO). Also there was 16 % of an unidentified amorphous phase. In heat treated Gabonese ore (1200 °C for 4 hours in CO atmosphere) Sorensen et al. found 9.4% of an unidentified phase.

### Induction Furnace Experiments

The experiments conducted with the induction furnace are listed in table 1. During the experiments the temperature on top of the coke bed was around 200 °C higher than the temperature on top of the charge mix. This temperature gap decreased when the amount of reduction increased.

When the temperature was increased above 1200 °C the sinter started to soften and melt. The melted and reduced sinter drained down into the coke bed. Three different categories were used to characterize the sinter; sinter with original shape, partially reduced sinter and melted and reduced sinter.

The area fraction of the reduced sinter, partially molten sinter and sinter with original shape is given in figure 1(a) and 1(b).

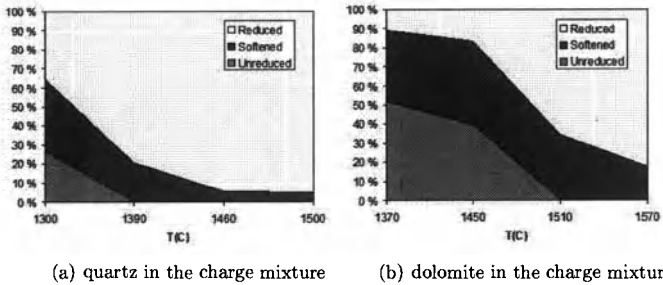


Figure 1: Area fraction of unmelted, melted and reduced sinter as a function of temperature for Gabonese ore

Slizovkiy et al.[3] investigated the reduction of different manganese ores and sinters using the same S.C.I.C.E. technique used in this work. When the sinter is mixed with quartz the temperature needed for melting and reduction is lower compared to a charge without quartz. At 1450 °C, without quartz, they found only around 40% of reduced ore compared to 90 % found in these experiments. The decrease in melting and reduction temperatures, with quartz, are expected from the phase diagram in figure 2(a) due to the increased

amount of Si in the charge.

Fluxing with dolomite gave the opposite effect of quartz. The melting and reduction temperature seems to be around 150°C lower than the temperature observed in the quartz experiments. Xakalashé [1] has found the same temperature effect of dolomite and quartz using Gabonese ore instead of sinter.

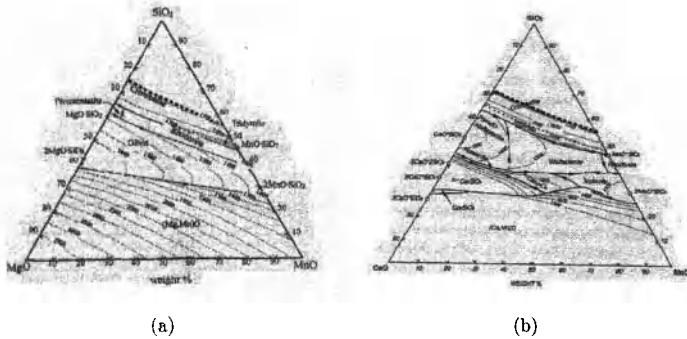


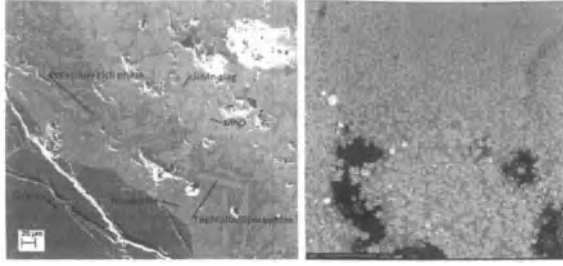
Figure 2: Ternary phase diagrams of MgO, SiO<sub>2</sub>, CaO and MnO from [4]

### EPMA Analysis

EPMA was used to analyse green sinter. Hausmannite is found as a light phase with straight edges and sharp corners. The Manganosite was found closer to the edge of the sintered particle and had rounder sides and edges. The hausmannite and manganosite particles were separated from each other by a tephroite matrix which is the medium gray phase in the figure. The last phase, which could be the amorphous phase found in XRD, is a mixture of a dark phase and a dendritic or lamellar light phase. Overall these two phases contain a high amount of potassium and some barium, indicating that the dark phase could be (kalsilite, kaliophilite( $KAlSiO_4$ )) and the light phase barium oxide.

Figure 3(b) shows the interface between pure slag, and slag with dolomite. In the area with high concentration of dolomite the pure MnO phase is considerably more fine grained. By comparing the particle size in this interface to the hausmannite particles in the raw sinter, it is evident that the addition of dolomite reduces the particle size in the slag. The reduction of the size of these particle could lower the viscosity of the slag, and promoted the flow of slag into the coke bed.

From the phase diagram it can clearly be seen that the melting point in (Mg,Mn)O increase considerably with increasing concentration of Mg. The phase diagrams 2(a) also shows that the olivine containing MgO has a higher melting point than tephroite. This indicates that MgO is important for the increase in melting temperature, and detrimental for the grain size of the solid MnO phase.



(a) SEM image of the interface between sinter and quartz at 1200°C. (b) Interface between slag and dolomite. The dolomite is placed on top.

Figure 3: Melting of sinter and dolomite.

The interface between quartz and sinter differs from the gradual composition change of the dolomite/sinter interface. Several different phases can be identified in the interface using EPMA. A SEM image from the interface between quartz and sinter is shown in fig 3(a). The phase closest to the quartz has the chemical composition of rhodonite ( $(Mn, Fe, Mg, Ca)SiO_3$ ) with mainly Mn. Between the rhodonite and MnO/SiMn slag, two phases can be seen; a dark phase with composition close to that of spessartine ( $Mn_3Al_2Si_3O_{18}$ ), and a light dendritic phase with the composition of tephroite. The dendritic structure indicates that parts of the interface zone were liquid at high temperatures, and solidified into rhodonite, tephroite, and kalsilite/kaliophilite. The spessartine is enriched in aluminium, subsequently leaving the slag close to the MnO phase low in aluminium. The interface between quartz and sinter can also contain a phase rich in potassium. The composition of this phase in sample Q2 matches the composition of kalsilite ( $KAlSiO_4$ ) and its high temperature polymorph kaliophilite. The presence of kaliophilite was predicted by Sorensen et al.[2] in Gabonese ore at 1000°C in CO atmosphere using factsage.

### Modeling

The softening and reduction of manganese ore has been modeled by Slizovskiy et al.[3], determining the rate constants for softening and reduction of ore. The time dependent reduction can be expressed by the rate constant, the area of reduction, the activity of MnO in the slag, and the calculated temperature dependent equilibrium activity of MnO in the slag[5]:

$$\frac{\delta w_{red}}{\delta t} = k_{1,red} A(t) (a_{MnO} - a_{MnO(eq)}) \quad (1)$$

The rate constant is estimated from an Arrhenius equation:

$$k_{1,red} = k_{0,red} \exp\left(\frac{-E_1}{RT}\right) \quad (2)$$

where  $k_{0,red}$  is a constant dependent on the ore,  $-E_1$  is the activation energy for the reduction,  $R$  is the gas constant and  $T$  the temperature. The area of reduction can be estimated by the amount of partly molten ore, since the contact area between solid particles are small. The amount of partly molten ore can also be expressed:

$$\frac{\delta w_{soft}}{\delta t} = k_{1,soft} w_0 \quad (3)$$

Where the rate constant of softening ore can be estimated from an Arrhenius equation:

$$k_{1,soft} = k_{0,soft} \exp\left(\frac{-E_2}{RT}\right) \quad (4)$$

Using the amount of softened ore found from equation 3 the area of reduction can be estimated:

$$a(t) = \frac{l}{\rho_{ore}} \frac{S_P}{V_P} \int \frac{\delta w_{soft}}{\delta t} dt \quad (5)$$

where  $\rho_{ore}$  is the density of the ore,  $V_P$  is the volume of one ore particle and  $S_P$  is the surface area of one ore particle.  $l$  is the reacting coefficient which is assumed to 0,33 in these calculations. If equation (3) is inserted into equation (5) the resulting equation can be expressed as:

$$a(t) = \frac{l}{\rho_{ore}} \frac{6w_0}{D_p} \int k_{0,soft} \exp\left(\frac{-E_2}{RT}\right) dt \quad (6)$$

where  $D_P$  is the diameter of an ore particle. Some assumption has to be made in order to use this model:

- The density of slag and ore is equal and constant during softening and reduction
- The ore particles are all spherical with the same diameter (15mm)
- The contact area between softened ore and coke is one third of the total surface area of the ore( $l=0,33$ )
- There is always solid MnO present in the slag and the activity of MnO in the slag is unity
- The equilibrium activity of MnO in the slag is calculated from the equilibrium constant

The values  $k_{0,red}$ ,  $k_{0,soft}$ ,  $E_1$  and  $E_2$  were found by comparing the model to the experimental results. The values were fitted by minimizing the squares of the difference between the model and experimental results.

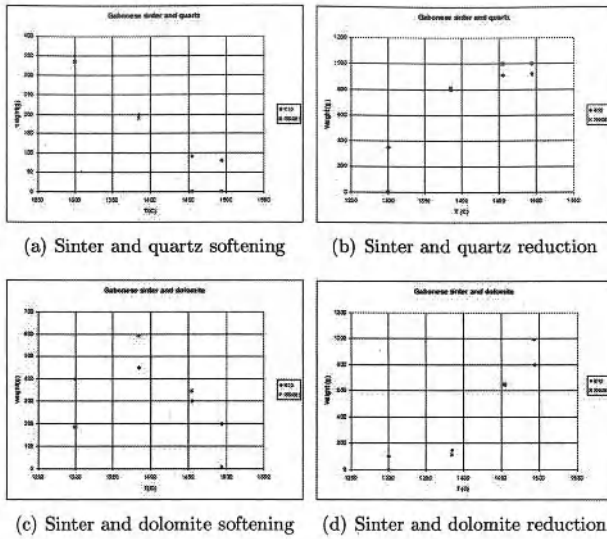


Figure 4: Comparison between model and experimental results

The values found for  $k_{0,red}$ ,  $k_{0,soft}$ ,  $E_1$  and  $E_2$  is given in table 2

Table 2: Parameter for modeling of reduction and softening

Sample	$k_{0,soft}$	$E_2$	$k_{0,red}$	$E_1$
Gabonese sinter and quartz	$7,00 \cdot 10^{12}$	409	$1,37 \cdot 10^{11}$	350
Gabonese sinter and dolomite	$2,50 \cdot 10^{14}$	485	$2,40 \cdot 10^{11}$	395

## Discussion

Slizovkiy et al.[3] investigated the reduction of different manganese ores and sinters using the same S.C.I.C.E. technique used in this work. When reducing Gabonese sinter at 1450°C they observed that around 40% of material was reduced. In this work it can be seen that adding quartz increased the amount of reduced sinter to 90 %. The decrease in melting and reduction temperatures are expected from the phase diagram in figure 2(a) as the Si content in the charge increases. Likewise the amount of reduced sinter at 1450°C with dolomite in the charge were only 12%. The increased meltingpoint of sinter when dolomite is introduced can also be seen from the phase diagram. The increased melting temperature will decrease the contact area between sinter and coke, subsequently decreasing the reduction rate.

The difference between the interfaces quartz/sinter and dolomite/sinter is clear. Whereas the calcium and magnesium seems to have diffused in to the partly molten sinter, the quartz/sinter interface seems to have been completely liquid. The dendritic growth of the spessartine indicates that the interface has been liquid already at 1200°C. In the case of the dolomite interface it seems like the sinter melts first, and then penetrates into the cracking dolomite.

Comparing the parameters for the modeling with those obtained by Slizovski et al. it is clear that adding dolomite will change the parameters  $k_{o,soft}$  and  $E_2$  closer to that of assmang ore, which is high in CaO, than Gabonese sinter. The values  $k_{o,soft}$  and  $E_2$  for the experiment with quartz is close to those for sinter alone found by Slizovskiy et al. The values found for  $k_{o,red}$  varies more from those found by slizovskiy, but this could be due to the fact that they had a fixed value for  $E_1$ .

### Conclusions

- The sinter has a larger melting interval compared to the ore, which could be explained by melting temperature difference between the low temperature melting phases of tephroite/rhodonite, and hausmannite.
- Addition of quartz lowers the melting temperature with around 100 °C. Several distinct phases are observed in the quartz sinter interface, indication that it has been completely liquid. High quartz content also lead to lower activation energy for melting and reduction.
- Dolomite has the opposite effect, rising the melting temperature with around 100 °C. The activation energy for both softening and reduction will increase with increasing dolomite content, which leads to slower reduction.
- Areas with dolomite has finer solid MnO particles in the slag.

### References

- [1] B.Xakalashc. Manganese ore melting temperatures for ferromanganese production. *internal report*, 2010.
- [2] Phase composition of manganese ores and their change in the process of calcination. B.sorensen and s.gaal and e.ringdalen and m.tangstad and r.kononov and o. ostrivski. *Internation journal of mineral processing 94*, 2010.
- [3] D.Slizovskiy, M.Tangstad, and S.Wasbo. Melting temperatures of ore for ferromanganese production. *To be published*, 2009.
- [4] A. Muan and E.F.Osborne. *Phase equilibria among oxides in steelmaking*. Addison-wesley, 1966.
- [5] S.E.Olsen, M.Tangstad, and T.Lindstad. Production of manganese ferroalloys. *SINTEF and Tapir academic press, trondheim*, 2007.

## **CERAMIC PIGMENTS WITH SPINEL STRUCTURE OBTAINED BY LOW TEMPERATURE METHODS**

E. A. Chavarriaga, L. J. Jaramillo, O.J. Restrepo

Universidad Nacional de Colombia, Medellín. E-mail: [ojrestre@unal.edu.co](mailto:ojrestre@unal.edu.co)

Keywords: Ceramic pigments, Spinel structure, Chemical methods, Characterization materials

### **Abstract**

This paper presents the results of the manufacturing ceramic pigments with spinel structure, using methods of synthesis of low temperature. In this work we obtained spinel structures type by the methods of Self-combustion, Coprecipitation, Microemulsion, Gel citrate and Pechini. These methods become an attractive alternative to traditional method (ceramic method), since we can work at a lower temperature, reducing manufacturing costs, lower fuel consumption, less wear on equipment and other environmental and economic implications. Also it is possible to have control over features such as stoichiometry, morphology of the products, reaction times and structures. The products obtained by these routes will be used in the manufacture of ceramic pigments and characterized using different techniques such as X-ray diffraction (XRD), scanning electron microscopy (SEM) and UV-VIS spectrophotometry.

### **Introduction**

Spinel is a ternary oxide  $AB_2O_4$ , where A and B are cations occupying tetrahedral and octahedral positions respectively. These oxides exhibit interesting electrical, magnetic and catalytic properties [1-4], depending on its nature, charging and intrinsic distribution of ions [5].

The most widely used method to prepare spinels has been through solid state reaction, which consists of mixed oxides at high temperatures [6, 7]. In the last years, there have been a strong tendency to use chemical routes for the synthesis of crystalline ceramic particles at low temperatures [8,9]. Unconventional methods currently employed for the synthesis of complex oxides are Gel citrate method, Pechini, Spontaneous combustion, Microemulsion and Coprecipitation. Pechini method [10, 11], based on polymeric precursors, does not require high temperatures and allows stoichiometric control for greater reproducibility. This method involves the formation of a polymeric resin between a metal quelate and polyhydroxy acid of alcohol by polyestirification.

Coprecipitation is important for many environmental problems related to water resources, including acid mine drainage, migration of radionuclides in waste repositories dirty, transport of contaminant metals in the industry, metal concentrations in aqueous systems and the technology of wastewater treatment. The coprecipitation process can vary in each case; the partition in the solid phase can be carried out by surface adsorption, ion exchange, surface precipitation, occlusion and formation of solid solution. The formation of solid solution is the result of structural incorporation of the marker in structural support sites resulting in a minor component in the solid solution with the host phase that has a very low solubility of pure solid [12]. Synthesis by gel citrate method allows the use of a route to obtain ceramic pigments from a very simple experimental system in which the stoichiometric control, the size and shape of the particles and the purity of the phases obtained can be controlled more accurately [13].

This study is focused on the preparation of solid solutions of spinels with chromium  $ACr_2O_4$ , (A is a cation that can be iron, zinc or calcium), and iron and zinc ferrite  $ZnFe_2O_4$  by citrate gel method, Pechini and coprecipitation assisted by ultrasound, in order to show the advantages of using unconventional methods to obtain spinel structures which are used as ceramic pigments. They were

characterized to determine structure by XRD, morphology by SEM and reflectance by spectrophotometry VIS.

### **Methodology**

For the synthesis of spinels we worked with chromium and iron structures known as chromites and ferrites. They were:  $ZnCr_2O_4$ ,  $FeCr_2O_4$ ,  $ZnFe_2O_4$  and  $CaCr_2O_4$ . These structures were synthesized by different methods and had the following procedures:

#### **Gel Citrate Method**

We prepared two solutions: For the first solution were weighted 5.25g of  $Ca(NO_3)_2 \cdot 4H_2O$  (Merck) 99% purity, 19.23 g  $Cr(NO_3)_3 \cdot 9H_2O$  (R-A Chemicals) 98% purity, and a solution was prepared in distilled water. For the second one 9.04g of citric acid mono-hydrated ( $C_6H_8O_7 \cdot H_2O$  Panreac) 99% purity were weighted and dissolved in distilled water. The two solutions were mixed while stirring until leaving to form a homogeneous mixture, the pH was raised to 8 with ammonia solution 26%, the temperature was slowly increased until 80 °C to the formation of a gel. Temperature was slowly increased until self-combustion reaction occurs at 175 °C. Finally, the obtained powders were milled and calcined at 700 °C for 6h.

#### **Coprecipitation Assisted by Ultrasound**

Raw materials used were iron  $FeCl_3 \cdot 4H_2O$  63% (Panreac), zinc  $ZnCl_2$  97% (Carlo Erba) and chromium chlorides  $CrCl_3 \cdot 6H_2O$  97% (Merck) as precursors. These salts with an aqueous solution were prepared using distilled water at a temperature of 70 °C. This solution was added drop wise to an aqueous solution containing NaOH, 99% (Merck), for pH regulation with respect to pH,  $KNO_3$  as oxidizing agent, 99% (Mallinkrodt), also at a temperature of 70 °C with vigorous stirring and permanent for several minutes. The solution was carried to the ultrasound machine and leaves it for an hour, then allowed to stand a few minutes and proceeded to vacuum filter. The precipitate is washed with water and ethanol to remove soluble salts and filtered again; this proceeding was done repeatedly until no traces of salts. We proceeded to dry in an electric oven at temperature of 95-100 °C for 12 hours and finally subjected to a heat treatment for 8 hours at 800 °C. The ramp was made to a scale of 5 °C per minute.

#### **Pechini Method**

Citric acid (18g, Carlo Erba) was weighed and was dissolved in distilled water at a constant stirring, then slowly increases the temperature between 60 and 70 °C. After 13.54g was added iron chloride (Carlo Erba). A salt of Zn (5.65g, Carlo Erba) was added, these cations are complexed with citric acid. The dissolution of the salts increase the temperature to 90 °C then it was added 12 g of ethylene glycol (Carlo Erba) to perform the polyesterification reaction. The reaction was terminated with the formation of a transparent resin. Subsequently, the resin is heated to 300 °C for 1h (primary calcination) allowing partial decomposition of the gel forming polymeric resin and expanded material consisting mainly of semi carbonized. After the first calcination the organic wastes rich powders were fired at 900 °C for 6h.

X-ray diffraction (XRD) was performed in order to determine the crystalline phases that are present in each of the samples on a PANalytical diffractometer brand, model XPert-Pro, using Cu K $\alpha$  radiation of 1.54060 Å, from 4 to 75°, at a rate of 0.02°/min and 400 cps.

To observe the morphology of the samples we used a scanning electron microscope JEOL model 5410 mark by retro projected signals and secondary electrons. The reflectance spectra and colorimetric coordinates were measured with a spectrophotometer UV VIS IR Glacier TM X with lineal arrangement CCD, range from 200nm to 1025nm, using an illuminant D65 CIE and the ASTM

E1349-06 [16], standard observer CIE 1964 and geometry 0°:0°, software is BWspec 3.26. In Table 1 is shown the nomenclature and the conditions of preparation of the samples that were characterized.

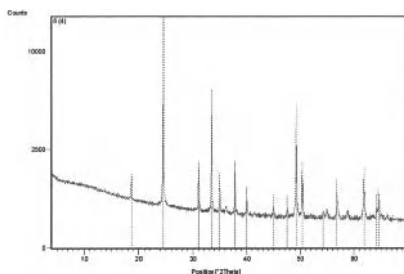
**Table 1.** Nomenclature and condition of samples.

Sample	Synthesis method	Synthesis time (Hours)	Synthesis Temperature (°C)
$\text{CaCr}_2\text{O}_4$	Gel citrate	6	700
$\text{ZnCr}_2\text{O}_4$	Coprecipitation assisted by ultrasound	8	800
$\text{MgCr}_2\text{O}_4$	Coprecipitation assisted by ultrasound	8	800
$\text{ZnAl}_2\text{O}_4$	Pechini	6	900

## Results and Discussion

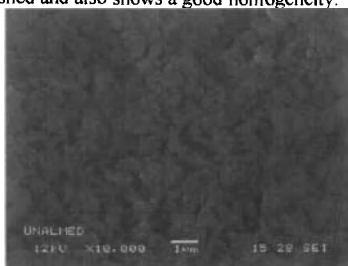
### Gel Citrate Method

Figure 1 shows the phase formation  $\text{CaCr}_2\text{O}_4$  through gel citrate method, there is a high purity of phase, there are peaks corresponding to low intensity  $\text{Cr}_2\text{O}_3$ .



**Figure 1.**  $\text{CaCr}_2\text{O}_4$  XRD

SEM results shown in Figure 2, note that a 10000X is possible to see some small and regular particles. Particles are clearly distinguished and also shows a good homogeneity.



**Figure 2.** SEM for  $\text{CaCr}_2\text{O}_4$ . 10000X

Figure 3 shows the diffuse reflectance spectrum for  $\text{CaCr}_2\text{O}_4$ , it shows a reflectance band characteristic of green (510 - 550 nm).

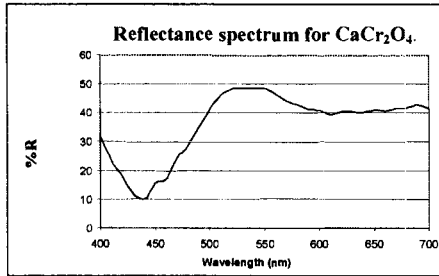


Figure 3. Reflectance spectrum for  $\text{CaCr}_2\text{O}_4$ .

### Coprecipitation Assisted by Ultrasound.

Two structures were prepared by this method  $\text{ZnCr}_2\text{O}_4$  y  $\text{FeCr}_2\text{O}_4$ .

Figure 4 shows crystalline structure of  $\text{ZnCr}_2\text{O}_4$  without secondary phases. Peaks are adjusted at similar intensity. It means that this method is correct to obtain this structure.

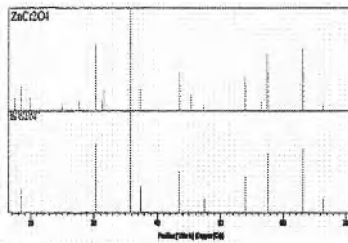


Figure 4. Indexed peaks of  $\text{ZnCr}_2\text{O}_4$

SEM results shown in Figure 5, note that a 5000X is possible to see different crystals and some small particles that may be traces of salt that was not removed. Particle size distribution is about 1 to 3 micrometers. Particles are clearly distinguished and also shows a good homogeneity.

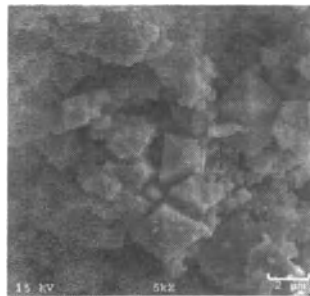


Figure 5. SEM for  $\text{ZnCr}_2\text{O}_4$ . 5000x

Reflectance curve (Figure 6) shows that has a reflectance maximum of 20% and most notable peaks of the curve are at 450 nm, a maximum in 530nm and another at approximately 630nm, indicating that the predominant colors are green and yellow respectively.

In Table 2 is shown colorimetric coordinates. It shows that the coordinate  $a^*$  is negative which indicates a hue green. Coordinate  $b^*$  is positive, it means yellow, thus resulting in a grayish hue that is shown in Figure 7.

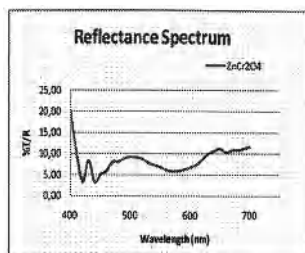


Figure 6. Reflectance spectrum for  $ZnCr_2O_4$ .

Table 2. Colorimetric coordinates  $L^*a^*b^*$   $ZnCr_2O_4$ .

Label	Value
$L^*$	32,536
$a^*$	-1,982
$b^*$	4,020



Figure 7.  $ZnCr_2O_4$  pigment

Figure 8 shows the peaks of the diffractogram  $FeCr_2O_4$ . There are two main crystalline phases, iron chromite and  $Fe_{0.7}Cr_{1.3}O_3$ .

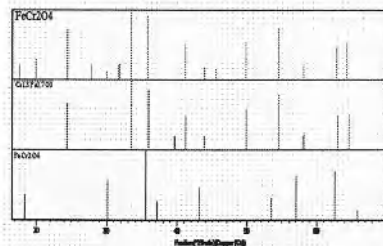
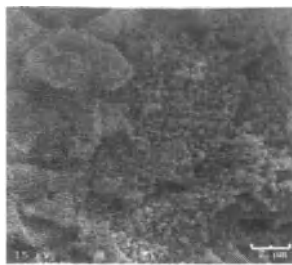


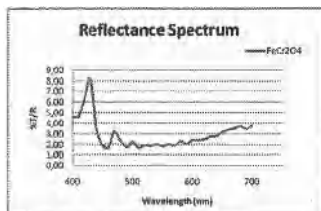
Figure 8. Indexed peaks of  $FeCr_2O_4$

In Figure 9 is possible to see that there is formation of agglomerates, they show that has a homogeneous chemical composition.



**Figure 9.** SEM for FeCr<sub>2</sub>O<sub>4</sub>. 5000X

Figure 10 shows the reflectance spectrum. This curve gives an indication of the behavior of the pigment. This curve not exceeding 10%, that is dark and also shows the highest peaks are between 450 and 500 nm which is the presence of blues and the rest shows no more lengths dominant wave, but covers them all.



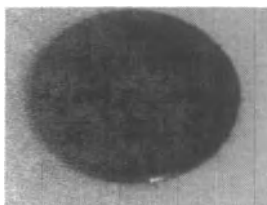
**Figure 10.** Reflectance spectrum for FeCr<sub>2</sub>O<sub>4</sub>.

Table 3 shows the colorimetric coordinates of the pigment. It shows a low brightness and presence of blue hues as seen with the coordinate b\* that is negative.

**Table 3.** Colorimetric coordinates L\*a\*b\* FeCr<sub>2</sub>O<sub>4</sub>.

Lab	FCO
	16,091
	9,158
	-8,784

Figure 11 shows FeCr<sub>2</sub>O<sub>4</sub> pigment obtained by coprecipitation assisted by ultrasound method.



**Figure 11.** FeCr<sub>2</sub>O<sub>4</sub> Pigment

### Pechini Method.

Figure 12 shows the diffractogram for the pigment obtained by Pechini method at a temperature of 900°C. There occurs the formation of spinel phase  $ZnFe_2O_4$  and the phase formation hematite  $Fe_2O_3$ , which have a maximum of intensity characteristic of the spinel to  $2\theta=35^\circ$ .

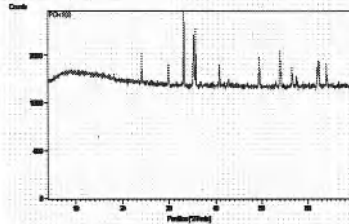


Figure 12. XRD for  $ZnFe_2O_4$  Pechini method at 900°C

Figure 13 shows the SEM micrograph that shows the formation of agglomerates and octahedra which are the characteristic shape of the spinel structure, with particle sizes of about 1 micrometer.

Figure 14 shows a high reflectance in the yellow and red region of the spectrum, which are complementary colors at purple and green regions, respectively, showing a dominant wavelength of about 678nm.

Table 4 shows a high luminance ( $L^*$ ) but low colorimetric coordinate  $a^*$  and  $b^*$  positive, which shows its low saturation. These coordinates show the red and yellow components, respectively.



Figure 13. SEM of  $ZnFe_2O_4$  5000X  
Reflectance spectrum  $ZnFe_2O_4$

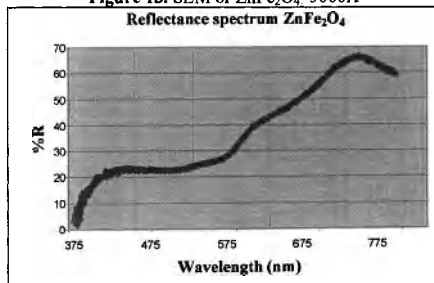


Figure 14. Reflectance spectrum for  $ZnFe_2O_4$ .

**Table 4.** Colorimetric coordinates  $L^*a^*b^*$  ZnFe<sub>2</sub>O<sub>4</sub>.

Lab	ZFO
L*	58,863
a*	13,39
b*	9,86

### Conclusion

By using the coprecipitation assisted by ultrasound method get chromites of zinc and iron with the right stoichiometry and structure, although in iron chromite there is a formation of a second crystalline phase and agglomeration occurs more than in the zinc chromite. CaCr<sub>2</sub>O<sub>4</sub> phase was obtained through the gel citrate method lower temperatures than required with traditional method.

ZnFe<sub>2</sub>O<sub>4</sub> ceramic pigment with spinel structure was obtained by Pechini method which shows that with the alternative method results in a good homogeneity in chemical composition. On the Pechini method is also observed regularity in particles, but at 900°C results in a well-defined morphology and no agglomeration.

Finally we can say that unconventional methods are a good alternative for the production of ceramic pigments and more specifically those with a spinel structure as shown throughout this work, and also obtained at temperatures below 1000°C, where traditional methods are not met to form such structures and also obtained good morphological and colorimetric conditions.

### References

- [1] Nathawan P, Darshane VS. Structural, Transport, magnetic and infrared studies of the oxidic spinels Co<sub>2</sub>-XTi<sub>1</sub>-XFe<sub>2</sub>XO<sub>4</sub>. *Journal of Physics*. 1988;21(6):3191-3203.
- [2] Vlasenko VM, Chernobrivets VL. Methane chlorination on spinel copperchromiumcatalyst in the presence of oxygen. *Russian Journal of Applied Chemistry*. 1998; 71(8):1393-1396.
- [3] Erran E, Trifino F, Vaccari A, Richter M. Structure and reactivity of Zn-Cr mixed oxides Role of non-stoichiometry in the catalytic synthesis of methanol. *Catalysis Letter*. 1989; 3(1):65-72.
- [4] Câmara MSC, Lisboa-Filho PN, Cabrelon MD, Gama L, Ortiz WA, Paiva- Santos CO, Leite ER, et al. Synthesis and characterization of Li<sub>2</sub>ZnTi<sub>3</sub>O<sub>8</sub> spinel using the modified polymeric precursor method. *Materials Chemistry and Physics*. 2003; 82(1):68-72.
- [5] McClure D. The distribution of transition metal action in spinels. *Journal of Physical Chemistry Solids*. 1957; 3:311-317.
- [6] Preudhomme J, Tarte P. Infrared studies of spinels-III. The normal II-III spinels. *Spectrochimica Acta Part A: Molecular Spectroscopy*. 1971; 27(90):1817-1835.
- [7] Chokkaram S, Srinivasan R, Milbrun DR, Davis BH, Conversion of 2-octanol over nickel-alumina, cobalt-alumina, and alumina catalysts. *Journal of Molecular Catalysis A: Chemical*. 1997; 121(2-3):157-169.
- [8] L. Chen, Y. Liu, and Y. Li, *J. Alloy Compd.*, 381, 266, (2004).
- [9] Z. Lu, Y. Tang, L. Chen, and Y. Li, *J. Cryst. Growth*, 266, 539, (2004).
- [10] Pechini M P. US Patent. 3330697, 1967.
- [11] Lessing PA Mixed-cation powders via polymeric precursors. *American Society Ceramic Bulletin*. 1989; 68(5):1002-1007.
- [12] C. Zhu, S. Martin, R. Ford, N. Nuhfer. "Experimental and modelling studies of coprecipitation as an attenuation mechanism for radionuclides, metals and metalloid mobility". *Geophysical research abstracts*, Vol. 5, 06552, 2003.
- [13] A. Bardhan, C.K. Ghosh, M.K. Mitra, G.C. Das, S. Mukherjee, K.K. Chattopadhyay. *Solid State Sciences* 12 (2010) 839–844.

## **MECHANICAL CHARACTERIZATION OF CELLULAR CERAMIC MATERIAL**

Wilson Acchar<sup>1,2</sup>, Fernando Barcelos<sup>2</sup> and Luis Carlos Pereira<sup>3</sup>

<sup>1</sup>Department of Physics, Federal University of Rio Grande Norte (UFRN),  
59072-970 Natal-RN, Brazil;

<sup>2</sup>Post-Graduation Program in Materials Science and Engineering, Federal University of Rio  
Grande Norte (UFRN), 59072-970 Natal-RN, Brazil;

<sup>3</sup>Post-Graduation Program in Metallurgical Engineering and Material, Federal University of Rio  
Janeiro (UFRJ), Ilha do Fundão, Cidade Universitaria, 21941-972 Rio de Janeiro-RJ, Brazil

Keywords: Cellular ceramic, mechanical properties, alumina

### **Abstract**

Porous ceramics have been extensively investigated as structural materials for flow of fluids in many applications, such as filters for molten metals, water purification and hot gases, thermal protection systems and heat exchangers. This class of material must have two special features: high permeability and mechanical strength. However, these parameters are influenced in different ways by the processing method and the consequent cellular structure. In this work two different types of commercial ceramic filter materials are investigated. Characterization included the evaluation of the strength values as well as the permeability behavior and microstructural analyzes of the surface fracture. The results indicate that the strength values are strong dependent on the filament defects.

### **Introduction**

Ceramic materials with a cellular structure have been extensively investigated as structural materials for flow of fluids applications [1-3]. Microstructural aspects such as morphology, size of the cell and the degree of interconnectedness are mainly parameters that influence the properties of these porous materials [4-6]. The most used industrial process to produce cellular ceramics for filter application is the polymeric sponge replication method. This technique consists in dipping the polymer foam into slurry containing an appropriate binder and the necessary ceramic materials, followed by a heating treatment [2,5].

Mechanical properties of cellular ceramics depend basically on cell size, degree of interconnectedness and density [1,2,5,8,9]. Materials used as filters required a good strength and also permeability values. These properties are inversely proportional to each other. Higher porosity increases permeability values but decreases the strength values [1,2,5]. The objective of this work is to study the strength resistance of a commercial porous ceramic material (10, 20 and 30 ppi) based on silicon carbide.

## Experimental Procedure

Cellular ceramic materials with 10, 20 and 30 pores per linear inch (ppi) tested in this work were supplied by Technicer, SP-Brazil. Samples were disks with a diameter of 30 mm. Mechanical tests were carried out in specimens with dimensions of approximately 30 mm×15 mm×10 mm at room temperature. The ceramic materials were also coated with a suspension containing  $\text{Li}_2\text{O}+\text{ZrO}_2+\text{SiO}_2$ , in order to improve the mechanical properties. Strength values (average five bodies for each value) were measured with a universal testing machine (Zwick-Roell) in four-point bending tests at a constant cross-head speed of 0.5 mm/min.

Crystalline phases were identified by X-ray diffraction (Shimadzu XRD 600) in the  $2\theta$  range of 10 to  $90^\circ$  with a  $2\theta$  scanning rate of  $2^\circ \text{ min}^{-1}$ . The cell geometry and the macrostructure of the ceramic foams were characterized by optical camera and the struts and the fracture surface were observed by scanning electron microscope (Schimadzu).

Permeability parameters were evaluated from airflow rate versus pressure drop measurements using the following equations:

$$(P_i - P_0) / (2P_0 L) = (\mu v_s) / k_1 + (\rho v_s^2) / k_2 \quad (1)$$

Where  $P_i$  and  $P_0$  are the absolute air pressures at the entrance and exit of the sample, respectively;  $v_s$  is the superficial fluid velocity;  $L$  is the sample's thickness and  $\mu$  is the air density. The  $k_1$  and  $k_2$  values are known as Darcian and non-Darcian permeabilities, in reference to Darcy' law.

## Results and Discussion

A typical morphology of the ceramic materials investigated in this work is showed in figure 1. The materials show a homogeneous pore size distribution and the presence of some closed cells that can degrade the permeability behaviour.

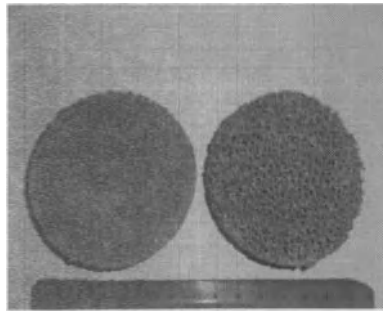


Figure 1. Morphology of the sample.

Table I shows the permeability parameters. The values of  $k_1$  and  $k_2$  are very useful to indicate the pressure drop of the fluid used to flow. The values founded in this work (Table I) are coherent with data presented in the literature [5] and indicated a strong dependence of the cell size and the permeability values.

Table 1. Permeability values ( $k_1$  and  $k_2$ ) of the materials used in this work.

Nominal pore counting (ppi)	$k_1 [10^{-7} \text{ m}^2]$	$k_2 [10^{-3} \text{ m}]$
10	9.42	6.20
30	2,71,	1.90

Figure 2 shows the X-ray diffraction patterns of the ceramic material. The ceramic material is constituted basically by silicon carbide. No other crystalline phases were founded.

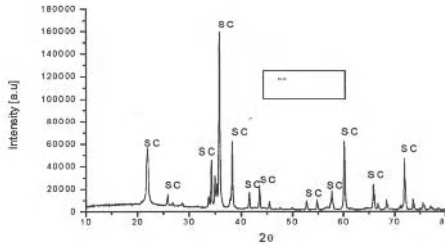


Figure 2. X-ray diffraction.

The effect of cell size and the coating treatment on the mechanical strength is showed in figure 3. The low strength values observed for all tested materials are related to the presence of macro and microdefects in the material such as triangular voids inside filaments (struts), internal microcracks distributed between the filaments and the pores and microcracks into the filaments (figure 4). As described in the literature [1,5] the strength of the cellular ceramic materials depends strongly of the presence and density of these defects. Figure 3 shows that the coating process realized in the ceramic materials has caused an increase in the strength values.

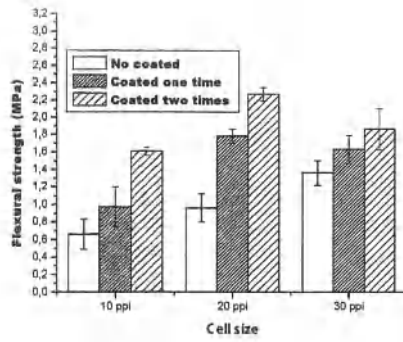


Figure 3. Flexural strengths values.

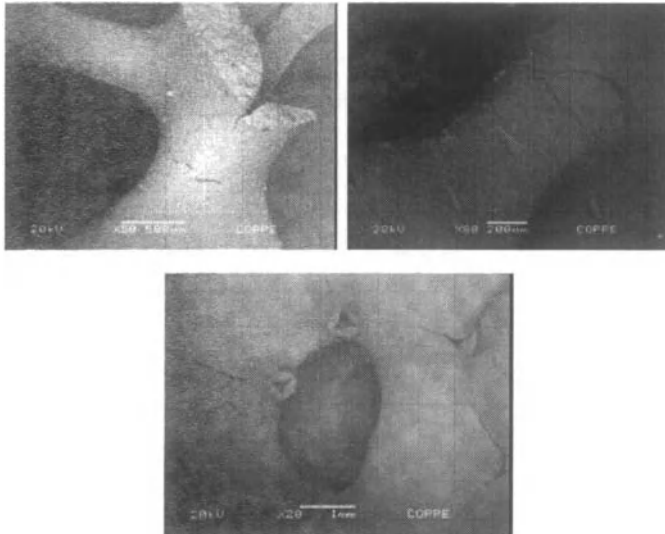


Figure 4. Fracture aspects of the fracture without coating.

Figure 5 shows the fracture surface for coated and no-coated ceramic materials. It can be noted that the coated material shows a decrease of the cracks density on the surface of the filament. It may conclude that the LZSA material has filling the surface cracks, improving the strength values of the material.

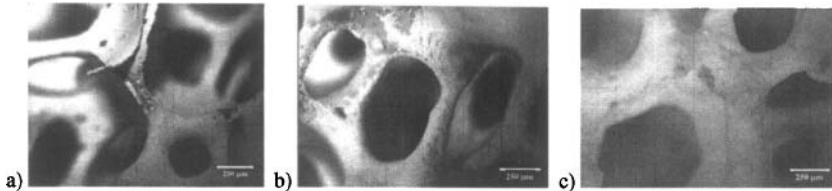


Figure 5 Fracture aspects of the fracture: a) No coated b) coated one time and c) coated two times.

### Conclusions

Commercial cellular ceramic materials with 10, 20 and 30 ppi were analyzed. The results obtained in this work show that the ceramic material is constituted mainly by silicon carbide. All materials show the presence of macrodefects (triangular voids) and also microdefects into the filaments (cracks and micropores) that causes the low strength values. Strength and permeability have shown an inverse dependence, as expected. The 40 and 10 ppi cell sizes showed higher permeability and strength values, respectively. The strength increase observed in coated samples is associated to the decrease of the cracks density.

### References

1. L. J. Gibson, M. F. Ashby and B. A. Harley, *Cellular Materials in Nature and Medicine*, Cambridge University Press, 2010.
2. M. Scheffler, P. Colombo, *Cellular Ceramics: Thermal Properties*, Wiley-VCH, 2005.
3. V.R. Salvini, M.D.M. Innocentini, V.C. Padolfelli, Optimizing permeability, mechanical strength of ceramic foams, *American Ceramic Society Bulletin* 79 (2000) 49-54.
4. D.D. Brown, D.J. Green, Investigation of strut crack formation: In open cell alumina ceramics, *Journal American Ceramic Society* 77 (1994) 1467-72.
5. L.J. Gibson, M.F. Ashby, *Cellular Solids-Structure and Properties*, 2nd Ed., Pergamon Press, New York, 1998.
6. P.Colombo, Ceramic foams: fabrication,properties and application, *Key Engineering Materials* 206-213 (2002) 1913-1918.
7. P. Colombo, J.R. Hellman, Ceramic foams from preceramic polymers, *Materials Research Innovations* 6 (2002) 260-271.

8. R. Brezny, D.J. Green, The mechanical behavior of cellular ceramics, in: R.W. Cahn, P. Haasen, E.J. Kramer, *Materials Science and Technology - A Comprehensive Treatment*, VCH Publishers, Weinheim, Germany, vol.11, Ch. 9, 1991.
9. J. She, T. Ohji, Thermal shock behavior of porous silicon carbide ceramics, *Journal American Ceramic Society* 85 (2002) 2125-2127.

## STUDY OF ATTAPULGITE FOR HUMAN HEALTH

Wilson Acchar<sup>1</sup>, Antonio Carlos Silva da Costa<sup>1</sup>, Tulio Flávio Accioly de Lima e Moura<sup>2</sup> and Ledjane Barreto<sup>3</sup>

<sup>1</sup>Post-Graduation Program in Materials Science and Engineering, Federal University of Rio Grande Norte (UFRN), 59072-970 Natal-RN, Brazil;

<sup>2</sup>Post-Graduation Program in Pharmacia, Federal University of Rio Grande Norte (UFRN), 59072-970 Natal-RN, Brazil;

<sup>3</sup> Post-Graduation Program in Materials Science, Federal University of Sergipe (UFS), Brazil

Keywords: Attapulgite, clay, properties, microstructure

### Abstract

Clays are common ingredients in pharmaceutical products both as excipients and active substances. Clay minerals are naturally cationic exchangers and they may undergo ion exchange with basic drugs in solution. Smectites, and montmorillonite have been studied due their high cation exchange capacity as compared to other silicates. Recently a patented study reports the use of attapulgite as the encapsulating agents both for the protecting the active substance and modulating release into the body. Some clays such as kaolinite, smectites, talc, etc are also used as dermatological protectors. Sepiolite and smectites have the ability to form complexes with organic compounds with absorb ultra-violet radiation, enabling them to be used in sun screens with protection factors. The objective of this work is to characterize the attapulgite in order to study the potential use of this clay material in the human health.

### Introduction

Since the beginning of time, nature has served humanity as a source of various raw materials. Among these, clays such as kaolinite and illite are common ingredients in the tile production. Recently, special clay materials have been investigated in order to identify new potential uses of these class of materials. Clay materials are natural raw material and have excellent properties such as low toxicity, good biocompatibility, making them a good material to be used in biological applications. Attapulgite (paligorskite) and sepiolite is so called special clays. These special clay materials are very similar and have a great potential to be used in some technological areas due their special catalytic, sorptive and colloidal-rheological properties [1-8]. Recently some works have reported the use of these special clays materials for many applications such as drug delivery, wound dressing, oil absorbent, pesticides, fertilizers [9-12]. Brazil has a significant reserve of attapulgite located in Piauí state, making the study of the potential of this mineral in special areas, very attractive. Attapulgite is classified a fibrous aluminous silicate material and shows the presence of micropores and channels, fine particle size and high surface area making this material a good candidate alternative material to be used in many industrial applications [6,8,9,11,12]. The objective of this work is to characterize the physical and microstructure of attapulgite.

### Experimental Procedure

A typical attapulgite clay material from Teresina-Pi, Brazil was collected directly from the industry. Paligorskite (attapulgite) is used today in Brazil only in domestic application. The clay material was physically characterized. The characterization included chemical composition (X-ray fluorescence (XRF), Shimadzu EDX-700), mineralogical composition (X-ray diffraction (XRD), Shimadzu XRD-60) and thermal behavior (differential thermal analysis (DTA), Shimadzu DTA-50, and thermogravimetric analysis (TGA), Shimadzu TGA-51). Crystalline phases were identified by X-ray diffraction (Shimadzu XRD 600) in the range of 5 to 70 ° with a 2θ scanning rate of 2° min<sup>-1</sup>. Morphology and microstructural aspects of the attapulgite were observed by a transmission electron microscopy (Philips).

### Results and Discussion

Table I gives the chemical composition of the attapulgite investigated in this work. The attapulgite is very similar to other clay materials and shows the expected typical composition: rich in silica and alumina (minor contents of Mg, Ti, Ca, Na and K oxides), accompanied by 5.1 wt. % iron oxide.

Table I. Chemical composition (wt.%, XRF) of the attapulgite material investigated in this work.

	SiO <sub>2</sub>	Al <sub>2</sub> O <sub>3</sub>	Fe <sub>2</sub> O <sub>3</sub>	K <sub>2</sub> O	CaO	Na <sub>2</sub> O	TiO <sub>2</sub>	MgO	BaO	P <sub>2</sub> O <sub>5</sub>	SO <sub>2</sub>
Attapulgite	67.7	12.9	5.1	5.4	0.6	0.2	1.0	---	---	---	0.2

Figure 1 shows the X-ray diffraction patterns of attapulgite. It can be seen that the clay material contains quartz and attapulgite peaks, and minor amounts of dolomite, which is in agreement with the chemical results presented in table I.

Figure 2 shows the thermal analyses of attapulgite. The material shows some weight loss that could be associated with water loss, adsorbed water loss, structural water loss and volatile elements.

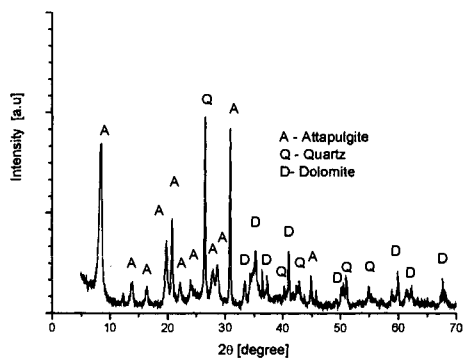


Figure 1. X-ray diffraction pattern of attapulgite.

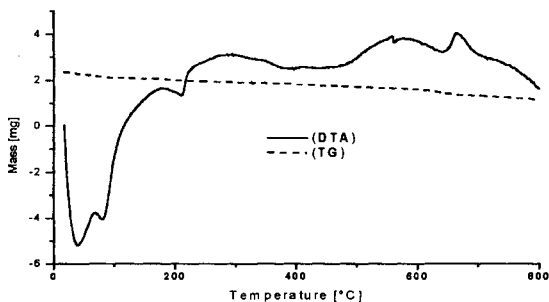


Figure 2. Thermal analyzes of attapulgite.

Figure 3 shows the microstructural aspects of the attapulgite. The transmission electron microscopy enables to see that the microstructure of attapulgite is fibrous and is formed by microchannels. The microstructure of attapulgite is very similar to sepiolite [1,3,9]. Both materials show a fibrous structure with channels running parallel to the fiber length. The fibrous of attapulgite are very fine, showing a diameter of approximately 50 nm. The presence of micropores and channels in attapulgite and sepiolite together with the fine particle size and fibrous structure are responsible to the high surface area of these materials [1,9].

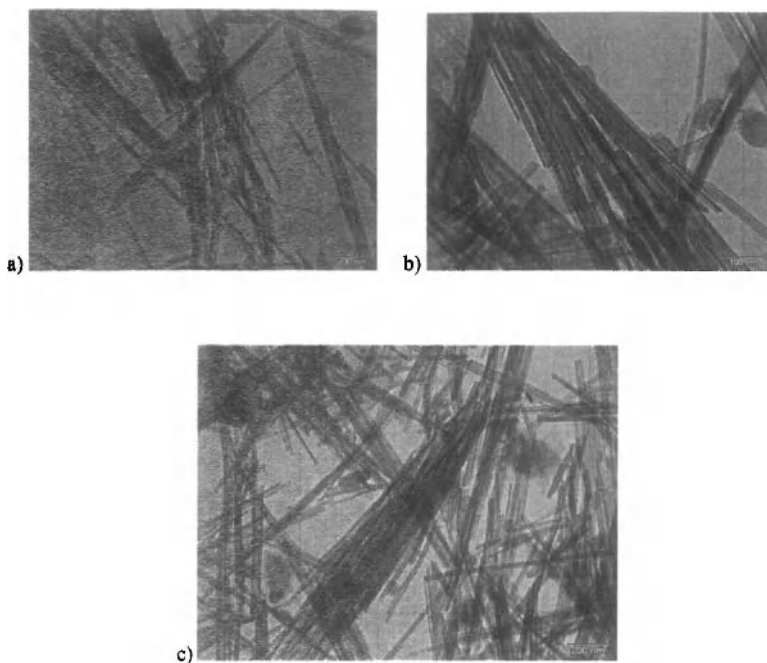


Figure 3. Microscopy electronic of transmission of attapulgite.

### Conclusions

A commercial clay material was analysed in this work. X-ray diffraction results have identified the attapulgite as the main crystalline phase. The morphology of attapulgite shows a fibrous structure with the presence of channels, very similar to sepiolite. The results obtained in this work show that the attapulgite (paligorskite) has a similar microstructure and properties to that of sepiolite, clay used in many branches of industry, because of its technological properties. Results indicate the viability of the application of attapulgite in pharmaceutical field.

### Acknowledgments

The authors thank FAPERN and CNPq for financial support.

### References

1. C. Viseras, Pharmaceutical Applications of some spanish clays, Applied Clay Science 14 (1999) 69-82.

2. M.C.Hermosin, J.White, S.L.Hem, Sepiolite, a potential excipient for drugs subject to oxidative degradation, *J. Pharm. Sci.* 70 (1981) 189-192.
3. A Del Hoyo, M.A. Vicente, V.Rives, Application of phenyl salicilate-sepiolite systems as ultraviolet radiation filters, *Clay Mineral* (1998) 33, 467-474.
4. M.I. Carretero, Clay minerals and their beneficial effects upon human health. A review, *Applied Clay Science* 21 (2002) 155-163.
5. A.C.V. Coelho, P. S. Santos, *Argilas Especiais: O que são, Caracterização e Propriedades*, *Quim. Nova* 30 (2007) 146-152.
6. A.L. Viçosa, A.C. Gomes, B.G. Soares, C.M. Paranhos, Effect of sepiolite on the physical properties and swelling behaviour of rifampicin-loaded nanocomposite hydrogels, *eXPRESS Polymer Letters* 3 (2009) 518-524.
7. Y. Xiang, Z.Peng, D.Chen, A new polymer-clay nano-composite hydrogel with improved response rate and tensile mechanical properties, *European Polymer Journal* 42 (2006) 2125-2132.
8. M.S. Augsburger, E. Strasser, E. Perino, R.C. Mercader, FTIR and Mossbauer investigation of a substituted palygorskite:Silicate with a channel structure, *Journal of Physics and Chemistry of Solids* 59 (1998) 175-180.
9. E. Galan, Properties and applications of palygorskite-sepiolite clays, *Clay Minerals*, 31 (1996) 443-453.
10. M. Kokabi, M. Sirousazar, Z.M.Hassan, PVA-clay nanocomposite hydrogels for wound dressing, *European Polymer Journal* 43 (2007) 773-781.
11. C. Aguzzi, P.Cerezo, C.Viseras, C.Caramella, Use of clays as drug delivery systems:Possibilities and limitations, *Applied clay Science* 36 (2007) 22-36.
12. J-Ho. Choy, S-Jin. Choi, J-Min. Oh, T.Park, Clay minerals and layered double hydroxides for novel biological applications, *Applied Clay Science* 36 (2007) 122-132.

*Characterization of Minerals, Metals, and Materials*  
Edited by: Jiann-Yang Hwang, Sergio Neves Monteiro, Chengguang Bai,  
John Carpenter, Mingdong Cai, Donato Firrao, and Buoung-Gon Kim  
TMS (The Minerals, Metals & Materials Society), 2012

# **Characterization of Minerals, Metals, and Materials**

## **Characterization Technologies**

Session Chairs:  
**Mingdong Cai**  
**John Carpenter**

## 3D METALLOGRAPHY OF MULTIPHASE STEELS

Martin Fischer<sup>1</sup>, Pierre Lutomski<sup>1</sup>, Andreas Stieben<sup>1</sup>, Wolfgang Bleck<sup>1</sup>

<sup>1</sup>RWTH Aachen University; Institute of Ferrous Metallurgy; Intzestr. 1, 52072 Aachen, Germany

Keywords: light optical microscopy, 3D metallography, serial sectioning, image stacks

### Abstract

For steel investigation and development, exact knowledge about the microstructural state is required. The information gained from 2D images often can't properly reflect the real 3D microstructural properties. In order to gain reliable information for meaningful models, simulations and correlations, it is necessary to accompany standard metallography with 3D information, which, unfortunately, is very difficult to access. This article presents a procedure for serial sectioning in combination with light optical microscopy. Only standard metallographic tools are employed in combination with image manipulation freeware. 3D microstructural data were extracted from three multiphase steel grades and in two cases virtual 3D-models of microstructural phases were generated.

### Three Dimensions Of Microstructures

Since the invention of steel, craftsmen, inventors and engineers tried to improve its properties and tailor them to the requirements of new developments. For systematic development and enhancement of steels, the capability to investigate its inner structure is highly important, because it represents the linchpin between material production and properties. By having an in-depth understanding how production conditions form the microstructure and also how the microstructural state determines the material properties, steel design can be drastically improved. With this knowledge, microstructures can be designed to provide target material properties and process conditions can be identified that form these structures. Due to the key role of microstructure, the capability to gain accurate information about it is indispensable. It is the task of metallography to access and extract descriptive quantitative microstructural data like fractions, sizes, shapes and distributions of the different constituents. The most commonly used investigation tool in metallography is the light optical microscope (LOM). Besides this tool, additional high resolution techniques like Scanning Electron Microscopy (SEM) or Transmission Electron Microscopy (TEM) have become increasingly important. With these and other available methods, extensive information on the microstructural state of a material can be gained. Unfortunately, most metallographic methods have a major loss of information systematically built in. Analyses of microstructures are usually performed on surfaces, i.e. on 2D areas that emerge by cutting through the 3D material structure. This means, a complete dimension of information is not taken into account. How serious this reduction of information is and how it can affect interpretation of structures is exemplarily demonstrated in **figure 1**, which displays the planar structure emerging from a random cut through a simple 3D structure. It is very difficult to deduce or even imagine the original spatial structure from which this projection emerged and it is impossible to reconstruct it with absolute certainty without further information. The image has emerged from a random cut

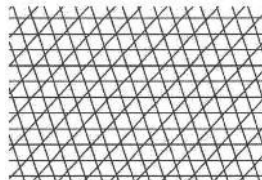


**Figure 1:** 2D cut through an unknown simple 3D structure

through a 3D structure of stacked cubes that is displayed in figure 2. The area shown in figure 1 is outlined. Although artificially constructed, this example demonstrates how distorted and misleading the view on structures can become by ignoring a spatial dimension.

The deduction of data on 3D structures from 2D information is task of the "stereology". Unfortunately this deduction generally provides an infinite number of possible solutions. For instance, a circular surface with a defined diameter can emerge by cutting through a sphere, a cylinder, a cone and other geometric bodies, which can also vary in size. Due to this problem, stereological methods are generally only applicable in metallographic analysis for constituents with defined and convex shapes [1]. In other words: In order to gain reliable information about the 3D properties of microstructural constituents from 2D analysis, it is necessary to know their general shape characteristics beforehand. The constituents must also have concave geometry, because otherwise they could be cut multiple times by a single plane and appear as several separate constituents. As an additional constraint due to practical reasons, the general shape of constituents has to be isometric, because non-isometric bodies display a much larger statistical variety of appearances when cut from different angles [1]. These constraints limit the validity of analysis data gained from 2D-images for modern steel grades for several reasons. Modern steels often comprise complex microstructures with constituents of various shapes, often concave, that can't be abstracted by a single general geometry. What is more, the 3D shape of investigated microstructural constituents is usually unknown. Indeed, in most cases, even the 2D structure is unknown before the analysis is carried out. For these reasons microstructural analyses in 2 dimensions can lead to distorted data on size, shape, spatial distributions, connectivity, et cetera. In order to gain accurate data as input for correlations, models and simulations on phase transformation or microstructure evolution, it is necessary to access information on the 3D microstructural state directly. In the following section, available methods for this are briefly reviewed.

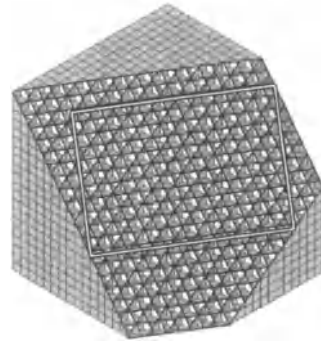


Figure 2: 2D cut through a simple 3D structure

### 3D Analysis Techniques

#### Serial Sectioning With LOM

A straightforward approach to access the 3D microstructural features of a steel grade is "serial sectioning" which means to investigate the microstructure at the same sample spot in different depths by a stepwise removal of material layer between analyses. The resulting 2D image series are then combined with the depths data to provide 3D-information. For serial sectioning with LOM, material is usually removed by polishing and the microstructural constituents are contrasted by etching. Images are taken with a digital camera and afterwards analyzed by differentiating the colors of the constituents [2]. The distances between the layers can be measured by utilization of a Vickers hardness indent. This indent has the shape of a pyramid with a square basis. The angle between two opposite faces is  $136^\circ$ . The depth  $h$  of an indent can be calculated by the formula  $h=d/2*\tan(\alpha)$  with  $\alpha=15,994^\circ$  and  $d$  as the length of one diagonal [3]. In order to convert the 2D information layers into a 3D-data set, the images have to be exactly aligned to each other and stacked [4]. The free space in between the analyzed layers has

to be assigned to microstructural constituents. Usually, this is done according to the layer above or below.

Despite the simple principle, there are several hindrances, when applying serial sectioning to the analysis of steel grades, especially of complex and multiphase ones. One major problem is the detection of microstructural constituents by etching and image analysis, which has to be highly consistent for all images of a series in order to provide usable data-sets. Because etching methods are highly sensitive to parameters like etching time, freshness of the solution, temperature and surface quality, the reproducibility and consistency of results is often limited [5]. It is very difficult to achieve consistent etching results for all images of a series. Image analysis can be a second hindrance, if different phases display similar spectral values [5]. These difficulties increase with rising microstructural complexity and decreasing constituent sizes [4, 6]. An additional major problem is the removal of surface layers of appropriate thickness and the measurement of the according distances between the image layers. In modern steel grades, microstructural constituents often have sizes on a  $\mu\text{m}$ -scale or below. The distances between slices have to be accordingly small and their measurement accurate. Due to these difficulties, 3D-LOM combined with serial sectioning was hitherto only applied to the investigation of distinct microstructural details and single phases, like the 3D structure of pearlite, the shape of cementite precipitations, the shape of proeutectic ferrite precipitates and the 3D-structure of single phase austenitic steel [7, 8].

#### Serial Sectioning Using FIB

Other popular approaches to serial sectioning employ a focused ion beam (FIB) for removing material layers of constant thickness by ion sputtering. This technique can for instance be combined with FIB-microscopy. In alternating sputtering and image taking steps, a series of images through a volume can be produced [9]. FIB-sectioning can also combined with other high resolution microscopy techniques - the most common approach is a combination with Electron Backscatter Diffraction (EBSD) measurements, which provide extensive crystallographic information for each measurement point [10]. The advantages of these approaches are their precision and the possibility to perform automated measurements. They also provide very consistent results and, in case of EBSD analysis, extensive microstructural data. The main drawback of these 3D analysis methods is the speed of data acquisition. First, the material removal is time consuming. Zaefferer reported a time consumption of about 15 minutes for each removal of a  $20 \times 20 \times 1 \mu\text{m}^3$  material volume by FIB sputtering in a low alloyed steel sample [11]. The measurement process consumes additional time, especially for EBSD measurements. A compromise between investigation volume size, measurement resolution and resource consumption including time has to be found. For an investigation volume of  $30 \times 20 \times 5 \mu\text{m}^3$  with a resolution of  $0,1 \times 0,1 \times 0,1 \mu\text{m}^3$  (i.e. 50 slices), a measurement time of about 30 hours is reported [12]. This shows that covering a statistically significant investigation volume with sufficient resolution can consume enormous resources. Additionally, a high level of expertise is necessary for effective measurements and correct interpretations of the data. For these reasons, 3D-EBSD at the moment does not have the potential to become a widespread analysis technique, but because the data gained are extensive, it is an excellent tool for information focused microstructural analyses of selected cases. Rowenhorst for instance investigated the 3D-shape of martensite crystals in a high-strength low-alloy steel [13] and Zaefferer investigated a variety of special microstructural configurations like the lamella structure of pearlite, nanocrystalline NiCo deposits and fatigue cracks in aluminum [12].

### Other 3D Imaging Techniques

Other 3D imaging methods are available, but they do not meet the requirements for "micro"-structure analysis. One technique is 3D Atom Probe, which can detect type and position of distinct atoms within an investigated material volume. Because measurements are performed on atomic level, this method is not applicable for structure analyses on a microscopic scale [14]. Another technique is X-ray computer tomography. X-ray projections from different angles provide information on position and density of absorbing structures in an investigated sample, which can be combined to reconstruct the 3D-volume. The high X-ray energy necessary for the examination of metallic materials results in a focal spot of a few micrometers at minimum. This is too large to identify grain boundaries and therefore proper microstructural analysis is impossible [15].

### Experimental Procedure

A procedure for 3D investigations of multiphase microstructures with LOM has been developed based on the principles of serial sectioning. For the development, a cold-rolled 1mm thin sheet of Dual Phase steel was used, which consists of martensite and ferrite (steel 1). After completion of the routine, it was also used on two additional steel grades - one experimental steel with a bainitic-martensitic microstructure (steel 2) and a tool steel with vanadium carbides embedded in an austenitic matrix (steel 3). The chemical compositions of the steels are also listed in table I.

Table I: Investigated steel grades

	Microstructure	Etchant	Layers	Magnif.	Volume/ $\mu\text{m}^3$	l x w x h / $\mu\text{m}^3$	$\varnothing$ layer distance
Steel 1	ferrite-martensite	Nital	48	1000x	88.000	77 x 62 x 18	0,3 $\mu\text{m}$
Steel 2	bainite-martensite	Nital	75	500x	1.770.000	230 x 165 x 47	0,6 $\mu\text{m}$
Steel 3	austenite-carbides	Klemm	71	500x	889.000	171 x 113 x 46	0,6 $\mu\text{m}$

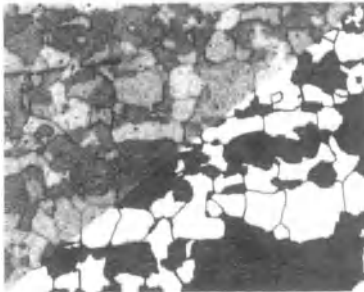


Figure 3: Steel 1, layer 23:  
original image (b/w) and phase-ID layer

3D metallographic data were acquired with LOM by repeated removal of surface layers from the sample by manual polishing with 1 $\mu\text{m}$ -diamond paste and metallographic analysis of the emerging new surfaces. The distances between the analyzed surface layers were determined using a Vickers-hardness-indent (HV1). For steel 1, the indent depths were determined for each layer in two ways: 1<sup>st</sup> by measurements of the indent diagonals and using the formula given above and 2<sup>nd</sup> with a confocal microscope, which allows surface topography measurements with a precision of 2nm in vertical direction [16]. A new indent was set after each four images, because edges and surfaces of the indents became blurred by etching and polishing, which hampered measurements. The 2 depth measurement data sets were evaluated in comparison to each other (see the discussion section). For steels 2 and 3, only diagonals measurements were employed. Measurements were also performed for each layer. After each polishing step, the microstructure was contrasted by etching with 3% alcoholic HNO<sub>3</sub> dilution in case of steels 1 and 2. For contrasting the V-carbides in steel 3, Klemm color etching was used. The digital images were taken with a Leica DM 2500M light optical microscope at a magnification of 1000x (resolution: 2048x1536 px) for steel 1 and 3 and 500x (resolution: 2560x1920 px) for steel 2. A sample adapter was used to minimize rotation of the sample and to

ensure high congruence of the imaged areas. These steps were repeated the number of times listed in table 1 for the different steels. The digital images were processed using the free "GNU Image Manipulation Program" GIMP, version 2.6.7. They were manually aligned to each other and cropped to the largest area covered by all images. White balance and contrast of the images were adjusted for better results. For steels 1 and 3, the two present phases were separated using GIMP, creating phase-ID layers for all images with unambiguous assignment of areas to distinct phases as shown in figure 3. Utilizing a combination of the phase-ID layers with the distance data, virtual models of the phases could be reconstructed for steels 1 and 3 by developing appropriate routines in MATLAB. The details of phase separation and model development are not explained here, because this would be beyond the scope of this article.

## Results

The number of layers investigated for each of the steel grades and the investigated volume sizes can be found in table 1. For visualization, the image series have been stacked in the measured distances using GIMP, as shown in figures 4(l.), 5 and 6(l.). For steel 1, a virtual volume element was created by combining the phase ID-layers with the layer distances, which represents the phase distribution (fig. 4(m.)). Also the ferrite grains were reconstructed using the MATLAB software (fig. 4(r.)). For steel 3, the carbides were reconstructed as visualized in figure 6(r.).



**Figure 4:** Steel 1 - image stack (l.), RVE (m.), reconstructed ferrite grains (r.)

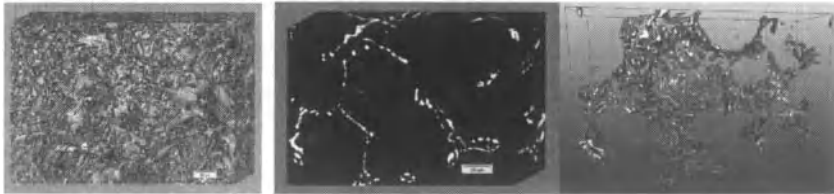


**Figure 5:** Steel 2 - image stack



**Figure 6:** Steel 3 - image stack (l.), reconstructed carbides (r.)

## Discussion

There have been several hindrances to cope with in order to access 3D-metallographic data with serial sectioning and LOM. These will be discussed in the following.

### Distance Measurements

For steel 1, the layer distance data were acquired with two different techniques for comparison. The first was usage of a confocal microscope, which is capable of surface topography measurements with a precision of 2nm in vertical direction. The second was calculation of the

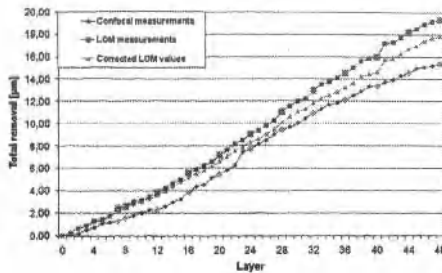


Figure 7: Surface removal

indent depths from the indent diagonal lengths. The graphs in figure 7 show the averaged results of the two methods for the distances in steel 1 in comparison. The values clearly deviate due to several influences, which distort the two measurement techniques. The confocal microscope measurements were hampered because the measurement software can't automatically detect the deepest point of the indent. The manual detection leads to failures in the range of 0,1 µm for each measurement. Additional difficulties were

introduced by noise, which often occurs near the indent tip and hinders a correct depth determination.

For the geometric depth calculations from the indent diagonal lengths, one error source is the elastic springback of the indented material. The upper graph in figure 7 was calculated with an angle of 15,94° according to the HV-indenter geometry. But the material springs back due to its elasticity. Thereby the angle is reduced. For the investigated materials, springbacks between 0,6° and 1,0° were recorded using the confocal microscope. Without correction, the calculated layer distances are slightly increased. The failure in depth calculation increases with decreasing indent depth. Without knowing the true angle, it's advised to set new indents regularly in order to keep the error small. Another source of measurement deviations comes from the bulge of pushed aside material which occurs around each set indent. Without its removal, an error in height is introduced, because the indent is larger on top of the bulge than on ground level. Therefore for steel 1, the indent diagonals were measured only after the first polishing step under the assumption that the bulge would then be removed. However the upper graph in figure 7, which represents the accumulated depth calculations derived from these diagonal measurements, still shows above-average distance jumps when new indents were employed. Further investigations with the confocal microscope revealed that the bulge was not always completely removed with one polishing step, which increases the layer distance. The middle graph in figure 7 shows a recalculation of the indent diagonals values, with use of the true angle and correction of the bulge error. A third error source for depth values can be induced by the etching process if etchants are applied that remove material like e.g. Nital. The surfaces of the indents are also etched and deviations from the original shape occur, which increase with each additional etching step. The edges of the indents become frayed, which can result in increased measured diagonal lengths and a slight decrease of the calculated distances.

The described effects can explain the deviations between the two depth measurement approaches. Apparently, for the indent-diagonals measurements, the distance increasing effects of the material springback and the indent bulge are dominant. These and the distance measurement failures during confocal measurement are the source of the deviations between the two approaches. The method using the confocal microscope is considered to be more accurate, but the diagonal measurements are much easier and faster to apply and the time saving is very high. This method was therefore applied to steels 2 and 3 with correction factors for the angle and bulge effects.

### Image Analysis

In order to access the 3D information in multiphase steels, accurate and consistent phase detection is essential. For LOM, the standard method for phase differentiation is color-thresholding. For highly contrasted phases like for steels 1 and 3, this approach usually provides sufficiently accurate results for single images. But for complete image series, this approach comes to its limits, because contrasting of microstructures based on etching is not a highly reproducible procedure. After etching, each image appears somewhat different in terms of color, brightness, contrast, shadows et cetera. This translates into little variations of the phase detection results. While this is no problem for the analysis of distinct image, in a 3D-stack the information in the image layers are mutually dependent and analysis inconsistencies can drastically decrease the quality of the final result. Standard color-thresholding is not capable to provide the required high level of consistency. Therefore, phase detection for steels 1 and 3 was performed with advanced image manipulation tools and techniques. The freeware tool GIMP was used for all necessary steps - alignment, quality improvement and phase separation. Sufficiently accurate and consistent phase separation was achieved for all images.

### 3D Results

The presented results show clearly the potential of LOM in combination with serial sectioning to provide 3-D metallographic data for multiphase steel grades. For steels 1 and 3, virtual 3D-models of the microstructure were created. This type of microstructural data will provide unprecedented input for simulations and models. It can be used for investigations of 3D grain shapes, phase distributions and phase connectivity and will help to gain a better understanding of phase formations, phase transformations and correlations between different spatial microstructural configurations and material properties.

The workflow of the presented procedure is simple, reproducible and employable with standard metallographic facilities. Several error sources have been identified, especially for depth measurements using indent diagonals. The creation of virtual microstructural models from this method heavily depends on the consistency of phase detections. But even without 3D-reconstruction, highly valuable qualitative insights may be gained from stacked images.

A comparison with the increasingly popular 3D investigation techniques using EBSD and FIB reveals that both methods could benefit from each other, because they cover different scales. The volumes covered by 3D-EBSD using FIB mentioned in literature have dimensions of about  $30 \times 20 \times 5 \mu\text{m}^3$  ( $3.000 \mu\text{m}^3$ ) up to  $50 \times 30 \times 7 \mu\text{m}^3$  ( $10.500 \mu\text{m}^3$ ). The dimensions of the presented volumes are considerably larger in each dimension. The method is therefore capable to investigate large volumes and to provide statistically significant data, which is one of the major problems of the 3D-EBSD approach. On the other side, EBSD measurements provide much more detailed and higher resolved microstructural information. This allows much deeper evaluations of the material state than possible with LOM. Therefore, the two methods operate on distinct scale levels and can mutually complement each other with EBSD providing crystallographic details at high resolutions, which can be used to correctly interpret information on large scales provided by LOM.

The presented results show clearly the problematic of applying stereology for the analysis of modern multiphase microstructures even for apparently simple cases like the ferritic phase in the steel 1 or the carbides in steel 3. The phase constituents miss all criteria required to derive reliable information on the 3D microstructural properties from 2D-images with stereologic methods, as their shapes are neither defined nor convex nor uniform. This shows the necessity

for direct investigation of microstructural information like 3D-grain sizes, -shapes, spatial phase distributions and phase connectivity of components. Apart from being necessary for the "understanding" of microstructures, these data are needed as reliable input for correlations, models and simulations on phase transformation and microstructure evolution.

### Conclusions

A method for accessing 3D metallographic data based on serial sectioning and LOM was developed and applied to three multiphase steel grades. For the required determination of the layer distances, Vickers hardness indents were employed. In order to gain 3D-information, highly consistent analysis of all images is crucial. In the presented work, consistent phase separation was achieved using advanced image manipulation tools from the free software GIMP. Volumes between 88.000 and 1.770.000  $\mu\text{m}^3$  were investigated. These are considerably larger than those volumes reported in literature that were investigated with techniques capable of resolving structures small enough for the differentiation of grain boundaries. Virtual 3D models were created for two steels reflecting spatial phase distributions as well as shapes of phase constituents.

### References

- [1] Velichko, A.; Mücklich, F.; *Praktische Metallographie* 45 (2008) 9, pp. 423-439
- [2] Chawla, N.; Ganesh, V.V.; Wunsch, B.; *Scripta Materialia* 51 (2004), pp. 161-165
- [3] Oettel, H.; Schumann, H.; *Metallografie*, 14. Auflage, WILEY-VCH Verlag, Weinheim, 2005
- [4] Kral, M.V.; Spanos, G.; *Acta Materialia* 47 (1999) 2, pp. 711-724
- [5] Leunis, E.; Halon, D.; Rijkenberg, A.; Scott, C.; Drillet, J.; Hackl, R.; Report EUR 22387; Science Research Development, (2006)
- [6] Thomser, C.; Unger, M.; Zhang, Z.; Ohm, J. R.; Bleck, W.; *Praktische Metallographic Sonderband* 38 (2006), pp. 89-95
- [7] Kral, M. V., Mangan, M. A.; Spanos, G.; Rosenberg, R. O.; *Materials Characterization* 45 (2000) 1, pp. 17-23
- [8] Lewis, A.C.; Bingert, J.F.; Rowenhorst, D.J.; Gupta, A.; Geltmacher, A.B.; Spanos, G.; *Materials Science and Engineering A* 418 (2006), pp. 11-18
- [9] Keehan, E.; Karlsson, L.; Bhadeshia, H. K. D.H.; Thuvander, M.; *Materials Characterisation* 59 (2008), pp. 877-882
- [10] Inkson, B.J.; Mulvihill, M.; Möbus, G.; *Scripta Materialia* 45 (2001), pp. 753-758
- [11] Zaefferer, S.; European Workshop on Modern Developments and Applications in Microbeam Analysis, 2009, Gdynia
- [12] Zaefferer, S., Wright, S. I., Raabe, D.; *Metallurgical and Materials Transactions A* 39A (2008), pp. 374-389
- [13] Rowenhorst, D.J.; Gupta, A.; Feng, C.R.; Spanos, G.; *Scripta Materialia* 55 (2006), pp. 11-16
- [14] Muraleedharan, K.; Balamuralikrishnan, R.; Das, N.; *Journal of Materials Science* 44 (2009), pp. 2218-2225
- [15] Becker, S.; Brunke, O.; Sieker, F.; *Prakt. Met. Sonderband* 41 (2009), pp. 297-302
- [16] Brozek, T.; *Handbuch  $\mu$ surf explorer*, Oberhausen, 2007

## Characterization of Open-Pored Metals Using Image Processing

Björn Hinze<sup>1</sup>, Joachim Rösler<sup>1</sup>

<sup>1</sup>TU Braunschweig, Institute for Materials, Langer Kamp 8, D-38106 Braunschweig,  
Germany

Keywords: porosity, pore size, noise reduction, absorber material

### Abstract

The most important characteristic of open-pored metals is porosity, since it enables all of their functional applications as filters or sound absorbers. Due to the notch effect of the pores, mechanical properties of porous metals are better than the ones of comparable structures made of polymers or ceramics. Consequently, only open-pored metals can be used in aircrafts to reduce flow noise or noise resulting from the core engine by acoustic absorption. Absorption properties depend highly on pore size and porosity of the material, which must be characterized as precisely as possible in order to analyze the correlation between morphology and noise reduction performance. Here, a line segmenting method is explained in order to characterize pore size and porosity of absorber materials using image processing based on two dimensional microscopy images, including sample preparation and specification of the set-up. Then, the influence of the pore structure on the measured absorption behavior is discussed. Finally, the correlation of acoustic behavior, pore morphology, and porosity is outlined.

### Introduction

Significant noise loads affect everyone causing anxiety, depression, insomnia and other effects which impair health and productivity [1],[2]. Due to the rising number of flights and aircrafts, air traffic noise increases dramatically. To counter this development, various approaches have been developed to reduce the different noise sources resulting from airframe, jet or engine [3],[4],[5],[6]. One approach to reduce this noise is the application of noise reducing liners in the hot gas path [7]. This is especially important, since the engine is becoming the dominant noise source of modern airplanes during take-off [8]. Due to the elevated temperatures and high fatigue loading in this part of the aero-engine, conventional passive absorber materials cannot be used. Polymers would not be able to bear the heat and ceramic fibers would crack under the mechanical loading due to the notch effect. Consequently, this study focuses on metals with open pores, which can resist elevated temperatures and fatigue loading and additionally resemble geometrically conventional passive absorbers. Based on the production processes, e.g. sintering of metal fibers [7], powder processing using a foaming agent [9], coating of polymer foams [10], or using melt infiltration techniques [11], the characteristic dimension of the porosity is usually in the range of 0.01-10mm. In this work, sintered metals and metal sponges are analyzed after the theory of sound absorption is briefly outlined. Then, measurements of the acoustic absorption of metal sponges and sintered metals in an impedance tube are performed. To understand and predict the acoustic properties of metals with open porosity, it is necessary to characterize the materials as precisely as possible. This is explained in detail using a line segmenting technique, followed by a discussion of the connection of pore characteristics and acoustic absorption. Finally, a conclusion is given.

## Sound Absorption

Acoustic absorption  $\alpha$  is the reduction of sound energy. The absorption is maximal if the reflection of the sound absorber surface approaches zero and the sound absorption coefficient within the absorber material is maximum. The acoustic absorption  $\alpha$  can be expressed by the reflection  $R$  or the reflection coefficient  $r$  which can also be written using the impedance  $Z$  for perpendicular sound incidence:

$$\alpha = 1 - R = 1 - |r|^2 = 1 - \left| \frac{Z_{\text{absorber}} - Z_{\text{air}}}{Z_{\text{absorber}} + Z_{\text{air}}} \right|^2 \quad (1)$$

The impedance  $Z$  of air and an absorber with infinite thickness is according to [12]:

$$Z_{\text{air}} = \rho c \quad \text{and} \quad Z_{\text{absorber}} = \rho c \frac{\sqrt{\chi}}{\sigma} \sqrt{1 - j \frac{\sigma \Xi}{2\pi f p \chi}} \quad (2)$$

where  $j$  is the imaginary unit,  $\rho$  the density of air,  $c$  the velocity of sound and  $f$  the frequency of sound. Therefore, impedance and sound absorption are only dependent on the frequency and on three material properties:

1. Porosity  $\sigma = \frac{V_L}{V_A} < 1$   
 $V_L$  acoustic effective volume of pores meaning only volume of open pores  
 $V_A$  bulk volume of absorber
2. Structure factor  $\chi = \frac{V_K}{V_B} \geq 1$   
 $V_K$  air volume of compression  
 $V_B$  air volume of acceleration
3. Flow resistivity  $\Xi = -\frac{\Delta p}{v \Delta x}$   
 $\Delta p$  pressure drop  
 $v$  velocity  
 $\Delta x$  distance

For minimum reflection  $R \rightarrow 0$  of absorber, the impedance value of the absorber must approach the impedance value of air:

$$\rho c \frac{\sqrt{\chi}}{\sigma} \sqrt{1 - j \frac{\sigma \Xi}{2\pi f p \chi}} \rightarrow \rho c \quad \text{if} \quad \chi \rightarrow 1, \quad \sigma \rightarrow 1, \quad \sqrt{1 - j \frac{\sigma \Xi}{2\pi f p \chi}} \rightarrow 1 \quad (3)$$

The root term  $\rightarrow 1$  if flow resistivity  $\Xi \rightarrow 0$ . In practical applications, absorbers have finite thicknesses and are located in front of a sonically hard wall. Consequently, sound must be dissipated via transformation of acoustic energy into heat. The coefficient of absorption  $\alpha^*$  is defined as follows:

$$\alpha^* = k \sqrt{\frac{\chi}{2} \left[ \sqrt{1 + \left( \frac{\Xi \sigma}{\omega \rho \chi} \right)^2} - 1 \right]} \quad (4)$$

where  $k$  is a constant. If the coefficient of absorption  $\alpha^* \rightarrow \infty$ , the dissipation is maximum. Therefore, flow resistivity  $\Xi \rightarrow \infty$  and porosity  $\sigma \rightarrow 1$  for optimal dissipation properties. The result is an optimization problem for the value of the flow resistivity, since, the flow resistivity must be low enough that sound is not reflected by the material, but high enough that sound is sufficiently dissipated. Meaning on the one hand that open pores are necessary for acoustic absorption and on the other hand that there is an optimum pore structure for maximum absorption.

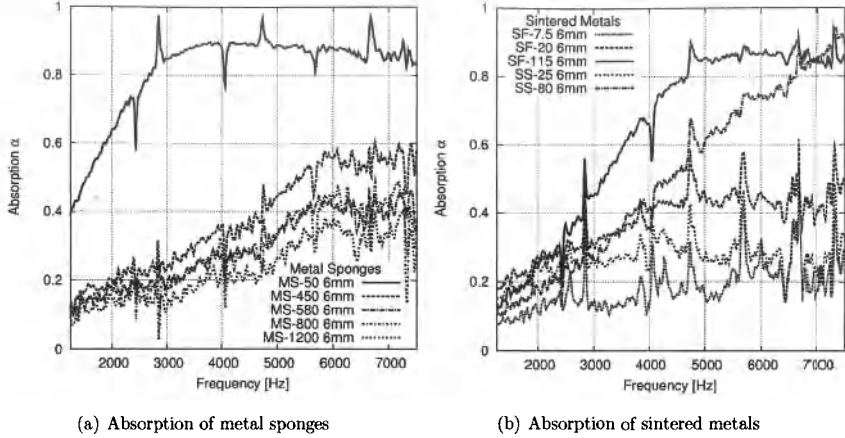


Figure 1: Acoustic absorption of absorber materials, for pore characteristics see Tab.1

### Sound Absorption of Metals with Open Porosity

Acoustic absorption was tested in an impedance tube [13]. The principle is that a noise generator emits a plane wave within the tube. The angle of incidence between the surface of the absorber material and the direction of the sound wave is  $90^\circ$ . Two microphones measure the sound pressure difference between incident and reflected waves, which gives the reflection factor  $r$  and, thus, the absorption  $\alpha$  in dependence of the sample thickness, according to Eq. (1). Due to the tube diameter, only frequencies from 1000 Hz to 7500 Hz were analyzed. Samples were machined to fit perfectly into the tube, which was additionally greased, to reduce errors resulting from small gaps between sample and tube. Measurements were performed on different metal sponges and sintered metals, see Fig. 1. The sample stacks had the same thickness within each material group to avoid the influence of the absorber thickness. According to the given theory, the acoustic absorption behavior of the different samples varies based on the pore characteristics, e.g. pore size and porosity. Hence, the pore characteristics of samples need to be characterized to explain absorption behavior.

### Characterization of Pore Characteristics

For the characterisation of pores, microscopy images are taken after sample preparation including embedding samples into a polymer, grinding and polishing to generate smooth surfaces. The image must show a representative area of the sample containing a reasonable amount of pores, while details still contain a sufficient amount of pixels and resolution to guarantee a clear differentiation between ligaments and pores, see Fig. 2(a-d). Since the porous material is not perfectly homogenous, several images were taken and the results obtained by image processing were averaged. To generate a black and white image, the original images are binarized exemplarily shown for the metal sponge; see Fig. 2(e). The generated image contains image noise resulting from the image acquisition. Therefore, a smoothing routine is applied to remove areas of less than ten connected white pixels in

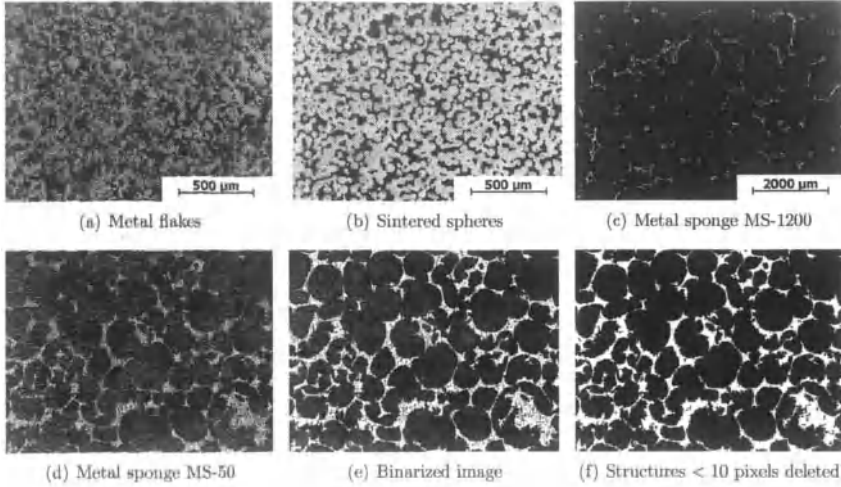


Figure 2: (a)-(d) Light microscopy images of absorber materials; (e)-(f) following steps of image pre-processing for the line segmenting method

a black area and vice versa. The result is shown in Fig. 2(f). Note, that the black phase represents pores and the white phase the metal ligaments. The pixel ratio of black and white pixels gives the porosity of the material. Furthermore, this image is prepared for the analysis of the pore characteristics using a line segmenting method.

### Line Segmenting Method

The principle of the line segmenting method is that black and white images, like Figs. 2(f) or 3(a), are superimposed with a lattice of parallel lines with a defined spacing, usually one pixel. This grid is rotated in discrete 1°-steps from 0° to an angle of 180°. Due to symmetry, the full 360° need not be analysed, since, a grid rotated by 180° gives the same transitions. Along the superimposing lines, all phase transitions, i.e. transitions from a black to a white pixel or vice versa, are detected. In Fig. 3(b), the transitions are marked with a grey "+". Afterwards, all segment lengths within each phase are summed up for every angle. Finally, the arithmetic average segment length  $\bar{x}$  and the sample standard deviation  $s$  are calculated:

$$\bar{x} = \sum_{i=1}^n \frac{x_i}{n} \quad (5)$$

$$s = \sqrt{\frac{\sum_{i=1}^n (x_i - \bar{x})^2}{n - 1}} \quad (6)$$

where  $x_i$  is a single segment length and  $n$  the amount of all detected segments per phase at one angle. The calculated average segment lengths are plotted in a polar coordinate system forming a microstructure ellipse for each phase (see Fig. 3(c)). Due to symmetry, a half

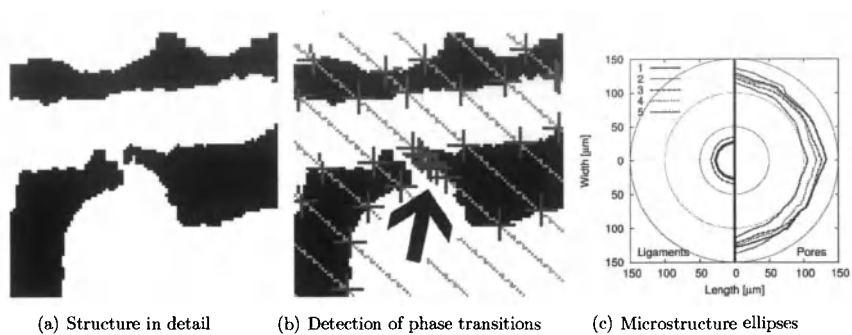


Figure 3: A black and white image (a) is superimposed by lines in order to detect phase transitions (b), the arrow marks an area of short segments due to virtual intersections; The average segment lengths are plotted in an polar coordinate system for every angle to generate microstructure ellipses (c), here based on five different images of the material shown in Fig. 2(d)

ellipse contains all information. Consequently, the half ellipses representing the white phase or metal ligaments are plotted on one side and the half ellipses representing the black phase ore pores on the other side. The measured values are visualized in this way in order analyse the ellipse's shapes or the scattering of different measurements within one material. If the ellipses are circular, there is no preferred orientation and the segment lengths can be averaged for all angles resulting in the average pore size.

However, if the superimposed images are studied in detail, there are short segments resulting from the digital or pixel based image processing, marked by the arrow in Fig. 3(b). Since the phase boundaries are not along the pixel raster, they are, approximated by stepped pixel formations. If such structures are superimposed by pixel based lines, virtual intersections occur due to the imperfect reproduction resulting in numerous short segments with lengths of just a few pixels. To reduce the influence of the short segments resulting from virtual intersections, a threshold must be used, defining the minimum segment length which is included in the calculation of the arithmetic average segment length  $\bar{x}$  and the sample standard deviation  $s$ . The microstructure ellipses are based on the average segment lengths, consequently the shape is highly dependent on this value. The higher the threshold value, the larger the ellipses become since short segment lengths are neglected in the calculation of the average length. Note, that the interface of the black and white phases is the same, accordingly the influence of virtual intersections is always higher in the phase with the smaller phase fraction. Characterizing highly porous materials, the threshold value must be selected accurately which is outlined in the following section.

### Specifying the Threshold Value

The principle is that even if the superimposing lines are rotated, the analyzed structure stays the same. Consequently, the black and white phase fractions should ideally be constant at every angle. Without setting a threshold value, all segment lengths are included in the calculation of the average segment length. For some angles with numerous short segments due to virtual intersections, this means a noticeable reduction of the average segment. Since

Table 1: Material properties of metal sponges (MS), sintered flakes (SF) and sintered spheres (SS); \*information of producer; \*\*values influenced by hollow struts

Material	Alloy	Porosity	Cell / pore size*	Average pore size
MS-50	Haynes Alloy 230	82%	n/a	121 ± 9 μm
MS-450	NiFe22Cr22Al6	90%	450 ± 45 μm	380 ± 19** μm
MS-580	NiFe22Cr22Al6	92%	580 ± 60 μm	445 ± 18** μm
MS-800	NiFe22Cr22Al6	94%	800 ± 80 μm	538 ± 58** μm
MS-1200	NiFe22Cr22Al6	95%	1200 ± 120 μm	656 ± 59** μm
SF-7.5	Hastelloy X	20%	7.5 ± 2.5 μm	8.6 ± 1.2 μm
SF-20	Hastelloy X	35%	20 ± 5 μm	22 ± 2 μm
SF-115	Hastelloy X	50%	115 ± 15 μm	113 ± 13 μm
SS-25	CuSn12	30%	25 ± 3 μm	25 ± 2 μm
SS-80	CuSn12	25%	80 ± 10 μm	80 ± 12 μm

the impact on the phase with the smaller phase fraction is bigger, the phase fraction of this phase is for some angles even smaller. If the threshold value is set too high, too many short segments are excluded from the calculation of the average segment length, meaning a noticeable increase of the average segment length. The result is that, the phase fraction of the smaller phase is particular overestimated for some angles, since the impact on this phase is bigger. Therefore, the ideal threshold is found, when the sample standard deviation of the phase fraction is minimal. Note, that the sample standard deviation is the same for the black and the white phase.

To select the ideal threshold, the phase fractions  $f_{black,i}$  and  $f_{white,i}$  of both phases are measured for each angle  $i$  and then their standard deviation  $s_{black}$  or  $s_{white}$  are determined as follows:

$$f_{black,i} = \frac{\bar{x}_{black,i}}{\bar{x}_{white,i} + \bar{x}_{black,i}} \quad \text{and} \quad f_{white,i} = \frac{\bar{x}_{white,i}}{\bar{x}_{black,i} + \bar{x}_{white,i}} \quad (7)$$

$$\bar{f}_{black} = \frac{\sum_{i=1}^{180} f_{black,i}}{180} \quad \text{and} \quad \bar{f}_{white} = \frac{\sum_{i=1}^{180} f_{white,i}}{180} \quad (8)$$

$$s_{black} = s_{white} = \sqrt{\frac{\sum_{i=1}^{180} (f_{black,i} - \bar{f}_{black})^2}{179}} = \sqrt{\frac{\sum_{i=1}^{180} (f_{white,i} - \bar{f}_{white})^2}{179}} \quad (9)$$

After the correct threshold value is found, the line segmenting method can be applied to the prepared black and white images. The results for the different absorber materials are listed in Tab. 1.

## Discussion

The relevant material properties in regard to sound absorption are porosity  $\sigma$ , structure factor  $\chi$  and flow resistivity  $\Xi$ . In highly porous metals, as used in this work, the structure factor  $\chi \rightarrow 1$  and can thus be neglected. The flow resistivity  $\Xi$  is based on the pore characteristic, e.g. pore size and pore morphology. According to the law of Hagen-Poiseuille, the flow resistivity is dominated by the pore size due to resulting internal friction. Therefore, it is possible to correlate flow resistivity  $\Xi$  and pore size in direction of flow. Note, that pore size inversely correlates with flow resistivity  $\Xi$ . In this investigation, the tortuosity of pores which also impacts the flow resistivity was not measured. The characterization was done using a

line segmenting method for values see Tab. 1. Comparing the pore size values measured for sintered metals by the producer using a Coulter porometer according to ASTM E 1294 and the values measured by the line segmenting method, the results are in agreement with each other. For metal sponges, just the cell size was measured by the producer. The pore sizes measured by the line segmenting method are smaller since it does not calculate the pore diameter. Additional divergence between the two values results from hollow struts of the metal sponges which are only included in the measurement using the line segmenting technique.

In order to predict the acoustic absorption by characterizing the pore morphology, acoustic tests using an impedance tube were performed. All materials listed in Tab. 1 were machined to stacks with the thickness of 6 mm in order to avoid the influence of the absorber thickness which also influences the flow resistivity. The absorption tests of metal sponges, compare Fig. 2, show that the smaller the pore size the better is the acoustic absorption. Note, that the finest pore size is  $121 \pm 9 \mu\text{m}$  and the largest  $656 \pm 59 \mu\text{m}$ . The measurements of the sintered metals suggest that the bigger the pore size, the better the acoustic absorption; see Fig. 2. Note, that the biggest pore size of the analyzed materials is  $113 \pm 3 \mu\text{m}$  indicating an absorption optimum in the range of  $100 \mu\text{m}$  to  $150 \mu\text{m}$ . It can be concluded that it is possible to describe acoustic absorption by pore size and porosity even if the relative pore length and the structure factor  $\chi$  are neglected.

## Conclusions

One possibility to reduce noise of aero-engines is the application of metallic absorber materials with open porosity. Three different material properties, porosity  $\sigma$ , structure factor  $\chi$  and flow resistivity  $\Xi$ , are needed to describe the acoustic behavior. Since they depend on the pore characteristics, in particular pore size and tortuosity, it is possible to predict the acoustic behavior based on the pore characteristics. In this work, the materials were characterized by image processing of microscopy images using a line segmenting method. Concluding that the best absorption behavior for an absorber thickness of 6mm was reached with materials containing open pores in the range of  $100 \mu\text{m}$  to  $150 \mu\text{m}$ .

## Acknowledgements

The authors would like to thank Philipp Seiler for writing the line segmenting program, Alantum Europe GmbH and GKN sinter metals for providing sample materials. Financial support by the German federal state of Lower Saxony through the research program "Bürgernahe Flugzeug" is greatly appreciated.

## References

- [1] M.M. Haines, et al., "Chronic aircraft noise exposure, stress responses, mental health and cognitive performance in school children" (Psychol. Medicine, 31, 2001), 265-277.
- [2] E. Franssen, et al., "Aircraft noise around a large international airport and its impact on general health and medication use" (Occup Environ Med, 61(5), 2004), 405-413.
- [3] G. M. Lilley, "The Prediction of Airframe Noise and Comparison with Experiment" (Journal of Sound and Vibration, 239(4), 2001), 849-859.

- [4] C. Tam "Supersonic Jet Noise" (Annu. Rev. Fluid Mech., 27, 1995), 17-43.
- [5] D. Papamoschou "New Method for Jet Noise Reduction in Turbofan Engines" (AIAA Journal, 42(11), 2004) 2245-2253.
- [6] W. Neise, and L. Enghardt "Technology approach to aero engine noise reduction" (Aerospace Science and Technology, 7, 2003), 352-363.
- [7] I.O. Golosnoy, J.C. Tan, and T.W. Clyne, "Ferrous Fibre Network Materials for Jet Noise Reduction in Aeroengines Part I: Acoustic Effects" (Adv. Eng. Mater., 10, 2008) 192-200.
- [8] M. Janic, "Aviation and externalities: the accomplishments and problems" (Transportation Research Part D: Transport and Environment, 4(3), 1999), 159-180.
- [9] C.-J. Yu, et al., "Metal foaming by a powder metallurgy method: Production, properties and applications" (Mater. Res. Innovat., 2, 1998), 181-188.
- [10] S. Pickering, "Inco invests in its nickel future at Clydach" (Met. Powder Rep., 53, 1998), 24-27.
- [11] A. Brothers, et al., "Processing and structure of open-celled amorphous metal foams" (Scripta. Mater., 52, 2005) 335-339.
- [12] E. Lotze, "Technischer Lärmschutz", ed. W. Schirmer (Springer, 2006), 191-199.
- [13] DIN EN ISO 10534-2

## **THERMOGRAPHY ASSISTED FATIGUE TESTING**

Anil Saigal<sup>1</sup>, Rongbiao Gu<sup>1</sup>, Christopher San Marchi<sup>2</sup> and Douglas M. Matson<sup>1</sup>

<sup>1</sup>Department of Mechanical Engineering, Tufts University, Medford, MA 02155, USA

<sup>2</sup>Sandia National Laboratories, Livermore, CA 94551, USA

Keywords: Thermography, fatigue testing, temperature rise

### **Abstract**

Hydrogen embrittles most structural metals, although the form and magnitude of embrittlement depends on the source of the hydrogen as well as the stress in the metal. Hydrogen fuel cell systems typically store gaseous hydrogen fuel at high-pressure, which provides both a source of hydrogen and high stresses in the containment materials. Understanding and measuring the effects of hydrogen on the mechanical properties of common structural metals, especially fatigue properties, is important for safe, long-term operation of such systems. This work explores the use of thermography to efficiently and quantitatively evaluate hydrogen-assisted fatigue of type 304 austenitic stainless steel. In particular, thermographic analysis was used with rotating-beam fatigue testing and shown to provide repeatable results which are in general independent of test cycle frequency while reducing test times by several orders of magnitude. The effects of hydrogen were studied by thermally precharging fatigue test specimens in gaseous hydrogen prior to thermography-assisted fatigue testing and then compared to testing of non-charged specimens. Hydrogen-precharging increased the strength of this type 304 austenitic stainless steel and increased the fatigue life by a factor of about 50-100.

### **Introduction**

The world is facing a severe energy and environmental challenge: how to provide competitive and clean energy for its citizens in light of an escalating global energy demand and concerns over energy supply security, climate change and local air pollution. As a carbon-free energy carrier, hydrogen provides a promising vector for storing and distributing renewable energy. Hydrogen is an important industrial gas that is used extensively in many industries. However, with growing demand for clean energy, hydrogen fuel cell systems are being developed for use in consumer products, such as fuel cell vehicles, which changes the landscape for safe design of high-pressure gaseous hydrogen systems.

Efficient production, storage and distribution of hydrogen in the consumer market requires high-pressure, thus high stress in the hydrogen containers, and cyclic loading as fuel systems are charged/discharged. Additionally, structural steels are known to suffer from hydrogen embrittlement (HE) in gaseous hydrogen environments, a phenomenon that causes deterioration of their mechanical properties. The severity of HE depends on composition, microstructure, processing history and strength of the steel, as well as the mechanical conditions of the application [1]. Therefore a systematic understanding of the strength and fatigue performance of materials in gaseous hydrogen environments is critical for materials selection from both engineering and economical perspectives.

Austenitic stainless steels are commonly employed in high-pressure systems due to their high corrosion resistance. Despite their high cost, austenitic stainless steels are also used in gaseous hydrogen systems because austenitic alloys tend to be more compatible with gaseous hydrogen environments than ferritic alloys. Performing tests in gaseous hydrogen environments is challenging and expensive, thus testing is commonly performed in surrogate environments. It has been shown, for example, that tensile testing of thermally precharged austenitic stainless steels results in nominally the same measured properties as tests performed in gaseous hydrogen [2]. Thermal precharging is a method where test specimens are soaked in high-pressure gaseous hydrogen at elevated temperature to enhance the rate of penetration of hydrogen into the materials by diffusion and, if left for sufficient time, allows the material to become saturated with hydrogen throughout the volume of the specimen [3, 4]. Upon cooling to room temperature the diffusivity of hydrogen in austenitic stainless steel is sufficiently slow that hydrogen remains in the specimen during the test. During tests that require extended time scales, such as fatigue tests, there is concern that hydrogen may diffuse out of the specimen during the test, such that the effects of hydrogen are reduced or not measured.

La Rosa et al. demonstrated the validity of the thermographic method for rapid determination of fatigue properties [5]. This method, also called the Risitano method, can reduce the time for construction of a fatigue-life curve (S-N curve) to a fraction of the conventional method. The thermographic methodology is based on an energy balance between the energy necessary to achieve failure and the energy dissipated per cycle, the former assumed to be a constant for the system undergoing fatigue and the latter being related to the heat generated in the sample during fatigue. Heating of the sample during fatigue cycling can be measured and generally shows a profile as shown in Figure 1. The plateau temperature can be used to determine the cycles to failure ( $N_f$ ) for the applied stress amplitude as  $N_f = \Phi/\Delta T$ , where  $\Phi$  is a constant related to the failure energy of the specimen and  $\Delta T$  is the temperature difference between the plateau and the temperature at the endurance limit. Additionally, the initial slope of the temperature profile can be used to determine the endurance limit by plotting this slope as a function of stress amplitude and extrapolating to zero slope [5].

Combining the thermographic method with thermal precharging, the fatigue test can be performed in air while the internal hydrogen can be maintained in the specimen over the test duration, resulting in an efficient and effective means of determining the fatigue-life behavior of austenitic stainless steels. The fatigue-life properties of type 304 austenitic stainless steels with high concentration of internal hydrogen are studied in this paper. The thermographic method is utilized to enhance the efficiency of constructing fatigue-life curves, the so-called S-N curve, in rotating bending fatigue.

### Experimental Procedures

In this study, fatigue testing was performed at room temperature using a R.R. Moore rotating beam machine. With this method the specimen load is completely reversed such that the stress ratio ( $R$ ) is -1 and the mean stress is zero. Frequencies can be adjusted by changing the power output of the machine. Failure during testing was determined by a shut-off mechanism. When the sample is completely fractured or bent to  $\sim 3$  degrees (3 mm in deflection), the shut off switch is triggered and the test is stopped. Conventional tests were carried out with constant load amplitude to failure at a frequency of 50 Hz for providing baseline fatigue-life data.

Additionally, the effect of frequency was evaluated by performing a limited set of tests at frequencies of 30 and 100Hz.

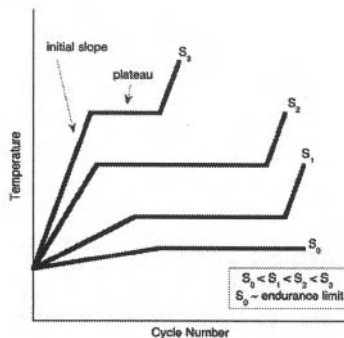


Figure 1. Schematic of idealized temperature profile during fatigue cycling; S represents the stress amplitude.

For accelerated testing using the thermographic test method, a series of short fatigue segments are used, referred to as temperature rise tests. These segments were designed to be ~5 minutes long (10,000 to 20,000 cycles) at a constant load amplitude and frequency of 50 Hz, in order to establish a stable temperature profile, while limiting the time that the sample is tested. The load after each segment is increased, such that the data necessary to produce the fatigue-life curve is generated with a single specimen.

Infrared technology is a non-contact, non-destructive and non-interruptive technique for temperature measurement and was used for temperature monitoring in this study. The Fluke thermometer model 568 was used for this purpose; this device is a single point pyrometer with laser guidance with a temperature range of  $-40^{\circ}\text{C}$  to  $800^{\circ}\text{C}$  and accuracy of  $\pm 1\%$  or  $\pm 1.0^{\circ}\text{C}$ . The minimum spot size is 19 mm. Real-time data collection at the highest sampling frequency of 1 Hz provides averaging over the rotating surface of the specimen.

Fatigue specimens were machined from a 95 mm (3/8 inch) round bar stock of type 304 austenitic stainless steel according to ASTM E466-96 specifications [6]. After nominal machining, all specimens were sent to a specialty machine shop for centerless grinding. Half of the specimens were thermally precharged following procedures in Refs. 2 and 3: exposure to gaseous hydrogen at pressure and temperature of 138 MPa and 573K for approximately twenty days. These procedures result in a uniform hydrogen concentration of approximately 140 wt ppm [2,3]; the average hydrogen content was verified by inert gas fusion on a witness specimen. After thermal precharging and prior to testing, the specimens were maintained at  $< 268\text{ K}$  to ensure minimum loss of hydrogen due to diffusion. Tensile specimens with a gauge diameter of 4 mm (ASTM E8, sub sized specimens) were also tested at a nominal strain rate of  $10^{-3}\text{ s}^{-1}$  (see refs. 2 and 3 for additional description of the tensile testing procedures).

Table 1 - Mechanical properties of type 304 austenitic stainless steel

	Yield Strength (MPa)	Ultimate Strength (MPa)	Reduction Area (%)	Elongation (%)
non-charged	490	700	80.3	44.0
H-precharged	598	756	26.5	25.1

### Results and Discussion

The tensile properties of the type 304 austenitic stainless steel before and after hydrogen precharging are shown in Table 1. Thermal precharging with hydrogen increases the strength of the alloy and reduces the ductility as previously observed for similar alloys [2, 4].

The temperature-time profiles for a representative selection of the conventional fatigue-life tests in rotating beam fatigue are shown in Figures 2 and 3. The results from these tests are plotted on a conventional fatigue-life (Wöhler) curve as shown in Figure 4a. The tests at frequency of 30 Hz and 100 Hz are also plotted in Figure 4a. Based on t-tests, it is found that measured fatigue life was in general independent of test cycle frequency within the range of frequencies investigated; the hydrogen-precharged material tested at this highest frequency is the exception (Figure 4a). The fatigue life of 304 austenitic stainless steel was 50-100 times greater when hydrogen-precharged as compared to no precharging. This non-intuitive result is consistent with prior studies [7,8]. Normalizing the stress amplitude by the yield strength for the non-charged material and hydrogen-precharged materials respectively, however, shows that the endurance limit is essentially unaffected by hydrogen, while at high stress (in the low-cycle fatigue regime) the fatigue life is slightly lowered by hydrogen (Figure 4b).

The thermal profile of a rotating beam fatigue test is shown in Figure 5. The thermal behavior of the tests in this study is different from the ideal thermal profiles found by La Rosa and Risitano [5]. Instead of a clear thermal plateau at a temperature above ambient, the temperature continued to increase over the course of the test. After an initially step temperature rise, the temperature reaches a sloped plateau that is approximately linear until a second rapid temperature rise occurs associated with fracture of the specimen. The plateau slope region is steeper for higher applied stresses.

Results of temperature rise tests are shown in Figure 6. The figures show sample temperature plotted as a function of test time for type 304 austenitic stainless steel with no hydrogen and with hydrogen precharging, respectively. The temperature rises rapidly during the first 100 seconds or so, followed by a stable plateau, described by the plateau slope. The initial thermal rise is used to characterize the endurance limit (Figure 7a): below the endurance limit the initial thermal rise is not a function of stress amplitude, while above the endurance limit the initial thermal rise is an increasing function of stress amplitude. The endurance limit is determined by plotting a line through the data for stress amplitudes greater than the endurance limit and extrapolating to zero slope [5]. The plateau slope is an indicator of the transition from high-cycle to low-cycle fatigue. At low stress amplitude (high-cycle fatigue regime), the plateau slope is a weak function of stress amplitude, while at high stress amplitude (low-cycle fatigue regime) the plateau slope is a much stronger function of stress amplitude. The transition between these two regimes is clearly identifiable in Figure 7b. The thermographic determination of the endurance limit and low-cycle

to high-cycle transition stress are given in Table 2, along with the values determined from the conventional fatigue-life tests (Figure 4).

The thermographic method provides an energy-based method of determining the endurance limit and the transition between low-cycle and high-cycle fatigue. For type 304 austenitic stainless steel, the thermographic transitions are consistent with conventional, empirically-determined values. The fatigue-life curve was not estimated with the thermographic data because the non-ideal thermal profiles made it difficult to establish the parameter  $\Phi$  for these particular tests; however, the excellent correlation of the endurance limit and transition stress allows for an estimate of the entire fatigue-life curve that is an adequate representation of the conventionally measured data.

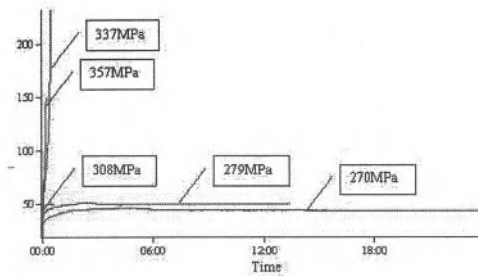


Figure 2 - Temperature-time curves for non-charged type 304 austenitic stainless steel: conventional fatigue-life measurement

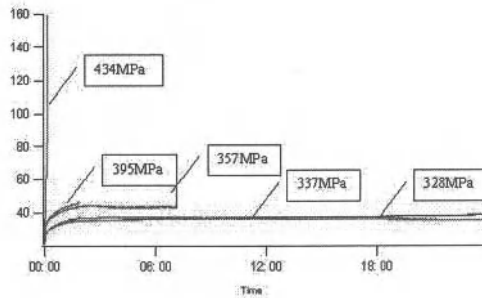


Figure 3 – Temperature-time curves for hydrogen-precharged 304 austenitic stainless steel: conventional fatigue-life measurement

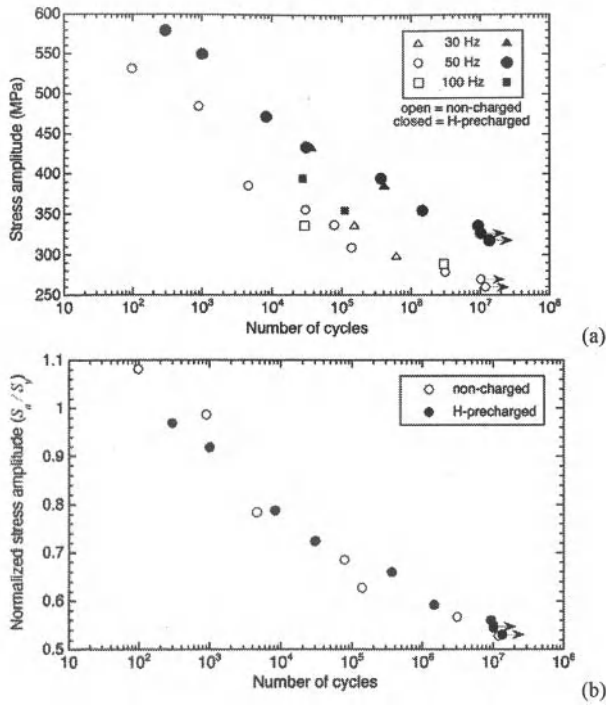


Figure 4 – Fatigue –life curves for type 304 austenitic stainless steel; (a) conventional fatigue-life curve (Wöhler curve); (b) stress amplitude normalized by yield strength (50 Hz only).

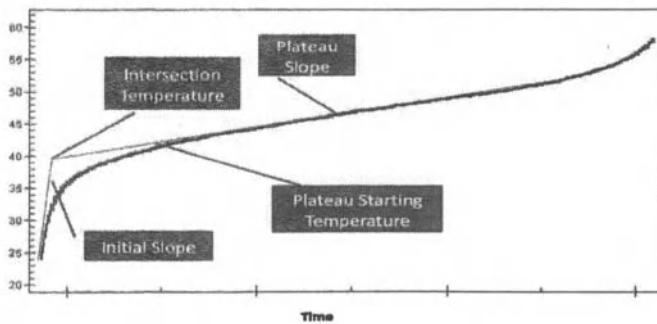


Figure 5 - Thermal profile of specimen during rotating beam fatigue to failure, showing initial thermal rise and plateau slope.

Table 2 – Characteristics of fatigue life for type 304 austenitic stainless steel

	Endurance Limit (MPa)		Low-cycle / high-cycle Transition stress (MPa)	
	Thermographic prediction	Conventional determination	Thermographic prediction	Conventional determination
H-precharged	310	320	407	430
non-charged	241	270	331	330

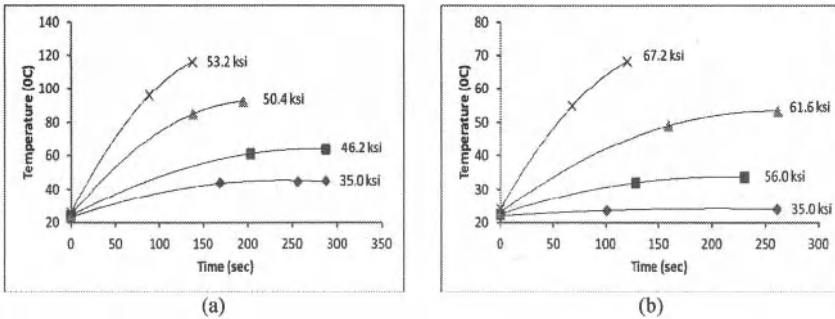


Figure 6 – Thermal profiles from temperature rise tests: (a) non-charged, (b) hydrogen-precharged.

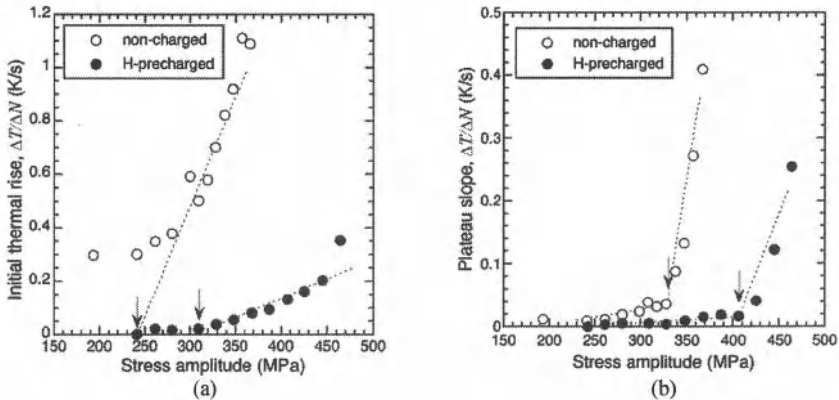


Figure 7 – Thermographic results for rotating beam fatigue of type 304 austenitic stainless steel; (a) initial thermal rise; (b) plateau slope. The arrows indicate the thermographic predictions of the endurance limit and the transition stress, respectively; the dotted lines are visual aid.

## Conclusions

Based on this study, the following conclusions can be drawn:

- a) Type 304 stainless steel experienced about 50-100 times longer fatigue life when hydrogen-precharged due to the strengthening effect of high concentration of internal hydrogen.
- b) The rapid determination method using thermometric techniques can significantly reduce the time and testing required to construct the fatigue-life curves.
- c) Frequency generally does not have significant impact on fatigue life measurements, with the exception of hydrogen-precharged type 304 austenitic stainless tested at 100 Hz.

## References

1. A. Thompson, Selection of structural materials for hydrogen pipelines and storage vessels, *International Journal of Hydrogen Energy* 2, 1977, 163-173.
2. C. San Marchi, T. Michler, K.A. Nibur and B.P. Somerday, On the physical differences between tensile testing of type 304 and 316 austenitic stainless steels with internal hydrogen and in external hydrogen, *Int J Hydrogen Energy* 35, 2010, 9736-9745.
3. C. San Marchi, D.K. Balch, K. Nibur and B.P. Somerday, Effect of high-pressure hydrogen gas on fracture of austenitic steels, *J Pressure Vessel Technology* 130, 2008.
4. C. San Marchi, B.P. Somerday, X. Tang and G.H. Schiroky, Effects of alloy composition and strain hardening on tensile fracture of hydrogen-precharged type 316 stainless steels, *Int J Hydrogen Energy* 33, 2007, 889-904.
5. G. La Rosa and A. Risitano, Thermographic methodology for rapid determination of the fatigue limit of materials and mechanical components, *International Journal of Fatigue* 22, 2000, 65-73.
6. *Standard Practice for Conducting Force Controlled Constant Amplitude Axial Fatigue Tests of Metallic Materials*, ASTM E466-96, 2002.
7. C. Skipper, G. Leisk, A. Saigal, D. Matson and C. San Marchi, Effect of internal hydrogen on fatigue strength of type 316 stainless steel, B.P. Somerday, P. Sofronis and R. Jones (Eds.) *Effects of Hydrogen on Materials*, Proceedings of the 2008 International Hydrogen Conference, Moran, WY, 2008, 139-146.
8. K. Murakami, T. Kanezaki and Y. Mine, Hydrogen effect against hydrogen embrittlement, *Metal Mater Trans* 41, 2010, 2548-2562.

## Acknowledgements

The authors wish to acknowledge Jeff Campbell of Sandia National Laboratories for his assistance conducting the hydrogen precharging. Sandia National Laboratories is a multi-program laboratory managed and operated by Sandia Corporation, a wholly owned subsidiary of Lockheed Martin Corporation, for the U.S. Department of Energy's National Nuclear Security Administration under contract DE-AC04-94AL85000. Partial support for this work provided under NASA grant NNX08AL21G.

*Characterization of Minerals, Metals, and Materials*  
Edited by: Jiann-Yang Hwang, Sergio Neves Monteiro, Chengguang Bai,  
John Carpenter, Mingdong Cai, Donato Firrao, and Buoung-Gon Kim  
TMS (The Minerals, Metals & Materials Society), 2012

# **Characterization of Minerals, Metals, and Materials**

## **Characterization of Environmental and Construction Materials**

Session Chairs:

**Naiyang Ma**

**Gaifeng Xue**

## **TILE PRODUCTION USING WASTES FROM MINING INDUSTRY OF THE MINING DISTRICT PACHUCA AND REAL DEL MONTE**

**Juan Hernández A.\***, Eleazar Salinas R., Francisco Patiño C., Isauro Rivera L., Javier Flores B.,  
Norma Trapála P., Miguel Pérez L., Mizraim. U. Flores G., Iván. A. Reyes D.

Centro de Investigaciones en Materiales y Metalurgia, Universidad Autónoma del Estado de Hidalgo. Carretera Pachuca-Tulancingo Km. 4.5, C.P. 42184 Pachuca, Hidalgo, México. Tel. y Fax: (01 771)7172-000 ext. 2280; Fax: (01 771)7172-000 ext. 6730, Email: [herjuan@uah.edu.mx](mailto:herjuan@uah.edu.mx)

Keywords: Mining wastes, reusing of wastes, tile production

### **Abstract**

This work is related with the production of tiles using wastes from mining and metallurgical industry of Hidalgo State, as raw material. These wastes present a majority particle size (60 %), minor than 53  $\mu$ m (mesh 270, in Tyler Series) with the following composition; 70.01 % wt. of SiO<sub>2</sub>, 12.82 % wt. of Al<sub>2</sub>O<sub>3</sub>, 3.80 % wt. of Fe, 0.70 % wt. of Mn, 3.98 % wt. of K<sub>2</sub>O, 3.34 % wt. of CaO, 2.50 % wt. of Na<sub>2</sub>O, 0.04 % wt. of Zn, 0.026 % wt. of Pb, 56 grams per ton of Ag and 0.6 grams per ton of Au. In this work, the partial results and experimental conditions for the preparation of some composites to produce tiles are shown. The composite that offers the best results in productions of tiles was that with 66.67 % wt. of mining waste, 26.67 % wt. of red mud and 6.67 % wt. of black mud.

### **Introduction**

To now, mining activities carried out during more than 457 years in Hidalgo State, México; has lead a great volume of wastes; which can be classified into different types, having among the more common; Acid mining water, solid transport water, elements in radical form, abandoned minerals without processing and processing minerals wastes known as burrows, being these the most abundant in the region counting with an approximated volume of 110 million of tons, presenting a fine particle size that can affect population health during windy epochs [1 - 4].

Form metallurgical point of view, is well known that a fundamental characterization study it is necessary to know the viability of reusing or recycling of these wastes. According this, these residues can also be considered as raw materials in other economical activities, due its Si, Fe, Al, Ca, Na and P oxides contents, its mineralogy and the distribution of chemical elements in the primary and secondary phases [1,2,5,6].

Chemical composition, particle size analysis and physical properties of the wastes from Pachuca revealed that this kind of residues can be used as raw material to ceramic industry joint with an agglutinant that allows have a good material for production of resistant issues. Also, this material can be a good alternative to cement industry due its SiO<sub>2</sub> content and to production of construction materials [7 - 9], and also as mixed feldspar substitute [9]. This is the reason because this work is related to production of tiles and bricks for construction industry, using wastes giving so an aggregated value and also a rational and sustainable use.

## Experimental procedure

Characterization of wastes was carried out using the following methods: X – Ray Diffraction to determinate the principal mineralogical phases present in this kind of residues. Atomic Absorption Spectrometry, both to determinate the chemical composition of wastes and clays used to elaborate mixes for tiles production. Scanning Electron Microscopy (in conjunction with Energy Dispersive Spectrometry of X – Ray), to reveal morphologic and semi quantitative analysis of waste particles. Finally, a particle size analysis were performed by wet sieving using standard sieves of Tyler series with a sample of 100 grams, drying the obtained fractions and then weighted.

In the same way, 7 mixtures of different chemical composition of clay and waste were made. With these composites it was sought high plasticity and green strength to produce tiles and brick of good quality.

## Results and discussion

The average chemical composition of waste from south dam in the mining district of Pachuca – Real del Monte, is shown in table 1 where can be appreciate that the majority compounds are silica, alumina and iron oxide.

Table 1. Average chemical composition of wastes.

Element	% in weight.	Element	% in weight
SiO <sub>2</sub>	70.01	P <sub>2</sub> O <sub>5</sub>	0.08
TiO <sub>2</sub>	0.30	K <sub>2</sub> O	3.98
Al <sub>2</sub> O <sub>3</sub>	12.82	CaO	3.34
Fe <sub>2</sub> O <sub>3</sub>	3.80	Na <sub>2</sub> O	2.50
MnO	0.70		
MgO	1.01		

The mineral species identified in the obtained diffractograms by X – Ray Diffraction (figure 1), were; silica, bertinita, feldspar, orthoclase, anorthoclase, calcite, gypsum, hematite, pyrite, sphalerite, galena and chalcopyrite.

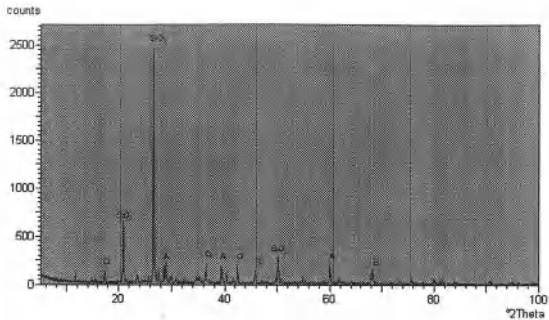


Figure 1. X – Ray Diffractogram of wastes, showing the principal mineral species: quartz ( $\text{SiO}_2$ ), orthoclase (O) albite (A) and berlinita (B).

In figure 2, can be seen a general image of waste particles analyzed by SEM - EDS, where can be observed the presence of majority elements such as silicon, aluminum, potassium, and iron, as well as minority elements such as magnesium, manganese and sulfur; showing also trace elements such as copper (observed in figure 2b).

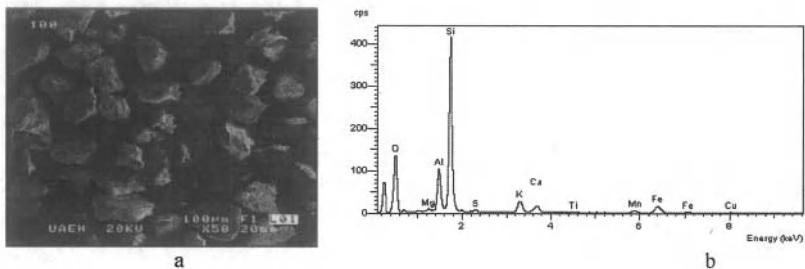


Figure 2. Image and spectra of waste particles obtained by SEM a) General image mesh 100, 50X (SEM), b) semi quantitative analysis (SEM – EDS).

In figure 3 are shown the results obtained by particle size analysis, where can be seen a relatively big particle sizes with a particle size distribution of standard size in mesh 80 ( $177 \mu\text{m}$ ) and an average size in mesh 200 ( $74 \mu\text{m}$ ), so it is observed that higher retained weight is found in mesh 100 with a 19.18 %, so the particle size is too big, later presents a very steep drop to mesh 400 that is where the minimum retained weight that is of the order of 4.50 %. Therefore we can say these are tailings with relatively coarse particles, but adequate for use as alternative industrial material.

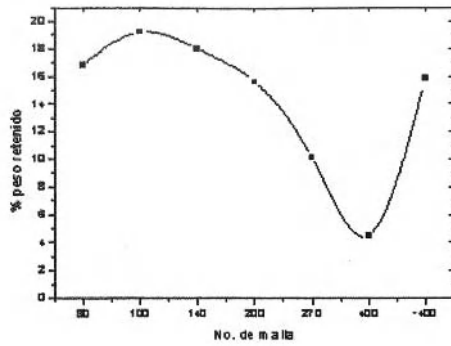


Figure 3. Particle size distribution

Table II shown average chemical compositions of clays used to make mixtures, showing the majority phases to silica, alumina, sodium oxide, potassium oxide and calcium oxide, which favor the stickiness of composites.

Table II. Average chemical compositions of clays.

Clay	SiO <sub>2</sub>	Al <sub>2</sub> O <sub>3</sub>	Na <sub>2</sub> O	K <sub>2</sub> O	CaO	MgO	TiO <sub>2</sub>	Fe <sub>2</sub> O <sub>3</sub>
1	62.34	20.59	1.34	1.67	1.09	0.44	1.70	10.84
2	68.79	18.95	1.50	1.52	1.66	0.45	0.98	6.15
3	66.94	21.44	0.32	2.11	0.39	0.83	1.41	6.56
4	59.53	28.47	0.41	1.17	0.26	0.80	1.13	8.23
5	62.34	20.59	1.34	1.67	1.09	0.44	1.70	10.84
6	42.52	32.18	0.45	0.45	0.26	0.45	1.77	18.93

Seven compounds were prepared from a mixture of waste and clays, obtaining the following composites with high plasticity, as shown in the table III.

Table III. Composition of representative composites for the manufacture of tiles.

Composite	% wt. of waste	% wt. of high plasticity clay	% wt. of low plasticity clay
1	66.67%	26.67%	6.67%
2	63%	31%	6%
3	63%	31%	6%
4	63%	31%	6%
5	60%	34%	6%
6	60%	34%	6%
7	60%	34%	6%

Based on the preparation of these composites, were produced seven briquettes, with each of the aforementioned composites (figure 4), found that the composite number one had the best properties of stickiness and plasticity; whereby some tiles were produced using this composite, getting high quality tiles (figure 5).

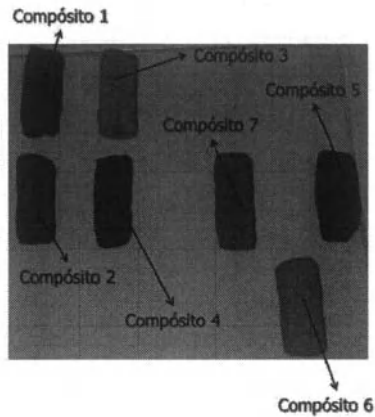


Figure 4. Briquettes obtained from the mixture of waste and clays.

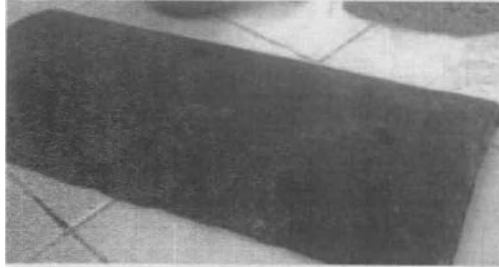


Figure 5. Tile produced with waste and clay.

According to the obtained results in the preparation of seven representative composites for fabrication of tiles, we can conclude that have been generated products with high plasticity and high green strength using wastes. These tiles also have good properties of burning that are upper to similar product elaborated in conventional processes, getting so a burnt red color.

### Conclusions

1. According to chemical composition and particle size distribution of wastes, these can be considered as a mixed feldspars substitute, which can be used as alternative raw material to fabrication of tiles.
2. Products of high plasticity and high green strength were obtained using wastes as majority compound in mixtures, getting similar or upper properties after burning in comparison of the products elaborated in conventional processes.
3. With the addition of clay to waste can be obtained composites of different shades to production of tiles, bricks and vault.

### References

1. Francisco Patiño, Juan Hernández, Isauro Rivera, Eleazar Salinas R, Luis Carlos Longoria G. And Juan Manuel Gonzalez, "Characterization and kinetics of the grinding of the Dos Carlos burrows in the state of Hidalgo," *International Precious Metals Institute*, EU. (2007).
2. Eleazar Salinas R., Francisco Patiño C, Juan Hernández A., Leticia E. Hernández Cruz, Isauro Rivera L, "La problemática de los jales en el estado de Hidalgo," *Memoria del IV Congreso Nacional de Metalurgia y Materiales*, México, septiembre (2006), 327- 328.
3. A.R. Geyne, Carl Fries et.al., "Geology and Mineral deposits of the Pachuca – Real del Monte District, State of Hidalgo," *Consejo de Recursos Naturales no Renovables*, (1963), 5-E.
4. Cía. Real del Monte y Pachuca, "Inventario de las presas de Jales de la CRMyP," (2006).
5. Juan Hernández A., Francisco. Patiño C., Isauro. Rivera L., Eleazar Salinas R., Martin Alamilla M., Eduardo Cerecedo S. Martin Reyes P., Miguel. Pérez L., "Silver Dissolution From The Waste Mounds Of Pachuca, Hidalgo State, Mexico – Effect Of Cyanide Concentration On Dissolution Rate," *European Metallurgical Conference EMC*. 3 (2009), 1037 – 1046.

6. Norma Oficial Mexicana NOM-O-13-1992.
7. Norma ASTM-C-24-56
8. Juan Hernández A., Eleazar Salinas R., Francisco Patiño C., Isauro Rivera L., Martín Reyes P., Miguel Pérez L., J. César Juárez T., Eduardo Cerecedo S., "Characterization Of Burrows From Mining District Of Pachuca Real Del Monte, In Hidalgo State And Viability Study To Use These Residues As Alternate Industrial Material," *TMS (The Minerals, Metals & Materials Society)*, (2011), 73-80.
9. Juan Hernández Avila, Eleazar Salinas Rodríguez, Isauro Rivera Landero, Francisco Patiño Cardona, Miriam Yta, Miguel Pérez Labra, "Caracterización de los jales del distrito Pachuca-Real del Monte, Hgo., y su posible uso como material industrial," *X Coloquio de Mineralogía, Pachuca, Hidalgo México*, (2006), 129-134.

### **Acknowledgments**

The authors thank to FOMIX - Hidalgo for the support for the realization of this work, involved in the Project 128491.

## **CONCRETE WITH CEMENTITIOUS STEEL SLAG COMPOSITES AND ITS APPLICATIONS**

Honghui Fang, Jiannyang Hwang, Gaifeng Xue and Lijun Lu

R&D center of WISCO, Wuhan 430080, China

Keywords: Steel slag, BF slag, granulated slag, free lime, concrete stability and expansion, concrete without cement.

### **Abstract**

Steel slag has been stockpiled in many steel mills due to its poor performance in various construction related applications. Free lime in steel slag has been considered as a major barrier for its utilizations. Composite of steel slag and powders of granulated blast furnace slag have been found an excellent cementitious material for concrete. Portland cement is not required in this kind of concrete. Concretes with various amounts of steel slag and powders of granulated blast furnace slag additions have been investigated. Physical and chemical properties of the products were examined. High performance concrete can be obtained. Field testing of the concrete products was conducted for various applications, including buildings and pavements, and the results demonstrated the soundness of the concrete. Drill cores of field tested concrete, with ages up to 26 years, were examined for the microstructures under SEM.

### **Introduction**

In the steel industry, a major source of the solid waste is steel slag. Steel slag has poor stability in construction applications. This is a major reason that only a small amount of steel slag has been utilized. Some of the reported applications include the land filling/creation in the sea, road base materials, soil treatment for acid neutralization and micronutrients supply, and sintering aid in the sintering plant of the steel industry [1].

To solve the stability problem for using steel slag as construction materials, the common approach is to find a method capable of depressing or eliminating the expansion of steel slag. Free lime in steel slag is the major component that causes the expansion. Aging and hydration pretreatment of free lime in steel slag are the well known methods for increasing the steel slag stability. However, there has been limited success on these approaches due to that a large portion of free lime is locked in the grains during the pretreatment process.

Based on the mineral compositions of steel slag and the characteristics of their hydraulic reactions, a new approach was studied and reported here. This approach utilizes the composites of steel slag and granulated blast furnace slag as major ingredients to accomplish the cementing requirements for concrete, while solving the steel slag stability and expansion problems in concrete.

### **Experiment**

#### **Materials**

There are two major components to make the no cement concrete. One is the steel slag and

the other is primarily the granulated blast furnace slag powder composites containing some additives. The composites of the two components react and provide the cementitious materials for the sand and aggregate in concrete.

Several steel slag samples were collected from different steel companies. These slag samples have been crushed to passing 4.75mm and magnetically separated to recover the iron metals. The granulated blast furnace powder composites are prepared by mixing powders of gypsum and silicates. Less than 4.5% of the materials have particle sizes above 80 $\mu$ m. The specific surface area is greater than 400 m<sup>2</sup> per Kg. Chemical compositions of the materials are given in Table 1.

Table 1. Chemical compositions of steel slag and granulated BF slag powder composite.

Sample	SiO <sub>2</sub>	Al <sub>2</sub> O <sub>3</sub>	CaO	MgO	Mn	P <sub>2</sub> O <sub>5</sub>	MFe	FeO	Fe <sub>2</sub> O <sub>3</sub>	S	Alkalinity*
SS1-TS	10.36	2.14	43.52	6.09	1.92	1.69	2.3	11.90	11.20	0.077	3.61
SS2-HS	8.68	1.63	42.96	7.50	1.89	1.26	0.4	13.28	12.49	0.040	4.32
SS3-DQ	8.34	1.12	39.03	9.95	2.29	1.48	2.3	23.35	6.65	0.038	3.97
SS4-AB	8.72	1.53	37.46	10.54	1.85	2.04	0.52	15.12	19.24	0.032	3.48
SS5-TS	10.59	1.69	38.28	7.76	2.61	1.52	/	26.02	9.24	0.106	3.16
SS6-HS	9.46	5.36	38.33	10.38	0.73	0.95	0.60	11.69	10.39	0.179	3.68
GP	33.70	14.49	37.35	9.73	0.19	0.023	/	0.81	1.30	0.755	1.10

Note: \*Alkalinity=CaO/(SiO<sub>2</sub>+P<sub>2</sub>O<sub>5</sub>); SS=Steel Slag, GP=Granulated BF Slag Powder Composites, TS=Thermal Stewed, HS=Hot Splashed, DQ=Drum Quenched, AQ=Air Blasted.

### Experimental Procedures

Samples for experiments were prepared with two different weight distributions, depending on the kind of materials utilized. For the GC and HS samples, the ratios are granulated powder mix 450g, steel slag 675g, and sand 675g. For the R and AB samples, the ratios are granulated powder mix 500g, steel slag 750g, and sand 750g. The amount of water utilized is determined by Chinese standard method GB/T2419 with mortar fluidity at 175 $\pm$ 5mm. Molding, curing and testing was carried out according to Chinese standard method GB/T 17671-1999.

### Concrete Preparation and Strength Testing

Concretes were prepared based on the formula shown in Table 2. Strength testing was carried out based on Chinese standard method GB/T50081-2002.

Table 2. Weight distribution for various concrete preparations.

No.	Strength Design	Slump mm	Addition (kg/m <sup>3</sup> )					Water Reducer	Water
			Granulated Powder Mix	Steel Slag*	Sand	Aggregate			
1	C50	140	480	500 (HS)	370	1100	5.8 (FDN)	170	
2	C30	260	390	400 (HS)	410	1250	4.7 (FDN)	165	
3	C50	180	480	500 (GC)	320	1100	5.8 (FDN)	190	
4	C30	140	390	400 (GC)	416	1250	4.7 (FDN)	180	
5	C50	165	450	800 (RCD)	/	1200	5.4 (FDN)	160	
6	C30	270	390	600 (RCD)	260	1200	4.7 (FDN)	165	
7	C50	265	450	800 (AB)	/	1200	5.4 (FDN)	160	

8	C30	265	390	600 (AB)	260	1200	4.7 (FDN)	160
9	C50	270	450	800 (RCD)	/	1200	9 (PA)	150
10	C70	260	550	800 (RCD)	/	1100	9 (PA)	150
11	C50	270	450	800 (AB)	/	1200	9 (PA)	145
12	C70	260	550	800 (AB)	/	1100	9 (PA)	145

### Field Sampling of Road Concrete and Strength Test

After the concrete was field tested on road for a period of time, samples were collected by drill cored as a cylinder with diameter of 100mm. The cylinder was cut to 100mm length for strength test.

## **Results and Discussion**

### Steel Slag Microstructure

The microstructures of steel slag cooled under various conditions were examined.

Drum quenched steel slag: Dicalcium silicate is the major component, followed with tricalcium silicate and periclase. The matrix is glassy. Dicalcium silicate is colorless and rounded in shape. Tricalcium is colorless, platy, showing better crystallinity. Periclase is yellowish, also rounded in shape. Magnesium is in solid solution with iron. It is bounded with iron rich glassy phase. The iron rich glassy phase is reddish-brown to black in color and is semi-transparent. It forms nets to separate dicalcium silicate and tricalcium silicate. The slag is relatively homogeneous, as shown in Figure 1.

Air blasted steel slag: Minerals are mostly rounded in shape. Dicalcium silicate is the major component, followed with periclase and glass, and minor calcium ferrite. Dicalcium silicate is shown in small grains. Matrix is the glass, with small amount of calcium ferrite, which is reddish brown in color. Periclase is yellowish, also rounded in shape. They are disseminated in the sample, although local enrichment has also been observed. The air blasted steel slag grains are covered with a thin layer of glass. No obvious hydration phenomenon was observed. The microstructure of air blasted steel slag is shown in Figure 2.

Hot splashed steel slag: Sample is easily hydrated. Crystal boundaries are difficult to be observed on the polished thin section. A hydrated rim on the steel slag grains can be found. Most of the fine powders are hydrated. Structures are not homogeneous. Dicalcium silicate is the major component, followed with tricalcium silicate, periclase and glass. Dicalcium silicate is mostly rounded, with some in other shapes. Cementing phase between the crystals is in less quantity. Periclase is present in isolated forms between the dicalcium silicates. It has yellow to black color. It is in high solid solution with iron. Figure 3 shows the microstructures of the hot spreaded slag.

Thermal stewed steel slag powder: Dicalcium silicate is the major component, followed with tricalcium silicate, periclase and glass. Calcium ferrite is observed in a few spots. Some of the steel slag grains are hydrated. Fine powders are basically all hydrated. Only the phases that do not hydrate are unchanged in the fine powders, primarily periclase and glass. Dicalcium silicate has a wide distribution in particle size and various granular shapes. Tricalcium is platy. Periclase sits between calcium silicates. Cementing phase between calcium silicates is in less quantity, mostly in glassy phase. There are a small amount of

calcium ferrite. Figure 4 shows the microstructures of the thermal stewed slag.

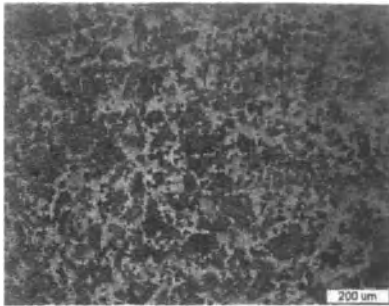


Fig.1. Microstructure of drum quenched slag.

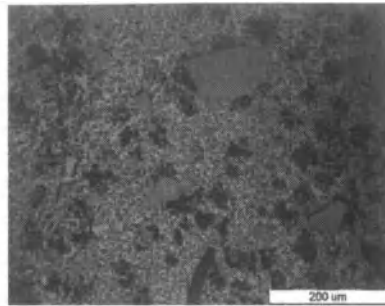


Fig.2. Microstructure of air blasted slag.

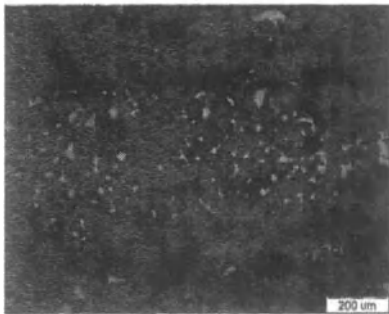


Fig.3. Microstructure of hot splashed slag.

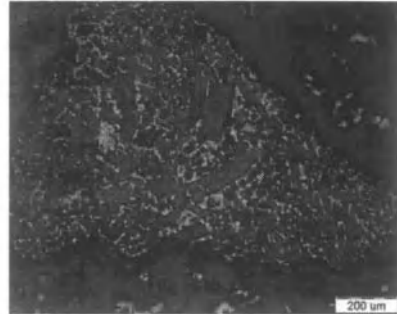


Fig.4. Microstructure of thermal stewed slag.

All of the four slag samples (Figure 1-4) contain dicalcium silicate and tricalcium silicate, which are the common cement ingredient [1]. From the mineral composition and occurrence standpoint, drum quenched slag and air blasted slag are similar. Both are cooled rapidly. Hot splashed slag and thermal stewed slag are cooled relatively slower.

Rapid cooled slags have relatively homogeneous glassy phase, which forms the nets enclosed the dicalcium silicate and free calcium oxide grains.

The slow cooled hot splashed and thermal stewed slags have the fast cooled outside shell and the slow cooled inside core. The microstructure is not homogeneous. Grain sizes of dicalcium silicate and tricalcium silicate are widely distributed and sometimes connected in sheets. Free calcium oxide grains are usually aggregated. Glassy phase is in smaller quantities and is distributed unevenly. A hydrated crust is frequently observed. The hydration is especially severe for those particles with less glassy phase.

The cooling rate obviously has strong effects on the microstructure of the slags [2]. The rapid cooled slag has less free calcium oxide, more glass, and is more homogeneous and more stable. The slowly cooled slag is not homogeneous and has more free calcium oxide, which is

usually in aggregates.

### Strength Test

The strength tests of the composites formed with steel slag and granulated BF slag powders are shown in Table 3. The strengths of the concrete using the composites and sand and gravel are shown in Table 4.

Table 3. Strength of the composites formed with granulated BF slag powder mixture and various kinds of steel slag.

Steel Slag <sup>1</sup>	Setting Time (Hour: Minute)		Boiling Stability	Flexural Strength (MPa)		Compressive Strength (MPa)	
	Initial	End		3d	28d	3d	28d
Hot Splashed	3: 25	7: 40	Passed	6.7	11.2	28.5	39.9
Thermal Stewed	2: 20	5: 45	Passed	7.6	13.3	30.7	43.9
Drum Quenched	1: 57	4: 32	Passed	10.3	17.0	47.5	71.2
Air Blasted	1: 25	2: 55	Passed	10.9	15.6	48.4	65.5

<sup>1</sup> All slag samples were utilized within one month of generation.

Table 4. The strengths of the concrete using the sand and gravel and the composite of steel slag and granulated BF slag powder mixture.

No.	Compressive Strength of Concrete (MPa)						
	3d	7d	28d	60d	90d	150d	360d
1	48.2	51.6	62.3	/	/	/	/
2	40.5	45.4	52.4	/	/	/	/
3	50.1	55.3	65.0	/	/	/	/
4	43.1	48.1	52.7	/	/	/	/
5	56.0	64.1	72.4	73.3	/	78.4	/
6-DQ	47.9	53.5	59.3	63.0	/	67.5	/
7	57.0	66.6	72.1	73.0	/	75.0	/
8-AB	44.5	53.5	59.7	61.0	/	64.3	/
9-DQ	/	84.2	88.7	/	93.4	/	95.0
10-DQ	76.8	82.0	93.4	/	97.0	/	99.6
11-AB	/	65.6	77.9	/	79.6	/	84.2
12-AB	74.3	81.5	91.5	/	93.1	/	100.3

Table 3 shows that the composite of granulated BF slag powder mixture and steel slag has good cementitious property and the composite has good mechanical properties. The composites formed with various kinds of steel slags can all meet the cement requirements of various grades. The early strengths are good. Setting times are normal. Boiling stabilities are passed. The flexural strengths are outstanding.

Table 4 presents the compressive strength of the concrete made of sand, gravel, and the composite of granulated BF slag powder mix and steel slags of various kinds. The designed

grades are C30, C50, and C70. It can be observed that all of the products meet the strength requirements of their corresponding grade. The early strength is outstanding. The strength is continuously increasing with time. Air blasted slag is utilized for the No. 12 test. The compressive strength exceeds 70MPa in 3 days, 90MPa in 28 days, and 100MPa in 360 days. Drum quenched slag is utilized for the No. 10 test. It has similar results as the No.12.

Concretes made of same steel slag (e.g. No. 6, 9 and 10 with DQ slag and No. 8, 11 and 12 with AB slag) show increased strengths with the increase of composite and the increase of composite to water ratio. Based on the theory of W/C (water to cement ratio) [3], the strength of hardened concrete relies more on the W/C ratio than the cement quantity. Low W/C means thicker slurry, which results in higher strength. This indicates that the increase of the concentration of cementitious materials in a concrete will yield concrete of higher strength.

Strength is the most important mechanical property of concrete [4]. This is simply because concrete is mostly utilized for load bearing or force resisting. For the concrete of this study, the hardening of the cementitious materials (produced by the composite of BF slag and steel slag, plus other additives) and the sand and aggregates determines the strength that is developed from them. The mechanical strength of the artificial stone depends on the characteristics, quantities, ratios, and structures of the mineral constituents. The composite of BF slag and steel slag produces intermixed needle like aluminum sulfate hydrates and velvet like silicate hydrates within one day. In three days, it can be observed that the aluminum sulfate hydrates are covered with the velvet silicate hydrates. In addition, the rod shape and granular shape silicate hydrates also appeared. After 28 days, dense structures of intermixed aluminum sulfate hydrates and silicates hydrates are formed.

A microhardness test was conducted on a 7 days sample. A polished section was made from the sample and the microhardness was examined along a line from the center of a aggregate to the matrix. The results are shown in Figure 5. The microhardness is 620 Kg/mm<sup>2</sup>, 231 Kg/mm<sup>2</sup> and 71 Kg/mm<sup>2</sup> for the aggregate grain center, boundary and matrix, respectively. The microhardness of the boundary is 3 times of that of the matrix. This demonstrates that the boundary of the grain and the matrix is hydrated and well bounded with the hardened hydrated products. This is different from the bounding from the Portland cement. In a previous study [6], it was shown that the boundary of the grain and matrix in concrete using the Portland cement has the lowest microhardness than the grain and the matrix. It is the weakest part of a concrete, with the hardness of about 40 to 90% of the matrix (Figure 6). Therefore, the composite of the granulated BF slag powder mix and the steel slag offers much better cementing property than the regular Portland cement on making a concrete.

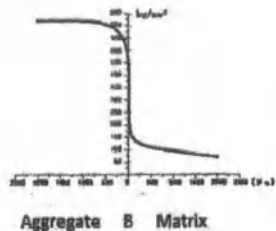


Figure 5. Microhardness around boundary.

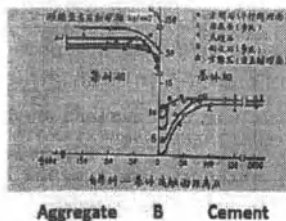


Figure 6. Microhardness near cement boundary.

## Engineering Applications

The concrete using the composite of BF slag and steel slag has been evaluated in many engineering projects to understand their long term performance. Some of these projects were carried out about 30 years ago. The results of these tests show that the composite based concrete has long life, excellent structures, and continuously increasing strength. Their microstructures are dense without any fractures around the grains observed. A few examples are presented here.

A project was carried out in 1985 to build a natural gas maintenance workshop with the composite concrete, including the foundations and pillars to support the crane operations. The pillars were prefabricated with steam curing, which reached 57% of the design strength within one day. After one day curing, the pillar was removed from the mold and lifted with a crane to the place. No cracks or damages were found. The workshop has been operated until now without showing any problems. An external agency has been called to examine the project 4 years after its construction. Nondestructive ultrasound and rebound hammer tests were conducted (Figure 7). Its conclusions include:

- a. The foundations and steel beam reinforced concrete corbels have satisfied the designed strength requirements according to the nondestructive testing, and hence achieved its load bearing requirements.
- b. The composite concrete is dense and has no cracks or other damages.
- c. Both the interior and field tests show excellent quality.
- d. There is no inside or out damages after years of use.

A road using the composite concrete was constructed along the dorm of the company in 1984 (Figure 8). The concrete is 200 mm thick. The designed strength is grade C20, and the tested strength is 28.5 MPa. After 22 months of use, a core was obtained and the strength has increased to 113%. After 26 years in use, another core was obtained and the strength was 35.1 MPa, equivalent to 123% increase. The strength is increasing with time. The surface of the road is still smooth, without seeing pitting and sand detaching.



Fig.7. Nondestructive test on 4 years old corbels.



Fig.8. 26 years old road using composite concrete.

Figure 9 is a SEM picture of the 26 years sample. Figure 10 shows the elemental analysis of the marked point in Figure 9. The point shows that this grain is a solid solution of Mg, Fe and Mn in oxide form (RO phase). This RO phase is surrounded by the velvet phase in a steel slag grain. In the typical steel slag, RO phase disseminated within the dicalcium silicates. The

velvet surroundings suggest that these dicalcium silicates have been hydrated in the last 26 years to form the hardened hydrated gels. The RO phase is stable. It didn't participate to hydration reaction. The steel slag grains and the surrounding matrix are densely connected. No cracks or fissures are observed, indicating no expansion. In the petrographic analysis, it shows that small steel slag particles have been hydrated, which consumes the calcium and leaving Mg and Fe RO grains behind, sticking out as an island in the hydrated products (Figure 11).

Fe metals left in the slag can be observed in Figure 12. There is no oxidation of the Fe metal grain after 26 years use, which is an additional evidence supporting that the composite concrete is dense.

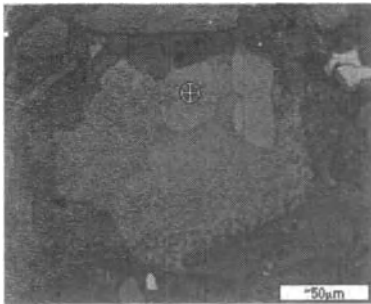


Fig.9. Solid solution phase ⊕ of Fe, Mg and Mn.

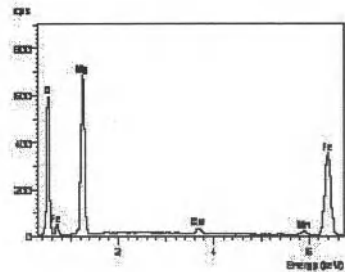


Fig.10. Elemental analysis of spot "⊕"

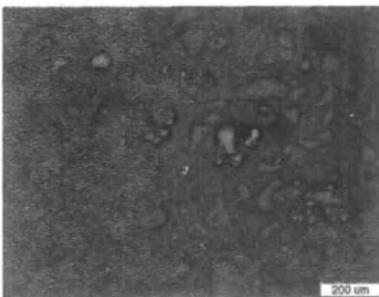


Fig.11. Small particles left in the hydrated matrix.

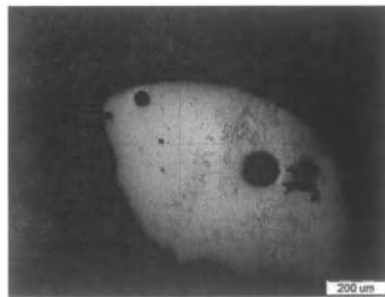


Fig.12. Metal particles in the composite concrete after 26 years.

### Conclusions

1. Composite of granulated BF slag powder mix and steel slag is a good cementitious material.
2. Concrete can be made using the composite to replace the Portland cement.
3. The hydrated products from the composite include various aluminum sulfate hydrates and silicate hydrates. These hydrates are densely intermixed. Steel slag particles are part of the

reactants. The final products are the hardened hydrates with very dense microstructures.

4. The nondestructive testings show that the composite concrete utilized in various civil projects are sound. The strength increases with time.

5. The composite concrete is still stable after 26 years in field use. Petrographic analysis of the core sample shows that the active ingredients in the large steel slag particles reacts first, which exposes the stable RO phase. Small slag particles also hydrates, consuming calcium and leaving RO of Mg and Fe as islands in the hydrates matrix. Steel slag particles forms dense mass with the matrix. Iron particles in the slag were not oxidized. There were no expansion from the free CaO and free MgO.

#### **Acknowledgement**

We are thankful to the assistance of Xin Xu and Dazhong Yu, Shengyang Building and Construction Materials Center, China Academy of Science in Building and Construction Materials, on the strength testing of our products.

#### **References**

- [1] Guiling Zhu, Shusan Sun, "Current status on steel slag utilizations", 2003 Proceedings for the Symposium of Energy and Environmental Technology in Metallurgical Industry, China Metallurgical Industry Publications, pp.18-23.
- [2] Jizheng Li, Honghui Fang, "Microstructure analysis of various steel slags", Henan Construction Materials, Issue 6, 2009.
- [3] Shaozheng Sun, Surfactants, Chemical Industry Publications, 1984, pp.419-436.
- [4] Xincheng Pu, Concrete, Chap.5, China Construction Publications, 1981, pp.67-68.
- [5] Honghui Fang, Steel slag cementitious materials and applications, Industrial Construction, v.2, 1991.
- [6] Xincheng Pu, Concrete, Chap.3, China Construction Publications, 1981, pp.53-54.

## **CHARACTERIZATION OF DUST GENERATED IN THE BOF CONVERTER**

Eduardo Junca<sup>1</sup>, José Roberto de Oliveira<sup>2</sup>, Denise Crocche Romano Espinosa<sup>1</sup>, Jorge Alberto Soares Tenório<sup>1</sup>

<sup>1</sup> University of São Paulo; Av. Prof. Mello Moraes, 2463; São Paulo, São Paulo, 05508-030, Brazil.

<sup>2</sup> Instituto Federal do Espírito Santo; Av. Vitória, 1729; Vitória; Espírito Santo; 29040-780, Brazil.

**Keywords:** Mineralogical characterization, waste steel.

### **Abstract**

Steel industry has been expanding every year, consequently there has been an increase in waste generation in this area. Thus, companies in this sector are finding it difficult to give a correct destination of waste. For example, only in a basic oxygen furnace (BOF) converter are generated about 18kg of dust per ton of steel. The aim of this work was the characterization of dust generated in the BOF converter. The characterization was performed by chemical analysis (titration for iron and its oxides and Inductively Coupled Plasma Atomic Emission Spectroscopy for other elements), scanning electron microscopy, size analysis using Mastersizer 2000 equipment and X-ray diffraction. It was observed that dust is composed mainly iron in form of magnetite, metallic iron and wustite with approximately 99% of the particle size below 100µm.

### **Introduction**

Today, steel is an important metal for the world. It can be produced for two routes, blast furnace/basic oxygen furnace (BOF) converter and electric arc furnace (EAF) [1].

First route, the iron is produced from the reduction of iron ore and coke for fuel injection and/ or natural gas for a production of pig iron in blast furnace. The pig iron is sent until BOF converter to perform the blowing of oxygen to obtain the steel. In the second route, the steel is produced using scraps or direct reduced iron (DRI) using electric arc.

During steel production are generated a lot of wastes like slag, sludges, scraps and dust [2]. Only in the first six months of 2010, world steel production totaled 706 million tons [3]. According to Watson and Wang [4], some 10 to 20 kg of dust is generated per tonne of liquid steel produced. Thus, the reuse of these wastes can be a great to companies, because it reduces the amount of raw material to be extracted and reducing disposal costs [5,6].

Basic oxygen furnace is responsible for over 60% of the total steel production, and it is the second largest generator of solid waste in an integrated steel mill, contributes with 27 wt.% of

the solid waste generated in the plant. In this sector are generated about 5 to 7 million tons per year worldwide [7,8 ,9].

The BOF dust is generated by blowing of oxygen in pig iron. When occurs oxygen contact with the pig iron small particles are generated. These particles are removed from furnace off-gases in bag-houses [4]. The figure 1 shows the process of particle generation in the BOF converter.

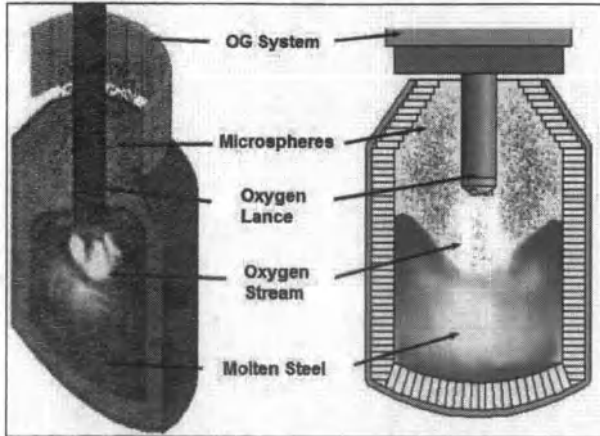


Figure 1: Process of particle generation in the BOF converter.

\*Footnote: Mendes, 2009 [10].

The main elements present in the BOF dust are Fe, Ca, Mn, Pb, Mg and Zn [11,12]. The Fe can be present as wustite and magnetite [6]. In the table I can be seen some composition of BOF dust.

Table I: Components present in the BOF dust.

Components	wt. %	wt. %
Total Fe	55.4	47.9
SiO <sub>2</sub>	2.3	1.4
MnO	1.8	0.3
CaO	10.6	13.0
MgO	3.7	0.5
ZnO	1.7	6.7
Pb	-	0.5
Na <sub>2</sub> O	0.3	0.7

\*Footnotes: Hay and Rankin, 1994 [13];OXIFINE, 2002 [14].

The BOF dust usually is dumped in landfill sites. Thus, it can cause environmental problem because the heavy metals like Pb and Zn can be leaching [11].

The steel industry is growing. Therefore this results in increased waste generation. There is potential for the development of fundamental studies and innovations for the exploitation and use of waste as raw material to be introduced into the productive cycle.

However for the development of new techniques for reuse of waste is necessary to know it. The aim of this work is to perform the characterization of the BOF dust for developments of new routes for its reuse.

### Materials and Methods

Initially was colected about 20kg from BOF dust. It was dried in muffle furnace at 60°C for 48 hours and it was manually homogenized. The next step, the dust was characterized by chemical analysis, scanning electron microscope coupled with EDS, X-ray diffraction and size analysis.

Chemical analysis was carried out by titration for iron and its oxides. For other elements, the chemical analysis was performed by Inductively Coupled Plasma Atomic Emission Spectroscopy (ICP). For perform ICP analysis the sample was digested in aqua regia for 24 hours and diluted in distilled water.

For accomplish scanning electron microscope the sample was coated with gold. The images were obtained for secondary electrons. The size analysis was realized using Mastersizer 2000 equipment. In this test was used water as dispersant and ultrasound for 5 minutes. The X-ray analysis was carried out in SIEMENS equipment, model 500. It was conducted between 5 to 70 degrees.

### Results and Discussion

In the table II shows results obtained from BOF dust by titration and Inductively Coupled Plasma Atomic Emission Spectroscopy.

Table II: Chemical analysis obtained from BOF dust.

Components	wt. %
Total Fe	46.9
Metallic Fe	2.2
Fe <sup>+2</sup>	44.4
Fe <sup>+3</sup>	0.3
CaO	23.2
MnO	3.4
MgO	2,1
SiO <sub>2</sub>	2.0
ZnO	1.9
PbO	0.1

It can be observed in the table II that total Fe (46.9 wt.%) is the main component found in BOF dust. The total Fe was found in three forms, metallic Fe (2.2 wt.%),  $\text{Fe}^{+2}$  (44.4 wt%) and  $\text{Fe}^{+3}$  (0.3 wt%). It also found 23.2 wt.% of CaO. According to Mendes, CaO is coming from calcite that is introduced into basic oxygen furnace [10].

Other elements also were found in less proportion like MnO, MgO, ZnO,  $\text{SiO}_2$  and PbO. The  $\text{SiO}_2$ , CaO, MgO are from slag. According to brazilian laws, this dust is classified as class I, hazardous waste [15].

Figure 2 shows X-ray obtained from BOF dust. It can be seen that main iron's phases found were wustite, magnetite and iron. It also was found quartz and calcite, magnesium peaks. According to Yi et al [16],  $\text{FeO}$  or  $\text{Fe}_2\text{O}_3$  are the main phases components from BOF dust. In this work, the main phase found was  $\text{FeO}$ . The  $\text{SiO}_2$  peak can be from slag.

The X-ray proves the results obtained by chemical analysis that showed that the main phases found was  $\text{Fe}^{+2}$  from wustite and magnetite.

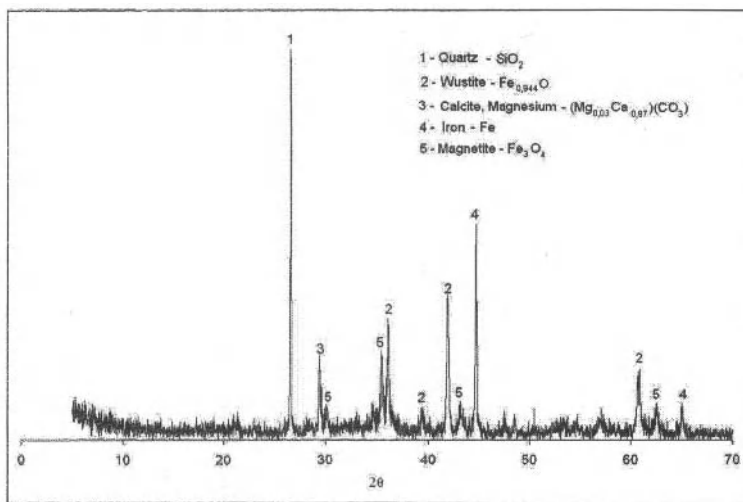


Figure 2: X-ray spectra of BOF dust sample.

Figure 3 shows images obtained from scanning electron microscopy and figure 4 shows EDS analyses performed together with scanning electron microscopy. It can be observed that the main peaks found were Fe, Ca, Mn, Mg and O. These results shows that Fe is present in greater proportion than other constituents.

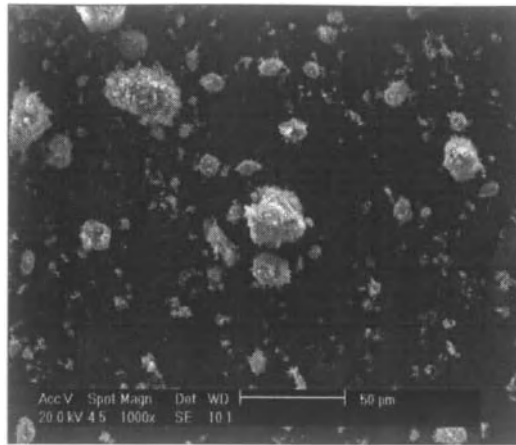


Figure 3: Images secondary electrons from BOF dust 1000x.

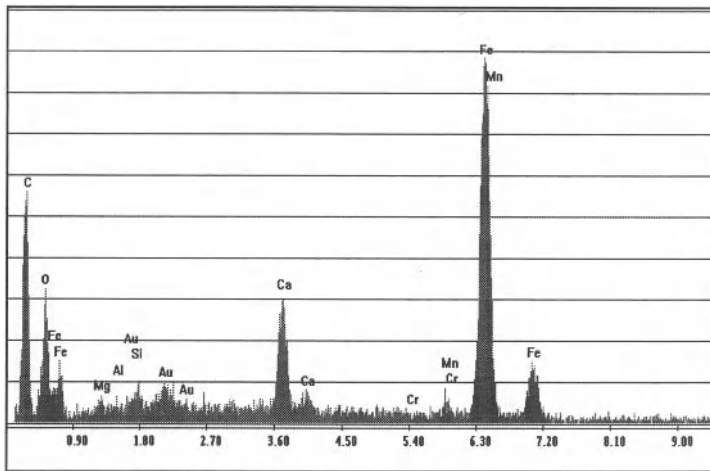


Figure 4: EDS spectra of BOF dust.

Figure 4 shows size analysis obtained by mastersize equipment from BOF dust. It can be seen that particle size distribution is situated in the range 0.128 to 158.5  $\mu\text{m}$ , with 98.2% smaller than 100  $\mu\text{m}$ . It was also observed that 50% of the particles were less than 10.08  $\mu\text{m}$ .

The fine particle size is one of the major problem found for recycling of this dust. Thus, it is necessary process of agglomeration to use this dust [7].

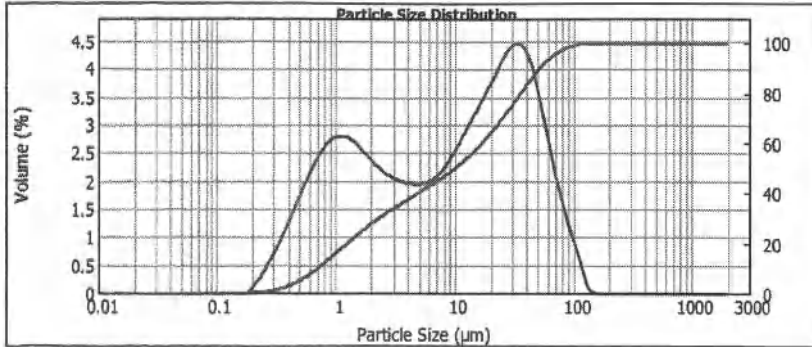


Figure 5: Size analysis from BOF dust.

Similar results were obtained for Mikhail and Turcotte [7]. Their data showed that almost all the BOF dust is under 100 µm.

### Conclusions

The characterization of the BOF dust showed that the main element was Fe (46.9 wt%). The main Fe phases found were wustite and magnetite. These phases are constituted mainly for  $Fe^{+2}$ . The size analysis showed that approximately 98% smaller than 100 µm, thus is necessary process of agglomeration to use this dust.

### References

- 1 Y. Kim and E. Worrell. "International comparison of CO<sub>2</sub> emission trends in the iron and steel industry". *Energy Policy*, 30 (10) (2002), 827–838.
- 2 C.M.F. Vieira et al., "Incorporation of fine steel sludge waste into red ceramic". *Materials Science and Engineering A*, 427 (1-2) (2006), 142–147.
- 3 WORLD STEEL ASSOCIATION. (2010). Steel Statistical Yearbook 2009. Brussels: WORLD STEEL ASSOCIATION. Available at: <<http://www.worldsteel.org/pictures/publicationfiles/SSY%202010.pdf>>, Accessed: 4/20/2009
- 4 J. L. Watson and Y. Wang. "Multi-stage, Multi-force Dewatering of Steelmaking Sludges". *Powder Technology*, 58 (1) (1989), 49 – 53.

- 5 V. P. Della et al., "By-product Utilization of Metallic Recovering of Stainless Steel Slags in The Ceramic Pigments Synthesis: Raw Material Characterization". *Cerâmica*, 51 (318) (2005), 111-116.
- 6 P. M. Andrade et al., "Recycling of Steel Sludge into Red Ceramic". *Materials Science Forum*, 530-531 (2006), 544-549.
- 7 S. A. Mikhail and A. M. Turcotte. "Thermal reduction of steel-making secondary materials I. Basic-oxygen-furnace dust". *Thermochimica Acta*, 311 (1-2) (1998), p.113-119.
- 8 S. Kelebek, S. Yörük and B. Davis. "Characterization of basic oxygen furnace dust and zinc removal by acid leaching". *Minerals Engineering*, 17 (2) (2004), 285-291.
- 9 M. Evestedt and A. Medvedev. "Model-based slopping warning in the LD steel converter process". *Journal of Process Control*, 19 (6) (2009), 1000-1010.
- 10 J. J. Mendes, "Influência da adição da lama fina de aciaria a oxigênio nas características físicas e microestruturais de pelotas queimadas de minério de ferro" (Master. Dissertation, Universidade Federal de Ouro Preto, 2009), 20.
- 11 M.L. Sammut at al., "Determination of zinc speciation in basic oxygen furnace flying dust by chemical extractions and X-ray spectroscopy". *Chemosphere*, 70 (2008), 1945-1951.
- 12 B. Das et al. "An overview of utilization of slag and sludge from steel industries". *Resources, Conservation and Recycling*, 50 (1) (2007), 40-57.
- 13 S. M. Hay and W.J. Rankin. "Recovery of iron and zinc from blast furnace and basic oxygen furnace dusts: A thermodynamic evaluation". *Minerals Engineering*, 7 (8) (1994), 985-1001.
- 14 J. V. Scheele and M. Johansson, "OXYFINES a new technology for in-plant recycling of dust and sludge in metal production industries, Recycling and waste treatment in mineral and metal processing". *Technical and economic aspects*, 1.1 (2002) 109-118.
- 15 F. F. Grillo, "Recuperação do zn e fe da poeira de aciaria elétrica proveniente da produção de aço carbono" (Master. Dissertation, Instituto Federal do Espírito Santo, 2011), 14-69.
- 16 C. Yi et al., "Experimental Research on Reducing the Dust of BOF in CO<sub>2</sub> and O<sub>2</sub> Mixed Blowing Steelmaking Process". *ISIJ International*, 49 (11) (2009), 1694-1699.

## **EXPERIMENTAL RESEARCH TO IMPROVE THE SOUNDNESS OF CEMENTITIOUS MATERIAL BLENDED WITH CYCLED FLUIDIZED BED ASH**

Shujing Zhu<sup>1</sup> and Xinghua He<sup>2</sup>

<sup>1</sup>Department of Resource and Environment, Wisco R&D Center, 430080 Wuhan,  
China

<sup>2</sup>Department of Water Supply, South Company of China Metallurgical Group, 430070  
Wuhan, China

Key words: Cycled fluidized bed ash (CFBA), soundness, cement clinker, free CaO ,  
cementitious material

### **Abstract**

Cycled fluidized bed ash (CFBA), a significant portion of fly ash produced from coal-fired power plants and rejected from the ash classifying process, has remained unused due to its high free CaO and SO<sub>3</sub> content. It is necessary to extend research on the method to reduce the expansion and improve the compressive strength by some effective chemical activator. This paper presents experimental results on the expansion by Le chatelier tester and the compressive strength. Hydraulic ash-zeolite (HAZ) cementitious material was blended as the chemical activator to study the effects of the activator on the expansion and the compressive strength. The results show that HAZ can not only reduce the expansion, but also increase the prisms compressive strength. Scanning electron microscope observation and X-ray diffraction analysis indicate that the main hydrated products of the sample are calcium hydroxide, ettringite, zeolite and calcite, which can explain the results of the expansion and the strength tests.

### **Introduction**

Nearly 80% of the electricity in China is produced by coal-fired plants, which results in the production of a large quantity of coal combustion residues, among which coal fly ash is the major component. Because of that the air-pollution becomes heavier as time going on. Cycle-fluidized-bed-combustion systems are retrofitted to meet air-emission standards mandated by China Clean Air Act. Cycle fluidized bed ash (CFBA) will present new challenges for coal-combustion byproduct management. The use of cycle-fluidized-bed ash as a cement replacement in concrete is the most attractive one because of its high volume utilization and widespread construction. However, the replacement of cement with cycle fluidized bed ash in Portland cement concrete usually increases the expansion and decreases the early strength of concrete. In many research of this field, most of them were focus on the activation of

pozzolanic activity of CFBA and to make all kinds of blend cement. A number of studies had been carried out on the activation of CFBA using chemical activators. These studies involved using different activating methods including alkali activation and sulfate activation [1, 2]. The former involved the breaking down of the glass phases in an elevated alkaline environment to accelerate the reaction [3, 4]. The later is based on the ability of sulfates to react with aluminum oxide in the glass phase of CFBA to produce ettringite that contributes to the strength at early ages [5-7]. With respect to sulfate activation, the use of gypsum and sodium sulfate had been well studied [5-8]. HAZ is one of HAS sub-products which is a patented chemical activator made by Wuhan University (ZL98113594.3). It had been used to activate CFBA to produce blend cement in many Chinese engineering projects and time has told us that it is a good activator.

Great progress has been made in this field in recent years and then there was an emphases assignment given by Technology committee of Wuhan city to make high pozzolanic activity cement material in which CFBA mix ratio exceed 40 percents. It was inferred by Shunsuke that calcium hydroxide is insufficient for proceeding of pozzolanic reaction in CFBA cement paste. When the substitution rate of CFBA is as high as 60%, calcium hydroxide is so insufficient that self-neutralization may occur. Therefore, it is desirable to not exceed 40% of the CFBA substitution rate of cement [9]. In this study, the focus is on the activation of activity of CFBA using HAZ. The purpose of this study is to find an effective and simple mix ratio of HAZ to keep the soundness and to increase the strength of blend cement in which CFBA mix ratio can range from 40 percents to 70 percents.

### Materials

The CFBA used in this study was from Tianmushan Power Plant in Hangzhou City. Its chemical compositions and main physical properties are given in Table 1. It can be seen that free CaO and SO<sub>3</sub> in the form of lime and anhydrite. In addition to pozzolanic properties, they can have hydraulic activity with just the ash itself [10, 11]. These ashes can form, with water, relatively strong materials without the need of an activator. The content of SO<sub>3</sub> and f-CaO are higher than 3%, which are the max ratio to mix with the clinker of fly ash allowed in China codes.

Table 1. Chemical composition of the sample from Tianmushan power plant.

Oxides	Content %
SiO <sub>2</sub>	31.15
Al <sub>2</sub> O <sub>3</sub>	18.07
Fe <sub>2</sub> O <sub>3</sub>	4.21
Total CaO	26.51
f-CaO	5.8
MgO	1.06

SO <sub>3</sub>	9.56
Loss on Ignition	8.12

The cement and the cement clinker used in this experiment were bought in Wuhan city. Its chemical compositions are given in Table 2.

Table 2. Chemical composition of cement clinker.

C <sub>3</sub> S	C <sub>2</sub> S	C <sub>3</sub> A	C <sub>4</sub> AF	CaSO <sub>4</sub>
56.47	14.04	6.93	13.62	1.00

Hydraulic ash-zeolite (HAZ) is one sub-products of Hydraulic ash-slag cementitious material (HAS) that is a patented chemical activator made by Wuhan University (ZL98113594.3). It is a kind of Hydraulic ash-slag cement material which was made up of pozzolanic concrete dust, byproduct of alkali industry, high blast furnace slag and some chemical agents. HAZ can make the expansion lower by give crystalloid inducement and change pH of the surroundings. Figure 1 gives the XRD pattern of HAS motar .

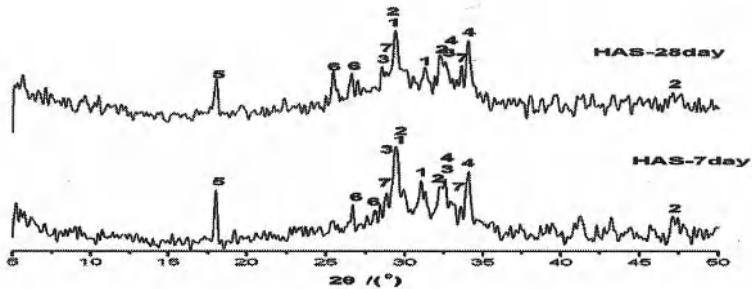


Fig. 1. XRD of HAS motar: (1: CaMgSi<sub>2</sub>O<sub>7</sub>; 2: CaAl<sub>2</sub>Si<sub>2</sub>O<sub>7</sub>; 3: CaAl<sub>2</sub>SiO<sub>7</sub>; 4: CaAlSiAlO<sub>7</sub>; 5: Ca(OH)<sub>2</sub>; 6: CaSiO<sub>3</sub>; 7: CaAl<sub>4</sub>O<sub>7</sub>)

### Experimental Procedure

The test specimens were prepared in two different batches. The first batch was used for determining the effect of HAZ content and amount of mixing CFBA on the cylinder expansion. Cylindrical specimens of 2.50 cm in height and diameter were made in this batch, which was molded by Le chaterlier tester. The water-to-binder ratio was 0.35 for all the mixes. To study the effect of CFBA content on prisms expansion, the ratios of CFBA and cement clinker in the mix were varied from 30:70% to 70:30%. For comparison, the same experiments were done on pastes with 30% CFBA and 70% cement without any HAZ. To study the effect of HAZ content on mortar strength and the expansion, the ratio of HAZ dosage was varied from 0.5% to 2%. All the component mix together and were ground in a lab ball mill to produce fine powders with a particle size of less than 75µm.

The second batch specimens were used for determining the effect of HAZ content and amount of mixing CFBA on mortar strength. The mix was cast into a 70.7×70.7×70.7 mm mold by hand. They were made from CFBA cementitious material-sand mortars, containing 60% mix of CFBA cementitious material and 40% sand. The ratios of CFBA and cement clinker in the mix were varied from 30:70% to 70:30% in the CFBA cementitious material.

After molding, test specimens were cured in a moisture chamber with a temperature of 20± 2°C and RH>90%. After a certain period of curing in the above-mentioned trial environments, the mortar specimens were tested for compressive strength. At the same time the paste specimens were analyzed using Scanning electron microscope, FT-IR, Differential Thermal Analyzer–Thermogravimetric (DTA-TG) and X-ray diffraction, and the composition and structure for new formations of the cementing matter were determined.

## Result and Discussion

### Expansion Decrease

Table 3 shows the results of soundness tested by Le chatelier tester, in which the CFBA dosage ranges from 30% to 70%. In Table 3, it can be seen that the pastes was broken when the CFBA replacement beyond 30%, in which there was no HAZ dosage. Figure 2 shows the photos of the broken cylinder and the soundness one. Table 3 shows that the maximum rate of the expansion reduction of the prism was achieved at 2% HAZ dosage. Expansion of CFBA-cement clinker with 2%(wt) of HAZ reduced by 47.8% compare to the same mix with no HAZ dosage. In Table 3 it can also be seen that expansion increased with increasing CFBA content at a constant HAZ dosage. For the mixes replacement of disposed CFBA increase from 40% to 70%, the expansion increased by 5.3%, 21.1% and 78.9% when 2%(wt) HAZ added. With 1% HAZ dosage, the expansion increased by 7.4%, 11.1% and 33.3%. On the other hand, it can be seen in Table 3 that the expansion changed at different HAZ dosages and all of the results of expansion show that the decrease at every replacement of disposed CFBA is 42%, 45%, 30.4%, and 17% when the HAZ dosage changed from 1% to 2%. It can be concluded that the major parameter of the expansion is not the replacement of disposed CFBA but the HAZ dosage.

Table 3. Schemes and results of expansion.

Samples	cement	Cement clinker	CFBA	HAZ	Expansion	Le chaterlier value(mm)
1	70%		30%		Broken	
2		60%	40%	2%	Soundness	1.9
3		50%	50%	2%	Soundness	2.0
4		40%	60%	2%	Soundness	2.3

5	30%	70%	2%	Soundness	3.4
6	60%	40%	1%	Soundness	2.7
7	50%	50%	1%	Soundness	2.9
8	40%	60%	1%	Soundness	3.0
9	30%	70%	1%	Soundness	3.6
10	30%	70%	0.5%	Soundness	4.3

Table 4. Schemes and results of strength.

Samples	CFBA	Cement clinker	HAZ dosage	MPa compressive strength		
				3d	7d	28d
1	70	30	0.5%	8.0	18.2	39.8
2	70	30	1%	9.2	19.6	41.4
3	70	30	2%	8.4	20.4	43.6
4	60	40		5.8	10.1	25.8
5	50	50		6.0	10.8	27.7
6	40	60		10.6	19.3	40.7



Figure 2. The photos of the broken and the soundness prism.

The reason may be that, during the hydraulic reaction, the free CaO in CFBA reacted with water and produced C-H, which caused the volume expansion. As the free CaO has good surface activity, it can absorb the water in the capillary pore and produce  $\text{Ca}(\text{OH})_2$ , which can keep the C-H out of capillary pore as its crystal size and kind, which make the volume bigger than the compute, and then the cubes broken [12,13]. In Tables 3 and 4 it can be seen that the higher CFBA ratio come without a bigger expansion as the HAZ added. The reason maybe the high pH of HAZ solution resulted in the breakdown of the covalent bonds of Ca-O, Si-O, and Al-O from the glassy surface of CFBA [14]. This causes the dissolution of calcium, silicon, and aluminium ions, and as a result, calcium silicate hydrate (C-S-H) gels are formed quickly by giving the crystalloid inducement, which is responsible for the expansion reduction and the compressive strength development of the prisms.

#### Compressive Strength Development

The mortar strength test results are shown in Table 4. The development of HAZ activated cementitious material containing CFBA was conducted at different concentrations. It is observed that the rate of mortar strength development of the

prisms decreased with the increasing concentration of the CFBA. The maximum rate of strength development of prisms were achieved at 2% dosage of HAZ is 15%. These values were much higher than those of the mortar cubes, which showed an increase of 15%, 12.1% and 9.5% at 3, 7 and 28 days curing time, respectively.

From Table 4, it is also found that the strength of the mix decreased with the increasing concentration of the CFBA. For the mixes containing 50% and 60% CFBA, the compressive strength decreased by 76.7%, 78.7% and 46.9% after curing for 3, 7 and 28 days, respectively. This reduction in compressive strength was reported to be caused by the increasing replacement of disposed CFBA [15], where similar values were obtained. But the pastes containing HAZ generally had higher compressive strength than those without in spite of less replacement of disposed CFBA. This maybe due to HAZ reacted with CFBA and cement clinker during the hydraulic reaction, and made the hydration products with zeolite. When the zeolite is formed, it could directly affects the hydration rate of CFBA cementitious material. As a result, the strength of the prisms with HAZ blended is greatly higher than that of those prisms without HAZ blended. This confirmed that HAZ is the direct parameter of the expansion reduction and the compressive strength development of the prisms.

#### SEM Observation on Hydration Products

The microstructure of the fractured surface of the pastes with different HAZ dosages were studied by SEM and the ratio of HAZ dosage were 0%, 0.5%, 1% and 2%. Figure 3a shows the micrographs of the paste without any HAZ dosage cured for 28 days. It can be found that a number of particles of CFBA had already been etched although smooth ones still existed. Compared with others that containing HAZ, the surface of the CFBA particle was smoother and rounder. This suggested that CFBA has not yet entered into an active state of reaction, which was consistent with the results of the compressive study.

The CFBA particles also remained smooth in the paste mix with 0.5%(wt) HAZ dosage. Figure 3b shows that no obvious salty crystal was observed. As for the pastes with 0.5%(wt) HAZ dosage, the CFBA particles were etched sharply and appeared to have reacted partly. In Figure 3c, it was found that the surface of CFBA particles appeared to be broken and reacted significantly, in which the HAZ dosage was 1%. It shows that the CFBA particles had reacted with the HAZ, resulting in more platy crystals and gel-like products surrounding the CFBA particles. The boundary between CFBA and the other hydration products can not be distinguished easily.

Figure 3d shows that more broken particles of CFBA could be seen and the system became much denser at 2% HAZ dosage. This is due to the possibility of CFBA activation mainly lies in the breaking down of its glass phase and the CFBA can react with HAZ in the binder system [16]. The hydration products of HAZ, zeolite, may absorb a large amount of expansion inducers. This is consistent with the results of the

exansion test.

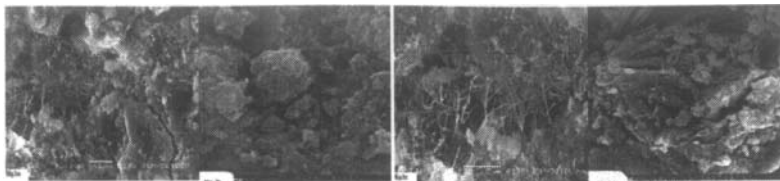


Fig.3 SEM Photos

Fraay et. al. [17] reported that in the presence of aqueous lime, the pH value required to the dissolution of alumina and silica in fly ash was about 13.3 or higher. The pH value of a saturated solution of HAZ is 13.4, so the addition of HAZ did have obvious effect on the VFBA-cement system.

#### X-ray Diffraction Analysis on Hydration Products

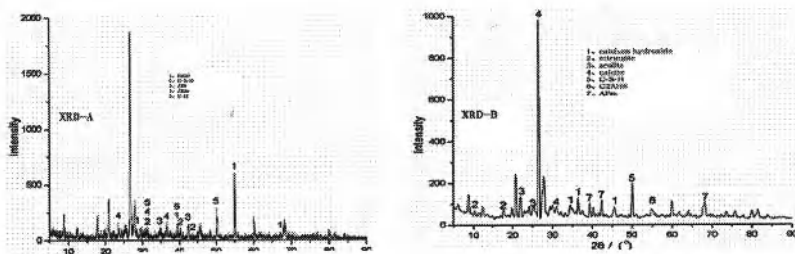


Figure 4. X-ray diffraction patterns of hydration products

Figure 4 shows the X-ray diffraction (XRD) patterns of the samples hydrated for 3 and 28 days with 2% HAZ dosage. In Figure 4, the XRD-A is the patterns of 3 days hydrated of the sample with 2% HAZ dosage. This figure shows that the CFBA hydrated production takes up most of the place. Quartz, C-S-H, Aft, AFm and C-H peaks can be identified with certainty. The reason is that CFBA take the controller role in this stage of the hydrated reaction with high content in the mixer. In the patterns of XRD-B, it can be seen that the main hydrated products of the sample are calcium hydroxide, ettringite, zeolite and calcite in the 28 days hydrated production. When 70% CFBA was substituted for cement, the hydration products of the mixture were mostly same as that of pure cement excluded zeolite. All crystal minerals of CFBA can be seen in Fig.4 (XRD-B). The diffraction peak strength of calcium hydroxide and ettringite basically were the same as that of Portland cement, and the diffraction peak strengths of the hydration products clearly decreased. The main reason is that the addition of CFBA to the binder may cause a significant dilution effect. Therefore the hydration degree of binder has been decreased more than the Portland cement. As the

zeolite is the hydration product of HAZ and binder, the absorption and other domino effect of it can be responsible for the expansion deduce and the compressive strength development of the prisms. Therefore acting as an activator with its addition into the binder, HAZ can not only deduce the expansion, but it can also make the prisms compressive strength increased obviously.

### FTIR Spectroscopy on Hydration Products

In spectroscopic investigations, the spectra of the 4000-300cm<sup>-1</sup> region were recorded. The FTIR spectra of the samples hydrated for 3, 14, and 28 days with 2% HAZ dosage are given in Figure 5.

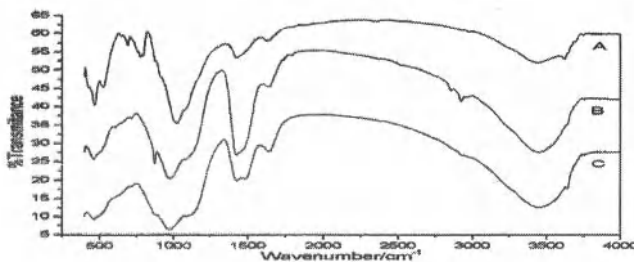


Fig.5. Infrared spectrum of specimens

The coordination-sensitive ring stretching modes of silica quartz (Si-O-Si) are observed at 470cm<sup>-1</sup> and the vibrational spectral of silica quartz are observed around 1030-1050cm<sup>-1</sup>. The spectra A is the spectra of the sample hydrated for 3 days with 2% HAZ dosage. In the spectra it is can be seen that the vibrational spectral of Si-O-Al, Mg-O-H, Al-O-H and H<sub>2</sub>O were observed at 525-530cm<sup>-1</sup>, 840cm<sup>-1</sup>, 915cm<sup>-1</sup> and 1635-1645cm<sup>-1</sup>, respectively. The coordination-sensitive ring stretching modes of H<sub>2</sub>O were observed at 3015-3630cm<sup>-1</sup>. This was mainly performed for the quantification of calcium hydroxide (CH) present in the CFBA hydration and HAZ dosage was not the major parameters in the hydration reaction at this stage. The spectra B and C are the spectra of the samples hydrated for 14 and 28 days with 2% HAZ dosage. As it is well known that with the curing time going, the hydration reaction is developing. In the spectra B and C it can be seen that there are obviously vibrational spectral appeared: vibrational spectral of calcium hydroxide, ettringite and calcite are observed around 500-1750cm<sup>-1</sup> clearly. There are also some characters of zeolite hydration products in this range of the spectra. In fact, the CH content of all specimens is continuously increasing with hydration age, as a result of the hydration of CFBA in this stage. And HAZ hydration products were increasing and the high pH of HAZ solution resulted in the breakdown of the covalent bonds of Ca-O, Si-O, and Al-O from the glassy surface of CFBA. This causes the dissolution of calcium, silicon, and aluminium ions, and as a result, calcium silicate hydrate (C-S-H) gels are formed quickly by

given the crystalloid inducement, which is responsible for the expansion deduce and the compressive strength development of the prisms macroscopically.

It has been well established that the pozzolanic reactions are highly dependent on the calcium hydroxide that exists on the cementitious matrix, the primary HAZ content in each mixture. Therefore, the CH contents that remained unbound in the systems were also calculated in unitary terms, that is, as a function of the cement mass in each mixture. And it is obvious that HAZ hydration control the expansion deduce and the compressive strength development of the whole reaction in this stage.

### Conclusion

1. The strength development of CFBA cementitious material in the presence of HAZ was considerably higher than the strength development of those without the compound. The maximum strength development was achieved at 2% dosage of HAZ.
2. The addition of HAZ compensates the expansion induced by the 70% replacement of disposed CFBA. The study results show that HAZ can not only deduce the expansion, but it can also make the prisms compressive strength increased.
3. In the hydration products, there were some kinds of zeolite produced, which is consistent with the results of XRD result.

### References

- [1] C.S. Poon, S.C. Kou, L. Lam, Z.S. Lin, Activation of fly ash cement systems using calcium sulfate anhydrite  $\text{CaSO}_4$ , *Cement and Concrete Research*, 2001, 31: 873 -881.
- [2] Ya Mei Zhang, Wei Sun, Han Dong Yan, Hydration of high-volume fly ash cement pastes, *Cement & Concrete Composites* 22 (2000) 445-452.
- [3] A. Xu, S.L. Sarkar, Microstructural study of gypsum activated fly ash hydration in cement paste, *Cem. Concr. Res.* 21(1991)1137-1147.
- [4] A.L.A. Frany, J.M. Bijen, Y.M. de Haan, The reaction of fly ash in concrete, a critical examination, *Cem. Concr. Res.* 19 (1989) 235-246.
- [5] C.J. Shi, Early microstructure development of activated lime-fly ash pastes, *Cem Concr. Res.* 26 (9) (1996) 1351-1359.
- [6] C.J. Shi, Pozzolanic reaction and microstructure of chemical activated lime-fly ash pastes, *ACI Mater. J.* 95(5) (1998) 537-545.
- [7] W. Ma, C. Liu, P.W. Brown, S. Komarneni, Pore structures of fly ashes activated by  $\text{Ca}(\text{OH})_2$  and  $\text{CaSO}_4 \cdot 2\text{H}_2\text{O}$ , *Cem. Concr. Res.* 25(2) (1995) 417-425.
- [8] A. Katz, Microscopic study of alkali-activated fly ash, *Cem. Concr. Res.* 28(2) (1998) 197-208
- [9] Shunsuke Hanchara, Fuminori Tomosawa, etc. Effects of water/powder ratio, mixing ratio of fly ash, and curing temperature on pozzolanic reaction of fly ash in cement paste.

- Cem. Concr. Res. 31 (2001) 31-39.
- [10] Gomes S. Characterization and comparative study of coal combustion residues from a primary and additional flue gas secondary desulfurization process [ J ]. Cement and Concrete Research, 1998, 28 (11): 1605 -1619.
- [11] E.J. Anthony, A.P. Iribbame. Study of Hydratration During Curing of Residues from Coal Combustion with Limestone Addition. 1995 International Conference on Fluidized Bed Combustion. Vol.2. 1113.
- [12] Khandaker M. Anwar Hossain, Blended cement using volcanic ash and pumice, Cement and Concrete Research 33 (2003) 1601–1605.
- [13] Huxing Chen, Xiawei Ma, Bolian Chen , Pore Structures of Cement Stone Containing Slag or Fly Ash, Journal of Materials Science & Engineering, Vol.21, No.3, 2003
- [14] Suwimol Asavapist, Duangruedee Chotklang, Solidification of electroplating sludge using alkali-activated pulverized fuel ash as cementitious binder, Cem. Concr. Res. 34 (2003) 349-353
- [15] C. Freidin, Hydration and strength development of binder based on high-calcium oil shale fly ash, Cement and Concrete Research, 1998 Vol. 28, No. 6, pp. 829–839
- [16] C.S. Poon, X.C. Qiao, Z.S.Lin, Pozzolanic properties of reject fly ash in blended cement pastes, Cen. Concr. Res. 33(2003) 1857-1865.
- [17] A.L.A. Fraay, J.M. Bijen, Y.M. de Haan, The reaction of fly-ash in concrete –a critical examination, Cem. Concr. Res. 19(1989) 235-246.

## **PRODUCTION OF APATITIC MATERIAL USING TURKISH COLEMANITE MINERAL**

Çağatay Moral<sup>1</sup>, Tuğba Başargan<sup>1</sup>, Gülhayat Nasun-Saygılı<sup>1</sup>

<sup>1</sup>Istanbul Technical University Chemical and Metallurgical Engineering Faculty  
Chemical Engineering Department, 34469, Maslak, Istanbul, TURKEY

Keywords: Boron, Colemanite, Hydroxyapatite

### **Abstract**

The aim of this study is to prepare the apatitic material using colemanite mineral ( $2\text{CaO}\cdot 3\text{B}_2\text{O}_3\cdot 5\text{H}_2\text{O}$ ) which was obtained from Eastern Anatolia, Turkey. For this purpose, colemanite mineral was reacted with different phosphate sources, namely, dipotassiumhydrogen phosphate, ammoniumhydrogen phosphate and orthophosphoric acid at various temperatures and time periods. Experiments were run in batch system. The apatitic material was prepared by a wet method and followed by heat treatment at various temperatures. Structure of the samples was analyzed by XRD, FTIR, XRF and SEM. The particle size analysis was also made for the result product. The experiments showed that reaction temperature, contact time and heating temperature are important parameters to transform the colemanite into apatitic structure. Reaction of colemanite with dipotassiumhydrogen phosphate and ammoniumhydrogen phosphate results in amorphous, non-stoichiometric hydroxyapatite type structure, while acid based phosphate source gives brushite and monetite type product before and after heat treatment, respectively.

### **Introduction**

Boron which has properties intermediate between metals and non-metals is a member of semiconductor group of elements. Its atom is very small and has three valence electrons. Boron exists in Earth's crust (from 5 mg/kg in basalts to 100 mg/kg in shale) and in the oceans (4.5 mg/l) [1]. Turkey has 60% of world's boron reserves which is mostly in the form of colemanite ( $2\text{CaO}\cdot 3\text{B}_2\text{O}_3\cdot 5\text{H}_2\text{O}$ ). Colemanite is the most important calcium containing commercial borate mineral with 5 mol of crystal water [2].

Calcium phosphate cements are very useful for bone repair applications because of its chemical structure. They are injectable, easy to shape and can be maintained locally. Because of those reasons calcium phosphate cements are very effective to fill bone defects with an irregular shape [3]. Hydroxyapatite ( $\text{Ca}_{10}(\text{PO})_6(\text{OH})_2$ ) is the major component of the bone (70 wt%). However, hydroxyapatite stoichiometry, composition and crystallinity differ in human skeleton system [4, 5].

The main objective of the present work was to study the transformation of colemanite to apatitic material using different phosphate solutions at several time spans and temperatures. The experiments were run in a batch system, change in pH and also weight loss were measured after the experiments. Several analysis methods were used to investigate the chemical and structural changes.

## Materials and Methods

Colemanite mineral that was obtained from Eti Bor Kutahya Emet-Espey field was grinded and then was sieved by JEL Apparatebau through stainless steel sieves to produce size ranges between 180-250  $\mu\text{m}$  for the experiments.

Table I. Compound Information of Espey Colemanite

Compound	Espey Colemanite	
$\text{B}_2\text{O}_3$	wt%	48.830
$\text{SiO}_2$	wt%	1.390
$\text{Fe}_2\text{O}_3$	wt%	0.320
$\text{Al}_2\text{O}_3+\text{TiO}_2$	wt%	0.240
CaO	wt%	26.260
MgO	wt%	1.090
SrO	wt%	0.660
As	ppm	150
$\text{SO}_4$	wt%	0.020
$\text{K}_2\text{O}$	wt%	0.16
$\text{Na}_2\text{O}$	wt%	0.040

Three different phosphate solutions were prepared to use in the conversion of colemanite to apatite form.  $\text{K}_2\text{HPO}_4$  solution was prepared dissolving  $\text{K}_2\text{HPO}_4$  (Merck, 98%) in deionized water to give a 0.25 M concentration. pH of the solution was adjusted to 7 by adding a few drops of dilute HCl into the solution for approximating solution's pH to human body fluid [6].  $(\text{NH}_4)_2\text{HPO}_4$  solution was prepared by using  $(\text{NH}_4)_2\text{HPO}_4$  (Merck, 99%) as the same principal of  $\text{K}_2\text{HPO}_4$  solution and its concentration adjusted to 0.3 M with deionized water. 0.6 M  $\text{H}_3\text{PO}_4$  solution was prepared in deionized water with using 85 %vol.  $\text{H}_3\text{PO}_4$  (Merck). Colemanite particles were reacted in each solution for a specified time at 37°C and 75°C. The amount of reactants was calculated according to Ca/P ratio of hydroxyapatite. After the reaction, the product was obtained by removing the solution with filtering flask. Product was decanted three times with deionized water and then two times with alcohol. After drying at 90°C for 12 hours in an oven, samples had heat treatment at 400°C and 700°C for 3 hours then they were stored in a dessicator. pH was measured in specified time intervals and selected temperatures while the reaction was going by using inoLab pH/Cond 720. These measurements give some information about the ion transfer between colemanite and phosphate solutions. The weight of the colemanite was specified before the experiments. So, the weight loss was calculated by subtracting the specified weight of the colemanite from samples that were washed with three times deionized water and two times alcohol, and dried at 90°C in an oven after the reactions. Structural and chemical changes in both colemanite and the phosphate solution that was resulted after the reactions were monitored using several techniques. Boron content of the samples was measured using volumetric titration method. After the heat treatment the functional bounds of the solid particles were analyzed by FT-IR (Perkin Elmer) in 650-4000  $\text{cm}^{-1}$  frequency interval. The XRD patterns of the samples before and after heat treatment phases were collected over a 2 $\theta$  range from 10° to 90° at a scan rate of 0.05°/s with a counting time of one second. The data collected from Bruker D8 Advance X-ray diffractometer. Some selected samples' qualitative and

quantitative analyses were made by Rigaku ZSX-Primus II X-ray fluorescent. Also the surface spectrums extended in 200-25,000 of those samples were obtained from JEOL 5410 scanning electron microscope.

## Results and Discussion

### Weight Loss, B<sub>2</sub>O<sub>3</sub> Concentration and pH Changes

Fig.1 shows the pH changes of the reactions. Ca<sup>2+</sup> ions of the colemanite react with PO<sub>4</sub><sup>3-</sup> ion from K<sub>2</sub>HPO<sub>4</sub> and (NH<sub>4</sub>)<sub>2</sub>HPO<sub>4</sub> solutions and precipitate apatite. Na<sup>+</sup>, BO<sub>3</sub><sup>3-</sup>, and SiO<sub>4</sub><sup>4-</sup> ions from colemanite dissolve into the solutions. The strongly basic NaOH that is formed from the Na<sup>+</sup> ions of the colemanite overwhelms the weak acidic tendency of B(OH)<sub>3</sub> and Si(OH)<sub>4</sub>, so the pH increases [6]. From the experiments that were maintained in K<sub>2</sub>HPO<sub>4</sub> solution, it is seen that the pH difference is decreasing as the reaction time increases. Besides, the pH values of higher temperature experiments are greater than the lower temperature experiments.

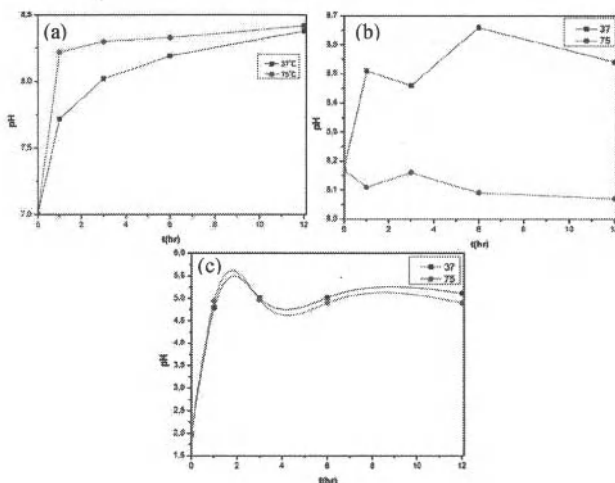


Figure 1. pH changes of the reactions that was made in the (a) K<sub>2</sub>HPO<sub>4</sub> solution (b) (NH<sub>4</sub>)<sub>2</sub>HPO<sub>4</sub> solution (c) H<sub>3</sub>PO<sub>4</sub> solution

Dissolution rate of colemanite is proportional to the temperature [7,8]. In this case, the rate of dissolution of B<sub>2</sub>O<sub>3</sub> from the colemanite increases as the increasing temperature, so the acidity of the solution increases and the pH decreases. Ca<sup>2+</sup> ions of the colemanite react with PO<sub>4</sub><sup>3-</sup> from the H<sub>3</sub>PO<sub>4</sub> solution and forms brushite and monetite. pH values of the reactions which were carried out at 37°C are greater than the 75°Cs because of the direct proportion of dissolution rate of B<sub>2</sub>O<sub>3</sub> to the reaction temperature [7]. Weight loss percent and change in B<sub>2</sub>O<sub>3</sub> concentration of the solutions are seen in the Fig.2 and Fig.3, respectively. Since dissolution of the B<sub>2</sub>O<sub>3</sub> from the colemanite increases, weight loss percent also increases as the temperature and the time for all the reactions.

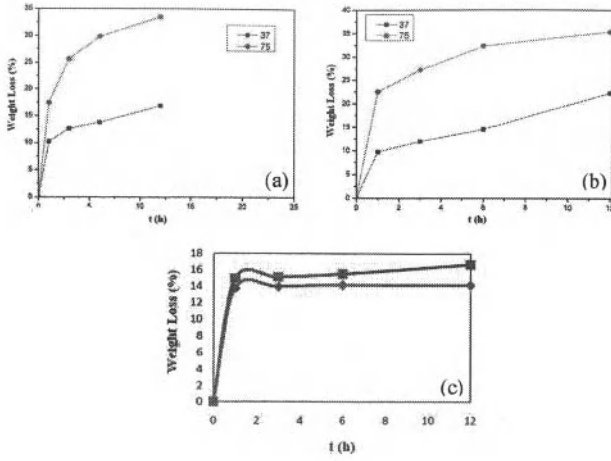


Figure 2. Weight loss of the reactions that was made in the (a)  $K_2HPO_4$  solution (b)  $(NH_4)_2HPO_4$  solution (c)  $H_3PO_4$  solution

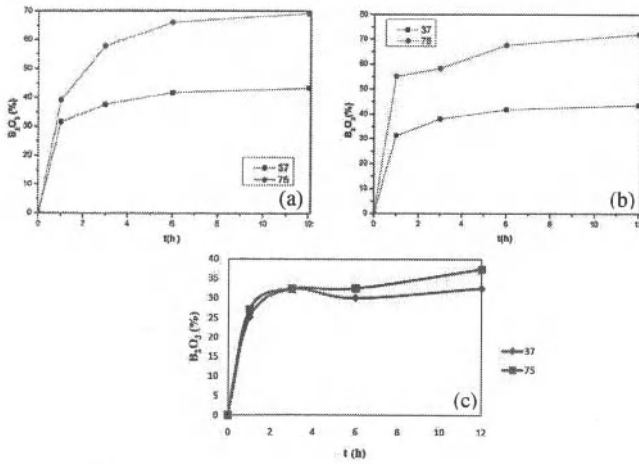


Figure 3.  $B_2O_3$  concentration of the solutions for the reactions that was made in the (a)  $K_2HPO_4$  solution (b)  $(NH_4)_2HPO_4$  solution (c)  $H_3PO_4$  solution

### Structural and Chemical Changes of Colemanite

FTIR analysis before the heat treatment of 1 hour experiments that was made with  $K_2HPO_4$  solutions is seen in Fig.4. The dominant bonds to represent hydroxyapatite are the phosphate  $\nu_3$  which are centered at  $1094\text{ cm}^{-1}$  and  $1032\text{ cm}^{-1}$ [5]. The phosphate  $\nu_3$  bond is seen at  $1024.05\text{ cm}^{-1}$  for the reaction at  $37^\circ\text{C}$  and  $1023.87\text{ cm}^{-1}$  for the reaction at  $75^\circ\text{C}$ .  $\nu_3$  band for the stoichiometric hydroxyapatite is located at  $1030\text{ cm}^{-1}$ , besides for non-stoichiometric hydroxyapatite  $\nu_3$  band is located at nearby  $1020\text{ cm}^{-1}$ [9]. The band comes from water is seen very weak at  $3248.50\text{ cm}^{-1}$  for the reaction at  $75^\circ\text{C}$ . The peaks at  $1200\text{ cm}^{-1}$  and  $1600\text{ cm}^{-1}$  interval represents the trigonal  $BO_3$  bonds in the structure [5]. Trigonal  $BO_3$  bond is seen at the  $37^\circ\text{C}$  experiment's curve but gives weak peak when the temperature is raised to  $75^\circ\text{C}$ .  $\nu_3$  phosphate bands are seen at  $1023.33\text{ cm}^{-1}$  at  $37^\circ\text{C}$  and  $1022.54\text{ cm}^{-1}$  at  $75^\circ\text{C}$  for 3 hours experiment. The intensity of the phosphate band increases as the temperature increment while the  $BO_3$  bond intensity is weaker than 1 hour experiment because of the increase in  $B_2O_3$  dissolution rate by time. For the 6 hours experiment the phosphate bands are seen at  $1023.09\text{ cm}^{-1}$  at  $37^\circ\text{C}$  and  $1023.31\text{ cm}^{-1}$  at  $75^\circ\text{C}$ . In the 12 hours experiment, phosphate bands are seen at  $1022.03\text{ cm}^{-1}$  at  $37^\circ\text{C}$  and  $1022.71\text{ cm}^{-1}$  at  $75^\circ\text{C}$ .

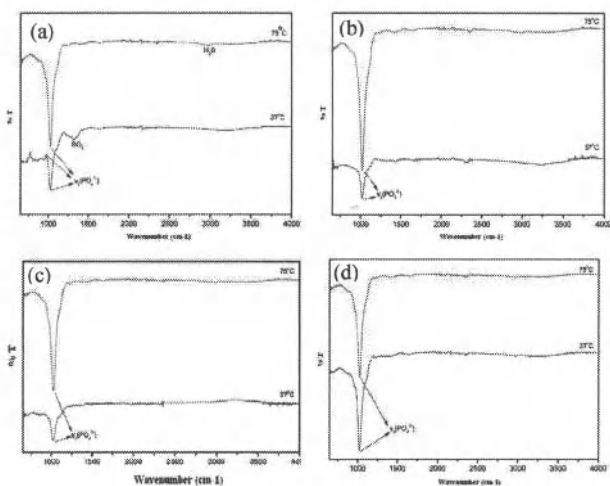


Figure 4. FTIR spectra for the samples that was in  $K_2HPO_4$  solution before heat treatment (a) 1 hour (b) 3 hours (c) 6 hours (d) 12 hours

The FTIR data before the heat treatment for the reactions that were done with  $(NH_4)_2HPO_4$  are seen in the Fig.5. Phosphate bands are seen at  $1025.56\text{ cm}^{-1}$  at  $37^\circ\text{C}$ ,  $1025.70\text{ cm}^{-1}$  at  $75^\circ\text{C}$  for 1 hour experiment;  $1025.38\text{ cm}^{-1}$  at  $37^\circ\text{C}$ ,  $1025.12\text{ cm}^{-1}$  at  $75^\circ\text{C}$  for 3 hours experiment;  $1022.52\text{ cm}^{-1}$  at  $37^\circ\text{C}$ ,  $1024.84\text{ cm}^{-1}$  at  $75^\circ\text{C}$  for 6 hours experiment and  $1023.30\text{ cm}^{-1}$  at  $37^\circ\text{C}$ ,  $1025.76\text{ cm}^{-1}$  at 12 hours experiment. The band strengths are getting stronger as both the time and temperature increment.

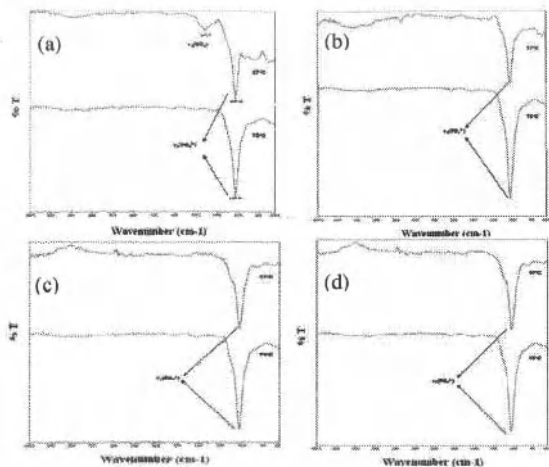


Figure 5. FTIR spectra for the samples that was in  $(\text{NH}_4)_2\text{HPO}_4$  solution before heat treatment (a) 1 hour (b) 3 hours (c) 6 hours (d) 12 hours

FTIR spectra analysis for the reactions done with  $\text{H}_3\text{PO}_4$  solution is seen in Fig.6. For 1 hour reaction, the peaks  $3161.50\text{ cm}^{-1}$  at  $37^\circ\text{C}$ ,  $3475.55\text{ cm}^{-1}$  and  $3158.70\text{ cm}^{-1}$  at  $75^\circ\text{C}$  represent O-H stretching bonds.  $1644.15\text{ cm}^{-1}$  at  $37^\circ\text{C}$  and  $1643.83\text{ cm}^{-1}$  at  $75^\circ\text{C}$  is for the H-O-H bonds that come from free water substance of the structure. The peaks represent asymmetric stretching of PO bonds are seen  $1123.21\text{ cm}^{-1}$ ,  $1055.05\text{ cm}^{-1}$  and  $984.82\text{ cm}^{-1}$  at  $37^\circ\text{C}$ ;  $1122.71\text{ cm}^{-1}$ ,  $1054.34\text{ cm}^{-1}$  and  $984.82\text{ cm}^{-1}$  at  $75^\circ\text{C}$  [10,11,12]. P-O(H) stretching bonds are seen  $869.11\text{ cm}^{-1}$  at  $37^\circ\text{C}$  and  $868.20\text{ cm}^{-1}$  at  $75^\circ\text{C}$  [13]. The peaks of  $768.08\text{ cm}^{-1}$  at  $37^\circ\text{C}$ ,  $783.26\text{ cm}^{-1}$  and  $868.20\text{ cm}^{-1}$  at  $75^\circ\text{C}$  represent the B-O bending bonds that come from  $\text{B}_2\text{O}_3$  from the structure. For 3 hours reaction, O-H stretching peaks are seen between  $3150\text{-}3480\text{ cm}^{-1}$ , H-O-H peaks that come from hydrate structure is seen nearby  $1644\text{ cm}^{-1}$ ; PO peaks are at  $948\text{-}1123\text{ cm}^{-1}$ ; P-O(H) stretching peaks are at nearby  $868\text{ cm}^{-1}$  and B-O bending peaks are at  $780\text{-}790\text{ cm}^{-1}$ . For 6 hours reaction, O-H stretching peaks are seen nearby  $3160\text{ cm}^{-1}$ , H-O-H peaks that come from hydrate structure is seen nearby  $1643\text{ cm}^{-1}$ ; PO peaks are at  $948\text{-}1123\text{ cm}^{-1}$ ; P-O(H) stretching peaks are at nearby  $869\text{ cm}^{-1}$  and B-O bending peaks are at  $780\text{-}795\text{ cm}^{-1}$ . For 12 hours reaction, O-H stretching peaks are seen nearby  $3160\text{ cm}^{-1}$ , H-O-H peaks that come from hydrate structure is seen nearby  $1643\text{ cm}^{-1}$ ; PO peaks are at  $984\text{-}1124\text{ cm}^{-1}$ ; P-O(H) stretching peaks are at nearby  $869\text{ cm}^{-1}$  and B-O bending peaks are at  $785\text{-}792\text{ cm}^{-1}$ .

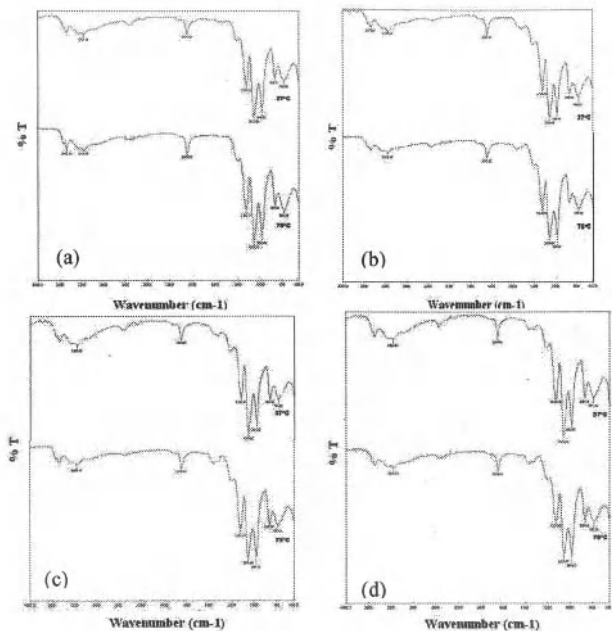


Figure 6. FTIR spectra for the samples that was in  $H_3PO_4$  solution before heat treatment (a) 1 hour (b) 3 hours (c) 6 hours (d) 12 hours

The XRD pattern for the 1 hour reaction that was happened in  $K_2HPO_4$  solution before the heat treatment contains  $16^\circ$  and  $32^\circ$   $2\theta$  peaks that represents hydroxyapatite in both  $37^\circ C$  and  $75^\circ C$  temperatures [7]. In the  $37^\circ C$  reaction, the dominant structure is calcium borate hydrate ( $Ca_2B_{10}O_{17} \cdot 5H_2O$ ) is seen in Fig.7.

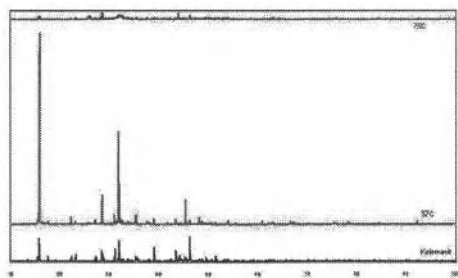


Figure 7. XRD patterns for 1 hour reactions.

Calcium borate hydrate is also dominant in the 12 hours reaction that is seen in Fig.8. The heat treatment in 700°C with 10°C/min temperature rise was applied on the sample for 3 hours and its effect is seen in Fig.9. The XRD patterns show that the apatite structure is formed and boron is diffused into the hexagonal system that was made by calcium and phosphate bonding [14].

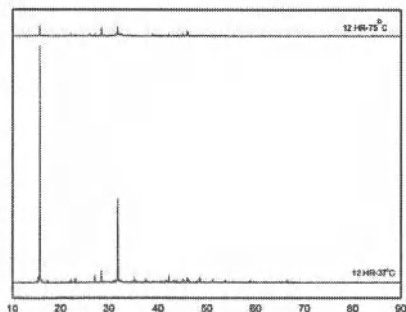


Figure 8. XRD patterns for 12 hours reactions.

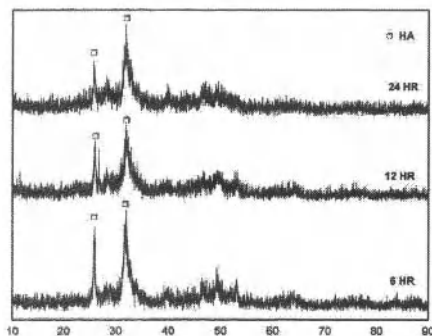


Figure 9. XRD patterns after 700°C heat treatment.

Calcium borate hydrate structure is seen in the XRD patterns of the products of the  $(\text{NH}_4)_2\text{HPO}_4$  solutions at 15.78° and 31.82° in Fig.10 [7]. After the heat treatment, hydroxyapatite peaks are seen in the structure.

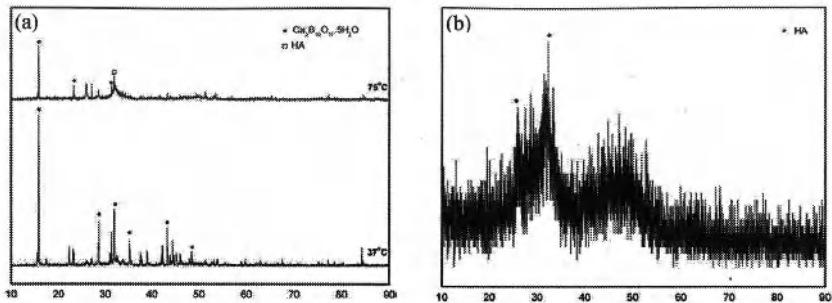


Figure 10. XRD patterns of  $(\text{NH}_4)_2\text{HPO}_4$  (a) 12 hours reaction without heat treatment (b) 12 hours and  $37^\circ\text{C}$  temperature reaction with  $400^\circ\text{C}$  heat treatment for 3 hours.

The XRD patterns of the selected cases for the  $\text{H}_3\text{PO}_4$  reactions (Fig.11) show that the structure of the colemanite remains but with the direct proportion to temperature and time, brushite ( $\text{CaHPO}_4 \cdot 2\text{H}_2\text{O}$ ) is seen in the structure. After the  $400^\circ\text{C}$  3 hours heat treatment, the water that was bonded to the structure is vapoured and the brushite turns into the monetite ( $\text{CaHPO}_4$ ) [7].

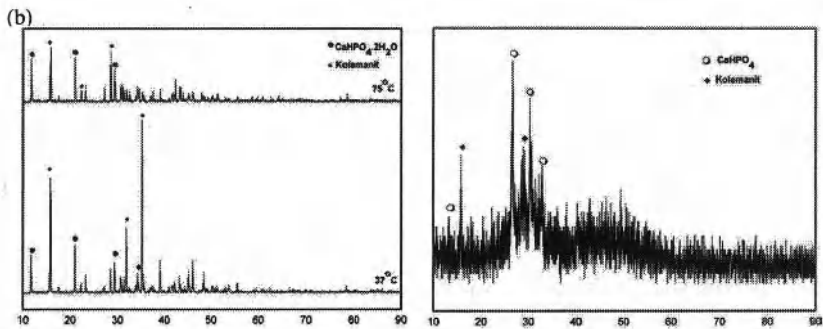


Figure 11. XRD patterns of  $\text{H}_3\text{PO}_4$  (a) 12 hours and  $75^\circ\text{C}$  reaction without heat treatment (b) 12 hours and  $75^\circ\text{C}$  temperature reaction with  $400^\circ\text{C}$  heat treatment for 3 hours

SEM images of the selected samples are seen in Fig.12. Plate like surface and the porous structure is seen in the 6 hours  $37^\circ\text{C}$  and  $75^\circ\text{C}$  temperature experiments that were made in  $\text{K}_2\text{HPO}_4$  solutions [6,15]. For the experiments with  $(\text{NH}_4)_2\text{HPO}_4$  solutions, after the  $700^\circ\text{C}$  heat treatment the plate like surface is obtained. Besides, calcium phosphate substances are formed on the plate like surface before the heat treatment [3,16].

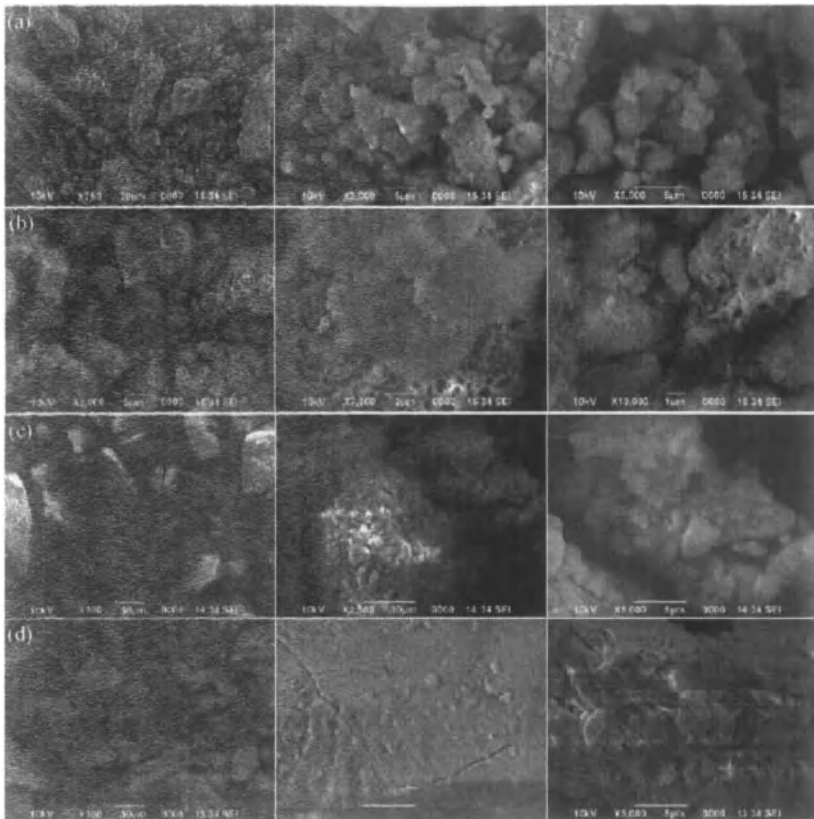


Figure 12. SEM images of (a) 6 hours and 37°C reaction in  $K_2HPO_4$  solution with 700°C heat treatment (b) 6 hours and 75°C reaction in  $K_2HPO_4$  solution with 700°C heat treatment (c) 12 hours and 75°C reaction in  $(NH_4)_2HPO_4$  solution (d) 12 hours and 75°C reaction in  $(NH_4)_2HPO_4$  solution with 700°C heat treatment

XRF analysis of some selected products that was made in the  $K_2HPO_4$  solutions is seen in the Table II. It is seen that non-stoichiometric hydroxyapatite structure is formed in the reactions.

Table II. XRF analysis

	CaO	P <sub>2</sub> O <sub>5</sub>	Ca/P
<b>3 hr 75°C</b>	49.08	36.89	1.68
<b>6 hr 37°C</b>	53.29	36.92	1.82
<b>6 hr 75°C</b>	48.98	35.73	1.73

### Conclusions

The apatitic structure was successfully obtained from colemanite using basic phosphate solution. The products from the reactions that were made in both K<sub>2</sub>HPO<sub>4</sub> and (NH<sub>4</sub>)<sub>2</sub>HPO<sub>4</sub> solutions have hydroxyapatite structure after the heat treatment. It was concluded that B<sub>2</sub>O<sub>3</sub> substance in the powder was diffused into the hexagonal cage system after the heat treatment. In the SEM images, it is seen that the plate like surface is formed after the heat treatment but the heat treatment causes cracks on the surface. Apatitic structure cannot be gained in the acidic phosphate solutions; however, monetite and brushite formation was obtained in the H<sub>3</sub>PO<sub>4</sub> solutions.

### References

- [1] L. Bolaños, K. Lukaszewski, I. Bonilla and D. Blevins, "Why Boron?", *Plant Physiology and Biochemistry*, 42 (2004), 907-912.
- [2] Ö. Yıldız, "The Effect of Heat Treatment on Colemanite Processing: A Ceramics Application", *Powder Technology*, 142 (2004), 7-12
- [3] R. P. del Real, J. G. C. Wolke, M. Vallet-Regi and J. A. Jansen, "A New Method To Produce Macropores in Calcium Phosphate Cements", *Biomaterials*, 23 (2002), 3673-3680
- [4] T. K. Anee, M. Ashok, M. Palanichamy and Kalkura S. Narayana, "A Novel Technique to Synthesize Hydroxyapatite at Low Temperature", *Materials Chemistry and Physics*, 80 (2003), 725-730
- [5] X. Han and D. E. Day, "Reaction of Sodium Calcium Borate Glasses to Form Hydroxyapatite", *J. Mater. Sci.: Mater. Med.*, 18 (2007), 1837-1847
- [6] W. Huang, D. E. Day, K. Kittiratanapiboon and M. N. Rahaman, "Kinetics and Mechanism of the Conversion of Silicate (45S5), Borate, and Borosilicate Glasses to Hydroxyapatite in Dilute Phosphate Solutions", *J. Mater. Sci.: Mater. Med.*, 17 (2006), 583-596
- [7] H. Temur, A. Yartaşı, M. Çopur and M.M. Kocakerim, "The Kinetics of Dissolution of Colemanite in H<sub>3</sub>PO<sub>4</sub> Solutions", *Ind. Eng. Chem. Res.*, 39 (2000), 4114-4119
- [8] M. Tunç, M.M. Kocakerim, Ö. Küçük and M. Aluz, "Dissolution of colemanite in (NH<sub>4</sub>)<sub>2</sub>HPO<sub>4</sub> solutions", *Korean J. Chem. Eng.*, 24 (2007), 55-59
- [9] M. Kumar, J. Xie, K. Chittur and C. Riley, "Transformation of modified brushite to hydroxyapatite in aqueous solution: effects of potassium substitution", *Biomaterials*, 20 (1999), 1389-1399
- [10] Y. Hsu, E. Chang and H. Liu, "Hydrothermally-Grown Monetite (CaHPO<sub>4</sub>) on Hydroxyapatite", *Ceramics International*, 24 (1998), 249-254

- [11] M. P. Hofmann, A. M. Young, U. Gbureck, S. N. Nazhat and Barralet, J. E., "FTIR-Monitoring of a Fast Setting Brushite Bone Cement: Effect of Intermediate Phases", *J. Mater. Chem.*, 16 (2006), 3199-3206
- [12] C.Q. Ning and Y. Zhou, "On the Microstructure of Biocomposites Sintered from Ti, HA and Bioactive Glass", *Biomaterials*, 25 (2004), 3379-3387
- [13] J. Xu, D.F.R. Gilson and I.S. Butler, "FT-Raman and High-Pressure FTInfrared Spectroscopic Investigation of Monocalcium Phosphate Monohydrate,  $\text{Ca}(\text{H}_2\text{PO}_4)_2 \cdot \text{H}_2\text{O}$ ", *Spectrochimica Acta Part A*, 54 (1998), 1869-1878
- [14] T. Itakura, R. Sasai and H. Itoh, "Precipitation Recovery of Boron from Wastewater by Hydrothermal Mineralization", *Water Research*, 39 (2005), 2543-2548
- [15] Y. Li, M.N. Rahaman, Q. Fu, S. Bal, A. Yao and D.E. Day, "Conversion of Bioactive Borosilicate Glass to Multilayered Hydroxyapatite in Dilute Phosphate Solution", *J. Am. Ceram. Soc.*, 90 (2007), 3804-3810
- [16] A. Ferreira, C. Oliveira and F. Rocha, "The Different Phases in the Precipitation of Dicalcium Phosphate Dihydrate", *Journal of CrystalGrowth*, 252 (2003), 599-611

## **SETTING TIME OF CONCRETE MATERIAL; LABORATORY MEASUREMENTS VERSUS FIELD APPLICATIONS**

Mourad Y. Riad<sup>1</sup>, Samir N. Shoukry<sup>2</sup>, and Gergis W. William<sup>1</sup>

<sup>1</sup>West Virginia University, Dept. of Civil and Environmental Eng., Morgantown, WV 26506

<sup>2</sup>West Virginia University, Dept. of Mechanical and Aerospace Eng., Morgantown, WV 26506

Keywords: Concrete setting time, curing fresh concrete, bridge deck cracking.

### **Abstract**

Setting of concrete material is defined as the transitional period between states of true fluidity and true rigidity. Initial and final setting times are measured in the laboratory on the mortar sieved from the mix in a controlled environment where temperature and moisture values are constant. On the other hand, field applications are held in outdoor environments where environmental variations have direct impact on setting time values. In this study, initial setting time of class K concrete, usually used for bridge decks and concrete pavements, are investigated highlighting discrepancies between laboratory and field measurements. 72 mixes have been cast in variable environments and collected data from concrete mixes and the ambient conditions are reported. In light of the collected data, the effects of variable setting times on early age cracking of concrete material are studied and means to minimize such cracks are presented.

### **Background**

Setting of concrete material is defined as the transitional period between states of true fluidity and true rigidity [1]. Continuous hydration of the cement within the matrix transfers the mix from a state of setting to hardening. Initial and final Setting times are measured in a laboratory setting following ASTM C 403 specifications. Initial setting approximates the time at which the cement paste can no longer be plastic under compaction (or can be handled in a proper fashion), while the final setting approximates the time at which hardening occurs. The standard test described in ASTM C 403 is conducted on the mortar sieved from the mix (paste passing from 4.75 mm sieve opening). Initial and final settings are described as the elapsed time after the initial contact of water and cement till the mortar reaches a penetration resistances of 3.5 MPa (500 psi), and 27.6 MPa (4000 psi) respectively.

Temperature evolution of the concrete mix plays a leading role in defining the paths to setting then hardening of the concrete material. Much experimental data put into evidence that temperature plays a significant role in the development of concrete strength during

the curing process [2]. Mathematical models that describe early age hardening of concrete mixes incorporate temperature effects in their formulation [3, 4]. The most known of those is the maturity method, that provides an equivalent age of the concrete mix based on the mix's temperature time history, in reference to a known temperature. The method is described in ASTM C1074-98 where the maturity index is expressed in terms of a temperature-time factor and equivalent age established from recorded temperature history of the concrete in the field.

While setting times of a concrete mix are measured in a controlled laboratory environment, the actual application of any mix takes place in the field, where temperature, relative humidity, solar radiation, and wind velocity cannot be controlled. This work sheds some light on discrepancies between initial setting results obtained from laboratory measurements versus those obtained from the field, and offer analysis on the contribution of such discrepancies in early age cracking of bridge decks.

### Experimental Program

Six class K concrete mixes ( $M_1$  to  $M_6$ ) were designed and cast in the laboratory as well as in various outdoor environments. Each mix composition featured either a set accelerator or a set retarder admixture that gives a variety of setting times for each mix. An additional plain concrete mix was also cast as a reference. Such mixes were subjected to a variety of environmental settings which constitute typical pouring days during late spring and summer seasons in West Virginia. During this construction period, the average high temperature is around 29°C (85° F) with peaks of 35°C to 40°C (95°F to 105°F) around noon. Typically, this ambient temperature is sustained during the afternoon, and decline to around 25°C- to 20°C (77°F to 68°F) during the early evening. The purpose of this set of tests is to gather an array of data that describe the environmental elements and their effects on concrete curing, specifically setting times and heat of hydration. Sets of slab specimens 0.3m×0.25m×0.13m (12in×10in×5in) of each mix are cast outdoors at four different times along the day. The selected pouring times are:

$T_1$ : between 9:00 AM and 10:00 AM; (morning pour)

$T_2$ : between 12:00 PM and 01:00 PM; (early afternoon pour)

$T_3$ : between 02:30 PM and 03:30 PM; (afternoon pour)

$T_4$ : between 05:00 PM and 06:00 PM; (early evening pour).

Time of initial set was evaluated through penetration tests on prisms of dimensions 0.20m×0.20m×0.13m (7.5in×7.5in×5in). Those were manufactured with mortar sieved from each batch of concrete and exposed to the same ambient conditions as the slab specimens. Two curing measures were applied to the concrete specimens in order to control the rise of temperature as a result of exposure to solar radiation and to prevent water evaporation from exposed surfaces. For this purpose, for each mix, two sets of samples were tested. The first set was cured with wet

burlap wrapped with a white polyethylene sheets while the second set was cured with a white pigmented resin-based curing compound.

The total number of 72 mixes was cast outdoors for this study. Each cast ( $T_1$  to  $T_4$ ) defined above consisted of one sample of the accelerated or retarded mix cured with wet burlap and polyethylene sheets; another similar mix sample sprayed with the curing compound and one reference sample of plain concrete mix that was cured with wet burlap and polyethylene sheets. For every set (three specimens), temperature time history was recorded at an interval of 10 minutes for at least twenty four hours after casting. A thermistor type YSI 44005 with an accuracy of  $\pm 0.5^\circ\text{C}$  was embedded into each specimen to provide temperature data while a data acquisition system model 8020 and multiplexer model 8032 manufactured by Geokon Inc. were used for data collection and storage.

A weather station model WMR200A manufactured by Oregon Scientific was installed at the site to provide records of environmental data. The weather station recorded continuous data of air temperature, relative humidity, wind speed and direction, barometric pressure and rain fall. Setting time penetration tests were performed both in open air and in the laboratory on samples of mortar sieved from each batch of concrete and subjected to the same ambient conditions and curing measures. Figure 1 shows the concrete specimens while being cured in an outdoor environment, while Figure 2 demonstrates measurement of setting time through penetration tests.

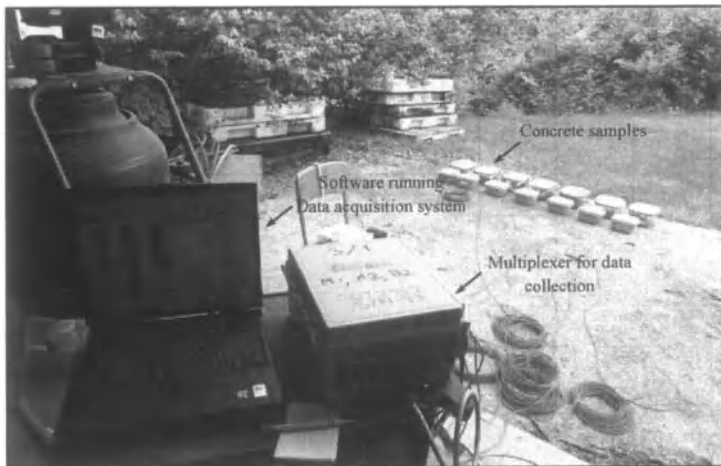


**Figure 1 Curing of concrete specimens in outdoor environment**

### Concrete Mix Composition

This study is carried out using Class K concrete, satisfying the requirements of the West Virginia Division of Highways [5] which are usually intended for bridge decks, sidewalks, parapets, and median barriers as a part of the bridge superstructure. Class K concrete was prepared at the laboratory using Type I Portland cement, type F fly ash provided by HeadWaters Resources, No. 57-67 limestone coarse aggregate and silica sand. Two admixtures (Sika air entrainer AEA-14 & High Range Water Reducing Admixture Sikament 686) were added in order to obtain required entrained air and adequate workability respectively; without the addition of excessive water. Table 1 summarizes the mix composition of concrete material used in this research.

Set retarding admixtures consisting of BASF POZZOLITH-100XR with concentration of 130 ml/100kg, SIKALASTIMENT with concentrations of 130 and 105 ml/100kg were used respectively for the 3 concrete mixes carrying set retarding admixtures. SIKALASTOCRETE 161FL with concentrations of 392, 2288, and 6080 (ml/100kg) were adopted for those 3 set accelerated mixes.



**Figure 2 Measurement of concrete setting time**

**Table 1 Materials and Mix Proportions used for Class K Concrete.**

<b>Material</b>	<b>Nominal Proportions (kg/m<sup>3</sup>)</b>
Type I Portland Cement	300
Class F Fly Ash (19% of cement weight)	57
Coarse aggregate No 57 - SSD	946
Fine aggregate - SSD	829
Water	142
Air content	7%
Air - entraining admixture	85 ml/100 kg
HRWR admixture	850 ml/100 kg
Water/cement binder ratio	0.40
Water + Admixtures/cement binder ratio	0.41
Total Weight including liquid admixtures	2277

### **Results and Analysis**

Figure 3 illustrates an example of temperature evolution of Mix 3 recorded while curing in an outdoor environment. In this plot, the zero on the horizontal axis corresponds to 8:00 AM. As can be noticed, although same mix properties and similar curing measures are cast along the day, the temperature evolution of such mixes follow different patterns depending on the ambient air temperature and relative humidity. Similar plots could be obtained for the other mix compositions. Table 2 lists maximum temperature values measured for the test mixes while they are set to cure in wet burlap and plastic sheets in various environments. The overall trends indicate that peak temperatures tend to decrease as time of pouring advanced through the afternoon and early evening. Accelerated mixes displayed the closest peak temperatures values for those specimens poured during T1, T2 and T3. Comparing temperature evolutions of samples cured with Wet Burlap opposed to the Curing Compound indicate that the concrete temperature patterns for the curing compound follow similar trends but with smaller amplitudes with a range difference of 3°C (5°F) to 8°C (14°F). A possible reason is that the white pigment of the curing compound, which according to the manufacturer is 65% light reflective, was more effective than white plastic sheet in reflecting solar radiation. Another factor that can be considered here is that the plastic covers limit the exposure of concrete surface to air and wind, thus contribute to the increase in concrete temperature [6]. Since temperature evolution curves are correlated to mix setting times, it was expected that measurements of times of initial settings will vary accordingly.

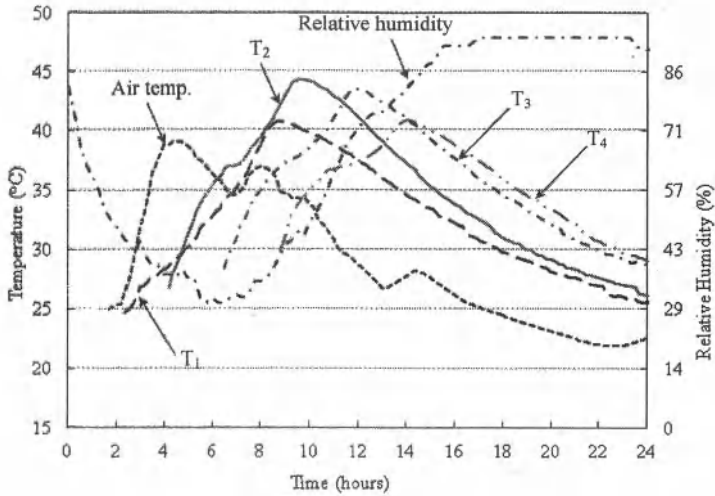


**Figure 3 Temperature evolution of Mix 3 cast along the day in outdoors environment**

Table 3 lists average results of times of initial settings measured both in the laboratory, compared to those measured in the field. Clearly the effectiveness of set retarders was diminished when samples were exposed to ambient conditions where continuous changes in temperature and humidity occur along the day. On the other side, the set accelerated mixes experienced faster setting times in the field than those cast in the laboratory environment.

The maximum reduction in times of initial setting in field conditions compared to those measured in the laboratory were found for those mixes poured around noon and mid afternoon for which ambient temperatures reached maximum values and remained at similar levels for at least three hours. After this time period, times of initial setting increased as ambient temperature decreased. This behavior is shown more evident in mixes M1, M2, and accelerated mixes M4 and M5.

It is evident from the initial setting time results, that conducting such measurements on concrete samples in the laboratory is not indicative of such mix behavior when cast in the field. The discrepancy between laboratory and field measurements in both, maximum curing temperature or initial setting time values, as listed in Tables 2 and 3 amounts to as much as 100 %.

**Table 2 Peak temperatures of concrete mixes measured in various environments (°C)**

Mix ID	Plain conc.	Set retarded mixes			Set accelerated mixes		
	Reference	M <sub>1</sub>	M <sub>2</sub>	M <sub>3</sub>	M <sub>4</sub>	M <sub>5</sub>	M <sub>6</sub>
Laboratory	28	26	27	27	29	28	27
Field-T1	45	51	36	41	43	42	37
Field-T2	42	47	36	44	43	40	37
Field-T3	41	42	35	43	42	40	43
Field-T4	36	38	30	41	37	37	35

**Table 3 Times of initial setting of concrete mixes measured in various environments (hours)**

Mix ID	Plain conc.	Set retarded mixes			Set accelerated mixes		
	Reference	M <sub>1</sub>	M <sub>2</sub>	M <sub>3</sub>	M <sub>4</sub>	M <sub>5</sub>	M <sub>6</sub>
Laboratory	5.9	10.6	9.3	8.1	5.3	3.9	2.8
Field-T1	3.67	5.3	6.23	5.35	2.98	3.00	2.31
Field-T2	3.64	4.19	5.55	4.44	2.82	2.37	2.14
Field-T3	2.82	3.83	6.07	4.03	2.82	2.49	2.14
Field-T4	3.35	4.86	6.58	3.92	3.14	2.57	2.33

In light of the measured setting times and temperature values for mixes cured in the field environment, it is evident that utilizing a unique mix composition and curing measure to pour a bridge deck segment that might take an entire working day will produce non-uniform deck regions. Despite the fact that compressive and tensile strengths of all mixes were found satisfactory, variations in the thermal and mechanical properties of different parts of the deck are bound to occur, which will lead to variations in the deck response to environmental changes. Expansion and contraction of different parts of the deck will vary in response to temperature increase or decrease. Temperature gradients developed across the deck thickness will also have another curling effect that will become non-uniform along the deck surface. Such a variation in behavior in adjacent parts of the deck would ultimately lead to initiation of cracks especially in the early age, when the concrete material is still to develop its full tensile strength. From another perspective, it is required by the WVDOT bridge design manual that the initial concrete stays plastic over the entire casting operation of the poured segment. According to the current pouring practice, this requirement is obviously almost impossible to meet. Therefore, it is recommended to design a pouring sequence for bridge decks that takes into account the field environmental effects on properties of fresh concrete mixes. This can be done by utilizing set accelerators for those mixes cast in the afternoons, and set retarders for mixes in the morning pours in a sequence that would reduce the variation in initial and final setting times between such pours. This can only be done if the initial setting time of concrete mixes could be estimated in field conditions. Once applied, the entire deck would have uniform thermo-mechanical properties, and a substantial reduction in the potential for early age cracking would be accomplished.

### Conclusions

In this investigation, variations in values of initial setting times of class k concrete mixes versus those in field applications are studied. More than 72 mixes were cast both in the laboratory, and also in various field conditions along normal summer working days in West Virginia with a wide range of setting times using set accelerators and set retarding admixtures. The collected results indicate that initial setting time measurements conducted in laboratory environments do not represent actual field performances of such fresh mixes. Discrepancies amounting up to 100% difference were observed when comparing measurements in the laboratory versus those in field conditions in both maximum temperature as well as values of initial setting times. When pouring a bridge deck along an entire day with a unique mix composition, variations in mix setting times are bound to occur along the day, producing non-uniform segments of the deck. In order to reduce the potential for early age cracking, a pouring sequence taking account the effects of environmental conditions on the properties of fresh concrete mixes must be designed.

### Acknowledgment

The authors would like to acknowledge The West Virginia Department of Transportation, Division of highways for sponsoring this research work. A special appreciation is extended to Mr. Jimmy Wriston, the project monitor, for his continuous support and dedication to this research.

### References

1. S. Mindess, and J. F. Young, 1981. '*Concrete*', 1st Edn., Englewood Cliff, New Jersey.
2. M. Cervera, R. Farla, J. Oliver, and T. Prato, "Numerical modelling of concrete curing, regarding hydration and temperature phenomena", *Computers and Structures* No. 80 (2002), pp. 1511-1521
3. K. Van Breugel, "Numerical Simulation of Hydration and Microstructural Development in Hardening Cement-based Materials", *Cement and Concrete Research*, Vol 25, No. 2 (1995), pp. 319-331.
4. J.K. Kim, Y.H. Moon, and S.H. Eo, "Compressive strength Development of Concrete with Different Curing Time and Temperature", *Cement and Concrete Research*, Vol 28 No. 12 (1998) pp. 1761-1773.
5. West Virginia Department of Transportation, Bridge design manual. WVDOT, Division of Highways, Charleston, WV, (2004) Sec 3.1.5.
6. M.A. Issa, "Investigation of cracking in concrete bridge decks at early ages", *Journal of Bridge Engineering*, vol. 4, no. 2 (1999), pp. 116-124.

## **GAS EMISSION AND STRUCTURAL CHANGES IN THE FIRING OF RED CLAY CERAMICS WITH ADDITION OF SANITARY WARE MASS WASTES**

Faria Jr., R. T.<sup>1</sup>; Souza, V. P.<sup>1</sup>; Cosin, S.<sup>2</sup>; Toledo, R.<sup>1</sup>; Vargas, H.<sup>1</sup>

<sup>1</sup>Universidade Estadual do Norte Fluminense Darcy Ribeiro – UENF  
Laboratório de Ciências Físicas - LCFIS

Av. Alberto Lamego, 2000, Pq. Califórnia, 28013-602, Campos dos Goytacazes, RJ  
Brasil

<sup>2</sup>LIEC - Laboratório Interdisciplinar de Eletroquímica & Cerâmica- Universidade Federal de São Carlos (UFSCAR) – 13565-905 São Carlos – SP, Brasil

Keywords: ceramic, pollutant gas, thermal properties, photothermal techniques

### **Abstract**

With the purpose of decrease environmental impact, caused by industrial residues (just discarded in the environment) and clay extraction in the ceramic industry, sanitary ware wastes were incorporated into clay. In contrast, it is important to evaluate not only the technological essays but also gases emissions in the ceramic firing process. The pollutant gases emitted in ceramic with residues can be in much larger concentrations than that in a pure clay ceramic firing or, on the other hand, can decrease the pollutant gas concentrations. With the aid of thermal analyses and photoacoustical techniques it was observed that sanitary ware waste can reduce the CO<sub>2</sub> emission. The gas emissions were shown as in function of firing temperature from 300 °C to 1100 °C. In order to analyze phase transformations during the firing process, clay samples and wastes were both analyzed by x-rays fluorescent chemical analysis and x-rays diffraction.

### **Introduction**

Research works on the structural and physical changes that wastes, mainly industrially produced, cause to the final ceramic product has been rapidly expanding in these last two decades. See, for instance references in [1]. In spite of these examples of a continuous effort to incorporate wastes into clay ceramic motivated by technical and economical advantages, environmental issues are still a matter of concern. However, the gas emission due to the clay firing process and its related atmospheric pollution may be enhanced as a consequence of an incorporated waste [2]. It is known that the firing of clay ceramics in conventional furnaces using fuels such as wood, charcoal, heavy oil and natural gas generates appreciable amounts of gaseous components, mainly carbon dioxide (CO<sub>2</sub>), carbon monoxide (CO) and methane (CH<sub>4</sub>). Additionally to the atmospheric pollution, these gas sets could be harmful to the human health and can corrode equipments [3,4].

Works on the effect of gas emission caused by the firing of clay ceramics incorporated with industrial wastes are practically inexistent. Therefore one of the mean objectives of this research was to investigate the gas emission resulting from the firing of clay ceramics incorporated with different industrial residues. Here, sanitary ware mass wastes were incorporated to the clay and already commercialized by a ceramic industry of São Paulo state.

Moreover, one of the main ceramics features was not yet well concerned by the community, that is, its thermal behavior. Urban buildings of equatorial and tropical countries are often subjected to constant solar radiation. Thus, thermal properties play a significant role in the quality of end-products. While technological properties of those materials are frequently found in the literature, information about the thermophysical characteristics of red ceramics is very scarce [5,6].

In order to show methodologies to characterize ceramics here depicted, the samples under study were clay from São Paulo state. Firstly, the raw materials without residues, named from now on CLAY is presented and throughout characterized. In a second stage, the aggregation of the residue is pointed out and named here as CLAY 20. Characterizations are performed and compared with CLAY.

### Ceramic Samples and Methods

The raw material was collected from a neocenozoic sedimentary soil placed in Jundiaí city, 60 Km far from São Paulo city in São Paulo state. About 20 kg of material collected in situ were dried, grounded, and passed through a sequence of sieves yielding a homogeneous powder with particle size smaller than 75  $\mu\text{m}$ , corresponding to 95 % of the original mass. According to their chemical properties they can be considered fluxes clays mainly by the alkaline elements ( $\text{Na}_2\text{O}$ ,  $\text{K}_2\text{O}$ ,  $\text{CaO}$  and  $\text{MgO}$ ), which are responsible for the ceramic sintering. The high values of  $\text{Na}_2\text{O} + \text{K}_2\text{O}$  come from the minerals illite and albite, while  $\text{CaO} + \text{MgO}$  are linked with calcite and dolomite minerals. To put side by side, samples of pure clay and clay with 20 % of sanitary ware mass wastes were considered for this research.

For measurements, a quantity of the powder was mixed with water and then extruded at 36 MPa into a rectangular prismatic mould with a 20x10 mm cross-section, cut into bars 100 mm long which were left drying in air for two weeks at room temperature. Before the firing process, the samples were placed in an oven at  $(110 \pm 5 \text{ }^\circ\text{C})$  for 24 hours.

To simulate the continuous sintering process of the ceramic material up to 1100  $^\circ\text{C}$ , and to accompany the changes that occur, 8 thermal treatment steps were chosen, each step being denoted  $T_F$  henceforth. The heating cycle was such that the sample was heated at a rate of 2  $^\circ\text{C}/\text{min}$  up to 600  $^\circ\text{C}$ , left at this temperature for one hour, and then heated at a rate of 4  $^\circ\text{C}/\text{min}$  up to the selected firing temperature, where it was left for 3 hours before cooling down to room temperature at a rate of 1.5  $^\circ\text{C}/\text{min}$ .

#### Characterization by X-Ray

The chemical composition and crystalline phases of the raw material with and without residues and only of the residues were presented. The microstructure of the samples as in function of the firing temperature was represented by X-ray diffractions.

The chemical characterizations were obtained by energy dispersive X-ray spectroscopy (EDS), using a SHIMADZU equipment. The resulting values of this quantitative analysis are shown in Table 1.

Observing Table 1 we can classify the clay as flux-based clay (higher fluxes oxides), as explained in the previous section. In addition to  $\text{SiO}_2$  and  $\text{Al}_2\text{O}_3$ , there are considerable amounts of  $\text{Fe}_2\text{O}_3$ ,  $\text{K}_2\text{O}$ , and  $\text{TiO}_2$ , which is favorable for red ceramics production. Iron oxide accounts for the bodies' red pigmentation after firing. The residue is a silt-clay with very low plasticity which should enhance the structural quality of the ceramic.

Table 1. Chemical composition of the clay and the sanitary ware mass residue (wt.%).

Oxides in wt%	CLAY	Sanitary ware mass residue
$\text{SiO}_2$	59.61	64.8
$\text{Al}_2\text{O}_3$	21.19	21.5
$\text{MnO}$	0.048	0.06
$\text{MgO}$	1.07	0.78
$\text{CaO}$	0.33	0.32
$\text{Na}_2\text{O}$	0.12	0.51
$\text{K}_2\text{O}$	2.33	2.53
$\text{TiO}_2$	0.944	0.89
$\text{Cr}_2\text{O}_3$	-	0.05
$\text{P}_2\text{O}_5$	0.13	0.13
$\text{SO}_3$	-	0.06
$\text{Fe}_2\text{O}_3$	5.45	5.96
$\text{ZnO}$	-	0.03
$\text{ZrO}_2$	-	0.13
LoI	9.28	2.25

The X-ray diffraction experiments were performed at room temperature using the  $\text{Cu K}\alpha$  radiation of a Seifert URD65 diffractometer, equipped with a diffracted beam monochromator. Diffractograms were obtained from 3 to 75° with step sizes of 0.03° and accumulation time of 3 s. From the diffractograms the sample crystallinities were determined as the ratio between the integrated intensity of the sharp diffraction peaks to the total area of the diffraction pattern, which includes the non-coherent intensity. It was just analyzed the 110 °C sample CLAY.

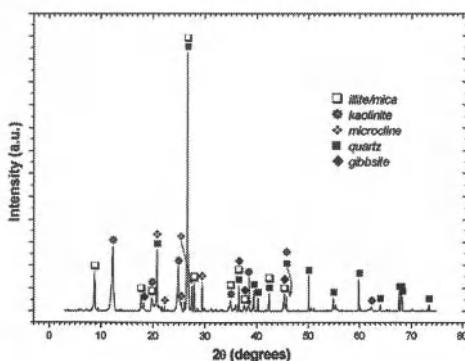


Fig.1. X-ray diffractogram of CLAY at 110 °C drying temperature.

Fig. 1 shows the XRD patterns of the clay raw material. These diffractograms indicate the presence of a micaceous mineral, quartz, microcline, and clay minerals.

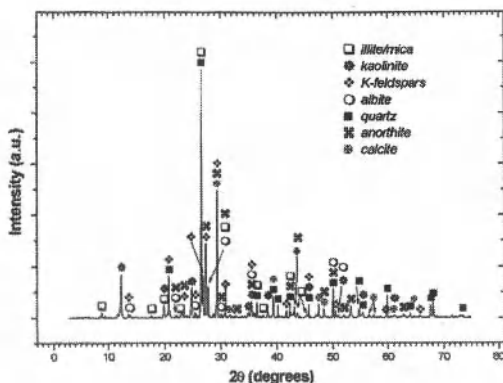


Fig. 2. X-ray diffractograms sanitary ware mass residues at 110 °C drying temperature.

Fig. 2 shows the waste of sanitary ware mass diffractogram, which points out the presence of micaceous material, albite, anorthite, k-feldspars, clay minerals, quartz, and calcite. We observed a variety of flux materials. Feldspars and microcline are sources of alkaline flux materials, such as  $K_2O$  and  $Na_2O$ , which make possible the formation of a liquid phase above 700 °C [7]. The fluxing capacity of this residue, which is associated with lower porosity after firing, is also confirmed by the presence of  $K_2O$  and  $Na_2O$  containing minerals. Then, the sanitary ware mass is the source of  $K_2O$  and  $Na_2O$ , which act as fluxes to improve the sintering process.

### Technological Essays

Considering the technological measurements of the clay and the sanitary ware mass residue, table 2 presents the technological properties of volumetric shrinkage, bending strength and water absorption for the product at the sintering temperature, considered the best temperature for commercial purposes.

Table 2 – Technological properties of end-product ceramic without residue (CLAY) and with 20% in wt of sanitary ware residue (CLAY 20).

Sample	Volumetric Shrinkage (%)	Bending Strength (MPa)	Water Absorption (%)
CLAY	2.1	3.3	20.3
CLAY 20	1.5	2.6	20.9

Comparing CLAY and CLAY 20, we can infer that no significant changes were observed.

### Thermal Diffusivity, using Photoacoustical Technique

Thermal diffusivity, a particular property that evaluates the heat propagation behavior within the sample, is quite sensitive to the material structure as well as preparation and sintering conditions. Experiments concerning with thermal diffusivity and samples thickness were performed five and ten times, respectively, to produce the deviations.

The experimental set-up, the sample is mounted directly onto a commercial electrets microphone presenting a good linear frequency response above 20 Hz (Omnidirectional back electrets condenser microphone cartridge, model WM-61A - Panasonic), fixed with a silicone grease, illuminated by the light beam from a He-Ne laser (Unilaser mod. 025) and modulated with a mechanical chopper (EG&G Instruments mod. 651), before it reaches the sample's surface. It consists of an Open Photoacoustical cell (OPC) configuration in the sense that the sample is placed on top of the detection set-up itself [8]. As a result of the periodic sample heating by modulated light absorption, the pressure inside the cell oscillates at the chopping frequency and can be detected by the microphone. The resulting PA signal is then subsequently fed into a field-effect-transistor (FET) pre-amplifier and leads directly to a "Lock-in" amplifier (Perkin Elmer Instruments mod. 5210), where it is possible to obtain the photoacoustical amplitude and the phase signal, which are recorded as a function of the modulation frequency in an appropriate software program.

According to the model proposed by [9] for thermal diffusion, the equation that leads us to the pressure fluctuation ( $\delta P$ ) in the air chamber is

$$\delta P = \frac{\gamma^2 I_0 (\alpha_g \alpha_s)^{1/2} \exp j(\omega t - \pi/2)}{2\pi l_g T_0 k_s f \sinh(\sigma_s l_s)}, \quad (4)$$

where  $\gamma$  is the air specific heat ratio,  $P_0$  the ambient pressure,  $T_0$  ambient temperature,  $I_0$  is the absorbed light intensity,  $f$  is the modulation frequency, and  $l_s$ ,  $k_s$  and  $\alpha_s$  are the length, thermal conductivity and the thermal diffusivity of the sample, respectively. Here, the subscripts denote the absorbing samples ( $s$ ) and the gas ( $g$ ) media, respectively, and  $\sigma_s = (1 + j)\alpha_s$ , is the complex thermal diffusion coefficient of  $i$  medium. It is assumed in the equation (1) that the sample is optically opaque  $l_p \ll l_s$ , where  $l_p$  is the optical penetration depth. For thermally thin sample  $\mu_s > l_s$ ;  $f < f_c$ , where  $\mu_s$  is the thermal diffusion length and  $f_c = \alpha_s / \pi l_s^2$  is the cut-off frequency.

The amplitude of the PA signal for a thermally thick sample decreases exponentially with the modulation frequency as  $S_{PA} \propto 1/f \exp(-b\sqrt{f})$ , where  $b = l_s \sqrt{\pi/\alpha_s}$ . In this case,  $\alpha_s$  is obtained from the experimental data fitting from the parameter  $b$ .

Taking values of thermal diffusivity from the literature, the cut-off frequency  $f_c$  is about 5.87 Hz, i.e. the frequency domain is regarded as thermally thick.

**Results and discussion:** Thermal diffusivity values are in close agreement with the literature [5,6,10]. Analyzing the thermal diffusivity and the diffractograms, we can explain that the lower diffusivity value in 900 °C and 1050 °C is possibly due to the Al-Si rearrangements, owing to a crystallization process followed by a lattice formation [11]. The kaolinite  $2Al_2(OH)_4Si_2O_5$  evolution, which reaches the spinel phase formation, with an intermediate phase, namely

metakaolin  $2Al_2Si_2O_7 + 4H_2O$ . The high diffusivity value at 1000 °C could be possible connected to the liquid phase formation within the beginning of the vitreous phase. The heat can be transported easier in this kind of phases than through the clay mineral grains. In support of this explanation for the highest thermal diffusivity, we note the clear modification of structure shown to occur above 1050 °C. At 1100 °C, the thermal diffusivity decreases. Through sintering at this temperature, formation of mullite  $2/3[3Al_2O_3 \cdot 2Si_2]$  and cristobalite  $5/3SiO_2$  starts from the spinel phase  $Al_4Si_3O_{12}$ , as reported by references in Ref. [11]. We suggest that there is a reduction of liquid phase surface and pores. This is due mainly to formation of mullite, which is characterized by a high proportion of oxygen vacancies that lead to low thermal diffusivity.

Table 3. Thermal properties of the pure clay and clay with 20% residue as in function of some possible sintering temperatures.

Temperature (°C)	CLAY Thermal diffusivity (cm <sup>2</sup> /s)	CLAY 20 Thermal diffusivity (cm <sup>2</sup> /s)
900	0.003 ± 0.0004	0.008 ± 0.0001
950	0.005 ± 0.0000	0.004 ± 0.0005
1000	0.007 ± 0.0000	0.009 ± 0.0008
1050	0.004 ± 0.0000	0.006 ± 0.0004
1100	0.004 ± 0.0002	0.004 ± 0.0009

We note that the aggregation of 20% of sanitary ware mass residue in the clay matrix generates higher values of the ceramic thermal properties. Probably, in 900 °C took place a pseudo sinterization due to the presence of alkaline salts (from the waste) in CLAY 20, which could justify the high value reached, although the ceramic structure is not well defined.

#### Pollutant Gases from the Firing of Clay Ceramic Added with Residues

The gas released from the furnace was directly connected to an infrared model URAS 14, ABB gas analyzer under a suction flux of 0.3 L / min. This gas analyzer detected and quantified simultaneously CO, CO<sub>2</sub>, CH<sub>4</sub>, NO, N<sub>2</sub>O, NH<sub>3</sub> e SO<sub>2</sub>. Gas samples were collected 20 min. after settled temperature stages of respectively, 150, 300, 450, 550, 650, 800, 950, 1050 and 1100 °C.

The emitted gases from the firing process were quantitatively measured by means of a photothermal technique. The gas analyzer measurement process is based on resonance absorption at the characteristic vibrational rotation spectrum bands of non-elemental gases in the middle infrared range between 2 μm and 12 μm. Because of their bipolar moment, the gas molecules interact with infrared emissions. For selectivity, the receiver is filled with the applicable sample components to establish reference and sensitivity to these components (~1 ppm). It consists of the cell divided into two identical compartments: one in the measuring cell, through which the sampled gas is flowed, and the other acts as reference, filled with nitrogen. The light emitted from a hot filament is modulated by a mechanical chopper and divided by a beam splitter. Each beam goes simultaneously through the measuring cell and the reference cell. The detector consists of two sealed chambers separated by a diaphragm capacitor. Both chambers are filled with pure gas of the chemical species under study. The light beams emerged from the sample and reference cells reach independently the two detector chambers, causing a differential pressure that

is proportional to the light absorption by the sample. The pressure difference is converted by the diaphragm capacitor into an electrical signal [12]. A detailed description of the Uras performance can be found in the literature [13]. Before each sample analyses the cells were calibrated using pure standard N<sub>2</sub>.

**Results and discussion:** CO<sub>2</sub>, in the range of 300 °C to 500 °C are emitted due to the organic matter oxidation. Moreover, the reaction of the kaolinite and goethite dehydroxilation deals to a metakaolinite, that is, an amorphous phase.

Values reached in this section were just proportional to a laboratory furnace.

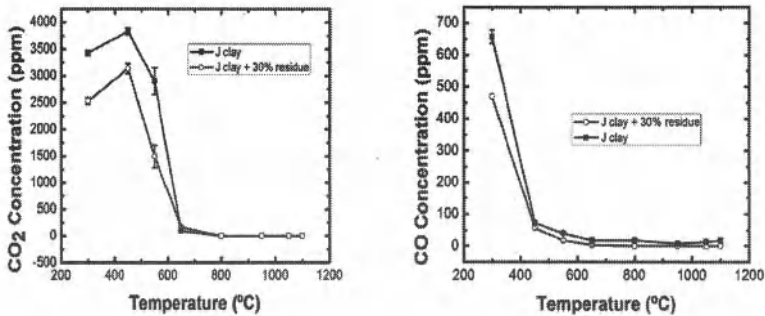


Fig. 5. CO<sub>2</sub> and CO emitted during the ceramic firing process as in function of the firing temperature.

Figure 5 shows the CO<sub>2</sub> and CO emissions as in function of firing temperature from the clay without and with 20% in weight of sanitary ware mass residue. Firstly, we observed that the addition of the residue diminishes around 15 % the amount of CO<sub>2</sub> emission. The amount of CO<sub>2</sub> emitted between 300 and 550 °C is due to organic matter oxidation and the dehydroxilation of clay minerals.

## Conclusions

Here, red ceramic samples from São Paulo state were analyzed as in function of firing temperature. In order to study the ceramics quality, technological essays were prepared.

The Thermal property of red ceramic samples as well as their crystalline phases was analyzed as a function of sintering temperature. Photoacoustical technique was used to measure the thermal diffusivity and the microstructures were identified by x-ray diffraction, in order to compare structural and thermal features of the samples. It was shown that there is an intrinsic relationship between the structure and the thermal diffusivity. When the crystalline structure undergoes strong perturbations the thermal diffusivity values decrease and vice-versa. When liquid phases achieve the highest concentration at around 1000 °C, the thermal diffusivity shows its maximum peak. Afterwards, there is a decrease, although the thermal diffusivity maintains high values, due to mullite enhancement and vitreous phase consolidation in the red ceramics. Considering thermal

features, it was shown that for this red ceramic, the sintering temperature should be greater than 1000 °C.

It is possible that sanitary ware residues can attenuate the pollutant gas release from the ceramic firing. We concentrate in this chapter the CO and CO<sub>2</sub> gases, in order to facilitate the point of view of our study. It will appear elsewhere the complete set of measured gases from this research.

### Acknowledgment

The authors thank the Brazilian agencies FAPERJ and CAPES for the financial support.

### References

- [1] Vieira, C.M.F. & Monteiro, S.N. (2009). Incorporation of solid wastes in red ceramics: an updated review. *Matéria (Rio J.)*, vol.14, nº .3, pp. 881-905. ISSN 1517-7076.
- [2] Souza, V.P.; Toledo, R.; Holanda, J.N.F.; Vargas, H. & Faria Jr, R.T. (2008). Pollutant gas analysis evolved during firing of red ceramic incorporated with water treatment plant sludge. *Cerâmica*, vol. 54, pp. 351-355.
- [3] Parsons, A. J.; Inglethorpe, S. D. J.; Morgan, D. J. & Dunham, A. C. (1997). Evolved gas analysis (EGA) of bricks clays. *J. Therm. Analysis*, vol. 48, pp.49.
- [4] Morgan, D. J. (1993). Thermal analysis including evolved gas analysis of clay raw materials, *Applied Clay Science*, vol. 8, pp. 81.
- [5] Alexandre, J.; Saboya, F.; Marques, B. C.; Ribeiro, M. L. P.; Salles, C., da Silva, M. G.; Sthel, M. S., Auler, L. T. & Vargas, H. (1999). Photoacoustic thermal characterization of kaolinite clays. *The Analyst*, vol. 124, pp. 1209–1214.
- [6] Mota, L.; Toledo, R. ; Machado, F.A.L.; Holanda, J.N.F.; Vargas, H. & Faria Jr., R.T. (2008). Thermal characterization of red clay from the Northern Region of Rio de Janeiro State, Brazil using an open photoacoustic cell, in relation to structural changes on firing. *Appl. Clay Science*, vol. 42, pp. 168–174.
- [7] Reed J.S. (1976). *Principles of the Ceramics Processing*. John Wiley and Sons, New York.
- [8] Vargas, H. & Miranda, L.C.M. (1988). Photoacoustic and related photothermal techniques. *Physics Reports*. vol. 161, pp. 43–101.
- [9] Rosencwaig, A. & Gersho, A. (1976). Theory of the photoacoustic effect with solids. *Journal of Applied Physics*, vol. 47, pp. 64–69.

*Characterization of Minerals, Metals, and Materials*  
Edited by: Jiann-Yang Hwang, Sergio Neves Monteiro, Chengguang Bai,  
John Carpenter, Mingdong Cai, Donato Firrao, and Buoung-Gon Kim  
TMS (The Minerals, Metals & Materials Society), 2012

# **Characterization of Minerals, Metals, and Materials**

## **Characterization of Energy, Electronic and Optical Materials**

Session Chairs:  
**Sergio Monteiro**  
**Zheng Zhang**

## **INFLUENCE OF $\text{La}_2\text{O}_3$ ADDITIVE CONTENT ON THE PHASE STABILITY, SINTERING AND MICROSTRUCTURE OF 8 MOL% $\text{Y}_2\text{O}_3$ STABILIZED CUBIC ZIRCONIA (8YSZ) CERAMIC USED FOR SOLID OXIDE FUEL CELL APPLICATIONS**

Suleyman TEKELI<sup>1</sup>, Bulent AKTAS<sup>2</sup> and Serdar SALMAN<sup>3</sup>

<sup>1</sup>Gazi University, Technology Faculty, Metallurgical and Materials Engineering Department, 06500, Beşevler-ANKARA/TURKEY

<sup>2</sup>Harran University, Engineering Faculty, Mechanical Engineering Department, Osmanbey Kampüsü, SANLIURFA/TURKEY

<sup>3</sup>Marmara University, Technology Faculty, Metallurgical and Materials Engineering Department, Göztepe-ISTANBUL/TURKEY

Key words: Cubic zirconia,  $\text{La}_2\text{O}_3$ ,  $\text{La}_2\text{Zr}_2\text{O}_7$ , Sintering, Microstructural investigation

### **Abstract**

The effect of  $\text{La}_2\text{O}_3$  content up to 15 wt% on phase stability, sintering and microstructure of cubic zirconia (8YSZ) was investigated. XRD results showed that the specimens containing up to 15 wt%  $\text{La}_2\text{O}_3$  were composed of only cubic structure. Also, the specimens doped up to 5 wt%  $\text{La}_2\text{O}_3$  revealed no  $\text{La}_2\text{O}_3$  peaks, indicating that  $\text{La}_2\text{O}_3$  was completely solubilized in the cubic structure. However, when > 5 wt%  $\text{La}_2\text{O}_3$  was added, the peak of  $\text{La}_2\text{Zr}_2\text{O}_7$  compound emerged, showing that the overdoped  $\text{La}_2\text{O}_3$  was not solubilized in the 8YSZ matrix. The lattice parameter of the 8YSZ slightly decreased with the increasing  $\text{La}_2\text{O}_3$  content up to 1 wt% but further increase in the  $\text{La}_2\text{O}_3$  amount resulted in an increased lattice parameter. The comparison of grain size of the 8YSZ specimens with various  $\text{La}_2\text{O}_3$  content showed that grain size slightly increased with the increasing  $\text{La}_2\text{O}_3$  content up to 1 wt% but further increase in the  $\text{La}_2\text{O}_3$  amount resulted in a decreased grain size.

### **Introduction**

At atmospheric pressures, three polymorphic forms of  $\text{ZrO}_2$  are stable at different temperatures i.e. monoclinic, tetragonal and cubic. A high-pressure orthorhombic form of  $\text{ZrO}_2$  has also been reported[1]. The successful production of pure  $\text{ZrO}_2$  bodies is not possible all the time due to the large volume expansion associated with the martensitic tetragonal–monoclinic transformation. This fact restricts the applications of zirconia, in spite of its excellent mechanical and thermal properties. However, the stabilization of the high temperature polymorphs at room temperature as stable phases is made possible by addition of suitable dopants. Fully stabilized cubic  $\text{ZrO}_2$  and partially stabilized tetragonal  $\text{ZrO}_2$  show interesting properties and are widely used as ionic conductors, coatings and gas sensors in solid oxide fuel cells and structural applications[2]. Most frequently used dopants include  $\text{Y}_2\text{O}_3$ , CaO, MgO and  $\text{CeO}_2$ , although other oxides, such as those of rare earth elements, can also act as stabilizers of the high temperature structures. The incorporation of aliovalent cations to the lattice, forming substitutional solid solutions, allows to control the concentration of anionic vacancies in the structure. This aspect is particularly

important in designing ionic conductors[3], and is also determinant in the stabilization process[4]. The process of stabilization with larger ionic radii dopants is rationalized by the crystal chemistry model[5], that describes the dopant cations as typical stabilizer when they have larger ionic size, lower charged state and higher ionicity than  $Zr^{4+}$ . The ionic radius of  $Zr^{4+}$  is 0.84 Å and that for  $La^{3+}$  is 1.016 Å [6].

In addition to the possibility of stabilization of high temperature structures, the  $ZrO_2-La_2O_3$  system includes the existence of  $La_2Zr_2O_7$ , with pyrochlore structure [7,8]. This compound finds application as catalyst[9] and as thermal barrier[10]. It can be synthesized by solid state reaction between the oxides at 1500–1600 °C, or by the sol-gel process[11]. In this study, the effect of various amounts of  $La_2O_3$  addition on the phase equilibrium, sinterability and microstructure of 8YSZ was investigated.

### Experimental Procedure

In this study, 8 mol % yttria stabilized cubic zirconia (8YSZ) (Tosoh, Japan) powders as a matrix material and  $La_2O_3$  powders (Taimei, Japan) up to 15 wt% as an additive were used. The average grain sizes were 0.3 µm for 8YSZ and 0.25 µm for  $La_2O_3$ . The chemical compositions of the powders used in the experiments are given in Table 1.

**Table 1: The chemical composition of the powders used in the experimental works.**

	wt %								
	ZrO <sub>2</sub>	Y <sub>2</sub> O <sub>3</sub>	La <sub>2</sub> O <sub>3</sub>	TiO <sub>2</sub>	FeO <sub>2</sub>	Na <sub>2</sub> O <sub>3</sub>	CaO	Al <sub>2</sub> O <sub>3</sub>	SiO <sub>2</sub>
8YSZ	85.9	13.6	-	0.1	0.003	0.01	0.02	0.25	0.1
La <sub>2</sub> O <sub>3</sub>	-	-	99.99	-	0.003	-	0.005	-	0.002

The specimens for the microstructural investigations were produced by means of colloidal processing. Doping process was carried out in a plastic container by mechanical mixing of  $La_2O_3$  up to 15 wt% and 8YSZ powders with zirconia balls and ethanol. Mechanical mixing was done in a "speks" type mixer at 200 rev/min for 12 hours. The prepared slurries were left to dry for 24 hours by leaving the lid open. After the drying process, the agglomerated powders with medium hardness were ball milled by a spex for 10 minutes to obtain a good dispersion and to break-up the agglomerates. The powders obtained were sieved through 60 µm sift, pressed under a 40 MPa pressure in a single axis die and the pellets with a radius of 10 mm and a height of 4mm were produced. Inner surface of the steel die was cleaned after each dry-pressing process and stearic acid was applied to the side walls of the die. Sintering was carried out in a box type furnace under normal atmospheric conditions. The pressed pellets were first subjected to a pre-sintering process at 1000 °C and then sintered at temperatures between 1200 and 1550 °C for 1 hour at a heating and cooling rates of 5 °C /min in order to determine the effect of the  $La_2O_3$  on the sinterability of the 8YSZ. The density of the sintered specimens was evaluated by the ratio between weight and volume, which was determined by a geometrical method. The relative density was estimated on the assumption that the sintered body was of the cubic phase and based on the theoretical density of 5.68 and 6.51 gr/cm<sup>3</sup> for 8YSZ and  $La_2O_3$ , respectively.

The surfaces of the specimens were ground and polished by normal metallographic way after the sintering process and the specimens were thermally etched by keeping them in a furnace at 50 °C below the sintering temperature for 1 hour. Microstructural investigation of the sintered specimens was done by a Scanning Electron Microscope (SEM Jeol Lv 6060). Grain sizes were measured by mean linear intercept method.

XRD (Shimadzu XRD 6000,  $\text{CuK}\alpha$ ,  $\lambda=1.5405 \text{ \AA}$ ) was used to determine probable changes in the crystal structure of various amount of  $\text{La}_2\text{O}_3$  doped 8YSZ and lattice parameter of 8YSZ. The specimens doped with 0-15wt%  $\text{La}_2\text{O}_3$  were tested between the scan span  $0^\circ$  and  $70^\circ$  at a scan speed of 0.03 degree/sec and the diffraction angles were measured. The lattice parameters were evaluated for each composition by using these diffraction angles.

### Experimental Results and Discussion

XRD patterns from various amounts of  $\text{La}_2\text{O}_3$  doped 8YSZ specimens are shown in Figure 1. The specimens containing up to 15 wt%  $\text{La}_2\text{O}_3$  were composed of only cubic crystal structure. The specimen doped up to 5 wt%  $\text{La}_2\text{O}_3$  revealed no  $\text{La}_2\text{O}_3$  peaks, indicating that  $\text{La}_2\text{O}_3$  was completely solubilized in the 8YSZ matrix and did not remain in the specimens as a secondary phase. However, when  $> 5 \text{ wt\%}$   $\text{La}_2\text{O}_3$  was added, the  $\text{La}_2\text{Zr}_2\text{O}_7$  pyrochloric compound peaks emerged, showing that overdoped  $\text{La}_2\text{O}_3$  was not solubilized in the 8YSZ matrix, forming a secondary phase of the  $\text{La}_2\text{Zr}_2\text{O}_7$  at high temperatures. It was also seen that this new phase preferentially precipitated around and at the grain boundaries of the 8YSZ. The formation of the  $\text{La}_2\text{Zr}_2\text{O}_7$  pyrochloric compound was due to the different ionic radius and crystal structure of  $\text{La}^{+3}$  and  $\text{Zr}^{+4}$  ions. As known, the ionic radius of  $\text{La}^{+3}$  with hexagonal structure is 1.016 Å and that of  $\text{Zr}^{+4}$  with a cubic crystal structure is 0.84 Å. The pyrochloric structure is defined as two distinct and intertwined structures. Of these two distinct structures, the first is the one in which octahedral  $\text{ZrO}_6$  is sequenced as a cation-centred. The other is anion-centred layout of tetrahedral  $\text{La}_4\text{O}$ .

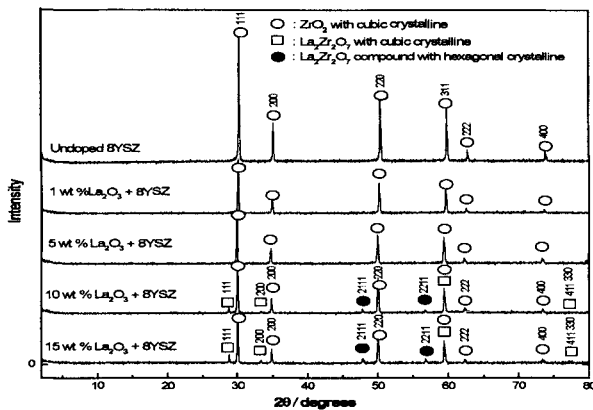


Figure 1. XRD patterns of undoped and  $\text{La}_2\text{O}_3$  doped 8YSZ specimens

The unification of two octahedral and one tetrahedral structures forms the compound  $\text{La}_2\text{Zr}_2\text{O}_7$  with  $\text{La}^{+3}$  cations situated in the hexagonal window of octahedral lattice[12]. The effect of the  $\text{La}_2\text{O}_3$  addition on the lattice parameter of the 8YSZ is given in Figure 2. While the lattice parameter of undoped 8YSZ is 5.146 Å, it increased to 5.181 Å with the addition of 15wt%  $\text{La}_2\text{O}_3$ . That is, the mean lattice parameter of the 8YSZ increased with the addition of  $\text{La}_2\text{O}_3$ . This increase in the lattice parameter, which corresponds Vegard's rule, can be attributed to the replacement of  $\text{La}^{+3}$  ions with  $\text{Zr}^{+4}$  and  $\text{Y}^{+3}$  ions in the cubic crystal of 8YSZ ( $\text{La}^{+3}$  ions, which are 20% bigger than the ionic radius of  $\text{Zr}^{+4}$ , increased the lattice parameter of the 8YSZ). The effect of the  $\text{La}_2\text{O}_3$  addition and rate on the sinterability of the 8YSZ is given in Figure 3.

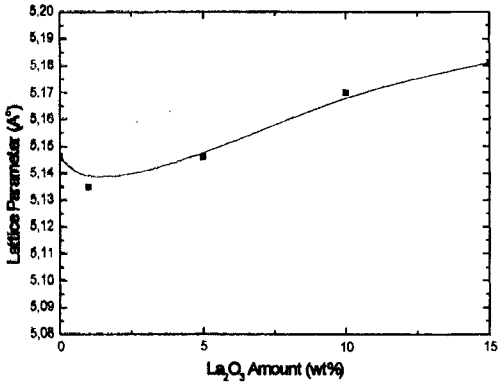


Figure 2. Lattice parameter variation of the 8YSZ with  $\text{La}_2\text{O}_3$  content.

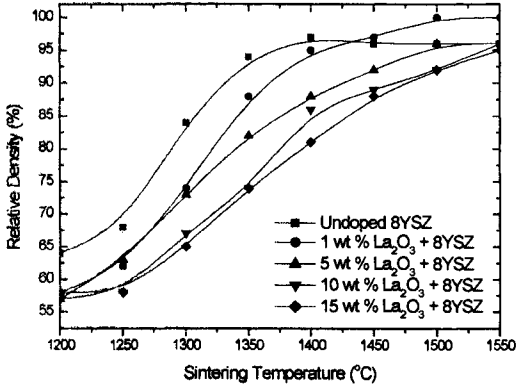


Figure 3. Relative density of the specimens doped with different amounts of  $\text{La}_2\text{O}_3$  sintered at various temperatures for 1 hour.

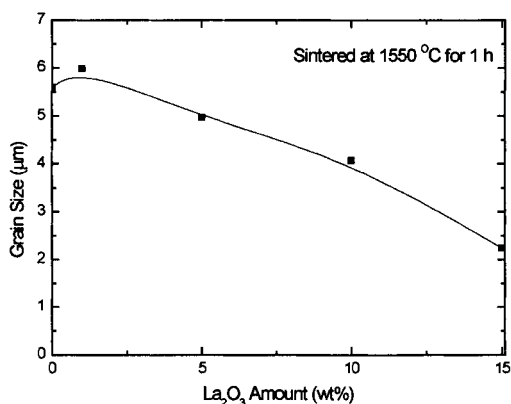


Figure 4. Grain size variation of the 8YSZ with La<sub>2</sub>O<sub>3</sub> amount

Here, the La<sub>2</sub>O<sub>3</sub> doped 8YSZ specimens were sintered without pressure at various temperatures for 1 hour after presintering at 1000 °C. As can be seen from the results, the relative density of the specimens increased with the increasing sintering temperature and decreased with the increasing La<sub>2</sub>O<sub>3</sub> amount at all temperatures. This decrease in the relative density was resulted from the porosities in the main matrix and around the grain boundaries especially at high amount of La<sub>2</sub>O<sub>3</sub> doped 8YSZ specimens. Also, the fact that the La<sub>2</sub>Zr<sub>2</sub>O<sub>7</sub> compound, which is formed in high amount of La<sub>2</sub>O<sub>3</sub> doped specimens at a high sintering temperatures and precipitated at the grain boundaries, prevented 8YSZ grains from touching each other and thus slowed the diffusion rate of the atoms in the grain boundaries as a result of an increase in grain boundary diffusion could be one other reason. The change in the grain size depending on La<sub>2</sub>O<sub>3</sub> amount is given in Figure 4. It can be seen from this figure that up to 1 wt% La<sub>2</sub>O<sub>3</sub> addition increased the grain size. This increased grain size could be due to the complete dissolution of the La<sub>2</sub>O<sub>3</sub> in the 8YSZ structure providing easy diffusion path at grain boundaries. However, further increase in the La<sub>2</sub>O<sub>3</sub> content led to a decrease in the grain size. This decrease in the grain size can be explained by the fact that the La<sub>2</sub>Zr<sub>2</sub>O<sub>7</sub> pyrochloric compound, which is formed around and at the grain boundaries at high temperatures, increased grain boundary cohesive resistance by pinning effect and thus, grain boundary mobility and energy decreased.

The microstructures of the specimens doped with various amounts of La<sub>2</sub>O<sub>3</sub> after sintering at 1550 °C for 1 hour are given in Figure 5. The undoped and up to 5 wt% La<sub>2</sub>O<sub>3</sub> doped 8YSZ specimens have an equiaxed, faceted, uniform and coarse-grained structure (Figure 5 a-c). The microstructures of the 10 and 15 wt% La<sub>2</sub>O<sub>3</sub> doped 8YSZ specimens, on the other hand, involve faceted 8YSZ grains together with round and smaller La<sub>2</sub>Zr<sub>2</sub>O<sub>7</sub> grains (Figure 5 d-e). It was also seen in Figure 5 that the porosity amount increased with increasing La<sub>2</sub>O<sub>3</sub> addition. The EDS analysis, taken from different parts of 15 wt% La<sub>2</sub>O<sub>3</sub> doped 8YSZ specimen are given in Figure 6. While the amount of La<sup>+3</sup> ions in the 8YSZ grains was 6.438 wt%, this rate was 37.067 wt% at

the grain boundaries. These EDS results are also an evidence of the existence of the  $\text{La}_2\text{Zr}_2\text{O}_7$  pyrochloric compound, which precipitated at the grain boundaries of the 8YSZ.

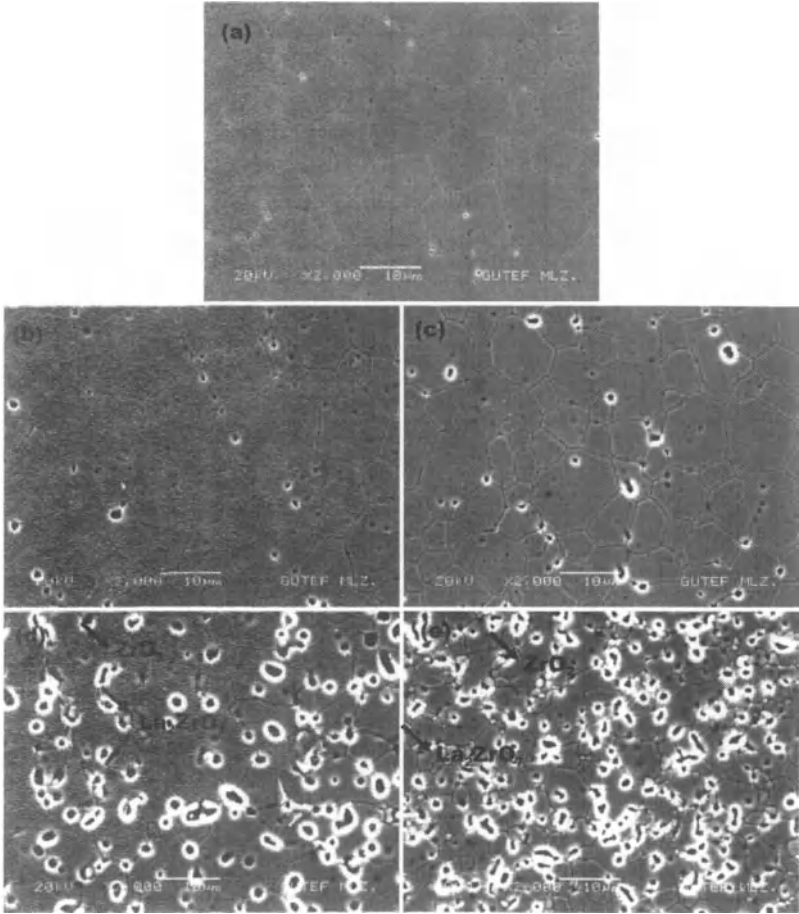
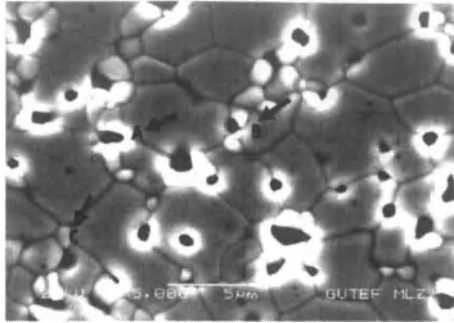


Figure 5. SEM micrographs of the thermally etched specimens with a) undoped, b) 1wt%, c) 5 wt%, d) 10 wt% and e) 15 wt%  $\text{La}_2\text{O}_3$  addition after sintering at 1550 °C for 1 hour.



EDS analys points	Wt (%)			
	Zr <sup>4+</sup>	La <sup>3+</sup>	Y <sup>3+</sup>	O <sup>2-</sup>
A	63.551	6.438	13.291	16.719
B	42.994	37.067	4.588	15.352
C	64.552	4.734	14.271	16.443

Figure 6. EDS results of 15 wt% La<sub>2</sub>O<sub>3</sub> doped 8YSZ specimen sintered at 1550 °C for 1 hour.

### Conclusions

- 1) XRD results showed that the 8YSZ specimens doped with up to 15 wt% La<sub>2</sub>O<sub>3</sub> have a cubic crystal structure and no change occurred in the crystal structure of the 8YSZ with the addition of La<sub>2</sub>O<sub>3</sub>. The specimen doped up to 5 wt% La<sub>2</sub>O<sub>3</sub> revealed no La<sub>2</sub>O<sub>3</sub> peaks, indicating that the La<sub>2</sub>O<sub>3</sub> was completely solubilized in the 8YSZ matrix and did not remain in the specimens as a secondary phase. However, when > 5 wt% La<sub>2</sub>O<sub>3</sub> was added, the La<sub>2</sub>Zr<sub>2</sub>O<sub>7</sub> pyrochloric compound peaks emerged, showing that the overdoped La<sub>2</sub>O<sub>3</sub> was not solubilized in the 8YSZ matrix forming a secondary phase of La<sub>2</sub>Zr<sub>2</sub>O<sub>7</sub> at high temperatures.
- 2) The relative density of the specimens decreased as the La<sub>2</sub>O<sub>3</sub> amount increased. This decrease was due to the existence of the La<sub>2</sub>Zr<sub>2</sub>O<sub>7</sub> pyrochloric compound, which precipitated at the grain boundaries at high temperatures and the porosities seen in the specimens with high amount of La<sub>2</sub>O<sub>3</sub> additions.
- 3) The grain size increased with the increasing La<sub>2</sub>O<sub>3</sub> amount up to 1 wt% and further increase in the La<sub>2</sub>O<sub>3</sub> content resulted in the decreased grain size. These results indicate that the La<sub>2</sub>O<sub>3</sub> addition within solubility limit accelerated the grain growth. The decrease in the grain size can be explained by the fact that the secondary phase of the La<sub>2</sub>Zr<sub>2</sub>O<sub>7</sub> pyrochloric compound, which is formed at the grain boundaries at high temperatures, increased grain boundary cohesive resistance and thus, limited grain boundary mobility and energy.

### Acknowledgements

The authors thank Gazi University and Marmara University, TURKEY, for the provision of laboratory facilities.

## References

1. A.H. Heuer and L.K. Lenz, "Stress-Induced Transformation during Subcritical Crack Growth in Partially Stabilized Zirconia," *J. Am. Ceram. Soc.*, 65 (1982), C-192-194.
2. R. Stevens, *Introduction to Zirconia* (Twickenham, Middx, :Magnesium Elektron Ltd., 1986), 12.
3. S.P.S. Badwal, *Ceramic Superionic Conductors* (New York, Materials Science and Technology A Comprehensive Treatment, vol. 11, VCH Publishers, Inc., 1994), 588.
4. P. Li and I.W. Chen, "Effect of Dopants on Zirconia Stabilization an X-ray Absorption Study: I. Trivalent Dopants," *J. Am. Ceram. Soc.*, 77 (1) (1994), 118-128.
5. S.M. Ho, "On the Structural Chemistry of Zirconium Oxide," *Mater. Sci. Eng.*, 54 (1982), 23-9.
6. R.C. Weast and M.J. Astle, *Handbook of Chemistry and Physics* (Florida, CRC Press, 1981), F-175.
7. R.S. Roth, "Pyrochlore-Type Compounds Containing Double Oxides of Trivalent and Tetravalent Ions," *J. Res. Natl. Bur. Std.*, 56 (1) (1956), 17-25.
8. A. Rouanet, "Zirconium Oxide-Lanthanide Oxide Systems Close to the Melting Point," *Rev. Hautes Temp. Refract.*, 8 (2) (1971), 161-180.
9. S.J. Korf, H.J.A. Koopmans, B.C. Lippens, A.J. Burggraaf, and P.J. Gellings, "Electrical and Catalytical Properties of Some Oxides with the Fluorite and Pyrochlore Structure," *J. Chem. Soc. Faraday Trans.*, 1 83 (1987), 1485-1491.
10. X.Q. Cao, R. Vassen, W. Jungen, S. Schwartz, F. Tietz, and D. Stöver, "Thermal Stability of Lanthanum Zirconate Plasma-Sprayed Coating," *J. Am. Ceram. Soc.*, 84 (9) (2001), 2086-2090.
11. H. Kido, S. Komarneni, and R. Roy, "Preparation of  $\text{La}_2\text{Zr}_2\text{O}_7$  by Sol-Gel Route," *J. Am. Ceram. Soc.*, 74 (2) (1991), 422-424.
12. B.G. Hyde, J.G. Thompson, and R.L. Withers, "Crystal Structures of Principal Ceramic Materials," *Materials Science and Technology A*, 11 (1994), 35.

## **DEVELOPMENT AND CHARACTERIZATION OF CARBONACEOUS MATERIALS INCORPORATED WITH METAL (Ti, V AND Zn)-ORGANIC COMPOUNDS FOR HYDROGEN STORAGE**

Mala Nath, Asheesh Kumar and Arjit Mallick

Department of Chemistry, Indian Institute of Technology Roorkee, Roorkee-247667, Uttarakhand, India

Keywords: Hydrogen storage; Metal-organic compounds; Sorption study; X-ray diffraction

### **Abstract**

The present research work is aimed to focus on the development of chemically stable light weight microporous carbonaceous material, such as activated charcoal incorporated either with titanium *n*-butoxide, titanium diisopropoxide bis(2,4-pentanedionate), vanadium 2,4-pentanedionate or zinc 2,4-pentanedionate having varying wt% of the metal (2–8%) using ethanol as solvent at 40–50 °C followed by calcinations at 100, 150 and 200 °C, except the samples with titanium diisopropoxide bis(2,4-pentanedionate) which are calcinated at 80 °C. Atomic absorption studies along with FESEM revealed that the maximum incorporation of metals (Zn, V and Ti) in activated charcoal was observed with 4 wt% of zinc 2,4-pentanedionate calcinated at 150 °C, 4 wt% of vanadium 2,4-pentanedionate at 100 °C, 2 wt% of titanium *n*-butoxide at 100 °C and 2 wt% of titanium diisopropoxide bis(2,4-pentanedionate) at 80 °C, and equilibration time of 20-24 h was used in each case. Hydrogen sorption behavior in these carbonaceous materials has also been studied at 77.4 K and low pressure up to 1 bar. The highest hydrogen uptake obtained was 1.45 wt% (164.5 cm<sup>3</sup> (STP)/g at P/P<sub>0</sub> = 1.0) for activated charcoal incorporated with 4 wt% of zinc 2,4-pentanedionate calcinated at 150 °C.

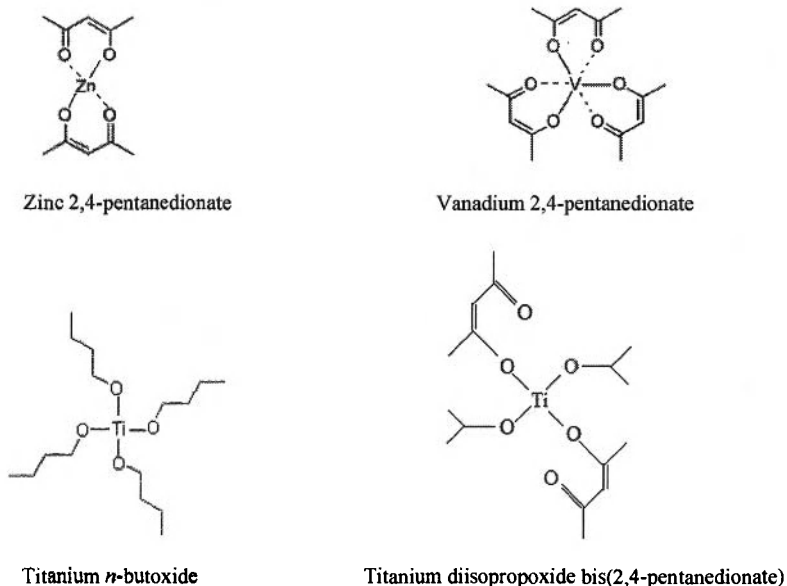
### **Introduction**

Two of the major challenges for humanity in the next twenty years are the shrinking availability of fossil fuels, the global warming and potential climate changes that result from their ever-increasing use. So it is necessary to find an energy source that is convenient, flexible and controllable. One possible solution to these problems is to use an energy carrier such as hydrogen, and ways to produce and store hydrogen in electric power plants and vehicles. Hydrogen storage is the bottleneck for the breakthrough of hydrogen as energy carrier in automotive applications [1].

The overarching technical challenge for hydrogen storage is how to store the amount of hydrogen required for a conventional driving range (>300 miles), within the vehicular constraints of weight, volume, efficiency, safety, and cost. Hydrogen storage is a major research focus for material scientists and chemists [2-7].

The different types of hydrogen storage materials have been used such as metal hydrides [8-10], formic acid [11], carbon nanotubes [12-14], carbonite substances [15], MOFs [16-18], and activated carbon [1, 19]. For hydrogen storage carbonaceous materials have attracted a lot of interest because of their excellent kinetics, which is based on weak Van der Waals forces between H<sub>2</sub> and the surface of materials [20]. In this paper carbonaceous material such as

activated charcoal incorporated with different metal (Ti, V, and Zn)-organic compounds as shown in Scheme 1 were prepared and their H<sub>2</sub> sorption behavior has been studied.



Scheme 1. Structures of different metal-organic compounds incorporated with charcoal.

## Experimental

### Materials

Activated charcoal (Merck), isopropanol (Rankem), ethanol (Rankem), titanium *n*-butoxide (Alfa Aesar), titanium diisopropoxide bis(2,4-pentanedionate) (Alfa Aesar), zinc 2,4-pentanedionate monohydrate (Alfa Aesar) and vanadium 2,4-pentanedionate (Alfa Aesar) were used without further purification.

### Preparation Of Carbonaceous Materials Incorporated With Zinc Using Zinc 2,4- pentanedionate Monohydrate And Vanadium Using Vanadium 2,4- pentanedionate

Zinc 2,4-pentanedionate monohydrate having 2 wt%, 4 wt% and 8 wt% of zinc (0.1611g, 0.322g and 0.6450g, respectively) were dissolved in ethanol (25mL) in a round bottom flask. Activated charcoal (2.0 g) was added to it and mixed properly. The mixture was stirred for 20–24 h at temperature 40–50 °C. Then the product was separated by filtration and washed with ethanol. The filtrate was stored for AAS analysis. The product was dried in hot air oven at 50 °C for 2 h. Then it was calcinated at different temperatures 100 °C, 150 °C and 200 °C in a heating furnace for 3 h to produce carbonaceous materials incorporated with zinc. Similar procedure was used for incorporation of vanadium using vanadium 2,4-pentanedionate.

### Preparation Of Carbonaceous Materials Incorporated With Ti Using Titanium *n*-Butoxide And Titanium Diisopropoxide Bis(2,4-pentanedionate)

Titanium *n*-butoxide having 2 wt%, 4 wt% and 8 wt% of titanium (0.2901 mL or 0.2843g, 0.5802 mL or 0.5686g and 1.160 mL or 1.137g, respectively) were mixed with isopropanol (25mL) in a round bottom flask. Charcoal (2.0 g) was added to it and mixed properly. The mixture was stirred for 20–24 h at temperature 40–50 °C. Then the product was separated by filtration and washed with isopropanol. The filtrate was stored for AAS analysis. The product was dried in hot air oven at 50 °C for 2 h. Then it was calcinated at different temperatures 100 °C, 150 °C and 200 °C in a heating furnace for 3 h to produce carbonaceous materials incorporated with titanium. Similar procedure was used for incorporation of titanium, using titanium diisopropoxide bis(2,4-pentanedionate) but calcination temperature was 80 °C .

### Measurements

The concentration of titanium, vanadium and zinc was determined by atomic absorption spectrometer (AAS) GBC Avanta using N<sub>2</sub>O-acetylene gas in the working range of 50–200 ppm and sensitivity 1.10 ppm. The FE-SEM micrographs and EDAX were taken using a FEI – QUANTA 200F scanning electron microscope having magnification up to 3000 KX, resolution 2 nm and acceleration voltage 20 kV. The X-ray patterns of the samples were recorded on Bruker AXS D8 Advance X-ray diffractometer with Cu-K $\alpha$  radiation ( $\lambda = 1.54 \text{ \AA}$ ) at 40 kV between the scan ranges of  $2\theta$  from 5–80 degree by the scan rate of 2 degree/min.

Gas Sorption Measurements The low pressure adsorption measurements were performed at 77.4 K on a Quantachrome QuadraWin-Data Acquisition and Reduction for Quadra Sorb SI Quantachrome instrument version 4.01. Sorption measurements were performed using high purity hydrogen (99.9995%) on samples of 0.1296 g to 0.0732g with the temperature maintained at 77.4 K by liquid nitrogen. These experiments were performed in National Chemical Laboratory, Pune, India.

### **Results And Discussion**

Hydrogen storing capacity of carbonaceous materials incorporated with transition metal depends on the amount of incorporated transition metal. The XRD of pure activated charcoal (d, 3.36, 2.07), zinc- (d, 10.47, 3.36)/vanadium 2,4-pentanedionate (d, 6.73, 3.18) and carbonaceous materials incorporated with transition metal indicated the presence of metal-organic compound in activated charcoal. The initial concentration and final concentration of the metal after adsorption on activated charcoal were determined by atomic absorption. From which the wt% of metal incorporated in activated charcoal (2.0 g) was determined. AAS analysis revealed that zinc 2,4-pentanedionate (2 wt% zinc) show maximum adsorption of 98.30 % (1.96 wt%), (2 wt%) vanadium 2,4-pentanedionate 95.50 % (1.91 wt%), (2 wt%) titanium *n*-butoxide (a) 87.68 % (1.75 wt%) and (2 wt%) titanium diisopropoxide bis (2,4-pentanedionate) (b) 47 % (0.94 wt%) on charcoal (Figure 1).

FE-SEM micrographs show the wt% of the metal present on the surface of charcoal due to adsorption of different metal-organic compounds. Few representative FE-SEM micrographs are shown in Figure 2 to Figure 4. It has been found that different surface of activated charcoal adsorbed different amount of metal. Therefore, the wt% of metals adsorbed on activated charcoal

was taken as average and data for maximum adsorption are given in Table I and Figure 5. The main constituent of charcoal is carbon whose wt% is above 90 in all FE-SEM micrographs.

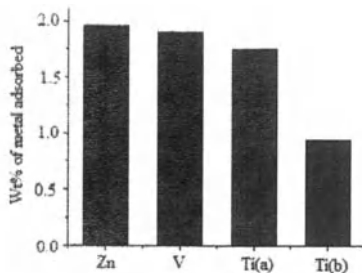


Figure 1. Wt% of metals adsorbed on charcoal using (2 wt%) zinc 2,4-pentanedionate (Zn), (2 wt%) vanadium 2,4-pentanedionate (V), (2 wt%) titanium *n*-butoxide (Ti(a)), (2 wt%) titanium diisopropoxide bis(2,4-pentanedionate) (Ti(b)) (AAS Results).

Table I. Maximum wt % of metal adsorbed on charcoal using FE-SEM results

Samples	Wt% of metal adsorbed (Calcinated Temperature °C)	Average wt% of metal adsorbed
Zinc-2,4 pentanedionate (4 wt%)	3.11 (150 °C)	3.05
Vanadium-2,4 pentanedionate (4 wt%)	3.01 (100 °C)	2.96
Titanium <i>n</i> -butoxide (2 wt%)	2.00 (100 °C)	1.52
Titanium diisopropoxide - bis (2,4-pentanedionate) (2 wt%)	1.11 (80 °C)	0.94

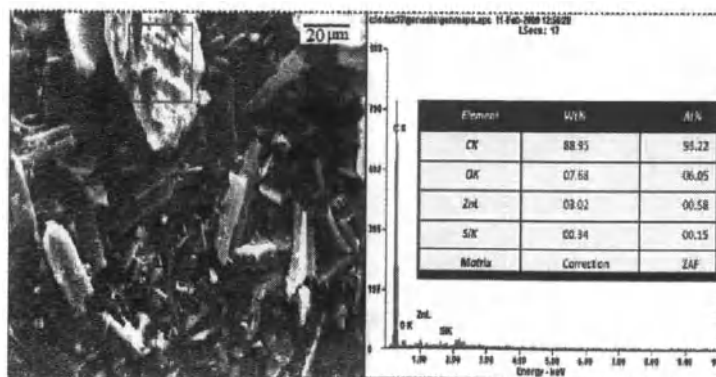


Figure 2. FE-SEM of charcoal incorporated with zinc using (4 wt%) Zn 2,4-pentanedionate calcinated at 150 °C.

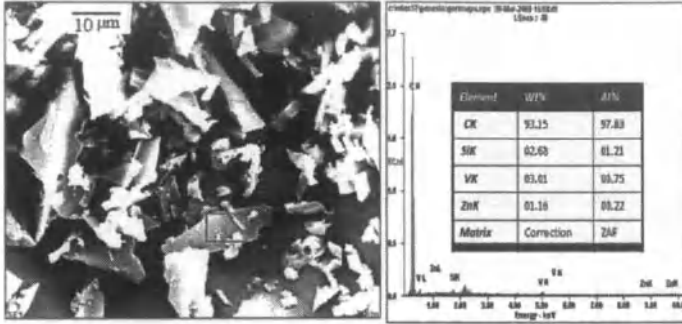


Figure 3. FE-SEM of charcoal incorporated with vanadium using (4 wt%) vanadium 2,4-pentanedionate calcinated at 100 °C.

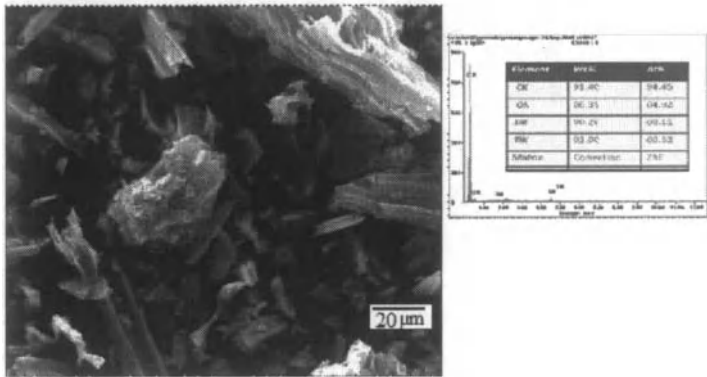


Figure 4. FE-SEM of charcoal incorporated with titanium using (2 wt%) titanium *n*-butoxide calcinated at 100 °C.

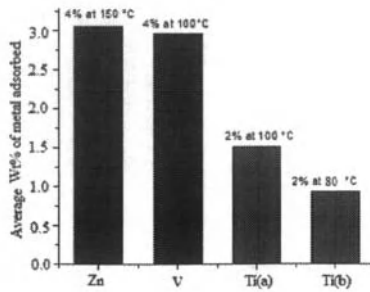


Figure 5. Average wt% of metal adsorbed on charcoal using zinc 2,4- pentanedionate (Zn), vanadium 2,4-pentanedionate (V), titanium *n*-butoxide (Ti(a)), titanium diisopropoxide bis(2,4-pentanedionate) (Ti(b)) (FE-SEM Results).

The high porosity and incorporation of metal in the porous carbonaceous material such as activated charcoal prompted us to evaluate its hydrogen adsorption performance. Low-pressure hydrogen sorption isotherms of activated charcoal incorporated with metal-organic compounds at 77.4K revealed reversible hydrogen sorption as shown in Figure 6. The abbreviations for the samples were given as Pure Activated Charcoal (CH), Charcoal incorporated with (2 wt%) titanium *n*-butoxide (TB), (2 wt%) titanium diisopropoxide bis(2,4-pentanedionate) (TC), (4 wt%) Zinc 2,4-pentanedionate (Z) and (4 wt%) Vanadium 2,4-pentanedionate (V). The maximum H<sub>2</sub> adsorption behaviour of samples at 77.4 K is shown in Table II. The H<sub>2</sub> adsorption in Activated Charcoal (CH) increases abruptly at the start of experiment and reaches to maximum of 155cm<sup>3</sup> (STP) /g at P/P<sub>0</sub> = 1.0 and maximum uptake of 1.37 wt% of hydrogen at 77.4K. The hydrogen adsorption in activated charcoal already has been investigated 0.05 wt% at room temperature, 298 K and pressure of 9.5 bar. While carbon nanotubes have 0.185 wt%, it is because of lattice defect in carbon nanotubes [20].

Table II. Mmaximum H<sub>2</sub> uptake in different carbonaceous materials

Carbonaceous materials	Maximum volume @STP cc/g	Maximum Wt% of hydrogen adsorbed
CH	155.6	1.37
TB	102.17	0.90
TC	119.4	1.05
Z	164.5	1.45
V	133.6	1.17

CH, Activated Charcoal; TB, Activated charcoal incorporated with 2% titanium *n*-butoxide; TC, Activated charcoal incorporated with 2% titanium diisopropoxide bis(2,4-pentanedionate); Z, Activated charcoal incorporated with 4% Zinc 2,4-pentanedionate; V, Activated charcoal incorporated with 4% Vanadium 2,4-pentanedionate.

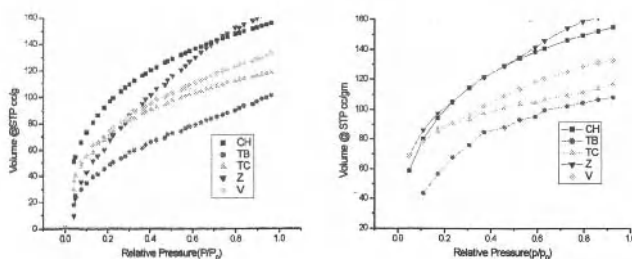


Figure 6. Adsorption-desorption isotherms of different carbonaceous materials at 77.4K on H<sub>2</sub>(g).

Samples TB, TC and V exhibited H<sub>2</sub> uptake of 102.17 cm<sup>3</sup> (STP) /g, 119.4 cm<sup>3</sup> (STP) /g and 133.6 cm<sup>3</sup> (STP) /g at P/P<sub>0</sub> = 1.0 (0.90, 1.05 and 1.17 wt%, respectively). Due to intercalation of metal the porosity of activated charcoal changes and different isotherms can be classified according to the interaction of metal with activated charcoal. This is why relatively low hydrogen uptake of 0.9–1.17 wt% at 77.4K in samples TB, TC and V than that of activated charcoal (CH) 1.37 wt%. It was found that in case of activated charcoal incorporated with (4 wt%) zinc 2,4-pentanedionate (Z) H<sub>2</sub> uptake was 164.5 cm<sup>3</sup> (STP) /g at P/P<sub>0</sub> = 1.0 (1.45 wt%). It was maximum than that of other incorporated carbonaceous materials and pure activated charcoal (1.37 wt%) also. The adsorption and desorption isotherms indicate that the process responsible for hydrogen adsorption in these carbonaceous materials may involve both physisorption and chemisorption. In conclusion it should be noted that the precise nature of interaction between the activated charcoal and transition metals is purely speculative and difficult to evaluate with precision.

The hydrogen storage on carbonaceous materials can be explained with Henry's law which is valid for a diluted layer adsorbed on the surface. At the temperature, the intercalation based on van der Waals forces between H<sub>2</sub> and carbon is the same order as the thermal motion energy of H<sub>2</sub> molecule on the surface. In order to increase the H<sub>2</sub> storage capacity, one should operate at a much lower temperature or under high pressure [21].

### Conclusions

In conclusion, carbonaceous materials incorporated with metal-organic compounds were successfully prepared. It was found that H<sub>2</sub> uptake was 164.5 cm<sup>3</sup> (STP) /g at P/P<sub>0</sub> = 1.0 (1.45 wt%) in case of activated charcoal incorporated with (4 wt%) zinc 2,4-pentanedionate. It was maximum than that of other incorporated carbonaceous materials and pure activated charcoal (1.37 wt%) also. Adsorption process is mainly affected by the pressure and temperature of the gas. High hydrogen uptake happens when the pressure is high.

### References

1. B.Panella, M. Hirscher, and S. Roth, "Hydrogen Adsorption in Different Carbon Nanostructures," *Carbon*, 43 (2005), 2209-2214.
2. A. Züttel, P. Wenger, S. Rentsch, P. Sudan, and Ph. Mauron, and Ch. Emmenegger, "LiBH<sub>4</sub> A New Hydrogen Storage Material," *J. Power Sources.*, 118 (2003), 1-7.
3. X. Hu, M. Trudeau, and D. M. Antonelli, "Hydrogen Storage in Microporous Titanium Oxides Reduced by Early Transition Metal Organometallic Sandwich Compounds," *Chem. Mater.*, 19 (2007), 1388-1395.
4. S. Proch, R. Kempe, C. Kern, A. Jess, L. Seyfarth, and J. Senker, "Pt@MOF-177: Syntheses, Room Temperature Hydrogen Storage and Oxidation Catalysis," *Chem. Eur. J.*, 14 (2008), 8204-8212.
5. T. Spassov, V. Rangelova, H. Chanev, S. Stoyanov and O. Petrov, "Synthesis and Hydrogen Adsorption in Cu-Based Coordination Framework Materials," *Scripta Materialia*, 58 (2008), 118-121.
6. A.R. Biris, D. Lupu, E. Dervishi, Z. Li, V. Saini, D. Saini, S. Trigwell, M.K. Mazumder, R. Sharma, and A.S. Biris, "Hydrogen Storage in Carbon-Based Nanostructured Materials," *Particulat. Science Technology*, 26 (2008), 297-305.

7. S. Ma, J.M. Simmons, D. Sun, D. Yuan, and H. Zhou, "Porous Metal-Organic Frameworks Based on an Anthracene Derivative: Syntheses, Structural Analysis, and Hydrogen Sorption Studies," *Inorg. Chem.*, 48 (2009), 5263-5268.
8. S.C. Amendola, S.L. Sharp-Goldman, M.S. Janjua, M.T. Kelly, P.J. Petillo, and M. Binder, "An Ultra Safe Hydrogen Generator: Aqueous Alkaline Borohydride Solution and Ru Catalyst," *J. Power Sources*, 85 (2000), 186-189.
9. Y. Kojima, K. Suzuki, K. Fukumoto, M. Sasaki, T. Yamamoto, Y. Kawai, and H. Hayashi, "Hydrogen Generation Using Sodium Borohydride Solution and Metal Catalyst Coated on Metal Oxide," *Int. J. Hydrogen Energy*, 27 (2002), 1029-1034.
10. Z.P. Li, B. H. Liu, K. Arai, N. Morigazaki, and S. Suda, "Protide Compounds in Hydrogen Storage Systems," *J. Alloys Compd.*, 356-357 (2003), 469-474.
11. J. Ferenc, "Breakthroughs in Hydrogen Storage-Formic Acid as A Sustainable Storage Material for Hydrogen," *Chem. Sus. Chem.*, 1 (2008), 805-808.
12. S. Iijima, "Helical Microtubules of Graphitic Carbon," *Nature*, 354 (1991), 56-58.
13. P. Chen, X. Wu, J. Lin, and K.L. Tan, "High H<sub>2</sub> Uptake by Alkali-Doped Carbon Nanotubes Under Ambient Pressure and Moderate Temperatures," *Science*, 285 (1999), 91-93.
14. L. Ci, H. Zhu, B. Wei, C. Xu, and D. Wu, "Annealing Amorphous Carbon Nanotubes for their Application in Hydrogen Storage," *Applied Surface Science*, 205 (2003), 39-43.
15. D.C. Elias, R.R. Nair, T.M.G. Mohiuddin, S.V. Morozov, P. Blake, M.P. Halsall, A.C. Ferrari, D.W. Boukhvalov, M.I. Katsnelson, A.K. Geim, and K.S. Novoselov, "Control of Graphene's Properties by Reversible Hydrogenation: Evidence for Graphane," *Science*, 323 (2009), 610-613.
16. S.J. Yang, J.Y. Choi, H.K. Chae, J.H. Cho, K.S. Nahm, and C.R. Park, Preparation and Enhanced Hydrostability and Hydrogen Storage Capacity of CNT@MOF-5 Hybrid Composite," *Chem. Mater.*, 21 (2009), 1893-1897.
17. M. Xue, Y. Liu, R.M. Schaffino, S. Xiang, X. Zhao, G.-S. Zhu, S.-L. Qiu, and B. Chen, "New Prototype Isoreticular Metal-Organic Framework Zn<sub>4</sub>O(FMA)<sub>3</sub> for Gas Storage," *Inorg. Chem.*, 48 (2009), 4649-4651.
18. N.L. Rosi, J. Eckert, M. Eddaoudi, D.T. Vodak, J. Kim, M.O' Keeffe, and O.M. Yaghi, "Hydrogen Storage in Microporous Metal-Organic Frameworks," *Science*, 300 (2003), 1127-1129.
19. R. Chahine, and T.K. Bose, "Low Pressure Adsorption Storage of Hydrogen," *Int. J. Hydrogen Energy*, 19 (1994), 161-164.
20. N.H.A. Hassan, A.R. Mohamed, S.H.S. Zein, "Study of Hydrogen Storage by Carbonaceous Material at Room Temperature," *Diamond & Related Materials* 16 (2007), 1517-1523.
21. Y. Zhou, K. Feng, Y. Sun, and L. Zhou, "Adsorption of Hydrogen on Multiwalled Carbon Nanotubes at 77 K," *Chem. Phys. Lett.*, 380 (2003), 526-529.

## CHARACTERIZATION OF NICKEL OXIDE NANOPARTICLES FOR HYDROGEN ADSORPTION WITH EXTERNAL ELECTRIC FIELD

Zheng Zhang, Xiang Sun, Zhiwei Peng, Jiann-Yang Hwang  
Michigan Technological University  
1400 Townsend Drive, Houghton, MI 49931, USA

Keywords: Nickel oxide, Hydrogen adsorption, Electric field.

### Abstract

Nickel oxide nanoparticles were synthesized using sodium dodecyl sulfate as the surfactant and urea as the hydrolyzing agent and different calcination temperatures and time were selected for preparation. Nitrogen adsorption (BET), X-ray diffraction (XRD) and scanning electron microscope (SEM) were subsequently used to characterize the prepared samples. The effect of an external electric field on hydrogen adsorption over a prepared nickel oxide was carried out. The electric field was introduced by a piezoelectric element, which is capable of autogenously generating charges under hydrogen pressure. Increased hydrogen adsorption was obtained from this study, which indicated a stronger interaction between the adsorbent surface and hydrogen.

### Introduction

Metal oxide has attracted great attention for adsorption because of their wide application in catalysis [1-7], gas storage [8,9] and sensors [10,11]. However, with respect to the usage in hydrogen adsorption, few research outcomes have been reported [12,13], since there remains the difficult task of synthesizing highly porous metal oxides with unsaturated metal centers, which account for the strong interaction with hydrogen [14,15]. Nickel oxides are polar materials with an intrinsic dipole moment. The external applied electric field could further enhance the dipole moment so that the hydrogen could be more strongly adsorbed.

Piezoelectric elements are energy transformation devices that are capable of transforming mechanical energy into electricity and vice versa. They are found in useful applications such as the production and detection of sound, generation of high voltages, electronic frequency generation, and so on. In our study, a piezoelectric element, which is a thin slab was buried inside the sorbent. Under hydrogen pressure, charges will be generated and accumulate at surface of the element in response to the applied mechanical stress. The electrical charge created at the element surface under static hydrogen pressure can be estimated by [16]

$$Q = d_{33}PS \quad (1)$$

where  $Q$  is the electrical charge,  $d_{33}$  is the piezoelectric charge constant,  $P$  is the hydrogen

pressure, and  $S$  is the surface area upon which hydrogen pressure is exerted. As nickel oxide is non-conductive, the electric field can be preserved inside the material and the induced increase of adsorption could be expected.

## Experimental

### Synthesis of Porous Nickel Oxide

Porous nickel oxide used in this study was prepared following previously developed techniques. 13.19 g  $\text{NiCl}_2 \cdot 6\text{H}_2\text{O}$ , 32.01 g sodium dodecyl sulfate (SDS), 100 g urea and 60 ml DI water were mixed together and stirred at 40 °C for 1 h to obtain a transparent solution. The solution was then transferred to an 80 °C oil bath and kept for 6 h. The obtained slurry was cooled and filtered and then dried at 120 °C overnight. The solid were ground and washed several times with ethanol to remove the surfactant. The final product was dried and calcined at different temperature for desired time to obtain porous oxides. The final products were denoted as NiO-SDS.

### Characterization

The surface area and micropore volume were measured with a Micromeritics ASAP2000 instrument using nitrogen adsorption at liquid nitrogen temperature (77 K). The samples were evacuated by heating at 200°C under vacuum for 12 hours before testing. X-ray diffraction (XRD) was carried out using a Scintag XDS2000 powder diffractometer at a scan rate of 0.08 °/s with Cu radiation at 45 kV, 35 mA. A Hitachi S-4700 field emission-scanning electron microscope (FE-SEM) was used to examine the microstructure of the samples.

### Hydrogen Adsorption Measurement

Hydrogen adsorption measurements at 0-140 bars were carried out with a volumetric sorption measurement instrument (PCT-Pro 2000, Hy-Energy, LLC). The experimental setup is illustrated in Figure 1. Sorbent and a piezoelectric element were placed inside a glass container, which was capped by a paper filter and put inside the stainless sample holder to prevent the generated charges from spreading out. The piezoelectric element was a PMT-PT slab purchased from Morgan Electroceramics with a dimension of  $5 \times 5 \times 1$  mm. The positive side of the slab was covered by a  $\text{BaTiO}_3$  thin film to ensure the generation of only negative charges. The  $d_{33}$  value of this kind of material is in a range of 1200-2000 pC/N [17].

Prior to the test, the sample were dried in an oven at 105 °C for 12 h and then moved into the sample holder and evacuated at 100 °C for 2 h to ensure the removal of any contaminations on the sample surface. Around 300 mg sample was used in each run. Ultrapure (99.99999%) hydrogen and helium gases were used for all calibrations and measurements. All the adsorption measurements were conducted under room temperature ( $22 \pm 0.8$  °C). A blank test was also performed to exclude possible adsorption of hydrogen on the inner wall of the sample holder.

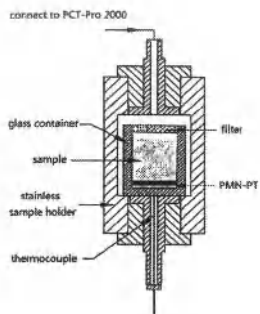


Figure 1 Experimental setup for hydrogen adsorption measurement.

## Results and Discussion

### Characterization of Porous Nickel Oxides

The adsorption isothermals of NiO-SDS calcined at 300 °C and 360 °C for various time are shown in Figure 2a. All the samples prepared preserved mesoporous characteristic. The corresponding pore size distributions calculated by BJH desorption are shown in Figure 2b. The NiO-SDS calcined at lower temperature presented to have narrower pore size distribution which concentrated around 4 to 5 nm. With the calcinations temperature increased to 360 °C, the pores were clearly widened and the pore size distribution was enlarged.

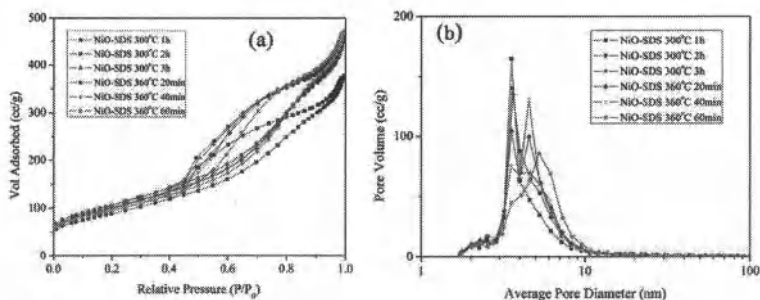


Figure 2 (a) Nitrogen adsorption/desorption isotherms and (b) pore size distribution (calculated by BJH desorption) of nickel oxides.

Surface area and pore size properties of calcined products were summarized in Table 1. The BET surface area of NiO-SDS increased with increase of calcination time from 1 hour to 2 hours at 300 °C and further calcination caused negligible enhancement on the total surface area. At such

temperature, the decomposition of Ni(OH)<sub>2</sub> slowly developed and the pore skeleton generated was very stable. With the calcinations temperature increased from 300 °C to 360 °C, the total surface area dropped and longer heating time resulted in lower surface area. Obviously, the decomposition of Ni(OH)<sub>2</sub> took place too fast at such temperature and the pore structure collapsed upon heated. And as the calcinations proceeded longer, the pore size was enlarged and the small pores began to be sintered, as observed that the pore diameter increased to 8 nm for 1 hour heating at 360 °C.

Table 1 Surface properties of calcined nickel oxides

Samples	BET surface area (m <sup>2</sup> /g)	Average pore diameter (nm)	Pore volume (cc/g)
NiO-SDS 300 °C 1h	318.29	6.95	0.553
NiO-SDS 300 °C 2h	382.23	7.08	0.677
NiO-SDS 300 °C 3h	382.56	7.08	0.677
NiO-SDS 360 °C 20min	361.82	7.47	0.675
NiO-SDS 360 °C 40min	357.57	7.48	0.668
NiO-SDS 360 °C 60min	341.25	8.09	0.689

XRD analysis was used to confirm if the hydroxides were totally transformed into oxides. As shown in Figure 3, the hydroxide decomposition was not completed after 1 hour heating at 300 °C. This was identified from a small remaining peak of nickel hydroxide hydrate at around 23°. Total decomposition was achieved at 300 °C after 3 hours. A higher temperature of 360 °C resulted in complete calcination even for 20 minutes duration time.

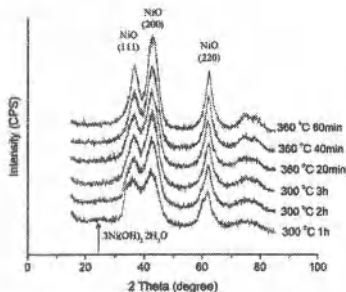


Figure 3 XRD patterns of nickel oxide.

Figure 4 shows the FE-SEM images of the nickel oxide calcinated at 300 °C for 3h. Uniform crystals can be observed.

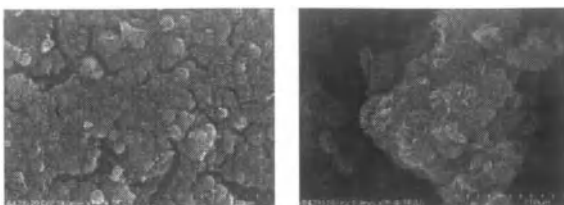


Figure 4 FE-SEM images of porous nickel oxide (NiO-SDS 300 °C 3h).

#### Hydrogen Adsorption Measurement

For better results, here we chose the nickel oxide with the highest surface area (NiO-SDS 300 °C 3h) for hydrogen storage test. Hydrogen adsorption isotherms at room temperature for porous NiO and NiO with PMN-PT are shown in Figure 5. The porous nickel oxide had a total hydrogen capacity of about 0.08 wt % at 135 bar. The shape of the adsorption curve was almost linear, indicating a further increase in capacity could be obtained at a pressure >135 bar. The results also showed that the hydrogen uptake had been remarkably enhanced to 0.11 wt % at 135 bar in the presence of PMN-PT, which was about 37.5% increase. It should be noted that the PMN-PT alone had zero adsorption at the same conditions. Such significant enhancement was due to the effect of electric field on nickel oxide.

Physisorption played the most important role in this process. Negative charges created would stay around the surface of PMN-PT and work as the source of electric field. Electric cloud of both sorbent and hydrogen molecule could subsequently be polarized and form a stronger interaction. On the other hand, nickel oxide was said to have relatively weak catalytic effect on hydrogen storage comparing to metal nickel [18]. By embedding the piezoelectric material into the ionic adsorbent, the negative charges generated could charge the nearby catalytic sites. Dissociation of hydrogen would involve charge transfer between the dissociated hydrogen and the charged site to form hydrogen ions ( $H^+$  or  $H^-$ ). These ions could easily diffuse into the porous nickel oxide under electric field, resulting in enhanced catalytic effect. Moreover, it is noted that the magnitude difference between the two lines continuously increased from 0 to 60 bar and then remained almost constant at pressures higher than 60 bar. This implies there was a saturation point from which further increase of the electrical strength has no effect on the hydrogen adsorption.

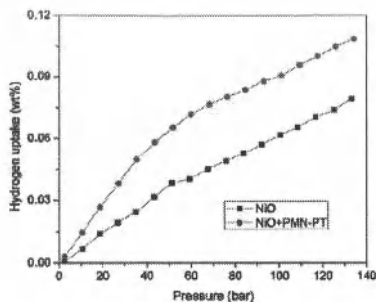


Figure 5 Hydrogen uptake isotherms on porous nickel oxide

### Conclusions

Porous nickel oxides were synthesized utilizing sodium dodecyl sulfate as the growth templates and the calcination temperature and time were varied for an optimized result. Taking the sample with the highest surface area as sorbent, we demonstrated that placing a piezoelectric element inside nickel oxide sorbent could significantly increase hydrogen adsorption. 37.5% uptake increase was observed at 135 bar at room temperature. The increase is attributed to a stronger interaction between hydrogen and host induced by negative charges that are generated at the surface of piezoelectric element under hydrogen pressure. Enhanced catalytic effect of nickel oxide under electric field could be an important factor on increased adsorption.

### Acknowledgement

This work was supported by U.S. Department of Energy's Hydrogen Program. (Award Number DE-FC36-05GO15003)

### Reference

- [1] A. Berman, R. K. Karn, and M. Epstein. "Steam Reforming of Methane on a Ru/Al<sub>2</sub>O<sub>3</sub> Catalyst Promoted with Mn Oxides for Solar Hydrogen Production," *Green Chem.*, 9(2007), 626-631.
- [2] V. Demidouk, V. Ravi, J. O. Chae, D. Y. Lee, and T. G. Jung, "Pt-Al<sub>2</sub>O<sub>3</sub> Catalyst and Discharge Plasma Pre-treatment Techniques for Enhancing Selective Catalytic Reduction of Nitrogen Oxides: A Comparative Study," *React. Kinet. Catal. L.*, 85(2005), 239-244.
- [3] A. Hadi, and I. I. Yaacob, "Synthesis of PdO/CeO<sub>2</sub> Mixed Oxides Catalyst for Automotive Exhaust Emissions Control," *Catal. Today*, 96(2004), 165-170.
- [4] Lian, Y. X.; Wang, H. F.; Zheng, Q. X.; Fang, W. P.; Y. Q. Yang, "Effect of Mg/Al Atom Ratio of Support on Catalytic Performance of Co-Mo/MgO-Al<sub>2</sub>O<sub>3</sub> Catalyst for Water Gas

- Shift Reaction," *J. Nat. Gas Chem.*, 18(2009), 161-166.
- [5] I. V. Mishakov, E. V. Ilyina, A. F. Bedilo, and A. A. Vedyagin, "Nanocrystalline Aerogel VOx/MgO as a Catalyst for Oxidative Dehydrogenation of Propane," *React. Kinet. Catal. Lett.*, 97(2005), 355-361.
- [6] W. M. Yeoh, K. Y. Lee, S. P. Chai, K. T. Lee, and A. R. Mohamed, "Synthesis of High Purity Multi-walled Carbon Nanotubes over Co-Mo/MgO Catalyst by the Catalytic Chemical Vapor Deposition of Methane," *New Carbon Mater.*, 24(2009), 119-123.
- [7] Y. H. Hu, and E. Ruckenstein, "Effect of Pre-treatments on Hydrogen Storage in Li<sub>3</sub>N-based Materials," *Adv. Catal.*, 48(2004), 297-301.
- [8] N. V. Mozharova, V. V. Pronina, A. V. Ivanov, S. A. Shoba, and A. M. Zagurskii, "The Formation of Magnetic Ferric Oxides in Soils over Underground Gas Storage Reservoirs," *Eurasian Soil Sci.*, 40(2007), 636-648.
- [9] X. P. Dai, R. J. Li, C. C. Yu, and Z. P. Hao, "Unsteady-State Direct Partial Oxidation of Methane to Synthesis Gas in a Fixed-Bed Reactor Using AFeO<sub>3</sub> (A=La, Nd, Eu) Perovskite-Type Oxides as Oxygen Storage" *J. Phys. Chem. B*, 110(2006), 22525-22531.
- [10] A. Lari, A. Khodadadi, and Y. Mortazavi, "Semiconducting Metal Oxides as Electrode Material for YSZ-based Oxygen Sensors," *Sens. Actuators B*, 139(2009), 361-368.
- [11] G. Korotcenkov, "Metal Oxides for Solid-State Gas Sensors: What Determines Our Choice?" *Mater. Sci. Eng. B* 139(2007), 1-23.
- [12] X. Hu, B. O. Skadchenko, M. Trudeau, and D. M. Antonelli, "Hydrogen Storage in Chemical Reducible Mesoporous and Microporous Ti Oxides" *J. Am. Chem. Soc.*, 128(2006), 11740-11741.
- [13] Z. P. Guo, L. Yuan, K. Konstantinov, Z. G. Huang, and H. K. Liu, "Preparation of Spherical Clusters of Metal Oxide Nanorods and Their Hydrogen Storage Behavior," *Mater. Lett.*, 60(2006), 3891-3894.
- [14] J. E. Bushnell, P. R. Kemper, P. Maitre, and M. T. Bowers, "Insertion of Sc<sup>+</sup> into H<sub>2</sub>: The First Example of Cluster-Mediated  $\sigma$ -Bond Activation by a Transition Metal Center" *J. Am. Chem. Soc.*, 116(1994), 9710-9714.
- [15] X. He, and D. Antonelli, "Recent Advances in Transition Metal Containing Mesoporous Molecular Sieves" *Angew. Chem., Int. Ed.* 41(2001), 214-229.
- [16] J. van Randerat, and R. E. Settingington, *Piezoelectric Ceramics* (London, UK: Mullard Ltd, 1974), 96.
- [17] <http://www.morganelectroceramics.com/piezomaterials/pzmat4a.html>.
- [18] A. Borgschulte, R. J. Westerwaal, J. H. Rector, B. Dam, and R. Griessen, "Hydrogen sorption mechanism of oxidized nickel clusters," *Appl. Phys. Lett.*, 85(2004), 4884-4886.

## **NANOCRYSTALLINE CdS THIN FILMS PREPARED BY VACUUM EVAPORATION**

Shadia J. Ikhmayies

Al Isra University; Faculty of Information Technology, Department of Basic Sciences-Physics;  
Amman, 16197, Jordan.

**Keywords:** II-VI Semiconductors, CdS/CdTe solar cells, heterojunctions, nanocrystallites, thin films.

### **Abstract**

Nanocrystalline CdS thin films were prepared by vacuum evaporation on glass substrates at ambient temperature. The films were characterized by recording and analyzing their transmittance, X-ray diffraction (XRD) patterns, scanning electron microscope (SEM) images and Energy dispersive X-ray (EDAX) spectra. X-ray diffractograms revealed that the material is nanocrystalline with predominant cubic crystal structure and preferential orientation along (1 1 1) plane. SEM micrographs confirmed the nanostructure of the material and showed uniform and well covered surfaces. EDAX reports revealed that the films are cadmium rich and contain oxygen. The first derivative of the absorbance was used to estimate the effective bandgap energies of the nanocrystallites and the hyperbolic band model was used to estimate their radii. The results were compared with those obtained by XRD and SEM measurements.

### **Introduction**

CdS thin films are of considerable interest as they can be used in fabrication of solar cells and other opto-electronic devices. In particular, heterojunction solar cells with a narrow band gap base and wide band gap window have been investigated in an attempt to develop efficient, stable and low-cost solar cells [1]. The CdS quantum dot embedded in a glass matrix is one of the well-known quantum dot systems and its electronic and luminescent properties have been studied extensively [2]. Three-dimensional confinement of carriers within the quantum dots leads to the blue shift of the optical band-gap and to modification of many properties of semiconductor material [3]. It has been argued that in these semiconductor nanoparticles the hyperbolic band model gives a better fit to the observed quantum size effect as compared to the effective mass approximation [4].

There are different ways to synthesize CdS nanoparticles such as colloidal particulates [5], chemical deposition [6], sol-gel [7], spray pyrolysis [8], chemical bath deposition [3], vacuum-evaporation [9], etc. In the present work, vacuum evaporation technique has been chosen for the deposition of nanocrystalline CdS thin films as it is simple compared with other new and sophisticated techniques.

Most studied nanocrystalline semiconductors belong to the II-VI group as they are relatively easy to synthesize and generally prepared as particulates or in thin film form. Among II-VI compounds, CdS is one of the most studied materials. For example, Némec et al. [3] reported on the control of nanocrystal sizes in CdS nanocrystalline films prepared by ammonia-free chemical bath deposition technique. Datta et al. [10] achieved size tunability of thiophenol capped CdS nanoparticles (NPs) by controlling the temperatures at the time of synthesis. In this work CdS

nanocrystallites were produced by vacuum evaporation on glass substrates at ambient temperature. The grain size was estimated by using XRD diffractograms, SEM micrographs, and first derivative with the hyperbolic model. The obtained values from these different methods are compared and discrepancies are explained.

### Experimental Part

Undoped CdS thin films were deposited by vacuum evaporation at ambient temperature on glass substrates of dimensions ( $6 \times 2.6 \times 0.1 \text{ cm}^3$ ) in a high vacuum system ( $\sim 10^{-5}$  mbar) provided with a Turboe pump. The evaporation rate was about  $10 \text{ \AA/s}$  and it was measured by a cooled quartz crystal monitor. The distance between the source and the substrate was about 30 cm. Films of thickness 50-495 nm were produced through different individual evaporations.

The transmittance of the films was measured by using a double beam Shimadzu UV 1601 (PC) spectrophotometer with respect to a piece of glass similar to the substrates in the wavelength range 300-1100 nm. The thickness of the films was estimated from the interference maxima and minima in the transmittance by using the method of Alvin [11]. X-ray measurements were recorded by a Philips PW1840 Compact X-ray diffractometer system with  $\text{Cu K}\alpha$  ( $\lambda = 1.5405 \text{ \AA}$ ). The SEM micrographs were taken by a FEI scanning electron microscope (Inspect F 50), which was supplied by energy dispersive analysis by X-rays (EDAX), so the compositional analysis of the films was performed by the same system.

### Results and Discussion

Fig.1 displays the X-ray diffractograms of two CdS films with different thickness. As the figure shows, the structure is mainly identified as zinc blende, where the characteristic lines of the cubic phase C(1 1 1), C(2 2 0), C(3 1 1) and C(2 2 2) are evident in the diffractogram. The C(1 1 1) peak at  $2\theta$  about  $26.2^\circ$  is overlapped by a broad band produced by the amorphous glass substrate. Němec et. al. [3] says that cadmium sulfide nanocrystallites tend to crystallize in cubic (zinc-blende) structure unlike the bulk CdS which is usually hexagonal (wurtzite). But the diffractogram also shows some lines of the hexagonal phase, which are the H(1 0 0), H(1 0 1) and the H(0 0 2) lines. On the other hand it is known that the peak produced by the C(1 1 1) crystalline planes of the cubic CdS and that of the H(0 0 2) crystalline planes of the hexagonal structure coincide within 1 per cent. As the figure shows, the C(1 1 1) is the preferential orientation for crystal growth, but it is stronger and narrower in the case of the 300 nm film, indicating that the grain size in this film is larger.

The grain size was calculated by using Scherrer formula and the line C(1 1 1) in the XRD pattern of the film with thickness 300 nm, where it has the largest intensity.

$$d = \frac{\lambda}{D \cos \theta} \quad (1)$$

where  $d$  is the grain size (diameter of the nanocrystallites),  $\lambda$  is the X-ray wavelength used,  $D$  is the angular line width of the half-maximum intensity and  $\theta$  is Bragg angle. The grain size was found to be about 15 nm for the crystallites grown in this direction, or the average radius of the nanocrystallites is about 7.5 nm. It is necessary to remind by the fact that, lines of smaller intensity give smaller values of  $d$  in both films.

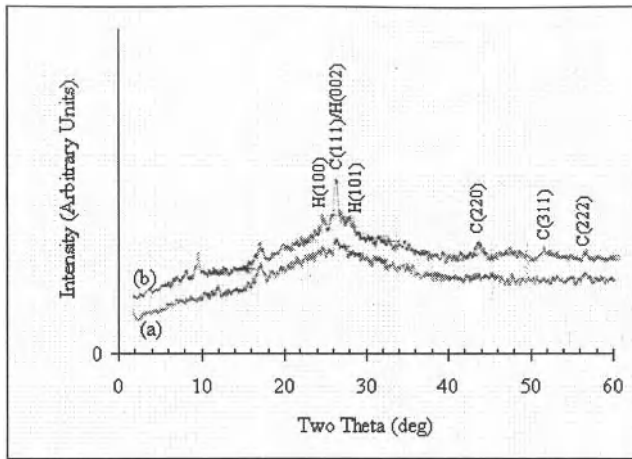
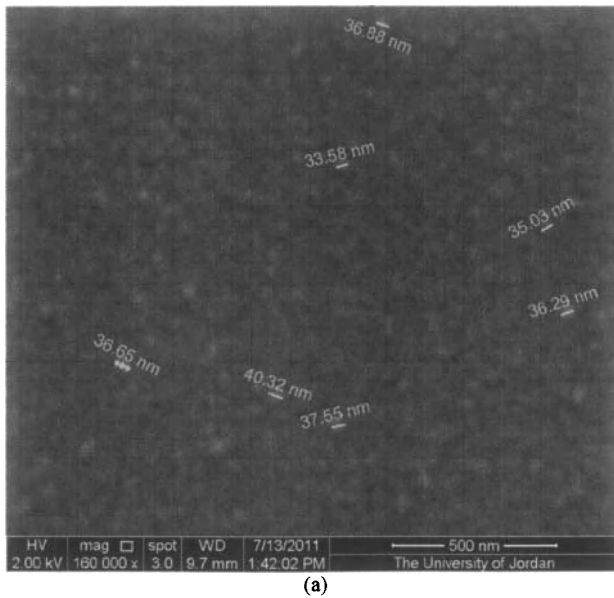
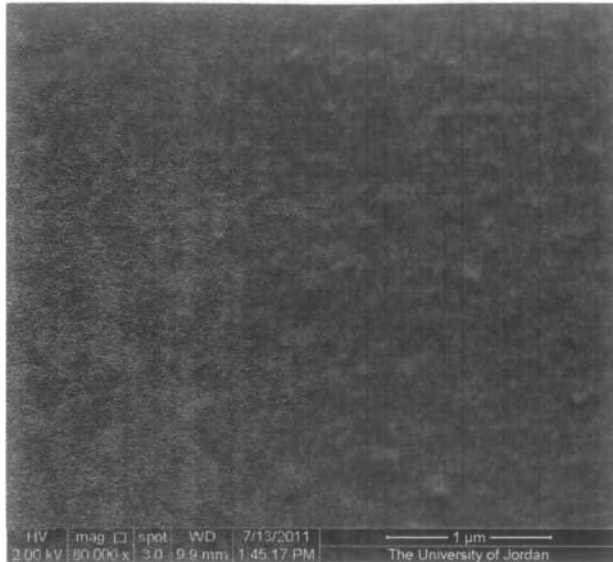


Figure.1 X-ray diffractogram of vacuum evaporated CdS thin films of thickness a) 100 nm. b) 300 nm.



(a)



(b)

Figure.2 SEM micrographs of vacuum evaporated CdS thin films with thickness a)  $t = 400$  nm. b)  $t = 100$  nm.

Fig.2 depicts the SEM micrographs for two films of thickness 100 and 400 nm. The images show uniform and close-packed films with complete coverage of the substrates. The micrograph of the thicker film shows larger grain size than the thinner one. The grain size was estimated for seven nanocrystallites randomly in the image of the 400 nm film, and the average grain size obtained by this method is about  $36.57 \pm 2.10$  nm, which gives an average radius of about 18.0 nm.

Fig.3 shows a typical EDAX pattern for the film of thickness 100 nm beside a SEM image to show the position where the compositional analysis was performed. It is found that the ratios of Cd: S: O concentrations in the film are 45.33: 36.30: 18.37. This means that the CdS films are Cd rich and the ratio of Cd to S is 1.25. This result is consistent with the findings of Nanda et. al. [12] who showed that CdS nanoparticles have excess Cd, the amount of which increases on decreasing the size. It is known that excess Cd can produce acceptor states within the gap of CdS. These states together with those originating from quantum size effect will form a continuum of localized states near the valence band edge [12]. The presence of oxygen in the films is because of the long exposure to atmosphere.

The transmittance curves which are recorded at room temperature for five values of film thickness are shown in Fig.4. The transmittance is as high as 100% for films thicker than 100 nm for values of wavelength larger than the cut-off value for CdS which is about 513 nm. Films of thickness more than 100 nm showed interference maxima and minima, while thinner films didn't show this, because the minima and maxima are more separated in this case. The sharpness of the absorption edge decreases with decreasing film thickness, which is evidence of the presence of

nanocrystallites. These results are in excellent agreement with the results obtained by Sahay et al [13] that for sulfide films deposited on the glass substrate; nano-confined effects begin to play substantial role in the optical spectra near the band edge.

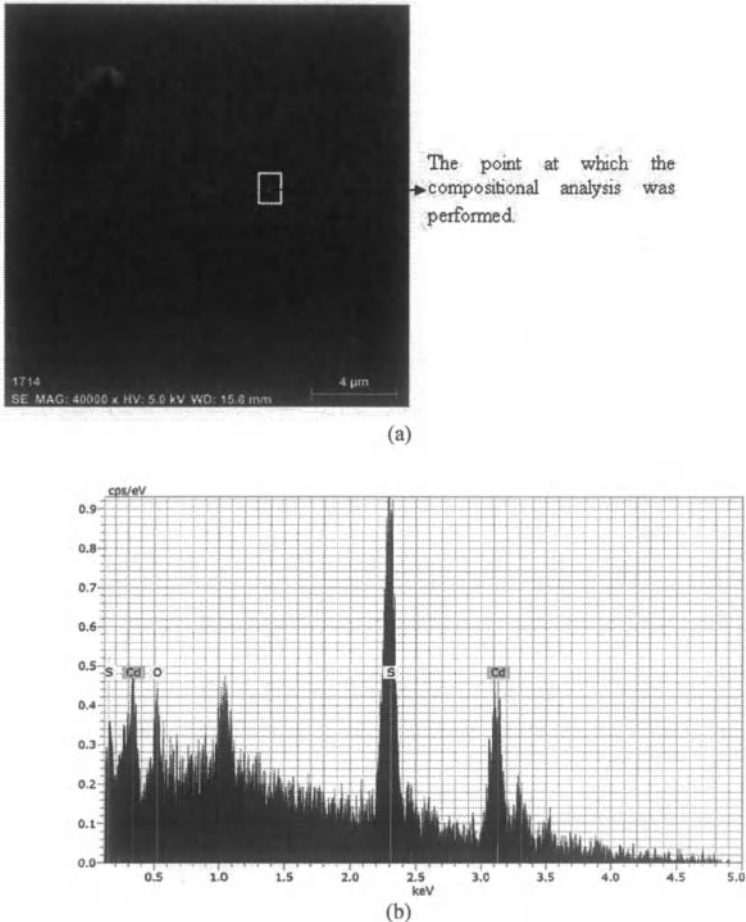


Figure.5 a) The EDAX pattern for the vacuum evaporated CuS film of thickness 100 nm. b) The SEM image of the film and the position where the compositional analysis was performed.

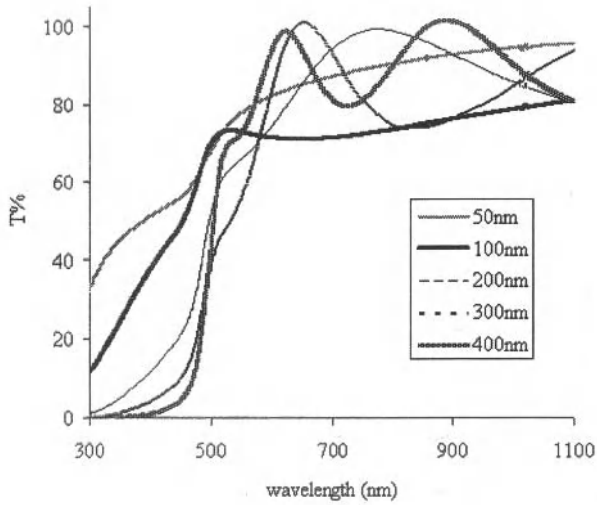


Figure.4 Transmittance curves of vacuum evaporated CdS thin films of different values of film thickness.

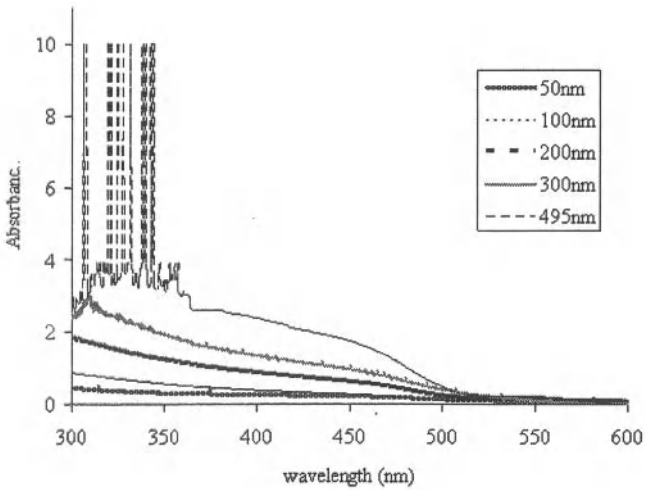


Figure.5 The absorbance curves of vacuum evaporated CdS thin films of different values of film thickness.

The absorbance curves for CdS films of different thickness are displayed in Fig.5 where the absorbance is high in the UV region and low for values of wavelength larger than the cut-off wavelength of CdS. These curves show that the absorption edge is not sharp, but it is graded. This phenomenon is evidence on the presence of nanocrystallites or quantum dots with different sizes and then the presence of different values of the bandgap energies [14]. To confirm this expectation, the first derivative of the absorbance curves was plotted in Fig.6.

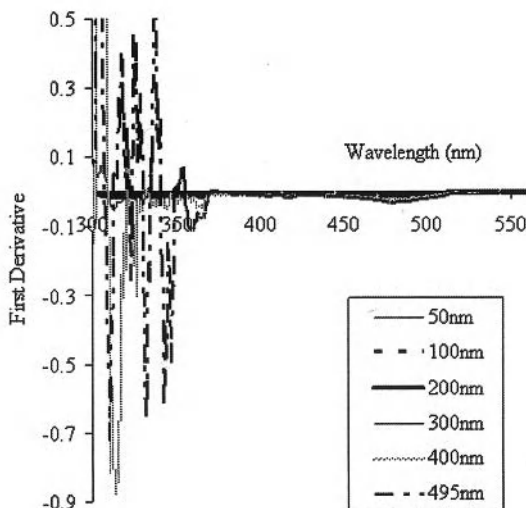


Figure.6 The first derivative of the absorbance curves of CdS thin films of different thickness.

The minima of the first derivative for the films of thickness 300 and 400 nm were displayed in tables I and II respectively and used to find the optical bandgap energies. As we see there is a wide range of bandgap energies that is; 2.594-3.930 eV and 2.594-4.113 nm for the films of thickness 300 and 400 nm respectively. The increase in the bandgap energy could be explained as follows; the nanoparticles have the crystalline structure of their bulk counter parts and hence are characterized by the fully occupied valence band and an empty conduction band separated by the energy gap ( $E_g$ ). However, the charge carriers in these bands e.g., the electrons in the conduction band and holes in the valence band experience an overall confining potential due to the finite size of these particles. As a result there will be size-dependent discrete states in the conduction and valence bands resulting in the effective enhancement of the bandgap; the so-called quantum size effect [4, 9]. It has been argued that in these semiconductor nanoparticles the hyperbolic band model gives a better fit to the observed quantum size effect as compared to the effective mass approximation [4]. So it was used in this work to estimate the size of the

nanocrystallites. The equation derived for the bandgap,  $E_{gn}$  of nanocrystallites according to [12] is:

$$E_{gn} = \left[ E_{gb}^2 + 2\hbar^2 E_{gb} \left( \frac{\pi}{R} \right)^2 / m_e^* \right]^{1/2} \quad (2)$$

where  $E_{gb}$  is the bandgap for the bulk semiconductor which equals to 2.42 eV [15],  $R$  is the particle's radius, and  $m_e^*$  is the effective electron mass. Taking  $m_e^* = 0.2 m_e$  [16] for CdS, where  $m_e$  is the mass of a free electron. The calculated values of particle's radii for the two aforementioned films are displayed in table I and II. From table I the average value of the radius is  $R \pm \Delta R = 5.2 \pm 2.8$  nm, and from table II it is  $R \pm \Delta R = 5.7 \pm 2.7$  nm. The large values of the standard deviation are due to the first value in each table which is 11.4 nm. If we look at Fig.6 we find that this minimum is very small and it could be neglected. In this case the average values with standard deviations will be  $3.9 \pm 0.4$  and  $4.3 \pm 1.0$  for the 300 and 400 nm values of film thickness respectively. So a narrow range of the nanoparticles radii is obtained by the vacuum evaporation technique. It is noticed that the nanocrystallites are smaller and have narrower size distribution in the case of the thinner film. So, decreasing film thickness results in smaller size of the nanoparticles and narrower distribution of their radii.

By comparing the average value of  $R$  in table I with the value obtained from the X-ray diffractogram of the film of thickness 300 nm, it is found that there is a considerable difference. The reason of this discrepancy is that the C(1 1 1) line of the cubic phase that was used in the calculation is overlapped with the H(0 0 2) line of the hexagonal phase, which results in increasing its intensity and hence reducing its full width at half maximum. The result of this is a larger value of the estimated grain size. The comparison between the average value of  $R$  in table II and the average value obtained from the SEM micrograph for the film of thickness 400 nm shows that the value obtained by the SEM is too much larger. This can easily be explained by saying that crystallites in the SEM micrographs are aggregates which consist of a collection of smaller particles.

Table I. Values of  $E_{gn}$  estimated from Fig.6 and the calculated values of the nanocrystallites' radii for film of thickness 300 nm.

No.	Position of the minima (nm)	$E_g = hc/\lambda$ (eV)	$R$ (nm)
1	478	2.594	11.4
2	365	3.397	4.5
3	353.5	3.508	4.2
4	337	3.670	3.9
5	325.5	3.810	3.6
6	315.5	3.930	3.4

Table II. Values of  $E_{gn}$  estimated from Fig.6 and the calculated values of the nanocrystallites' radii for film of thickness 400 nm.

No.	Position of the minima (nm)	$E_g = hc/\lambda$ (eV)	R(nm)
1	478	2.594	11.4
2	416.5	2.977	6.1
3	382	3.246	4.9
4	365	3.397	4.5
5	344	3.605	4.0
6	314	3.949	3.4
7	301.5	4.113	3.2

### Conclusions

Nanocrystalline cadmium sulfide CdS thin films were produced by vacuum evaporation on glass substrates at ambient temperature. The films were characterized by recording their XRD diffractograms, SEM observations, EDAX spectra and transmittance measurements. XRD diffractograms and SEM micrographs revealed the nanocrystalline nature of the films. EDAX spectra showed that the films are cadmium rich and that, they contain oxygen. The transmittance and absorbance curves confirmed the presence of quantum dots. The bandgap energy for the different nanocrystallites  $E_{gn}$  was estimated from the first derivative of the absorbance. These values of bandgap energy were used to calculate the particles' sizes according to the hyperbolic model. The estimated values of the optical band gap are found to be 2.594-4.113 eV, corresponding to nanocrystallites of radii 11.4-3.2 for CdS films of thickness 300 and 400 nm. These results are compared with the results obtained by XRD diffractograms and SEM images.

### Acknowledgments

I would like to thank Sameer Farrash from the physics department in the University of Jordan for producing the films by vacuum evaporation. Also I want to thank Waddah Fares Mahmoud and Azzam Karadshah from the department of geology in the University of Jordan for taking the SEM micrographs and for taking XRD diffractograms respectively.

### References

1. M. Singh, Y. K. Vijay, and B. K. Sharma, "A Variable Electron Beam and its Irradiation Effect on Optical and Electrical Properties of CdS Thin Films," *Pramana Journal of physics*, 69 (4) (2007), 631–638.
2. A. Ates, M. A. Yildirim, M. Kundakçi, and M. Yildirim, "Investigation of Optical and Structural Properties of CdS Thin Films," *Chinese Journal of Physics*, 45 (2-1) (2007), 135-141.
3. P. Němec, I. Němec, P. Nahálková, K. Knížek, P. M alý, "Ammonia-Free Chemical Bath Deposition of CdS films: Tailoring, the Nanocrystal Sizes," *Journal of Crystal Growth*, 240 (2002), 484–488.
4. K. K. Nanda, S. N. Sarangi, S. N. Sahu, S.K. Deb, S.N. Behera, "Raman Spectroscopy of CdS Nanocrystalline Semiconductors," *Physica B*, 262 (1999), 31-39.
5. V. L. Colvin, A. P. Alivisatos, J. G. Tobin, "Valence-Band Photoemission from a Quantum-Dot System," *Physical Review Letters*, 66 (21) (1991), 2786-2789.
6. R. S. Singh, and S. Bhushan, "Structural and Optical Properties of Chemically Deposited Cd(S-Se): CdCl<sub>2</sub>, Sm films," *Bull. Mater. Sci.*, 32 (2) (2009), 125–133.

7. Jialong Zhao, Kai Dou, Shaozhe Lu, Yinmin Chen, Shihua Huang, Jiaqi Yu, Weidong Xiang, and Zishang Ding, "Photoluminescence of CdS Semiconductor Nanocrystals in Sodium Borosilicate Glasses," *Journal of Materials Science Letters*, 15 (1996), 702-705.
8. I. K. Battisha, H. H. Affify, G. Abd El Fattah and Y. Badr, "Raman and Photoluminescence Studies of Pure and Sn-Enriched Thin Films of CdS Prepared by Spray Pyrolysis", *FIZIKA A*, 11 (1) (2002), 31-42.
9. Shadia J. Ikhmayies and Riyad N. Ahmad-Bitar, "Optical Properties of Nanocrystalline CdTe Thin Films," *Physica B*, 405 (2010), 3141-3144.
10. A. Datta, A. Priyam, S. N. Bhattacharyya, K. K. Mukherjea, and A. Saha, "Temperature Tunability of Size in CdS Nanoparticles and Size Dependent Photocatalytic Degradation of Nitroaromatics," *Journal of Colloid and Interface Science*, 322 (2008), 128-135.
11. Goodman M. Alvin, "Optical Interference Method for the Approximate Determination of Refractive Index and Thickness of a Transparent Layer," *Applied Optics*, 17 (17) (1978), 2779-2787.
12. K. K. Nanda, S. N. Sarangi, S. Mohanty, and S. N. Sahu., "Optical Properties of CdS Nanocrystalline Films Prepared by a Precipitation Technique," *Thin Solid Films*, 322 (1998), 21-27.
13. P. P. Sahay, R. K. Nath, and S. Tewari, "Optical Properties of Thermally Evaporated CdS Thin Films," *Cryst. Res. Technol.*, 42 (3) (2007), 275 - 280.
14. Gary Hodcs, Ana Albu-Yaron, Franco Decker, and Paulo Motisuke, "Three-Dimensional Quantum-Size Effect in Chemically Deposited Cadmium Selenide Films," *Physical Review B*, 36 (8) (1987), 4215-4221.
15. Ziaul Raza Khan, M. Zulfequar, and Mohd. Shahid Khan, "Chemical Synthesis of CdS Nanoparticles and their Optical, and Dielectric Studies," *J. Mater Sci.*, 46 (2011), 5412-5416.
16. M. Bedir, M. Öztas, Ö. F. Bakkaloğlu, and R.Ormanci, "Investigations on Structural, Optical and Electrical Parameters of Spray Deposited ZnSe Thin Films with Different Substrate Temperature," *Eur.Phys.J.B.*, 45 (2005), 465-471.

## STRUCTURE-PROPERTY CORRELATION OF $x\text{Pb}(\text{Ni}_{0.33}\text{Nb}_{0.67})\text{O}_3-(1-x)\text{Pb}(\text{Zr}_{0.31}\text{Ti}_{0.69})\text{O}_3$ BASED RELAXOR-FERROELECTRIC CERAMICS SYNTHESIZED VIA COLUMBITE PRECURSOR METHOD

B.Mallesham<sup>1</sup>, T. V. Jayaraman<sup>2</sup>, A.R.James<sup>3</sup>, D.Das<sup>1\*</sup>

<sup>1</sup>School of Engineering Sciences & Technology, University of Hyderabad, Hyderabad 500046, India

<sup>2</sup>Department of Mechanical and Materials Engineering, University of Nebraska, Lincoln 68588, United States

<sup>3</sup>Defence Metallurgical Research Laboratory, Hyderabad 500058, India

Keywords: Relaxor ferroelectrics, perovskite, pyrochlore, piezoelectric charge coefficient

### Abstract

The PNN-PZT  $x\text{Pb}(\text{Ni}_{0.3}\text{Nb}_{0.67})\text{O}_3-(1-x)\text{Pb}(\text{Zr}_{0.31}\text{Ti}_{0.69})\text{O}_3$  ( $0.2 \leq x \leq 0.6$ ) based relaxor-ferroelectric material was synthesized by columbite precursor ( $\text{NiNb}_2\text{O}_6$ ) method via conventional solid state reaction. Homogeneous mixture of required oxides and precursor was calcined at  $850^\circ\text{C}$  for 4 hrs to obtain phase pure perovskite. Pellets of PNN-PZT ceramics were sintered at  $1100^\circ\text{C}$  for 4 hrs. Phase pure perovskite structure was confirmed by the X-ray diffraction analysis. From the X-ray diffraction analysis it is also confirmed that there is a structural transformation from the rhombohedral to tetragonal with increase in PZT content and existence of morphotropic phase boundary (MPB) at  $x = 0.5$  composition. The morphology and microstructure of the sintered pellets were observed using the scanning electron microscope. P-E loop measurement shows the high remnant polarization ( $19.12 \mu\text{C}/\text{cm}^2$ ) and low coercive field ( $6.89 \text{ kV}/\text{cm}$ ) at MPB compared to all other compositions. The electromechanical planar coupling coefficient ( $k_p$ ) was measured through the resonance and anti-resonance method using the LCR meter. The piezoelectric strain coefficient ( $d_{33}$ ) measured directly using the  $d_{33}$ -meter. At  $x = 0.5$  composition the highest value of  $d_{33} = 398 \text{ pC}/\text{N}$  is obtained.

### Introduction

Lead nickel niobate (PNN) is one of the first known relaxor ferroelectrics, reported by Smolenskii and Agranovskaya in 1958, and have been extensively investigated over the years [1-2]. The phase pure PNN was prepared using the columbite precursor method by Veitch in 1983 [3]. At room temperature the PNN has the perovskite crystal structure with cubic unit cell and lattice parameter  $a = 4.03 \text{ \AA}$ . The PNN exhibits diffused phased transition around  $-120^\circ\text{C}$ . Lead zirconate titanate ( $\text{Pb}(\text{Zr}_x\text{Ti}_{1-x})\text{O}_3$  (PZT), a solid solution of lead titanate (PT) and lead zirconate (PZ), is known for its various applications such as transducers, sonars, micropositioners, rotary actuators, and pyroelectric sensors due to its outstanding ferroelectric, piezoelectric, and optoelectronic properties. Because of this reason it has been studied extensively for several decades [4]. The solid solution of normal ferroelectric and relaxor ferroelectric materials is of particular

interest during the recent years owing to their better piezoelectric and dielectric properties; among these one of the interesting material is PNN-PZT. Buyanova et. al. studied the PNN-PZT in detail and investigated morphotropic phase boundary (MPB) of the system in 1965 [5]. Piezoelectric properties of PNN-PZT was studied by Luff et. al.; and they observed their highest values at the composition 0.5PNN-0.35PT-0.15PZ [5]. Due to its enhanced piezoelectric properties and excellent response to characteristic strain it is a promising candidate for piezoelectric microactuators application.

A significant problems involved in the synthesis of the relaxor ferroelectrics are formation of pyrochlore phase ( $\text{Pb}_3\text{Nb}_4\text{O}_{14}$ ) prior to perovskite phase formation and hence their loss during the sintering process due to low melting point of lead. However conventional solid state route (columbite precursor method) is known to be a better method to synthesize phase pure perovskite [6]. In this work we synthesized the pyrochlore-free single phase PNN-PZT via columbite precursor method, characterized their physical and electrical properties, and studied the effect of crystal structure on the physical and electrical properties of the material.

## Experimental Details

### Synthesis

The powders of  $x\text{PNN}-(1-x)\text{PZT}$  ( $0.2 \leq x \leq 0.6$ ) were synthesized via columbite precursor method. The raw materials used for the synthesis were high purity (~99%)  $\text{PbO}$ ,  $\text{TiO}_2$ ,  $\text{ZrO}_2$ ,  $\text{NiO}$ , and  $\text{Nb}_2\text{O}_5$ . The nickel niobate (columbite precursor) was synthesized using  $\text{NiO}$ ,  $\text{Nb}_2\text{O}_5$  powders taken in stoichiometric proportion. Then mixing and grinding of the powders was performed for 2 h in an agate mortar. The calcination of the homogeneous mixture was carried out using an alumina crucible at 900 °C, 1000 °C, 1100 °C, and 1200 °C in a muffle furnace for 4h. Once the single phase nickel niobate has formed other oxides such as  $\text{PbO}$ ,  $\text{TiO}_2$ ,  $\text{ZrO}_2$ ,  $\text{NiNb}_2\text{O}_6$  and 2 mol.% excess lead oxide has been taken in stoichiometric proportion to obtain the PNN-PZT. Then mixing and grinding of these powders has been done for about 2 h in an agate mortar using acetone. The homogeneous mixture of the oxides has been calcined using an alumina crucible at 800 °C, 850 °C in a muffle furnace for 4 h.

The chemical reactions involved were,

Calcination at 1200 °C:



Calcination at 850 °C:



After the formation of the single phase PNN-PZT, the powders were pressed (200 MPa) into cylindrical disks of 9 mm diameter and 1 mm thickness using a hydraulic press. Subsequently the pellets were sintered in a closed alumina crucibles at 1100 °C for 4 h. During sintering an equivalent amount of lead zirconium oxide ( $\text{PbZrO}_3$ ) powder was placed around the pellets in order to suppress the lead loss from the sintered pellets [6].

## Characterization

The structural and microstructural characterization were performed using x-ray diffractometer (XRD) (Bruker D-8 advance) and scanning electron microscopy (SEM) (HITACHI S-3400N) respectively. For the electrical characterization of PNN-PZT ceramics the electrical contacts were made by using silver paste with the curing temperature  $\sim 500$  °C. Sintered pellets were polished using fine emery paper to get the flat surface. Silver paste was deposited on both sides of the pellet. Firing was performed in a furnace at 500 °C for 15 min to get good adhered electrodes. Ferroelectric hysteresis loops were recorded at room temperature using an automatic  $P$ - $E$  loop tracer from Marine India Company. In order to measure the piezoelectric properties samples were polled by applying DC electric field three times of coercive field for 30 min in a silicone oil bath at 100°C. After poling the pellets were kept in a silver foil for 24 h for the charge dissipation prior to testing. Piezoelectric charge coefficient  $d_{33}$  was directly measured using the Piezo  $d_{33}$  system (Model SS01 sensor technology limited). The electromechanical planar coupling coefficient ( $k_p$ ) was calculated using resonant and ant resonant frequencies measured using an Agilent E4980A LCR meter.

## Results and Discussion

Figure 1 shows the XRD spectra of  $x$ PNN-(1- $x$ )PZT ( $0.2 \leq x \leq 0.6$ ) sintered at 1100 °C for 4 h. The XRD patterns (Fig 1a.) clearly reveal that the structure is single phase perovskite for all the compositions. In the present study the single phase perovskite structure without pyrochlore was

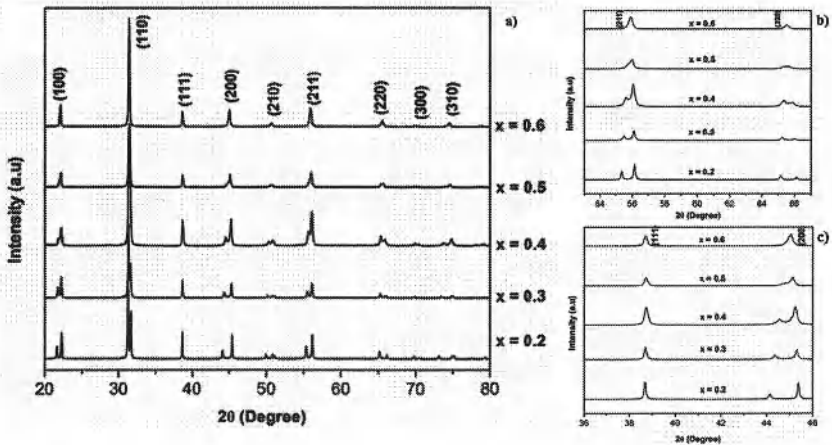


Figure 1. a) XRD patterns of  $x$ PNN-(1- $x$ )PZT ceramics sintered at 1100 °C for 4 hrs ( $0.2 \leq x \leq 0.6$ ); Enlarged x-ray diffraction patterns of b) (211), (220) and c) (111), (200) peaks

synthesized by columbite precursor method. The crystal structure of PZT at room temperature is tetragonal [6]. From the XRD spectra it can be observed that with increasing PZT content in

$x$ PNN-(1-x)PZT the broadening and splitting of peaks takes place except for the peak (111). The degree of splitting also increases with increasing PZT content. This indicates that there is a structural transformation from rhombohedral to tetragonal phase with increasing PZT content in PNN-PZT system. In order to show the structural change with decreasing PNN content, enlarged XRD reflection from (111), (200), (211), (220) peaks for all the compositions are shown in Fig 1b & 1c. At  $x = 0.5$  the broadening of peaks was observed, indicating the coexistence of rhombohedral and tetragonal phase [7]. It also evident that the splitting of peaks (200), (211), (220) started at  $x = 0.4$ , the degree of splitting increases with decrease in PNN content in the range  $x = 0.4-0.2$ . This is due to increasing tetragonal phase appearing in the PNN-PZT system with decreasing PNN content. Quantitative analysis of the XRD spectra (Rietvelt refinement) is currently underway.

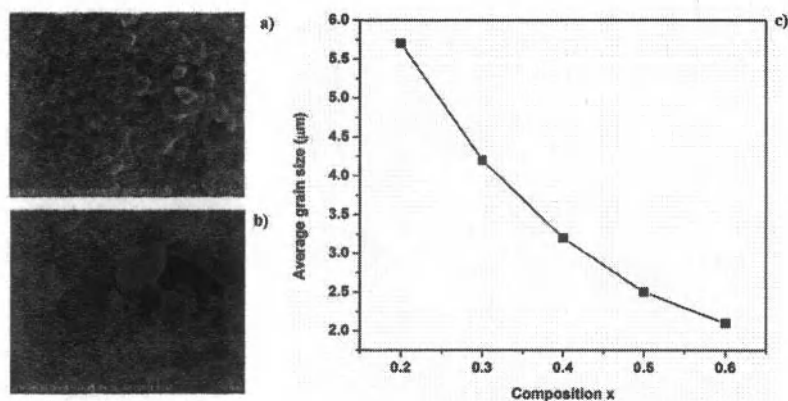


Figure 2. SEM Micrographs of: (a) 0.6PNN-0.4PZT, (b) 0.2PNN-0.8PZT ceramics, and (c) Average grain size versus composition ( $x$ ) of  $x$ PNN-(1-x)PZT ( $0.2 \leq x \leq 0.6$ ) ceramics

The SEM images of fractured surface of the samples ( $x = 0.6$  &  $0.2$ ) sintered at  $1100^\circ\text{C}$  for 4 h is shown in Fig. 2a & 2b as a representative. Since the samples are non-conductive gold was coated on the samples using the sputter coater to make it conductive. From these images it was observed that the grain growth was not uniform. Existence of pores indicates that the samples do not have high density. The morphology of most of the grains is polyhedron. The average grain size of the samples is estimated by taking the average of  $\sim 25$  grains in an image. These images clearly show that with varying PNN content the grain size and distribution varies. At higher PNN content the grain size is small or as PNN content decreases the grain size increases. Figure 2(c) shows the composition ( $x$ ) dependence of average grain size in  $x$ PNN-(1-x)PZT ceramics. Decreasing grain size with increasing PNN content ( $x$ ) is evident.

Figure 3(a) shows the  $P$ - $E$  loops of PNN-PZT ceramics measured at room temperature using  $P$ - $E$  loop tracer. The loops are symmetric and fully saturated for all compositions. Among all compositions 0.6PNN-0.4PZT exhibits a slim loop; 0.2PNN-0.8PZT exhibits a fat loop. This

indicates that as the PNN content decreases the relaxor property also decreases and the material exhibits the property closer to normal ferroelectric material (at  $x = 0.2$ ). From the  $P$ - $E$  loop

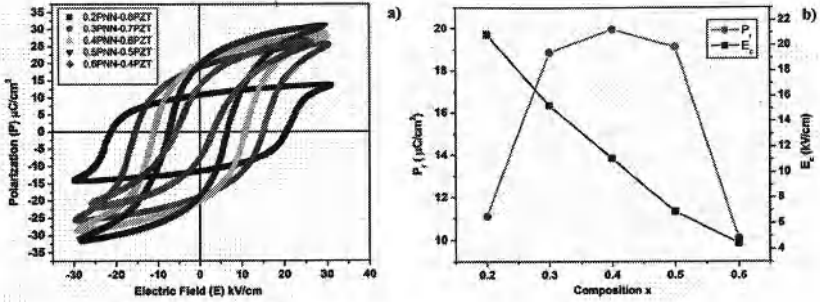


Figure 3. (a)  $P$ - $E$  loops, (b)  $P_r$  versus  $x$ , and (c)  $E_c$  versus  $x$  of the  $x$ PNN-(1- $x$ )PZT

measurements it is observed that 0.2PNN-0.8PZT has the least remnant polarization ( $P_r$ ), 0.4PNN-0.6PZT has the largest remnant polarization, and 0.5PNN-0.5PZT has the largest saturation polarization ( $P_s$ ). In comparison with all other compositions the 0.5PNN-0.5PZT exhibits smaller value of coercive field ( $E_c$ ) and larger value of remnant and saturation polarizations. This is due to the existence of MPB at this composition. At MPB the coexistence of rhombohedral and tetragonal phases leads to enhancement of possible spontaneous polarization directions to 14 [8]. Due to the enhancement of spontaneous polarization directions the long range interactions exists between the ferroelectric dipoles at MPB. Figure 3(b) shows the variation of  $P_r$ ,  $E_c$  with  $x$ . It is evident that remnant polarization  $P_r$  increases initially, reaches maximum at  $x = 0.4$  and subsequently decreases with further increase in  $x$ ; while coercive field  $E_c$  decreases with increase in PNN content. The estimated  $P_r$  values are less than the reported results of this system [5, 8]. This may be due to the low density (presence of pores) of the sintered samples. The presence of pores causes high dielectric loss in the samples [4]. Due to high dielectric loss lower polarization is expected for materials with porosity.

To measure the electromechanical coupling coefficient of PNN-PZT ceramics the resonance and anti-resonance method is used. Resonant anti resonant frequencies are recorded using an Agilent E4980A Precision LCR Meter. The value of  $k_p$  is determined using the relation given below. From the measured  $k_p$  values it was observed that for  $x$ PNN-(1- $x$ )PZT ( $0.2 \leq x \leq 0.6$ ) ceramics it increases initially from  $x = 0.2$ - $0.5$ , peaking at  $x = 0.5$  and then decreases at  $x = 0.6$ . The maximum value of  $k_p$  (33.8%) is obtained at  $x = 0.5$  which is the MPB composition of the PNN-PZT samples that leads to enhancement of coupling coefficient. The reason for enhancement in  $k_p$  at MPB is due to the existence of larger domain reorientation directions. Because of the larger reorientation directions the piezoelectric ceramics are easily poled compared to the material which does not have MPB.

$$k_p = \sqrt{\frac{2.51(f_a - f_r)}{f_a}} \quad (3)$$

where,  $f_a$  = anti-resonance frequency,  $f_r$  = resonance frequency

The piezoelectric charge coefficient ( $d_{33}$ ) is measured using Piezo  $d_{33}$ -meter (Sensor Tech SS01) directly. The  $d_{33}$  reaches a maximum value of 398 pC/N at  $x = 0.5$ , due to the location of MPB at

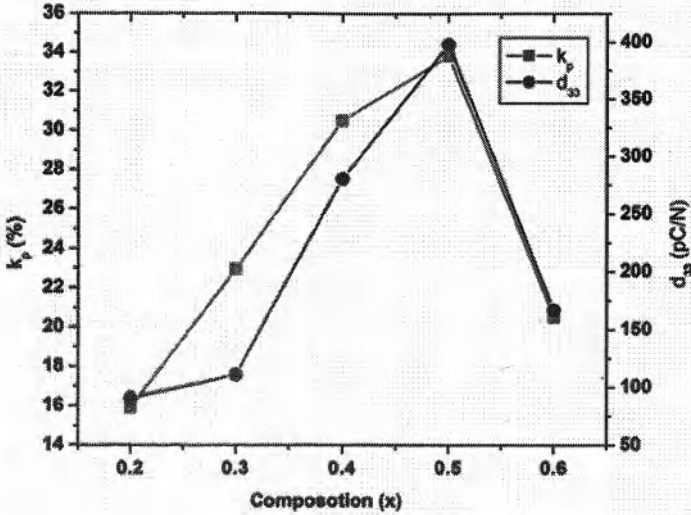


Figure 4. Variation of  $k_p$  and  $d_{33}$  with composition ( $x$ ) in  $x$ PNN-(1- $x$ )PZT ceramics

this composition. Figure 4 shows the variation of  $k_p$ ,  $d_{33}$  with  $x$ . The variation in  $k_p$ ,  $d_{33}$  with structural changes is similar to the data reported earlier [7]. Both  $k_p$  and  $d_{33}$  increases initially with  $x$  and then decreases with increase of PNN content. But, the estimated  $k_p$ ,  $d_{33}$  are less than the reported values. This is mainly because of the improper poling of the samples due to low density, in homogeneity in the microstructure. The samples with low density do not withstand a field of 3-4 times the coercive field ( $E_c$ ) during poling. So poling has been done at an applied field of less than 3 times the coercive field. But, in order to obtain a properly poled sample poling has to be done at an applied field of 3-4 times the  $E_c$ .

### Conclusions

Relaxor ferroelectric ceramics  $x$ PNN-(1- $x$ )PZT ( $0.2 \leq x \leq 0.6$ ) were synthesized via columbite precursor method. Phase pure perovskite structure was confirmed by X-ray diffraction analysis. From the X-ray diffraction analysis it is also confirmed that there is a structural transformation from the rhombohedral to tetragonal phase with increase in PZT content and existence of morphotropic phase boundary (MPB) at  $x = 0.5$ . The morphology and microstructure of the sintered pellets were observed using the SEM. From the SEM micrographs it is observed that the grain growth is non-uniform, morphology is polyhedron. The average grain size increases with increasing PZT content. P-E loop measurements show high remnant polarization ( $\sim 19 \mu\text{C}/\text{cm}^2$ )

and low coercive field ( $\sim 7$  kV/cm) at MPB compared to all other compositions. At  $x = 0.5$  composition the highest value of  $d_{33} \sim 398$  pC/N and  $k_p \sim 33\%$  is obtained.

### Acknowledgement

The authors acknowledge the financial support from the School of Engineering Sciences and Technology at the University of Hyderabad. The help extended by Mr. Ajit kumar of Composites and Ceramics Research Group at DMRL Hyderabad and Ms. Mamatha and Mr. Ashok of Physics Department at the Vardhaman Engineering College, Hyderabad in carrying out the piezoelectric measurements is greatly appreciated.

### References

1. G A Smolenskii, and A I Agranovskaya, "Dielectric polarization of and losses of some complex compounds, Sov. Phys. Tech. Phys. (1958) 1380.
2. Edward F. Alberta, Amar S. Bhalla, "Low-temperature properties of lead nickel-niobate ceramics," *Materials Letters*, 54 (2002), 47–54.
3. L C Veitch, Processing lead nickel niobate and its dielectric properties, B S Thesis, The Pennsylvania State University, University park, PA (1983)
4. L.B. Kong, T.S. Zhang, J. Ma, F. Boey, "Progress in synthesis of ferroelectric ceramic materials via high-energy Mechanochemical technique," *Progress in Materials Science*, 53 (2008), 207–322.
5. Sandeep Mahajan, Chandra Prakash, O.P. Thakur, "Piezoelectric properties of  $0.5(\text{PbNi}_{1/3}\text{Nb}_{2/3})\text{O}_3-0.5\text{Pb}(\text{Zr}_{0.32}\text{Ti}_{0.68})\text{O}_3$  ceramics prepared by solid state reaction and mechanochemical activation-assisted method," *Journal of Alloys Compounds*, 471 (2009), 507–510.
6. Naratip Vittayakorn, Gobwute Rujjanagul, Xiaoli Tan, Meagen A. Marquardt, and David P. Cann, "The morphotropic phase boundary and dielectric properties of the  $x\text{Pb}(\text{Zr}_{1/2}\text{Ti}_{1/2})\text{O}_3-(1-x)\text{Pb}(\text{Ni}_{1/3}\text{Nb}_{2/3})\text{O}_3$  perovskite solid solution," *J. Appl. Phys.*, 96 (2004), 5103-5109.
7. Ruijuan Cao, Guorong Li, Jiangtao Zeng, Suchuan Zhao, Liaoying Zheng, and Qingrui Yin "The piezoelectric and dielectric properties of  $0.3\text{Pb}(\text{Ni}_{1/3}\text{Nb}_{2/3})\text{O}_3-x\text{PbTiO}_3-(0.7-x)\text{PbZrO}_3$  ferroelectric ceramics near the morphotropic phase boundary," *J. Am. Ceram. Soc.*, 93 (2010), 737–741.
8. B.-J. Fang, Q.-B. Du, L.-M. Zhou, Y.-H. Shen, and J. Wang, "Development of perovskite structure and electrical properties of  $\text{Pb}(\text{Zr}_{1/2}\text{Ti}_{1/2})\text{O}_3\text{-Pb}(\text{Ni}_{1/3}\text{Nb}_{2/3})\text{O}_3$  system," *Eur. Phys. J. Appl. Phys.*, 51 (2010), 10301-10307.

## **THE CHARACTERISTICS OF OPTICAL RECORDING MEDIA AFFECTED BY THE ACCELERATING AGING TEST**

Der-Ray Huang<sup>1</sup>, Jing-Xuan Lin<sup>1</sup>, Tzu-Chien Lin<sup>1</sup>, Jiin-Sen Chen<sup>2</sup>, Ming-Yu Lin<sup>2</sup>, Jack Tsai<sup>2</sup>,

<sup>1</sup>Graduate Institute of Opto-Electronics, National Dong Hwa University, Taiwan  
No. 1, Sec. 2, Da Hsueh Rd., Shoufeng, Hualien 97401, Taiwan

<sup>2</sup>Electro-Optics Laboratories, Industries Technology Research Institute, Taiwan  
No. 195, Sec. 4, Chung Hsing Rd., Chutung, Hsinchu 31040, Taiwan

Keywords: Recording media, DVD-R

### **Abstract**

In this paper, some DVD-R discs have been selected for long time light exposure test and high temperature and humidity test. Generally, recordable media under long time light exposure maybe be defected seriously. If we use Jitter value 8% as a reference to determine the life time of DVD-R samples, some discs defect after 5 hours of light exposure while some discs can endure over 25 hours. Also if we use reflectivity 45% to determine the life time, some discs defect after 30 hours light exposure while some discs can endure over 40 hours. From our results, the good samples show good characteristics of PI error. The absorption spectrum of recordable media is a good reference to justify the quality of dye media. These results can be used to estimate the life time of recordable discs.

### **Introduction**

In general, the life time of DVD-R with a layer of organic dye recording layer is required for preservation in decades. In addition to optical characteristics and thermal properties, we still need to consider the stability of the dye in recording media. The presentation of the color on organic dye is not only related to the material's property but also related to the light exposure. In this study, we focus on the absorption characteristics and reflectivity of organic dye in optical recording layer after light exposure. The optical properties of discs depend on the functional groups and molecular structure [1]. According to "DVD Specifications for Recordable Disc (DVD-R)", the reflectivity should higher than 40%. From measured reflectivity, we can confirm that the important issue is whether dye be affected by light exposure or not. Because each specific functional group absorbs the specific spectrum, we can check the characteristics of functional groups from their UV/Visible Spectra. We also use High-performance liquid chromatography (HPLC) to detect the different components of dye on the recording layer [2]. The jitter value

test is to test the error cause by digital signal of recording media. If we use jitter value 8% as a reference to determine the life time of DVD-R samples, the purpose of this study is to investigate the Jitter values of recording media after high light exposure and high temperature/humidity test. The results of these test will be helpful for the development of long-life optical storage media .

### Experimental

In order to test the life time of the recording media under light exposure, more than 20 brand samples of commercial DVD-R discs were selected for light exposure testing. The testing method is according to the ISO-105-802 standard. In our experiment, the light exposure was tested by using Atlas Ci4000 Xenon Weather-Ometer (Fig. 1). The light source is Xenon with wavelength 420nm and light cycle irradiance 1.10w/m<sup>2</sup>. During the testing, the black panel temperature is 63°C , chamber temperature is 42°C and the relative humidity is 30% .



Fig. 1. ATLAS Ci4000 Xenon weather-Ometer

Another life testing of DVD-R samples was measured by using "Weiss Sb22/160 temperature and humidity tester. The testing procedure was following the Standard ISO/IEC 10995[3]. The reference temperature and humidity was set (85°C/85%RH) for accelerating test. The samples after each run testing (5 hours) were automatically measured the PI-error values.

The characteristics of DVD-R discs were measured by using DVD-R/RW Testers as shown in Fig. 2. The characteristics (Jitter, reflectivity, PI-error, ...) of samples before the light exposure were measured as reference data. Then the characteristics of samples were measured after the samples tested for each run with five hours. If the jitter value is greater than 8%, the signal may be read as error; so the sample is defined as fail. The absorption spectra of samples were tested by using UV/VIS absorption spectrometer. The sample un-exposure and after light exposure

were dissolved in the solvent ethanol, and measure the absorbance with wavelength from 200nm to 800nm.



Fig. 2.DVD-R/RW Testers

## Results and Discussion

### 3.1 Light Exposure Test

According to “DVD Specifications for Recordable Disc (DVD-R)”, the jitter value should lower than 8%. In our experiment, five type DVD-R discs were selected to compare the different characteristics. Fig.3 shows the effect of Jitter values of five DVD-R samples after the light exposure testing. The initial jitter values before light exposure for five DVD-R samples are sample-A(6.7%)、sample-B(6.9%)、sample-C(7.41%)、sample-D(6.66%)、sample-E(5.43%) which are lower than the standard jitter value 8%. If we test the jitter values of samples after the light exposure for 40 hours (each run testing 5 hours), the results represent the characteristics of photosensitivity are: sample-A<sample-C<sample-E<sample-B<sample-D. This represents that the photosensitivity of sample-D is the most sensitive under solar illumination. From above comparison, although the jitter values of DVD-R discs before light exposure still maintain in the range of 5% to 7% which satisfy the format requirement, some samples are very unstable after light exposure. If the dye layer is more sensitive to light, the conversion efficiency between light and thermal is better. Therefore the characteristics of samples with different dyes on recording media show different results after they tested in the Xenon arc lamp spectrum for more ten hours.

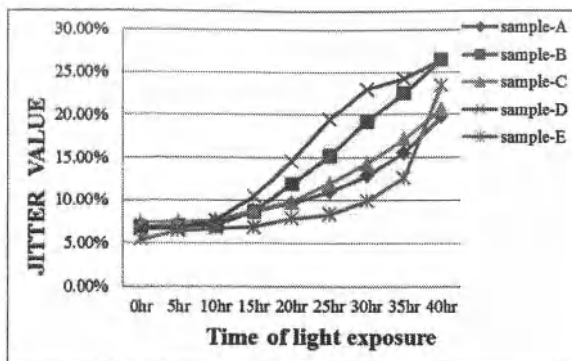


Fig. 3. The effect of jitter values for DVD-R samples after the light exposure testing

### 3.2 High Temperature and Humidity Test

To evaluate the life time of recording media, the jitter values of the samples before high temperature and humidity test are good reference for evaluating the properties of recording media. From Fig.4, we can see that the relative stability of the Jitter values of different DVD-R samples are :sample-D> sample-B> sample-E> sample-C> sample-A in condition (85 °C /85%RH). This result is almost the same as that obtained from the light exposure test as shown in Fig.3. The distribution curves of most samples are similar except for sample-E. The conclusion is that the more sensitive to light exposure of dye, the more stability of samples in the high temperature and humidity test

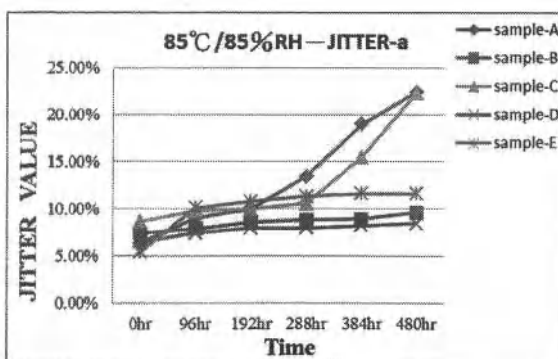


Fig. 4. The effect of jitter values for DVD-R samples after the high temperature and humidity test(85°C/85%RH)

### 3.3 Absorption Spectrum of Recording Media

In absorption spectrum of DVD samples, we generally can use UV/visible absorption peaks to make sure whether the functional groups have changed or not. From this, we select sample-C to explain the phenomenon. Comparing the UV/visible absorption spectra of blank DVD-R samples before light exposure (Sample-ST) and after 40 hour light exposure (sample-SP), we can find the degradation of the absorption spectra. From Fig.5 and Fig.6, we can find the absorption peaks of samples distribution between 540nm ~ 600nm which correspond to the required absorption spectrum of laser head. In our experiment, the trend of spectral distribution broadly divided into three categories, which are single peak, double peaks and triple peaks. From this results, we know that all of the dyes in different samples are different structure. Fig.5 shows the triple peaks of spectrum of the sample-A before light exposure, we can see that the triple peaks 511nm, 559 nm and 598 nm respectively. After light exposure, the triple peaks are still exist, but the intensities of absorption are degraded obviously. Fig. 6 shows the absorption curves with double peaks of the sample-C. The more narrow absorption range, the higher the purity of the color. However, it is almost no different for double peaks in the curves of exposure and un-exposure. We can find that the absorption intensity is also decreased for sample-C after light exposure. From our results, the degradation of absorption is a good reference to evaluate the stability of recording media.

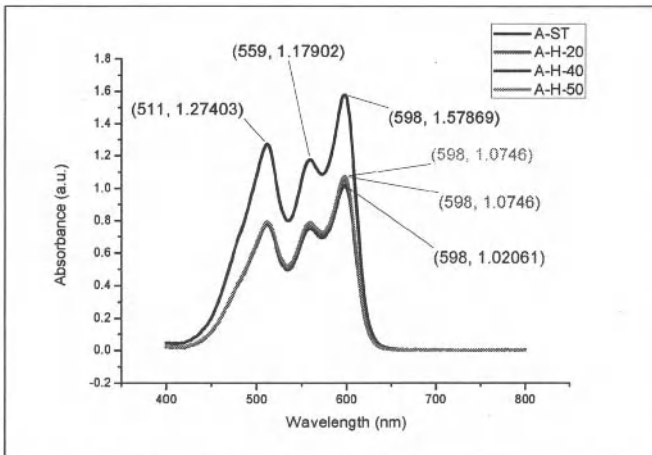
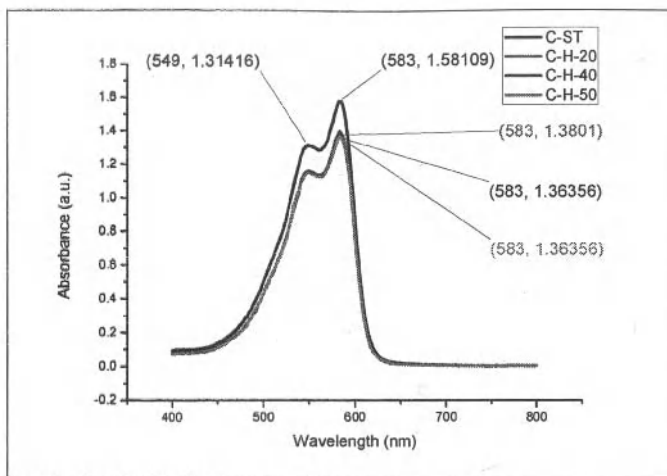


Fig. 5. Absorption curves of samples A discs before and after high temperature-humidity test



**Fig. 6.** Absorption curves of samples C discs before and after high temperature-humidity test

According to “DVD Specifications For Recordable Disc (DVD-R)” the reflectivity should be in the range of 85%–45%. From the results in Fig.7, we can see that the reflectivity of no-written/written sample-C begin to decrease after 30 hour light exposure, We conclude that the reflectivity is affected by light exposure obviously. The reflectivity of recorded sample is lower than that of blank sample. Considering the jitter values of sample-C after light exposure, the jitter value is begun to rise after 30 hours. From the variation of jitter-value and reflectivity for sample-C, we can find that the values have different change after light exposure testing 30hours to 40hours. We can make sure that the properties of dye layer on sample-C begin to change. It is a good method to estimate the life time of the recording media. Another method to estimate the life time of recording is using high temperature and humidity test. To test the jitter value and PI error of samples after high temperature and humidity testing, we can verify the stability of dye on recording media. In our experimental results, the sample with two peaks shows better characteristics, while the samples with one peak and three peaks in the high temperature and humidity test is relatively poor.

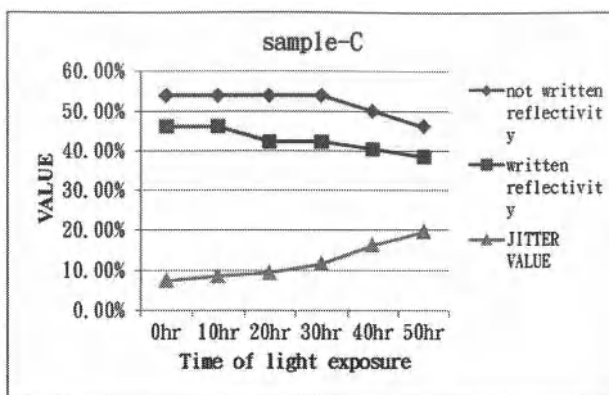


Fig.7. The no-written/written reflectivity and jitter values of sample-C before and after light exposure testing.

Generally we use HPLC to confirm the results. We test the reflectivity and jitter value of different samples to confirm the results by using the test of HPLC to observe whether the dye is decomposed or not. Fig.8 shows the property decay (%) of Samples A, B, C after long time test. From PI-error values of samples, there is just a little change in a short time, but the influence becomes obvious for samples A and B after long-time test. However, the sample-C shows good properties of PI-error values even after 20 hours and 40 hours. The results indicate that the property of sample-C is better than those of sample-A and sample-B.

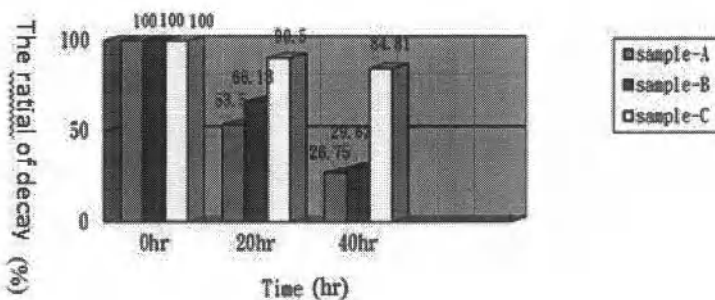


Fig.8. Comparison of the property decay of Samples A, B, C after long time test.

### **Conclusion**

The jitter value test is to test the error caused by digital signal of recording media. If the jitter value is too large, the signal may be error. According to "DVD Specifications for Recordable Disc (DVD-R)", the jitter value should lower than 8%. In our experiment, five type DVD-R discs were selected to compare the different characteristics after light exposure and high temperature and humidity test. Generally, the recordable media under long time light exposure may be defected seriously. Some discs are defected after 5 hours of light exposure, while some discs can endure over 25 hours. Also if we use reflectivity 45% as reference to determine the life time, some discs are defected after 30 hours light exposure while some discs can endure over 40 hours. The absorption spectrum of recordable media is a good reference to justify the quality of dye media. The distribution of the spectrum with single peak and triple peaks in the high temperature and humidity test is relatively poor. From the jitter-value and reflectivity of sample-C, we can find that after light exposure testing from 30hours to 40hours, the value have no difference change. These results can be used to estimate the life time of recordable media. The results will be helpful for developing long life media.

### **Acknowledgement**

The work was supported by the National Science Council, Taiwan under the Contract No. NSC 100-2221-E-259-016. The authors would like to thank ITRI for providing testing equipments and supporting the research analysis.

### **References**

- [1] D. A. Skoog, F. J. Hooller, T. A. Nieman, "Principle of Instrumental Analysis, Fifth edition, Harcourt Brance and Company Florida, pp.673~696,725~750 (1997)
- [2] Milton Ohring, "The Material Science of Thin Films", Academic Press, 65(1992).
- [3] ISO/IEC 10995, "Information technology — Digital recorded media for information interchange and storage — Test method for the estimation of the archival lifetime of optical media", (2008).

## **A COMPARISON BETWEEN THE PROPERTIES OF SPRAY- PYROLYZED SnO<sub>2</sub>:F/CdS:In STRUCTURES PREPARED BY USING NH<sub>4</sub>F AND HF AS A SOURCE OF FLUORINE**

Shadia J. Ikhmayies<sup>\*1</sup> and Riyad N. Ahmad-Bitar<sup>2</sup>

<sup>1</sup>Al Isra University, Faculty of Information Technology, Department of Basic Sciences-Physics;  
Amman, 16197, Jordan.

<sup>2</sup>University of Jordan, Faculty of Science, Physics Department; Amman, 11942, Jordan

Keywords: Spray Pyrolysis, CdS/CdTe Solar Cells, Transparent Conducting Oxides, Cadmium Compounds.

### **Abstract**

SnO<sub>2</sub>:F/CdS:In structures were prepared by the spray pyrolysis technique on glass substrates at a substrate temperature  $T_s = 450$  °C. NH<sub>4</sub>F and HF were both tried as the sources of fluorine in the precursor solution of SnO<sub>2</sub>:F. A comparison between the properties of structures obtained by using the two doping compounds was performed. X-ray diffraction (XRD), scanning electron microscopy (SEM) and transmittance measurements were used to characterize the films. The structures prepared by using HF as a fluorine source were found to have more ordered crystal growth, larger grain size and sharper absorption edge. From the inspection of the first derivative of the absorbance it is expected that more interdiffusion on the SnO<sub>2</sub>:F/CdS:In interface takes place in the structures made by using HF. These results confirm that these films are better as forecontacts for CdS/CdTe solar cells.

### **Introduction**

Thin film CdS/CdTe solar cells built in the superstrate geometry rely on transparent conducting oxides (TCOs) to make the front contact. The investigation of combined CdS-TCO films has recently been developed owing to the great interest of better understanding the effect of these bilayers on the absorbers [1]. Usually SnO<sub>2</sub> is utilized as a front contact for these solar cells. Optimizing the properties of the SnO<sub>2</sub>/CdS structures is an important step on the way to get high performance CdS/CdTe solar cells.

There are different methods to prepare SnO<sub>2</sub> thin films, such as reactive sputtering [2], evaporation [3], chemical vapour deposition [3, 4], dip coating [5] and spray pyrolysis [6-9]. At the same time CdS thin films can be prepared by different techniques such as chemical bath deposition [10], thermal evaporation [11], screen printing [12] and spray pyrolysis [7, 13]. However, the spray pyrolysis technique is a very low cost and simple technique that enables intentional doping and getting large area and uniform thin films [14]. For these reasons it is chosen to prepare SnO<sub>2</sub> and CdS thin films in this work. To improve the properties of these compound semiconductors, SnO<sub>2</sub> was doped with fluorine and CdS was doped with indium where such doping is well known for these compounds.

Few studies are conducted on studying the SnO<sub>2</sub>/CdS structures, because CdS/CdTe interface had attracted attention. Niles et al. [15] had investigated the formation and thermal stability of the SnO<sub>2</sub>/CdS interface by soft X-ray synchrotron radiation photoemission. Krishnakumar et al. [16] had investigated the band alignment of differently treated TCO/CdS interface, where they

determined the band offset at differently prepared and treated ITO/CdS and SnO<sub>2</sub>/CdS interfaces using photoelectron spectroscopy and sputter depth profiling. In this work we produced the SnO<sub>2</sub>:F/CdS:In bilayers by the spray pyrolysis technique. The SnO<sub>2</sub>:F was produced by using two different doping compounds NH<sub>4</sub>F and HF, and the CdS:In layer was deposited onto this layer in both cases. A comparison between the bilayers produced by using the different fluorine sources was performed. Considerable differences were observed and it is found that bilayers produced by using HF are better for the production of CdS/CdTe solar cell.

### Experimental Part

To prepare the precursor solution for SnO<sub>2</sub>:F thin films, stannous chloride SnCl<sub>2</sub>.2H<sub>2</sub>O was used. Ammonium fluoride NH<sub>4</sub>F (BDH Chemicals. Ltd Poole England) and hydrofluoric acid HF (40%) were used as the sources of fluorine. Two different solutions were made: The first solution was prepared from  $5.03 \times 10^{-3}$  moles of stannous chloride (SnCl<sub>2</sub>.2H<sub>2</sub>O) and  $4.73 \times 10^{-3}$  moles of ammonium fluoride (NH<sub>4</sub>F). These were dissolved in 45 ml of methanol CH<sub>3</sub>OH (MAY AND BAKER LTD DAGENHAM ENGLAND), 5 ml of distilled water, and 1 ml of HCl. The ratio of fluorine ions to tin ions in the solution was 0.94 which is approximately the same as that used by Gordillo et al. [8] at which they got the best quality of SnO<sub>2</sub>:F films prepared by using NH<sub>4</sub>F. This solution was intermittently sprayed on glass substrates of dimensions  $2.5 \times 6 \times 0.1$  cm<sup>3</sup> that were ultrasonically cleaned in methanol for at least 15 minutes at substrate temperature T<sub>s</sub> = 450 °C. The set of films prepared from this solution is called NH<sub>4</sub>F-films. The second solution was made by dissolving  $5.01 \times 10^{-3}$  moles of SnCl<sub>2</sub>.2H<sub>2</sub>O with  $5.71 \times 10^{-3}$  moles of HF in 45 ml of methanol, 5 ml of distilled water and 1 ml of HCl. The ratio of fluorine ions to tin ions in the solution was 1.14 which is also approximately the same as that used by Gordillo et al. [8] at which they got the best SnO<sub>2</sub>:F films prepared by using HF. Also this solution was sprayed by the same method on glass substrates of the same dimensions as those used for the NH<sub>4</sub>F-films after cleaning them ultrasonically in methanol for the same period of time. The set of films prepared from this solution is called HF-films.

To prepare CdS:In thin films a solution was prepared by taking  $2.06 \times 10^{-2}$  moles of extra pure CdCl<sub>2</sub>.H<sub>2</sub>O (MERCK Art. 2011) and  $2.24 \times 10^{-2}$  moles of thiourea (NH<sub>2</sub>)<sub>2</sub>CS (>97% S) in 350 ml of distilled water. Indium chloride InCl<sub>3</sub> (MERCK Art.12471) was used as the source of indium. The ratio of the concentration of indium ions to that of cadmium ions in the solution ( $[In^{+3}]/[Cd^{+2}]$ ) which is approximately the same ratio of the corresponding atoms was 10<sup>-4</sup>. This ratio which was used as an indication of the doping ratio may differ from that in the films due to the dynamic nature of the spray pyrolysis. In-doped CdS thin films have been deposited onto the NH<sub>4</sub>F-films and HF-films prepared before at a substrate temperature T<sub>s</sub> = 450 °C. The produced structures are denoted by NH<sub>4</sub>F-structures and HF-structures respectively.

The spraying system used for film deposition has been described elsewhere [7]. The spray rate was usually in the range 15-18 ml/min. The optimum carrier gas pressure for this rate of solution flow was around 5 kg/cm<sup>2</sup>, where nitrogen was used as the carrier gas. The transmittance of the films was measured in the wavelength range  $\lambda = 290-1100nm$  by using a double beam Shimadzu UV 1601 (PC) spectrophotometer with respect to a piece of glass similar to the substrates. X-ray diffraction measurements were made with a Philips Analytical Compact X-ray diffractometer system with Co anode material K<sub>α1</sub> ( $\lambda_1 = 1.78897\text{\AA}$ ) and K<sub>α2</sub> ( $\lambda_2 = 1.79285\text{\AA}$ ). The surface morphology of the films was analyzed by a LEITZ-AMR 1000A scanning electron microscope. Energy dispersive X-ray analysis (EDAX) was performed for both types of SnO<sub>2</sub>:F films (the NH<sub>4</sub>F-films and the HF-films) by FEI Inspect F50.

## Results and Discussion

### Structural Properties

Fig.1 shows the X-ray diffractograms of two SnO<sub>2</sub>:F/CdS:In structures prepared at a substrate temperature T<sub>s</sub> = 450 °C. Fig.1a is for NH<sub>4</sub>F-structures, Fig.1b is for HF-structures, and the thickness of the CdS:In layer is approximately the same in both structures which is about 0.50 μm. The diffractograms show the crystallographic orientations of the hexagonal CdS:In, but it is not easy to recognize the lines characteristic of SnO<sub>2</sub>:F films which are weaker than those of CdS:In and sometimes overlapped with them. Table I contains the XRD data for the two films including the d value which is the distance between nearest neighbor (hkl) planes measured for the two cobalt anodes (α<sub>1</sub> = 1.78897 Å and α<sub>2</sub> = 1.79285 Å), intensity of the peaks and Miller indices.

The comparison between the two diffractograms shows that first, the orientation of crystal growth is more ordered in Fig.1b. Second, the intensities of the lines (100), (102), (110), (103) and (112) in Fig.1b became smaller than their intensities in Fig.1a. Third, the line C(111)/(002) had grown and became the preferential orientation in Fig.1b, while the line (101) which was the preferential orientation in Fig.1a became weaker. Fourth, the intensity of the peaks of positions 2θ < 23° that are related with the formation of complex compounds which decompose to CdS [17], had too much suppressed in Fig.1b. Finally, from table I it is noticed that the spacing d is always larger for the NH<sub>4</sub>F-structures, or in other words the whole spectrum was shifted towards smaller d values for the HF-structures. This behavior can be interpreted depending on the results of the compositional analysis taken for the SnO<sub>2</sub>:F films by using EDAX measurements shown in table II. As the table shows the ratio of oxygen atoms to tin atoms in the HF-films is 1.96 which is close to the stoichiometric ratio 2.0, but in the NH<sub>4</sub>F-films it is 8.47 which is far from the stoichiometric ratio. It is known that the ionic radius of tin is smaller than that of O<sup>2-</sup>, so the larger density of oxygen ions enlarges the lattice and hence lattice parameters and spacing distance d, which is the case in the NH<sub>4</sub>F films.

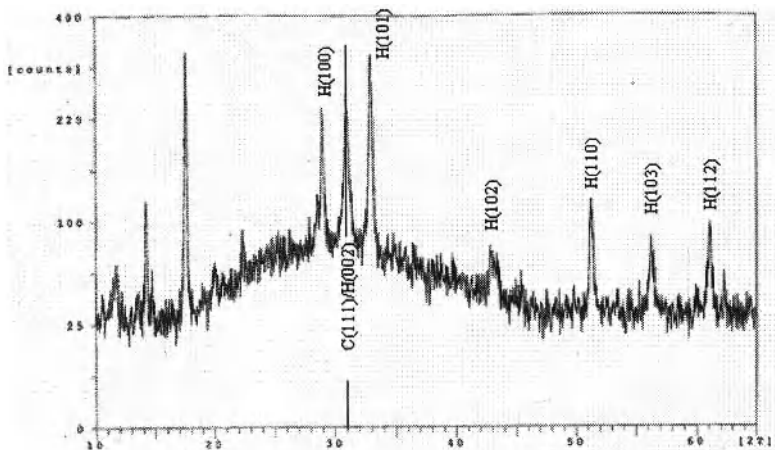
The grain size was calculated by using Scherrer formula and the line (101) in the XRD diffractograms.

$$d = \frac{\lambda}{D \cos \theta} \quad (4)$$

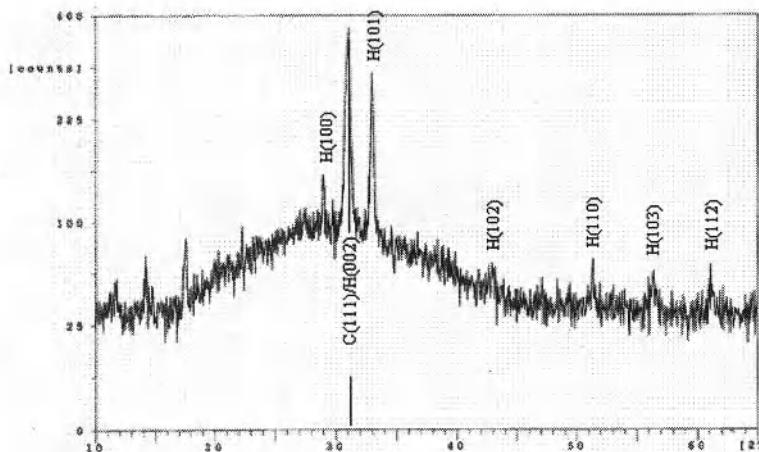
where *d* is the grain size, *λ* is the X-ray wavelength used, *D* is the angular line width of the half-maximum intensity and *θ* is the Bragg angle. It was about 26 nm for the NH<sub>4</sub>F-structures and 31 nm for the HF-structures. These values can be compared with the grain size of CdS:In thin films on glass substrates which is 29 nm at T<sub>s</sub> = 460 °C [17].

Fig.2 depicts the SEM images of CdS:In deposited on a glass substrate (Fig.2a) and on the SnO<sub>2</sub>:F substrates, which are the NH<sub>4</sub>F-films and HF-films (Fig.2b and c respectively). The difference in the morphology of the surfaces is apparent in the three cases, and it is obvious that the smallest grain size of CdS:In was obtained for CdS:In on the NH<sub>4</sub>F-films. The larger grain size in the case of the HF-structures may be due to the larger concentration of fluorine in the HF-films relative to oxygen concentration. Gordillo et al. [8] concluded that the addition of HF leads

to a small increase of the growth rate of the  $\text{SnO}_2:\text{F}$  films. On the contrary, the addition of  $\text{NH}_4\text{F}$  results in a small decrease of the growth rate.



(a)



(b)

Figure 1. X-ray diffractograms of  $\text{SnO}_2:\text{F}/\text{CdS}:\text{In}$  structures deposited at  $T_s = 450^\circ\text{C}$  by using the fluorine sources. a)  $\text{NH}_4\text{F}$ . b)  $\text{HF}$ .

Table I. The XRD data of the NH<sub>4</sub>F-structures and HF-structures.

2θ of the peaks (°)	d for α <sub>1</sub> (Å)	NH <sub>4</sub> F d for α <sub>2</sub> (Å)	(hkl)	Height (Counts)	2θ of the peaks (°)	d for α <sub>1</sub> (Å)	HF d for α <sub>2</sub> (Å)	(hkl)	Height (Counts)
11.695	8.77967	8.79874		32	11.660	8.80594	8.82506		14
13.390	7.67242	7.68909		14					
14.175	7.24952	7.26527		96	14.185	7.24444	7.26017		19
14.675	7.00381	7.01902		24					
17.560	5.86005	5.87277		313	17.560	5.86005	5.87277		49
19.945	5.16518	5.17640		18					
22.370	4.61127	4.62128		29	22.290	4.62761	4.63766		24
28.950	3.57854	3.58631	H(100)	172	28.975	3.57552	3.58328	H(100)	58
31.005	3.34661	3.35387	H(002)	164	31.010	3.34608	3.35335	H(002)	292
32.930	3.15592	3.16278	H(101)	262	32.940	3.15499	3.16184	H(101)	193
42.790	2.45201	2.45734	H(102)	26	42.850	2.44874	2.45406	H(102)	11
51.260	2.06789	2.07238	H(110)	90	51.325	2.06545	2.06993	H(110)	26
56.320	1.89535	1.89947	H(103)	42	56.370	1.89381	1.89792	H(103)	17
61.110	1.75953	1.76335	H(112)	67	61.065	1.76070	1.76452	H(112)	18

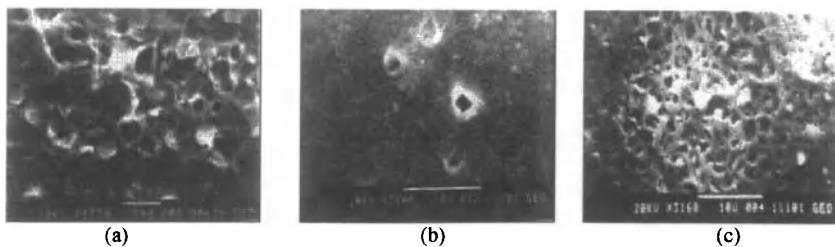


Figure 2. SEM images of: a) CdS:In on glass substrates at  $T_s = 460$  °C [17]. b) NH<sub>4</sub>F-structures. c) HF-structures.

Table II. The results of the EDAX analysis for the NH<sub>4</sub>F-films and the HF-films.

Element	NH <sub>4</sub> F Norm.(wt%)	HF Norm.(wt%)
O	88.47 ± 28.4	65.62 ± 21.5
F	1.08 ± 1.3	0.85 ± 1.6
Sn	10.44 ± 5.0	33.52 ± 13.2

### Optical Properties

Fig.3 depicts the transmittance and absorbance of two NH<sub>4</sub>F-structures and two HF-structures. As Fig.3a shows, all of the films have approximately the same transmittance after  $\lambda \geq 510\text{nm}$ , i.e. after the absorption edge of CdS. This is because the transmittance in this region is determined by the CdS:In layer. But before the absorption edge of CdS at  $\lambda \leq 510\text{nm}$  there are apparent differences. The transmittance of the NH<sub>4</sub>F-structures in this region is larger than that of the HF-structures. This means that the absorbance of the HF-structures is higher in this region. Fig.3b confirms this expectation, where it is obvious that the absorbance of the HF-structures is larger than that of the NH<sub>4</sub>F-structures before the absorption edge of CdS. The higher absorption is due to the larger density of free charge carriers which are electrons in the case of SnO<sub>2</sub>:F. From table II it is seen that the NH<sub>4</sub>F-films are richer in oxygen and poorer in tin than the HF-films. This means that the density of the defects such as  $O^-$ ,  $O_2^-$  and Sn deficiency is larger in the NH<sub>4</sub>F-films. These defects reduce the density of free charge carriers (electrons) in the films. Although the NH<sub>4</sub>F-films contain more fluorine than the HF-films and they have a higher doping ratio, where the doping ratio is the ratio of the concentration of fluorine ions to that of tin ions that is approximately the same as the ratio of the atoms [F]/[Sn], and it is 2.5% in the HF-films and 10.34% in the NH<sub>4</sub>F-films, but the ratio of the concentration of fluorine ions to that of oxygen ions which is approximately the same as that of the atoms is 13% for the HF-films, but 1.22% for the NH<sub>4</sub>F-films. It is known that fluorine replaces oxygen in the SnO<sub>2</sub> lattice, and hence it increases the density of free electrons.

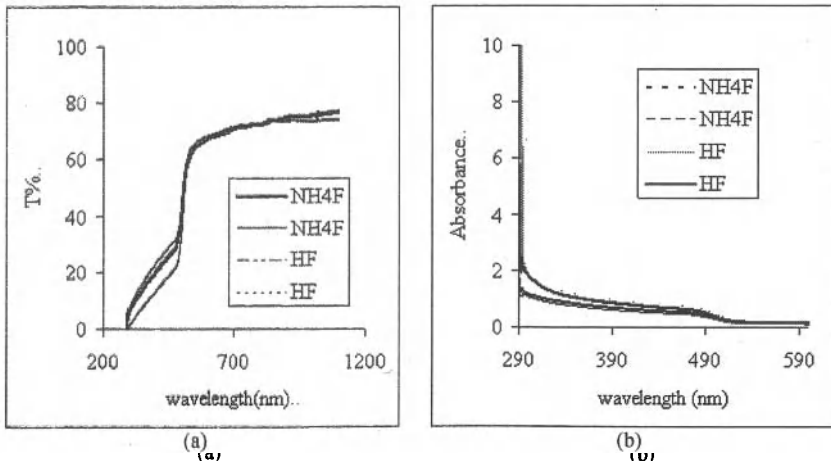


Figure 3. a) The transmittance curves of the SnO<sub>2</sub>:F/CdS:In structures. b) The absorbance curves of the SnO<sub>2</sub>:F/CdS:In structures.

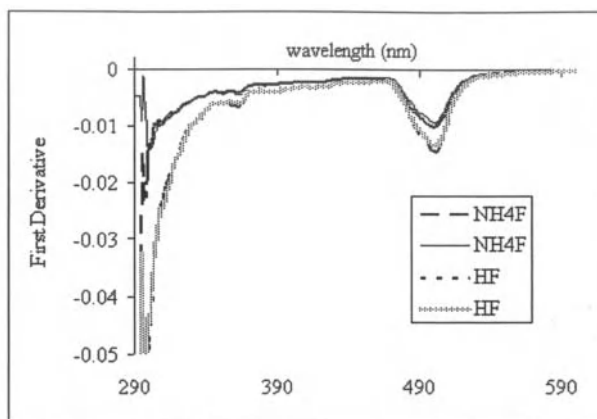


Figure 4. The plot of the first derivative of the absorbance against the photon's energy of the  $\text{SnO}_2\text{:F/CdS:In}$  structures.

Fig.4 displays the first derivative of the absorbance against wavelength. The minima in the graph refer to the bandgap values. At least two minima are observed in the graph, one for  $\text{CdS:In}$  and the other for  $\text{SnO}_2\text{:F}$ . The minima at about 500 nm refer to the bandgap of  $\text{CdS:In}$  which is about 2.48 eV. As the figure shows the positions of these minima are approximately the same for the  $\text{NH}_4\text{F}$ -structures and the  $\text{HF}$ -structures. But it is obvious that the minima are deeper in the case of the  $\text{HF}$ -structures, which means that the absorption edge is sharper. The other minima refer to the bandgap of  $\text{SnO}_2\text{:F}$  which is about 4.17 eV. Also all of the films showed approximately the same positions of the minima and the minima are deeper and wider in the case of the  $\text{HF}$ -structures. The width of the minima could be due to the distribution in the grain size in the  $\text{SnO}_2\text{:F}$  films, where each size results in a certain minimum and the superposition of these minima produces the wide minimum that we have. Also it could be related to interdiffusion on the junction and the formation of a solid solution of the form  $\text{CdS}_x\text{Sn}_{1-x}$  on the  $\text{SnO}_2$  side, i.e. diffusion of S towards  $\text{SnO}_2\text{:F}$ . Wider minima with structure were found in the case of the  $\text{HF}$ -structures which may mean more interdiffusion takes place for these films, which is better for the  $\text{CdS/CdTe}$  solar cells.

### Conclusions

A comparison between  $\text{SnO}_2\text{:F/CdS:In}$  structures prepared by the spray pyrolysis technique by using  $\text{NH}_4\text{F}$  and  $\text{HF}$  as sources of fluorine was performed. XRD diffractograms revealed that the  $\text{HF}$ -structures have more ordered crystal growth and larger grain size than the  $\text{NH}_4\text{F}$ -structures. SEM micrographs showed different morphologies and larger grain size for the  $\text{HF}$ -structures. EDAX analysis revealed that the  $\text{NH}_4\text{F}$ -films are richer in oxygen and poorer in tin which reduces the density of free charge carriers. The transmittance of the  $\text{HF}$ - structures is smaller in the high energy region before the absorption edge of  $\text{CdS}$  due to stronger absorption. From the first derivative curves the bandgap energies of  $\text{CdS:In}$  and  $\text{SnO}_2\text{:F}$  did not change, but the wide minima of  $\text{SnO}_2\text{:F}$  may refer to interdiffusion on the  $\text{SnO}_2\text{:F}$  side. The deeper minima in the case of  $\text{HF}$ -structures refer to sharper absorption edge. From these results it is found that  $\text{HF}$  is a

better fluorine source in the SnO<sub>2</sub>:F layer to be used as a forecontact in superstrate CdS/CdTe solar cells.

### References

- [1] M.A. Martínez, C. Guillén, M.T. Gutiérrez, and J. Herrero, "Optimisation of CdS-TCO Bilayers for their Application as Windows in Photovoltaic Solar Cells," *Solar Energy Materials and Solar Cells*, 43 (1996), 297-310.
- [2] S. S. Pan, C. Ye, X. M. Teng, H. T. Fan, and G. H. Li, "Preparation and Characterization of Nitrogen-Incorporated SnO<sub>2</sub> Films," *Appl. Phys. A*, 85 (1) (2006), 21-24.
- [3] P. Montmeat, "Thin Film Membranes for the Improvement of Gas Sensor Selectivity" (Doctorate thesis. École Nationale Supérieure des Mines de Saint-Étienne (ENSMSE): a graduate school for science and technology, France, 1999).
- [4] Jonas. Sundqvist, and Anders. Hårsta, "Growth of SnO<sub>2</sub> Thin Films by ALD and CVD: A Comparative Study," *Proceedings of the sixteenth Int. CVD Conf.* Paris, France, 1 (2003), 511.
- [5] Viviany. Geraldo, Luis Vicente de Andrade Scalvi, Evandro Augusto de Morais, Celso Valentim Santilli, and Sandra Helena Pulcinelli, "Sb Doping Effect and Oxygen Adsorption in SnO<sub>2</sub> Thin Films Deposited via Sol-Gel," *Mat. Res.*, 6 (4) (2003), 451-456.
- [6] A. E. Rakhshani, Y. Makdasi, and H. A. Ramazaniyan, "Electronic and Optical Properties of Fluorine-Doped Tin Oxide Films," *J. Appl. Phys.*, 83 (2) (1998), 1049-1057.
- [7] Shadia J. Ikhmayies, "Production and Characterization of CdS/CdTe Thin Film Photovoltaic Solar Cells of Potential Industrial Use" (Ph.D Thesis, University of Jordan, 2002).
- [8] G. Gordillo, L. C. Moreno, W. de la Cruz., and P. Teheran, "Preparation and Characterization of SnO<sub>2</sub> Thin Films Deposited by Spray Pyrolysis from SnCl<sub>2</sub> and SnCl<sub>4</sub> Precursors," *Thin Solid Films*, 252 (1994), 61-66.
- [9] E. Shanthi, A. Banerjee, V. Dutta, and K. L. Chopra, "Electrical and Optical Properties of Tin Oxide Films Doped with F and (Sb + F)," *J. Appl. Phys.*, 53 (3) (1982), 1615-1621.
- [10] Hülya Metin and R. Esen, "Photoconductivity Studies on CdS Films Grown by Chemical Bath Deposition Technique," *Erciyes Üniversitesi Fen Bilimleri Enstitüsü Dergisi*, 19 (1-2) (2003), 96-102.
- [11] P. P. Sahay, R. K. Nath, and S. Tewari, "Optical Properties of Thermally Evaporated CdS Thin Films," *Cryst. Res. Technol.*, 42 (3) (2007), 275-280.
- [12] D. Patidar, R. Sharma, N. Jain, T. P. Sharma, and N. S. Saxena, "Optical Properties of CdS Sintered Film," *Bull. Mater. Sci.*, 29 (1) (2006), 21-24.
- [13] A. Ashour, "Physical Properties of Spray Pyrolysed CdS Thin Films," *Turk J Phys*, 27 (2003), 551-558.
- [14] Shixing Weng, and Michael Cocivera, "Cadmium Sulphide Prepared from Cadmium Oxide Thin films," *Solar Energy Materials and solar cells*, 36 (1995), 301-309.
- [15] David W. Niles, Dennis Rioux, and Hartmut Höchst, "A Photoemission Investigation of the SnO<sub>2</sub>/CdS Interface: a Front Contact Interface Study of CdS/CdTe Solar Cells," *J. Appl. Phys.*, 73 (9) (1993), 4586-4590.
- [16] V. Krishnakumar, K. Ramamurthi, A. Klein, and W. Jaegermann, "Band Alignment of Differently Treated TCO/CdS Interfaces," *Thin Solid Films*, 517 (2009), 2558-2561.
- [17] Shadia. J. Ikhmayies, and Riyad N. Ahmad-Bitar, "The Influence of the Substrate Temperature on the Photovoltaic Properties of Spray-Deposited CdS:In Thin Films," *Applied Surface Science*, 256 (2010), 3541-3545.

## CHARACTERIZATION AND PREPARATION OF ANTI-REFLECTION COATINGS IN THE RANGE OF 3-5 $\mu\text{m}$ FOR Si OPTICAL WINDOW

K. Iqbal, A. Maqsood, M. Mujahid and M. H. Asghar

School of Chemical and Materials Engineering, National University of Sciences and Technology, Pakistan

**Keywords:** Annealing; Characterizations; Multilayer; RF magnetron sputtering

### Abstract

Thin film multilayer anti-reflection coatings ( $\text{SiO}_2/\text{Si}/\text{SiO}_2$ ) having thicknesses 286/571/143nm were deposited by RF magnetron sputtering deposition technique on 0.5mm thick Si(100)-substrates. Post-deposition annealing is also carried out in the temperature range 150-650 $^\circ\text{C}$  for 4hr at the rate of 10 $^\circ\text{C}$  /min. Si Optical window was designed at 4.2 $\mu\text{m}$  wavelengths and correlated with modeling software. The films are transparent in the 3-5 $\mu\text{m}$  band of the electromagnetic spectrum, firmly adhered to the substrate. The prepared multilayer thin films are characterized optically and structurally using a spectrophotometer, an atomic force microscope, x-ray diffraction and a scanning electron microscope. Optical and structural characterizations show that the %transmittance is between 60% and 75%, no appreciable change in crystal structure and roughness of coatings vary between 9 and 25 nm when annealed in the temperature range of 150-650 $^\circ\text{C}$ . Local elemental characterization on the surface of the thin film was carried out using energy dispersive spectroscopy. The quantitative result of energy dispersive spectroscopy has also shown that the ratio of Si to O on the film is 0.67:1.

### Introduction

$\text{SiO}_2$  thin films have unique properties in the interfaces with Si and most studied materials in the field of microelectronics and optical devices [1]. Multilayer thin films are using nowadays in the design and fabrication of the shrinking systems with a variety of fields such as optoelectronic devices. The physical properties and parameters can be controlled at scales of microns down to nanometers by using RF magnetron sputtering system [2].

Silicon and Silicon dioxide are used as coating materials [3]. These thin films are laid on top of each other in  $\text{SiO}_2/\text{Si}/\text{SiO}_2$  order by RF magnetron sputtering on top of a substrate as given in Table 1.

**Table 1** Design data for  $\text{SiO}_2/\text{Si}/\text{SiO}_2$

S.No.	Material	Physical thickness (nm)
1	Substrate(Si)	$5 \times 10^5$
2	$\text{SiO}_2$	143
3	Si	571
4	$\text{SiO}_2$	286

Antireflection (AR) coating has significant role on optical and electro-optical applications [4, 5]. In some applications, these are required for the reduction of surface reflections. In

others, not only is the reflection reduced but transmittance is also increased considerably [5, 6].

This work was designed at 4.2 $\mu\text{m}$  wavelength, prepared and characterized for non-quarter-wave thick multilayer AR coatings based on low-high refractive indexes in the 3–5 $\mu\text{m}$  bands and total thickness was determined by Fresnel equations [7] as given in equation 1 and 2. At 4.2 $\mu\text{m}$  wavelength, mainly carbon dioxide takes part in reducing the %transmittance [8].

$$n_{\text{AR}}^2 = n_s \times n_{\text{air}} \quad (1)$$

$$d = \lambda_0 / (4 n_{\text{AR}}) \quad (2)$$

Experimental efforts are increasingly supported by computational software TFCAL [9] that address %transmittance versus wavelength in microns, saving time and cost.

The films were subjected to post deposition annealing under various temperatures, 150–650 $^{\circ}\text{C}$ . The furnace temperature was raised to above temperatures at a rate of 10 $^{\circ}\text{C}/\text{min}$  and kept constant for 4hr then cooled for room temperature at a rate of 5 $^{\circ}\text{C}/\text{min}$ . After annealing, we studied effects of annealing by the Fourier Transform Infrared Spectroscopy (FTIR), X-Ray Diffraction (XRD), Scanning Electron Microscope (SEM), Energy Dispersive Spectroscopy (EDS) and Atomic Force Microscopy (AFM) characterization techniques. Results of combined experimental and theoretical are tailored.

### Design of Si/SiO<sub>2</sub> Thin Films

The hybrid antireflective coating model was designed using thin film design TFCALC software to minimize the reflectance of a Si substrate in the wavelength range 3–5 $\mu\text{m}$ . In TFCALC software, the illuminant, stored in the illuminant database, is given as a table of spectral intensity versus wavelength. The incident angle may vary from 0 to 89.999 degrees. The substrate and the incident and exit mediums are selected from the substrate database. The thickness of the substrate, which is considered a massive layer, may be specified. The materials that compose the front and back layers are selected from the Materials database (or from a name in the Variable Materials or Mixture Materials windows). Currently, there is a limit of 5000 layers. The optical properties of substrates and materials are stored as tables or dispersion formulas of complex refractive index (n-ik) versus wavelength. It is possible to specify which surface the light encounters first: Front or Back. That is, light can come from either side of the coating [10].

SiO<sub>2</sub> was used as the low index material, while high index material was Si as shown in Figure 1 and their refractive indices were calculated by Sellmeiers dispersion equation [7, 10] is given in equation 3 and values of constants are given in Table 2. Alternate layers of Si and SiO<sub>2</sub> were used to achieve the required spectral performance. Spectral performance of Antireflection Coating (ARC) design is shown in Figure 2.

$$n^2 - 1 = A_1 \lambda^2 / (\lambda^2 - C_1^2) + A_2 \lambda^2 / (\lambda^2 - C_2^2) + A_3 \lambda^2 / (\lambda^2 - C_3^2), \quad [C_1, C_2, C_3 \text{ and } \lambda] = [\mu\text{m}] \quad (3)$$

**Table 2** Parametric values of Sellmeier equation

S.No.	Material	A <sub>1</sub>	A <sub>2</sub>	A <sub>3</sub>	C <sub>1</sub> ( $\mu\text{m}$ )	C <sub>2</sub> ( $\mu\text{m}$ )	C <sub>3</sub> ( $\mu\text{m}$ )
1	SiO <sub>2</sub>	0.696166	0.407943	0.897480	0.068404	0.116241	9.89616
2	Si	10.668429	0.00304347	1.5413341	0.30151648	1.1347511	1104.0

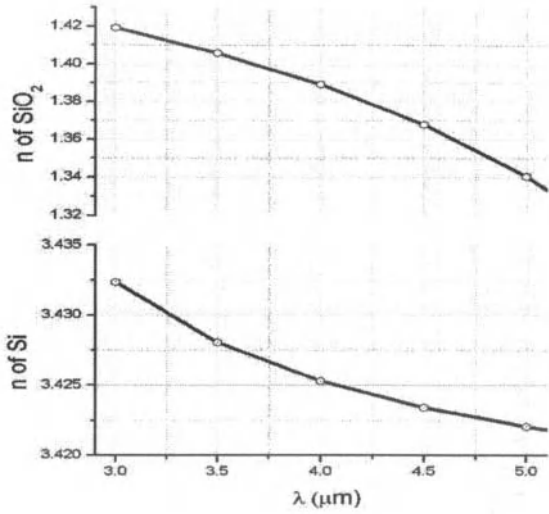


**Fig.1.** Refractive indices of  $\text{SiO}_2$  & Si in the 3-5 $\mu\text{m}$  wave band

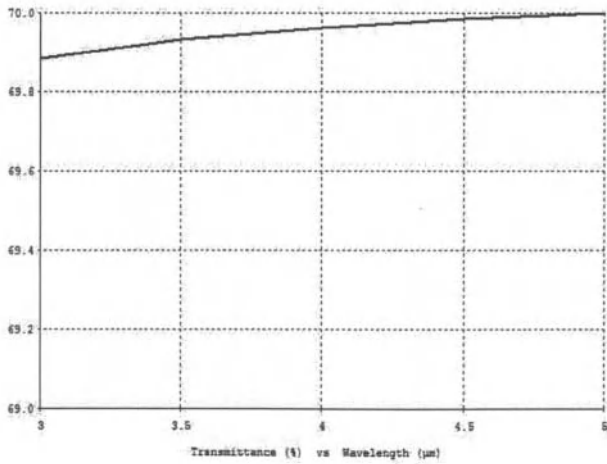


**Fig.2.** Transmittance % vs. wavelength ( $\mu\text{m}$ ) profile of Si/ $\text{SiO}_2$  layers

## Experimental details

### Sputtering System

Si/SiO<sub>2</sub> films were deposited on silicon substrates by using RF magnetron sputtering deposition technique [10, 11]. The sputtering target was taken with diameter of 4 inches. The forward power P<sub>f</sub> and the reflected power P<sub>r</sub> used in the growth process were 2.74kW and 0.16kW respectively, and the distance between the target and the substrate was 10cm. The sputtering chamber was evacuated to a pressure less than 5.0×10<sup>-4</sup> Pa. Argon (99.999%) flow rate and oxygen (99.999%) flow rate and deposition rate for the individual layers are given in the Table 3.

**Table 3** Deposition rate, Argon flow rate and Oxygen flow rate for the individual layers

S.No.	Material	Deposition rate (Å/sec)	Argon flow rate (sccm)	Oxygen flow rate (sccm)
1	SiO <sub>2</sub>	1.1	190	21
2	Si	1.5	130	-

### Annealing of Samples

Si/SiO<sub>2</sub> thin films were firstly prepared on Si(100) substrates using RF magnetron sputtering system. Then the samples were annealed at different temperatures (150-650°C for 4hr) in oxygen ambient and their properties were investigated particularly as a function of annealing temperature. The microstructure, morphology and optical property of Si/SiO<sub>2</sub> films were studied by XRD, AFM, UV/VIS/IR Spectrometer, EDS and SEM.

### Film Characterization

The linear transmission spectra of the films were recorded on UV/VIS/IR Spectrometer (U-3501, Hitachi) at room temperature in the 3–5µm regions. Structural analysis of the films and multilayered structures were determined by a SEM (JSM-6490A, Joel) and EDS. Prior to SEM, the samples were coated with a thin layer of gold to prevent charging of the specimens. The structure of the deposited Si/SiO<sub>2</sub> films was studied using XRD. A Siemens/Bruker D 8 X-ray diffraction was used at the conditions “tube voltage 40kV, current 40mA and wavelength Cu Kα, λ=0.154178nm”. The 2θ scan range is from 20° to 90°, step is 0.04 and scan speed is 1°/min.

The films morphology was investigated by AFM (JSPM5200, Jeol). It had a Si<sub>3</sub>N<sub>4</sub> cantilever tip, operated in AC mode, with the cantilever frequency of 174.161 kHz, and force constant of 1.00N/m, respectively. The scans were performed in air. The images were acquired at 512×512 pixels.

## Results and Discussion

### Structural Identification

Film compositions were analyzed with EDS in the SEM. A 10 kV accelerating voltage and 1.0 nA probe current was used in EDS. EDS results were shown for as-deposited and annealed at 650°C sample in the Figure 3(a) and 3(b) respectively. Atomic compositions were computed with the help of ZAF method [12] are shown in Figure 4, along with the Si/O ratio for all the films. With the exception of first four samples, the films appear close to stoichiometric with respect to O content and all films reveal no contamination of the samples by argon.

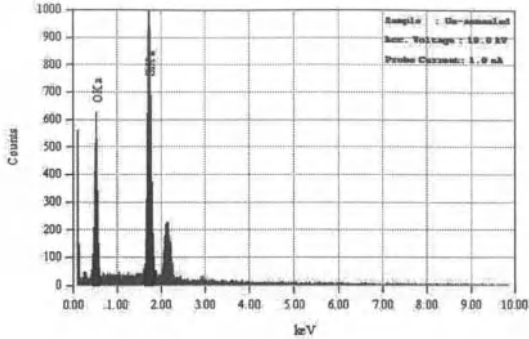


**Fig.3. (a)** EDS analysis of as-deposited sample

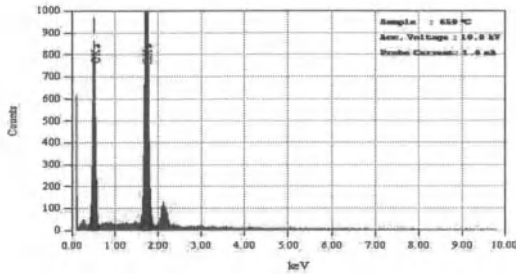


**Fig.3. (b)** EDS analysis of sample 650°C

The significant effect of heat treatment on various properties of Si/SiO<sub>2</sub> coatings is due to the micro-structural changes during heat treatment. In order to study the crystallographic structure of Si/SiO<sub>2</sub> coatings as well as the effect of heat treatment on their microstructure was conducted as shown in Figure 5. A comparison of different structures was made by taking into consideration relative intensity and location of the peaks. The crystal structure was determined and lattice parameters  $a = 5.44 \text{ \AA}$  of the samples were calculated by using Bragg's equation at  $\theta = 69.1^\circ$  and  $(hkl) = (100)$  as given in equation 4. Also Figure 5 illustrates that the un-annealed and annealed samples (150-650°C for 4hr) are in polycrystalline structures and the peak with maximum relative intensity was that of substrate silicon. In addition, satellite peaks (or doublet or rocking curves) near at  $69^\circ$  degree shows unstrained from top layer to silicon substrate and also shows  $K\alpha_1$  and  $K\alpha_2$  radiation diffract at the same angle.

$$\sin^2 \theta / (h^2 + k^2 + l^2) = \lambda^2 / 4a^2 \quad (4)$$

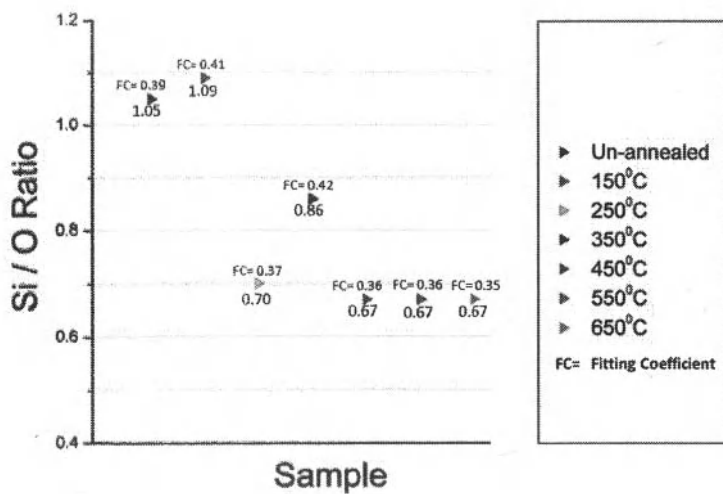


Fig.4. Si/O ratio of the surface of Multi-layer Thin Films

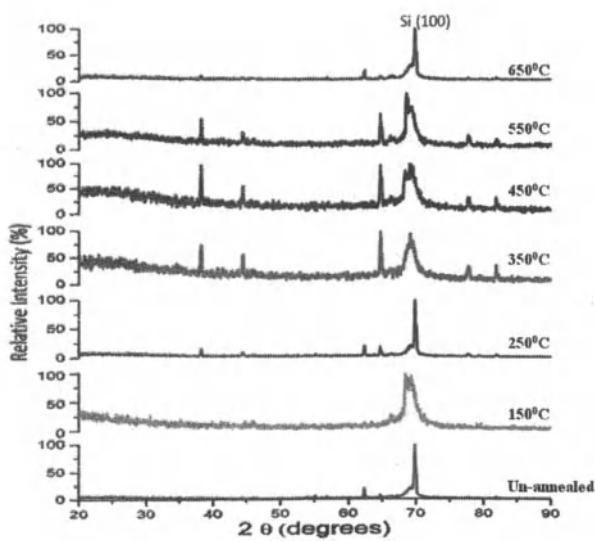


Fig.5. XRD analysis of un-annealed and annealed samples between intensity and angle 2θ

### Film Surfaces and Roughness

The comparison of film surfaces before and after heat treatment was made through SEM and spectrophotometer studies. From Figures 6(a) and 6(b), the film surface has no evident defaults such as small impurity, small holes and cracks before and after annealing at 650°C respectively and the cross-sectional morphology exhibits a uniform structure as shown in Figure 6(c). Whereas Figures 7(a) and 7(b) also shows that film surface has no defaults. From Figures 8(a) and 8(b), the surface of the film is composed of very uniform tiny “islands” with an average cluster size of approximately 9 to 25nm. RMS roughness of the samples is shown in Figure 9. Both of SEM and AFM observations indicate that films have columnar structure and the surface of the film is smooth and featureless.



**Fig.6. (a)** Typical SEM image of the surface of the as-deposited sample

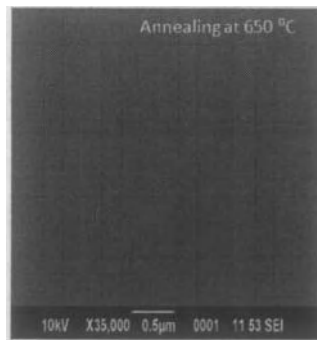


**Fig.6. (b)** Typical SEM image of the surface of the annealed sample 650°C

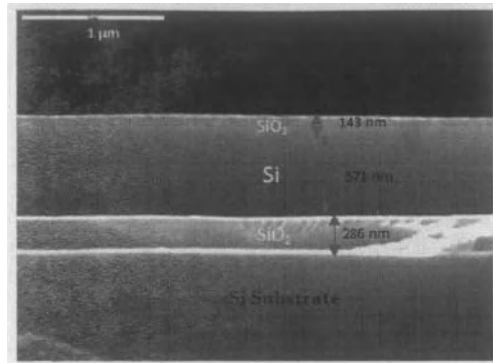


**Fig.6. (c)** Typical SEM image of cross-sectional morphologies of the as-deposited sample

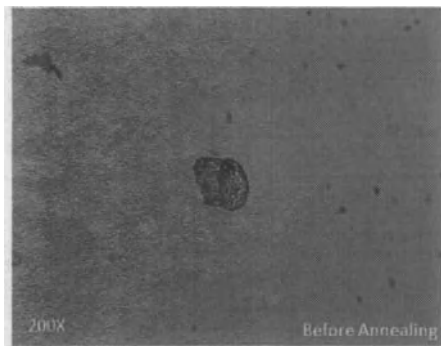


**Fig.7. (a)** Optical image of the surface of the as-deposited sample

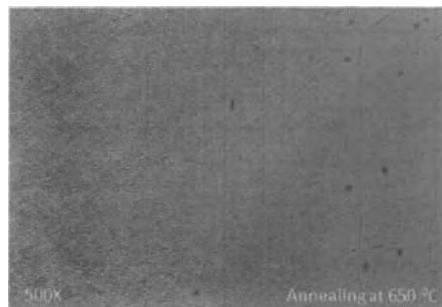


**Fig.7. (b)** Optical image of the surface of the annealed sample 650°C

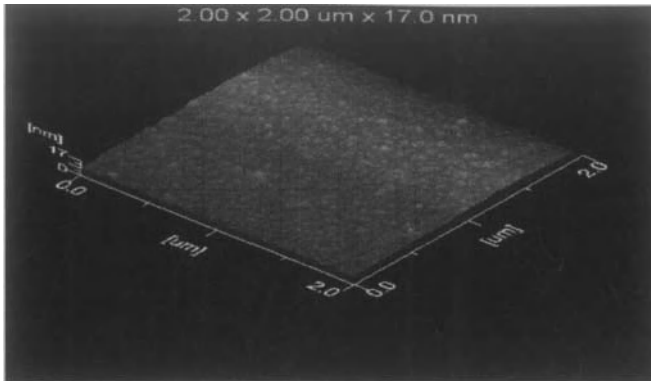


**Fig.8. (a)** Three-dimensional AFM image of the as-deposited sample

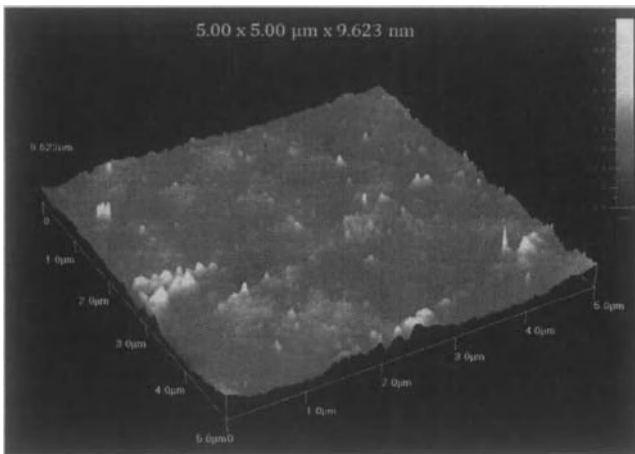


**Fig.8. (b)** Three-dimensional AFM image of the annealed sample 650°C

**Spectral Distribution of Si/SiO<sub>2</sub> Coatings Transmittance**

Annealing effects were seen by spectral distribution. An Average transmission of Si/SiO<sub>2</sub> coatings is achieved 75% in the 3-5μm wave bands as shown in Figure 10. The figure shows that these films are transparent (T+R=1) in the 3-5μm wavelength range and also shows that blockage of transmission appears at 4.2μm due to absorbance of carbon dioxide (CO<sub>2</sub>) except a sample which annealed at 650°C.

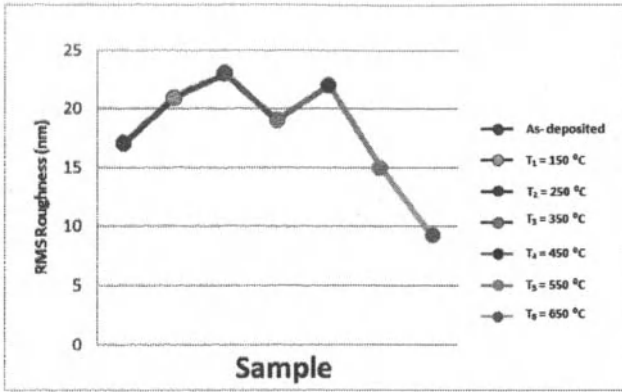


Fig.9. RMS roughness of the as-deposited and annealed samples

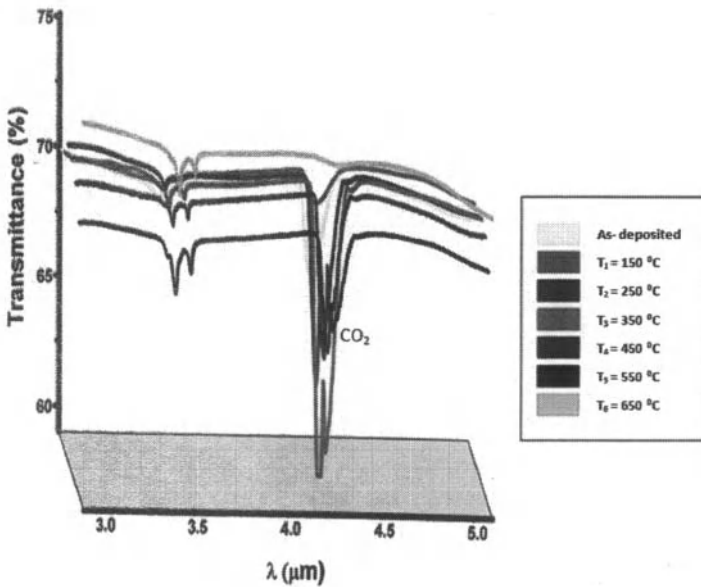


Fig.10. Measured transmission spectra for the as-deposited and annealed samples

## Conclusions

Multilayer thin-films of Si and SiO<sub>2</sub> are successfully prepared by RF magnetron sputter deposition. Annealed at 650°C generates smooth films as well as enhanced optical properties. The resulting models were helpful for determining the errors in deposition processes of each of the utilized deposition techniques, and this was the main goal. Thus, it has been found that the thicknesses of the coatings were controlled mainly within the expected accuracy. The main problem in deposition of the studied samples is control of the desired refractive index by means of better determination of deposition rate of high index material or by avoiding the undesired co-deposition when only the low index material is supposed to be deposited.

## Acknowledgements

One of the Authors (K. Iqbal) expresses his gratitude to Professor A.A. Khan for guiding me during my research work, reported in this paper. He also thanks all family members for their support. He also acknowledges the financial support of NUST.

## References

- [1] J. Y. Kim, D. W. Kim, H. S. Jung and K. S. Hong, *Jpn. J. Appl. Phys.*, Vol. 44, 2005, pp. 6148.
- [2] K. C. Park, D. Y. Ma, K. H. Kim, The physical properties of Al-doped zinc oxide films prepared by r.f. magnetron sputtering, *Thin Solid Films*, Vol. 305, 1997, pp. 201–209.
- [3] S. Sanjabi, S. K. Sadmezzaad, K. A. Yates, Z. H. Barber, *Thin Solid Films*, Vol. 491, 2005, pp. 190-196.
- [4] M. H. Asghar, F. Placido and S. Naseem, *Eur. Phys. J. Appl. Phys.*, Vol. 36, 2006, pp. 119.
- [5] M. Kuo, D. J. Poxson, Y. S. Kim, F. W. Mont, J. K. Kim, E. F. Schubert, and S. Lin, "Realization of a near-perfect antireflection coating for silicon solar energy utilization," *Opt. Lett.* 33, 2527-2529 (2008)
- [6] U. Bach, D. Lupo, P. Comte, J. E. Moser, F. Weissortel, J. Salbeck, H. Spreitzer and M. Gratzel, *Nature*, Vol. 395, 1998, pp. 583.
- [7] J. D. Rancourt, *Optical Thin Films User Handbook*, SPIE Publishing, Washington USA, 1996.
- [8] M. Bessell, *Encyclopedia of Astronomy and Astrophysics*, Nature Publishing Group and Institute of Physics Publishing, UK, 2001.
- [9] TFCALC: <http://www.sspectra.com/>
- [10] I. H. Malitson, Interspecimen comparison of the refractive index of fused silica, *J. Opt. Soc. Am.*, Vol. 55, 1965, pp. 1205
- [11] D. Josell, W. C. Carter and J. E. Bonevich, *Nanostruct. Mater.*, Vol. 12, 1999, pp. 387.
- [12] M. H. Asghar, F. Placido and S. Naseem, *Eur. Phys. J. Appl. Phys.*, Vol. 35, 2006, pp. 177.

*Characterization of Minerals, Metals, and Materials*  
Edited by: Jiann-Yang Hwang, Sergio Neves Monteiro, Chengguang Bai,  
John Carpenter, Mingdong Cai, Donato Firrao, and Buoung-Gon Kim  
TMS (The Minerals, Metals & Materials Society), 2012

# **Characterization of Minerals, Metals, and Materials**

## **Characterization of Carbon and Soft Materials**

Session Chairs:  
**Shadia J. Ikhmayies**  
**Jinhui Peng**

## **THERMAL PROPERTIES OF POLYESTER COMPOSITES INCORPORATED WITH COIR FIBER**

Helvio Pessanha Guimarães Santafé Jr., Nuã Simonassi, Sergio Neves Monteiro

State University of the Northern Rio de Janeiro, UENF, Advanced Materials Laboratory,  
LAMAV; Av. Alberto Lamego, 2000, 28013-602, Campos dos Goytacazes, Brazil  
[santafejr@uenf.br](mailto:santafejr@uenf.br)

Keywords: coir fiber, polyester composites, thermogravimetric analysis, fiber/matrix interaction

### **Abstract**

Thermoset polymers, like the polyester, become harder with increasing temperature owing to molecular crosslink formation, which is a thermal benefit for composite matrix applications. Natural lignocellulosic fibers, however, have low thermal resistance and tend to degrade with increasing temperature. Therefore, the combination of a lignocellulosic fiber, as reinforcement, with a thermoset polymer, as the matrix, results in a composite material with complex thermal behavior. In the present work, a thermal analysis was conducted on polyester composites with different amounts of coir fibers. Both TGA and DTG curves were analyzed to determine the effect of the coir fiber on the thermal resistance of the composites. It was found that the coir fiber sensibly affects the thermal behavior of the polyester matrix for fiber amounts above 10% in volume. This effect is associated with an increase in thermal degradation.

### **Introduction**

In recent years, there has been an increase application of natural fibers as reinforcement of polymer matrix composites in several industrial sectors, with special participation in automobile components [1-3]. Figure 1 illustrates the different components of a modern BMW sedan that are fabricated with lignocellulosic reinforced polymer composites.



Figure 1. BMW sedan and its different parts made of polymer composites reinforced with lignocellulosic fibers. ([www.bmwgroup.com](http://www.bmwgroup.com))

In fact, not only environmental benefits are motivating the substitution of natural fibers for glass fiber in polymer composites [4], but also technical, economical and societal advantages [5,6]. A number of reasons favor the use of natural fibers, mainly those obtained from cellulose-based vegetables, also known as lignocellulosic fibers such as cotton, flax, sisal, jute, hemp, wood, pineapple, to mention a few. Actually, it is estimated that more than 500 lignocellulosic fibers are known and have potential to be used in engineering applications. Most of these fibers are native of tropical regions in Africa, South Asia, Central and South Americas. The plant cultivation, extraction and processing of lignocellulosic fibers represent an important source of income for people and countries in these regions.

In the Amazonian region, for instance, lignocellulosic fibers such as curaua, piassava, buriti, guarumã, tucumã and many others that have been for long time used in simple products like ropes, baskets, brooms and carpets, are recently being investigated as possible reinforcement for composites [7-9]. In particular, the coir fiber, Fig. 2, the lignocellulosic fibers, is at the present time extensively investigated for this purpose [10-21]. As any lignocellulosic fiber, however, the coir fiber is subjected to thermal degradation at temperatures around 280°C [22], which would impair the performance of a polymer composite subjected to such higher temperature.

Araujo [22], working on coir fiber up to a fraction of 20% reinforcing both polyurethane and polypropylene composites, found by thermogravimetric analysis (TGA) and by its derivative thermogravimetry (DTG), two stages of composite decomposition between 300-380°C and 400-440°C. Since a thermal analysis of coir fiber composites has not been performed thus far on thermoset polymer matrix, the objective of this work was to investigate the effect caused by different amounts of coir fibers on the thermal behavior of polyester matrix composites.

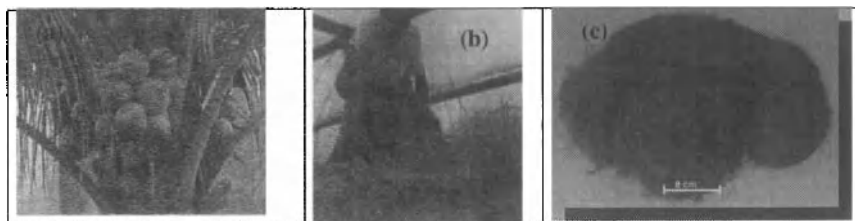


Figure 2 - Plantation (a), manual processing (b) and bundle (c) of coir fibers.

### Experimental Procedure

A lot of processed coir fibers was purchased from a Brazilian firm, “Coco Verde Reciclado”, which commercializes lignocellulosic fibers cultivated in the many regions. From the as-received lot, one hundred fibers were separated for a statistic analysis of length and diameter as shown in Fig. 2. This figure reveals that the dimensions of the coir fibers as any other lignocellulosic fiber [4-6], are heterogeneous with a significant dispersion in values.

Another relevant information from the histograms in Fig. 3 is that the average length of 846 mm is more than 15 times its critical length of 3 mm, obtained in epoxy pullout tests [20]. This is considered a condition for long and continuous fiber [23] and assures the most effective

strengthening of the matrix. Here it is important to mention that the statistical distribution in Fig. 2 is similar to others recently reported on coir fibers [16,17]

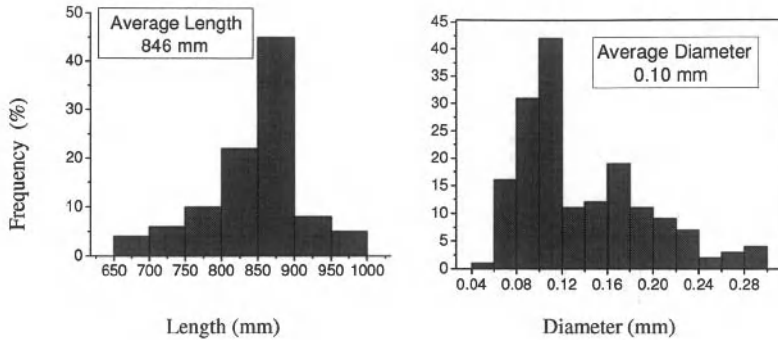


Figure 3 – Histogram of the statistical distribution: (a) length and (b) diameter of coir fibers.

Composites were fabricated by placing, separately, amounts of 0, 10, 20 and 30% in volume of continuous and aligned coir fibers inside a small cylindrical mold with 5.5 mm in diameter and 20 mm in length. Still fluid commercial orthophthalic polyester resin added with 0.5% methyl-ethyl-ketone hardener was poured into the mold to serve as the composite matrix. The composites were allowed to cure at 25°C for 24 hours. After removing each composite from its cylindrical mold, thin-cut discs with 2 mg in weight, corresponding to approximately 1 mm in thickness, were used as samples for thermal analysis. TGA and DTG analyses were conducted in a model 2910 TA instrument equipment shown in Fig. 4.

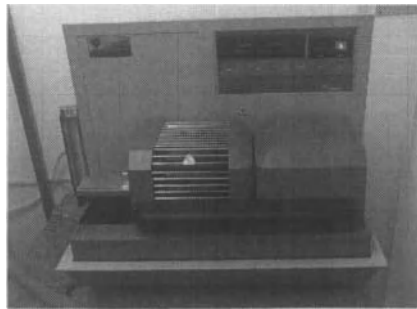


Figure 4. Thermal analysis TGA and DTG equipment.

## Results and Discussion

Figure 5 shows both the TGA and DTG curves for the coir fiber reinforced polyester composites as well as the corresponding curves for the pure (0% fiber) polyester resin.

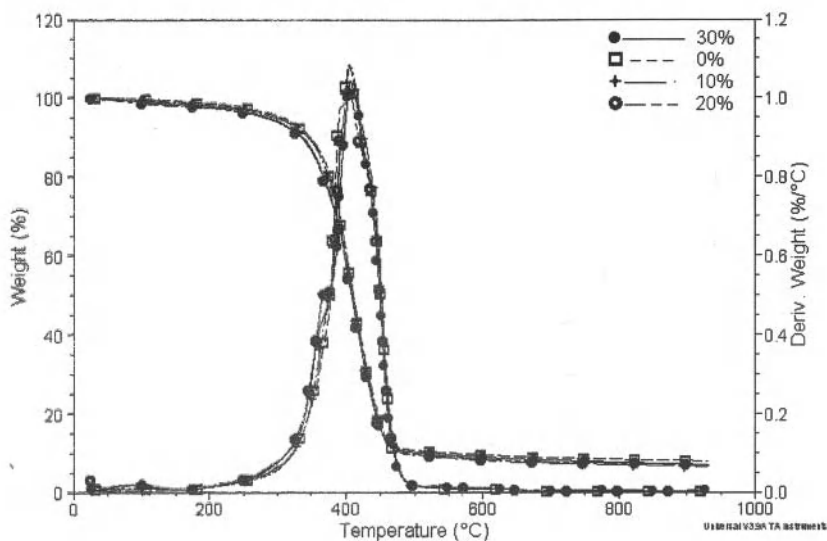


Figure 5. TGA and DTG curves for the pure polyester and the polyester composites reinforced with different volume fractions of coir fibers.

The TGA and DTG curves shown in Fig. 5 reveal the thermal stability of the composites in terms of weight loss. In this figure, it is important to notice that the polyester used as matrix, corresponding to 0% fiber, begin to decompose around 300°C and finishes around 500°C. This is expected for this type of thermoset polymer in which thermal degradation starts with the evolution of volatile compounds followed by breaking and depolymerization of molecular chains [24]. It should also be noticed in Fig. 5 that, for both types of curves TGA and DTG, there is an apparent superposition of all investigated composites with respect to the pure polyester curves. In principle, this would indicate that, at least up to a volume fraction of 30%, no effect on the thermal behavior of the polyester composite could be attributed to the coir fibers. Such result is difficult to be explained since the coir fiber deteriorates at temperatures lower [22] than those, 300-500°C, associated with the polyester matrix decomposition.

A careful observation of the DTG curve, which is amplified in Fig. 6, reveals a sensible effect caused by the coir fiber.

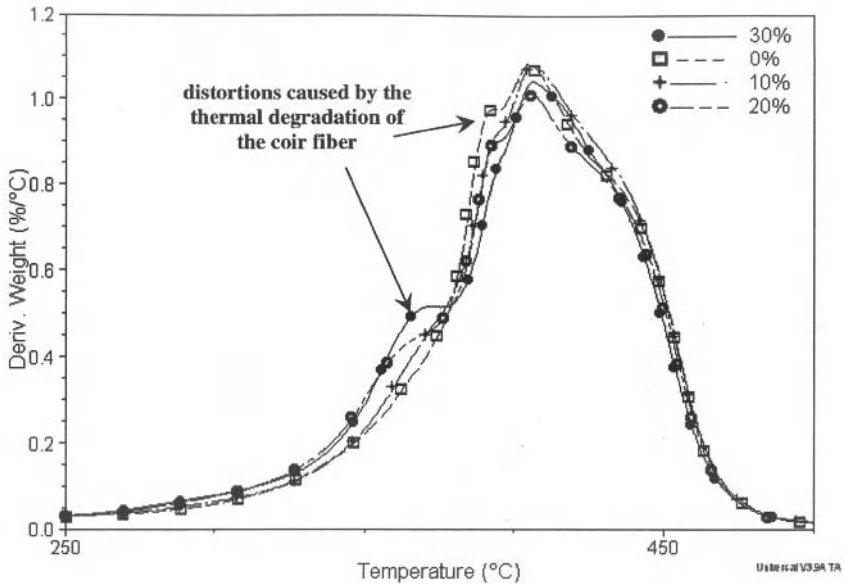


Figure 6. Amplified DTG curves for the pure polyester and the polyester composites reinforced with different volume fractions of coir fibers.

The effect of the coir fibers on the thermal behavior of the polyester composites can be detected by distortions caused in the DTG curve as compared to the pure polyester curve (0% fiber) around 370 and 390°C. These distortions are more pronounced the greater the volume fraction of coir fiber.

A possible interpretation for this behavior can be apprehended if one considers that the actual curves for the composites are formed by three peaks. One peak is that corresponding to the pure polyester with a maximum around 410°C. The two other peaks around 370 and 390°C would correspond to the influence of the coir fiber degradation.

The possibility of the coir fiber to contribute with two thermal degradation peaks was also reported by Araujo [22] in thermoplastic matrix composites. In that work, a better definition of the two peaks was facilitated by the decomposition of the matrix, which occurs through two thermal peaks. The reason for the two decomposition peaks in the coir fiber could be apparently related to the decomposition of cellulose and lignin as found in other natural lignocellulosic fibers [25]. For the particular case of coir fibers, it was concluded [14] that in oxidative atmosphere it is not possible to separate the different degradation processes of the fiber components such as hemicellulose, cellulose and lignin. Degradation reactions in the coir fiber

are complex and overlap in the range of 220 to 350°C [14]. This temperature range is lower than the peaks around 370 and 290°C, Fig. 6, suggested in the present work. However, the protection of the polyester matrix could be responsible for allowing the degradation of the coir fiber to begin at higher temperatures.

### Conclusions

- A thermal analysis based on TGA and DTG curves revealed the effect of coir fibers incorporated up to a volume fraction of 30% into a polyester matrix composite.
- The TGA curves of the composites fail to show any sensible difference to the pure polyester curve. By contrast, the DTG curves were able to reveal a noticeable effect caused by the coir fiber, as evidenced by distortions towards lower temperatures in comparison to the pure polyester curve.
- It is suggested that these distortions are due to peaks around 370 and 390°C superimposed with the main polyester peak at 410°C. These coir fiber related peaks can be possibly attributed to the separate decomposition of cellulose and lignin in the fiber.

### Acknowledgements

The authors thank the support to this investigation by the Brazilian agencies: CNPq, CAPES, FAPERJ and TECNORTE/FENORTE.

### References

1. S. Hill, "Cars that grow on trees". *New Scientists*, 153(2067) (1997) 36-39.
2. G. Marsh, "Next step for automotive materials". *Mater. Today*, 6(4) (2003) 36-43
3. R. Zah, R. Hischer, A.L. Leão, I. Brown, "Curaua fibers in automobile industry – A sustainability assessment". *J. Cleaner Production*, 15, (2007) 1032-1040.
4. P. Wambua, I. Ivens and I. Verpoest, "Natural fibers: can they replace glass and fibre reinforced plastics?". *Composites Science and Technology*, 63 (2003) 1259-1264.
5. Crocker, J., "Natural materials innovative natural composites". *Materials Technology*, 2-3 (2008) 174-178.
6. S.N. Monteiro, F.P.D. Lopes, A.S. Ferreira and D.C.O. Nascimento, "Natural fiber polymer matrix composites: cheaper, tougher and environmentally friendly". *JOM*, 61(1) (2009) 17-22.
7. K.G. Satyanarayana, J.L. Guimarães, F. Wypych, "Studies on lignocellulosic fibers of Brazil. Part I: Source, production, morphology, properties and applications". *Composites: Part A*, 38, (2007) 1694-1709.
8. S.N. Monteiro, F.P.D. Lopes, L.C. Motta, L.S. Marques and T.G.R. Portela, "Statistical analysis to characterize the uniformity of mechanical properties of buriti fibers". *Proceedings of Characterization of Materials Symposium, TMS 2009* (San Francisco, CA, USA, March 2009) 1-6.
9. N.S.S. Santos, C.G.B.T. Dias, "Mechanical properties of plant braided fabrics/post-consumer polypropylene composites". *Proceedings of the 41<sup>st</sup> International Symposium on Macromolecules – MACRO 2006* (Rio de Janeiro, Brazil, July 2006) 1-2.

10. A.L. Leão, I.H. Tan and J.C. Caraschi, "Curaua Fiber – A tropical natural fibre from Amazon – Potential and applications in composites", *Proceedings of the International Conference on Advanced Composites*, (Hurghada, Egypt, 1998) 557-564.
11. S.N. Monteiro, J.F. de Deus and J.R.M. d'Almeida, "Interfacial strength of curaua fiber reinforced polyester composites", *Proceedings of SAM-CONAMET* (Mar del Plata, Argentina, 2005) 1-6.
12. S.N. Monteiro, R.C.M.P. Aquino, F.P.D. Lopes, E.A. Carvalho and J.R.M. d'Almeida, "Mechanical behavior and structural characteristics of polymeric composites reinforced with continuous and aligned curaua fibers". *Rev. Mater.*, 11(3) (2006) 197-203.
13. S.N. Monteiro, J.F. de Deus and J.R.M. d'Almeida, "Mechanical and structural characterization of curaua fibers", *Proceedings of Characterization of Minerals, Metals & Materials - TMS Conference*, (San Antonio, USA, March, 2006) 1-8.
14. F. Tomczak, K.G. Satyanarayana, T.H.D. Sydenstricker, "Studies on lignocellulosic fibers of Brazil. Part III: Morphology and properties of Brazilian curaua fibers". *Composites: Part A*, 38, (2007) 2227-2236.
15. S.N. Monteiro, R.C.M.P. Aquino, and F.P.D. Lopes, "Performance of curaua fibers in pullout tests". *J. Mater. Sci.* 43 (2008) 489-493.
16. S.N. Monteiro, A.S. Ferreira and F.P.D. Lopes, "Rupture mechanisms in composites reinforced with curaua fibers", *Proceedings of Characterization of Minerals, Metals & Materials - TMS Conference*, (New Orleans, USA, March, 2008) 1-8.
17. R.V. Silva, E.M.F. Aquino, L.P.S. Rodrigues and A.R.F. Barros, "Curaua/Glass Hybrid Composite: The Effect of Water Aging on the Mechanical Properties", *J. Reinforced Plast. & Comp.*, 28 (2009) 1857-1868.
18. S.N. Monteiro, A.S. Ferreira and F.P.D. Lopes, "A comparative study of curaua fiber reinforced epoxy matrix composites as building materials", *Proceedings of the Global Symposium on Recycling, Waste Treatment and Clean Technology – REWAS2008*, (Cancun, Mexico, October 2008) 1653-1658.
19. R.V. Silva and E.M.F. Aquino, "Curaua fiber: A new alternative to polymeric composites", *J. Reinforced Plast. & Comp.*, 27(1) (2008) 103-112.
20. S.N. Monteiro, A.S. Ferreira and F.P.D. Lopes, "Pullout tests of curaua fibers in epoxy matrix for evaluation of interfacial strength", *Proceedings of Characterization of Minerals, Metals & Materials - TMS Conference*, (San Francisco, USA, March, 2009) 1-7.
21. S.N. Monteiro, A.S. Ferreira and F.P.D. Lopes, "Izod impact energy of polyester matrix composites reinforced with aligned curaua fibers", *Proceedings of Characterization of Minerals, Metals & Materials - TMS Conference*, (San Francisco, USA, March, 2009) 1-8.
22. C.R. Araujo, "Kinetics of thermal decomposition of polymeric composites with curaua fibers" (in Portuguese) *D.Sc. Dissertation*, School of Chemistry, Federal University of Rio de Janeiro – UFRJ (Rio de Janeiro, Brazil, 2003).
23. W.D. Callister Jr., *Materials Science and Engineering – An Introduction*, 5 ed., (New York, NY: John Wiley & Sons, 2000).
24. H.F. Mark, N.M. Bikales, C.G. Overgerger, G.Menges, *Encyclopedia of Polymer Science and Engineering*, John Wiley & Sons, New York, 1988.
25. J.R.M. d'Almeida, R.C.M.P. Aquino, S.N. Monteiro, "Tensile mechanical properties, morphological aspects and chemical characterization of piassava fibres", *Composites- Part A*, 37 (2006) 1473-1479.

## INVESTIGATING THE RHEOLOGY OF LCPS THROUGH DIFFERENT DIE GEOMETRIES

Arash Ahmadzadegan, Michael A. Zimmerman and Anil Saigal

Mechanical Engineering Department  
Tufts University  
Medford, MA, 02155

Keywords: Rheology, Extrusion, Die Swell, LCP, Finite Element

### Abstract

In this study, the rheology of liquid crystalline polymer (LCP) melts through simplified 2-D and 3-D die geometries is simulated using Polyflow™. It is known that rheological properties of LCPs are close to long chain polymers and their directionality is close to those of small molecule liquid crystals (SMLCs). As a result, different rheological models (both viscoelastic and generalized Newtonian) for long chain polymers in Polyflow™ were investigated based on the available capillary rheometer data. By varying the parameters in these models, it is possible to adjust the effect of shear viscosity, normal stress differences and relaxations times on the rheology of the polymer. The free surface of the extrudate coming out of the die is simulated and the amount of die swell for different types of rheological models is compared. This study indicates that the Bird-Carreau model best applies to thermotropic LCP materials as quantified by die swell. Since the rheology of the LCPs affects the orientation of the crystals, the result of this simulation can be further used to predict the orientation of crystallines inside and outside the die.

### Introduction

Any rod like molecule or crystal tends to orient itself in the direction of shear as it moves within a flow. Since polymers consist of long chains of molecules, they experience the same phenomena when flowing in the melt condition. For most polymers, the molecules change direction and distribute uniformly in space during the solidification. However due to the higher inertia of the crystals in the liquid crystalline polymers, the oriented crystals will keep their order during the solidification and as a result the final product will show anisotropy in material properties.

This investigation focuses on the film casting of the liquid crystalline polymers and the rheology of these materials inside and outside of the die.

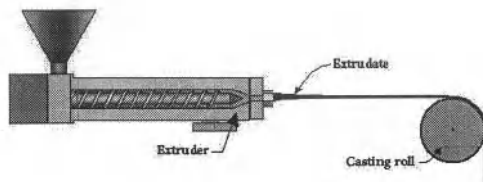


Figure 1. The extrusion process including a casting roll

Figure 1 shows the extrusion process inside and outside the die. In this study, we investigate the domain of simulation that starts from inside the die and ends close to the casting roll. The major physical and simulation phenomenon that happens in this region are (a) boundary layer inside the die, (b) die swell at the lip of the die, (c) free surface and (d) the reduction in area of extrudate whenever the pulling velocity of the casting roll is more than the velocity of the extrudate.

### Numerical Method

The commercial software used for the simulations is Polyflow™. Unlike most generic flow solvers (like FLUENT™) that use finite volume method [1], Polyflow™ uses a finite element scheme to solve the constitutive equations governing the rheology of materials inside and outside of the die. There are advantages and disadvantages to this method of numerical simulation and the way it has been implemented in Polyflow™ compared to the finite volume method and is described in Table 1.

Table 1. Advantages and disadvantages of finite element simulation in Polyflow™

Advantages	Disadvantages
The accuracy of the solution is higher and for each cell it is possible to increase the accuracy.	It needs extreme amount of memory which makes it impossible to increase the number of cells depending on memory.
The values on the nodes of elements are readily known which makes it possible to change the shape of the cells according to physical changes in the domain. (Convenient for finding the shape of the free surface accurately.)	Unlike FLUENT™, the method that Polyflow™ uses to solve the discretized equations does not allow users to control the convergence during the simulation.
Polyflow™ is optimized for polymer rheology and has a wide range of rheological models are available to choose from for different materials.	Polyflow™ has much less access points compared to FLUENT™ for defining user defined functions (UDFs) and it is harder and slower to customize it since it used language CLIPS for its UDFs.
	It is less stable than the Finite Volume Method (FVM) for flow simulations.

For generating mesh, GAMBIT was used for all the simulations [1]. GAMBIT is the mesh generation software for FLUENT™[1] and is capable of exporting the generated mesh to Polyflow™. It offers a single interface for geometry creation and meshing. GAMBIT's combination of CAD interoperability, geometry cleanup, decomposition and meshing tools results in one of the easiest, fastest and most straightforward preprocessing paths from CAD to quality CFD meshes. Special care has been taken to resolve the boundary layer and other high gradient regions like the lip of the die. Moreover, all the generated mesh for discretizing the flow domain is structured mesh. This type of mesh is useful especially when there is a free surface since some of the remeshing techniques in Polyflow™ need the mesh outside the die to be sliceable.

## Rheological Models

Since it is known that the rheology of the LCPs are close to long chain polymers and directionality of these materials are close to small molecule liquid crystals (SMLC), it is possible to use the rheological models used for long chain polymers and combine them with the theories that apply to SMLC[2].

There are a wide variety of rheological models available in Polyflow™. The simplest model which linearly relates the rate of deformation of the fluid at each point to the shear stress in all directions is the Newtonian model. Other models have more complicated relations between the physical and other material properties. It is also possible to define different relations and constants in different directions for anisotropic materials. Three different rheological models were investigated to compare the amount of die swell in different simulations. The first one is the Newtonian model with constant viscosity. Second model is the Power-Law model in which the viscosity is defined as:

$$\eta = K(\lambda\dot{\gamma})^{n-1} \quad (1)$$

In this equation  $\eta$  is viscosity and  $\dot{\gamma}$  is the local shear rate.  $K$  and  $n$  are consistency factor and power law index, respectively.  $\lambda$  is the natural time or the reciprocal of reference shear rate. Figure 2 shows the data from a capillary rheometer experiment used to determine the constants in this model. As can be seen, the capillary rheometer data can be approximated by a line when plotted on a log-log scale.

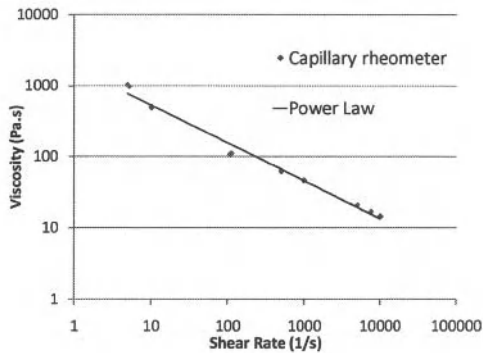


Figure 2. Power-law behavior of an LCP material

Table 2 shows the constants extracted from the capillary rheometer data. As can be seen in Table 2, the maximum and minimum shear rates based on the capillary rheometer data are 1029 and 14.4 Pa.s, respectively. The shear rates in the simulated extrusion processes are low compared to the information obtained from the capillary rheometer and for a more precise modeling of the rheology more data points in the low shear region are needed. The minimum shear rate is high as compared to the shear rate in the extrusion process. As such, it is better to define a viscosity for very low shear rates. Otherwise, the interpolation of viscosity versus shear rate increases indefinitely, which is not a physical phenomenon and causes the solution to diverge. This low

shear rate viscosity can be defined using the more advanced definitions of the Power-law model, such as the Bird-Carreau model which is shown in Table 3.

Table 2. Power-Law model constants

k (Pa.s <sup>n</sup> )	n	Max Viscosity (Pa.s)	Min Viscosity (Pa.s)	Temperature (°C)
1864	0.4651	1029	14.4	350

In the Bird-Carreau model,  $\eta_0$  is the viscosity of the material at zero shear-rate and  $\eta_\infty$  is the viscosity at very high shear rates. In addition, one viscoelastic fluid model is also considered for comparison with Newtonian and Bird-Carreau models. The choice of this viscoelastic model is arbitrary and is only considered to compare the existence of normal stresses and their effect on the die swell. Here the Oldroyd-B model has been used as shown in Table 3. The various parameters in the Oldroyd-B model are defined elsewhere [3]. In this model, it is possible to consider the pure viscous component of extra stress tensor,  $T_2$ . As such, use of the Oldroyd-B model results in a stable behavior during the numerical simulation.

Table 3. Rheological models [3]

Rheological Model	Correlation
Bird-Carreau	$\eta = \eta_\infty + (\eta_0 - \eta_\infty) (1 + \lambda^2 \dot{\gamma}^2)^{\frac{n-1}{2}}$ (2)
Oldroyd-B	$T = T_1 + T_2$ $T_2 = 2\eta_2 D$ $\overset{\nabla}{T}_1 = \frac{DT_1}{Dt} - T_1 \cdot \Delta v - \Delta v^T \cdot T_1$ $T_1 + \lambda \left( \overset{\nabla}{T}_1 \right) = 2\eta_1 D$ $-\Delta P + \nabla \cdot (T_1 + T_2) + f = \rho a$ $\nabla \cdot v = 0$ (3)

### Results and Discussion

The simulation in this study is divided into 3 main groups:

- 1) 2D simulation of the flow inside and outside the die for die-swell observation.
- 2) 2D simulation of the flow inside and outside the die with the effect of casting roll.
- 3) 3D simulation of the flow inside and outside the die.

The first model shown in Figure 3 is a 2-D cross section of a coat-hanger die which is taken from the middle section of a production die. As can be seen, the die swell observed for the viscoelastic material is much more than that predicted using the Newtonian or Bird-Carreau models. This difference comes from the absence of normal stress differences in the Newtonian and Bird-Carreau models. The expansion of the extrudate after exiting the die lip when using the Newtonian and Bird-Carreau models is only due to the velocity gradient inside the die. However, in the case of viscoelastic fluid (Oldroyd-B model), shear stresses results in normal stresses that are released upon exiting the die and expand the extrudate more. It is known that thermotropic

liquid crystalline polymers (TLCPs) show very small die swell [4]. This indicates that the Bird-Carreau model best applies to thermotropic LCP materials as quantified by die swell.

The second sets of results are for the case where a force is applied at the end of the extrudate after it exits the die to account for the force that the casting roll applies to the extrudate. Figures 4 and 5 show the velocity contours for Newtonian and Bird-Carreau models, respectively. As can be seen, the maximum velocity of the extrudate at the end of domain for Bird-Carreau model is slightly more than the case of Newtonian model. This difference seems to be as a result of shear thinning behavior of the Bird-Carreau model in presence of shear stresses.

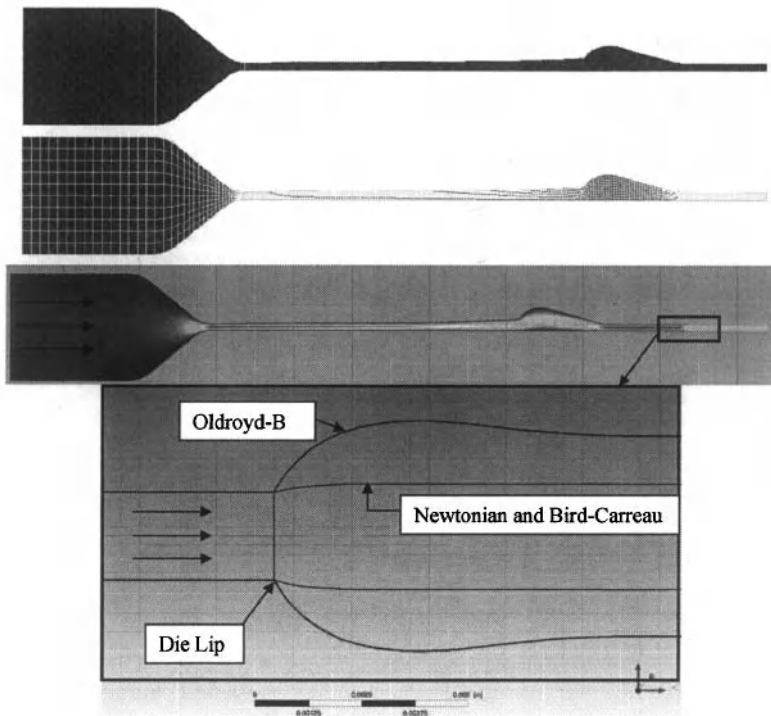


Figure 3. Geometry of 2D coat-hanger die and die-swell for Newtonian, Bird-Carreau and viscoelastic materials

Figure 6 shows the local shear rate contour inside and outside the die. Local shear rate changes from zero to 14.48/s, and the maximum shear rate occurs at the lip of the die where the extrudate exits the die.

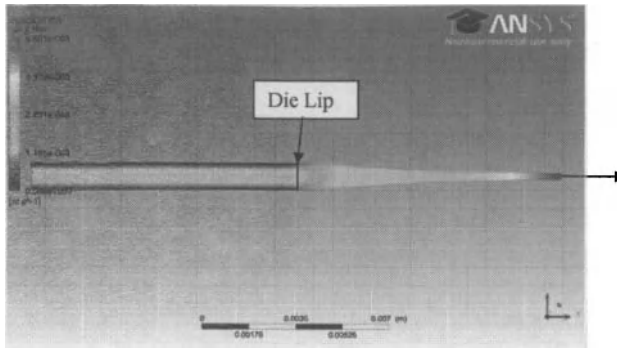


Figure 4. Effect of the casting roll on the 2D extrudate with Newtonian fluid model

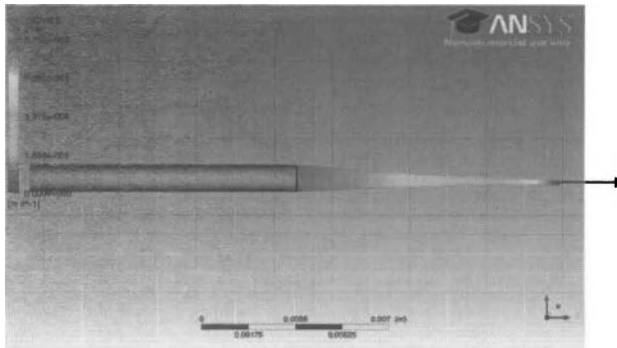


Figure 5. Effect of the casting roll on the 2D extrudate with Bird-Carreau model

The rest of the simulations are done in 3-D incorporating the Bird-Carreau model. Considering the periodic boundary condition on the sides of the simulation domain makes it possible to model a section of an infinite die. Another aspect of this die is that two separate streams enter the die from the left and after mixing they exit the die as a single stream.

In Figures 8 and 9 the effect of casting roll has been applied to the free part (end) of the extrudate and the velocity contours generated are shown inside and on the boundaries, respectively. The purpose of the two different streams of fluid at the inlet was to change the direction of the velocity coming into the die to simulate excessive warpage of the final product. However, the numerical solution always diverged when the exit velocity profile was not normal to the die lip surface.

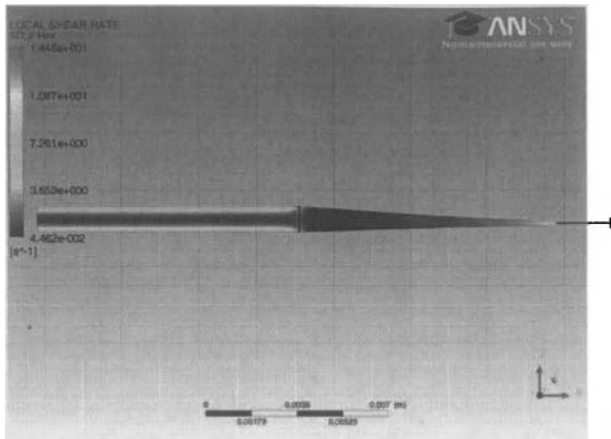


Figure 6. Local shear rate inside and outside the die in presence of casting roll for Bird-Carreau model

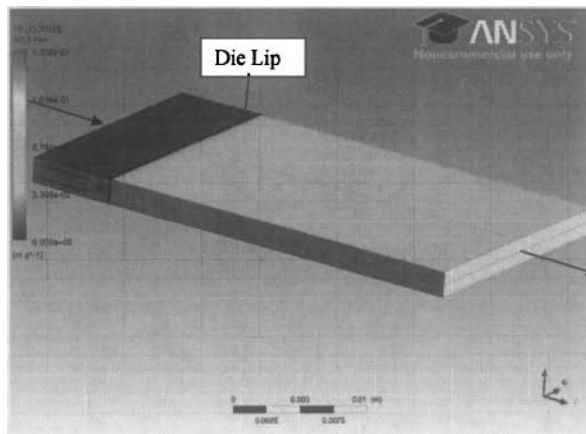


Figure 7. Velocity profiles inside and outside of the die in 3D simulation

### Conclusions

The free surface of the extrudate coming out of the die is simulated and the amount of die swell for different types of rheological models is compared. This study indicates that the Bird-Carreau model best applies to thermotropic LCP materials as quantified by die swell. Since the rheology of the LCPs affects the orientation of the crystals, the result of this simulation can be further used to predict the orientation of crystallines inside and outside the die.

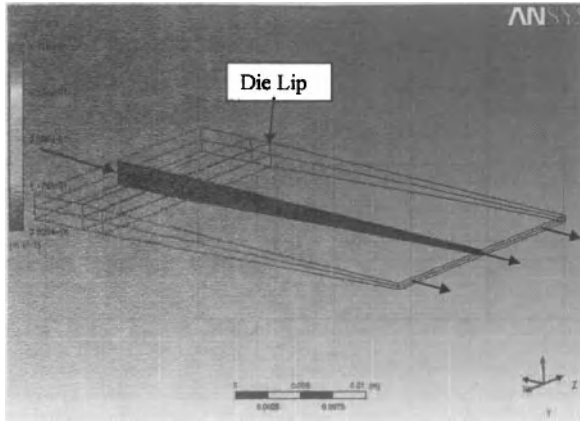


Figure 8. Velocity profile on a section of the die after applying the casting roll effect

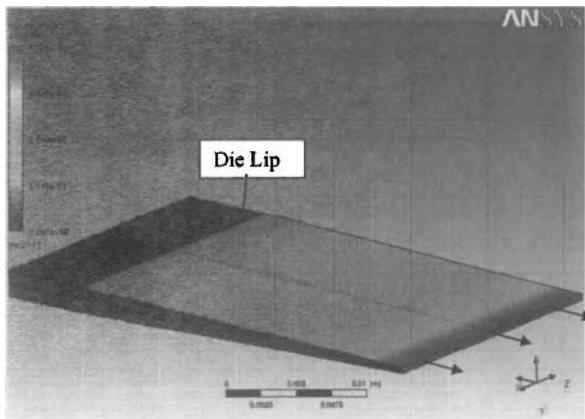


Figure 9. Contours of velocity on the 3D model with casting rolls

### References

1. ANSYS™ Fluent™ Documentation, Release 13, Sep. 2010.
2. A.M. Donald, et al., *Liquid Crystalline Polymers*, Cambridge University Press, 2006
3. ANSYS™ Polyflow™ Documentation, Release 13, Sep. 2010.
4. Tai-shung Chung, *Thermotropic Liquid Crystalline Polymers*, Technomic Publishing Company, Inc., 2001, p. 238.

## **EFFECT OF THE FIBER EQUIVALENT DIAMETER ON THE ELASTIC MODULUS AND DENSITY OF SISAL FIBERS**

Artur Camposo Pereira, Wellington Pereira Inácio, Frederico Muylaert Margem, Sergio Neves Monteiro

State University of the Northern Rio de Janeiro, UENF, Advanced Materials Laboratory,  
LAMAV; Av. Alberto Lamego, 2000, 28013-602, Campos dos Goytacazes, Brazil  
[arturcamposmv@hotmail.com](mailto:arturcamposmv@hotmail.com)

Keywords: sisal fibers, density elastic modulus, Weibull analysis, diameter correlation.

### **Abstract**

Natural fibers are currently gaining attention as reinforcement of polymer composites for uses in engineering parts for automobile and building construction. In spite of environmental, economical and societal advantages, the natural lignocellulosic fibers are not as uniform in their dimension and properties as compared to synthetic. In recent works it was found that the variation in strength could be correlate to the equivalent diameters for several lignocellulosic fibers including the sisal fibers. In the present work an investigation on a possible correlation of the equivalent diameter with changes in density and elastic modulus was carried out. Precise measurements of the equivalent diameter, conducted in a profile projector, were correlated with the density and the elastic modulus by means of the Weibull statistic analysis. The results showed that an inverse correlation with the diameter also applies for both the density and the elastic modulus with a high degree of precision. SEM observation of the sisal fiber in structure and fracture aspects strongly indicate that defects and microfibril participation could be responsible for the inverse correlation.

### **Introduction**

According to Kalia [1], cellulose-based fibers are currently being pushed owing to their "green" image. Contrary to synthetic glass fiber, extensively used in our modern technology, these lignocellulosic fibers are renewable and can be incinerated at the end of the material's lifetime without adding pollution in the atmosphere moreover, the amount of CO<sub>2</sub> released during incineration process is negligible as compared to the corresponding amount taken up by the plant throughout its lifetime. Even if an industrial processing equivalent of CO<sub>2</sub> release is added, the lignocellulosic fiber is considered neutral with respect to the emission of gases responsible for the global warming [2].

A growing industrial use of lignocellulosic fibers is under way in packaging, textiles, civil construction and automobile. One of their promising applications is as reinforcement for polymer composites. In fact, a considerable number of publications [3-8] has been dedicated to lignocellulosic fiber reinforced polymer composites. In particular, applications in the automotive industry are already in the market [9-12]. In spite of the environmental benefits as well as economical, technical and social advantages of lignocellulosic fibers, they also present shortcomings such as dimensional heterogeneities and low interfacial adhesion to hydrophobic polymer normally used as composite matrix [3-7]. Another characteristic that may significantly affect the properties of the lignocellulosic fiber is a sensible influence of the transversal dimensions or associated cross section area [3]. In recent works [13,14] it has been shown that the tensile strength of several lignocellulosic fibers display an universe correlation with their equivalent diameter. This correlation was also applied to sisal fibers for which values close to 1000 MPa were found for a mean equivalent diameter of 50  $\mu\text{m}$ . The mechanisms responsible

for this inverse correlation were indicated as due to the existence of proportionally more defects in thicker fibers that also present relatively more micro fibrils [14]. Based on these experimental evidences, the present work investigates whether a possible correlations. Could also exists between the density and the tensile elastic modulus with the corresponding sisal fiber equivalent diameter.

### Experimental Procedure

The sisal fibers were supplied by the Brazilian firm Sisalsul as a lot containing many thousands individual fibers. In a first moment, one hundred fibers were picked up from the as-received lot for a dimensional analysis. After leaning and drying at 60°C in a stove for one hour, the fibers diameter were measured in a Nikon profile projector at five equally spaced position along the fiber length. Two measurements were performed at each position by a 90° rotation, since the fibers are not perfect cylinders. The average of these measurements characterized the equivalent diameter of every evaluated fiber. Figure 1 presents the histogram associated with the statistical distribution of the equivalent diameters of the sisal fibers measured in the fibers step. In this

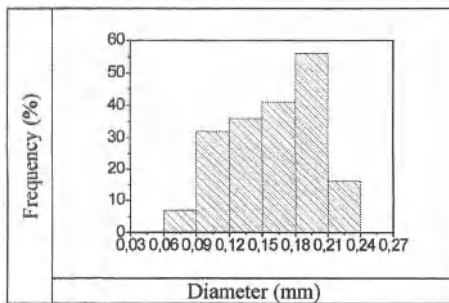


Figure 1: Statistical distribution of the equivalent diameter of the sisal fibers.

figure it is observed that the range of equivalent diameter extends from 0,4 to 0,22 mm, with a mean value of 0,13mm. Based on this range, six intervals of 0,06-0,09, 0,09-0,12, 0,12-0,15, 0,15-0,18, 0,18-0,21 and 0,21-0,24mm, were conventionally consider as division for the histogram in Fig. 1. For each one of these six intervals, a total of 20 fibers were them selected in a second moment and, after leaning and drying, had their diameter measured in the profile projector following the same above mentioned procedure. The 120 measured fibers, 20 for each interval, were them individually weighed in a scale with 0,001g of precision. The density,  $\rho$ , of individual fibers was them calculated by the expression

$$\rho = 4m/\pi d_e \quad (1)$$

where  $m$  is the mass and  $d_e$  the fibers equivalent diameter. These fibers, in a third moment, were tensile tested at a temperature of 25 °C in a model 5582 Instron machine. Special tensile grips were used to avoid both slippage and damage of the fiber. The tensile test strain rate was  $4,2 \times 10^{-2} \text{ s}^{-1}$ . Values of the elastic modulus were directly obtained from stress-strain curves. Both the density and elastic modulus values were statistically analyzed using the weibull method, used the computer program Weibull Analysis. The fracture tip of some tensile ruptured fibers were analyzed by scanning electron (SEM) microscopy in a model S5X-550 Shimadzu microscope

operating at an accelerating voltage of 15kV. The fiber sample was attached by means of a carbon tape onto a metallic support and then gold sputtered for SEM observation.

### Results and Discussion

Tensile results permitted the evaluation of modulus of elasticity the tensile strength for every fiber investigated. These values of strength were analyzed by the Weibull statistic method, in each of the six diameter intervals. Figure 2 shows the logarithmic graphs of the reliability vs. location parameter, also known as the Weibull graphs. In this figure the graphs are unimodal with just one straight fitting for all points in the same diameter interval. This indicates that every sisal fiber related to each one of the six intervals belongs to a group with same mechanical behavior.

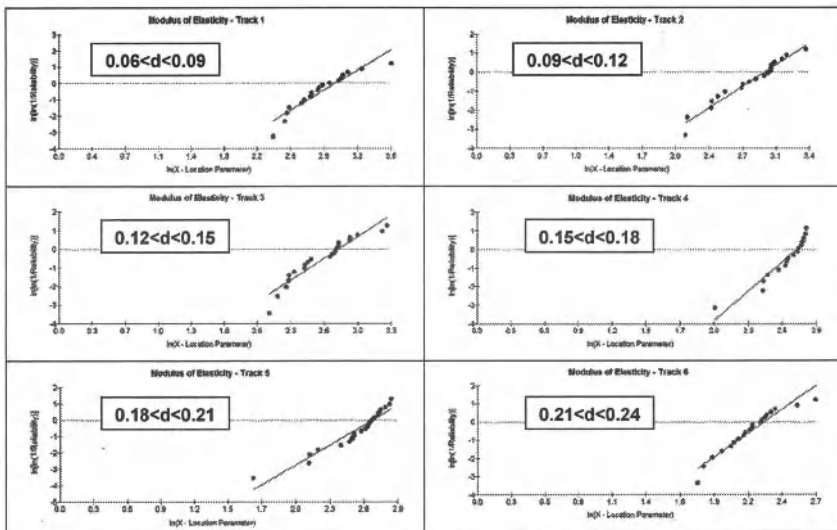


Figure 2: Weibull graphs characteristic strength modulus of elasticity for the different intervals.

Table 1 presents the values of the Weibull parameter associated with the statistical characteristic of each diameter interval. In this table, the parameter  $\theta$  in the statistical analysis of this work represents the most characteristic strength modulus of elasticity. The adjustment parameter  $R^2$  indicates the precision degree of the statistical analysis.

Table 1: Weibull parameters the modulus of elasticity with the ranges in diameter from sisal fibers.

Diameter Interval (mm)	Weibull Modulus $\beta$	Characteristic Strength $\theta$	Precision Adjustment $R^2$	Average Tensile Strength (GPa)	Statistical Deviation (GPa)
------------------------	-------------------------	----------------------------------	----------------------------	--------------------------------	-----------------------------

0.06-0.09	3.433	20.162	0.893	18.125	5.835
0.09-0.12	3.313	19.041	0.963	17.086	5.682
0.12-0.15	3.542	16.184	0.911	14.577	4.561
0.15-0.18	5.423	15.372	0.905	14.181	3.015
0.18-0.21	4.198	14.644	0.924	13.317	3.573
0.21-0.24	4.845	9.835	0.927	9.014	2.125

The variation of the characteristic strength modulus of elasticity with the fiber diameter, i.e., the mean value of the interval, is shown in Figure 3. In this figure there is a clear tendency for  $\theta$  to vary in an inverse way with respect to the fiber diameter. A physical consequence is that the thinner the fiber, the higher the characteristic strength modulus of elasticity.

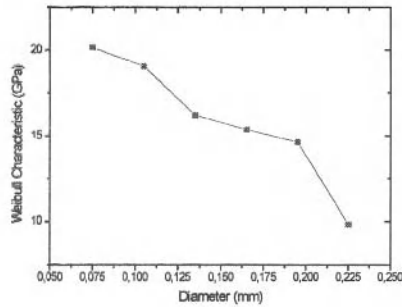


Figure 3: Variation of the characteristic stress with the mean diameter for each interval.

The corresponding values of  $R^2$  in Table 1 statistically support the inverse correlation between  $\theta$  and  $d$ . This correlation can be mathematically described as the following hyperbolic equation for sisal fiber.

$$\theta = 8.43/d - 0.97$$

Another Weibull parameter of relevance is the average modulus of elasticity strength,  $\bar{\sigma}_m$ . The interval of  $\bar{\sigma}_m$  and its deviation encompasses the corresponding values of  $\theta$ . In a normal distribution of strength modulus of elasticity, within a given diameter interval, the values of  $\bar{\sigma}_m$ ,  $\theta$  and the arithmetic average of the strength should coincide.

Figure 4 plots  $\bar{\sigma}_m$  and deviations as a function of the diameter. In this figure, within the error bars, a hyperbolic inverse correlation can be adjusted between  $\bar{\sigma}_m$  (GPa) and  $d$  (mm):

$$\bar{\sigma}_m = 7.91/d - 0.84$$

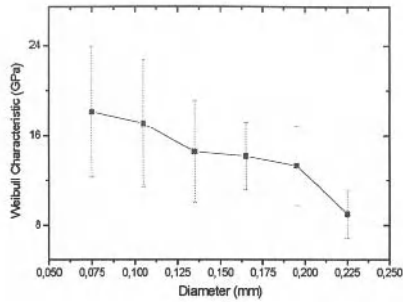


Figure 4: Variation of the average strength modulus of elasticity with the mean diameter for each interval.

By comparing Equation (1) and (2), it can be seen that both have very similar mathematical coefficients. It is then suggested that a hyperbolic type of equation is indeed the best statistical correlation between the sisal fiber strength modulus of elasticity and its diameter.

Figure 5 shows the logarithmic graphs of the reliability vs. location parameter, also known as the Weibull graphs. In this figure the graphs are unimodal with just one straight fitting for all points in the same diameter interval. This indicates that every sisal fiber related to each one of the six intervals belongs to a group with same mechanical behavior.

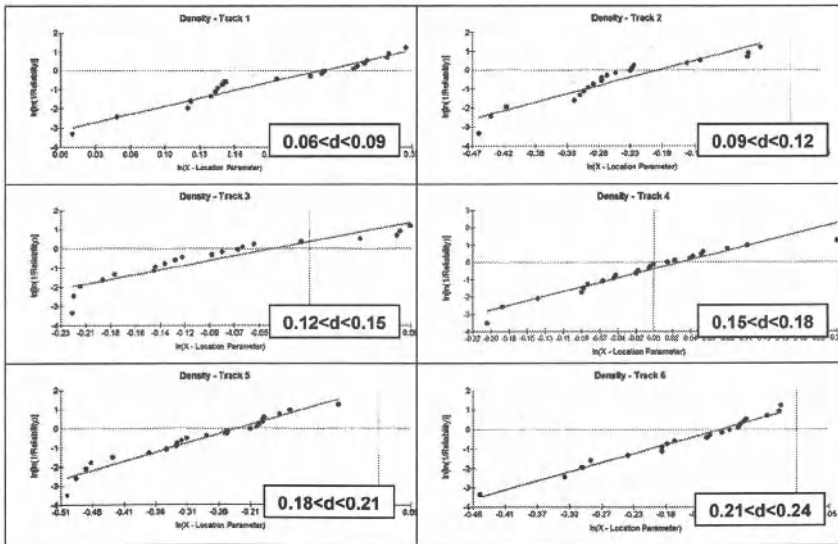


Figure 5: Weibull graphs characteristic density for the different intervals.

Table 2 presents the values of the Weibull parameter associated with the statistical characteristic of each diameter interval. In this table, the parameter  $\theta$  in the statistical analysis of this work represents the most characteristic density. The adjustment parameter  $R^2$  indicates the precision degree of the statistical analysis.

Table 2: Weibull parameter of sisal in different diameter interval.

Diameter Interval (mm)	Weibull Modulus $\beta$	Characteristic Strength $\theta$	Precision Adjustment $R^2$	Average Tensile Strength ( $g/cm^3$ )	Statistical Deviation ( $g/cm^3$ )
0.06-0.09	13.131	1.269	0.956	1.283	0.113
0.09-0.12	9.462	0.823	0.898	0.781	0.099
0.12-0.15	10.672	0.964	0.853	0.920	0.104
0.15-0.18	11.962	1.032	0.935	0.988	0.100
0.18-0.21	9.349	0.795	0.944	0.754	0.098
0.21-0.24	10.18	0.898	0.982	0.855	0.101

The variation of the characteristic density with the fiber diameter, i.e., the mean value of the interval, is shown in Figure 6.

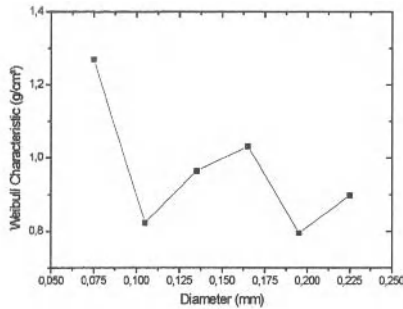


Figure 6: Variation of the characteristic stress with the mean diameter for each interval.

The corresponding values of  $R^2$  in Table 2 statistically support the inverse correlation between  $\theta$  and  $d$ . This correlation can be mathematically described as the following hyperbolic equation for sisal fiber.

$$\theta = 0.685/d - 0.036$$

Another Weibull parameter of relevance is the average density,  $\bar{\sigma}_m$ . The interval of  $\bar{\sigma}_m$  and its deviation encompasses the corresponding values of  $\theta$ . In a normal distribution of density, within a given diameter interval, the values of  $\bar{\sigma}_m$ ,  $\theta$  and the arithmetic average of the strength should coincide.

Figure 4 plots  $\bar{\sigma}_m$  and deviations as a function of the diameter. In this figure, within the error bars, a hyperbolic inverse correlation can be adjusted between  $\bar{\sigma}_m$  (g/cm<sup>2</sup>) and d (mm):

$$\bar{\sigma}_m = 0.60/d - 0.04$$

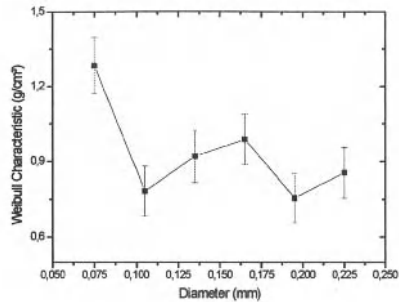


Figure 4: Variation of the average density with the mean diameter for each interval.

Figure 5 shows SEM fractographs of the tip of tensile-ruptured sisal fibers with different diameters. It can be seen in this figure that the thinner fiber with d = 0.05 mm, Fig 5 (a), displays a fracture associated with lesser fibrils. By contrast, the thicker fiber, with d= 0.15 mm, Fig 5 (b), shows a heterogeneous fracture comprising relatively more fibrils. As a consequence, there is a higher statistical chance that the thicker sisal fiber would prematurely break at lower stress than the thinner one.

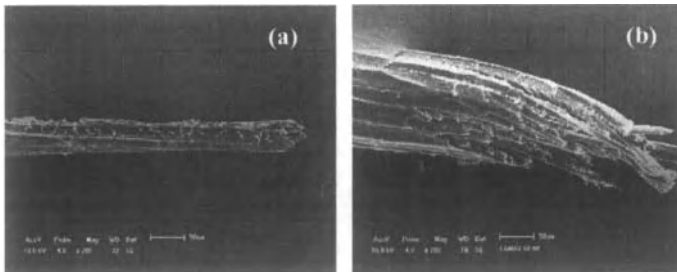


Figure 5: SEM fractograph of tensile-ruptured tips of sisal fibers (a) thinner, d = 0.05 mm and (b) thicker, d = 0.15 mm.

Finally, with the goal of future employment in composites, one can improve the process through a preliminary selection dimensional fibers, to determine certain characteristics for a specific project. Obviously, the smaller diameter fibers should be chosen since they have better features.

## Conclusions

- The Weibull statistics could provide a good inverse correlation between modulus of elasticity and diameter of the fibers, i.e. fibers with diameters smaller bands showed greater ability to absorb energy before fracture, revealing itself to be best ribs materials subject to impact.
- However, the low numerical value of the parameter  $\beta$  and  $R^2$ , with a high variance in resistance measurements indicated, could raise doubts about the correlation established in the workplace.
- However, as seen, the greater uniformity of fiber fracture related to the bands thinner in diameter, visualized in the results (presence or absence of knurl) as in fractografia, reaffirms that the modulus is inversely proportional to the equivalent diameter.

## Acknowledgements

The authors thank the support to this investigation by the Brazilian agencies: CNPq, CAPES, FAPERJ and TECNORTE/FENORTE.

## References

1. S. Kalia, B. S. Kaith, I. Kaurs, *Cellulose Fibers: Bio – and Nano – Polymer Composites* ( New York: Springer, 2011).
2. A. Gore, *An Inconvenient Truth. The Planetary Emergency of Global Warming and What We Can do About It* (Emmaus, Pennsylvania, USA: Rodale Press, 2006).
3. A .K. Bledzki, and J. Gassan, "Composites Reinforced With Cellulose-Based Fibers". *Prog. Polym. Sci.*, 4 (1999) 221-274.
4. D. Nabi Sahed and J.P. Jog, "Natural fiber polymer composites: a review", *Advances in Polymer Technol.*, 18 (1999), 221-274.
5. A.K. Mohanty, M. Misra and L.T. Drzal, "Sustainable biocomposites from renewable resources: opportunities and challenges in the green material world", *J. Polym. Environ.*, 10 (2002), 19-26.
6. Crocker, J., "Natural materials innovative natural composites". *Materials Technology*, 2-3 (2008) 174-178.
7. S.N. Monteiro, F.P.D. Lopes, A.S. Ferreira, D.C.O. Nascimento, "Natural fiber polymer matrix composites: cheaper, tougher and environmentally friendly", *JOM*, 61 (2009) 17-22
8. R. Malkapuram, V. Kumar, Y. S. Nezi "Recent development in natural fiber rein forced polypropylene composites" *J. Reinforced Plastics and composites*, 28 (10)(2009) 1169-1189.
9. G. Marsh, "Next step for automotive materials". *Mater. Today*, 6(4) (2003) 36-43.
10. J. Hulbery, D. Houston, "Natural fiber reinforced polymer composites in automotive application", *JOM*, 58 (2006) 80-86.
11. R. Zah, R. Hischer, A.L. Leão and I. Brown, "Curaua fibers in automobile industry – A sustainability assessment". *J. Cleaner Production*, 15, (2007) 1032-1040.
12. S. N. Monteiro, K. G. Satyanarayana, F. P. D. Lopes "High strength natural fibers for improved polymer matrix composites" *Mat. Sei. Forum* 638-642 (2010) 961-966.
13. S. N. Monteiro, F. P. D. Lopes, A. P. Barbosa, A. B. Bevitori, I. L. A. Silva, L. L. Costa "Natural Lignocellulose fibers as engineering materials – an overview" *Met. Mat. Tras. A*, 42A (2011) 2963-2974.

## **CORRELATION BETWEEN THE DENSITY AND THE DIAMETER OF BURITI FIBERS**

Anderson de Paula Barbosa, Michel Picanço Oliveira, Alexandre da Silva Crespo, Núbia Suely Silva Santos, Frederico Muylaert Margem, Sergio Neves Monteiro

State University of the Northern Rio de Janeiro, UENF, Advanced Materials Laboratory, LAMAV; Av. Alberto Lamego, 2000, 28013-602, Campos dos Goytacazes, Brazil  
State University of Pará, Center for Natural Science and Technology,  
Tv. Enéas Pinheiro, 2626, 66095-100 - Belém, PA – Brazil.  
[sergio.neves@ig.com.br](mailto:sergio.neves@ig.com.br)

Keywords: Buriti fiber, Weibull analysis, density/diameter correlation.

### **Abstract**

Environmental considerations in addition to technical, economical and societal benefits are increasingly promoting the substitution of natural fibers for glass fiber in polymer matrix composites. However, natural fibers are heterogeneous in their dimensions, specially the cross section, which plays an important role in their mechanical strength. The fibers extracted from the petiole of the buriti palm tree is a relatively un known but promising natural fiber for composite reinforcement. In this work, a statistical analysis of the density of buriti petiole fibers using the Weibull methodology was performed. An attempt to correlate the fiber density with the diameter, precisely measured by means of a profile projector, was carried out. The results revealed an inverse dependence between the buriti petiole fiber diameter and corresponding density. Fracture tip observation by SEM suggested a possible mechanism that could justify this inverse correlation.

### **INTRODUCTION**

In the past decade polymer composites reinforced with natural fibers obtained from cellulose-based plants, known as lignocellulosic fibers, have been applied in several engineering sectors, specially the automobile industry as both interior and outside component [1-4].

Environmental benefits as well as economical, social, and technical advantages are actually promoting the substitution of these lignocellulosic for the traditional glass fiber in polymer matrix composites [5]. Today several lignocellulosic fiber are being extensively investigated [6-11] and considered for reinforcement of polymer composites. Some relatively unknown lignocellulosic fiber with reinforcement potential, however, still need to be characterized aiming at future application in composites. This is the case of the fibers stripped of from the petiole of the buriti palm tree, which is endemic in the central and northern regions of South America [12,13]. Preliminary works on the possibility of using the buriti petiole fibers as composite reinforcement, has shown favorable results [14,15].

Figure 1 shows the buriti palm tree (*Mauritia flexuosa L.*) and a bundle of it e petiole fibers.

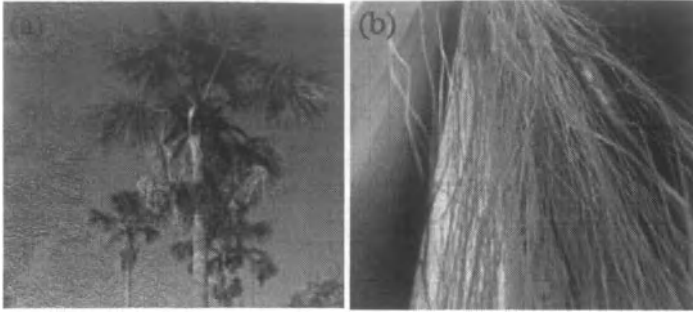


Figure 1. The buriti palm tree (a) and bundle of petiole fibers (b).

Several parts of the buriti palm tree, Fig 1(a), are traditionally used by the people from the Amazon region in Brazil as an abundant source of nuts for food and leaves for art crafts such as basket and hut roofing. The possibility of using its petiole fibers in engineering composites requires complete characterization of the fiber's physical and mechanical properties. One basic property that has not yet been investigated is the fiber density. Since the buriti petiole fiber, as any lignocellulosic fiber, is heterogeneous with variable diameters, the objective of this work is to precisely evaluate its density. This was carried out by means of profile projector measurements followed by a statistical analysis using the Weibull method to the density with the corresponding fiber diameter.

#### EXPERIMENTAL PROCEDURE

The buriti petiole fibers were supplied by one of the co-authors of this work, Núbia S. S. Santos from her property in the state of Para, North of Brazil. These fibers, were initially leached at 60°C for one hour. No chemical treatment was applied to the fibers surface.

From the as received lot of fibers, one hundred were randomly taken for statistical evaluations of the diameter. Each fiber was measured in five different positions along its length and then rotated by 90° for a second measurement, at the same positions, to obtain a mean value. The average of all measurements was taken as the equivalent diameter of that fiber. These measurements were performed in a Nikon profile projector with 0,01 mm of precision.

Figure 2 shows the histogram for the distribution of buriti petiole fiber diameters. The range of equivalent diameters found extended from 0.1 to 0.8 mm. Seven intervals of 0.1 were conventionally considered to construct the histogram. The overall average of equivalent diameter was calculated as 0.48mm. For each of the seven intervals of diameter that divided the histogram of Fig 2, a total of 20 fibers were then selected from the as received lot and had their diameters also measured in the profile projector, as above mentioned, in five locations equally distributed along the length with two measurements at the location separated by 90° rotation.

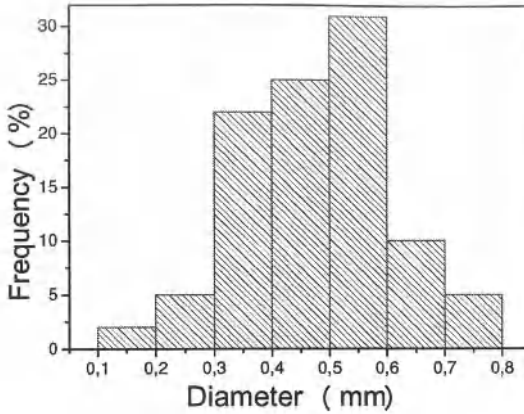


Figure 2. Histogram of the distribution of equivalent diameters of the buriti petiole fibers.

Each of this 140 fibers was weighed in a scale with 0.001g of precision. The density  $\rho$  of fiber was then calculated by

$$\rho = 4m / \pi d_e \quad (1)$$

Where  $m$  is the mass and  $d_e$  the fiber equivalent diameter. In order to investigate the effect of the microstructure, the tip of some tensile fractured samples were observed by scanning electron microscopy (SEM).

The fibers were attached with an electrical conducting carbon tape to a metallic support to be gold sputtered then observed in model SSX-550 Shimadzu microscope operating at 15 kV.

## RESULTS AND DISCUSSION

The experimentally calculated values for the buriti petiole fiber density, Eq (1), corresponding to the different intervals in the histogram in Fig (2) were analyzed by the Weibull statistic method using the computer program Weibull Analysis. This program was applied for the densities of the 20 fibers associated with each one of the seven intervals of equivalent diameter in Fig 2. The program generated the graphs shown in Fig (3), in this figure we should notice that all Weibull graphs are unimodal i.e. with just one fitting strength line.

This is an evidence that all fibers in every one of the seven intervals of equivalent diameter of the histogram in Fig 2, display the same behavior.

The Weibull Analysis program also provides the following parameters: characteristic density,  $\theta$ , Weibull modulus,  $\beta$ , and statistical precision,  $R^2$ , as well as the corresponding means density,  $\rho$ , and mean deviation,  $\Delta$ , for every interval of equivalent diameter. The Figure 4 shows the variation of the characteristic density with the mean fiber

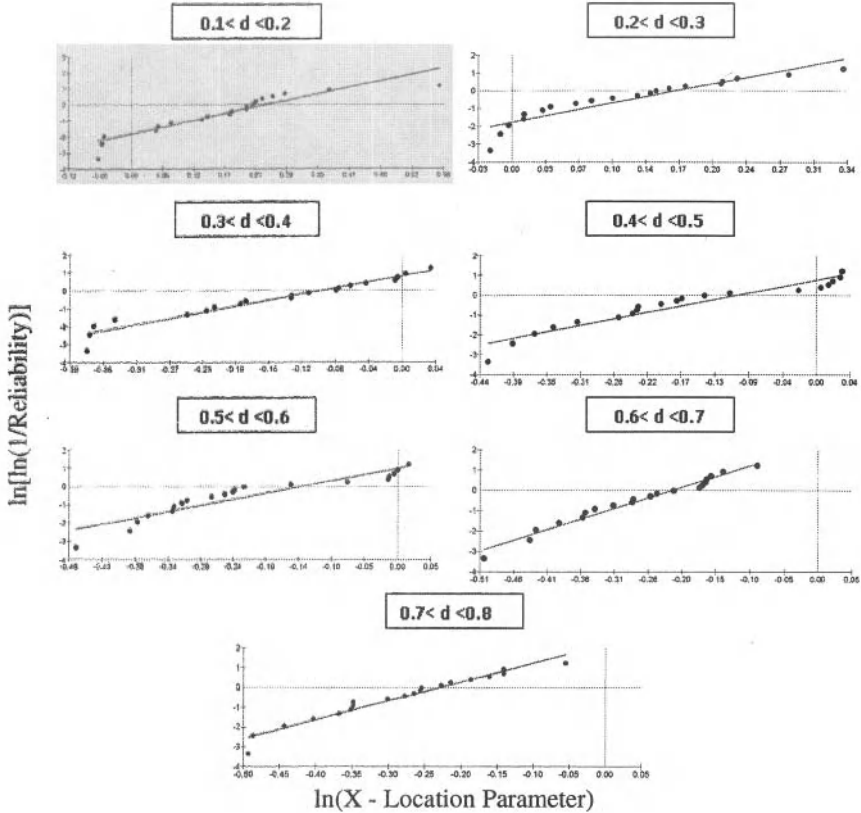


Figure 3 Weibull graphs for the different intervals of equivalent diameter (mm) present in fig 2.

Figure 4 presents the variation of the characteristic stress with the mean fiber diameter for each interval in the histogram of Fig. 2. In this figure, there is a clear tendency for the Weibull characteristic stress to vary in an inverse manner with the mean buriti fiber diameter. In other words, the thinner the fiber, the higher the characteristic stress. The corresponding values for the Weibull modulus,  $\beta$ , and precision adjustment,  $R^2$ , statistically support the inverse correlation between the characteristic stress,  $\theta$ , and the mean diameter,  $d$ . In fact, through a mathematical correlation, a hyperbolic equation (2) was found to fit the data in Fig. 4.

$$\theta = 0.68/d - 0.09 \tag{2}$$

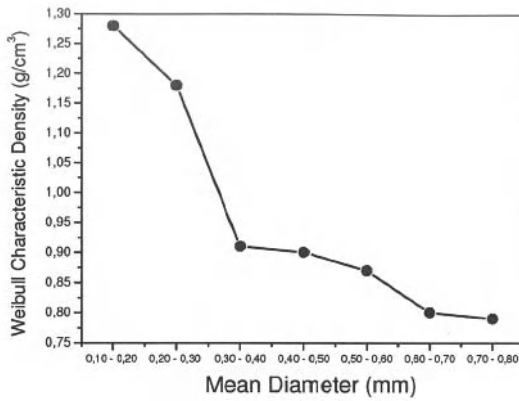


Figure 4. Variation of the characteristic density with the mean diameter for each interval in Fig.2.

In order to verify the physical significance of Eq. (2), the maxim density,  $\bar{\rho}_m$ , calculated for the buriti fibers was plotted as a function of the means diameter in Fig. 5. In this figure, within the error bars associated with the standard deviations, an unequivocal hyperbolic inverse correlation also exists between  $\bar{\rho}_m$  and  $d$ .

$$\theta = 0.95/d - 0.63 \quad (2)$$

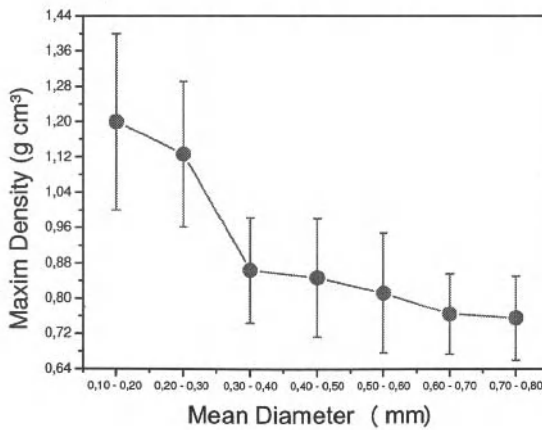


Figure 5. Variation of the maxim density with the diameter for each interval in Fig.2.

Finally, the nature of the filamentous buriti fibers can also be responsible for the results in Figure 6 (a) and (b). The figure 6(a) shows the more thin fiber that present less defects and malformations, so common in lignocellulosic fibers, what can justify the higher density for the thinner fibers, but at the figure 6(b) the thicker fibers shown a heterogeneous surface comprising relatively more holes and gaps what can tell us why the lower density.

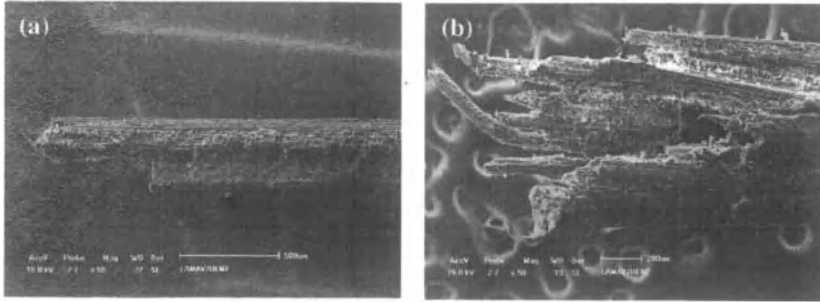


Figure 6. SEM fractograph of tips of tensile-ruptured buriti fibers: (a) thinner,  $d = 0.2$  mm and (b) thicker,  $d = 0.7$  mm.

Finally, it is worth mentioning that a hyperbolic correlation, Eq. (1) and (2) could in practice allow a selection of high density buriti fibers, with smaller diameters, to reinforce polymer composites with improved mechanical properties.

### Conclusions

- A Weibull statistical analysis of density-tested buriti fibers revealed an inverse hyperbolic correlation between the ultimate density and the fiber diameter.
- The density for the buriti fibers are inversely proportional to its diameter
- The non-uniform microstructure of the fiber palm tree, composed of filaments with voids between the fibrils, apparently contributes to the occurrence of inversely relation in density.

### Acknowledgements

The authors thank the support to this investigation by the Brazilian agencies: CNPq, CAPES, FAPERJ and TECNORTE/FENORTE. It is also acknowledged the permission to the use of the impact equipment of IQ/UFRJ and the SEM microscope by the PEMM from COPPE/UFRJ

### References

1. H. Larbig, H. Scherzer, B. Dahlke, R. Poltrock, "Natural fiber reinforced foams based on renewable resources for automotive interior applications" *Journal of Cellular Plastics* 34 (1998) 361-379.
2. G. Marsh, "Next step for automotive materials". *Mater. Today*, 6(4) (2003) 36-43.

3. J. Holbery, D. Houston, "Natural fiber reinforced polymer composites in automotive applications", *JOM*, 58 (2006) 80-86.
4. R. Zah, R. Hischer, A.L. Leão and I. Brown, "Curaua fibers in automobile industry – A sustainability assessment". *J. Cleaner Production*, 15, (2007) 1032-1040.
5. P. Wambua, I. Ivens and I. Verpoest, "Natural fibers: can they replace glass and fibre reinforced plastics?", *Composites Science and Technology*, 63 (2003) 1259-1264.
6. A .K. Bledzki, and J. Gassan, "Composites Reinforced With Cellulose-Based Fibers". *Prog. Polym. Sci*, 4 (1999) 221-274.
7. D. Nabi Sahed and J.P. Jog, "Natural fiber polymer composites: a review", *Advances in Polymer Technol.*, 18 (1999), 221-274.
8. A.K. Mohanty, M. Misra and L.T. Drzal, "Sustainable biocomposites from renewable resources: opportunities and challenges in the green material world", *J. Polym. Environ.*, 10 (2002), 19-26.
9. K.G. Satyanarayana, J.L. Guimarães, F. Wypych, "Studies on lignocellulosic fibers of Brazil. Part I: Source, production, morphology, properties and applications". *Composites: Part A*, 38, (2007) 1694-1709.
10. Crocker, J., "Natural materials innovative natural composites". *Materials Technology*, 2-3 (2008) 174-178.
11. S.N. Monteiro, F.P.D. Lopes, A.S. Ferreira, D.C.O. Nascimento, "Natural fiber polymer matrix composites: cheaper, tougher and environmentally friendly", *JOM*, 61 (2009) 17-22.
12. N.S.S. Santos, C.G.B.T. Dias, E.M.S. Sanches, C.A.C. Zavaglia, E.L. Albuquerque, "Microstructural and mechanical characterization of miriti fiber for utilization as reinforcement on polymeric composites" (in Portuguese), *Proceedings of the Brazilian Congress on Materials Science and Engineering – 18 CBECIMAT* (Porto de Galinhas, PE, Brazil, November 2008) 3565-3573.
13. T.G.R. Portela, L.L. Costa, F.P.D. Lopes, S.N. Monteiro, "Characterization of fibers from different parts of the buriti palm tree", *Proceedings of the Characterization of Mineral, Metals & Materials, TMS 2010* (Seattle, USA, February 2010) 1-8.
14. T.G.R. Portela, L.L. da Costa, N.S.S. Santos, F.P.D. Lopes, S.N. Monteiro "Tensile behavior of lignocellulosic fiber reinforced polymer composites: Part II buriti petiole/polyester" *Rev. Mater.*, 15(2) (2010) 216-222.
15. T.G.R. Portela, L.L. da Costa, R.L. Loiola, S.N. Monteiro "Flexural mechanical characterization of polyester composites reinforced with continuous buriti petiole fibers" *Proceedings of the characterization of minerals & materials symposiums*, TMS 20119 (San Diego, CA, USA, Feb – march 20110).

## THERMAL AND MORPHOLOGICAL BEHAVIOR OF EVOH/PIASSAVA FIBER COMPOSITES

Beatriz Ribeiro Nogueira<sup>1</sup>, Anne Chinellato<sup>2</sup>, Angel Visentim Ortiz<sup>1</sup>, Arifa Parveen<sup>3</sup>, Vijaya Kumar Rangari<sup>3</sup>, and Esperidiana A. B. Moura<sup>1</sup>

<sup>1</sup>Nuclear and Energy Research Institute, IPEN-CNEN/SP  
Av. Prof. Lineu Prestes 2242, 05508-000, São Paulo, SP, Brazil

[bia.ribnog@gmail.com](mailto:bia.ribnog@gmail.com)

[angelortiz@uol.com.br](mailto:angelortiz@uol.com.br)

[eabmoura@ipen.br](mailto:eabmoura@ipen.br)

<sup>2</sup>Federal University of ABC, UFABC  
R. Santa Adélia 166, 09210-170, Santo André, SP, Brazil

[anne.chinellato@ufabc.edu.br](mailto:anne.chinellato@ufabc.edu.br)

<sup>3</sup>Tuskegee University  
Department of Materials Science and Engineering  
1200 W. Montgomery Rd., Tuskegee, AL, 36088, U.S.A.

[arifa\\_p06@yahoo.com](mailto:arifa_p06@yahoo.com)

[rangariv@mytu.tuskegee.edu](mailto:rangariv@mytu.tuskegee.edu)

**Keywords:** Composite, Piassava Fibers, Morphological Properties, Thermal Properties, SEM

### Abstract

Composite consisting of ethylene vinyl alcohol (EVOH) with short piassava fibers were prepared by extrusion process and their thermal and morphological behavior were investigated. The EVOH reinforced with 5 and 10 % of piassava (*Attalea funifera* Mart) fiber particle, based on the percentage weight ratio (wt %), untreated and treated with a commercial silane coupling agent, were prepared and the influence of fiber loading and the effect of chemical treatment on their thermal and morphological behavior were evaluated by SEM, DSC and TG analyses. Melt flow index (MFI) of the composites have been determined to evaluate the effects of fiber reinforcement on dynamic viscoelastic melt of the EVOH. In addition, piassava fibers characterization by SEM, FTIR, and organic and inorganic composition have also been carried out. The SEM results of the composites showed surface micrographs without microvoids and a good distribution, dispersion and compatibility between the fillers and the EVOH matrix. Concerning the piassava fibers characterization, the results showed that piassava has higher lignin content than cellulose and hemicelluloses, and around 0.7 % of ash with 52 % of silica (SiO<sub>2</sub>). This high concentration of silica is consistent with the SEM analysis of the fiber that showed a large amount of "silica rings" encrusted on their surface.

### Introduction

Lately, great worldwide interest has arisen in developing new technologies that enable the use of products with less environmental impact. Effort has been put into seeking natural modifier applications, particularly regarding the use of natural fibers. Special attention has been given to the use of natural vegetable fibers, because of the huge variety of species available. Such vegetable fibers are usually referred to as lignocellulosic materials [1]. This work evaluated the effects of piassava (*Attalea funifera* Mart.) fiber incorporation in an ethylene and vinyl alcohol copolymer (EVOH). The EVOH belongs to a family of copolymers with excellent gas barrier

properties and resistance to organic compounds, which allow its application in different segments, from food packaging to gas tanks. However, EVOH is very sensitive to moisture, and in conditions of high humidity its gas barrier properties, thermal and mechanical properties are affected.

Piassava fiber, aim of this study, is a lignocellulosic stiff fiber extracted from the leaves of a palm tree occurring naturally at the Brazilian Atlantic rain forest. The production of piassava fibers is steadily increasing over the past years and the main use of these fibers is for industrial and domestic brooms, industrial brushes, ropes, baskets, carpets and roofs. It is estimated that around 20% of the fiber production is disregarded by the transformation industries. These leftover fibers, that do not meet the requirements for the uses cited above, are, however, undamaged and long enough to be used as reinforcement in fiber composites. The piassava fiber has a high lignin and silica content when compared to many other known lignocellulosic fibers. These may be responsible for its high flexural strength and low permeability to water. The fiber also presents an array of silicon rich star-like protrusions, which may help their mechanical interlock with resins when used as reinforcements in resin matrix composite materials [2]. In general, a shortcoming in the natural fiber-thermoplastic system is the poor bonding between the natural fiber and the plastic. This is due to a dissimilar chemical nature, once the surface of the natural fiber is usually hydrophilic while many plastics are generally hydrophobic. In order to develop composites with better mechanical properties, it is necessary to impart hydrophobicity to natural fibers by suitable treatments. The selection of proper coupling agents and even electron beam irradiation are important ways to improve fiber-matrix adhesion in order to produce composite materials with superior strength [3].

## Experimental

### Materials

The materials used in this study were EVOH with 38% mol of ethylene (commercial grade by EVALCA), piassava residues that were discharged by industry and Z-6030 silane ( $\gamma$ -methacrylate propyl trimetoxi silane) as coupling agent.

### Preparation and Incorporation of Piassava Fiber in the EVOH Resin

In order to eliminate impurities, the residues were washed and kept in distilled water for 24 h. The fiber was then dried at  $80 \pm 2$  °C for 24 h in a circulating air oven. Next, piassava fiber residues were scraped, washed and kept in distilled water for 24 h and again dried at  $80 \pm 2$  °C for 24 h in a circulating air oven. The resulting fibers were reduced to fine powder with particle size less than or equal to 125  $\mu$ m by using a ball mill. For fiber surface treatment, 1% of silane (percentage in weight) was dissolved in a methanol solution with acetic acid addition to adjust the solution pH to 3.5 with constant agitation for 10 minutes. The fibers were wet with this solution and after 6 hours they were dried at  $80 \pm 2$  °C for 24 h to reduce the moisture content to less than 2%. The EVOH/5% fiber composites and the EVOH/10% fiber composites were obtained by extrusion in twin screw ZSK 18 Megalab extruder machine by Coperion Werner & Pfeleiderer GmbH & Co. KG. The compounded materials were passed through the different zones of the extruder and finally extruded.

### Analyses

For this work, thermal and morphological behaviors were evaluated by SEM, DSC and TG analyses. Melt flow index (MFI) of the composites has also been determined to evaluate the effects of fiber reinforcement on dynamic viscoelastic melt of the EVOH. In addition, piassava

fibers characterization by SEM, FTIR, and organic and inorganic composition have also been carried out.

Scanning Electron Microscopy (SEM). The scanning electron microscopy (SEM) analyses were carried out using a LX 30 (Philips). The samples were freeze-fractured under liquid nitrogen, and then the fractured surface was coated with a fine layer of gold and observed by scanning electron microscopy.

Differential Scanning Calorimetry (DSC). The differential scanning calorimetry (DSC) analyses were carried out using a Mettler Toledo DSC 822e from 30 to 300°C at a heating rate of 5°C/min under nitrogen atmosphere.

Thermogravimetric Analyses (TG). The thermogravimetric analyses (TG) were carried out using a SDT Q 600 by TA Instruments. TG analyses of the materials were performed on samples at a heating rate of 10 °C/min (in an oxygen atmosphere) with temperature ranging from 25 to 600°C.

Melt flow index (MFI) measurements. The MFI measurements (190°C and 2.16Kg) were determined with a Microtest extruder plastometer [4].

Fourier transform infrared (FTIR) analysis. Treated fibers were analyzed using a Perkin-Elmer analyzer for FTIR spectroscopy.

Fiber Chemical Component analysis-Organic Characterization. All samples analyzed were free from extractives and previously dried. For the determination of the lignin content, 1 g of fiber was placed in a test tube with sulfuric acid (72 %) for 24 hours and then was hydrolyzed for 4 hours. The insoluble lignin was then filtered and after drying the sample was weighed. The insoluble lignin content was calculated using equation 1 [5,6].

$$Li = \frac{Wf}{Wi} \times 100 \quad (1)$$

where: Li is the percentage of insoluble lignin; Wi is the initial weight of the sample and Wf is final weight of the sample.

The soluble lignin evaluated was then in the obtained filtrate. Lignin concentration was determined using a UV/VIS – 1601PC spectrophotometer (Shimadzu, Japan) evaluating the absorbance at 280 and 215 nm. The values obtained were calculated using the equation 2 [5,6].

$$Ls = \frac{4.53 \times (A_{215} - A_{280})}{300} \quad (2)$$

where: Ls is the concentration (g/L) of soluble lignin, A<sub>215</sub> is absorbance value obtained at 215 nm and A<sub>280</sub> is absorbance value obtained at 280 nm.

The amount of lignin in the sample is the sum of soluble and insoluble lignin. The cellulose content was determined by the extraction of this compound by reflux in a solution of nitric acid and acetic acid. After this process, the sample was washed with water and ethanol and then filtered. It was then dried in an oven until constant weight. The values were calculated using equation 3 [5,6].

$$C = \frac{Wf}{Wi} \times 100 \quad (3)$$

where: C is the percentage of cellulose, Wi is the initial weight of the sample and Wf is the final weight of the sample.

The amount of hemicellulose in the sample was obtained by the difference in the total amount of the sample (100 %) minus the sum of the others compounds in the fiber.

Fiber Chemical Component analysis-Inorganic Characterization. Inorganic components were determined by wavelength dispersive X-ray fluorescence (WDXRF) using a Rigaku RIX 3000 analyzer.

### Results and Discussion

#### Scanning Electron Microscopy (SEM)

SEM micrographs of EVOH and EVOH/fiber composites with 5 and 10% of piassava fibers are shown in Figures 1, 2 and 3. Figure 1 shows the micrographs of EVOH surface and the treated and non-treated piassava fibers. Figures 2 and 3 show the composite surface micrographs. Comparing Figure 1(A) with Figures 2 and 3, it can be seen that there is no important differences on the EVOH macromolecular arrangement when non-treated piassava fiber or treated piassava fiber are incorporated. The four composites appear to present a smooth surface and good interfacial adhesion between phases.

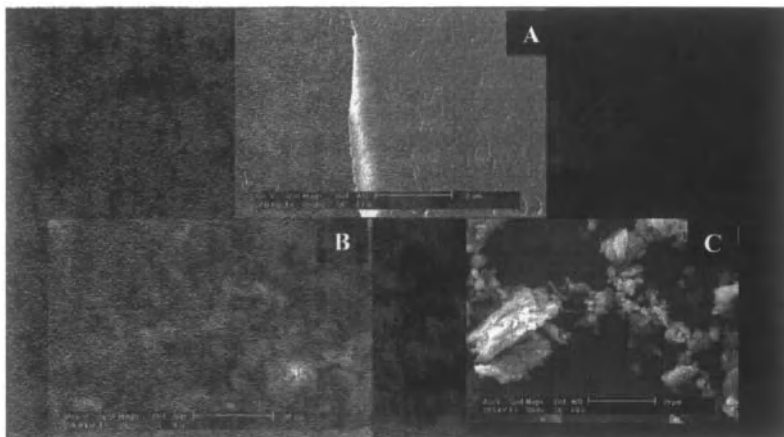


Figure 1. Scanning Electron Microscopy (SEM) surfaces micrographs of EVOH and piassava fibers. Figure 1(A) EVOH; Figure 1(B) piassava fiber; Figure 1(C) piassava treated fiber.

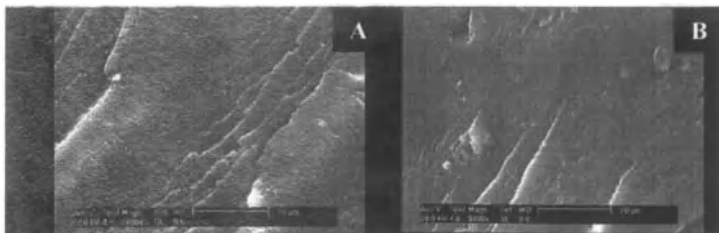


Figure 2. Scanning Electron Microscopy (SEM) surfaces micrographs of EVOH/piassava composites. Figure 2(A) EVOH/Piassava 5%; Figure 2(B) EVOH/Piassava 10%.



Figure 3. Scanning Electron Microscopy (SEM) surfaces micrographs for EVOH/treated piassava composites. Figure 3(A) EVOH/treated piassava 5 %; Figure 2(B) EVOH/treated piassava 10 %;

#### Differential Scanning Calorimetry (DSC)

The results of the DSC analysis for fusion enthalpy ( $\Delta H_m$ ) of the EVOH and EVOH/piassava composites with 5 and 10% of piassava fiber are presented in Table I. The results presented in Table 1 represent the average values calculated from the data obtained by DSC analysis. Crystallinity was calculated from melting peak area information. The percentage of crystallinity (X%) in each material was calculated by the equation 4.

$$X = \frac{\Delta H_m}{\Delta H_m^0} \times 100 \quad (4)$$

where:  $\Delta H_m$  is the melting enthalpy of the EVOH or EVOH/Piassava sample;  $\Delta H_m^0$  is the initial melting enthalpy of 169,2 J/g for the EVOH sample assuming 100% crystallinity, for EVOH 38% ethylene

Table I. Results of melting temperature, enthalpy and crystallinity percentage obtained by DSC analysis

	EVOH	C5%(d)	C10%(e)	C5%T(f)	C10%T(g)
Tm(°C)(a)	158,0±0,7	156,5±0,4	152,6±0,3	155,8±0,3	152,4±0,4
$\Delta H_m$ (J/g)(b)	73,8±5,2	83,3±2,3	72,01±2,86	73,6±1,0	74,61±1,7
X(%) (c)	43,63	49,21	42,46	43,50	44,10

(a) Melting temperature ; (b) fusion enthalpy ; (c) calculated crystallinity in percent; (d) Composite EVOH/5%fiber; (e) Composite EVOH/10%fiber; (f) Composite EVOH/5% treated fiber; (g) Composite EVOH/10% treated fiber.

The results of the crystallinity presented in Table I indicate that the addition of non-treated or treated piassava fiber in the EVOH allows the production of a composite with similar crystallinity of the pure EVOH. These results are consistent with the micrographs shown in Figure1 where no morphological changes can be detected when the pure EVOH surface and the composites surfaces are compared. Only the composite of EVOH with 5 % of non-treated piassava fiber present an increase of 13 % in crystallinity, while crystallinity variation is less than 3 % for all other composites.

#### Thermogravimetric Analyses (TG)

The results of the thermogravimetric analyses (TG) are presented in Table II.

Table II. The onset temperature of thermal degradation of the pure EVOH and the EVOH/Piassava composites

Material	Onset temperature (°C)	Material	Onset temperature (°C)
EVOH	306,2±4,4	C5%T <sub>(c)</sub>	297,1±2,1
C5% <sub>(a)</sub>	304,9±3,4	C10%T <sub>(d)</sub>	294,3±3,2
C10% <sub>(b)</sub>	296,5±1,9		

(a) Composite EVOH/5%fiber; (b) Composite EVOH/10%fiber; (c) Composite EVOH/5%treated fiber; (d) Composite EVOH/10% treated fiber.

Results indicate that the addition of piassava treated fibers to the EVOH tends to reduce the thermal stability of the material. The average onset temperatures of thermal degradation of the pure EVOH and the EVOH/Piassava composites indicate a decrease of 0.4 % for the EVOH/5 % treated fiber composite , 3.0 % for the EVOH/5 % fiber composite , 2.6 % for the EVOH/5 % treated fiber composite and 3.5 % for the EVOH/5 % treated fiber composite .

#### Melt flow index (MFI) measurements

The results of MFI measurements at 190 °C/2.16 Kg for pure EVOH was 2.63 g/10 min and for EVOH/Piassava 5 % and 10 % were 3.43 g/10 min and 2.59 g/10 min, respectively and for treated fiber composites were, 3.04 g/10 min and 2.82 g/10 min, respectively. These results shows that the incorporation of 5 % of piassava fibers promoted increases up to 30 % in MFI when compared with the pure EVOH. These results indicate that fiber addition affects the dynamic viscoelastic melting of resin.

#### Fourier transform infrared (FTIR) analysis

The treated piassava fiber spectrum indicated that it is not possible to confirm the incorporation of the silane coupling agent in the piassava fibers once additional transmission bands (–Si–O–C) at 1090 cm<sup>-1</sup> were not present in the spectra that were obtained. Results are shown in figure 4.

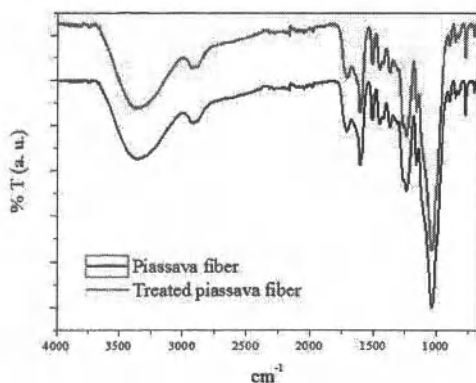


Figure 4. FTIR spectra of original and treated piassava fiber.

### Fiber Chemical Component analysis-Organic composition

Table III presents the results of the piassava fiber organic composition analysis. It also brings results from the literature for comparison.

**Table III. The organic composition of the piassava fiber**

	Literature [7]	Values Obtained
Content of extractives (%)	-	17.20
Hemicellulose (%)	11	13.25
Cellulose (%)	29	26.81
Lignin (%)	45	42.74

As it can be seen in Table III, the major component is lignin, followed by cellulose and hemicellulose. The results obtained are also in accordance with those found in the literature. For all values obtained, the standard deviations were below 1%.

### Inorganic composition

Piassava fiber was analyzed by means of wavelength dispersive x-ray fluorescence (WDXRF). Table IV presents each component found in the piassava fiber and their amount in  $\mu\text{g/g}$  of analyzed sample.

**Table IV. Inorganic components of the piassava fiber**

Component	$\mu\text{g/g}$	Component	$\mu\text{g/g}$	Component	$\mu\text{g/g}$
SiO <sub>2</sub>	3670 $\pm$ 100	Al <sub>2</sub> O <sub>3</sub>	253 $\pm$ 30	PbO	23 $\pm$ 10
CaO	968 $\pm$ 50	Na <sub>2</sub> O	232 $\pm$ 30	NiO	19 $\pm$ 10
SO <sub>3</sub>	675 $\pm$ 50	Cl	205 $\pm$ 20	CuO	14 $\pm$ 10
MgO	299 $\pm$ 30	K <sub>2</sub> O	186 $\pm$ 20	ZnO	<10
P <sub>2</sub> O <sub>5</sub>	271 $\pm$ 30	Fe <sub>2</sub> O <sub>3</sub>	177 $\pm$ 20		

Results indicate 0.7 % of inorganic components with a high content of silica. Figure 5 shows a micrograph of the piassava fiber studied in which an array of silicon rich star-like protrusions can be seen.



**Figure 5. Micrograph of a piassava fiber**

### Conclusions

The piassava addition resulted mostly in a composite with small gain in crystallinity when compared to the pure EVOH material. Results indicated that fiber addition affects the dynamic viscoelastic melting of the EVOH resin. Micrographs revealed dense and compact cryofractured surface morphologies. Both the pure EVOH and the composites exhibit smooth surfaces. Besides, it was possible to detect, for the studied piassava fiber, the array of silicon rich star-like protrusions by means of SEM. Considering that the burning of piassava fibers result in an amount of 0.7 % of ashes, basically inorganic compounds, and considering that inorganic analysis showed that for each gram of piassava the total of SiO<sub>2</sub> is 0,0037mg, it can be concluded that SiO<sub>2</sub> corresponds to over 52 % of piassava fiber ashes. Results also showed that there was no evidence that the silane coupling agent was able to treat and modify the fiber surface so that the resulting composite would have enhanced properties when compared to the non-treated fiber composite. All these results are very important as they can lead to obtaining materials with better properties.

### Acknowledgements

The authors wish to thank A. Schulman for the support in this work.

### References

1. A. L. Marinelli, et al., "Desenvolvimento de Compósitos Poliméricos com Fibras Vegetais Naturais da Biodiversidade: Uma Contribuição para a Sustentabilidade Amazônica", *Polímeros: Ciência e Tecnologia*, vol. 18, nº 2, p. 92-99, 2008
2. J.R.M. d'Almeida, R.C.M.P. Aquino, S.N. Monteiro, "Tensile mechanical properties, morphological aspects and chemical characterization of piassava (*Attalea funifera*) fibers", *Composites: Part A*, 37 (2006) 1473–1479
3. S. W. Kim , S. Ohb, K. Leeb, "Variation of mechanical and thermal properties of the thermoplastics reinforced with natural fibers by electron beam processing", *Radiation Physics and Chemistry*, 76 (2007), 1711–1714
4. American Society for Testing and Materials, *ASTM D1238 - 04 Standard Test Method for Melt Flow Rates of Thermoplastics by Extrusion Plastometer*.
5. I. A. T. Razera, "Fibras lignocelulósicas como agente de reforço de compósitos de matriz fenólica e lignofenólica". Thesis: MSc. Universidade de São Paulo. São Carlos, 2003.
6. A. P. Fuzeto, "Determinação do teor de lignina em amostras vegetais através de três métodos analíticos e correlação com digestibilidade in vitro". Thesis: PhD. Universidade Estadual do Norte Fluminense. Campos dos Goitacazes, 2003.
7. Aquino, R. C. M. P. Desenvolvimento de compósitos de fibra de piassava da espécie *Atalea Funifera* Mart e matriz de resina poliéster. Thesis: MSc. Universidade de São Paulo. Pirassununga, 2003.

## THERMAL BEHAVIOR OF BANANA FIBERS

Frederico Muylaert Margem, Lucas Barbosa de Souza Martins, Nathalia Carneiro Garcia Rosa,  
Sergio Neves Monteiro

<sup>1</sup>State University of the Northern Rio de Janeiro, UENF, Advanced Materials Laboratory, LAMAV;  
Av. Alberto Lamego, 2000, 28013-602, Campos dos Goytacazes, Brazil  
[sergio.ncvcs@ig.com.br](mailto:sergio.ncvcs@ig.com.br)

Keywords: Banana Fiber, TGA, DTG, DSC, thermal decomposition, water evolution.

### Abstract

A natural banana fiber extracted from the plant pseudostem has shown values of density and mechanical strength with potential for uses in engineering applications such as automobile interior parts and floating components. Moreover, natural fibers can also be used as insulating materials in packaging and building panels. In this case some thermal properties are required. Therefore, the objective of this work was to evaluate the thermal behavior of the banana fiber by means of TGA, DTG and DSC analysis. The TGA curves revealed weight loss related to release of humidity and molecular structure decomposition. Peaks in the DTG curves indicated two intervals in temperature associated with different decomposition processes. The only endothermic DSC peak found was attributed to the lignocellulosic water of hydration being lost around 121°C.

### Introduction

In recent times, environmental aspects related not only to pollution caused by non-degradable synthetic leftovers, specially polymeric wastes, but also to climate changes as a consequence of industrial activities, are motivating the use of natural materials. A particular case is fibrous composites, like the fiber grass composites. These synthetic materials, made from non-renewable polymers, are practically non-degradable and contribute to global warming by the CO<sub>2</sub> emission associated with the energy required for the fabrication process. In spite of these environmental shortcomings, fiber materials are essential for the production of many items such as insulating chests, automobile cushion, construction panels, etc. An environmentally correct alternative to replace synthetic fibers composites is the naturally existing ones extracted from plants such as ramie and sisal. These have some environmental advantages of being renewable and degradable, these banana plant provide a negative contribution to CO<sub>2</sub> emission by absorbing greenhouse gas during the plant lifecycle. Banana fibers have been used since long time in simple items such as ropes and rugs. Today they are used in engineering applications related insulation in building panels [2] and finish parts in automobile interior components [3].

In Brazil, the banana fiber obtained from the plant leaf is being used as a great substitute for synthetic polymer composites. A recent work [4] on the characterization of the banana fiber has shown its potential as a new engineering material with a density range that goes from 0,5g/cm<sup>3</sup> to 4,5g/cm<sup>3</sup>. This banana fiber could be used in reinforcement systems. Moreover, by its mechanical properties of strength and rupture, the banana fiber could be applied as reinforcement and insulation material. However, the thermal behavior of the banana fiber has not yet been evaluated. Therefore, the objective of this work was to conduct thermal gravimetric analysis, TGA and its derivate, DTG as well as differential scanning calorimetry, DSC, measurements up to a temperature associated with the degradation of this natural fiber.

## Experimental Procedure

The banana fibers investigated in this work were commercially supplied by a local producer. Figure 1 illustrates the typical banana plant and a bundle of fibers extracted from its stem.

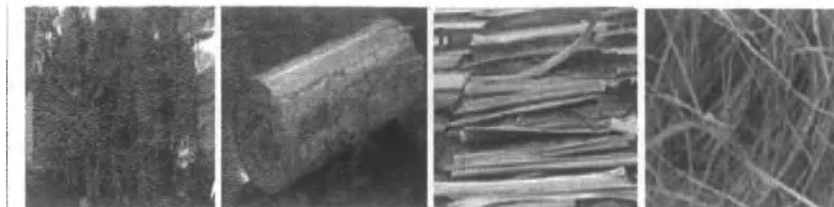


Figure 1. typical banana plant, the pseudostem with average diameter of 15-30 cm, the sun-dried for a week and the group of fibers after the defibrillation.

Samples of the banana fiber were prepared, for the thermal behavior characterization by TGA/DTG and DSC. The TGA/DTG analysis was carried out in a model 2910 TA Instrument, Fig. 2(a), equipment operating at a heating rate of  $10^{\circ}\text{C}/\text{min}$  in the interval of temperatures from 25 to  $800^{\circ}\text{C}$ . This operation was conducted under nitrogen and oxygen atmospheres. Thin discs with 2 mg in weight, corresponding to approximately 1 mm in thickness, were used as sample for the TGA/DTG analysis.

The DSC analysis was carried out in a model 2010 TA Instrument, Fig. 2(b), equipment operating from 25 to  $250^{\circ}\text{C}$ . For this particular analysis a 15 mg sample of banana fiber was placed inside a tight-closed aluminum container.

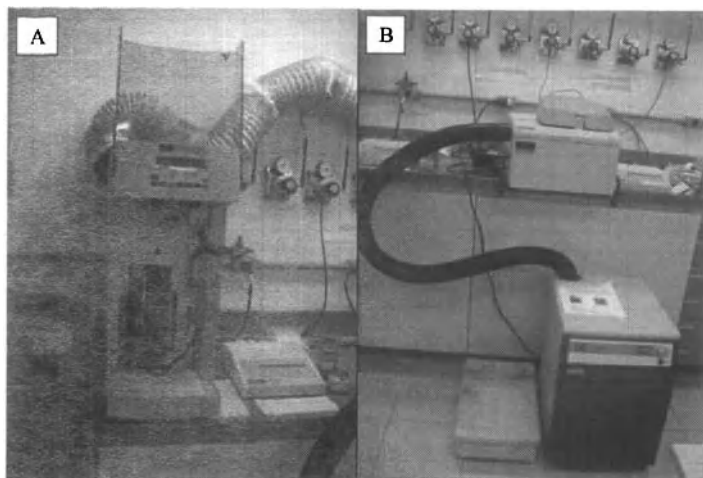


Figure 2 – Thermal analysis equipments: (a) TGA/DTG, and (b) DSC

## Results and Discussion

The thermal stability of the banana fiber measured by the loss in weight through TGA performed with increasing temperature under oxygen ( $O_2$ ) is shown in Fig. 3. In this figure it should be noticed that after a small initial drop in weight from 25 to 75°C, the curve remain constant up to approximately 220°C, characterizing a first constant stage. This initial drop in weight for natural materials is normally attributed to the release of water related to the humidity absorbed on the surface of a hydrophilic lignocellulosic structure [5]. After the first constant stage, a sharp decrease in weight then occurs until approximately 400°C. This sharp decrease can be associated with the decomposition of the banana fiber lignocellulosic structure by rupture of its macromolecular chains [5]. With increasing temperature, a second constant stage in both TGA curves, Fig. 3, exists up to the limit of 800°C established for the analysis.

Even though 200°C was indicated as the approximate end of the first constant stage in TGA curves, the onset of the banana fiber structure decomposition was determined by means of a formal procedure. The intercept of the horizontal extension of the first constant stage with the straight line, at the inflexion point, corresponding to the sharp decrease gives the onset of the structure decomposition. As shown in Fig. 3, this onset occurs at the relatively close temperatures of 300°C for TGA.

The end of the banana fiber structure decomposition process can also be determined using a similar procedure. This was done by considering the intercept of the same straight line tangent at the inflexion point of the sharp decrease with the second stage horizontal line. In this case, the decomposition ends at 379°C for TGA. Here a relevant aspect to be noted is the different levels for the second constant stage, Fig. 3, depending on the atmosphere of the thermogravimetric analysis.

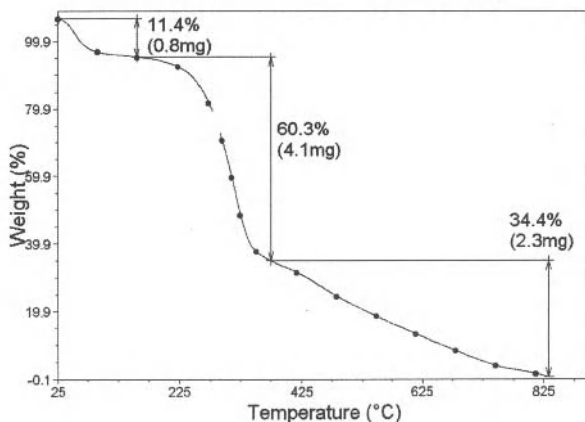


Figure 3. TGA curves to the banana fiber.

TGA curve at Fig. 3 shows the important levels of weight loss associated with events occurring to the banana fiber thermal degradation. The small first drop in weight due to the loss of absorbed humidity is relatively close, 11.4%. This result together with the close decomposition onset temperatures, Fig. 3, indicates that the initial release of humidity is not affected by the existent atmosphere. By contrast, the sensible differences in weight loss during the structure decomposition,

60,3%, together with corresponding significant differences between the decomposition temperatures, Fig. 3, indicate an effect of the atmosphere. This will be better understood in conjunction with the DTG curves.

The residual weight found at 825°C in the second stage, of 2,3%, corresponding to the thermal degradation in the banana fiber, can be interpreted as follows. However, the O<sub>2</sub> reaction during the banana fiber decomposition apparently left a thermal stable residue, probably oxides that did not decompose up to 800°C.

Figure 4 shows the DTG curves for the banana fiber under oxygen (O<sub>2</sub>) atmosphere. The first peaks at the same temperatures of 54,1°C and same amplitude confirm that the release of humidity is not affected by the distinct atmospheres.

The peaks corresponding to the maximum rate of banana fiber decomposition, 316,3°C in O<sub>2</sub>, indicate that oxygen induces a reaction with the banana fiber, causing a more effective degradation to occur at earlier temperatures. In fact the carbon and nitrogen that constitute the lignocellulosic structure of the banana fiber are expected to react with the oxygen releasing CO, CO<sub>2</sub> and H<sub>2</sub>O. Additionally, other free elements in the structure, like Ca, K, Na, Fe, etc, may also react with the O<sub>2</sub> to form oxides associated with inert ashes.

A relevant aspect of the larger peaks in Fig. 4 is their broadening observed in the left side as shoulders around 280°C. This can be attributed to lower temperature peaks, apparently at 290°C that are concealed by the larger peaks. Lower temperature peaks indicate a complex thermal degradation process related to the rupture of molecular chains with different energy levels.

Another feature in Fig. 4 is the existence of small peaks at 459,9°C for O<sub>2</sub> atmosphere. This is apparently an indication of another effective loss of weight taking place at temperatures higher than that associated with the first peaks. In fact, the existence of two peaks in the DTG curve of a natural fiber and its polymer composite was reported [5,6] at similar intervals of temperature. The lower temperature peak was attributed to the decomposition of more rigid molecular segments while the higher temperature peak would be related to the decomposition of more flexible segments [6].

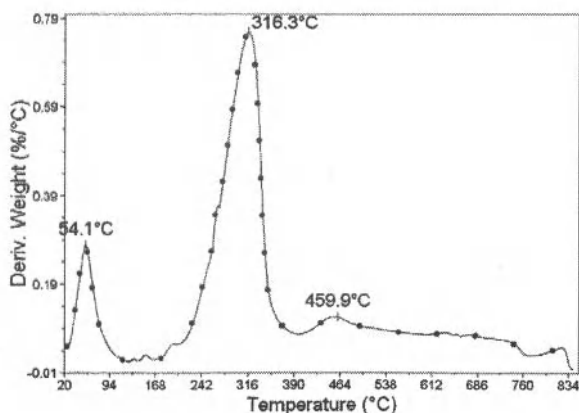


Figure 4. DTG curves for the banana fiber.

Figure 5 shows the DSC curve for the banana fiber. In this figure an endothermic event occurs in the interval of temperature from approximately 25°C to 225°C with a peak at 127,9°C. It is suggested that the heat absorbed in this endothermic event, 135 J/g, could be related to the release of water associated with the hydration of the lignocellulosic structure of the banana fiber, before macromolecular chain degradation occurred.

Finally, the thermal analysis performed in the banana fiber indicated that this natural material loses a relatively small amount of absorbed water up to 55,6°C. Its macromolecular chain structure begins the thermal degradation process around 225°C and, under an oxidizing atmosphere, leaves a solid residue of less than 10% of its total weight. These characteristics establish the limits for engineering applications of the banana fiber, especially as an insulating material.

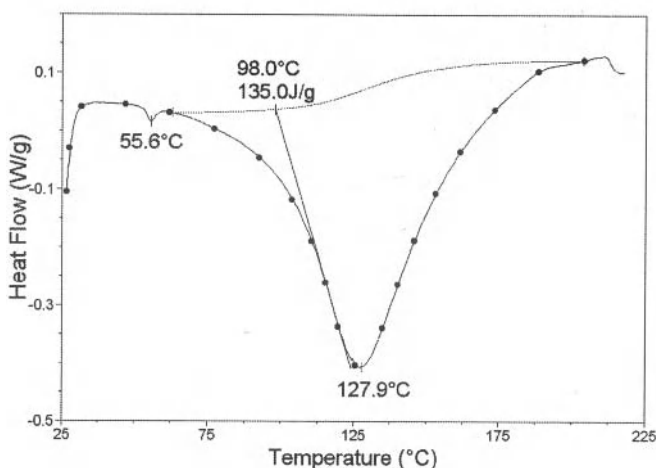


Figure 5. The DSC curve for the banana fiber heated under N<sub>2</sub> atmosphere.

### Conclusions

- The thermal behavior of a banana fiber analyzed by TGA, DTG and DSC revealed evidences of water loss and structural decomposition. Up to 75°C approximately 11,4% of humidity is released while the lignocellulosic water of hydration is lost around 121°C.
- Two events of structural decomposition displayed maximum weight loss associated with clear peaks at 316°C and 459°C, as well as apparently concealed peaks at 280°C, on oxygen atmosphere.
- Under oxygen, a constant amount around 9% of stable solid residue is formed as inert ashes from 400°C up to 825°C. This residue is composed of oxides from trace metals such as Ca, K, Na and Fe as contents of the banana fiber lignocellulosic structure.

### Acknowledgements

The authors thank the support to this investigation by the Brazilian agencies: CNPq, CAPES, FAPERJ and TECNORTE/FENORTE.

### References

1. W.D. Callister Jr., *Materials Science and Engineering – An Introduction*, 5 ed., (New York, NY: John Wiley & Sons, 2000).
2. T. Tondi, A. Pizzi and R.Olives, “Natural tannin-based rigid foams as insulation for doors and wall panels”, *Maderas – Ciencia y Tecnologia*, 10(3) (2008) 218-227.
3. B. Dahlke, H. Larbig, H.D. Schererzer, R. Poltrock, “Natural fiber reinforced foams based on renewable resources for automotive interior applications”, *J. Cell. Plast.*, 34(4) (1998) 361-382.
4. L.L. Costa, S.N. Monteiro, T.G.R. Portela, N.S.S. Santos, “Characterization of a natural banana fiber from the palm tree”. *Proceedings of Characterization of Minerals, Metals & Materials Symposium, TMS 2010* (Seattle, WA, USA, February 2010) 1-8.
5. B. Wielage, T. Lampke, G. Marx, K. Nestler, D. Starke, “Thermogravimetric and differential scanning calorimetric analysis of natural fibres and polypropylene”, *Thermochimica Acta*, 337(1999) 169-177.
6. C.G. Mothe, C.R. Araujo, M.A. Oliveira, M.I. Yoshida, “Thermal decompositions kinetics of polyurethane composites with bagasse of sugar cane”, *J. Thermal Analysis and Calorimetry*, 67(2002) 305-312.

## **COMPARATIVE STUDIES OF CRUSHING BEHAVIOR OF VARIOUS FIBER REINFORCED SKIN POLYURETHANE FOAM CORED COMPOSITE SANDWICH STRUCTURES**

K. V. Sharma<sup>1</sup>, M. Sripathy<sup>2</sup>

<sup>1</sup>Department of Mechanical Engineering, UVCE, Bangalore University, K.R Circle, Bangalore, Karnataka 560001, India

<sup>2</sup>Office of the Director, Technical Education, Palace Road, Bangalore 560001, India

Keywords: Polyurethane, Foam, Crushing behavior

### **Abstract**

The conventional fiber reinforced plastic does not participate in the plastic deformation or enter the large plastic deformation state during collision. On the other hand, sandwich structure allows more plastic deformation, which improves the energy absorption efficiency. The objective of this study is focused on the investigation of the crushing of sandwich structure made from sisal / coir / bamboo/ glass fabrics as reinforcement and with polyester resin to form the composites skin and with polyurethane foam as the core. Experiments were conducted, showing that the underlying crushing mechanism of sandwich structures is very different from that of solid-section thin-walled structures. When a sandwich is subjected to crushing, the core deforms in the shear mode and the face bends independently. The damage is through the width zone of crushed foam core accompanied by a residual crushing in the foam. It is shown that such damage causes a significant reduction of compressive strength. Results show that glass/polyester and bamboo/polyester skin based sandwich structures have superior compressive strength. Coir /polyester based sandwich structure come next to glass/polyester sandwich structures in this aspect which is then followed by Sisal /polyester based sandwich structures.

### **Introduction**

Cellular polymeric foam sandwich structures are often employed in shock mitigating applications. The cellular polymeric foam has several favorable properties, such as, low density, relatively high strength-to weight ratio and a significant degree of crushability. This high crushability is the result of the large void ratio in such materials, which also facilitates the collapse of cell walls via bending and buckling [1]. A few feasibility studies on FRP sandwich panels show that the panels efficiently provided high mechanical performance for minimum weight [2].

Presently, there is an increasing demand for environmentally friendly materials with the desire to reduce the usage of conventional fibers such as carbon, glass and aramid fiber. Many researchers [3-8] have explored various natural fibers, where good mechanical strength was achieved. Natural fibers are low-density material, yielding relatively lightweight composites with high specific properties. It also offers significant cost advantages and benefits associated with processing when compared to synthetic fibers. Natural fibers have been used to reinforce traditional thermoplastic polymers in automotive applications [9]. The influence of surface treatments of natural fibers on the interfacial characteristics was also studied [10]. However, at present, natural fiber is limited only for fiber reinforced plastics laminates. For the construction of sandwich structure's skin, conventional glass fiber and carbon fiber are used. This study is

aimed at developing sandwich structural skin members made from natural fiber like sisal, coir and bamboo reinforced with polyester and tested for crushing behavior. The objective of this work, is therefore to conduct face-wise cyclic compression tests and to investigate the crushing behavior of polyurethane foam cored composite sandwich structures.

### Experimental

The materials used in making the specimen beams were polyester resin, natural fibers (jute, bamboo and coir), E-glass fiber and polyurethane foam. The manually decorticated bamboo fibrous strips are dried off in the sun. These strips of fiber are removed from the culms contain tissues and gums. After decortivating, the dry fiber is extracted by means of a chemical process of decomposition called degumming, in which the gummy materials and the pectin are removed. The method of degumming was designed by Gangstad et al. and has been cited by Maiti [11]. This has been taken as the basis for chemical extraction. The chemical extraction process yields about 33% of fiber on weight basis. The green components of the jute plants were dried in an electric oven at a temperature of 90 °C for 24 h and the weights of the components were measured with an electronic balance. The coir's were used in the same condition in which they were received from the factory. The raw coir fibers were washed 10 times with of tap water till the pH value of water reached [7]. After a series of preliminary tests, it was found that 2 h of boiling in water was sufficient to reduce water soluble chemicals such as sugar, starch, fat, tannins, resin, quinines and phenols. Then coir fibers must then be washed with abundant tap water until the color of water became clear [12].

The natural fibers and the coupling agents are characterized as follows:

1. Natural fibers are mechanically separated, industrially purified and alkalized using less than 5% NaOH.
2. Treated fiber are separated by steam explosion

The sandwich specimens were then fabricated according to standard specifications. The primary chemicals used to produce the polyurethane foam were methylene di-isocyanate (MDI) and polyether polyol (PP). The specimen consists of laminates of glass fiber/polyester, jute/polyester, bamboo/ polyester, coir/polyester and PUF as core.

The procedure followed for fabricating the sandwich specimens are as follows:

1. Calculated amount of MDI and PP liquids were taken in separate clean and dry glass cups to produce PU foam of density 0.8 gm/cc.
2. Inner surface of the wooden die which was fabricated to suit the impact specimens was of the following dimension, 63.5mm x 12.5mm x 3 mm, and was covered with Teflon sheet.
3. MDI and PP were mixed by vigorous mechanical stirring
4. The mixture was poured into the die.
5. The die was covered with a Teflon coated metal plate and a pressure of 0.5 MPa was applied.
6. PU rigid foam was taken out of the die after curing for 20 minutes.
7. Woven fabric was laid-up on the polyurethane foam core
8. Polyester resin was laid up on each face of the fabric. The weight fraction specification is given in Table 1.
9. The specimens were cured in hot press at a pressure of 0.5 MPa and 120 °C for 3 hours

<b>Table 1 Material Composition of skin.</b>		
<b>Material Composition</b>	<b>Weight Fraction (in %)</b>	
	<b>Fiber</b>	<b>Polyester Resin</b>
<b>Glass /polyester composites</b>	65	35
<b>Jute /polyester composites</b>	50	50
<b>Bamboo/polyester composite</b>	50	50
<b>Coir / polyester composites</b>	50	50
<b>The fiber / resin ratio was taken as per Dhakal et al [13] and also natural fiber has porosity and hence it needs more resin comparing with glass fiber.</b>		

#### **Crushing (Lateral Compression) Tests**

Experimental study was conducted to investigate the physical phenomena of local damage and crushing in sandwich beams. The specimens for crushing tests were 100 mm x 100mm x50 mm. Crushing tests were conducted in an Instron Universal testing machine at cross-head displacement rate of 2 mm / min. To limit the overall bending, the sandwich beams were rested entirely on a steel plate. Load was applied through a steel plate as shown in Figure 1. The load is applied for all the specimen is up to 300 kg (uniform cross head).The deformation undergone by the sandwich is noted. Repeated crushing cycles are applied up to 10 cycles for all the specimens. In the result and discussion only two cycles of compression are given for clarity purpose. The following four types of specimens were used for crushing test for ten cycles: polyester / e-glass, polyester / bamboo, polyester / coir mat and polyester / sisal

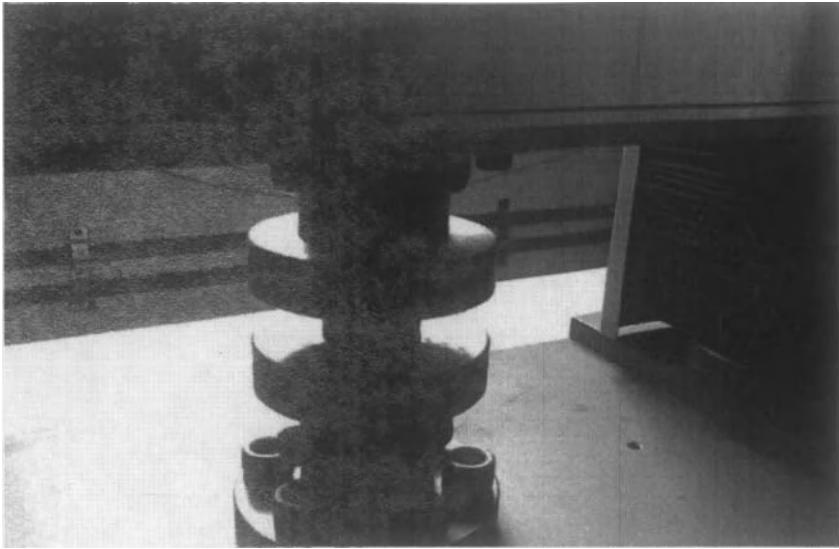


**Fig. 1** Crushing of sandwich structures

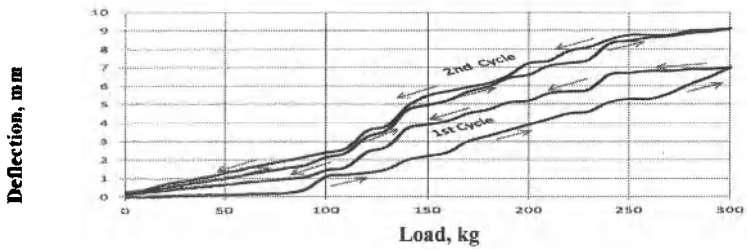


**Fig. 2** Cyclic compressive loading – Polyester / e-glass with double woven

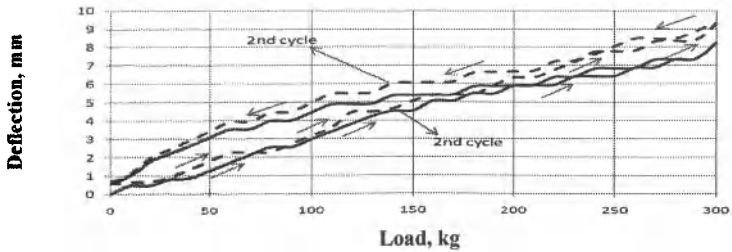


**Fig. 3** Cyclic compressive loading – Polyester / bamboo with double woven

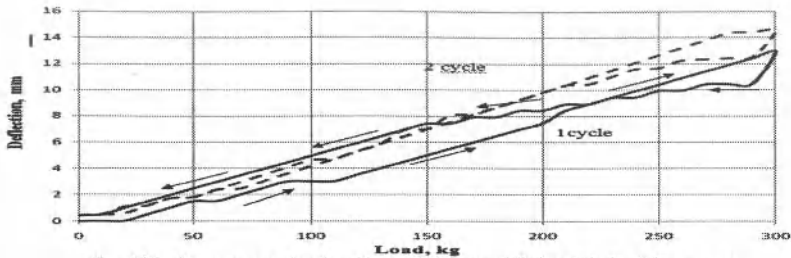


Fig. 4 Cyclic compressive loading – Polyester / Coir with double woven

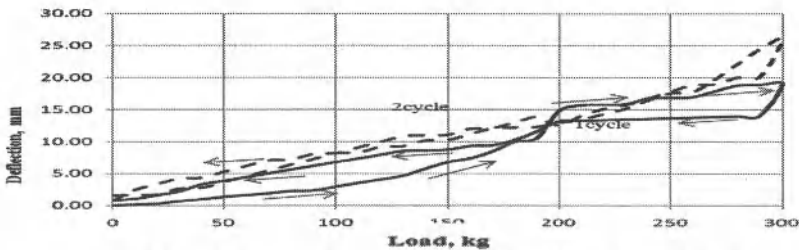


Fig. 5 Cyclic compressive loading – Polyester / Sisal with double woven

### Results and Discussion

Typical load–displacement curve sampled during the tests for e-glass/polyester, bamboo/polyester, coir/polyester and sisal /polyester is shown in Fig. 2, Fig. 3, Fig. 4 and Fig. 5 respectively. Only two cycles of crushing data are given in the form of figures for clarity purpose. However, the overall performance, that is, the maximum deflections of these sandwich structures are given in Fig. 6. The load-displacement curve shows pure elastic response of a specimen at first cycles. Then the onset of core crushing occurs accompanied the following cycles by a progressive growth of a crushed core zone which is shown in Fig. 6. There is relatively high deflection of about 20-30 mm for sisal /polyester sandwich structures. The faces emit popping sound which presumably indicates microscopic failure of individual fibers in the vicinity of the contact with the steel plate.

The crushed core zone was clearly observed during and after the crushing tests, since it had a specific appearance and color. An increase in the damage area caused substantial change in the crushing compression properties, namely the local squeeze buckling in the damaged zone followed by an instantaneous drop in the overall stiffness.

The specimens were then subjected to compressive loads up to 0.56% of their compressive strength. The compressive behavior was similar, irrespective of the skin material, which shows that in lateral compression the specimens behave similar to that of parallel springs. The skin transfers full load on to the foam. Hence, the lateral crushing strength of the sandwich structures

depends on only the strength of the foam. Very little difference in results was observed in lateral compression, among the samples. This could mean, only interfacial strength contributes to the crushing resistance of the sandwich structures.

In cyclic compression the structures absorb energy when compressive loads are applied and release energy when the loads are removed with a very small deformation. The experiments showed a small deformation in the initial cycles (up to 6 cycles) and no deformation in the subsequent cycles. The very large foam cells get fully damaged in the initial cycles of compression due to high air compression ratio and in the subsequent cycles, there will not be any effect of these large cells. The smaller cells act as dampers because of low air compression ratio. In compression the circular holes of PU foam become elliptical perpendicular to the axis of load. The compressive strain signature is non-linear due to the stiffening of the sandwich with an increase in compressive load. The deformation mechanism of foam is localized under-static compression conditions. They become even more localized and propagate through the material as crushing wave fronts which have some of the characteristics of waves [13-15].

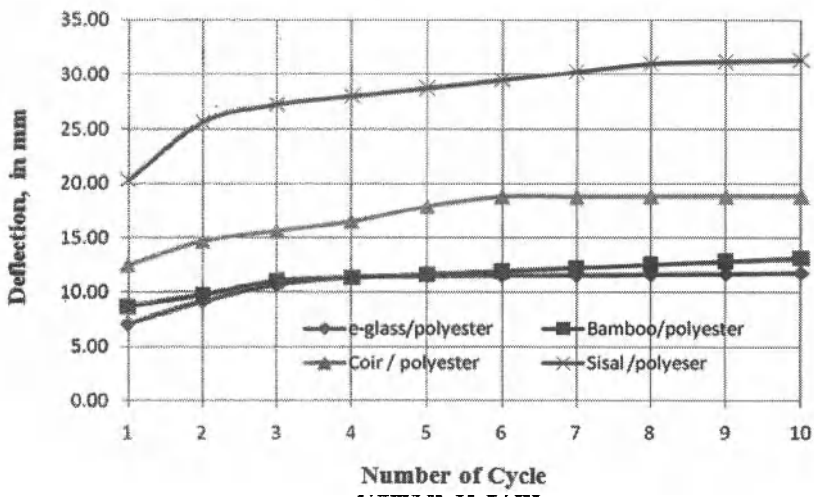


Fig. 6 Effect of number of cycles on deflection of sandwich structures at 300 kg force.

## Conclusions

The results of an extensive test program on crushing compression for the four types of sandwich structure specimens namely e-glass/polyester, bamboo/polyester, coir/polyester and sisal / polyester based sandwich structure are discussed. The particular focus was posed on the stability of the face sheets within the damaged zone. The main results can be outlined as follows:

- The experimental study revealed that a typical damage consists of a sub-interface zone of crushed core and bend in the face sheet without delamination between foam and face sheets.
- For one sandwich configuration subject to crushing loading, only core damage can be seen. This effect reduced considerably in face sheet.
- The crushing occurred in the damage zone and was proved by the residual square in the core. This failure mode caused substantial increase in the compression deformation, that is, reduction in the compression load capacity and overall stiffness.
- Of the four types of sandwich specimens' glass/polyester and bamboo/polyester exhibited highest crushing resistance and sisal /polyester exhibited the lowest crushing strength.

## References

1. Zonghua Zhang, Shutian Liu, Zhiliang Tang, Crashworthiness investigation of kagome honeycomb sandwich cylindrical column under axial crushing loads, *Thin-Walled Structures*, vol. 48 (1), 2010, pp. 9-18
2. D. Mohr, T. Wierzbicki, Crushing of soft-core sandwich profiles: experiments and analysis, *International Journal of Mechanical Sciences*, vol.45,(2),2003, pp. 253-271
3. Yanjun Xie, Callum A.S. Hill, Zefang Xiao, Holger Militz, Carsten Mai, Silane coupling agents used for natural fiber/polymer composites:A review, *Composites Part A*, vol.41,(7)2010, pp.806-819
4. S.V Joshi, L.T Drzal, A.K Mohanty, S Arora, Are natural fiber composites environmentally superior to glass fiber reinforced composites? *Composites Part A*, vol.35, 2004, pp. 371-76.
5. K. Murali Mohan Rao, K. Mohana Rao, Extraction and tensile properties of natural fibers: Vakka, date and bamboo, *Composite Structures*, vol.77,(3),2007, pp.288-295
6. Maya Jacob, Sabu Thomas, K.T. Varughese Mechanical properties of sisal/oil palm hybrid fiber reinforced natural rubber composites, *Composites Science and Technology*, vol. 64, (7-8),2004, pp. 955-965
7. Flavio de Andrade Silva, Nikhilesh Chawla, Romildo Dias de Toledo Filho, Tensile behavior of high performance natural (sisal fibers *Composites Science and Technology* vol 68, (15-16) 2008, pp. 3438-43
8. C.Alves, P.M.C. Ferrão, A.J. Silva, L.G.Reis, M.Freitas, L.B.Rodrigues, D.E.Alves, Ecodesign of automotive components making use of natural jute fiber composites, *Jou of Cleaner Production*, vol.18, 2010, pp.313-27
9. A. Awal, G. Cescutti, S.B. Ghosh, J. Müssig, Interfacial studies of natural fibre/polypropylene composites using single fiber fragmentation test (SFFT), *Composites Part A* vol. 42,(1), 2011, pp. 50-56
10. S.V Joshi, L.T Drzal, A.K Mohanty, S Arora, Are natural fiber composites environmentally superior to glass fiber reinforced composites *Composites Part A: vol 35, (3) 2004, pp. 371-376*

11. K. Murali Mohan Rao, K. Mohana Rao, Extraction and tensile properties of natural fibers: Vakka, date and bamboo, *Composite Structures* 77 (2007) 288–295
12. C. Asasutjarit, J. Hirunlabh, J. Khedari, S. Charoenvai, B. Zeghmami, U. Cheul Shin, Development of coconut coir-based lightweight cement board, *Construction and Building Materials* 21 (2007) 277–288.
13. H.N. Dhakal, Z.Y. Zhang, O.W. Richardson, O.A.Z. Errajhi, The low velocity impact response of non-woven hempfibre reinforced unsaturated polyester composites, *Composite Structures*, vol 81, (4), 2007, pp. 559-567
14. F.G. Torres, M.L. Cubillas, Study of the interfacial properties of natural fibre reinforced polyethylene. *Polymer Testing*, vol. 24,(6), 2005, pp. 694-698.
15. Amin Ajdari, Hamid Nayeb-Hashemi, Ashkan Vaziri, Dynamic crushing and energy absorption of regular, irregular and functionally graded cellular structures, *International Journal of Solids and Structures*, vol 48, (3-4), 2011, pp. 506-516.

## **ELASTIC MODULUS VARIATION WITH DIAMETER FOR RAMIE FIBERS**

Alice Barreto Bevitori, Isabela Leão Amaral da Silva, Renan Sopoletto Carreiro, Frederico Muylaert Margem, Sergio Neves Monteiro

State University of the Northern Rio de Janeiro, UENF, Advanced Materials Laboratory,  
LAMAV; Av. Alberto Lamego, 2000, 28013-602, Campos dos Goytacazes, Brazil  
[alicebevitori@gmail.com](mailto:alicebevitori@gmail.com)

Keywords: ramie fiber, elastic modulus, Weibull analysis, diameter correlation.

### **Abstract**

The ramie fiber is one of the strongest lignocellulosic fibers with applications ranging from simple items such as fabrics and ropes to engineering composites for automobile parts and building panels. Characterization of the ramie fiber has recently been conducted for physical and mechanical properties. In principle, thinner ramie fiber could be comparatively stronger and consequently more effective as a composite reinforcement. In this work an attempt to correlate the ramie fiber elastic modulus obtained in tensile test with its corresponding diameter, precisely measured by means of a profile projector, was carried out. Tensile results analyzed by the Weibull statistic showed a significant increase in elastic modulus with decreasing the diameter of ramie fiber. Scanning electron microscopy observation of the fracture of selected ruptured fiber revealed possible mechanisms that could justify the elastic modulus/diameter inverse dependence.

### **Introduction**

Engineering applications of natural fibers obtained from cellulose-rich plants, also known as lignocellulosic fibers, are currently being the focus of attention. In fact, they are considered an environmentally correct alternative to substitute synthetic fibers such as the glass fiber, associated with an intensive intake of energy during production, as reinforcement of polymer composites [1-4]. In recent years there has been a growing tendency towards the use of lignocellulosic fiber composites in several industrial sectors from civil constructions to car making. In particular, the automotive industry is expanding the number of both interior and exterior components made of natural fiber composites [5].

Among the several lignocellulosic fibers investigated and already used as composite reinforcement, that extracted from the bast of the ramie plant (*Boehmeria nivea*) is one of the strongest with reported tensile strength values above 1000MPa [6]. Figure 1 illustrates the ramie plant as well as a bundle of extracted fibers and a micrograph of the fibers surface.

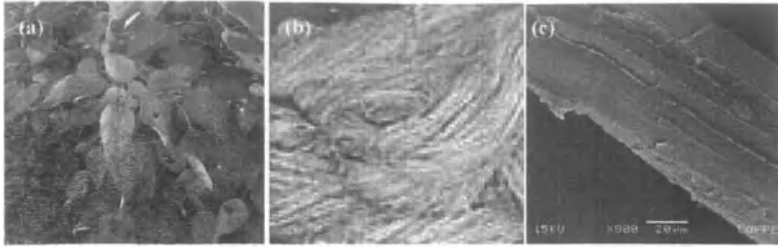


Figure 1. Illustration of: (a) Ramie plant; (b) bundle of fibers; (c) fiber micrograph.

In spite of imperfections and heterogeneities shown in Figure 1 (c), the ramie fiber has a special interest owing to the fact that its cellulose chain are much highly organized as compared to other natural fibers such as flex, jute and cotton [7].

Presently, the ramie plant, Figure 1 (a), is cultivated almost exclusively for fiber production. The ramie fiber is used mainly in the fabrication of textile, sackcloth, canvas and ropes. Moreover, due to its relatively high mechanical resistance, the cellulose obtained from the ramie fiber is partially used to produce the paper for currency bills. Other applications of the ramie fibers are related to reinforcement of fuel hoses, tires and parachute [8].

The properties of polymer composites reinforced with ramie fibers have been the subject of investigation [6, 9-11]. In particular, it was found that the tensile strength of ramie fibers display an inverse correlation with its equivalent diameter [6]. Furthermore, polyester composites reinforced with 30% of the ramie fibers would reach flexural strengths close to 300MPa.

Based on the inverse correlation between the tensile strength and the equivalent diameter of ramie fibers, the present work investigated the possibility of a similar correlation to apply for the elastic modulus of ramie fibers. By means of tensile tests and precise measurement of the fiber diameter, a statistical analysis was conducted to evaluate the ramie fiber elastic modulus dependence on the equivalent diameter.

### Experimental Procedure

The ramie fibers investigate were supplied by a Brazilian firm, Sisalsul. From the as-received lot, one hundred fibers were randomly taken for a statistic dimensional analysis. Figure 2 presents the statistical distribution of the equivalent diameter measured by a profile projector along the fiber length in five distinct locations.

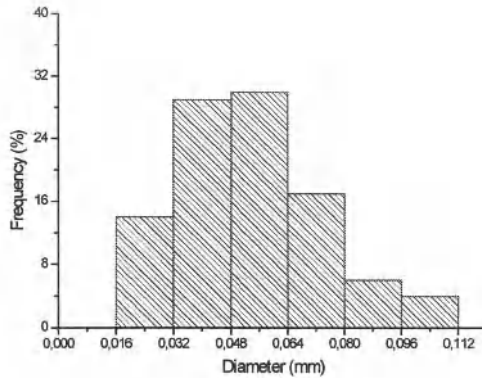


Figure 2. Statistical distribution of diameter of the ramie fibers.

Based in the histogram of Figure 2, six diameter intervals were considered. For each interval in Fig. 2, 20 fibers were then selected, through profile projector measurements. All this fibers were individually tensile tested at a temperature of  $25 \pm 2^\circ\text{C}$  in a model 5582 universal Instron machine. Especial tensile grips were used to avoid both slippage and damage of the fiber. The values obtained for the elastic modulus were interpreted by means of the Weibull statistics using the computer program Weibull Analysis.

To complement this investigation, the fracture of some tested fibers were attached with carbon tape to a metallic support, gold sputtered and then observed by scanning electron microscopy, SEM, in a model a model SSX-550 Shimadzu microscope operating at an accelerating voltage of 7- 15 kV.

### Results and Discussion

The digital recorded data obtained from the Instron machine allowed construct representation load vs. elongation curves for each diameter interval, such as those presented in Fig. 3. In these curves, it should be noted that the load vs. elongation graphs present common characteristics. The indicates that the ramie fiber act as brittle material without any plastic extension after the elastic regimen. Moreover, most curves presents evidence of serrations that have been suggested to be associated with partial rupture of fibrils that compose a lignocellulosic fiber. It is worth mentioning that thinner fibers are composed of relatively lesser fibrils, which result in superior mechanical behavior. This fact will be further discussed in the present work.

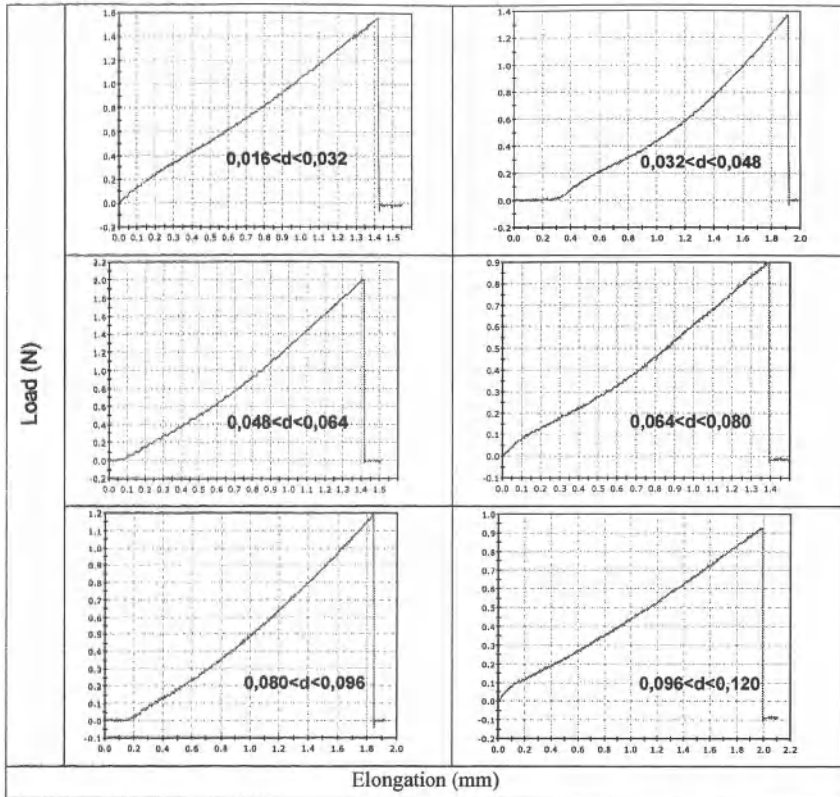


Figure 3. Typical tensile load vs. diameter of ramie fibers for the distinct intervals in the histogram of Fig. 2.

Table 1 present the Weibull parameter associated with the statistical characteristic of each diameter interval. In this table, the parameter  $\sigma$  in the statistical analysis of this work represents the most characteristic tensile strength. The adjustment parameter  $R^2$  indicates the precision degree of the statistical analysis.

Table 1. Weibull parameter the ramie fiber strength in different diameter interval.

Diameter Interval (mm)	Weibull Modulus $\beta$	Characteristic Strength $\sigma$	Prevision Adjustment $R^2$	Mean tensile Strength (GPa)	Deviation (GPa)
0.016-0.032	2,739	0,9486	0,9577	0,844	0,3328
0.032-0.048	2,6	0,6577	0,8649	0,5842	0,2413
0.048-0.064	2,121	0,4181	0,957	0,3703	0,1836
0.064-0.080	1,762	0,2255	0,9728	0,2008	0,1177

<b>0.080-0.096</b>	1,93	0,1748	0,8825	0,155	0,08369
<b>0.096-0,112</b>	2,228	0,1632	0,9084	0,1445	0,06857

Tensile results such as the ones exemplified in Fig. 3 permitted the evaluation of tensile strength for every fiber investigated. These values were analyzed by the Weibull statistic method, in each of six diameter intervals. Figure 4 shows the logarithmic graphs of the reliability vs. location parameter, also known as the Weibull graphs. In this figure the graphs are unimodal with just one straight fitting for all points in the same diameter interval this indicates that the ramie fiber related to each one of the seven intervals belong to a group with same mechanical behavior.

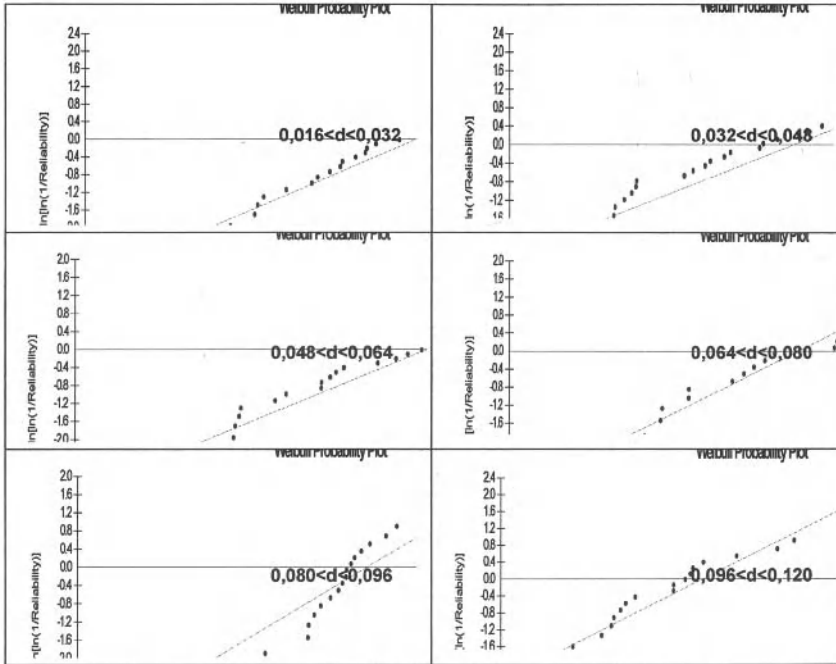


Figure 4. Weibull graphs for the different intervals in the histogram of Fig. 2.

Figure 5 presents the variation of the characteristic modulus with the mean fiber diameter for each interval in the histogram of Fig. 2. In this figure, there is a clear tendency for the Weibull characteristic modulus to vary in an inverse manner with the mean ramie fiber diameter. In other words, the thinner the fiber, the higher the characteristic stress. The corresponding values for the Weibull modulus,  $\beta$ , and precision adjustment,  $R^2$ , statistically support the inverse correlation between the characteristic modulus,  $\theta$ , and the mean diameter,  $d$ . In fact, through a mathematical correlation, a hyperbolic equation was found to fit the data in Fig. 5.

$$\theta = 0,02591/d - 0,08433 \quad (1)$$

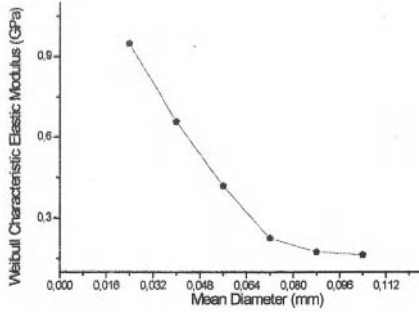


Figure 5. Variation of the characteristic elastic modulus with the mean diameter for each interval in Fig.2.

Another Weibull parameter of relevance is the average elastic modulus,  $\bar{E}_m$ , calculated for the ramie fibers was plotted as a function of the means diameter in Fig. 6. In this figure, within the error bars associated with the standard deviations, an unequivocal hyperbolic inverse correlation also exists between  $\bar{E}_m$  and  $d$ .

$$\bar{E}_m = 0,02307/d - 0,07591 \quad (2)$$

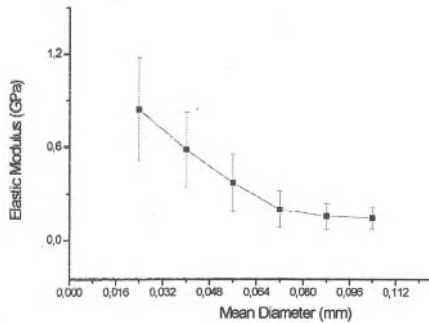


Figure 6. Variation of the average elastic modulus with the diameter for each interval in Fig.2.

By comparing Eq (1) and (2), it can be seen that both have very similar mathematical coefficients. It is then suggested that a hyperbolic type of equation it is indeed the best statistical correlation between the ramie fiber tensile strength and its diameter. Similar results have recently been reported for curaua and sisal fibers [6].

A SEM observation of the tip of tensile-ruptured ramie fibers, Fig. 7, provided additional evidence for the rupture mechanism related to the hyperbolic strength/diameter correlation. The fiber with smaller diameter, Fig 7(a) displays a more uniform fracture associated with lesser fibrils. By contrast, the fiber with larger diameter, Fig. 7(b), shows a heterogeneous fracture associated with more fibrils. These microstructure evidences indicate that there is a higher statistical chance that one of the many fibrils of the thicker ramie fiber, Fig. 7(b), could prematurely break and then nucleates the fiber rupture at a lower stress. Statistically, the many fibrils of a thicker ramie fiber tend to have one of them braking shortly during the application of a tensile load, as compared to the fewer fibrils of a thinner fiber.

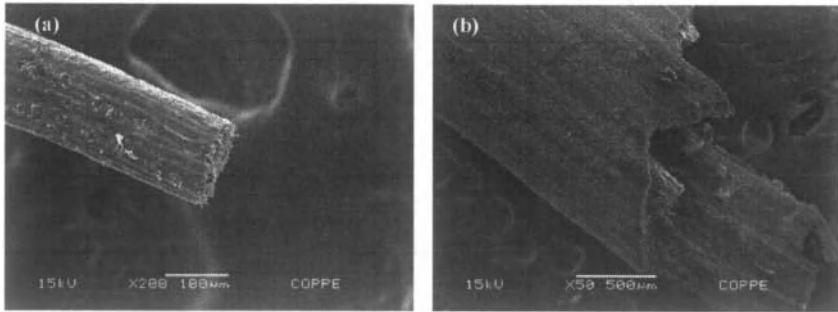


Figure 7. SEM fractograph of tips of tensile-ruptured ramie fibers: (a) thinner,  $d = 0.0183$  mm and (b) thicker,  $d = 0.1097$  mm

Finally, it is worth mentioning that a hyperbolic correlation, Eq. (1) and (2) could in practice allow a selection of stronger ramie fibers, with smaller diameters, to reinforce polymer composites with improved mechanical properties.

### Conclusions

- A Weibull statistical application to analyses of tensile strength revealed an inverse hyperbolic correlation with the equivalent diameter of ramie fibers
- The experimental results obtained for both the elastic modulus characteristic as for the average maximum modulus, showed a hyperbolic equation with similar coefficients.
- SEM observations showed that thicker fibers, consequently with more number of filaments, have a possible mechanism of premature rupture and still thinner fiber are considered strongest for reinforcement of composites with improved mechanical performance.

### Acknowledgements

The authors thank the support to this investigation by the Brazilian agencies: CNPq, CAPES, FAPERJ and TECNORTE/FENORTE.

## References

1. S.N. Monteiro, F.P.D. Lopes, A.S. Ferreira, D.C.O. Nascimento, "Natural fiber polymer matrix composites: cheaper, tougher and environmentally friendly", *JOM*, 61 (2009) 17-22.
2. P. Wambua, I. Ivens and I. Verpoest, "Natural fibers: can they replace glass and fibre reinforced plastics?", *Composites Science and Technology*, 63 (2003) 1259-1264.
3. J. Crocker, "Natural materials innovative natural composites". *Materials Technology*, 2-3, (2008) 174-178.
4. A.K. Mohanty, M. Misra, G. Hinrichsen, "Biofibers, biodegradable polymers and biocomposites: an overview", *Macromol. Mat. and Engineering*, 276/277 (2000), 1-24.
5. J. Holbery, D. Houston, "Natural fiber reinforced polymer composites in automotive applications", *JOM*, 58 (2006) 80-86.
6. S.N. Monteiro, K.G. Satyanarayana and F.P.D. Lopes, "High strength natural fibers for improved polymer matrix composites", *Proceedings of the International Conference on Processing & Manufacturing of Advanced Materials – THERMEC 2009*, (Berlin, Germany, August, 2009) 1-6.
7. C. M. Bezerra, D. C. S., Gonçalves, D. O. Freitas, K. K. O. Souto, R. X. Barbosa, T. R. Ferreira, *Fibras Celulósicas*. Universidade Federal do Rio Grande do Norte. Departamento de Engenharia e Produção Têxtil (2003).
8. BNDES. – *Produção e consumo de algodão e as indústrias de fiações de algodão e linho no Paraná*. Informe Setorial– Banco de Desenvolvimento Econômico e Social – BNDES (1998), site oficial – [www.bndes.gov.br](http://www.bndes.gov.br)
9. S. Nam, A.N. Netravali, "Green Composites II. Environment – friendly, biodegradable composites using ramie fibers and soy protein concentrate (SPC) resin", *Fibers and Polym*, 7 (4) (2006) 380-388.
10. S.N. Monteiro, L.F.L. Santos Jr., F.M. Margem, "Mechanical characterization of ramie fiber reinforced polyester composites ", *Proceedings of the TMS Conference*, (New Orleans, LA, USA, March, 2008) 1-6.
11. F.M. Margem, S.N. Monteiro, J. Bravo Neto, R.J.S. Rodriguez, B.G. Soares, "The dynamic-mechanical behavior of epoxy matrix composites reinforced with ramie fibers", *Rev. Mater.*, 15 (2) (2010) 167-175.
12. S.N. Monteiro, A. B. Bevitori, R. S. Rodriguez, I. L. A. Silva, F. P. D. Lopes, "Thermal Analysis Characterization of ramie fibers with different diameters, In: *Characterization of Minerals, Metals & Materials – TMS Conference*, Mar. 2011. San Diego, USA, p. 1-6.

## **COMPARATIVE STUDY OF THE SUGARCANE BAGASSE FIBER/HDPE COMPOSITE PROPERTIES USING ELECTRON-BEAM AND GAMMA RADIATION TREATMENTS**

Amanda C. S. Pereira<sup>1</sup>; Anne C. Chinellato<sup>2</sup>; Alejandra T. Soria<sup>3</sup>; Anibal V. Abreu<sup>3</sup>; Nélida L. del Mastro<sup>1</sup>; Esperidiana A. B. Moura<sup>1\*</sup>

<sup>1</sup>Nuclear and Energy Research Institute, IPEN-CNEN/SP  
2242 Prof. L. Prestes Av., São Paulo, SP, 05508-000, Brazil

<sup>2</sup>Federal University of ABC, UFABC,  
166 Santa Adélia Rua, Santo André, SP, 09210-170, Brazil

<sup>3</sup>Laboratório Tecnológico del Uruguay - Tecnología de Irradiación,  
6201 Italia Av, Montevideo, 11500, Uruguay  
[cabmoura@ipen.br](mailto:cabmoura@ipen.br)

Keywords: Sugarcane bagasse fiber, Composite, Thermo-mechanical properties, Electron-beam irradiation, Gamma irradiation

### **Abstract**

This work presents a comparative study of the thermo-mechanical and morphological properties of sugarcane bagasse fiber/HDPE composite treated with electron-beam and gamma radiation. The composite samples obtained by extrusion and injection molding processes were irradiated at 50 and 90 kGy using either a 1.5 MeV electron beam accelerator or gamma irradiator EMI-9, at room temperature in presence of air. The irradiated and non-irradiated samples were submitted to mechanical and MFI tests, differential scanning calorimetry (DSC), thermogravimetric analysis (TGA), scanning electron microscopy (SEM), sol-gel analysis and X-Rays Diffraction (XRD) and the correlation between their properties was discussed. Improvement of the bagasse fiber/HDPE composite properties, using electron-beam or gamma radiation, was found.

### **Introduction**

Residues of sugarcane bagasse fiber are widely produced in Latin America and other countries: in Southern Africa, Egypt, South-Eastern Asia, India, China, Australia, Cuba, among other producers, as by-products of the sugar and bioethanol industry. The sugarcane industry in Brazil and Uruguay is well established and expanding with large potential to increase the production of sugarcane bagasse in the next years [1-3]. Although the major portion of the bagasse is currently burnt for energy supply in the sugarcane industry, the disposal of this byproduct is still inefficient and, consequently, it is critical for agriculture profitability and environmental protection. Sugarcane bagasse is a lignocellulose fiber mainly constituted by around 46 % cellulose, containing hemicellulose, lignin, fat and waxes, silica and other elements [3, 4]. Studies have reported that sugarcane bagasse can be used to produce thermoplastic polymeric composites with excellent properties for many applications. [5-8]. Based on this survey, the transformation of bagasse into high quality industrial products, such as bagasse-polymer composites, can provide its more effective utilization.

High density polyethylene (HDPE) is a linear thermoplastic polymer widely used, presenting balanced mechanical properties, chemical resistance, impermeability to water, low cost and easy processing advantages [8-9]. The molecular weight, the molecular weight distribution and the amount of branching determine many of the mechanical and chemical properties of the end product. HDPE has been used with natural fibers to prepare composites with good performance [5-9]. A promising approach for the controllable modification of the polymer materials properties is based on ionizing radiation treatment. In general, the cross-linking and degradation processes occur, simultaneously, in amorphous regions of polymers as an effect of ionizing radiation. Cross-linking of HDPE into three-dimensional networks leads to improvement of properties such as tensile strength, chemical resistance and thermal characteristics [13].

## Experimental

### Materials

The materials used in this study were HDPE resin (HDPE JV060U – commercial grade by Braskem S/A), with MFI = 6.4 g/10 min at 190 °C/2.16 Kg, specific density = 0.957 g/cm<sup>3</sup> and sugarcane bagasse fiber from agro-industrial residues.

### Preparation of Sugarcane Bagasse Fiber/HDPE Composite

In order to remove the impurities, the sugarcane bagasse fiber residues were scraped, washed, and kept in distilled water for 24 h. The fiber was then dried at 80 ± 2 °C for 24 h in an air-circulating oven. The dry fiber was reduced to fine powder, with particle sizes equal or smaller than 250 µm, by using ball mills, and dried again at 80 ± 2 °C for 24 h to reduce the moisture content. The HDPE resin reinforced with 5.0 % (wt %) sugarcane bagasse fiber was obtained using an extrusion machine twin screw "extruder ZSK 18 Megalab" from Coperion Werner & Pfleiderer GmbH & Co. KG. The sugarcane bagasse fiber/HDPE composite was pelletized and fed into a "Sandretto 430/110" injection molding machine and specimen test samples were obtained.

### Irradiation Treatment

Sugarcane bagasse fiber/HDPE composite was irradiated at radiation dose of 50 kGy and 90 kGy using either a 1.5 MeV electron beam accelerator or gamma irradiator EMI-9, at room temperature, in the presence of air. Electron-beam irradiation was performed at Radiation Technology Center – CTR/IPEN-CNEN/SP, using an electrostatic accelerator (Dynamitron II, Radiation Dynamics Inc.), at dose rate 28.02 kGy/s, energy 1.007 MeV, beam current 5.65 mA and tray speed 6.72 m/min. Radiation doses were measured using cellulose triacetate film dosimeters, "CTA-FTR-125", from Fuji Photo Film Co. Ltd.. Gamma irradiation was performed at the Laboratorio Tecnológico del Uruguay, using a "EMI-9", gamma irradiator, dose rate 0.377 KGy/min. Gamma radiation doses were measured using dosimeters type Red 4032 batch KN, from Harwell.

### Assays

Mechanical tests: the tensile tests were performed according to ASTM D 638, the flexural tests were based on ASTM D 790 and the impact strength tests were based on ASTM D 256.

MFI Measurements: the MFI was determined with a Microtest extruder plastometer (ASTM 1238-04) in the conditions specified for HDPE;

Sol-Gel Analysis: the gel content of the cross-linked samples was determined by extraction of the samples in boiling xylene for 24 hours using Soxhlet apparatus. This procedure was

performed with four weighed samples,  $300 \pm 10$  mg, irradiated and non-irradiated materials. The extracted samples were dried in oven at  $50^\circ\text{C}$  and weighed until showing constant weight. The gel content was calculated as it follows:

$$\text{Gel fraction (\%)} = \frac{W_d}{W_i} \cdot 100\% \quad (1)$$

where:

$W_i$  = initial weight of the dried sample

$W_d$  = weight of the dried insoluble part of sample after extraction with xylene

Differential Scanning Calorimetry (DSC): the DSC analyses were carried out using a SDT Q 600 (TA Instruments), on four weighed samples with  $5.0 \pm 0.5$  mg of materials. Samples were heated from  $25$  to  $300^\circ\text{C}$ , at a heating rate of  $10^\circ\text{C}/\text{min}$  (in an oxygen atmosphere). The scans were taken from the second heating cycle to eliminate any thermal history of the samples. Crystallinity was calculated from melting peak areas. The percentage of crystallinity ( $X_c$ ) in a composite material was calculated by the following equation:

$$X_c = \frac{\Delta H_m \cdot 100}{\Delta H_m^0 \cdot w} \quad (2)$$

where:

$\Delta H_m^*$  = melting enthalpy of the HDPE/Piassava sample

$\Delta H_m^0$  = initial melting enthalpy of the HDPE assuming 100 % crystallinity,  $290 \text{ J/g}$  for HDPE

$W$  = polymer mass fraction in the composite

Thermogravimetric Analyses (TG): the TG were carried out using a a SDT Q 600 (TA Instruments). TG analyses of the materials were performed on three weighed samples with  $5.0 \pm 0.5$  mg of the materials. Samples were heated from  $25$  to  $600^\circ\text{C}$ , at a heating rate of  $10^\circ\text{C}/\text{min}$  (in an oxygen atmosphere).

X-rays diffraction (XRD): X-ray diffraction was carried out using a diffractometer Rigaku Denki Co. Ltd., Multiflex model with  $\text{CuK}\alpha$  radiation ( $\lambda = 1.5406 \text{ \AA}$ ) at  $40 \text{ kV}$  and  $20 \text{ mA}$ , with  $2\theta$  varying between  $2^\circ$  to  $50^\circ$ .

Scanning Electron Microscopy (SEM): The scanning electron microscopy (SEM) analyses for cryo-fractured under liquid nitrogen samples of the HDPE and sugarcane bagasse fiber/HDPE composite were carried out using a LX 30 (Philips). The fractured surface of samples was coated with a fine layer of gold and observed by scanning electron microscopy.

Statistical Analysis: The differences between the results of tests carried out were statistically evaluated by ANOVA using BioEstat software (version 5.0, 2007, Windows 95, Manaus, AM, Brazil). Significance was defined at  $p < 0.05$ .

## Results and Discussion

### Mechanical Tests Results

These results of the mechanical tests presented show the average values calculated from the data obtained in tests. The standard deviations for results were less than 10 % for all tests.

Figure 1 shows the results of the tensile strength at break and elongation at break (%) for non-irradiated sugarcane bagasse fiber/HDPE composite (*composite*) and for both electron-beam

(EB) and gamma-rays irradiated *composite*. As seen in this figure there were a significant increase in tensile strength and a large reduction in elongation at break for both, electron-beam and gamma-rays irradiated *composite*. The tensile properties provide an excellent measure of the degree of cross-linking provided by radiation processing to the composites *composite*. The increasing trend in tensile strength and reduction in elongation indicates that the high cross-linking was formed due to irradiation process causing embrittlement to the *composite* in all cases.

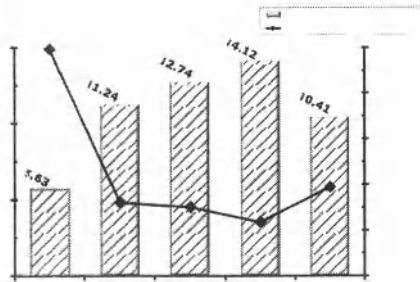


Figure 1. Tensile strength at break and elongation at break (%) for the sugarcane bagasse fiber/HDPE composite.

Figure 2 presents the results for flexural strength and flexural modulus tests. The results revealed that irradiation treatment had a significant effect on the flexural strength and modulus of *composite*. Fig. 2 shows a gain between 20 % and 30 % in flexural strength and between 35 % and 45 % in flexural modulus of *composite* due to electron-beam (EB) and gamma-rays treatment ( $p < 0.05$ ). However, the results suggest higher flexural strength and modulus values for *composite* treated by gamma-rays than electron-beam at some radiation dose.

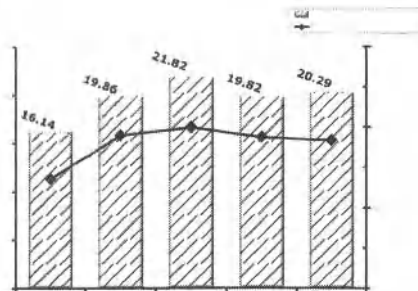


Figure 2. Flexural strength and modulus for the sugarcane bagasse fiber/HDPE composite

The results of the average values obtained in the impact strength tests of sugarcane bagasse fiber/HDPE composite are presented in Fig. 3. As seen there was a significant decrease ( $p < 0.05$ ) between 8 % and 25 % in impact strength of irradiated of *composite* when compared with neat *composite*, except for gamma irradiated *composite* at 50 kGy.

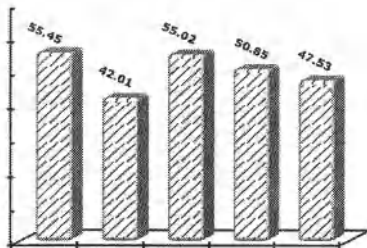


Figure 3. Impact strength for the sugarcane bagasse fiber/HDPE composite

**MFI Measurements.** These MFI measurements results showed a tendency to a slight decrease in MFI of HDPE from MFI = 6.41 to MFI = 6.06 (g/10 min at 190 °C/2.16 Kg) because of bagasse fiber incorporation, suggesting that the addition of this fiber may affect the dynamic viscoelastic melt, since it could reduce molecular mobility and, consequently, the flow. Under the MFI test conditions, the irradiated *composite* did not show any flow and therefore, the MFI could not be determined.

**Sol-Gel Analysis.** The sol-gel analysis results are showed in Table 1. The gel content for electron-beam irradiated *composite* increased with increase of radiation dose applied, while for *composite* treated with gamma-rays at 90 kGy the gel content was small than at 50 kGy. The extent of gel formation in the exposed samples is strongly dependent on the radiation dose and dose rate values. The higher gel content corresponds to a higher portion of the structural network formation in the amorphous region of the polymer that makes it insoluble in solvents. The sol content corresponds to the linear portion of the polymer in both amorphous and crystalline regions. These results showed that both electron-beam and gamma-rays irradiated *composite* predominantly undergo cross-linking. The smaller gel content for gamma irradiated *composite* at 90 kGy than at 50 kGy suggest a higher influence of air due to slower dose rate values of gamma-rays in comparison with electron-beam dose rate.

**Differential Scanning Calorimetry (DSC).** The results of the DSC analysis for melting enthalpy, melting temperature and crystallinity percentage for the sugarcane bagasse fiber/HDPE composite, as a function of electron-beam and gamma-rays radiation dose are given in Table 1. As it can be seen, there were significant gradient decrease ( $p < 0.05$ ) in melting enthalpy, melting temperature and crystallinity percentage of both, electron-beam and gamma irradiated *composite* when compared with non-irradiated *composite*.

**Thermogravimetric Analyses (TG).** The results of the thermogravimetric analyses (TG) are also presented in Table 1. The results showed a significant reduction ( $p < 0.05$ ) in the onset degradation temperature for all irradiated *composite*, when compared with non-irradiated *composite*. With relation to weight loss, there was significant decrease, about 10 %, for irradiated *composite*, except to electron-beam irradiated *composite* at 90 kGy. These results suggests that electron-beam radiation treatment with dose smaller than 90 kGy and gamma-rays up to 90 kGy lead to the more thermal degradation of *composite*.

Table 1. Melting enthalpy, melting temperature, crystallinity percentage, onset degradation temperature, total weight loss and gel content for the composite

Composite	DOSE (kGy)	$\Delta H_m^c$ (J/g)	$X_c^d$ (%)	$T_m^e$ (°C)	Onset Temp <sup>f</sup> (°C)	Weight Loss <sup>g</sup> (%)	Gel Content (%)
Non-irradiated	0	103.48	35.32	118.59	289.41	93.76	0.0
Gamma <sup>a</sup>	50	80.43	27.45	114.00	270.51	94.03	70.16
	90	75.23	25.67	114.63	271.05	95.14	64.00
EB <sup>b</sup>	50	82.74	28.24	114.86	264.59	91.96	76.00
	90	79.33	27.08	115.63	281.74	92.39	90.00

a. gamma-rays irradiated; b. electron-beam irradiated; c. melting enthalpy; d. crystallinity percentage; e. melting temperature; f. onset degradation temperature; g. total weight loss

**X-rays diffraction (XRD).** X-ray diffractograms of electron-beam (EB) and gamma irradiated of sugarcane bagasse fiber/HDPE composite are presented in Figure 4. The characteristic sharp peaks appearing at  $2\theta$  between  $20^\circ$  and  $25^\circ$  correspond to HDPE.

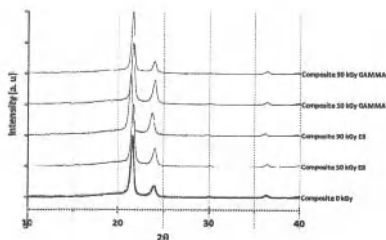


Figure 4. XRD curves of the sugarcane bagasse fiber/HDPE composite

The strongest peak presented at the position of  $21.43^\circ$  corresponds to (110) reflection crystalline and the second strongest peak presented at the position of  $23.80^\circ$  corresponds to (200) reflection crystalline plane. It can be seen a trend of change in intensity of diffraction peaks for the (110) and (200) planes of HDPE for the irradiated *composite*, in comparison with non-irradiated *composite*. The trend was more obvious at the electron-beam irradiated composite with 50 kGy and 90 kGy and at gamma irradiated composite with 50 kGy. This trend of change suggest differences in crystallinity of the composite, due to irradiation treatment, which was confirmed by crystallinity percentage results, calculated from melting peak areas of DSC curves of *composite*

**Scanning Electron Microscopy (SEM).** SEM micrographs of cryo-fractured surfaces of HDPE and sugarcane bagasse fiber/HDPE composite are shown in Figure 5. As it can be seen, non-irradiated HDPE showed a rough, dense and compact cryo-fractured surface revealed, while the non-irradiated *composite* also revealed a rough, dense and compact cryo-fractured surface, but with a large number of cavities in the matrix phase, which can indicate a poor interfacial adhesion between fiber and matrix. In contrast, the irradiated *composite* revealed a slightly smoother cryo-fractured surface. SEM micrographs of electron-beam irradiated *composite* indicated that the fibers were enveloped or surrounded by the bulk of the HDPE resins, but at 90 kGy some fibers were pulled out and broken, and gaps between the fibers and matrix can still be clearly seen.

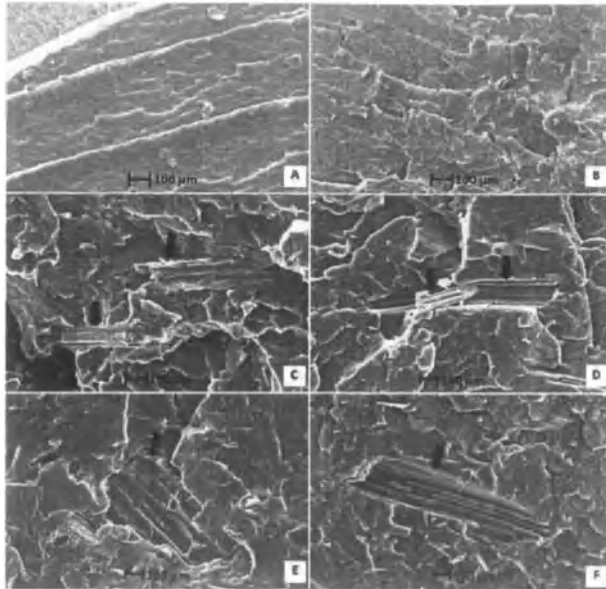


Figure 5. SEM micrographs (500 X) for cryo-fractured surfaces of the HDPE and sugarcane bagasse fiber/HDPE composite. (A) Non-irradiated HDPE, (B) non-irradiated composite; EB irradiated composite: (C) 50 kGy, (D) 90 kGy; and gamma irradiated composite: (E) 50 kGy, (F) 90 kGy.

On the other hand, at micrographs surfaces of gamma irradiated *composite* it can be seen a higher extent of the fibers pulled out with smooth grooves left in the matrix. Apparently, electron-beam irradiation plays more important role in adhesion of sugarcane fiber to HDPE matrix than gamma-rays, thereby, showing less fibers pulling out and therefore smaller numbers of holes on the micrographs surfaces of treated composite. This observation is in agreement with the results of tensile strength tests.

### Conclusion

The objective of the present work was to investigate the behavior of Sugarcane bagasse fiber/HDPE composite properties, irradiated by electron beam and gamma-rays. This process resulted in, a more rigid and a little more fragile composite material, while the thermal properties showed a small reduction in relation to the non-irradiated material. Apparently, electron-beam irradiation plays more important role in adhesion of sugarcane fiber to HDPE matrix than gamma-rays. However, the mechanical tests results showed that electron-beam irradiation was superior only as far as tensile strength properties are concerned. Regarding flexural properties, both ionizing radiation processes used showed similar results. It seems that both processes may be used to obtain composite materials with improved properties. Therefore, the choice between one of them will depend on which property is relevant for the final product application.

### Acknowledgements

The authors wish to thank A. Schulman for the support in this work.

### References

1. X. Li; L. G. Tabil; S. Panigrahi; W. J. Crerar, "Processing Flax Fiber-reinforced Polymer Composites by Injection Molding, *Proceedings of the CSAE/SCGR*," Meeting Winnipeg, Manitoba, Canada, June 26- 29 (2005).
2. "Acompanhamento da Safra Brasileira de Cana-de-Açúcar Safra 2009/2010, Terceiro Levantamento, Dezembro/ 2009, Companhia Nacional de Abastecimento - (Conab)," [http://www.conab.gov.br/conabweb/download/safra/3\\_levantamento2009\\_dez2009.pdf](http://www.conab.gov.br/conabweb/download/safra/3_levantamento2009_dez2009.pdf) (2010).
3. FAOSTAT. Food and Agriculture Organization of the United Nations. Crop production. In: <http://faostat.fao.org/site/567/DesktopDefault.aspx?PageID=567#ancor> Accessed on June 01, (2010)
4. "Dados e Cotações – Estatísticas, União da Indústria de Cana-de-Açúcar (UNICA)," <http://www.unica.com.br/dadosCotacao/estatistica> (2011).
5. Y. Lei; Q. Wu; F. Yao; Y. Xu, "Preparation and properties of recycled HDPE/natural fiber composites," *Journal Composites: Part A: Applied Science and Manufacturing*, Volume 38, pp.1664–1674 (2007).
6. D. R. Mulimari, H. J. C. Voorwald, M. O. H. Cioffi, M. L. C. P. Silva, S. M. Luz, "Preparation and properties of HDPE/sugarcane bagasse cellulose composites obtained for thermokinetic mixer," *Carbohydrate Polymers*, Volume 75, pp.317–321 (2009).
7. J. Z. Lu; Q. Wu; I. I. Negulescu; Y. Chen, "The influences of fiber feature and polymer melt index on mechanical properties of sugarcane fiber/polymer composites," *Journal Applied Polymer Science*, Volume 102, pp.5607–5619 (2006).
8. Y. Lei; Q. Wu; F. Yao; Y. Xu, "Preparation and properties of recycled HDPE/natural fiber composites," *Journal Composites: Part A: Applied Science and Manufacturing*, Volume 38, pp.1664–1674 (2007).
9. KROSCWITZ, J.I. Kirk-Othmer Encyclopedia of Chemical Technology, 4<sup>th</sup> edition, John Wiley & Sons, New York, USA, vol. 17, p.724-732, (1996).
10. RAGHAVAN, J. Evolution of cure, mechanical properties, and residual stress during electron beam curing of a polymer composite. *Composites: Part A*, v.40, p. 300–308 (2009)
11. GHEYSARI, D., BEHJAT, A., HAJI-SAEID, M., The effect of high-energy electron beam on mechanical and thermal properties of LDPE and HDPE. *European Polymer Journal*, v. 37 (2), p. 295–302 (2001).
12. BÉNGTSSON, M.; OKSMAN, K.; STARK, N.M., Profile Extrusion and Mechanical Properties of Crosslinked Wood-Thermoplastic Composites. *Polymer Composites*, p. 184–194, 2006.
13. KHONAKDARA, H.A.; JAFARIB, S.H.; WAGENKNECHTC, U.; JEHNICHENC, D., Effect of electron-irradiation on cross-link density and crystalline structure of low- and high-density polyethylene. *Radiat. Phys. Chem.* v.75, p.78–86, 2006.

*Characterization of Minerals, Metals, and Materials*  
Edited by: Jiann-Yang Hwang, Sergio Neves Monteiro, Chengguang Bai,  
John Carpenter, Mingdong Cai, Donato Firrao, and Buoung-Gon Kim  
TMS (The Minerals, Metals & Materials Society), 2012

# **Characterization of Minerals, Metals, and Materials**

## **Characterization of Light Metals**

Session Chairs:

**Xuewei Lv**

**Gulhayat Nasun Saygili**

## **INFLUENCE OF DEFORMATION ON THE PROPERTIES OF CARBON-FIBER REINFORCED 2024 ALLOY MATRIX COMPOSITES**

Linli Wu\*, Guangchun Yao

School of Materials and Metallurgy, Northeastern University, Shenyang 110004, PR China

Key words: Composites, 2024 aluminum alloy, Carbon fiber

### **Abstract**

The influence of deformation on the properties of short-carbon-fiber reinforced 2024 alloy matrix composites was investigated in this study. It was found that the distribution of carbon fibers changed from the random state before deformation to the ordered state that carbon fibers arranged along the direction of rolling and extruding after deformation. Under the temperature range in control, the increase of rolling and extruding temperature would benefit to improve strength and elongation of composites, but was not conducive to improve the hardness of composites. With the increment of total deformation, all the strength and the hardness of composites became greater, nevertheless the elongation decreased. After being rolled and extruded, the strength and the hardness of composites were all bigger than those of composites before being rolled and extruded; moreover, the strength of extruded 2024 alloy matrix composites was higher than that of rolled 2024 alloy matrix composites under the same heat treatment conditions.

### **Introduction**

Carbon fibers have been reckoned as very important reinforcements due to the high specific strength, specific modulus, high thermal and electric conductivity, low expansion coefficient and good self-lubricant properties [1-4]. Light metal composites reinforced with carbon fibers, such as carbon fibers in an aluminum matrix, are widely used and studied. Some studies have concentrated on the interfacial characteristic of CF/Al composites in order to search for the way of improving the bonding between carbon fibers and the matrix alloy [5-8], and on the influence of the carbon fiber percent composition in the composites [9-11]. Some researchers began to take interest in the deforming characteristic and failure behavior of carbon fiber reinforced metal matrix composites [12-16]. However, the same with other metal materials, most of CF/Al composites were prepared by some single processes, such as powder metallurgy, extrusion casting and vacuum press infiltration, which caused that the composites products could not be manufactured directly. In order to cover the shortage of the mentioned above processes and get composites products with perfect mechanical properties and dimensional accuracy, the composites should be reworked by rolling, extruding or forging process. Compared with research about manufacturing process, the correlative investigation on the reworking of CF/Al composites was much less evidently, which restricted the application and the further development of CF/Al composites.

Thus, the present paper is focused on the deformation behavior and properties of short-CF/Al composites with direct observation of the microstructure of the composites and by testing the properties of short-CF/Al composites before and after reworking.

## Experimental

### Material

The composites ingots used in rolling and extruding process were prepared by stirring vacuum casting, the 2024 aluminium alloy was used for the matrix alloy and the short carbon fiber (about 1-2 mm) for the reinforcing material, the mass percent of the short carbon fiber was about 4wt.% in the composites. And it was metalized on the carbon fiber with a thickness of 0.7  $\mu\text{m}$  of nickel by the way of electroplating before it was added into the matrix alloy. In order to avoid the dendritic segregation, promote the solution of no-equilibrium phase and the precipitation of over-saturation alloy elements, which made the solute concentration more homogeneous, first the annealing treatment process was performed for the composites, which could improve the plasticity and the deformability of composites.

### Roll and Extruding Forming

In the present study, the composites were rolled by hot rolling process, and the rolling temperature was controlled between 420  $^{\circ}\text{C}$  and 460  $^{\circ}\text{C}$ . The composites ingot should be hold for 30 min in the thermostat oven under the rolling temperature before rolling, and the rolling sheet of composites should be carried back in the furnace to hold for 10 min under the rolling temperature after four times of rolling (one circulation). The composites slab with primary thickness of 10 mm, finally, was rolled into 1.5 mm thickness sheet after several circulations (four times of rolling in every circulation) in which the reduction of the initial pass was 0.225 mm, the second was 0.45 mm, the third and the fourth were 0.225 mm. Double high rolling mill was used in the present study, the rolling schematic plan was shown in Fig.1(a).

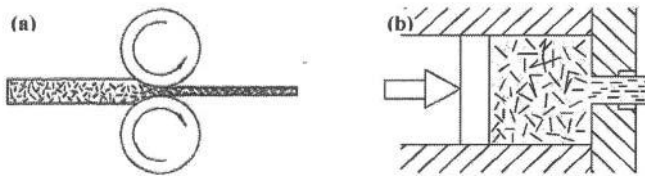


Fig.1 Schematic plans of composites deformation process  
(a)-rolling process; (b)-extrusion process

For the high resistance of deformation, it was very difficult for the carbon fiber reinforced aluminium alloy matrix composites to be extruded. A proper extruding process should be selected during extruding forming.

In the present study, the hot extrusion process was used during material deformation, and the essential parameters were shown as follow: extruding temperature was between 400 $^{\circ}\text{C}$  and 460 $^{\circ}\text{C}$  (temperature of billets), temperature of die was 450  $^{\circ}\text{C}$ , temperature of inwall of container was 450 $^{\circ}\text{C}$ , extrusion ratio was 4, and extrusion speed was 35 mm/s. The schematic plan of composites extrusion process was shown in Fig.1(b).

### Microstructure and Morphology Observation

Microstructures and morphologies of the alloys were characterized using digital camera (SONY-T300) and scanning electron microscope (SEM, JSM-6301F).

## Results and Discussion

### Effect of Deformation on the Microstructure of Composites

Fig.2 and Fig.3 showed separately the microstructures of the rolled and extruded composites. It could be seen that the grain of matrix alloy was elongated along the direction of rolling and extruding, which was due to the plastic deformation of composites under the huge deformational stress. Carbon fiber flowed with the matrix alloy during rolling and extruding, and matrix alloy deformed inhomogeneously in the elastic state during the flow, but for the high strength and high modulus, carbon fibers might rotate forward the direction of rolling and extruding, or break randomly. The distribution of carbon fibers changed from the random state before deformation to the ordered state that carbon fibers arranged along the direction of rolling and extruding after deformation, that is to say, the carbon fiber had the characteristic of orientation.

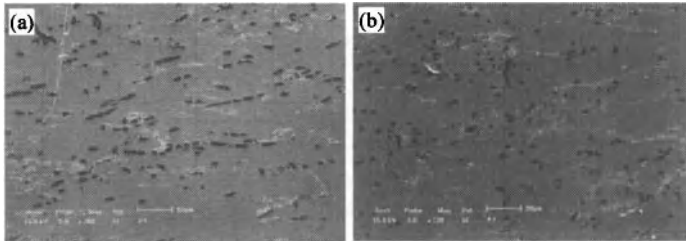


Fig.2 Comparison of composites structures with longitudinal and cross direction after being rolled  
(a)-longitudinal; (b)-cross

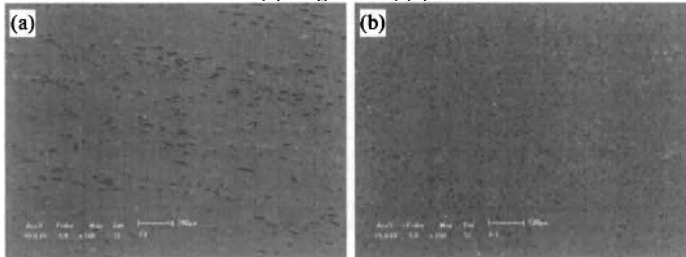


Fig.3 Comparison of composites structures with longitudinal and cross direction after being extruded  
(a)-longitudinal; (b)-cross

In addition, carbon fibers and matrix alloy also flowed forward both sides across the direction of rolling during the rolling deformation, so it could be observed that the grains of the matrix in the cross-section were elongated and there were many oblique sections of carbon fibers. On the contrary, there was no oblique section of carbon fiber in the extruded composites basically, probably because the carbon fibers and the matrix alloy only flowed forward the direction of extruding deformation.

As mentioned above, carbon fibers might break and orderly arrange along the direction of rolling and extruding, which might be comprehended by use of the rotation model of carbon fiber (shown in Fig.4). It is well known that the deformation resistance of matrix alloy will be greatly reduced during the hot rolling process and the hot extruding process, but for the strength of carbon fiber did not changed basically under the temperature of hot rolling and hot extruding, carbon fiber would flow with the matrix alloy during rolling and extruding, however, carbon fibers arranged disorderly in the matrix alloy in the initial stage of rolling and extruding process, the orientation of carbon fiber was not in accordance with the flowing direction of matrix alloy, so carbon fiber axial rotation would happen inevitably, which made the orientation of carbon fibers consistent with the plastic flow direction of the matrix alloy. As shown in Fig.4, when the angular velocity  $\omega_1$  of carbon fiber rotation was not equal to the angular velocity  $\omega_2$ , carbon fiber would bend, and when the suffered bending stress was less than or equal to the strength of carbon fiber, the fracture would not happen, when the suffered bending stress was bigger than the strength of carbon fiber, the fracture would occur. Additionally, because the flowability of matrix alloy became better when the rolling or the extruding temperature was increased, the bending stress would become smaller, which made the probability of carbon fiber failure becomes less.

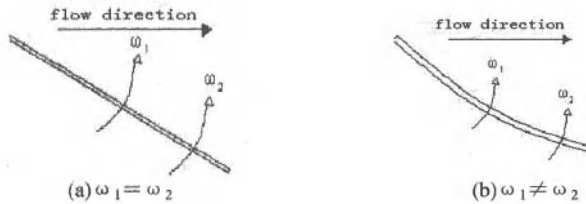


Fig.4 Model of carbon fiber moving in rolling and extrusion

#### Effect of Deformation Temperature

Fig.5 shows the mechanical properties of as-rolled composites sheets that were prepared respectively under the temperature of 420°C, 430°C, 440°C, 450°C and 460 °C. It could be seen that tensile strength ( $\sigma_b$ ), yield strength ( $\sigma_{0.2}$ ) and elongation ( $\delta$ ) were all improved along with the increment of the rolling temperature. The tensile strength enhanced from 426MPa to 443MPa, the yield strength from 350MPa to 364MPa, respectively increased by 3.99% and 4%, the elongation from 4.02% to 4.15%, however, the hardness was reduced from 151HB to 144HB, down 4.61%.

According to the above mentioned, it could be known that the increment of rolling temperature would help to improve the orientation ability of carbon fibers in the matrix alloy, the possibility of fracture of carbon fibers became smaller, which made the reinforced effect more significant, therefore, the strength of as-rolled composites sheet was improved with the increment of rolling temperature. On the other hand, for the increase of the rolling temperature, the ability to resist deformation of matrix alloy decreased and the residual stress of as-rolled composites sheet corresponding became less, which were benefit the improvement of tensile strength and elongation, however, the hardness was decreased with the reduction of deformation resistance.

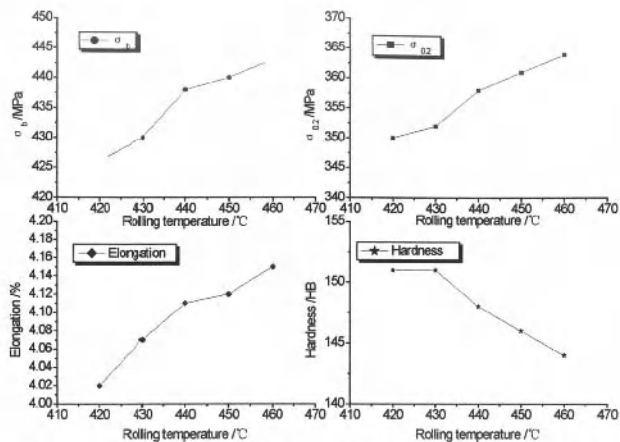


Fig.5 Effect of rolling temperature on the properties of composites plates

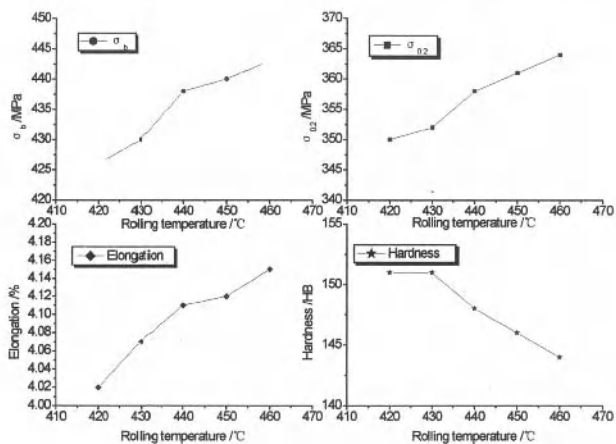


Fig.6 Effect of extruding temperature on the properties of composites Extruded Rod

In order to investigate the effect of extruding temperature on the properties of composites, four different extruding temperatures of 400°C, 420°C, 440°C, and 460 °C were selected according to the extruding temperature of 2024 alloy, usually between 380°C and 450°C, Fig.6 showed the effect of extruding temperature on the properties of composites bar. In accordance with the rolling process, the strength of as-extruded composites increased with the rise of extruding temperature, however, when extruding temperature was 460°C, the tensile strength fell slightly; it might be resulted from the grain growth during the extruding deformation, which was harmful to the improvement of composites strength.

### Effect of Total Deformation

The relationship between total deformation and properties of composites could be seen in Fig. 7. With the increase of total deformation, all the strength and the hardness of composites became greater, nevertheless the elongation decreased. The tensile strength was improved from 434MPa to 448MPa, the yield strength from 342MPa to 353MPa, respectively increased by 3.23% and 3.21%, the elongation dropped from 4.12% to 3.92%, in addition, the hardness was increased from 149HB to 156HB, down 4.7%. It was consistent with reference [17], bigger the total deformation was, better the microstructure was, and better the property was. In addition, it might be due to that, with the increment of total deformation, the deformation resistance of composites was improved and carbon fibers orientated along the rolling direction more obviously, which lead to the results as shown in Fig. 7.

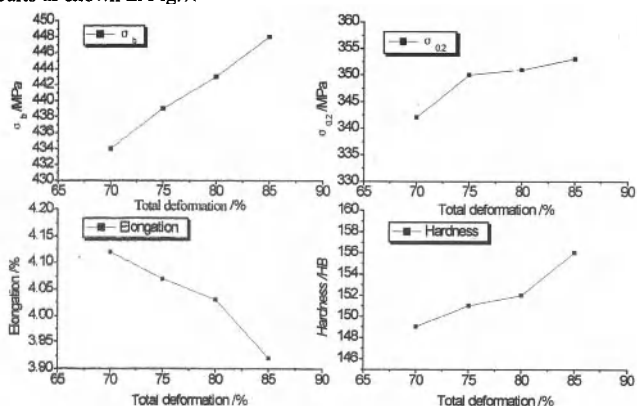


Fig.7 Effect of rolling total deformation on the properties of composites plates

### Comparison of the Performances

Fig.8 showed properties comparison of composites before and after rolling and extruding. It could be seen that the reworking was an effective way of improving the properties of composites, which might be due to the work-hardening of bulk alloy and the orientation of carbon fibers along the direction of rolling and extruding. In addition the elongation, all properties of extruded composites were bigger than those of rolled composites obviously, which might be so-called Extrusion Effect [18]. During the process of extruding, composites were subjected to the compression stress in three directions, and were in the state of being compressed across the axial direction and being extended deformation along extruding direction, and the bulk alloy flowed repositively and all the grains moved along the extruding direction, which resulted in the formation of strong [111] texture in the extruded composites, and [111] direction of most grains were in accordance with the extruding direction. For aluminium alloy with face-centered cubic lattice, the strength along [111] direction was the highest, therefore, the strength of extruded 2024 alloy composites was higher than that of rolled 2024 alloy matrix composites under the same heat treatment conditions.

### Comparison of the Performances

Fig.8 showed properties comparison of composites before and after rolling and extruding. It could be seen that the reworking was an effective way of improving the properties of composites, which might be due to the work-hardening of bulk alloy and the orientation of carbon fibers along the direction of rolling and extruding. In addition the elongation, all properties of extruded composites were bigger than those of rolled composites obviously, which might be so-called Extrusion Effect [18]. During the process of extruding, composites were subjected to the compression stress in three directions, and were in the state of being compressed across the axial direction and being extended deformation along extruding direction, and the bulk alloy flowed repositively and all the grains moved along the extruding direction, which resulted in the formation of strong [111] texture in the extruded composites, and [111] direction of most grains were in accordance with the extruding direction. For aluminium alloy with face-centered cubic lattice, the strength along [111] direction was the highest, therefore, the strength of extruded 2024 alloy matrix composites was higher than that of rolled 2024 alloy matrix composites under the same heat treatment conditions.

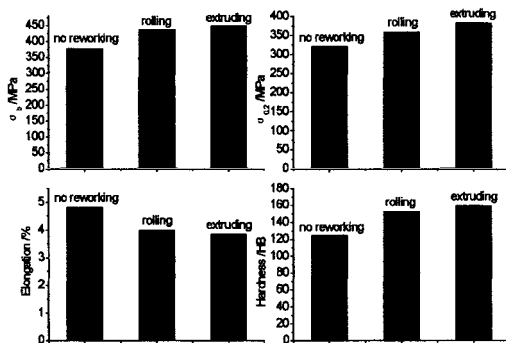


Fig.8 Properties comparison of composites fore and after rolling and extruding

### Conclusions

- (1) The distribution of carbon fibers changed from the random state before deformation to the ordered state that carbon fibers arranged along the direction of rolling and extruding after deformation.
- (2) Under the temperature range in control, the increase of rolling and extruding temperature would benefit to improve strength and elongation of composites, but was not conducive to improve the hardness of composites. With the increment of total deformation, all the strength and the hardness of composites became greater, nevertheless the elongation decreased.
- (3) After being rolled and extruded, the strength and the hardness of composites were all bigger than those of composites before being rolled and extruded; moreover, the strength of extruded 2024 alloy matrix composites was higher than that of rolled 2024 alloy matrix composites under the same heat treatment conditions.

### Acknowledgements

The authors wish to acknowledge the financial support of the New Teacher Fund, Education Ministry of China (grant number: 20070145058), and thank Dr. Luo Tianjiao for technical assistance and Mr. Wang Gang for help with the electron microscopy.

### References

- [1] P.J. Walsh. Carbon fibers. ASM Handbook. 21, 2001, p92-105.
- [2] S.J. Park, M.S. Cho. Effect of anti-oxidative filler on the interfacial mechanical properties of carbon-carbon composites measured at high temperature. *Carbon*. 38(7), 2000, p1053-1058.
- [3] S. Chand. Carbon fibers for composites. *J. Mater. Sci.* 35(6), 2000, p1303-1313.
- [4] R.J. Diefendorf, E. Tokarsky. High performance carbon fibers. *Polymer Engineering & Science*. 15(3), 1975, p150-159.
- [5] M.H. Vidal-Sétif, M. Lancin, C. Marhic, R. Valle, et al. On the role of brittle interfacial phases on the mechanical properties of carbon fibre reinforced Al-based matrix composites. *Materials Science and Engineering: A*. 272(2), 1999, p321-333.
- [6] L. Liu, W.W. Li, Y.P. Tang, et al. Friction and wear properties of short carbon fiber reinforced aluminum matrix composites. *Wear*. 266(7-8), 2009, p733-738.
- [7] E. Hajjari, M. Divandari, A.R. Mirhabibi. The effect of applied pressure on fracture surface and tensile properties of nickel coated continuous carbon fiber reinforced aluminum composites fabricated by squeeze casting. *Materials & Design*. 31(5), 2010, p2381-2386.
- [8] M. Lancin, C. Marhic. TEM study of carbon fibre reinforced aluminium matrix composites: influence of brittle phases and interface on mechanical properties. *J. Eur. Ceram. Soc.* 20(10), 2000, p1493-1503.
- [9] T. Matsunaga, K. Matsuda, T. Hatayama, et al. Fabrication of continuous carbon fiber-reinforced aluminum-magnesium alloy composite wires using ultrasonic infiltration method. *Composites Part A Applied Science and Manufacturing*. 38(8), 2007, p1902-1911.
- [10] B.B. Singha, M. Balasubramanian. Processing and properties of copper-coated carbon fiber reinforced aluminum alloy composites. *J. Mater. Proc. Tech.* 209(4), 2009, p2104-2110.
- [11] H. Naji, S.M. Zabarjad, S.A. Sajjadi. The effects of volume percent and aspect ratio of carbon fiber on fracture toughness of reinforced aluminum matrix composites. *Materials Science and Engineering: A*. 486(1-2), 2008, p413-420.
- [12] W.S. Lee, W.C. Sue, C.F. Lin. The effects of temperature and strain rate on the properties of carbon-fiber-reinforced 7075 aluminum alloy metal-matrix composite. *Compos. Sci. Technol.* 60(10), 2000, p1975-1983.
- [13] J. Su, G.H. Wu, Y. Li, et al. Effects of anomalies on fracture processes of graphite fiber reinforced aluminum composite. *Materials & Design*. 32(3), 2011, p1582-1589.
- [14] C.C. Poteet, I.W. Hall. High strain rate properties of a unidirectionally reinforced C/Al metal matrix composite. *Materials Science and Engineering: A*. A222, 1997, p35-44.
- [15] J. Cai, Y.J. Chen, V.F. Nesterenko, et al. Effect of strain rate on the compressive mechanical properties of aluminum alloy matrix composite filled with discontinuous carbon fibers. *Materials Science and Engineering: A*. 485(1-2), 2008, p681-689.
- [16] Y.X. Zhou, Y. Wang, S. Jeelani, et al. Experimental study on tensile behavior of carbon fiber and carbon fiber reinforced aluminum at different strain rate. *Applied Composite Materials*. 14(1), 2007, p17-31.
- [17] Z.T. Wang, L.Z. Tian. Handbook of aluminium alloys and processing. Changsha: Central South University of Technology Press; 2005. p422-423.
- [18] J.X. Xie, J.A. Liu. Theory and technology of metal extrusion. Beijing: Metallurgy Industry Press; 2002. p. 72-3.

## **MICROSTRUCTURE AND DEFORMATION BEHAVIOR OF Mg-Zn-Al-Re MAGNESIUM ALLOY**

Jing Zhang<sup>1,2</sup>, Fusheng Pan<sup>1,2</sup>, Chenguang Bai<sup>1</sup>

<sup>1</sup>College of Materials Science and Engineering, Chongqing University; Chongqing 400044, China

<sup>2</sup>National Engineering Research Center for Magnesium Alloys, Chongqing University; Chongqing 400044, China

Keywords: Magnesium alloy, Microstructure, Deformation

### **Abstract**

The microstructure and hot deformation behaviour of an Er-modified Mg-Zn-Al alloy were evaluated. The results showed that the addition of rare-earth Er changed the morphology of the quasi-continuous grain boundary networked eutectic compound to globular particles. Moreover, a self-strengthening effect was identified for the alloy, which determined its deformation behavior. After hot extrusion, the yield strength and elongation to failure of the Mg-Zn-Al-Re alloy at 200°C were increased by 105% and 120%, respectively, due to an emerged dynamic precipitation strengthening mechanism.

### **Introduction**

Magnesium alloys are attracting increasing attention for applications in automobile, electronic devices and hand tools for weight reduction and higher fuel efficiency, because of their lightweight and a high specific strength. However, application of Mg is still very limited. The largest applications are still those non load-bearing castings used at room temperature, such as box case, housing, and covering. One of the main reasons is the inadequate absolute strength both at room temperature and elevated temperatures (>100°C) of the commercially used AZ, AM series alloys, due to the incoherent interface between the secondary phase  $\gamma$ -Mg<sub>17</sub>Al<sub>12</sub> and Mg matrix, as well as the low thermal-stability of the  $\gamma$  phase [1]. Besides, the heat-resistant magnesium alloys which contain rare earth (Re) as the main alloying element are very expensive. The other reason is their poor deformability. The key solution is therefore to develop low-cost heat-resistant wrought alloys.

Larger quantity of ternary addition of Zn to binary Mg-Al alloys has shown complete suppression of the formation of the Mg<sub>17</sub>Al<sub>12</sub> phase, and the resultant ZA alloys have sound castability [2]. Moreover, effective age-hardening would be reasonably expected due to the large solubility variation of Zn and Al in Mg with temperature. In previous works [3], we aimed to elucidate the variation of the constituent phases with the Zn/Al ratio and the Al content, based on which the potential alloy compositions with improved elevated-temperature properties have been identified [3,4]. Moreover, it has been reported that minor addition of Re to Mg alloys is greatly beneficial to the deformability [5,6]. Therefore in this paper, the microstructure and hot deformation behavior of an Er-modified Mg-Zn-Al alloy were studied, in order to evaluate its potential as a deformable heat-resistant alloy.

## Experimental procedure

The nominal composition of the Mg-Zn-Al alloy studied in this work was Mg-7Zn-3Al (wt.%) with 0.4% addition of Er. Alloys were prepared by semi-continuous cast. Solution and aging treatment were carried out at 325°C for 50h, followed by quenching in water, and then aged at 200°C for 20h. Extrusion was conducted on a XJ-500 Horizontal Extrusion Machine using a billet with diameter of 85mm. The extrusion ratio was 25. Cylindrical samples of 50-mm gauge length and 10-mm diameter were used for tensile mechanical testing both at room temperature and elevated temperatures. Tensile properties were determined from a complete stress-strain curve. 0.2% yield strength (YS), ultimate tensile strength (UTS) and elongation to failure (elongation) were obtained based on the average of three tests. Isothermal hot tension tests were conducted in the temperature range of 150°C to 300°C and at a strain rate of 0.001 s<sup>-1</sup> to 0.1 s<sup>-1</sup> on a Gleeble 1500D thermo-mechanical simulator. Microstructures were observed by optical microscopy and scanning electron microscopy (SEM) using a TESCAN VEGA2 scanning electron microscope equipped with an INCA Energy 350 energy dispersive X-ray spectrometer (EDS).

## Results and discussion

### As-cast and as-aged microstructures of Mg-Zn-Al alloy

Figure 1 (a) shows the as-cast microstructure of the Mg-7Zn-3Al alloy. It manifests a networked  $\tau$ -phase ( $\text{Mg}_{32}(\text{Al,Zn})_{49}$ , BCC,  $a=1.416\text{nm}$ ) distributing in the interdendritic regions. After solution and aging treated, the majority of the coarse  $\tau$ -phase particles dissolved into the matrix, instead, nano-sized precipitates occurred uniformly in the matrix, as revealed by TEM and shown in Figure 1 (b). Due to the high stability of the  $\tau$  phase and the low  $\tau$  phase-matrix interface energy [3], the alloy had satisfied elevated-temperature stability. Mechanical property testing showed that the yield strength of the alloy reached 3/4 that at room temperature. However, the plasticity was unsatisfactory.

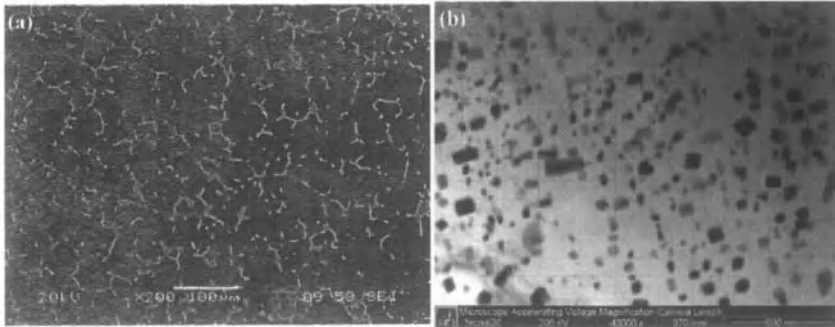


Figure 1. As-cast (a) and as-aged (b) microstructures of Mg-Zn-Al alloy.

### Microstructure and elevated mechanical properties of Mg-Zn-Al-Re alloy

Figure 2 shows the microstructure of Mg-Zn-Al-Er alloy. The quasi-continuous networked compounds were changed into discontinuous global particles with trace Er addition. EDS measurements revealed that these global particles were still the  $\tau$  compounds. Binary Al-Er particles were also occasionally detected.

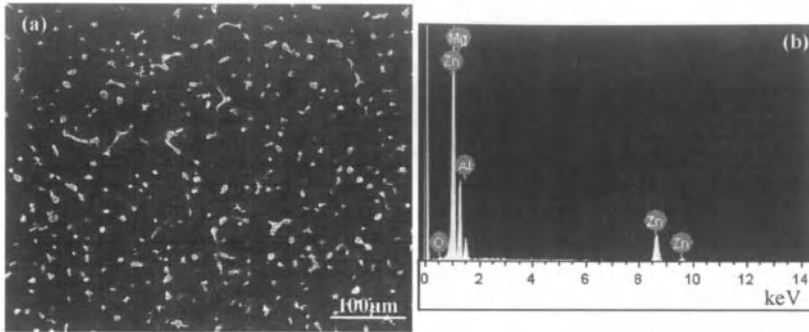


Figure 2. As-cast microstructure of Mg-Zn-Al-Er alloy (a) and typical EDS spectrum of the ternary Mg-Al-Zn particles (b).

The mechanical properties at 200°C of the alloys with and without Er addition were shown in Figure 3. It can be seen from Figure 3 that with Er addition, both the elongation and the strength are improved. It is interesting that when we compare the mechanical properties of the alloy with Er addition at room temperature and elevated-temperatures. It can be observed from Figure 4 that instead of falling down, the yield strength is increased and the elongation is also improved at higher temperatures. We call this a self-strengthening effect, which is believed to be associated with a dynamic precipitation during deformation. This finding provides a new way to develop heat-resistant wrought Mg alloy, i.e., utilizing the improved high temperature plasticity to realize hot plastic deformation, and dynamic precipitation to high strength at both room temperature and elevated temperature.

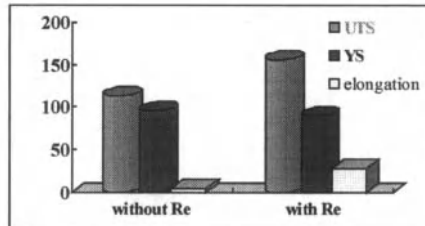


Figure 3. Mechanical properties at 200 °C of the alloys with and without Re addition.

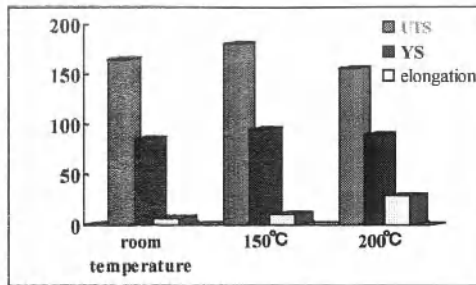


Figure 4. Mechanical properties of Mg-Zn-Al-Re alloy at room temperature and elevated-temperatures.

### Deformation behaviors

Deformation behaviors were evaluated by thermal analysis on a thermo-mechanical simulator. Figure 5 shows the typical flow curves under various deformation temperatures and strain rates. It is evident that for the ZA73 alloy, the hot plasticity is worse at lower temperature and strain rate and higher strain rate and temperature favor hot deformation; moreover, the poorest formability occurs at around 250°C. The addition of Er to the ZA73 alloy notably improves the hot plasticity for all deformation conditions, especially those under which the formability is relatively poor. Furthermore, these alloys manifest the best hot plasticity and stable flow stress when deformed at 300°C and a higher strain rate.

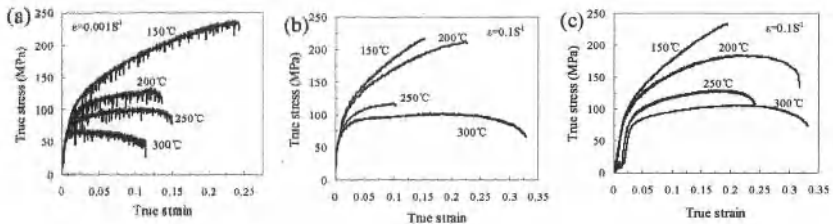


Figure 5. Typical flow curves under various deformation temperatures and strain rates during thermal simulation tests for alloys without (a and b) and with (c) Er addition.

### Fractographic analysis of as-deformed Mg-Zn-Al-Re alloy

Real extrusion experiments were carried out based on the optimum regimes determined by the thermal simulation. The Extrusion bars were tensile deformed both at room temperature and elevated temperatures. SEM fractographs revealed particles distributed in most of the dimples at the fracture surface of as-extruded Mg-Zn-Al-Er alloy tensile deformed at room temperature. EDS analysis results (Figure 6) showed that these particles were Al-Er binary phase. It has been reported that Er tends to form Al-Er phase in Mg alloys containing more Al element [7]. These fine dispersed Al-Er particles can act as heterogeneous nuclei to refine the microstructure [8]. On the other hand, excess Er addition will lead to coalescence of the Al-Er particles, resulting in stress concentration at the vicinity of the particles. Therefore, it is suggested that when the

precondition of a fine and homogeneous as-cast microstructure is satisfied, the addition amount of Er should be as less as possible.

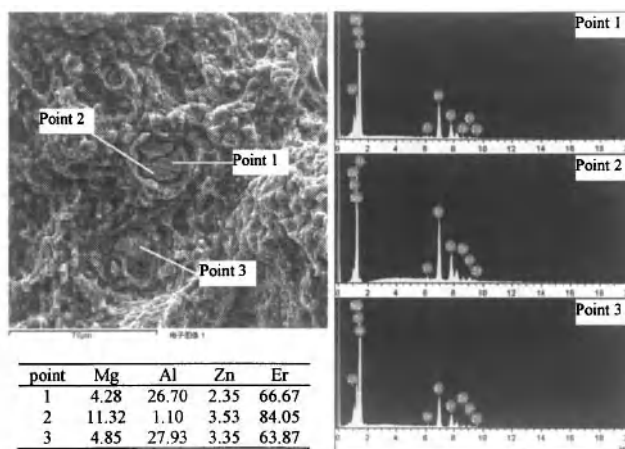


Figure 6. EDS analysis results of second-phase particles at fracture surface of as-extruded Mg-Zn-Al-Er alloy tensile deformed at room temperature.

Comparison of the tensile mechanical properties at 200°C between as-cast and as-extruded alloys revealed that both the yield strength and elongation to failure increased dramatically after hot extrusion, with the value being 105% and 120%, respectively. Furthermore, fractographs presented an obvious tough fracture feature when tensile deformed at 200°C for the extruded alloy. These phenomena all pointed to an emerged strengthening mechanism after hot deformation, i.e. dynamic precipitation, which endowed the alloy higher yield strength at elevated temperatures, in the mean time with the least harm effect on alloy plasticity.

### Conclusions

- 1) Feature of a self-strengthening effect was identified for the Mg-Zn-Al-Re alloy, which determined its deformation behavior.
- 2) The addition of rare-earth Er changed the morphology of the  $\tau$  phase to globular particles and enhanced alloy deformability.
- 3) After hot extrusion, the yield strength and elongation to failure of the Mg-Zn-Al-Re alloy at 200°C were increased by 105% and 120%, respectively, due to an emerged dynamic precipitation strengthening mechanism.

### Acknowledgements

The authors are grateful for the financial support of the Natural Science Foundation of CQ CSTC (No.2008BA4036) and China (No.50725413).

## References

- [1] C.J. Bettles, "The Effect of Gold Additions on the Ageing Behaviour and Creep Properties of the Magnesium Alloy AZ91E," *Materials Science & Engineering A*, **348**(2003), 280-288.
- [2] Z. Zhang, R. Tremblay, D. Dube, and A. Couture, "Solidification Microstructure of ZA102, ZA104 and ZA106 Magnesium Alloys and its Effect on Creep Deformation," *Canadian Metallurgical Quarterly*, **39**(2000), 503-512.
- [3] J. Zhang, Z.X. Guo, F.S. Pan, Z.S. Li, and X.D. Luo, "Effect of Composition on the Microstructure and Mechanical Properties of Mg-Zn-Al Alloys," *Materials Science & Engineering A*, **456**(2007), 43-51.
- [4] J. Zhang, R.L. Zuo, Y.X. Chen, F.S. Pan, and X.D. Luo, "Microstructure Evolution during Homogenization of  $\alpha$ -type Mg-Zn-Al Alloy," *Journal of Alloys and Compounds*, **448**(1-2)(2008), 316-321.
- [5] Y. Chino, M. Kado, and M. Mabuchi, "Compressive Deformation Behavior at Room Temperature - 773 K in Mg-0.2 mass%(0.035at.%)Ce Alloy," *Acta Materialia*, **56**(2008), 387-390.
- [6] N. Stanford and M. Barnett, "Effect of composition on the texture and deformation behaviour of wrought Mg alloys," *Scripta Materialia*, **58** (2008), 179-182.
- [7] C. Fang, "Researches on the Microstructures and Thermal Deformation Behaviors of Micro-alloyed Mg-Mn alloys" (Master thesis, Chongqing University, 2011), 28-30.
- [8] J.J. Yang, Z.R. Nie, T.N. Jing, H.Q. Ruan, and T.Y. Zuo, "Form and Refinement Mechanism of Element Er in Al-Zn-Mg Alloy," *The Chinese Journal of Nonferrous Metals*, **14**(2004), 620-625.

## **MICROSTRUCTURES AND TENSILE MECHANICAL PROPERTIES OF Mg-9Zn-0.6Zr-2Er MAGNESIUM ALLOY**

Jing Zhang<sup>a,b,\*</sup>, Baoxiang Zhang<sup>a</sup>

<sup>a</sup> College of Materials Science and Engineering, Chongqing University, Chongqing, China

<sup>b</sup> National Engineering Research Center for Magnesium Alloys, Chongqing, China

\*College of Materials Science and Engineering, Chongqing University, Chongqing 400044, China

Keywords: Mg alloy, Hot rolling, Solution, Tensile mechanical properties

### **Abstract**

As extruded Mg-9Zn-0.6Zr-2Er magnesium alloys were hot-rolled at 400 °C, followed by solution treatment at 400 °C for 1.5h and artificial aging at 200°C for 10h. Microstructures and tensile mechanical properties of the alloys after hot rolling, solution and aging treatment were examined respectively. Optical micrographs of the as-rolled and as-solution alloys showed fine grain structures, due to the formation of Er- and Zn- bearing compounds at grain boundaries which obviously improved the thermal stability of the alloy. Yield strength as high as about 335 MPa was obtained for the as-rolled alloy, showing that the mechanical properties of the alloy was greatly benefit from the grain refinement and dynamic precipitation of fine MgZn<sub>2</sub> during hot rolling. Due to solution heat treatment, vast majority of the Mg-Zn phases dissolved into the matrix, and precipitated out again as fine dispersoid during the subsequent aging, resulting in an enhanced aging-hardening effect.

### **Introduction**

With high specific strength and low density, magnesium alloy has stimulated significant interest for the applications in microelectronics, aerospace and automobile industries. Due to its HCP structure, magnesium alloys exhibit relatively poor strength and ductility. Great efforts have been made to improve the properties of magnesium alloys.

Thermo-mechanical processing which combined with subsequent heat treatment can strengthen magnesium alloys due to the strain-hardening mechanism, homogeneous distribution of second particles and grain refinement [1, 2]. However, commercial wrought magnesium alloys have high tendency of grain growth at high temperature due to lack of effective solutions to stabilize the microstructure [3, 4, and 6]. But Magnesium-RE alloys containing high rare earth were reported to have remarkable thermal-stability, Rare earth (RE), such as Y, Nd, Yb, Gd, Ce, were known to form second-phase particles that have higher thermal stability combining with Zn and matrix in Mg[12-17].

Although most of the commercial wrought Mg alloys are precipitation hardenable, but they rarely heat treated after wrought processes. This is because the age-hardening responses of commercial wrought alloys such as Mg-Zn (ZK) and Mg-Al-Zn (AZ) alloys are too low to achieve sufficient improvement by heat treatment (8). However trace element addition is a very effective way to enhance precipitation hardening effects [18].

In this paper, as-extruded Mg-9Zn-0.6Zr with 2% Er (wt%) magnesium alloy were undergone hot rolling, and then solution treated and T6 treated to enhanced mechanical properties. Effects of hot-rolling and heat treatment on the microstructure and tensile properties of Mg-9Zn-0.6Zr-2Er magnesium alloy were investigated. Thermal stability of the alloy was observed. Strengthening mechanism of the alloy is also discussed.

### **Material and Experimental Procedure**

The as-extruded magnesium alloy which is to be hot rolled has a nominal composition as following: 9%Zn, 0.6%Zr, 2%Er and balance magnesium. The cylindrical bars of 10 mm in diameter were machined into rectangular plates with a cross-section of 12mm×8 mm. Prior to processing, the plates were heated at 673K for 6 hours. The rolling process was carried out at 673K with cold rollers. The plates with 8mm starting thickness then were reduced to 2mm, and the reduction per pass was 0.5mm. The rolling plates were heated at 673K for 20min before rolling and 5 min during each pass to stabilize the rolling temperature. The rolling direction was parallel to extrusion direction of as extruded alloy. Hot rolled alloys were heated at 673K for 1.5h then undergone artificial aging at 473k for 10h.

The alloys were investigated in as-rolled, as-solutioned, and as-aged heat treated condition. Microstructures were observed by optical microscopy, as well as scanning electron microscopy (SEM) with a TESCAN VEDA3 scanning electron microscope. Dogbone tensile specimens of 2-mm gauge thickness, 5mm gauge width and 25mm gauge length were also machined from hot rolled and as-solutioned alloys for the ambient temperature tensile tests. Tensile tests were carried out in a Shimadzu AG-X10KN universal testing machine at a strain rate of 0.5mm s<sup>-1</sup>. The tensile axis was along the rolling direction. Tensile properties were determined from a complete stress-strain curve. Micro Vickers-hardness of the alloys was conducted using a 0.3 Kg load and hold time of 15s. Grain sizes of the alloy of each condition were statically calculated.

### **Results and Discussion**

#### Microstructures of the Prior-rolling and As-rolled Alloys

Fig1(a) shows optical micrograph(OM) of the alloy undergone pre-heating before hot rolling, the alloy has fine and even grains which are 5-10 $\mu$ m in size.

Microstructures of the hot rolled plate are shown in fig1.b (RD-TD plane), c(RD-ND plane), d(TD-ND plane) respectively. RD-ND plane and TD-ND plane emerged large amount of shearing bands. Shearing bands which consist of recrystallized grains are inevitable in the rolling process of magnesium alloy due to the macro-stress state [11]. As we know, dynamic recrystallization (DRX) has a high tendency to nucleate at the original grain boundaries. Compared with those boundaries which were parallel or perpendicular to the rolling direction (RD), boundaries that parallel to maximum shear stress have much more probability to accommodated strain during hot deformation. It was expected more and more grains would be formed at these soft oriented regions, producing ductile shearing bands inclined about 45°to the rolling direction (seen in fig1.c).

RD-TD plane of the as-rolled alloy emerged large amount of twinning while without shearing band.

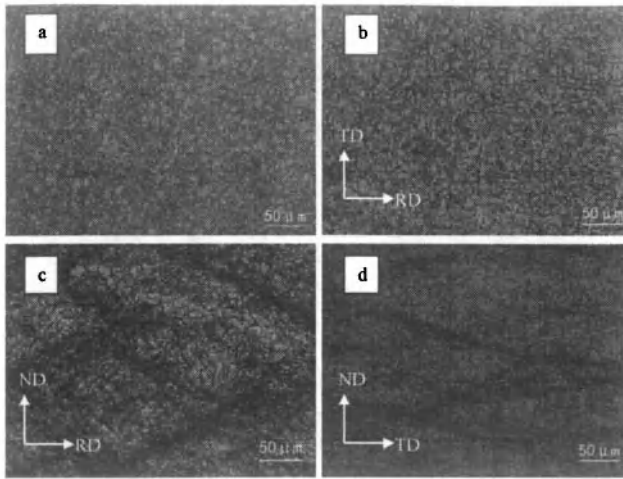


Figure 1. optical micrographs of prior-rolling Mg-9Zn-0.6Zr-2Er alloy (a), TD-RD plane (b), ND-RD plane (c), ND-TD plane (d) of as-rolled alloy.

#### Microstructures of the As-solutioned and As-aged Alloy

Microstructures of as-solutioned alloy in the (a) TD-ND plane, (b) RD-ND plane and (c) RD-TD plane can be seen in fig2 (a-c) respectively. The alloy has fully recrystallized, and twins were disappeared. The dynamic recrystallized grains used to located at the shearing bands of as-rolled alloy stayed almost the same size, what' more, average grain size of the as-solutioned alloy was just slightly higher than as-received extruded alloy(seen in Figure3), indicating that the alloy has excellent microstructural stability at elevated temperature (at least 673K). Figure4 shows SEM microstructure images of as-solutioned alloy, existence of the thermal stable Mg-Zn-Er phase particles at the grain boundaries that hinder grain growth during the solution treatment [2].

Optical microstructure characteristics of the alloy stay almost the same after aging treatment (seen in figure 2(d-f)). The aging treatment did not change the grain size, but it does change the second phase constitution, more second phases are static precipitate from the Mg matrix (seen in fig 4(c)), resulting in an aging-hardening effect.

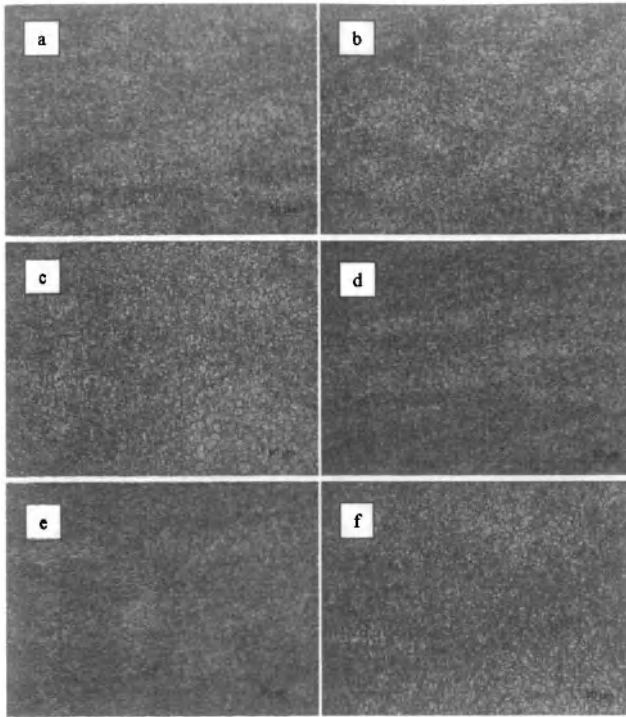


Figure 2. Optical micrographs of as-solutioned and as-aged alloys in TD-ND plane (a,d) ,ND-RD plane (b,e), and TD-RD plane (c,f) respectively.

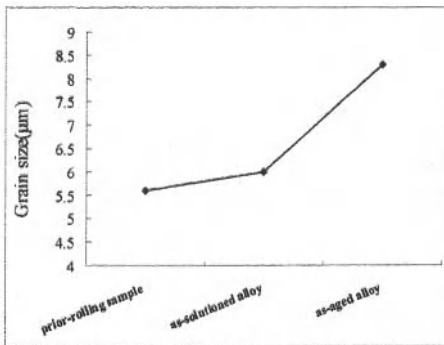


Figure 3. Average grain size of alloys that prior-rolling alloy, as-solutioned alloy and as-aged alloy.

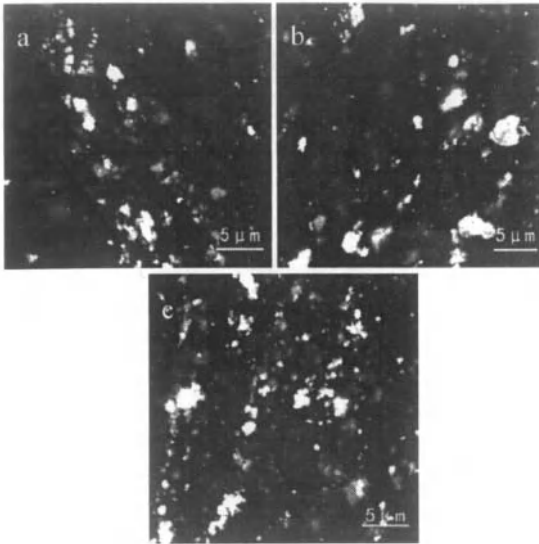


Figure 4. SEM images :( a) as-rolled alloy; (b) as-solutioned alloy; (c) as-aged alloy.

#### Tensile Properties of the Alloys with Different Processing

The tensile test results of the as-extruded alloy, as-rolled alloy and as-solutioned alloy are given in Table 1. As shown in the table, the yield strength (YS) of as-rolled alloy was 335Mpa which was 16Mpa higher than that of as-extruded alloy. The difference in the measured yield strength of the two alloys may be due to the not fully recrystallized grains in as-extruded alloy and, a better second phase strengthening effect in as-rolled alloy than that in as-extruded one. But the elongation of the as-rolled alloy is sharply decreased (2.1%) compared to the as-extruded alloy (16.58%). Compared to the as-rolled alloy, both the yield strength (YS) and ultimate tensile strength (UTS) of the as-solutioned alloy are dramatically decreased, whereas, the elongation is markedly increased (seen in table1). This is due to the following facts: (1) as-rolled alloy was statically recrystallized, density of dislocation was declined, effect of strain hardening has been eliminated after the alloy underwent solid solution treatment; (2) some grain boundary phases were dissolved during the solution treatment, resulting in a decreased precipitation hardening effect.

Table 1. Tensile properties of as-extruded, as-rolled and as-solution alloy.

Samples	YS ( $\sigma_{0.2}$ )	UTS ( $\sigma_b$ )	elongation (%)
As-extruded alloy	319Mpa	370.5Mpa	16.6
As-rolled alloy	335Mpa	370Mpa	2.1
As-solutioned alloy	205Mpa	271.5Mpa	12.3

Hardness of as-aged alloy is increased after aging treatment. (Seen in fig.5) This is due to static precipitation of  $MgZn_2$  phase particles [2], and inevitably, these particles are the obstruction of

the dislocation, thus they make an ageing strengthening effect on the materials. But hardness of as-aged alloy is lower than the as-rolled alloy, indicating that dynamic precipitation of second phases during hot deformation is more effective in hardening the alloy than static precipitation of second phases during aging treatment.

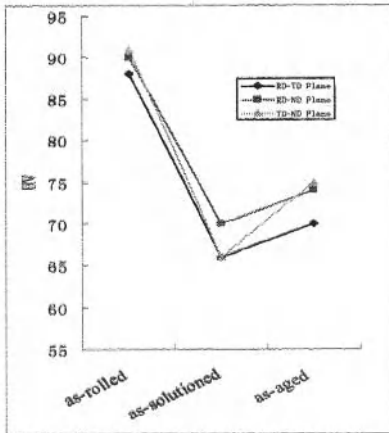


Figure5. Vickers hardness (HV) of as-rolled, as-solutioned and as-aged alloys.

### Conclusion

(1) Mg-9Zn-0.6Zr-2Er alloy plates can be consecutively rolled with the reduction of 75% at 673K with cold rollers, the as-rolled alloy exhibits shearing bands and twinning.

(2) Hot rolling processing can enhance the strength of Mg-9Zn-0.6Zr-2Er magnesium alloy, namely, the ultimate tensile strength is 370Mpa, and yield strength is 335Mpa, while elongation is 2.1%. The as-solutioned alloy exhibits lower strength but higher elongation than the as-rolled one, while the as-aged alloy shows higher Vickers hardness, indicating a considerable age-hardening effect.

(3) Due to the thermal stable second phases precipitating at grain boundaries, Mg-9Zn-0.6Zr-2Er magnesium alloy has excellent microstructural stability at high temperature (at least 673K).

### Acknowledgements

The authors are grateful for the financial support of the Natural Science Foundation of CQ CSTC (No.2008BA4036) and China (No.50725413).

### Reference

[1] Shouren Wang, Suk Bong Kang, JaeHyung Cho, "Effect of hot compression and annealing on microstructure evolution of ZK 60 Magnesium alloy", *J Mater Sci* (2009)44:5475-5484.

- [2] Jing Zhang, Qi Ma, Fusheng Pan, "Effects of trace Er addition on the microstructure and mechanical properties of Mg-Zn-Zr alloy", *Materials and Design* 31(2010) 4043-4049.
- [3] Bettles CJ, Gibson MA, "Current wrought magnesium alloys: Strengths and weaknesses". *JOM* 2005; 57:46-9.
- [4] Takuda H, Kikuchi S, Hatta N, "Possibility of grain refinement for super plasticity of a Mg-Al-Zn alloy by pre-deformation". *J Mater Sci*, 1992; 27:937-40.
- [5] Wenjiang Ding, Daquan Li, Qudong Wang, Qing Li, "Microstructure and mechanical properties of hot-rolled Mg-Zn-Nd-Zr alloys", *Mater. Sci. Eng. A*, 373 (2004) 320.
- [6] Z.P. Luo, S.Q Zhang, "Effect of Heat Treatments on Tensile Properties and Microstructures of Wrought Mg-Zn-Zr-RE alloys", *Advanced performance materials*, 2, (1995)299-304.
- [7] R.Mahmudi, F.Kabirian, Z.Nematollahi, *Materials and Design* 32(2011) 2583-2589.
- [8] K. Hoho, C.L.Mendis, T.T.Sasaki, K.Oh-ishi, *Scripta Materialia* 63(2010) 710-715.
- [9] Chunjiang Ma, Manping Liu, Guohua Wu, Wenjiang Ding, Yanping Zhu, *Mater Sci Eng A*, 2003, 349(1/2):207-212.
- [10] HE S M, ZENG X Q, PENG L M, GAO X, NIE J F, DING W J, *Journal of Alloys and Compounds*, 2007; 427(1/2):316-323.
- [11] Zhen Zhang, Mingpu Wang, Nian Jiang, Shuo Zhu, "Formation of shearing bands in the hot-rolling process of AZ31 alloy", *Journal of Alloys and Compounds*(2010).
- [12] Zheng XW, Dong J, Xiang YZ, Chang JW, Wang FH, Li J, et al, "Formability, mechanical and corrosive properties of Mg - Nd - Zn - Zr magnesium alloy seamless tubes". *Mater Design* 2010;31:1417 - 22.
- [13] Xu DK, Liu L, Xu YB, Han EH, "The effect of precipitates on the mechanical properties of ZK60-Y alloy", *Mater Sci Eng A* 2006;420:322 - 32.
- [14] Guo XF, Remennik S, Xu CJ, Shechtman D. "Development Mg-6.0%Zn-1.0%Y-0.6%Ce-0.6%Zr magnesium alloy and its microstructural evolution during processing", *Mater Sci Eng A* 2008;473:266 - 73.
- [15] Pelcova J, Smola B, Stulikova I, "Influence of processing technology on phase transformations in a rare-earth-containing Mg - Zn - Zr alloy", *Mater Sci Eng A* 2007;462:334 - 8.
- [16] Yu WB, Liu ZY, He H, Cheng NP, Li X, "Microstructure and mechanical properties of ZK60 - Yb magnesium alloys", *Mater Sci Eng A* 2008;478:101 - 7.
- [17] He S, Peng L, Zeng X, Ding W, Zhu Y, "Comparison of the microstructure and mechanical properties of a ZK60 alloy with and without 1.3 wt.% gadolinium addition", *Mater Sci Eng A* 2006;433:175 - 81.
- [18] Buha J. "Grain refinement and improved age hardening of Mg - Zn alloy by a trace amount of V", *Acta Mater*, 2008; 56:3533 - 42.

## **NANOBOND - THE PERFECT REFRACTORY CHOICE FOR QUICK LINING AND REPAIRING OF ALUMINIUM MELTING FURNACES**

Dr.-Ing. Thomas Schemmel<sup>1</sup>, Dr.-Ing Helge Jansen<sup>1</sup>, Dipl.-Ing. Bertram Kesselheim<sup>1</sup>,  
Dipl.-Ing. Uwe Kremer<sup>2</sup>

<sup>1</sup>Refratechnik Steel GmbH, Schiess Straße 58, 40549 Duesseldorf, Germany

<sup>2</sup>TRIMET ALUMINIUM AG, Aluminiumallee 1, 45356 Essen, Germany

Keywords: Nanobond, Refractory, Aluminium, No Cement Castables, Quick Drying

### **Abstract**

During the last decades the refractory life time of the different aggregates of the secondary aluminium production was improved significantly. However, each repair and installation of refractory material affects the operating schedule and can cause costs in the million range. The downtime of just one melting furnace generate costs of 100.000 to 400.000 \$ per day. Besides cooling down of the furnace and its repair, the heating-up procedure accounts for the longest time of the shutdown. Usually, heating-up of low cement or ultra low cement castables takes 120 to 150 hours. In order to reduce such expensive downtimes Refratechnik developed a unique and novel product series: Nanobond. These materials can be heated-up in only a third of the usual time. This paper talks about the theoretical aspects, as well as the mechanical and physical properties and especially practical experience of using Nanobond.

### **Theoretical Aspects and Laboratory Results**

Cement containing castables such as RCC, MCC, LCC or ULCC are considered standard in many refractory applications. Over the years a wide range of possible raw materials and practical installation methods were developed. However, all of these cement bonded refractory mixes possess one main important drawback. Such materials are characterized by the hydration of the cement bonding. As a result the physical bonded and the hydraulic water has to be removed in a relatively complicated drying procedure. The hydraulic water specifically demands a very careful and cautious heating up procedure. Most of the dreaded steam explosions can occur at a furnace temperature of approx. 250 °C. [1] To avoid such destructions, the heating-up of a new lined or repaired furnace can be very complex and slow. Depending on the furnace or the casted part a drying time of several days with long curing times are common.

Besides cooling down of the furnace and its repair, the heating-up procedure account the longest time of the shutdown. Additionally the cement bonding of usual castables is very often a weak point regarding the chemical wear of refractory materials. In order to solve such problems Refratechnik developed a unique, novel and patented product series: Nanobond. Nanobond is typically free of cement and water. It is a dry refractory mix that comes with a special liquid binder. This liquid binder acts as a mixing and binding agent. By adjusting the amount of the binder the setting time of the castable can be controlled individually. In contrast to other available cement free castables this two-component-system is completely safe to use and represents no health hazard. The absence of any acids means that no corrosion of the anchors can take place. There are no restrictions regarding transport or usage at plant. Table 1 provides a short comparison of cement bonded castables and Nanobond castables.

Table 1: Comparison of the main properties of usual cement bonded castables and Nanobond

	Usual cement castables	Nanobond
Type	regular, medium, low cement or ultra low cement castable	no cement castable
Mixing agent	water	special liquid binder
Variation of the setting time	usual additives	amount on liquid binder
Mechanical and physical properties	Comparable	
Available raw materials	no technical restrictions: chamotte, bauxite, tabular alumina, andalusite, fused corundum etc.	
Shelf life	max. 6 months	max. 12 months

The introduced Nanobond system is available for all type of alumina-based raw materials and has been tested in numerous different applications successfully. In addition to the mentioned castable and self-flow castable it is also available as a jet cast material. Many alumina melting furnaces are still applied with a safety lining. If this safety or permanent lining will be damaged during the break out a special Nanobond castable based on chamotte is available.

The Nanobond binder technology is mainly based on colloidal silica. It is a colloidal dispersion of nano-sized Silicon Dioxide (SiO<sub>2</sub>) particles. By drying the non-cross-linked or uncured sol a stable and cross linked gel is formed. After this gelation the binder system is temperature stable, insoluble in water and characterized by a very high mechanical strength.

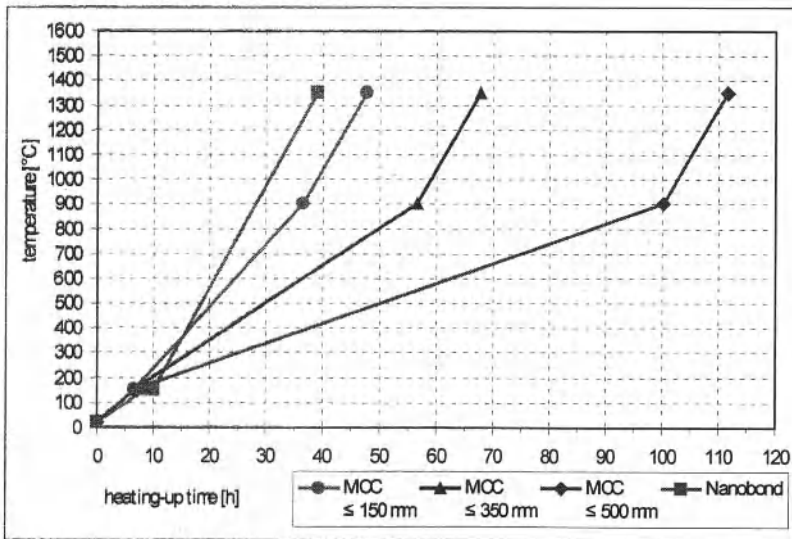


Figure 1: Heating-up procedure of different medium cement castables samples compared to Nanobond

Figure 1 clearly shows the main advantage of the Nanobond product series. The initial heating-up procedure of a typical medium cement castable is strongly depending on the size and the shape of the specimen. For larger samples or prefabricated parts the heating-up time is significantly longer. In the example shown the recommended heating-up time triples to ~110 h as the sample increases from 150 to 500 mm. For the shown Nanobond material the heating-up time is constant for specimens < 500 mm: 42 h.

In the Table 2 below some highlights of a conventional medium cement castable with that of Nanobond material are shown. The raw material base (corundum) and the installation method (casting, vibrating) are the same. Both materials contain a novel and patented system of different anti-wetting additives. Anti-wetting additives are thus frequently used in order to improve the life time of refractory products. Up until now, however, standard additives have been unable to prevent an intense corrosion from occurring, in particular with Aluminium-Magnesium alloys. These additives tend to dissolve when faced to the usual operating temperatures of >1000 °C. Not only is the desired effect lost but there is a risk of lasting damage to the brick structure from the decomposition products. The new developed anti-wetting system can withstand temperatures of up to 1200 °C without damaging the refractory material structure.

Table 2: Main properties of a medium cement castable compared to Nanobond

	Medium cement castable	Nanobond
<b>Main raw material</b>	corundum	
<b>Installation method</b>	casting, vibrating	
<b>Bonding system</b>	Hydraulic	Inorganic, chemic
<b>Mixing liquid</b>	Water	Special liquid binder
<b>Special anti-wetting additive</b>	Yes	Yes
<b>Maximum service temperature [°C]</b>	1250	1500
<b>Apparent porosity [%]</b>	22.0	15.0
<b>Cold crushing strength [N/mm<sup>2</sup>]</b>		
After curing at 110 °C	110.0	40.0
500 °C	110.0	120.0
1000 °C	110.0	120.0
1200 °C	110.0	120.0
1500 °C	---	120.0
<b>Permanent linear change [%]</b>		
After curing at 110 °C	- 0.05	- 0.05
500 °C	- 0.05	- 0.05
1000 °C	+ 0.05	- 0.10
1200 °C	+ 0.10	- 0.10
1500 °C	---	- 0.85

Due to the hydraulic bonding of the MCC the maximum service temperature of this product is limited to 1250 °C. The cold crushing strength after curing at at least 500°C is comparable for both materials. As a result of using a special binder and the absence of water the apparent porosity of the Nanobond material is significantly lower (15.0 %). Figure 2 shows different MCC and Nanobond crucibles in contact with liquid alumina alloy 7075. The tests were accomplished at 800, 1000 and 1200 °C with a curing time of 150 h. For both materials the infiltration and the

wear is similar. The special anti wetting additive prevents a massive corundum formation, which is well known as the main wear effect of refractories in aluminium melting furnaces. Importantly, what is not evident is the detrimental affect of the colloidal silica binder system on the wear of the materials. Due to its nano-sized structure the introduced silica is very reactive and can react with other refractory material components to uncritical phases like mullite.

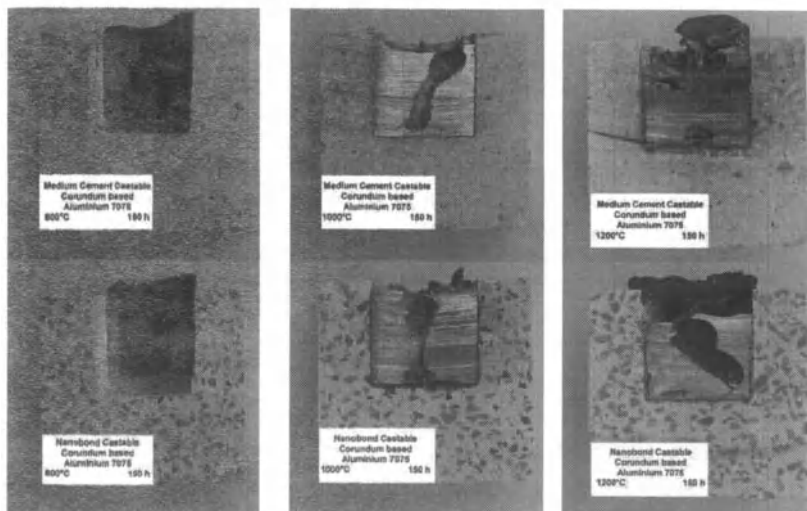


Figure 2: Cup tests of a Medium Cement Castable (MCC) and a Nanobond Castable with Aluminium alloy 7075

Aside from the obvious economical advantages of the heating-up procedure the fast and uncritical heating up procedure the Nanobond materials possess another big benefit for customers. After the initial heat-up the refractory lining is 100 % free of water. Consequently no hydrogen is delivered to the liquid aluminum. The Hydrogen pickup of the aluminum by the monolithic refractory lining is serious problems for many alumina foundries, therefore, by choosing the novel Nanobond bonded materials the quality of sensitive or demanding alloys and casted parts can be improved.

#### Usual Lining vs. Nanobond Lining and Repairing Practical Experience Report from TRIMET

To demonstrate the potential and to highlight some practical experience a report of the repair lining of a melting furnace at TRIMET Aluminium AG (Essen, Germany) is discussed.

After 4 years of production a service repair of the smelting furnace No. 6 was necessary. The furnace showed a premature wear in the bottom and the ramp. Based on their past TRIMET decided to reline the furnace with Nanobond material. This choice allowed the facility to shorten the stoppage and to recommence to production as soon as possible. After cooling down and

breaking out, the furnace was relined with Refratechnik Nanobond castable. Beside the usage of the special liquid binder the procedure of mixing, casting and vibrating is comparable to any other typical refractory castables. The setting time of the castable was controlled by the amount of the liquid binder. No special additives were needed to react on different ambient temperatures. Due to the perfect adhesive and bonding properties to the existing refractory lining no special pretreatment was required.

In total ~ 20 to of the corundum based Nanobond material was mixed and installed into the furnace. The following pictures are showing the furnace before breaking out, during relining and after heating up. Due to its perfect condition no repair of the safety lining necessary. After installation and a short drying time at ambient temperature the heating-up procedure was started. After only 22 h of heating-up and 12 of sintering with liquid metal at 850 °C the furnace No. 6 was ready to return to production. In total the complete relining of the bottom and the ramp took only 1 week.

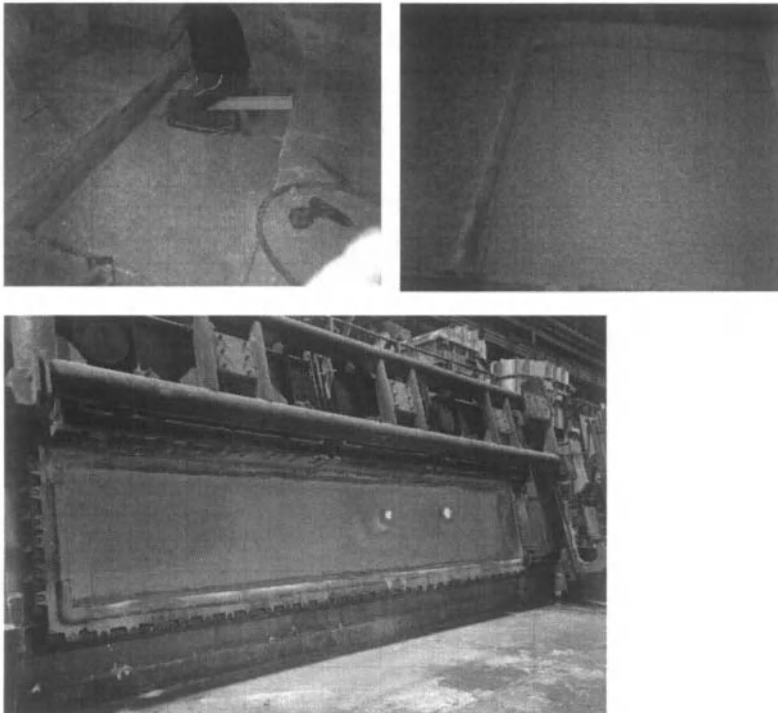


Figure 3: Different views into the aluminium melting furnace No. 6: during relining and after heating up and sintering with liquid metal

The chart diagram in figure 4 shows total timeline of the described relining of the furnace No. 6. The usual relining with common medium cement castables (MCC) is shown for comparative purposes. It is evident that by using Nanobond the total repairing time was significantly shorter. Compared to a lining with an usual medium cement castable the facility can win 5-6 days of production. Ultimately for an Aluminum producer such as like TRIMET this means an additional production of ~ 15 batches.

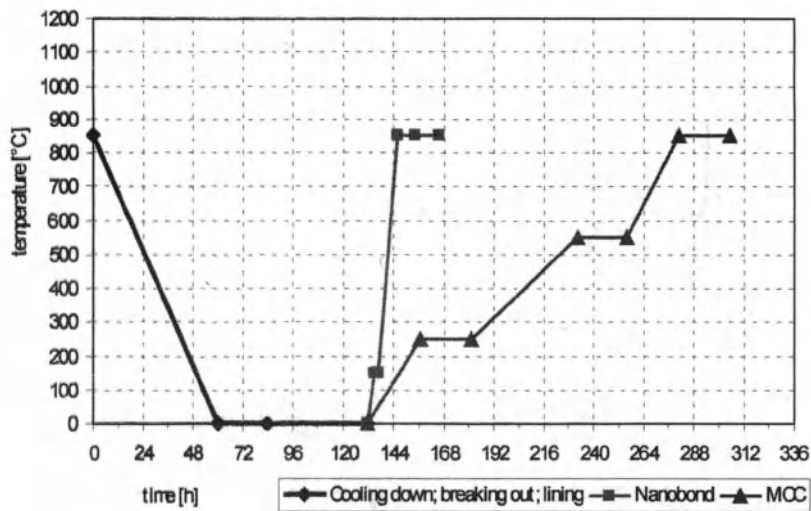


Figure 4: Total time schedule for relining the TRIMET aluminium melting furnace No. 6: Nanobond and Medium Cement Castable

Besides the shorter curing time and the increased reproduction ability, the easier heating up procedure is a big benefit to the Nanobond user. Table 3 below highlights the equipment needed and the associated costs caused for heating up a furnace. The drawn-out heating-up procedure of cement bonded castables requires special equipment. To maintain the essential low temperature increase external heating equipment is needed. In total the heating device including measurement technique and manpower can cause cost of in the region of 30.000 \$. Figure 5 shows a relined aluminium melting furnace and the external heating equipment that is need to heat-up the cement bonded castables proper. In contrast the Nanobond material does not need any special heating equipment. It can be simply cured with the furnace burners.

Table 3: Time schedule and cost/production plan for relining melting furnace No. 6

	Medium Cement Castable	Nanobond
<b>Heating up procedure</b>	7-8 days	2 days
<b>Special heating equipment</b>	External heating device including manpower, installation, measurement technique etc. (fig. 5)	No
<b>Costs</b>	~30.000 \$	Nothing
<b>Loss of production during total relining</b>	~ 40 batches	~ 20 batches

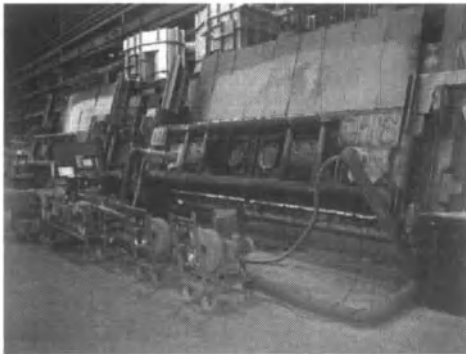


Figure 5: External heating device for drying / heating-up a MCC relined aluminium melting furnace

### Conclusion

Nanobond is a new product series especially developed for a fast, secure and save relining of aluminium melting furnaces. Due to the absence of water and the cement free bonding system the installed lining can be heated up 70 % quicker than common medium cement castables. In addition to straight forward curing process, Nanobond exhibits the following technical and economical benefits:

- no risk of introducing hydrogen into the process
- long shelf time
- 100 % safe and harmless liquid binder
- adjustable setting times
- perfect adhesion and bonding on existing refractory linings
- non wetting behavior

### Reference

[1] G. Routschka, H. Wuthnow: Pocket Manual Refractory Materials. 3<sup>rd</sup> Edition 2008, Vulkan-Verlag Essen, Germany

## **CHARACTERIZATION OF GRIT BLASTED METALLIC BIOMATERIALS BY THERMOELECTRIC POWER MEASUREMENTS**

H. Carreon<sup>1</sup>, S. Barriuso<sup>2</sup>, J. L. González-Carrasco<sup>2,3</sup>, F. G. Caballero<sup>2</sup>, M. Lieblich<sup>2</sup>

<sup>1</sup>Instituto de Investigaciones Metalúrgicas,  
Edif."U" C.U., 58000-888, Morelia, México

<sup>2</sup>Centro Nacional de Investigaciones Metalúrgicas,  
Avda. Gregorio del Amo 8, E28040, Madrid, España

<sup>3</sup>Centro de Investigación Biomédica en Red en Bioingeniería,  
Biomateriales y Nanomedicina (CIBER-BBN), Madrid, España

Keywords: Grit Blasting; Thermoelectric Measurements; Residual Stresses; Biomaterials

### **Abstract**

The grit blasting is a low-cost technique successfully used to enhance mechanical fixation of the implants through increasing their roughness. As a result of the severe plastic surface deformation, it produces subsurface effects such as grain refinement, hardening and compressive residual stresses which are generally evaluated with destructive techniques. In this research work, non-contacting and contacting thermoelectric power measurements are performed in blasted 316LVM and Ti-6Al-4V specimens using Al<sub>2</sub>O<sub>3</sub> and ZrO<sub>2</sub> particles which yield a coarse and a fine rough surface, respectively. This study correlates the microstructural changes induced by the grit blasting treatment and the limitations and advantages of each of the nondestructive thermoelectric techniques based on the Seebeck effect used to evaluate these biomaterials.

### **Introduction**

It is well known that surface properties play an important role in metallic materials used in bio-medical applications. Since the biological response is correlated directly with surface properties it is comprehensible the intense activity in superficial modification by physics or chemistry methods in this field. Grit blasting, one of the most popular surface modification of metallic biomaterials, enhances the mechanical fixation of the implant through the increase in roughness [1-3]. Roughening is developed by bombarding the surface with a high-velocity jet of ceramic particles, being the final roughness a function of the processing parameters (pressure, distance, time,...) and blasting particles (nature, shape, size). As the plastically deformed surface layer tries to expand relatively to the intact interior of the specimen, residual compressive stress gradients develops perpendicular to the surface at shallow depths with a maximum value at a depth in the range of 5 to 60  $\mu\text{m}$ . This surface treatment also may cause subtle variations in the subsurface material properties, such as increased hardness and grain size refinement, which are consequences of the significant plastic deformation through cold work. Blasted affected zones may extend to a depth of up to about 200  $\mu\text{m}$ . The subsurface hardening and the near-surface compressive stress gradient play a beneficial role by retarding fatigue crack nucleation and further

growth, ultimately extending the fatigue life of the metallic part [4]. In this work, two non-destructive thermoelectric techniques (NDTT), the non-contacting and contacting thermoelectric power measurements were used to analyze the subsurface induced changes on blasted Ti-6Al-4V and 316LVM specimens using  $Al_2O_3$  and  $ZrO_2$  particles. Detailed information on the microstructural induced effects and subsurface mechanical properties were published elsewhere [5-8]. Here the nondestructive evaluation of the involved microstructural changes is used to assess the global subsurface damage. Advantages of using nondestructive techniques during manufacturing are envisaged.

### Thermoelectric Techniques

Thermoelectricity is caused by coupled transport of heat and electricity in metals, which can be exploited for materials characterization [9]. In general, the thermoelectric methods are based on the Seebeck effect that is commonly used in thermocouples to measure temperature. The *contacting thermoelectric technique* monitors the thermoelectric power (TEP) of metallic conductor materials, which is affected by the different types of defects present in the atomic lattice such as atoms in solid solution, precipitates and dislocations. A schematic representation of the contacting thermoelectric apparatus is given in Figure 1. The sample is placed between two blocks of a reference metal that are subjected to a temperature gradient. The TEP value of the sample is a measure of the magnitude of the induced potential difference at the metal contacts in response to the temperature gradient across the sample. Several parameters can affect the changes in TEP of the test sample to be inspected. The most important parameters affecting the thermoelectric measurements are those associated with volumetric and contact effects. The volumetric effect is close-related to the thermoelectricity phenomena by the kinetics of the diffusion of electrons throughout the material. This effect is mainly affected by chemical composition, different heat treatment, precipitation process, grain boundaries, texture and fatigue of the material [10,11]. The contact effects are related to the imperfect contact between the test sample and the reference probe, amount of pressure applied to the probe, temperature of hot and cold junctions and probe material [12].

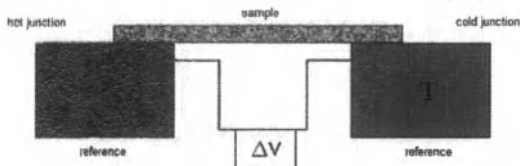


Figure 1. Schematic diagram of the contacting thermoelectric technique as used for the characterization of grit-blasted samples.

On the other hand, when the material gradient properties such as local plastic deformation, fretting, residual stress, localized texture, cold work, etc., occurs at the surface or subsurface region, the material properties variation can be detected more efficiently using the surrounding intact material as the reference electrode; thus providing a perfect interface between the region to be tested and the surrounding material [13-16]. This measurement process is called *non-contacting thermoelectric technique* in which the idea is to sense the weak thermoelectric currents around inclusions and other types of inhomogeneities or imperfections when the specimen to be tested is subjected to directional heating or cooling by using a high-sensitivity magnetic sensor as shown in Fig. 2. An external heating or cooling is applied to the specimen to produce a temperature gradient in the region to be tested. This leads to that different points of the boundary between the host material and the

imperfection will be at different temperatures, therefore also at different thermoelectric potentials. These potential differences will produce opposite thermoelectric currents inside and outside the imperfection. The thermoelectric currents form local loops that run in opposite directions on the opposite sides of the imperfection relative to the prevailing heat flux. These thermoelectric currents can be detected by magnetic sensing of the flux density  $B$  even when the imperfection is buried below the surface and the magnetic sensor is far away from the test sample.

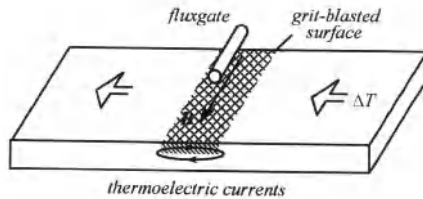


Figure 2. Schematic diagram of the noncontacting thermoelectric technique as used for the characterization of the grit-blasted samples.

### Experimental Method

The 316 LVM austenitic stainless steel was supplied as a bar. Specimens of 20 mm in diameter and 2 mm thick were machined and grit blasted by the implant manufacturer (SURGIVAL, Valencia, Spain). Grit blasting was performed with two different types of particles under a pressure of 350 kPa for 2 min and the distance between the nozzle and the target surface was 20 cm. A first set of samples (Zirconia) was blasted using  $ZrO_2$  embedded in silica vitreous phase microspheres sized between 125  $\mu m$  and 250  $\mu m$ . The second set of samples (Alumina) was blasted with alumina angular particles  $Al_2O_3$  of  $\sim 750 \mu m$ . On the other hand, a Ti-6Al-4V alloy was used in this study. The samples were grit blasted with the following conditions: A first set of samples (Zirconia) was blasted using  $ZrO_2$  embedded in silica vitreous phase microspheres sized between 125  $\mu m$  and 250  $\mu m$ . The second set of samples (Alumina) was blasted with alumina angular particles  $Al_2O_3$  of  $\sim 500 \mu m$ . In both cases, for comparative purposes unblasted samples were ground with consecutively finer SiC papers, and finely polished with diamond paste and colloidal silica (0.5  $\mu m$ ) to remove the slight layer of disturbed metal.

The contacting TEP measurements were performed using a calibrated TECHMETAL thermoelectric contact apparatus. The sample is pressed between two blocks of a reference metal (pure copper). One of the blocks is at 15°C, while the other is at 25°C to obtain a temperature difference,  $\Delta T$ . A potential difference,  $\Delta V$ , is generated at the reference metal contacts. The apparatus does not give the absolute TEP value of the sample ( $S^*$ ), but a relative TEP ( $S$ ) in comparison to the TEP of pure copper ( $S_0^*$ ) at 20°C. The relative TEP value ( $S$ ) is given by  $S = S^* / S_0^* = \Delta V / \Delta T$ . The measurements are performed very quickly (<1 min) and precisely ( $\pm 0.5\%$ ), with a resolution of about 0.001  $\mu V/K$ . On the other hand, in the non-contacting TEP measurements each sample is mounted into two pure copper supportters which are perforated by a series of holes and equipped with sealed heat exchangers to facilitate efficient heating and cooling and then mounted on a nonmagnetic translation table for scanning. In order to get a better heat transfer between the specimen and the copper heat exchangers, a layer of silicone heat sink compound was applied. One of the copper supportters is at 15°C, while the other is at 25°C. The temperature gradient is kept at  $\sim 1.2^\circ C/mm$  in all non-contacting TEP measurements, which is more than sufficient to produce detectable magnetic signals in grit blasted 316 LVM stainless steel and Ti-6Al-4V alloy samples. A pair of fluxgate sensors is used in a gradiometric arrangement in order to detect the thermoelectric

signals from the grit blasted zone. The inspection of the specimen is realized at the horizontal sensor polarization. The lift-off distance between the primary sensor and the sample surface is  $\sim 2$  mm. In this work, the material properties that significantly change during grit blasting are investigated in order to establish how they individually and collectively affect the thermoelectric measurements. It is important to mention the interesting role that cold work could play in the surface treatment and obviously on the final interpretation of the results. It is well known that the principal change in the hardness due to cold work occurs simultaneously with the matrix-material recrystallization. On actual grit blasted specimens the residual stress and cold work effects can be best modified by chosen adequate heat treatments that simulate thermally activated stress release. In the present case, the blasted 316 LVM samples were annealed at  $700^{\circ}\text{C}$  for 2 min, 10 min and 1 h, and subsequently, air-cooled down to room temperature. Moreover, the blasted Ti-6Al-4V samples were annealed at  $595^{\circ}\text{C}$  and  $710^{\circ}\text{C}$  for 1h and 2h respectively, and air-cooled down to room temperature.

### Results and Discussion

Microstructural examination of the surface that blasting causes a severe surface plastic deformation that leaves a rough surface with an average roughness,  $R_a$ , of  $0.9\ \mu\text{m}$  and  $6.7\ \mu\text{m}$  for 316 LVM samples, and  $0.12\ \mu\text{m}$  and  $5.43\ \mu\text{m}$  for Ti-6Al-4V samples, when blasting with Zirconia or Alumina, respectively. These differences should be understood within the framework of the specific features that distinguish the  $\text{ZrO}_2$  and  $\text{Al}_2\text{O}_3$  particles. As mentioned previously, the  $\text{ZrO}_2$  particles are rounded, whereas the  $\text{Al}_2\text{O}_3$  particles are some three times larger and have a rough surface characterized by edge-like facets. Therefore, the Zirconia particles produce a more homogeneous deformation without grinding down the material, unlike the  $\text{Al}_2\text{O}_3$  ones. As expected, contamination with ceramic particles, obviously remnants of the blasting particles, is also observed. In addition to the irregular rough surface morphology, grit blasting produces significant subtle microstructural variations that are consequence of the severe plastic deformation through cold work. As an example, Fig.3 shows representative cross sectional SEM images of the Alumina and Zirconia blasted 316LVM samples.

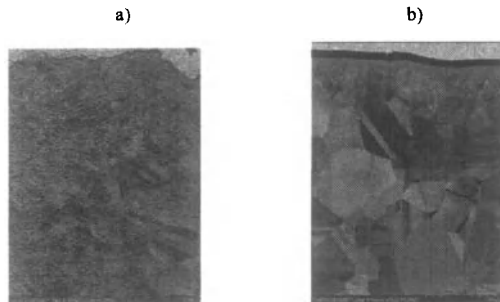


Figure 3. . Cross section SEM images of grit blasted 316LVM stainless steel samples using a) Alumina and b) Zirconia particles.

All the 316LVM stainless steel and Ti-6Al-4V samples were tested using the contacting and non-contacting thermoelectric techniques. TEP measurements with the contacting technique (Fig. 4) revealed an increase in the

relative TEP value of the 316LVM stainless steel blasted samples, Fig. 4a, with regards to the unblasted condition, with a somewhat higher value for the Alumina blasted samples. Annealing at 700°C caused a decrease in the relative TEP, being differences insignificant when increasing the soaking time. In the case of Ti-6Al-4V titanium alloy samples, Fig. 4b, the relative TEP value of the blasted samples also increases with regards to the unblasted condition at the two types of blasted surfaces. The relative TEP decreased gradually after the first and second stress relaxation treatments. In both cases, after annealing the relative TEP value was still much higher than that corresponding to the unblasted conditions, which correlates well with the remaining hardness gradients and grain size refinement reported for the 316 LVM steel [17].

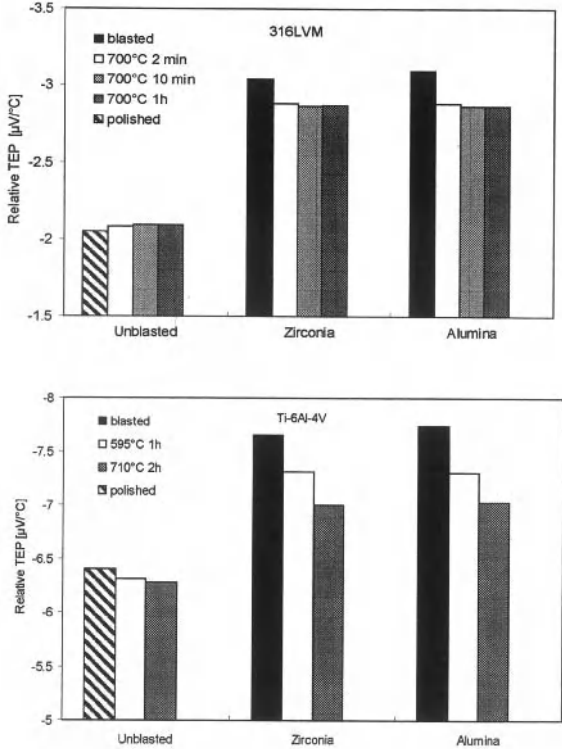


Figure 4. Relative TEP measurements of unblasted and blasted 316LVM stainless steel and Ti-6Al-4V titanium alloy samples by contacting.

As can be seen from Fig 5, inspection of the unblasted samples did not reveal any TEP variation, irrespectively the application or not of heat treatments. Interestingly, 316LVM stainless steel blasted samples failed to reveal any change when using the non-contacting technique. This behaviour is related to the presence of  $\alpha'$ -martensite in the microstructure [5]. The ferromagnetic nature of the martensitic phase can negatively affect the detection of the magnetic field produced by thermoelectric currents around the blasting affected zone. Annealing enhances the reverse (martensite  $\rightarrow$  austenite) transformation [18] recovering the magnetic field signal. Flux density decreased with increasing the soaking time and after 1 h was nearly identical to that observed for the unblasted specimens. After the first partial stress relaxation, the measured magnetic flux density decreased by  $\sim 9$  nT with the two different types of blasting processes using  $ZrO_2$  and  $Al_2O_3$  particles respectively. In comparison, on the second partial stress relaxation treatment at  $700^\circ C$  for 10 min the magnetic flux density was approximately  $\sim 82\%$  lower.

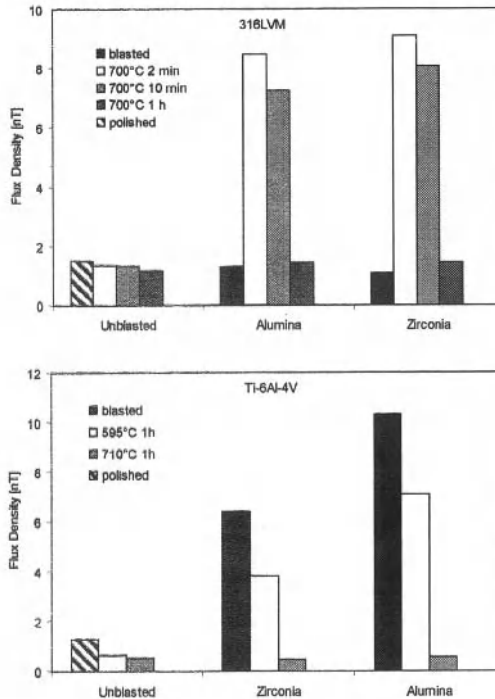


Figure 5. Relative TEP measurements of unblasted and blasted 316LVM stainless steel and Ti-6Al-4V alloy samples by noncontacting.

In the case of Ti-6Al-4V alloy samples, the flux density increased significantly  $\sim 7$  nT and  $\sim 11$  nT when using  $ZrO_2$  and  $Al_2O_3$  particles, respectively. Then, the flux density decreased gradually after the first stress relaxation treatment ( $595^\circ C/1h$ ). Finally, on the second stress relaxation treatment ( $700^\circ C/2h$ ), the flux density was reduced to a value similar to that of the unblasted condition. Correlation with the microstructural analysis and microhardness measurements indicated that such evolution of the flux density exclusively corresponds to the relaxation of the compressive residual stresses [17]. Overall this study reveals that the non-contacting technique is more sensitive to the presence of residual stresses, whereas the contact technique is strongly influenced by the grain size refinements and work hardening. The poor sensibility of the contacting TEP measurements to the simultaneous stress relaxation can be explained by the fact that the microstructural changes occurs mainly at the subsurface of the specimen, while this technique averages material properties throughout the entire thickness of the sample.

### Conclusions

It has been found that the contacting and non-contacting thermoelectric techniques are associated directly with the subtle material variations such as grain size refinement, work hardening and compressive residual stresses due to plastic deformation produced by grit blasting. In the case of the blasted 316 LVM, the TEP measurements clearly demonstrate that the non-contact NDTT technique is very sensitive to the reverse transformation of the  $\alpha'$ -martensite and the expected relaxation of compressive residual stresses with increasing the severity of the thermal treatment, while the contact NDTT results are closely related to the grain size refinement and work hardening. In general, the contacting and non-contacting thermoelectric techniques clearly demonstrated that the thermoelectric power measurement is a valuable intrinsic material property to microstructural assessment.

### Acknowledgments

This work was performed at UMSNH (Mexico) and CENIM-CSIC (Spain) with a partial funding from CONACYT (Mexico) under project CB-80883 and MAT2009-14695-C04. The author H. Carreon wishes to thank CONACYT (Mexico) for the financial support during the sabbatical in CENIM-CSIC.

### References

1. T. Jinno, V.M. Goldberg, D. Davy, S. Stevenson, *J. Biomed. Mater. Res A* 42:1, (1998) 20.
2. A. Wennerberg, T. Albrektsson, B. Andersson, *Int J Oral Maxillofac. Implants* 11 (1996) 38.
3. C. Aparicio, F.J. Gil, U. Thams, F. Muñoz, A. Padrós, J.A. Planell. *Key Eng. Mater.* 254-256 (2004) 737.
4. I. Altenberger, B. Scholtes, U. Martin, H. Oettel, *Mater. Sci. Eng. A* 264:1 (1999) 58.
5. M. Multigner, E. Frutos, J. L. González-Carrasco, J.A. Jiménez, P. Marín, J. Ibáñez. *Mater. Sci. Eng. C* 29 (2009) 1357.
6. E. Frutos, M. Multigner, J.L. González-Carrasco, *Acta Mater.* 58 (2010) 4191.
7. M. Multigner, S. Ferreira, E. Frutos, M. Jaafar, J. Ibáñez, P. Marín, T. Pérez- Prado, G. González-Doncel, A. Asenjo, J.L. González-Carrasco. *Surf. Coat. Technol.* 205 (2010) 1830.
8. M. Multigner, P. Fernández-Castrillo, S.Ferreira-Barragán, G. González-Doncel, J. L. González-Carrasco. *Revista de Metalurgia* (Madrid), 45 (2009) 52.
9. E.B. Henry, C.M. Stuart, W. Tomasulo, *Nondestructive Testing Handbook*, edited by P. McIntire, 9 (1995) 363.
10. F.G. Caballero, A. García-Junceda, C. Capdevila, C. García de Andrés, *Scr. Mater.* 52 (2005) 501.
11. F.G. Caballero, C. Capdevila, L. F. Alvarez, C. García de Andrés, *Scr. Mater.* 50 (2004) 1061.

- 12.J. Hu, P.B. Nagy, *Appl. Phys. Lett.* 73 (1998) 467.
- 13.H. Carreon , *NDT & E Int.* 39 (2006) 433.
- 14.K. Maslov , V.K. Kinra, *Mat. Eval.* 59 (2001) 1081.
- 15.E. Juzeliūnas , J.P. Wikswo, *J. Solid State Electrochem.* 10 (2006) 700.
- 16.H. Carreon , *Wear* 265 (2008) 255.
- 17.H. Carreon, S. Barriuso, G. Barrera, J. L. González, F. G. Caballero, *Surf. Coat. Technol.* (2011) in review
- 18.M. Sarasola and S. Talacchia, *Rev. Metal.* 35 (2001) 124.

## **CHARACTERIZATION OF THE TORSIONAL RESPONSE OF AS-CAST A359-SiC<sub>p</sub>-30% AT ELEVATED TEMPERATURES**

James DeMarco, Justin Karl, Yongho Sohn, Ali Gordon

University of Central Florida; 4000 Central Florida Blvd.; Orlando, FL 32816, USA

**Keywords:** metal-matrix composites, mechanical characterization, temperature-dependent modeling, strain-dependent modeling, hot rolling simulation

### **Abstract**

Aluminum metal-matrix composites are lightweight materials that have the potential to supplant steel in many applications. The current work helps to identify the parameters that confer maximal strength and ductility. Torsion tests were performed on the as-cast aluminum metal-matrix composite A359-SiC<sub>p</sub>-30% at a variety of temperatures and twist rates. Dependence of material properties on temperature and strain rate were identified from equivalent stress-strain curves constructed from the reduced data. Examination of the microstructure was performed on the as-cast material and on fracture surfaces. A temperature- and strain rate-dependent constitutive model was applied to simulation of the mechanical response of the torsion specimen. Trends in material properties corroborate and extend trends identified previously under tensile loading with regard to temperature and strain rate dependence. Shear properties of simulated specimens agree with properties obtained through experimentation.

### **Introduction**

Aluminum metal-matrix composites (Al-MMCs) have become increasingly popular in recent years. While unreinforced aluminum alloys have low densities and high ductilities, they are not suitable for many applications due to their lack of strength and stiffness. To provide added strength and stiffness while maintaining favorable densities, it has become common to reinforce aluminum alloys with silicon carbide in various forms, although usually the inclusions

are in the form of whiskers or particles. The result is a composite material with superior specific strength and stiffness. While whisker-reinforced composites are expensive due to the necessity of processing by nonstandard techniques and have low transverse properties when rolled, particle reinforced Al-MMCs have transverse material property values almost as high as the longitudinal properties and are not as expensive to process as whisker-reinforced Al-MMCs [1].

As-cast sheets of silicon carbide particle-reinforced Al-MMC are rolled at elevated temperatures to improve the mechanical properties of the resulting sheet. During this process, material is lost due to edge cracking, in which lateral expansion at the transverse edges of the billet results in the formation of cracks. Cracked material must be removed before further rolling. Additional cost savings can be attained in the processing of particle-reinforced materials through the reduction of edge cracking.

The rolling process imparts compressive and torsional stresses on the rolled material. Under the assumption of isotropy, previous work by the authors sought to characterize the tensile response of a candidate Al-MMC at elevated temperatures and various strain rates in order to predict material response during rolling. In the current work, investigation is expanded to the torsional response of specimens of as-cast A359-SiC<sub>p</sub>-30%. Study of the response of small samples of the as-cast material under carefully controlled conditions provides insight into the determination of parameters for the hot rolling process such as roll rate, roll temperature, reduction ratio, and so on, as noted in [2]. Hot working simulation tests include tensile testing, uniaxial compression, cam plastometer testing, and torsion testing. Tensile testing and compression suffer from limiting instabilities of necking and barreling, respectively, while compression and cam plastometer testing do not allow determination of limits to workability. Hot torsion has no limiting instability, and materials may be tested under torsion to failure [2]. For these reasons, torsion testing is often considered the best choice for testing hot workability.

While identification of the material properties at various temperatures and strain rates is in itself useful for increasing the efficiency of the rolling process, further insight is gained by the incorporation of microexamination of fracture surfaces and numerical modeling. Microexamination may reveal the mechanisms responsible for material failure and can provide a microstructural explanation for improvements in material properties under various conditions. If failure mechanisms are temperature or strain rate dependent, this dependence may be evident in features or patterns identified through microexamination. Numerical modeling provides

predictions of material response at temperatures and strain rates between those studied. Furthermore, if a constitutive model may be identified which provides a sufficiently accurate representation of material response under a variety of load configurations, temperatures and strain rates, it is possible to create a computational model of the rolling process, and a parametric study may be performed to identify the influence of temperature, strain rate, and other rolling parameters on the stresses and strains that result in the rolled sheet.

The remainder of this study is organized as follows. In Sec. 2, the experimental procedures employed for torsion testing, microexamination of fracture surfaces, and data reduction are described. In Sec. 3, a computational model of the mechanical response of the candidate material under torsion testing is developed. In Sec. 4, results of torsion experiments, microexamination, and numerical modeling are analyzed. Section 5 provides conclusions and avenues for future work.

### Experimental Procedure

The material under examination is the aluminum metal-matrix composite A359-SiC<sub>p</sub>-30%. Aluminum metal-matrix composites are valued for having high specific stiffness and a high strength-to-weight ratio. The matrix alloy, A359, is a high-silicon cast aluminum. Its chemical composition is given in Table 1. Previous studies of the composite or similar materials have addressed torsion [3], fracture [4], [5], [6], high-strain rate conditions [7] (compression), [8] (compression), [9] (tension), and creep [10], [11], [12]. However, previous studies have not examined the material as cast.

**Table 1:** Chemical composition of A359

Si	Fe	Cu	Mn	Mg	Zn	Sn	(Trace)	Al
9.45	0.11	<0.006	<0.05	0.67	<0.05	0.02	0.2	Bal

The microstructure of the composite shows four main regions: (i) solid solution fcc aluminum, (ii)  $\alpha$ -SiC, (iii) eutectic silicon, and (iv) precipitates and dispersoids rich in magnesium and iron. The average size of silicon-carbide reinforcement particles is  $17 \pm 5 \mu\text{m}$ , which is in agreement with measurements conducted in [13]. Distribution of silicon-carbide particles is non-uniform in the as-cast material, with some particle clustering and also some

regions sparse in particles. The uneven distribution may be attributed to a combination of solidification shrinkage and incomplete infiltration. Figure 1(a) shows the arrangement of SiC particles within the matrix in a sample region. Figure 1(b) shows the presence of eutectic silicon in the A359 matrix.

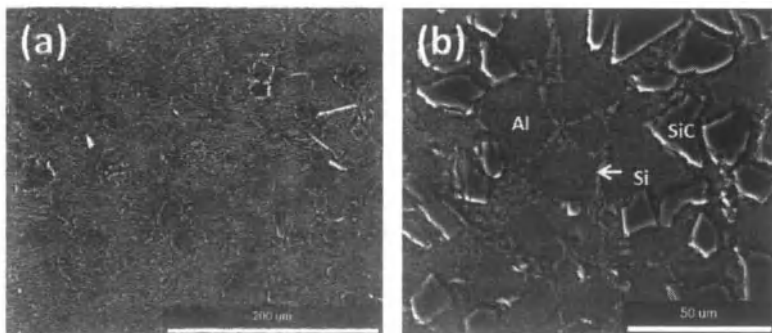


Figure 1: Microstructure of as-cast A359-SiC<sub>p</sub>-30%

A series of mechanical tests were performed in order to provide data regarding the response of the candidate material to torsion loadings under a variety of conditions. This information is used in the characterization of the behavior of the material in general, as well as to establish correlations with previously-performed tensile experiments and computational results. Unprocessed slabs of material were machined by an ISO-9001 compliant facility into specimens with a 2.0 inch (50.8mm) long and 0.25 inch (6.35mm) diameter gage section. Additional relevant dimensions are illustrated in Fig. 2.

Monotonic torsion tests were conducted under a variety of temperatures and strain rates. A total of 14 specimens of the as-cast material were tested in a static lab air environment on an MTS Bionix electromechanical load frame. Frame alignment was verified by the system manufacturer before testing, as an international standard has not yet been set. Torque and twist levels during each experiment were controlled and logged by an MTS Bionix control and acquisition system linked to a PC running MTS Systems TestWorks4 software. Temperature was maintained to within 1°F (0.55°C) of the target temperature in the middle of the gage section during elevated temperature testing, illustrated in Fig. 3.

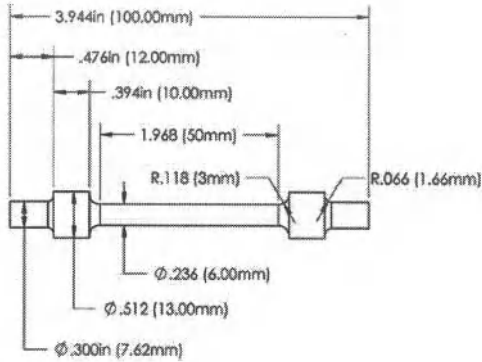


Figure 2: Torsion specimen dimensions

A resistance-type furnace manufactured by the Mechanics of Materials Research Group (MOMRG) lab at the University of Central Florida (UCF) provided heat. Heat application was regulated via a thermocouple and Watlow temperature controller coupled to a programmable Xantrex power supply.

Monotonic tests were conducted by applying twist rates that matched equivalent strain rates of  $10^{-5} \text{ s}^{-1}$ ,  $10^{-2} \text{ s}^{-1}$ , and  $10^{-1} \text{ s}^{-1}$  at the effective radii. Specimen ends were free to strain axially without restraint or load. Experiments were conducted at both room temperature and elevated temperatures. A standard for this specific torsion application is not yet available, but testing complied with specifications from similar ASTM standards E143 [14] and A938 [15]. Elevated temperature testing was performed at 97.2°C (207°F), 181.7°C (359°F), 315.6°C (600°F), 329.4°C (625°F), 343.3°C (650°F), 357.2°C (675°F), and 537.8°C (1000°F). High temperature test procedures conformed to suggested heat soak times and other guidelines from ASTM standard E21 [16].

For the purposes of simulation of the torsion tests, it was necessary to determine whether a non-uniform temperature distribution along the length of the specimen had an influence on simulated results; to this end, temperatures were recorded every 6.35 mm (0.25 in) along the specimen surface by thermocouples for three different target temperatures: 316°C (600°F), 399°C (750°F) and 538°C (1000°F). The resulting distributions are shown in Fig. 4.

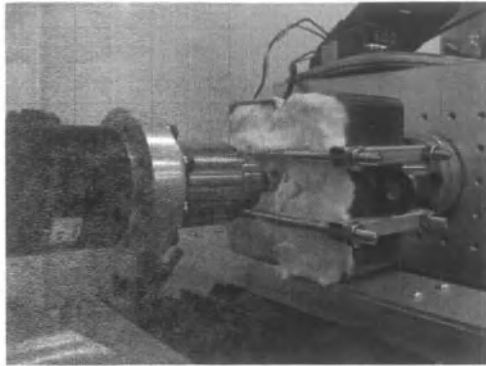


Figure 3: Profile of mechanical test specimen, heater, and extensometer

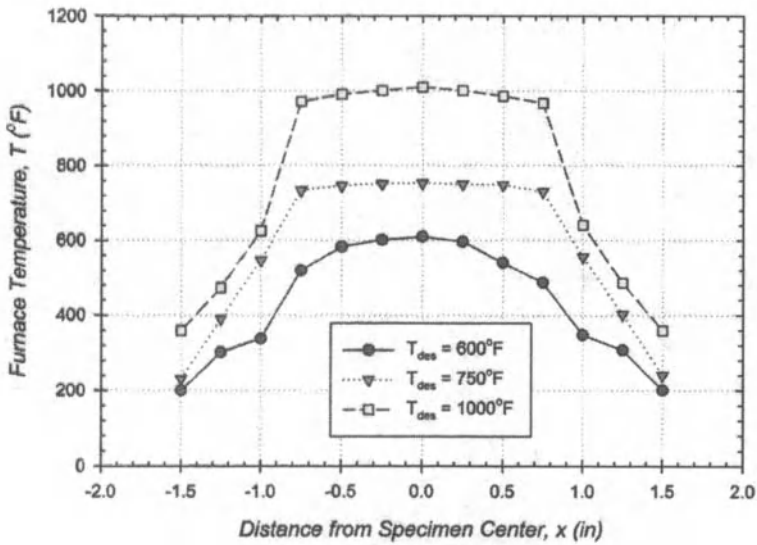


Figure 4: Temperature distributions along torsion specimen surface at specified target temperatures.

Torsion experiments provide measurements of torque and twist, which must be converted into quantities for shear stress and strain prior to application in the calibration or testing of constitutive models. The method applied in the current work was introduced by Barraclough et al. in 1973 [17]. It involves the introduction of an effective radius for calculation of strain and strain rate. The shear stress is computed as

$$\tau = \frac{3M}{2\pi R^3} \quad (1)$$

where  $M$  is the torque measured at the load cell and  $R$  is the specimen radius in the gage section. The shear strain is estimated to be

$$\gamma = \frac{r_{ef}}{L} \theta \quad (2)$$

where  $r_{ef} = 0.724R$  is the effective radius,  $\theta$  is the angle of twist measured at the grip, and  $L$  is the length of the gage section. The von Mises criterion is used to convert shear quantities into equivalent tensile quantities, so that

$$\sigma_{eq} = \frac{3\sqrt{3}M}{2\pi R^3} \quad (3)$$

is the equivalent stress, and

$$\epsilon_{eq} = \frac{r_{ef}}{\sqrt{3}L} \theta, \dot{\epsilon}_{eq} = \frac{r_{ef}}{\sqrt{3}L} \dot{\theta} \quad (4)$$

are the equivalent strain and strain rate, respectively. Twist rates for torsion experiments were set to provide a specified equivalent strain rate by application of the above rate equation. Equivalent stress-strain curves were used to identify equivalent material properties for comparison with results obtained previously through tensile testing.

### Computational Modeling

To study the hot rolling of as-cast A359-SiC<sub>p</sub>-30%, it is necessary to understand the behavior of the material at arbitrary temperatures and strain rates in the range of interest. To this end, a constitutive model was developed which is both temperature- and strain rate-dependent. The model is based on classical Perzyna viscoplasticity [18]. Elastic behavior is linear; since the equivalent Young's modulus under torsion did not show significant temperature dependence, the modulus for the model was defined to be the average modulus determined for all experiments performed under torsion. Inelastic response is assumed to be nonlinear, isotropic, temperature

dependent and strain rate dependent, with an onset yield strength which is temperature dependent at low temperatures and temperature and strain rate dependent at high temperatures.

The flow stress is based on that of Zhou and Clode [19]. It is defined as

$$K(\alpha; \dot{\alpha}_{avg}, T) = \sigma_{ys}(\dot{\alpha}_{avg}, T) + \sigma_{zc}(\alpha; \dot{\alpha}_{avg}, T) \quad (5)$$

where  $\alpha$  is the equivalent plastic strain,  $\dot{\alpha}_{avg}$  is the average strain rate, and  $T$  is the temperature in Kelvin. The yield strength  $\sigma_{ys}$  is to be determined and

$$\sigma_{zc} = C[1 - \exp(-b\alpha)] \sinh^{-1} \left[ B \dot{\alpha}^m \exp\left(\frac{Qm}{kT}\right) \right] \quad (6)$$

is the von Mises stress of the Zhou-Clode model. The hardening parameter  $b$  in the above is assumed to depend on the temperature-compensated strain rate,  $Z_\epsilon = \dot{\epsilon} \exp\left(\frac{Q}{kT}\right)$ , as follows:

$$b = \alpha_b Z_\epsilon^{\beta_b} \quad (7)$$

In order to complete the model, several parameters must be determined. These parameters, along with their influence on the resulting model, are shown in Table 2. The parameters were calibrated to provide the best model for the candidate material by extracting material properties from a series of tensile tests, as described in (DeMarco, Uribe-Restrepo, Karl, Sohn, & Gordon). The tests performed to calibrate the model are listed in Table 3. Properties of the as-cast AlMMC were determined at several temperatures and strain rates.

The yield strength model constructed for tension and described in (DeMarco, Uribe-Restrepo, Karl, Sohn, & Gordon) was not an effective predictor of yield strengths under torsion. Despite an RMS error of only 6.72% between the predicted and observed tensile yield strengths, the RMS error between predicted and observed equivalent torsional yield strengths was 27.9%. Therefore an improved model was defined which incorporated yield strength data for both the tension and the torsion tests. The improved model produced an RMS error of 11.49% for tension and 8.61% for torsion. The yield strength was defined to be a bilinear function of the absolute temperature and the equivalent strain rate for temperatures below 316°C (589K) and to follow an inverse exponential rule for temperatures above 589K. The revised equation for the yield strength is thus

$$\sigma_{ys}(T, \dot{\epsilon}) = \begin{cases} c_1 + c_2 \dot{\epsilon} + c_3 T, & T \leq 589 \\ (c_1 + c_2 \dot{\epsilon} + 589c_3) \cdot \left(1 - \exp\left(-\frac{c_4 \dot{\epsilon}^{c_5}}{T - 589}\right)\right), & T > 589 \end{cases} \quad (8)$$

where  $T$  is the temperature in Kelvin,  $\dot{\epsilon}$  is the equivalent strain rate, and  $c_1$  through  $c_5$  are constants to be determined to provide the best fit to experimental data. The inverse exponential form for the model at temperatures above 589K is to account for the observed yield strengths for tests performed just above 589K, which show a rapid decrease in yield strengths above this temperature.

The yield strength model constructed for tension and described in (DeMarco, Uribe-Restrepo, Karl, Sohn, & Gordon) was not an effective predictor of yield strengths under torsion. Despite an RMS error of only 6.72% between the predicted and observed tensile yield strengths, the RMS error between predicted and observed equivalent torsional yield strengths was 27.9%. Therefore an improved model was defined which incorporated yield strength data for both the tension and the torsion tests. The improved model produced an RMS error of 11.49% for tension and 8.61% for torsion. The yield strength was defined to be a bilinear function of the absolute temperature and the equivalent strain rate for temperatures below 316°C (589K) and to follow an inverse exponential rule for temperatures above 589K. The revised equation for the yield strength is thus

$$\sigma_{ys}(T, \dot{\epsilon}) = \begin{cases} c_1 + c_2\dot{\epsilon} + c_3T, & T \leq 589 \\ (c_1 + c_2\dot{\epsilon} + 589c_3) \cdot \left( 1 - \exp\left(-\frac{c_4\dot{\epsilon}^{c_5}}{T - 589}\right) \right), & T > 589 \end{cases} \quad (8)$$

where  $T$  is the temperature in Kelvin,  $\dot{\epsilon}$  is the equivalent strain rate, and  $c_1$  through  $c_5$  are constants to be determined to provide the best fit to experimental data. The inverse exponential form for the model at temperatures above 589K is to account for the observed yield strengths for tests performed just above 589K, which show a rapid decrease in yield strengths above this temperature.

The Levenberg-Marquardt algorithm was used to identify the flow stress parameters  $C$ ,  $B$ ,  $m$ , and  $Q$  that provide the best fit to strain rate and temperature dependence data. Since the flow stress is not activated until the yield strength is reached, the saturated stress level of the flow is identified with the difference between ultimate strength and yield strength. This difference may be obtained from the material properties extracted through tensile testing at different temperatures and rates. The Levenberg-Marquardt algorithm may then be applied to the data triples  $(T, \dot{\epsilon}, \sigma_{UTS} - \sigma_{ys})$  over the set of temperatures and rates tested.

**Table 2: Constitutive modeling constants for Zhou-Clode inelasticity model, as identified via tensile testing**

Parameter	Units	Value	Significance
$\alpha_b$	(unitless)	507.97	Scaling factor for temperature-compensated strain rate (TCSR) in strain hardening coefficient
$B$	s	1.202	Scaling factor for combined effect of rate and temperature
$\beta_b$	(unitless)	0.00315	Exponent for TCSR in strain hardening coefficient
$C$	MPa	15.06	Scaling factor for stress; does not affect rate or temperature dependence
$M$	(unitless)	0.1155	Exponent for combined effect of rate and temperature
$Q$	J/mol	175752.75	Exponent that differentiates effect of temperature from rate

**Table 3: Tensile experiments performed on A359-SiCp-30%**

Spec. ID	Temp., T (°F (°C))	Strain Rate, $d\epsilon/dt$ ( $s^{-1}$ )
TE10	68 (20)	$10^{-2}$
TE02	68 (20)	$10^{-3}$
TE11	68 (20)	$10^{-5}$
TE05	600 (316)	$10^{-2}$
TE03	600 (316)	$10^{-3}$
TE04	600 (316)	$10^{-5}$
TE06	1000 (538)	$10^{-2}$
TE07	1000 (538)	$10^{-3}$
TE08	1000 (538)	$10^{-4}$

A user-programmable feature (UPF) in the ANSYS finite element suite was created to implement the model. The discrete version of the Perzyna formulation with the flow stress as specified above was implemented on the basis of algorithms given in Simo and Hughes [18] for nonlinear isotropic/kinematic  $J_2$  plasticity and linear isotropic  $J_2$  viscoplasticity.

To study the mechanical response of the test samples, a 3D model of the torsion specimen was constructed in ANSYS. Exact dimensions of the machined specimens were used. Geometry was created by rotation of a plane drawing of a radial slice of the test specimen, and twenty-node SOLID186 elements were chosen to provide a regular pattern for the mesh. In actual tests, test specimens are gripped by chucks at the grip section. One end is axially fixed, and rotation is applied at this end. The other end is free to move axially, and torque is measured by a transducer at this end. Accordingly, for the computational model, the fixed end was established by setting all displacements to zero on one end of the specimen. Axial displacements at the free end were unconstrained. The free end was prevented from expanding radially by imposition of a pressure on the surface of the grip section. The pressure was arbitrarily chosen to be 40 MPa, which is between 30% and 70% of the material's yield strength at the temperatures and strain rates of

interest. This was found to be sufficient to minimize radial expansion while avoiding plastic deformation at the grip. Rotation was applied at the free end through the use of the ANSYS node-to-surface contact algorithm. A pilot node was defined along the specimen axis exterior to the specimen, and target nodes were set to be all nodes on the transverse surface of the free end. Through the resulting multipoint contact (MPC) elements defined internally by ANSYS, a rotation applied at the pilot node was conveyed to the transverse surface nodes, resulting in a rotation about the specimen axis. Simulations consisted of applying a rotation at least as large as the rotation associated to maximum torque for the specimen under consideration. The geometry, mesh and boundary conditions are illustrated in Fig. 5.

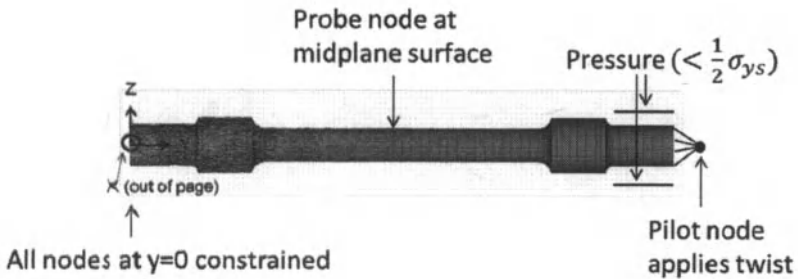


Figure 5: Image of ANSYS model geometry and mesh for torsion specimen

As noted in the previous section, temperature distributions along the specimen length were determined at each of three target temperatures. The resulting data were fitted by a function

$$T = T(T_0, y) \quad (9)$$

where  $T_0$  is the target temperature and  $y$  is the axial distance in millimeters from the fixed end of the specimen. For  $|y - 50.8| < 19.05$ , the distribution is defined by a best-fit surface to the temperature distribution data obtained at the target temperatures and a constant distribution imposed at room temperature, i.e., 20°C (68°F). This region corresponds to the gage section of the specimen, which is fully enclosed by the furnace. The temperature distribution is defined to be quadratic in  $y$  and  $T_0$  in this portion of the specimen. For  $19.05 \leq |y - 50.8| \leq 50.8$ , a similar approach is taken, with the resulting distribution defined as the maximum of 20°C (68°F) and a best-fit function to the temperature distribution data and a constant distribution imposed at

room temperature which is linear in  $y$  and quadratic in  $T_0$ , and which is required to produce the same temperature at  $|y - 50.8| = 19.05$  as the distribution obtained in the gage section. The surface fits were obtained via user functions created in TableCurve3D. The surface and data points for the gage section are shown in Fig. 6. The temperature distribution is defined in such a way that the user of the simulation software needs to specify only the target temperature, and the distribution is imposed automatically. For simulations below  $24^{\circ}\text{C}$  ( $75^{\circ}\text{F}$ ), the distribution is defined to be constant.

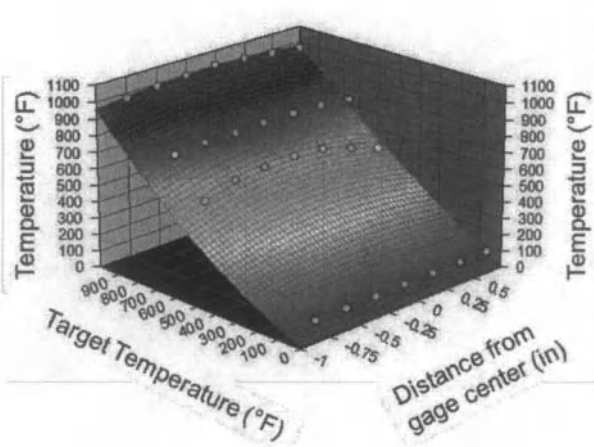


Figure 6: Temperature distribution fit.

## Results

Experiments performed on A359-SiC<sub>p</sub>-30% on the MTS Bionix torsion load frame resulted in torque and twist histories for each temperature and twist rate configuration studied. These histories were used to construct torque-twist, shear stress-strain, and equivalent stress-strain diagrams for each specimen. Shear and equivalent data were obtained by the method described in Sec. 2. The matrix of tests performed and material properties obtained under torsion is shown in Table 4. The resulting equivalent material properties were plotted against equivalent

strain rate and temperature and compared to tensile material properties obtained previously (see Table 3).

**Table 4:** Equivalent material properties of A359-SiC<sub>p</sub>-30% identified through torsion testing

Specimen ID	Temperature (°C (°F))	Equivalent Strain Rate (s <sup>-1</sup> )	Equivalent Young's Modulus (MPa)	Equivalent 0.02%-Offset Yield Strength (MPa)	Equivalent Ultimate Strength (MPa)	Equivalent Strain to failure (mm/mm)
C2	20 (68)	10 <sup>-5</sup>	89	100	234	0.0162
C1	20 (68)	10 <sup>-2</sup>	72	102	241	0.0233
C3	20 (68)	10 <sup>-1</sup>	80	113	254	0.021
C19	97 (207)	10 <sup>-5</sup>	90	115	225	0.016
C20	182 (359)	10 <sup>-5</sup>	75	99	194	0.0138
C5	316 (600)	10 <sup>-5</sup>	77	101	194	0.0161
C18	316 (600)	10 <sup>-2</sup>	75	109	181	0.0086
C4	316 (600)	10 <sup>-1</sup>	61	122	227	0.0171
C27	357 (675)	10 <sup>-5</sup>	88	87	187	0.011
C25	343 (650)	10 <sup>-5</sup>	70	92	150	0.0141
C24	329 (625)	10 <sup>-5</sup>	64	73	131	0.0119
C23	538 (1000)	10 <sup>-5</sup>	61	62	103	0.0121
C21	538 (1000)	10 <sup>-2</sup>	72	62	104	0.0218
C22	538 (1000)	10 <sup>-1</sup>	65	90	194	0.0287

Shear stress-shear strain curves produced from the reduced data show marked differences at varying strain rates and temperatures. In Fig. 7, it may be observed that temperature has a less pronounced effect on the shear response when the strain rate is high, which indicates an interaction of the strain rate and temperature dependences. Fig. 8 shows that, conversely, increased temperature leads to greater variation of the stress response with strain rate.

It is possible to identify further trends in the mechanical response through comparison of material properties obtained through torsion and tension testing at different strain rates and temperatures. Plots of the dependence of various properties on strain rate are shown in Fig. 9, and dependence on temperature is shown in Fig. 10; trends noted in the material properties are discussed below.

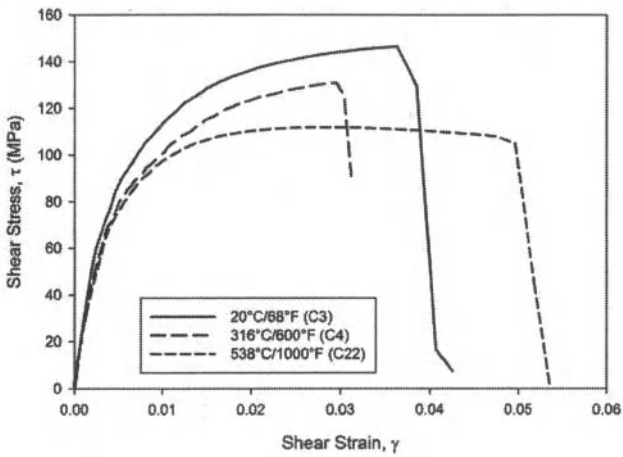
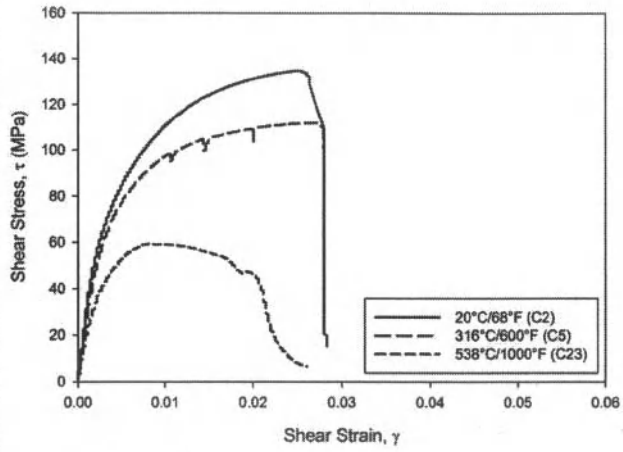


Figure 7: Torsion behavior of as-cast A359-SiC<sub>p</sub>-30% at various temperatures at a strain rate of (a)  $10^{-5} \text{ s}^{-1}$ , (b)  $10^{-1} \text{ s}^{-1}$

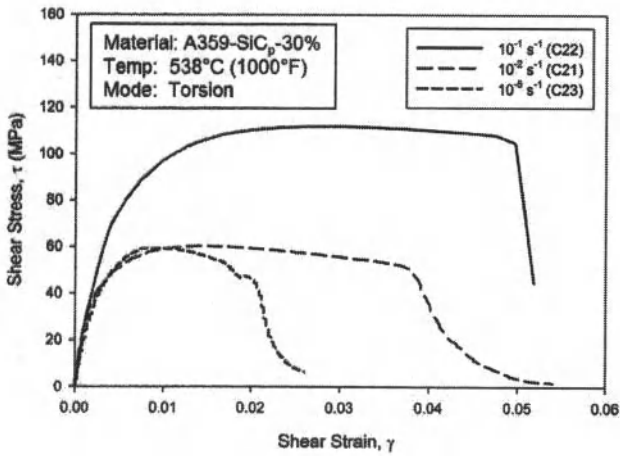
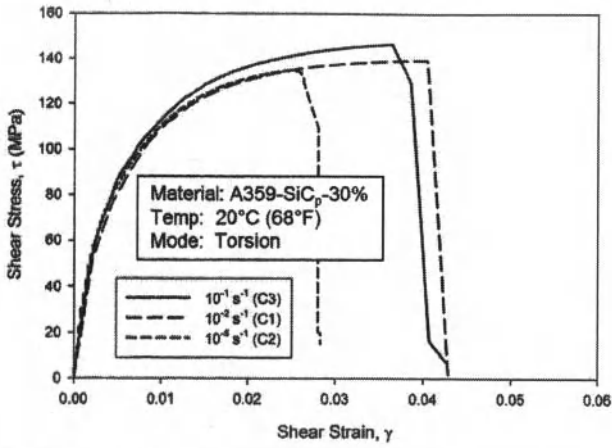


Figure 8: Torsion behavior of as-cast A359-SiC<sub>p</sub>-30% at various strain rates at temperatures of 20°C (68°F) and 538°C (1000°F)

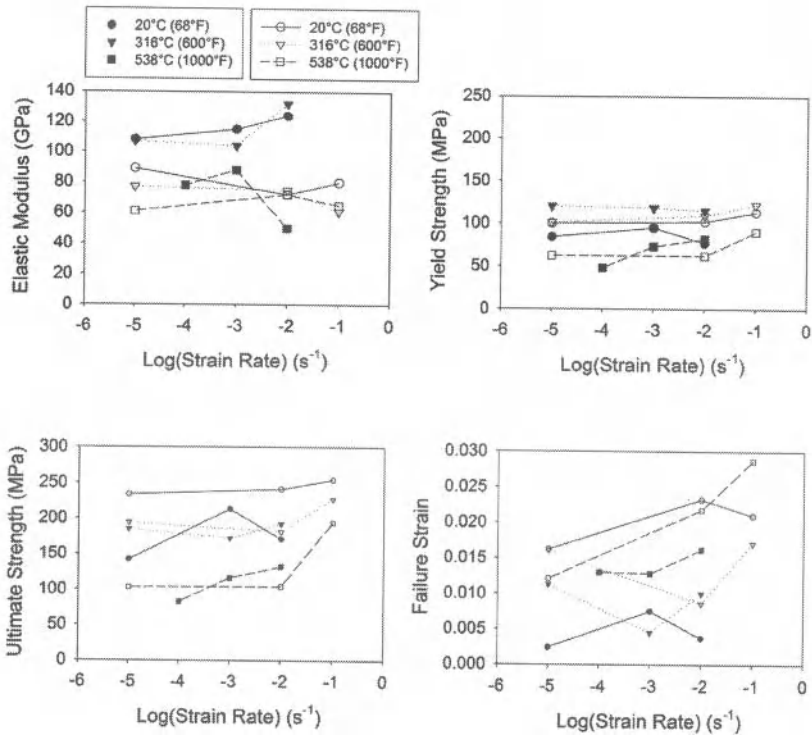


Figure 9: Dependence of equivalent material properties on strain rate for tension and torsion; filled symbols represent tension, empty symbols torsion.

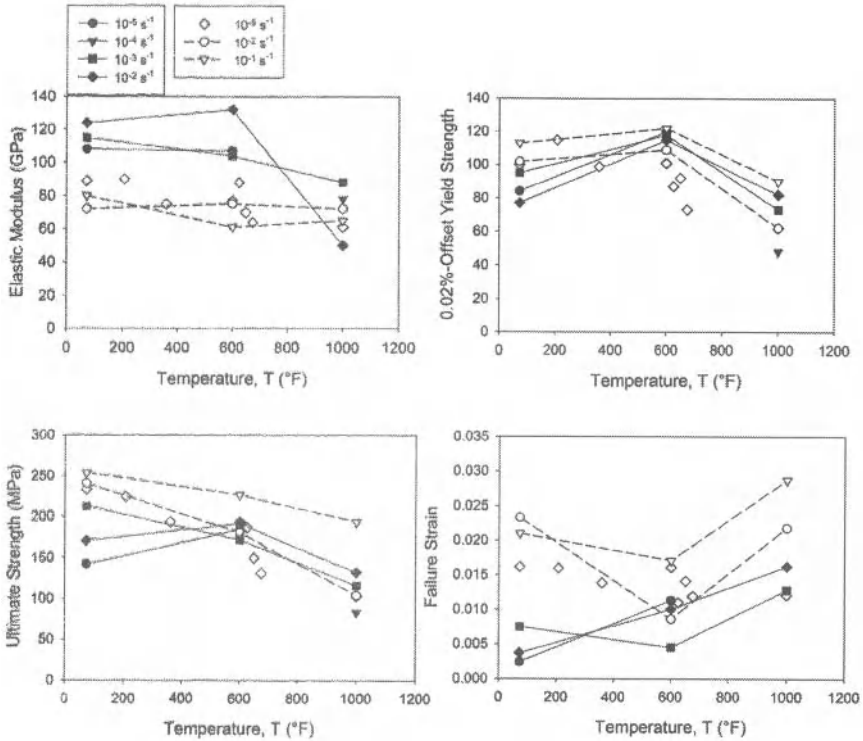


Figure 10: Dependence of equivalent material properties on temperature for tension and torsion; filled symbols represent tension, empty symbols torsion.

Elastic modulus clearly decreased at high temperature under tension, although the equivalent elastic modulus determined in torsion showed little if any consistent decrease with temperature. Equivalent elastic moduli remained around  $72 \pm 15$  GPa at all temperatures. In neither torsion nor tension did the elastic modulus show a consistent trend with strain rate.

The 0.02%-offset yield strength [20] was chosen to mark the onset of plasticity, due to the low ductility of the material at low temperatures. Yield strengths increased consistently with

strain rate at high temperatures only under tension. Under torsion, yield strengths were flat between  $10^{-5} \text{ s}^{-1}$  and  $10^{-2} \text{ s}^{-1}$  but increased at all three temperatures studied between  $10^{-2} \text{ s}^{-1}$  and  $10^{-1} \text{ s}^{-1}$ . Yield strength increase at high strain rate was slight at  $20^\circ\text{C}$  ( $68^\circ\text{F}$ ) and substantial at  $538^\circ\text{C}$  ( $1000^\circ\text{F}$ ). Of more interest is the trend in yield strength with temperature. Under both tension and torsion and at all rates studied, 0.02%-offset yield strengths peaked near  $316^\circ\text{C}$  ( $600^\circ\text{F}$ ). Increases between  $20^\circ\text{C}$  ( $68^\circ\text{F}$ ) and  $316^\circ\text{C}$  ( $600^\circ\text{F}$ ) were less substantial under torsion than under tension, but the trend is still apparent. Yield strengths dropped off significantly above  $316^\circ\text{C}$  ( $600^\circ\text{F}$ ) under both load scenarios.

Despite the peak in yield strengths in the vicinity of  $316^\circ\text{C}$  ( $600^\circ\text{F}$ ), ultimate strengths nevertheless generally decreased with increasing temperature for the temperatures and rates studied. Exceptions to this occurred at  $20^\circ\text{C}$  ( $68^\circ\text{F}$ ) at strain rates of  $10^{-5} \text{ s}^{-1}$  and  $10^{-2} \text{ s}^{-1}$  under tension. However, early failure of the specimen (prior to stress saturation) is the probable cause for these exceptions, as the material is rather brittle at low temperatures and is therefore more prone to rupture, particularly at high strain rates. As a function of strain rate, ultimate strengths followed the trends identified for yield strengths. A consistent increase in ultimate strength with strain rate was observed only at high temperature under tension, and ultimate strength was flat with increasing rate up to  $10^{-2} \text{ s}^{-1}$ , with temperature-dependent increases at  $10^{-1} \text{ s}^{-1}$ . The increase in ultimate strength between  $10^{-2} \text{ s}^{-1}$  and  $10^{-1} \text{ s}^{-1}$  for elevated temperatures was much larger than the increase in yield strength in this range of strain rates.

Failure strain was defined to be the strain level attained at the last data point prior to a 50% or greater drop in the stress below the ultimate stress level. Although wide scatter in failure strain data as a function of strain rate was observed under both torsion and tension, a general trend of increasing failure strain with strain rate was noted particular for elevated temperature torsion. With the exception of the same cases of early failure noted with regard to ultimate strengths at room temperature, failure strains at all rates reached a minimum around  $316^\circ\text{C}$  ( $600^\circ\text{F}$ ). Particularly at the higher strain rates for each test regime, failure strain increased substantially between  $316^\circ\text{C}$  ( $600^\circ\text{F}$ ) and  $538^\circ\text{C}$  ( $1000^\circ\text{F}$ ).

Simulated shear stress-strain curves were obtained in two ways. The first method was to capture the data at a surface node on the lengthwise midplane of the specimen at each step of the simulation. The location of the node used for data capture is shown in Fig. 5. The second method was to obtain time histories of the y-axis rotation and y-axis reaction torque at the pilot

node, which were then converted by standard mechanics of materials formulas to shear stress and strain histories.

Simulations were performed both with and without the imposition of temperature distributions discussed in the previous section; in the latter case, the temperature at all nodes was set to the target temperature regardless of position. Figure 11 shows simulated and experimental shear stress-strain curves for tests performed at 538°C (1000°F) and an equivalent strain rate of  $10^{-2} \text{ s}^{-1}$ . The simulated stress levels obtained under a distributed temperature distribution were nearly the same in all cases examined. It is noted that the model was calibrated under the assumption of constant temperature via tensile testing in which a similar furnace was used to heat the specimen. Since a similar temperature distribution to that identified in the torsion specimens may be presumed for the tension experiments, it may be expected that calibration performed by the aid of data obtained from such experiments under the constant-temperature assumption should be no less accurate for the torsion tests under a constant temperature assumption than for tests simulated with a temperature distribution in place. Furthermore, the temperature distribution is dependent on the specimen geometry, specifics of the furnace, and possibly other factors; therefore any distribution obtained in the current study may differ from those obtained elsewhere, so that findings based on a temperature-distributed model may not be considered to be general. On the basis of these considerations, the remainder of the results described in this section are obtained using a constant temperature distribution throughout the specimen.

Data obtained by direct acquisition of shear stress and strain at the specimen surface at the midplane of the gage section were found to be in better agreement with experimental data in the hardening portion of the shear stress-strain curve than data obtained through reduction of torque twist data obtained at the pilot node. While saturated stresses obtained by either method were nearly the same, in the hardening portion of the curve shear strains obtained through reduction were lower than those obtained directly in the gage section, as may be seen in Fig. 12. Since in most cases experimental data were fit better by the directly-captured shear stress-strain data than the data obtained through reduction of torque and twist from the pilot node, the remainder of the simulation results presented here are obtained directly from the gage surface.

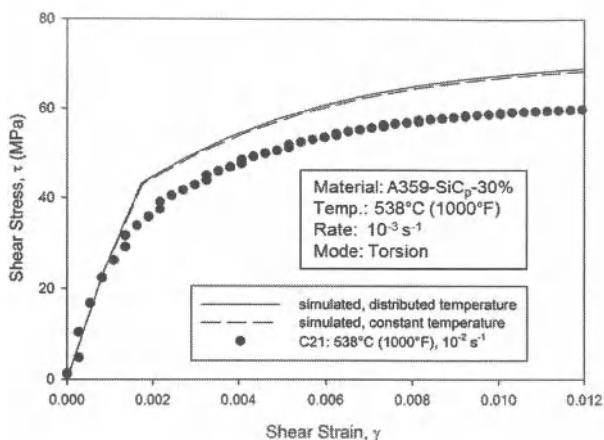


Figure 11: Comparison of shear stress-strain curves obtained with and without temperature distribution imposed on specimen.

Shear stress and von Mises stress contours at saturated stress were obtained at the specimen surface and at a transverse cross section at the midplane of the specimen. The shear and von Mises contours at the specimen surface for a simulation performed at 538°C (1000°F) and an equivalent strain rate of  $10^{-2} \text{ s}^{-1}$  are shown in Fig. 13. The contours were obtained after a rotation of 0.5 rad. It may be observed that the von Mises stress is essentially uniform in the gage section, does not depend on angle, and reduces as the radius expands throughout the rest of the model. Shear stress is also maximum in the gage section, although since the xy-component was chosen to represent shear stress, the value at a given point on any circumference depends on its angle with respect to the x-axis. Cross section contours at the specimen midplane are shown in Fig. 14 for the same test conditions. The cross section for von Mises stress shows that the stress is saturated or nearly saturated throughout most of the specimen, and drops quickly to zero in the interior closest to the specimen axis, where the amount of circumferential displacement is relatively low.

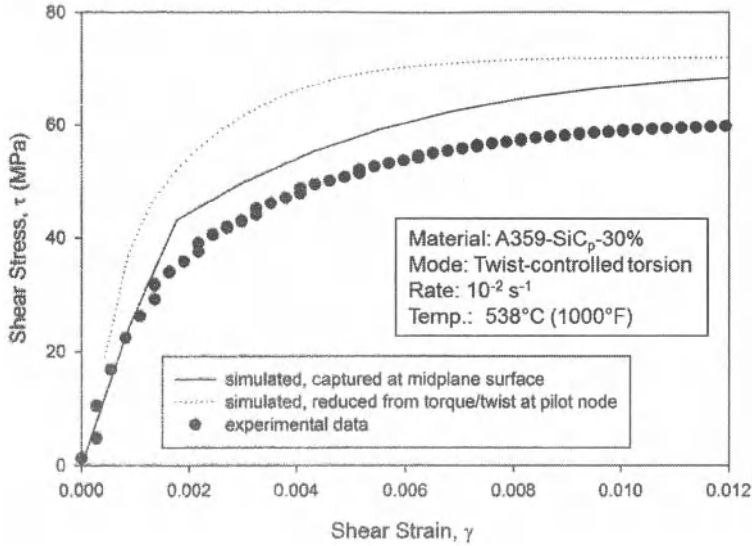


Figure 12: Comparison of shear stress-strain curves obtained directly from gage surface and by reduction of pilot-node torque-twist data.

Simulations of torsion tests were performed at constant temperatures of 20°C (68°F), 316°C (600°F) and 538°C (1000°F) and at equivalent strain rates of  $10^{-5} \text{ s}^{-1}$ ,  $10^{-2} \text{ s}^{-1}$ , and  $10^{-1} \text{ s}^{-1}$ , and the resulting shear stress-strain curves were plotted on the same sets of axes, along with experimental data. Figure 15 shows that while the simulated response diverges somewhat from the experimental results in the hardening portion of the curve, the simulations reliably reproduce acceptable approximations of the ultimate stress at each temperature. Simulations performed at the highest temperature studied, at which strain rate dependence is expected to be most significant, show that the rate dependence is captured well at rates which were used to calibrate the model, while underestimating the stress levels obtained at the highest rate, as may be observed in Fig. 16. It may also be seen that the shape of the hardening curves match well for the two lower-rate cases. In general, however, hardening was seen to occur at a greater rate in simulations than in actual tests. A difference in the rates of hardening in torsion versus tension testing has been observed repeatedly, as noted in [2], and may be due to a difference in the

effective strain rate under torsion as opposed to tension. Since rate dependence of the hardening parameter was calibrated under tension for the numerical model employed, the greater rate of hardening observed in simulations may be explained by the adherence of the model to hardening rates observed under tension.

### Conclusions

Torsion experiments were performed on the as-cast aluminum metal-matrix composite A359-SiC<sub>p</sub>-30% at a variety of temperatures and twist rates. The torque and twist histories obtained from the test apparatus were reduced to shear and equivalent stress and strain histories by application of the effective radius and von Mises equivalents. Stress-strain diagrams were constructed for the shear and equivalent quantities. These were used to determine equivalent material properties for the material, which were compared with properties previously obtained through tensile testing. The strain rate and temperature dependence of material properties were analyzed to determine trends.

A numerical model which was defined and calibrated to simulate the tensile response of the material was applied to simulate torsion tests at various twist rates and temperatures. The mesh used in simulations was a 3-D replica of the torsion specimen, and simulations were conducted with and without the imposition of experimentally-determined temperature distributions. Imposition of the temperature distribution was not found to improve accuracy of simulations. Shear stress-strain data was captured at the model specimen gage surface and also through the reduction of torque-twist data obtained from the pilot node used to twist the free end of the specimen model. Data obtained directly from the gage surface was found to provide shear stress-strain curves more closely aligned with experimental data than those obtained by reduction of torque-twist data at the pilot node. Simulated shear stress-strain curves produced under varying temperature and strain rate conditions sufficiently matched trends in experimental data to allow prediction of material response at intermediate temperatures throughout the range of temperatures studied, and at intermediate strain rates in the  $10^{-5}$ - $10^{-2}$  s<sup>-1</sup> range.

## References

- [1] K. Park, J. E. Lavernia, and F. A. Mohamed, "High temperature creep of silicon carbide particulate reinforced aluminum," *Acta metallurgica et materialia*, vol. 38, no. 11, pp. 2149-2159, 1990.
- [2] G. E. Dieter, H. A. Kuhn, and S. L. Semiatin, Eds., *Handbook of Workability and Process Design*. Materials Park, OH: ASM International, 2003.
- [3] Y. Li, K. T. Ramesh, and E. S. C. Chin, "The mechanical response of an A359/SiCp MMC and the A359 aluminum matrix to dynamic shearing deformations," *Materials Science and Engineering A*, vol. 382, pp. 162-170, 2004.
- [4] D. P. Myriounis, S. T. Hasan, N. M. Barkoula, A. Paipetis, and T. E. Matikas, "Effects of Heat Treatment on Microstructure and the Fracture Toughness of SiCp/Al Alloy Metal Matrix Composites," *Journal of advanced materials*, vol. 41, no. 3, pp. 18-27, 2009.
- [5] D. P. Myriounis, S. T. Hasan, and T. E. Matikas, "Microdeformation behaviour of Al-SiC metal matrix composites," *Composite Interfaces*, vol. 15, no. 5, pp. 495-514, 2008.
- [6] R. Rodríguez-Castro, R. C. Wetherhold, and M. H. Kelestemur, "Microstructure and mechanical behavior of functionally graded Al A359/SiCp composite," *Materials Science and Engineering A*, vol. 323, pp. 445-456, 2002.
- [7] Y. Li, K. T. Ramesh, and E. S. C. Chin, "Viscoplastic Deformations and Compressive Damage in an A359/SiCp Metal-Matrix Composite," *Acta mater.*, vol. 48, pp. 1563-1573, 2000.
- [8] Y. Li, K. T. Ramesh, and E. S. C. Chin, "The compressive viscoplastic response of an A359/SiCp metal-matrix composite and of the A359 aluminum alloy matrix," *International Journal of Solids and Structures*, vol. 37, pp. 7547-7562, 2000.
- [9] Y. Li, K. T. Ramesh, and E. S. C. Chin, "Plastic Deformation and Failure in A359 Aluminum and an A359-SiCp MMC under Quasistatic and High-strain-rate Tension," *Journal of Composite Material*, vol. 41, pp. 27-40, 2007.
- [10] O. A. Hamed, M. A. Shady, and A. R. El-Desouky, "Creep behavior of a cast 359/SiC/10p aluminum composite," *Materials and Design*, vol. 22, pp. 473-479, 2001.
- [11] N. P. Hung, C. S. Lim, Y. K. Ho, Y. C. Tan, and W. G. Tan, "Cumulative creep and hot isostatic pressing of particle-reinforced metal matrix composites," *Journal of Materials*

- Processing Technology*, vol. 101, pp. 104-109, 2000.
- [12] A. Madgwick, C. Ungpinitpong, T. Mori, and P. J. Withers, "Observation and quantitative analysis of damage caused by creep in an Al A359/SiCp composite," *Materials Science and Engineering A*, vol. 342, pp. 201-206, 2003.
- [13] W. H. Hunt, D. M. Schuster, M. D. Skibo, M. T. Smith, and D. R. Herling, "Lower Cost Cast Aluminum MMC Process and Products," in *State of the art in cast metal matrix composites in the next millentum; proceedings of a symposium*, 2000, pp. 265-272.
- [14] ASTM, *ASTM E143-02: Standard Test Method for Shear Modulus at Room Temperature*. West Conshohocken, PA.
- [15] ASTM, *ASTM A938-07: Standard Test Method for Torsion Testing of Wire*. West Conshohocken, PA.
- [16] ASTM, *ASTM E21-09. "Standard Test Methods for Elevated Temperature Tension Tests of Metallic Materials"*. West Conshohocken, PA, vol. 03.01.
- [17] D. R. Barraclough, H. J. Whittaker, K. D. Nair, and C. M. Sellars, "Effect of Specimen Geometry on Hot Torsion Test Results for Solid and Tubular Specimens," *Journal of Testing and Evaluation*, vol. 1, no. 3, pp. 220-226, May 1973.
- [18] J.C. Simo and T.J.R. Hughes, *Computational Inelasticity*, 1st ed., J.E. Marsden, L. Sirovich, and S. Wiggins, Eds. New York, U.S.A.: Springer-Verlag, 1998.
- [19] M. Zhou and M. P. Clode, "Hot torsion tests to model the deformation behavior of aluminum alloys at hot working temperatures," *Journal of Materials Processing Technology*, vol. 72, pp. 78-85, 1997.
- [20] ASTM, *ASTM B598-09: Standard Practice for Determining Offset Yield Strength in Tension for Copper Alloys*. West Conshohocken, PA.

*Characterization of Minerals, Metals, and Materials*  
Edited by: Jiann-Yang Hwang, Sergio Neves Monteiro, Chengguang Bai,  
John Carpenter, Mingdong Cai, Donato Firrao, and Buoung-Gon Kim  
TMS (The Minerals, Metals & Materials Society), 2012

# **Characterization of Minerals, Metals, and Materials**

## **Characterization of Ferrous Metals II**

Session Chairs:  
**Mingming Zhang**  
**Zhiwei Peng**

## COMPARISON OF CREEP LIFE ASSESSMENT BETWEEN TIN-BASED LEAD-FREE SOLDERS AND LEAD SOLDERS

Kenji Monden

Denki Kagaku Kogyo Kabushiki Kaisha (DENKA);  
3-5-1 Asahimachi; Machida-shi, Tokyo, 194-8560, Japan

Keywords: Creep life assessment, Imaginary initial strain rate, Lead solder, Lead-free solder

### Abstract

The creep properties of tin-based lead-free solders Sn<sub>3.0</sub>Ag<sub>0.5</sub>Cu and Sn<sub>0.7</sub>Cu<sub>0.1</sub>Ni and lead solders 10Sn90Pb and 50Sn50Pb were investigated at temperatures between 298 K and 398 K. The creep-rupture time decreases with increasing initial stress and temperature. The analysis of the solder creep curves uses the Omega method. The creep rate  $\dot{\epsilon}$  is expressed by following formula:  $\ln \dot{\epsilon} = \ln \dot{\epsilon}_0 + \Omega \epsilon$ , where  $\dot{\epsilon}_0$  and  $\Omega$  are experimentally determined. The parameter  $\dot{\epsilon}_0$  increases with increasing initial stress and temperature. The activation energy for  $\dot{\epsilon}_0$  is 108 kJ/mol for Sn<sub>3.0</sub>Ag<sub>0.5</sub>Cu and 85 kJ/mol for Sn<sub>0.7</sub>Cu<sub>0.1</sub>Ni. These energies suggest that the lattice diffusion of tin is dominant. The energy of 10Sn90Pb is 37 kJ/mol and that of 50Sn50Pb is 67 kJ/mol. The creep-rupture time is calculated using the parameters,  $\dot{\epsilon}_0$  and  $\Omega$ . The calculated creep-rupture time is in good agreement with the measured creep-rupture time.

### Introduction

Lead-free solders are replacing traditional tin-lead solders as part of a major trend toward protecting the earth's environment. However, tin-lead solders are currently needed for a high temperature range. Since creep is the main deformation mechanism in solder joints, understanding a constitutive model for creep and examining creep data for solders are important for reliability analysis of solder joints. A steady-state creep equation is generally used for solders [1, 2], and it supposes that the secondary-, or minimum-, creep rate occupies the entire creep life. However, secondary creep accounts for only about 15 % to 40 % of the entire creep life for solders. Thus, the equation may not represent the entire creep life.

Certain parametric methods [3, 4] have been used to predict the creep-rupture time of the solders. The physical significance of the parameters appearing in these parametric methods is not clear because they are usually determined based on creep-rupture data under a constant load. As an alternative to parametric methods, a modified theta-projection concept [5] can be determined by fitting a creep curve under constant stress for a specific equation. However, the creep curve expressed by the modified theta-projection concept is not well described near the failure point, and it underestimates the rupture strain.

In this study, the Omega method [6,7], which was developed to deduce the state equation for creep under a constant load and to predict the creep-rupture time, is applied to the analysis of creep curves of tin-based and lead-free solders [8]. The adaptability of the method to the creep deformation of tin-based lead-free solders Sn<sub>3.0</sub>Ag<sub>0.5</sub>Cu and Sn<sub>0.7</sub>Cu<sub>0.1</sub>Ni and lead solders 10Sn90Pb and 50Sn50Pb was also investigated. The Sn<sub>3.0</sub>Ag<sub>0.5</sub>Cu solder is one of the earliest commercially available lead-free solders. The Sn<sub>0.7</sub>Cu<sub>0.1</sub>Ni solder is expected to be a low cost solder because it does not include precious metals such as tin-silver alloys.

## Experimental

### Specimen Preparation

The creep specimen was machined from a cylindrical ingot, 130 mm long and 30 mm in diameter. Table I shows the chemical composition of the solders used in this study. The composition was analyzed by X-ray fluorescence analysis. The dimension of each creep specimen was 25 mm in gauge section and 7.5 mm in diameter. The shape and dimensions of a creep specimen are shown in Figure 1. Each specimen was subjected to 2 hour of heat treatment at a temperature corresponding to approximately 82 % of the melting point of the solder. The heat-treatment temperatures for 10Sn90Pb, 50Sn50Pb, Sn3.0Ag0.5Cu, and Sn0.7Cu0.1Ni are 440, 374, 400, and 410 K, respectively.

Table I. Chemical Composition of Tested Lead-Free Solders (Mass Ratio)

	Ag	Cu	Zn	Bi	Fe	Ni	Pb	Sn
10Sn90Pb	N.D.	N.D.	N.D.	N.D.	0.02	0.01	Bal.	10
50Sn50Pb	N.D.	N.D.	N.D.	N.D.	0.02	0.01	Bal.	50
Sn3.0Ag0.5Cu	2.7	0.45	N.D.	N.D.	0.01	0.01	0.02	Bal.
Sn0.7Cu0.1Ni	N.D.	0.70	N.D.	N.D.	0.03	0.06	N.D.	Bal.

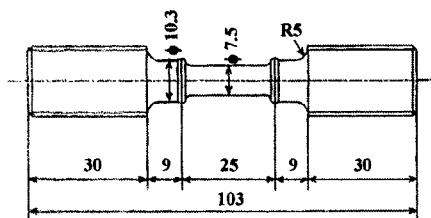


Figure 1. Shape and dimensions of the creep test specimen (Unit [mm])

### Creep Testing

The creep experiments in this study used a custom-built tension-creep apparatus. A gravity-loaded mechanical arm applied a force to the sample, and calibrated weights were loaded onto the mechanical arm. The test load was applied as quickly as possible, to approximate the real-life situation, in which load is applied instantaneously. The specimens were heated in a temperature chamber. The heating system maintained the temperature variation at less than 1 K.

The specimens had a collar at each end of the gauge part. An extensometer was attached to the two collars in order to measure the elongation of the gauge part during the test. A linear variable-differential transducer (LVDT) was directly linked to the extensometer. A data-acquisition unit collected signals from the LVDT.

To investigate the effects of temperature and initial stress, the creep tests were conducted at three different temperatures: 298, 343, 398, and 428 K. The elongation and temperature were continuously recorded. The stress applied in the creep test,  $\sigma_0$ , was calculated based on the initial cross-sectional area before the test.

## Results and Discussion

### Initial Strain Rate and Creep Equation

When the reloading creep stress is lower than that of the pre-creep, it suppresses the primary-creep. Therefore, the linearity between the logarithmic strain rate and true strain was obtained over almost the entire range of creep life. When primary and secondary creep regimes are minimal and tertiary creep is dominant, the strain rate  $\dot{\epsilon}_0$  is expressed by the following formula [8]:

$$\ln \dot{\epsilon} = \ln \dot{\epsilon}_0 + \Omega \epsilon, \quad (1)$$

where  $\dot{\epsilon}_0$  is the strain rate of being zero and  $\Omega$  is the slope of the line. Rewriting Equation (1) and integrating it with respect to time from zero to  $t$  results in Equation (2),

$$\epsilon = (1/\Omega) \ln[1/(1 - \Omega \dot{\epsilon}_0 t)]. \quad (2)$$

Using Equation (2), the creep curve can be drawn if  $\dot{\epsilon}_0$  and  $\Omega$  are known. There is  $t < 1/\Omega \dot{\epsilon}_0$  from the constraint on the independent variable of the logarithmic function. Therefore, the rupture time  $t$  can be defined by the following equation:

$$t_r = 1/\Omega \dot{\epsilon}_0. \quad (3)$$

Since the tertiary creep is dominant in the tin-based, lead-free solder, the Omega method is applied to the analysis of the solder creep curves.

### Creep Curve Properties

An example of the relationship between the logarithmic strain rate and true strain for Sn0.7Cu0.1Ni is shown in Figure 2. As the tertiary creep is dominant in the tin-based, lead-free solder Sn0.7Cu0.1Ni, the linearity between the logarithmic strain rate and true strain was obtained over almost the entire range of creep life. The parameters  $\dot{\epsilon}_0$  and  $\Omega$  are determined by least-squares regression to fit the data, as shown in Figure 2. Figure 3 shows an example of a creep curve obtained in the present work for Sn0.7Cu0.1Ni. The line and cross showing the rupture point are described by Equation (2) using  $\dot{\epsilon}_0$  and  $\Omega$ . The open circles are the experimental data. The calculated creep curve accurately describes the creep deformation and the rupture point.

### Effects of Stress and Temperature on the Parameters

When primary and secondary creep regimes are minimal and tertiary creep is dominant, the relationship between the imaginary initial strain rate and the expected initial stress is shown as follows [8]:

$$\dot{\epsilon}_0 = A_0 (\sigma_0/E)^{n_0} \exp(-Q_0/RT), \quad (4)$$

where  $A_0$  is the constant factor,  $E$  is Young's modulus,  $n_0$  is the stress exponent, and  $Q_0$  is the apparent activation energy for imaginary initial strain rate, which is independent of stress, provided that the normalized initial stress  $\sigma_0/E$  was used instead of  $\sigma_0$ . It is assumed that Equation (4) gives a reasonable representation of the imaginary initial strain rate, which would be roughly equal to the secondary creep rate.

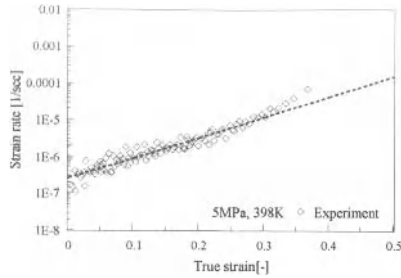


Figure 2. Relationship between strain rate and true strain for Sn0.7Cu0.1Ni

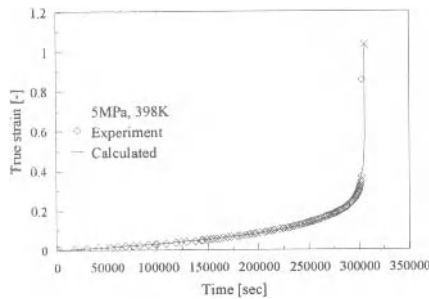


Figure 3. Measured and calculated creep curves for Sn0.7Cu0.1Ni

The effect of the temperature on the imaginary initial strain rate for lead-free solders is shown in Figure 4. The logarithmic imaginary initial strain rates  $\ln \dot{\epsilon}_0$  are plotted against the reciprocal temperatures  $1/T$ . The relationship of  $\ln \dot{\epsilon}_0$  and  $1/T$  appears to be linear, and the slope of the line shows  $-Q_0/R$ . The apparent activation energy for the imaginary initial strain rate of Sn0.7Cu0.1Ni is 85 kJ/mol under a constant stress of 7.0 MPa, and 108 kJ/mol under a constant stress of 7.8 MPa for Sn3.0Ag0.5Cu. These values are close to the activation energy for the lattice diffusion of tin, 104 kJ/mol [9].

The value  $\dot{\epsilon}_0 \exp(Q_0/RT)$  is plotted against the initial stress  $\sigma_0$  in Figure 5. All data points fall in the vicinity of a single line, explicitly demonstrating that a state equation for the imaginary initial strain rate exists. The slope of the line represents  $n_0$ . The parameter  $\dot{\epsilon}_0$  increases with increasing the initial stress and the temperature.

The effect of temperature on the strain rate acceleration factor for lead-free solders is shown in Figure 6. The logarithmic strain rate acceleration factor  $\ln \Omega$  is plotted against the reciprocal temperature  $1/T$ . The magnitude of  $\Omega$  decreases as the temperature increases. The following equation was derived to express the magnitude of  $\Omega$  [10]:

$$\Omega = A_S (\sigma_0/E)^{n_S} \exp(Q_S/RT), \quad (5)$$

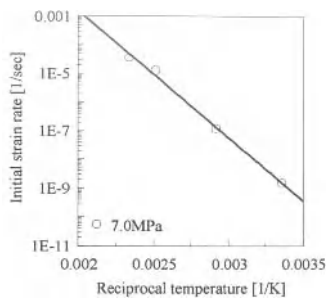


Figure 4. Relationship between the imaginary initial strain rate and the reciprocal temperature for Sn0.7Cu0.1Ni

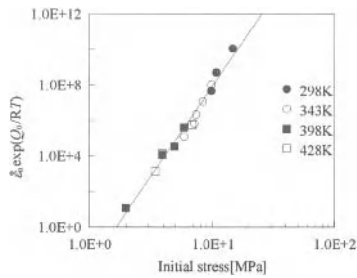


Figure 5 Temperature-compensated imaginary initial strain rate as a function of the initial stress for Sn0.7Cu0.1Ni

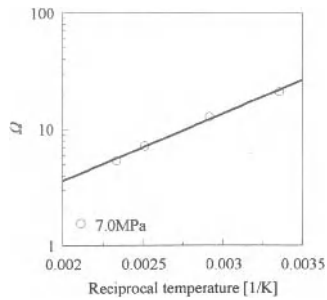


Figure 6 Relationship between the strain rate acceleration factor and the reciprocal temperature for Sn0.7Cu0.1Ni

where  $A_S$ ,  $n_S$ , and  $Q_S$  are constants, provided that the normalized initial stress  $\sigma_0/E$  was used instead of  $\sigma_0$ . The relationship of  $\ln \Omega$  and  $1/T$  appears to be linear, and the slope of the line shows  $Q_S/R$ . The constant  $Q_S$  of Sn0.7Cu0.1Ni is 11 kJ/mol under a constant stress of 7.0 MPa.  $A_S$ ,  $n_S$ , and  $Q_S$  are physically meaningless, but are useful in drawing the creep life assessment. The value  $\Omega/\exp(Q_S/RT)$  is plotted against the initial stress  $\sigma_0$  in Figure 7. All data points seem to fall in the vicinity of a single line. The slope of the line shows  $n_S$ . The parameter  $\Omega$  is temperature dependent but less dependent on the initial stress. Table II shows the present experimental data of the constants,  $n_0$ ,  $Q_0$ ,  $n_S$ , and  $Q_S$ .

### Creep Life Assessment

Rewriting Equation (1) results in Equation (6) as follows:

$$\dot{\epsilon} = \dot{\epsilon}_0 \exp(\Omega \epsilon) . \quad (6)$$

Integrating Equation (6) with respect to time, from  $t$  to  $t_r$ , results in Equation (7)

$$t_r - t = (1/\Omega \dot{\epsilon}_0) [\exp(-\Omega \epsilon) - \exp(-\Omega \epsilon_r)] , \quad (7)$$

where  $\epsilon_r$  is the rupture strain. The magnitude of  $\exp(-\Omega \epsilon_r)$  is generally much smaller than  $\exp(-\Omega \epsilon)$ , so Equation (7) can be simplified to Equation (8)

$$t_r - t = 1/\Omega \dot{\epsilon} . \quad (8)$$

Equation (8) suggests a very important result that the product of the strain rate and the remaining life  $t_r - t$  is constant  $1/\Omega$ . Therefore, the remaining life of the lead-free solder can be predicted if  $\Omega$  and strain rate are given.

Substituting zero into  $t$  in Equation (8) gives Equation (3). Equation (3) allows us to predict the creep-rupture time of specimens if  $\dot{\epsilon}_0$  and  $\Omega$  are known. The magnitude of  $\dot{\epsilon}_0$  and  $\Omega$  can be estimated from Equations (4) and (5) as a function of temperature and stress. Therefore, the creep-rupture time of specimens is predicted using Equation (9)

$$t_r = (A_0 A_S)^{-1} (\sigma_0/E)^{-(n_0+n_S)} \exp[(Q_0 - Q_S)/RT] , \quad (9)$$

if temperature and initial stress are known. Figure 8 shows the relationship between the initial stress and the creep-rupture time at each temperature. The data points are experimental results and the lines are described by Equation (9). The creep-rupture time decreases with increasing initial stress and temperature. Equation (9) gives a good fit for the initial stress versus the creep-rupture time at each temperature. The comparison of calculated creep-rupture time between tin-based lead-free solders and lead solders at 398 K is shown in Figure 9. The creep-rupture time of

Table II. Values of the Constants Estimated by this Study for the Lead-Free Solders

	$Q_0$ [kJ/mol]	$Q_S$ [kJ/mol]	$n_0$	$n_S$
10Sn90Pb	37	2.9	3.4	$-6.3 \times 10^{-2}$
50Sn50Pb	67	13	3.0	$-3.0 \times 10^{-1}$
Sn3.0Ag0.5Cu	108	7.2	7.8	$-7.7 \times 10^{-2}$
Sn0.7Cu0.1Ni	85	11	10	-1.6

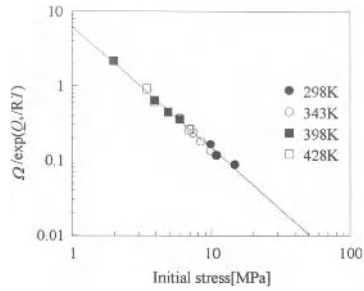


Figure 7. Temperature-compensated strain rate acceleration factor as a function of the initial stress for Sn0.7Cu0.1Ni

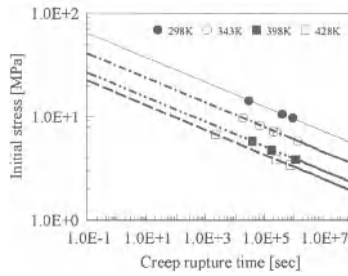


Figure 8. Relationship between the initial stress and the creep-rupture time for Sn0.7Cu0.1Ni

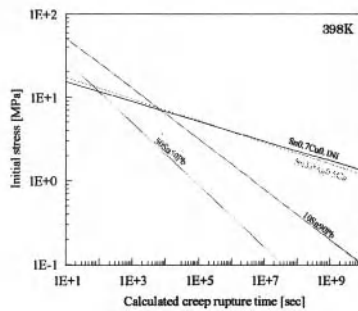


Figure 9. Comparison of calculated creep-rupture time between tin-based lead-free solders and lead solders at 398 K

tin-based lead-free solders is longer than lead solders less than 5 MPa of initial stress at 398 K. The creep-rupture time of Sn0.7Cu0.1Ni is comparable with that of Sn3.0Ag0.5Cu at 398 K.

### Conclusions

The creep properties of tin-based lead-free solders Sn3.0Ag0.5Cu and Sn0.7Cu0.1Ni and lead solders 10Sn90Pb and 50Sn50Pb were investigated at temperatures between 298 K and 398 K. The creep-rupture time decreases with increase in initial stress and temperature. Applying the Omega method to the analysis of creep curves of solders, the calculated creep curve accurately describes the creep deformation and rupture point. The parameter  $\dot{\epsilon}_0$ , which is the imaginary initial strain rate, increases as the initial stress and temperature increase. The apparent activation energy for  $\dot{\epsilon}_0$  is 108 kJ/mol in Sn3.0Ag0.5Cu and 85 kJ/mol in Sn0.7Cu0.1Ni. The energies of 10Sn90Pb and 50Sn50Pb are 37 kJ/mol and 67 kJ/mol, respectively. The remaining life of solder can be predicted if  $\dot{\Omega}$  and strain rate are known. If temperature and initial stress are known, the creep-rupture time of specimens is predicted using  $t_r = (A_0 A_S)^{-1} (\sigma_0 / E)^{-(n_0 + n_S)} \exp[(Q_0 - Q_S) / RT]$ . The creep-rupture time of lead-free solders is longer than lead solders less than 5 MPa of initial stress at 398 K. The creep-rupture time of Sn0.7Cu0.1Ni is comparable with that of Sn3.0Ag0.5Cu at 398 K.

### Acknowledgments

The help of Mr. T. Matsuda, Sumitomo Metal Technology, Inc., in acquiring solder mechanical properties and many helpful discussions with Mr. E. Mukai, Research Center, DENKA, are gratefully acknowledged.

### References

1. C.M.L. Wu and M.L. Huang, "Creep Behavior of Eutectic Sn-Cu Lead-Free Solder Alloy," *Journal of Electronic Materials*, 31 (5) (2002), 442-448.
2. M.L. Huang, L. Wang, and C.M.L. Wu, "Creep Behavior of Eutectic Sn-Ag Lead-Free Solder Alloy," *Journal of Materials Research*, 17 (11) (2002), 2897-2903.
3. I. Shohji, C. Gagg, and W.J. Plumbridge, "Creep Properties of Sn-8Mass%Zn-3Mass%Bi Lead-Free Alloy," *Journal of Electronic Materials*, 33 (8) (2004), 923-927.
4. M.L. El-Bahay, M.E.El Mossalamy, M. Mahdy, and A.A. Bahgat, "Some Mechanical Properties of Sn-3.5Ag Eutectic Alloy at Different Temperatures," *Journal of Materials Science: Materials in Electronics*, 15 (2004), 519-526.
5. Y. Kariya, M. Otsuka, and W. J. Plumbridge, "The Constitutive Creep Equation for a Eutectic Sn-Ag Alloy Using the Modified Theta-Projection Concept," *Journal of Electronic Materials*, 32 (12) (2003), 1398-1402.
6. J. Shi and T. Endo, "A New Approach for Creep Life Assessment Based on the Imaginary Initial Strain Rate," *Scripta Metallurgica et Materialia*, 32 (8) (1995), 1159-1162.
7. M. Prager, "Development of the MPC Omega Method for Life Assessment in the Creep Range," *Journal of Pressure Vessel Technology*, 117 May (1995), 95-103.
8. K. Monden, "Creep Life Assessment of Tin-Based Lead-Free Solders Based on Imaginary Initial Strain Rate," *Journal of Electronic Materials*, 36 (12) (2007), 1691-1696.
9. C. Coston and N.H. Nachtrieb, "Self Diffusion in Tin at High Pressure," *The Journal of Physical Chemistry*, 68 (1964), 2219-2229.
10. J. Shi, K. Tai, and T. Endo, "Creep Behavior Analysis of a Service-Exposed 2.25Cr-1Mo Steel," *Tetsu-to-Hagane*, 81 (8) (1995), 839-844 (in Japanese).

## **CORRELATIONSHIP BETWEEN $J_{IC}$ AND EQUIVALENT FRACTURE STRAIN DETERMINED BY SMALL-PUNCH TEST IN JN1, JJ1 AN JK2 AUSTENITIC STAINLESS STEELS**

Maribel L- Saucedo-Muñoz<sup>1</sup>, Toshiyuki Hashida<sup>2</sup>, Victor M. Lopez-Hirata<sup>1</sup>

<sup>1</sup>Instituto Politecnico Nacional (ESIQIE);

Apartado Postal 118-556, Mexico, D.F., 07730, Mexico

<sup>2</sup>Tohoku University (FRI); Sendai, Miyagi, 980-8579, Japan

**Keywords:** Thermal aging embrittlement, Austenitic stainless steels, Fracture toughness, Small-punch test.

### **Abstract**

Small-punch tests and determination of fracture toughness  $J_{IC}$  were conducted at 4 and 77 K on new cryogenic JN1, JJ1 and JK2 austenitic stainless steels, after isothermal aging. Equivalent fracture strain  $\epsilon_{qf}$  was determined by measuring the reduction of thickness in the small-punch test specimen. A linear dependence of  $J_{IC}$  on  $\epsilon_{qf}$  was found in these new materials. Regression analysis of experimental data produced the following linear relation  $J_{IC} = 1304.1 \epsilon_{qf} + 8.09$  [ $\text{kJm}^{-2}$ ]. An analysis of present work relation was pursued on the basis of material properties and evaluation method of  $J_{IC}$ . Results showed that the slope value has a strong dependence on material yield strength and  $J_{IC}$  evaluation method. This linear relation is useful for the evaluation of fracture toughness  $J_{IC}$ , measuring the equivalent fracture strain  $\epsilon_{qf}$  by means of small-punch test. Thus it can be useful for assessing the degradation of fracture toughness in small areas such as, the heat-affected zone in welded components.

### **Introduction**

Cryogenic structural materials for superconducting magnets of fusion nuclear reactor are required to possess a good combination of strength and toughness. The mechanical properties are required beyond the capability of conventional austenitic stainless steels [1]. New cryogenic JN1, JJ1 and JK2 austenitic stainless steels were developed by the Japan Atomic Energy Research Institute (JAERI) [1]. The structure of superconducting magnets is constructed by welding of 200 mm thick plates of these steels, which are solution treated at high temperatures and then water-quenched to avoid intergranular precipitation. However, the welding process involves heating and cooling [2], which cause microstructural changes in both base metal and weld. In this heterogeneous microstructure, it is important to estimate the fracture toughness of these materials at cryogenic temperatures. Therefore, it is necessary to evaluate the effect of aging process on the fracture toughness behavior of these new steels. To determine the cryogenic fracture toughness, the elastic-plastic  $J_{IC}$  value has been commonly used [2]; however, the specimen size is much larger than heat-affected zones in welded components. Small-punch (SP) testing method, employing miniature specimens, has permitted to evaluate the fracture toughness behavior at different temperatures in different nuclear reactor materials [3,4]. Mao et al. [5,6] and Misawa et al. [7] found a linear relation between  $J_{IC}$  value and equivalent fracture strain  $\epsilon_{qf}$ , determined by SP method in non-ferrous alloys and ferritic steels at room temperature and austenitic stainless steels at 4 and 77 K, respectively. So that, this kind of correlation would be

very useful to assess the fracture toughness  $J_{IC}$  values by means of SP test in small zones of welded components.

The goal of this work is to study the correlation of  $J_{IC}$  value and equivalent fracture strain ( $\epsilon_{qf}$ ), determined by small-punch test, at cryogenic temperatures in new austenitic stainless JN1, JJ1 and JK2 steels. These steels were isothermally aged in order to cause the fracture toughness deterioration due to precipitation of carbides and nitrides [7], similar to that one promoted by heating and cooling in welded parts. This study also analyses the effect of  $J_{IC}$  evaluation on the relationship between  $J_{IC}$  and  $\epsilon_{qf}$ .

### Experimental Procedure

Materials used in this work were forged plates of 200 mm thick of JN1, JJ1 and JK2 austenitic stainless steels and its composition is shown in Table I. Solution treatment of JN1, JJ1 and JK2 steels was carried out at 1348 K for 0.2 hours, 1333 K for 5.5 hours and at 1253 K for 5 h, respectively, and then water-quenched. The aging conditions were temperatures of 923, 973, 1023 and 1073 K for a time of 5 h. Tensile tests of these materials were conducted at 4 K and at cross-head speed of 0.5 mm/min with a tensile specimen of 5 mm diameter (number 14 of JIS Z2201 standard), following the procedure established in JIS Z2277 standard. Fracture toughness  $J_{IC}$  evaluation utilized the single-specimen unloading compliance method. T-L specimens were prepared according to ASTM E813-89 standard, employing 1TCT and 0.5TCT sizes, and subsequently precracked by fatigue test at room temperature. Precracking process employed an alternating stress intensity factor  $\Delta K$  of  $30 \text{ MPa}^{1/2}$ , a frequency of 10 Hz and a ratio of width to precrack length ( $a_0/W$ ) of 0.6. The cryogenic fracture toughness tests were conducted in an Instron tension machine, equipped with a cryostat, and with a cross-head speed of 0.1 mm/min in all tests. Testing temperatures were 4 and 77 K, reached after keeping the specimen for 10 minutes in liquid helium or nitrogen, respectively. Load-displacement curves were determined by the clip-gage method and crack length was measured with the unload compliance method.  $J$  integer and  $J_{IC}$  values were determined following ASTM E813-81 and E813-89 standards. SP test specimen of 10 mm x 10 mm x 0.5 mm were extracted in a way that the crack propagation in the specimen remains parallel to the longitudinal direction of plate. Testing temperatures were liquid nitrogen temperature (77 K) and liquid helium temperature (4 K). Figure 1 shows a schematic draw of the homemade apparatus for SP test at liquid nitrogen and helium temperatures. Specimen was mounted on the SP testing jig, and the LVDT for load-line deflection measurement is attached to the pull rod. SP test started by pressing the puncher, steel ball of 2.4-mm diameter, against the specimen. Tensile load was converted into compressive force through the puncher at a cross-head speed of  $0.1 \text{ mm min}^{-1}$ , and deflection was measured by a LVDT. Load-deflection curve was displayed using an X-Y recorder or computer. The upper and lower parts of dies are fixed with four screws with a torque of 0.5 Nm. Scanning electron microscopy (SEM) was used to observe the appearance and fracture surface of tested specimens. The fracture equivalent strain,  $\epsilon_{qf}$ , was determined by measuring the reduction of thickness in tested SP specimens. SP specimens were mounted on epoxy resin and cut it at its middle part with a diamond-disc in a low-speed saw machine. This section was prepared metallographically and then observed in an SEM.

Table I. Chemical composition (wt. %) of JN1, JJ1 and JK2 steels and materials of Misawa's work [4]

Material	C	Mn	Ni	Cr	Mo	N	Others
JN1	0.040	3.88	15.07	24.32	---	0.320	0.023 Al
JJ1	0.025	10.13	11.79	12.01	4.94	0.236	---
JK2	0.050	21.27	9.15	12.97	0.97	0.247	---
12Cr12Ni10Mn5Mo (ESR)	0.050	9.26	11.93	11.95	5.03	0.204	---
12Cr12Ni10Mn5Mo (VIM)	0.020	10.46	12.47	12.38	5.16	0.208	---
32Mn7Cr (ESR)	0.130	32.47	0.02	7.29	---	0.147	
18Mn5Cr (EF)	0.530	17.71	0.14	4.72	---	0.092	
A286 (ESR)	0.01	1.19	24.92	13.91	1.36	0.001	0.24 V, 2.39 Ti and 0.20 Al

## Results and Discussion

### Tensile Properties and Curves of Load-Deflection for SP Test

Table II shows the tensile properties at 4 and 77 K of JJ1, JN1 and JK2 steels solution treated and aged at 923, 973 and 1073 K for 5 h. In the case of solution treated samples, the highest yield ( $\sigma_0$ ) and ultimate tensile ( $\sigma_{ult}$ ) strengths were obtained in JN1 steel, which has the highest contents of interstitial solutes atoms and chromium. The highest elongation corresponded to JK2 steel with the highest and lowest contents of manganese and nickel, respectively. Aging process caused a decrease of tensile properties in all steels. Elongation of aged steels showed the highest drop among these properties. Figure 1 shows the curves of load-deflection of SP test at 4 K, for example, in both solution treated and aged JN1 steel samples. Load increases as a function of deflection until the maximum load is reached, shown by an arrow ( $\downarrow$ ) for each curve. After this maximum, load drops drastically or there is a change in the curve slope. This type of behavior was observed in all tested steels. It was also detected that the fracture took place at the maximum value of load during SP test. The maximum load and deflection at maximum load decreased with aging temperature for the three tested materials. This decreasing tendency varied with tested steel. Same type of behavior was observed in specimens tested at 77 K. Additionally, The presence of serrations or pop-in in load-deflection curves was observed as a characteristic event at 4 K [8]. For example, the appearance of regular and continuous serrations was detected after load reached a value about 1.2 kN in the case of both solution treated and aged at 923 K for 5 hours JN1 steel specimens. The amplitude of these serrations was larger at load values close to the maximum one. Load dropped drastically after reaching this maximum value. On the other hand, the load-deflection curve for the SP test specimens aged at higher temperatures exhibited a sharp change in the slope (bending point) at low values of load and no drastical drop of load was noticed at the end of test. The determination of load point for fracture was difficult in this case.

### Fractography and Fracture Appearance

SEM analysis of tested SP specimens was carried out to determine the fracture appearance of specimen and the fracture mode, after testing. SEM micrograph of SP test specimen of solution treated JN1 steel is shown in Fig. 2 (a). A semispherical cup is observed due to the shape of

Table II. Mechanical properties at 4 and 77 K of solution treated JN1, JJ1 and JK2 steels

Material	Heat treating condition	Testing temperature	$\sigma_0$ (Mpa)	$\sigma_{uts}$ (Mpa)	Elongation %
JN1	Solution treated	4 K	1349	1690	31
JN1	Aged 923K-5h	4 K	1318	1671	13
JN1	Aged 973K-5h	4 K	1310	1625	6.8
JN1	Aged 1073K-5h	4 K	1299	1564	2.4
JJ1	Solution treated	4 K	1169	1591	39
JJ1	Aged 923K-5h	4 K	1162	1517	17
JK2	Solution treated	4 K	1213	1576	44
JK2	Aged 923K-5h	4 K	1188	1534	21
JN1	Solution treated	77 K	843	1395	52
JN1	Aged 923K-5h	77 K	989	1358	--
JN1	Aged 1073K-5h	77 K	967	1199	--

puncher, steel ball. Fracture dimples were noticed in the fracture surface of this specimen, Fig. 2 (c). Similar results were also observed for solution treated JJ1 and JK2 steels. In the case of aged specimens, the fracture took place at the center of specimen at the moment of contact between puncher and specimen. An intergranular brittle fracture was also observed in this case. Figures 2 (b) and (d) show the fracture appearance and fractography of JN1 steel SP test specimen aged at 973 K for 5 h, after testing. Here, it can be noticed that the fracture occurred at the specimen center and propagated radially, and the fracture mode is composed of both dimples and intergranular brittle fracture. Besides, the fracture surface of specimens, aged at 973 K for times longer than 5 h, was almost composed of intergranular brittle fracture. Same results were observed for the aged JJ1 and JK2 steel specimens.

All the above results suggest that the SP test method is a good alternative to follow the fracture toughness deterioration originated in these new materials by isothermal aging.

Determination of  $\epsilon_{qf}$

Mao et al. [5,6] and Misawa et al. [7] have shown that the equivalent fracture strain  $\epsilon_{qf}$  can be selected as a fracture parameter for the SP test specimens under the biaxial Stress state.  $\epsilon_{qf}$  is defined by the following relation [5]:

$$\epsilon_{qf} = \ln (t_0/t) \tag{1}$$

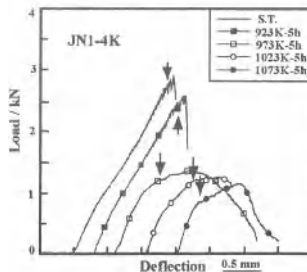


Figure 1. Load-deflection curves of JN1 steel in SP test at 4 K.

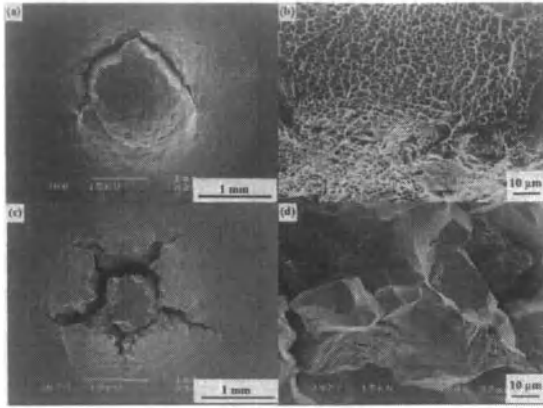


Figure 2. SEM photographs of SP test specimen of JN1 steel and its corresponding fractography for a) and c) solution treated, and b) and d) aged at 973 K for 5 h.

where  $t$  and  $t_0$  are the thickness of SP test specimen at the thinnest section and at the initial stage, respectively. Figures 3 (a) and (b) show a SEM micrograph of the thickness change of two sliced SP test specimens, corresponding to the JN1 steel solution treated and aged at 973 K for 5 hours, respectively. The former shows a drastical decrease of thickness, compared to the latter. The values of  $\epsilon_{qr}$  for the different tested materials were determined using similar SEM photographs. Figure 5 shows the  $\epsilon_{qr}$  values and its corresponding  $J_{IC}$  values determined experimentally using the ASTM E813-89 standard. Some  $J_{IC}$  values were determined from its corresponding  $K_{IC}$  value, employing the following relation:

$$J_{IC} = K_{IC}^2 (1 - \nu^2)/E \quad (2)$$

where  $E$  is the Young modulus and  $\nu$  the Poisson ratio.

#### Correlationship between $J_{IC}$ and $\epsilon_{qr}$

The plot of  $J_{IC}$  against  $\epsilon_{qr}$  is shown in Fig. 4 for all materials of present work. Some of these data were determined from welded parts. It is evident the linear relationship between them. The regression analysis of these data conducted to the following equation:

$$J_{IC} = 1304.1 \epsilon_{qr} + 8.09 \quad (3)$$

with a correlation coefficient,  $R^2$ , of 0.9546, which confirms the linear relation. This type of relation,  $J_{IC} = C_1 \epsilon_{qr} + C_2$ , is similar to the relation,  $J_{IC} = C_p \epsilon_{qr}$ , found by Bayoumi and Bassim [9] in a biaxial stress state for the case of elastic-plastic materials. They pointed out that the constant  $C_p$  depends on material and testing conditions and is defined as follows:

$$C_p = k m \sigma_0 L_p^*/C \quad (4)$$

Where  $\sigma_0$  is the yield strength,  $k$  a constant, which is usually less than one and which may vary with temperature and material conditions,  $m$  a constraint factor, which depends on the material and testing conditions and  $L_p^*$  the distance from crack tip, where initiation of ductile fracture occurs.

Figure 4 also shows the linear-relations found by Misawa et al. [7] in austenitic stainless steels. Besides, Table V summarized the linear dependence of  $J_{IC}$  on  $\epsilon_{qr}$  determined by Misawa et al. [7] and that of present work, as well as its corresponding testing temperature. It is evident from the

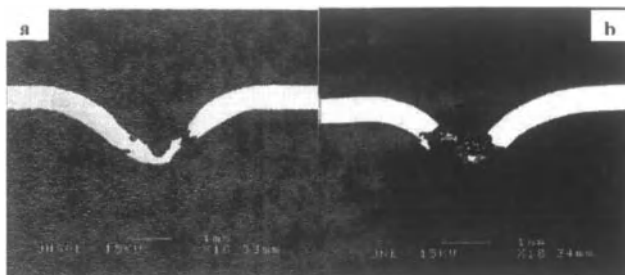


Figure 3. SEM photographs of thickness change for the SP test specimen of JN1 steel a) solution treated and b) aged at 973 K for 5 h.

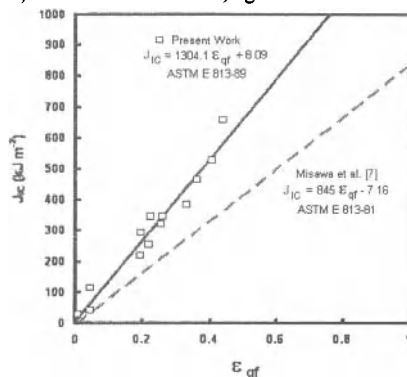


Figure 4. Plot of  $J_{IC}$  against  $\epsilon_{qf}$  for data from this present study and reference [7].

above Fig. 4 that Misawa's and present work relations are in good agreement with the relation proposed by Bayoumi and Bassim, since  $C_2$  is close to zero in both cases. However, the slope value,  $C_1$ , of present work is higher than that of Misawa's work.

Tables I and III show the chemical composition and some mechanical properties (yield strength and ultimate tensile strength) of materials tested by Misawa et al. [7]. By comparison of Tables II and III, it is clear that the average yield strength of materials for this work is similar to that of Misawa's materials. Thus, it would be expected a similar  $C_1$  value for both works.  $J_{IC}$  values reported by Misawa et al. were determined following the ASTM E913-81 standard.

Hence, their  $J_{IC}$  values are lower than the expected ones if the new ASTM E813-89 standard had been applied for  $J_{IC}$  determination. This means that the slope  $C_1$  of Misawa's work is underestimated.

To clarify the origin of a higher slope  $C_1$  for this work,  $J_{IC}$  values of JN1, JJ1 and JK2 were recalculated using the ASTM E813-81 standard. Figure 5 shows the plot of  $J_{IC}$  as a function of  $\epsilon_{qf}$ . A linear relation between these variables is evident. The regression analysis enabled to determine the following equation:

$$J_{IC} = 840.3 \epsilon_{qf} + 62.3 \quad (5)$$

The correlation coefficient,  $R^2$ , was 0.882. The  $C_1$  value of this equation,  $840.3 \text{ kJ m}^{-2}$  is close to the value of  $845 \text{ kJ m}^{-2}$  determined by Misawa. This suggests that the constant  $C_1$  is a constant value for same type of materials, and hence this kind of equation can be used for assessing the fracture toughness  $J_{IC}$  at cryogenic temperatures using the  $\epsilon_{qf}$  value determined by means of a SP test.

Table III. Mechanical properties at 4 and 77 K of steels used by Misawa [7]

Material	$\sigma_0$ (Mpa) at 4 K	$\sigma_v$ (Mpa) at 77 K
12Cr12Ni10Mn5Mo (ESR)	1249	851
12Cr12Ni10Mn5Mo (VIM)	1242	868
32Mn7Cr (ESR)	1145	759
18Mn5Cr (EF)	1320	820
A286 (ESR)	1027	892

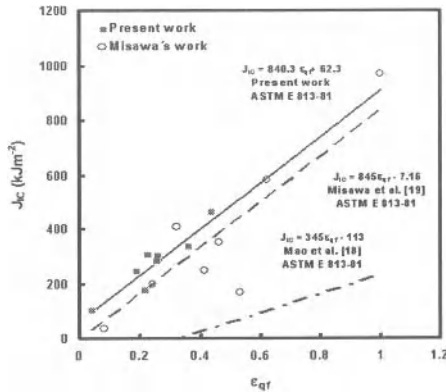


Figure 5. Plot of recalculated  $J_{IC}$  values from this current work vs.  $\epsilon_{qf}$ , according to ASTM 813-81 standard.

To determine the accuracy of these linear equations, it was assumed that the Bayoumi and Bassim relation could be applied for the analysis of experimental data:

$$J_{IC} = C_P \epsilon_{qf} \quad (6)$$

This assumption seems to be consistent for both works. Likewise, the constant  $C_P$  could be approximated to the  $\sigma_0$  value. Therefore,  $J_{IC}$  can be calculated using Eq. (6) and the experimental  $\sigma_0$  and  $\epsilon_{qf}$  values of each tested material. Both Misawa's and present work relations used data determined not only at 4 K, but also at 77 K. This fact confirmed that this kind of linear relation is independent of the testing temperature [7].

Therefore, the linear dependence of  $J_{IC}$  value on the  $\epsilon_{qf}$  value can be useful for assessing the fracture toughness deterioration not only in isothermally aged JN1, JJ1 and JK2 steels, but also in welded parts.

### Conclusions

A study of correlation between the fracture toughness value  $J_{IC}$  and the equivalent fracture strain  $\epsilon_{qf}$ , determined by the SP test, was carried out in solution treated and isothermally aged new JJ1, JN1 and JK2 steels and the conclusions are summarized as follows:

1. It was found a linear dependence of  $J_{IC}$  value on the  $\epsilon_{qf}$  value, as predicted by Bayoumi and Bassim for the biaxial stress state in an elastic-plastic material. The following linear relation was determined  $J_{IC} = 1304.1 \epsilon_{qf} + 8.09$  ( $\text{kJm}^{-2}$ ) in JN1, JJ1 and JK2 austenitic stainless steels.
2. The slope value  $C_1$  of  $1304.1 \text{ kJm}^{-2}$  is strongly dependent on the determination procedure of fracture toughness  $J_{IC}$  and on the yield strength value.
3. This linear relation can be used to assess the fracture toughness in both isothermally aged and welded JN1, JJ1 and JK2 steels.

### Acknowledgements

The authors wish to thank the financial support from SIP-COFAA-IPN and Fondo Sectorial para la Educacion-CONACYT 100584.

### References

1. H. Nakajima, K. Yoshida, and S. Shimamoto, "Development of New Cryogenic Steels for the Superconducting Magnets of the Fusion Experimental Reactor", *ISIJ International*, 30 (1990) 567-578.
2. H. Nakajima, Y. Nunoya, M. Nozawa, O. Ivano, K. Takano, T. Ando and S. Ohkita, "Development of High Strength Austenitic Stainless Steel for Conduit of Nb<sub>3</sub>Al Conductor", *Advances in Cryogenic Engineering*, 42 A (1996) 323-330.
3. J. Kameda and O. Buck, "Evaluation of the Ductile-to-Brittle Transition Temperature Shift due to Temper Embrittlement and Neutron Irradiation by Means of a Small Punch Test", *Journal of Materials Science*, 83 (1986) 29-38.
4. T. Misawa, T. Adachi, M. Saito and Y. Hamaguchi, "Small Punch Tests for Evaluating Ductile-Brittle Transition Behavior of Irradiated Ferritic Steels", *Journal of Nuclear Materials*, 150 (1987) 164-202.
5. X. Mao and H. Takahashi, "Development of a Further-Miniaturized Specimen of 3 mm Diameter for TEM Disk Small Punch Tests", *Journal of Nuclear Materials*, 150 (1987) 42-52.
6. X. Mao, T. Shoji, and H. Takahashi, "Characterization of Fracture Behavior in Small Punch Test by Combined Recrystallization-Etch Method and Rigid Plastic Analysis", *Journal of Testing and Evaluation*, 15, (1987) 30-37.
7. T. Misawa, S. Nagata, N. Aoki, J. Ishizaka and Y. Hamaguchi, "Fracture Toughness Evaluation of Fusion Reactor Structural Steels at Low Temperatures by Small Punch Tests", *Journal of Nuclear Materials*, 169 (1989) 225-232.
8. H. Kwon, S. Cheng, M. L. Saucedo M., T. Hashida and H. Takahashi, "Determination of Cryogenic Fracture Characteristics of Austenitic Stainless Steel JN1 Welded Joint and Heat-Treated Materials by Means of Small Punch Testing Method", *Trans JSME*, 63A (1997) 61-67.
9. M. R. Bayoumi and M. N. Bassim, "Study of the Relationship between Fracture Toughness ( $J_{IC}$ ) and Bulge Ductility". *Int. J. Fracture*, 23 (1983) 71-79.

## **EFFECT OF HEAT TREATMENT ON THE SURFACE CHARACTERISTICS OF AISI D2 STEEL MACHINED BY WIRE EDM**

M. M. Dhobe<sup>1</sup>, I. K. Chopde<sup>1</sup>, C.L. Gogte<sup>2</sup>

1. Mechanical Engineering Department, VNIT, Nagpur. (M.S)

2. Mechanical Engineering Department, MIT, Aurangabad. (M.S)

Keywords: - Heat treatment, Hardness, Surface roughness, white layer, W-EDM

### **Abstract**

The quality of machined surface is becoming more and more important to satisfy the increasing demand of component performance and its reliability. While machining any component, it is necessary to satisfy the surface integrity requirements. Heat treatment plays an important role in improving the characteristics of the material.

This work investigates the effect of heat treatment on the surface characteristics of AISI D2 tool steel after Wire-Electro Discharge Machining (W-EDM). The test specimens were prepared by hardening and tempering and then machined with Wire-Electro Discharge Machining process. Optical and scanning electron microscopy, surface roughness and micro hardness tests were conducted to study the surface characteristics of the machined surface.

After characterization based on microstructures and test results, it is observed that the recast layer droplets are of smaller size with reduced white layer thickness resulting in higher hardness and lower surface roughness.

### **Introduction**

With the development of mechanical industry, the requirement of alloy materials having high hardness, toughness and impact resistance is increasing. At the same time the quality of machined surface is becoming more and more important to satisfy the increasing demands of component performance and reliability. When machining any component, it is necessary to satisfy the surface integrity requirements. Surface integrity has two important parts. The first is surface texture, which governs mainly surface roughness. The second is surface metallurgy, which concerns to the nature of surface layer produced in machining [2].

Wire Electrical discharge machining (W-EDM) is nontraditional manufacturing process where the material is removed by a succession of electrical discharges, which occur between the electrode and work piece. These are submerged in a dielectric liquid such as de-ionized water. During the electrical discharge, a discharge channel is created where the temperature reaches approximately 12000 °C, removing the material by evaporation and melting. When the discharge ceases there is a fast cooling on the surface of work piece creating a zone affected by heat that contains the white layer. This layer contains several hollow, spheroids, fissures and micro fissures. Carbon is the main element of the white layer composition influencing simultaneously its hardness and thermal conductivity. The white layer caused by W-EDM process increases surface roughness, makes the surface hard and brittle and decreases the fatigue strength. The white layer thickness depends on the work piece material, on the power used to cut the work piece and on the applied electrical polarity[3]. Wire

Electrical discharge machining is governed by a thermal phenomenon, therefore not only removes material from the work piece but also changes the metallurgical constituents in the zone affected by the heat. Thus, during machining by W-EDM the surface of the material is subjected to heat treatment (locally) where the time of stage is the pulse duration and the temperature reached by the work piece is due to the applied current intensity being followed by a quick cooling[7].

The Wire-EDMed surface consists of many craters caused by electrical sparks. The larger the electrical discharging energy, the worse the surface quality will be. A large energy will produce a rippled surface, changes the structure and physical properties of material and result in cracks and residual stresses on the surface[4]. Ultimately the surface quality and life of the work piece will be decreased as well. The electrolytic erosion, which may occur during the process, will result in more micro cracks and lower surface hardness. Thermal nature of this process always produces a recast and underlying heat affected zone on the surface being machined and develops a residual tensile stress that often causes micro cracks [6, 7].

The thermal sensitivity or chemical complexity of the material can also affect the surface integrity. Optimum utilization of the capability of the Wire-EDM process requires the selection of an appropriate set of machining parameters. Hence the machining parameters should be chosen properly according to work piece properties so that better performance can be obtained. However, selection of appropriate machining parameters is difficult and relies heavily on the operators experience and machining parameters tables provided by the machine tool manufacturer. But these alternatives completely do not satisfy the requirements of both high efficiency and good quality. Hence in order to obtain the good surface properties after machining it is always essential to improve the internal structure and properties of the material by hardening and tempering appropriately[1,2].

Several studies have been carried out in order to determine appropriate work material/ machining parameters combinations to analyze surface integrity. These studies shows that the surface roughness is closely depend on the machining parameters. The structural changes of EDMed surface of steels have been studied and found that the top-most surface layer is non etchable layer, namely the white layer. Immediately beneath this layer, there is a heat affected zone, where heat causes micro structural transformations [2,3]. Relationship between EDM parameters and surface crack formation for D2 and H13 tool steel was studied. It was shown that crack formation and white layer thickness is related to the EDM parameters. An increased pulse on duration will increase both white layer thickness and induced stress[4,7,8]. Therefore in this paper it is tried to investigate the effect of heat treatment on surface integrity of AISI D2 tool steel used in manufacturing die and mould components by Wire EDM process.

## **Experimental**

### **Experimental And Measuring Apparatus**

The machine used for experimentation work is “spring cut” Electronica Make Wire EDM. The composition of AISI D2 steel used for experimentation is given in Table I. CuZn37 master brass wire with 0.25 mm diameter was used as an electrode. De-ionized water ( Ph Value 12.5) was used as the dielectric fluid. A Taylor Hobson make, surface finish Tester is used to measure the surface roughness. A SEM is used to investigate microstructure.

Table I. Chemical Composition of AISI D2 Steel (Wt %)

Sr.No	Constituent	Wt %	Range as per Standard
01	Carbon	1.57	1.40 - 1.60
02	Manganese	0.51	0.20 - 0.40
03	Chromium	12.50	11.50 - 12.50
04	Nickel	0.06	-
05	Molybdenum	0.41	0.70 - 0.90
06	Sulphour	0.024	-
07	Phosphorus	0.009	-
08	Silicon	0.40	0.10 - 1.0
09	Vanadium	0.25	0.20 - 1.0

### Specimen Preparations

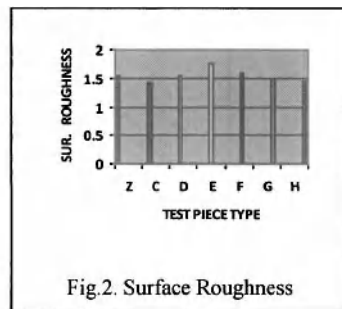
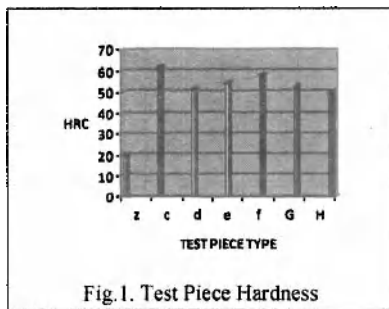
The specimens of die steel AISI D2 of 15 X 15 X 50 mm size are prepared by milling before heat treatment. The specimens are then hardened and tempered in different ways as shown in the Table II. The specimens are then machined by W-EDM process to obtain 15X15X9 mm thick test pieces. During machining the machining parameters i.e. pulse interval time (16  $\mu$ s), table feed rate (7.6mm/min), Wire tension (1800 g), pulse current on, pulse Current off, and Voltage were kept constant.

### Measurements

The hardness and the surface roughness of the machined test pieces is measured and tabulated in the Table II and its variation is presented graphically in Fig. 1 and 2 respectively. The machined surface is then prepared as per standard procedure for metallographic observations. Etching was done using 5% Nital reagent. The prepared surface is viewed under scanning electron microscope (SEM) for examining surface topography and is cross section for measuring white layer depth. The images of surface topography and white layer depth are shown in the Fig. 1-8. White layer depth from cross-section of machined surface was measured to determine its variation through heat-affected zone.

Table II Test Specimen Types, its Hardness and surface roughness

Sr.No	Type of Heat treatment	Notation	Hardness	Surface
			HRC	Roughness $\mu\text{m}$
01	As Annealed	Z	20.00	1.54
02	Hardened single tempered 250° C	C	62.33	1.43
03	Hardened double tempered 250° C	D	51.33	1.55
04	Hardened triple tempered 250° C	E	54.34	1.76
05	Hardened single tempered 450° C	F	58.33	1.59
06	Hardened double tempered 450° C	G	52.66	1.49
07	Hardened triple tempered 450° C	H	50.00	1.45



## Results and Discussion

### Surface Topography

During W-EDM each electrical discharge generates intense amount of heat, causing local melting or even evaporation of the work piece material. With each discharge, a crater is formed on the work piece and a smaller crater is formed on the tool electrode. Of the molten metal produced by the discharge, only 15% or less is carried away by the dielectric [8]. The remaining melt re-solidifies to form an undulating terrain. After magnification, the surface is observed to be covered with overlapping craters, globules of debris, and pocket marks or 'Chimneys', formed by entrapped gases escaping from the re-deposited material. Fig.3-6 shows typical topography of test pieces viewed under SEM. Variation of re-solidified craters are compared as circular and elongated one and are tabulated in Table III-VI.

The topographical images and table shows that the elongated and circular shaped droplets size is large in Z type and is small in C type specimen. At the same time more craters are formed in layers on the same surface, thereby increasing the surface roughness. In C type test piece the elongated droplets spread over the surface with few pocket marks of escaped gases. Where as in case of type E, droplets are more elongated and very few are in circular form and they spread over the area. In case of D type, droplets are more in circular shape and concentrated at a location like resolidified layers one above the other.

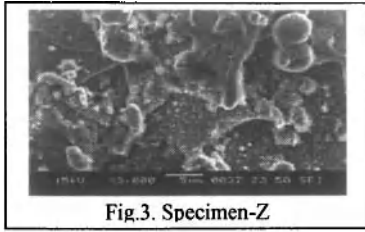


Fig.3. Specimen-Z

Table-III Specimen-Z		
Droplets Size	Circular in $\mu\text{m}$	Elongated in $\mu\text{m}$
Minimum	01	02
Maximum	05	20

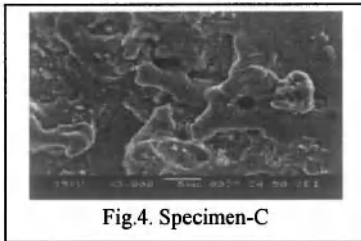


Fig.4. Specimen-C

Table-IV Specimen-C		
Droplets Size	Circular in $\mu\text{m}$	Elongated in $\mu\text{m}$
Minimum	01	02
Maximum	03	12

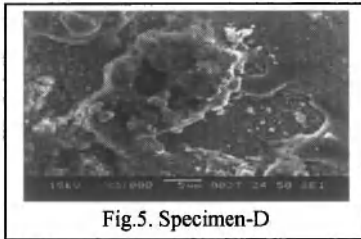


Fig.5. Specimen-D

Table-V Specimen-D		
Droplets Size	Circular in $\mu\text{m}$	Elongated in $\mu\text{m}$
Minimum	01	02
Maximum	05	13

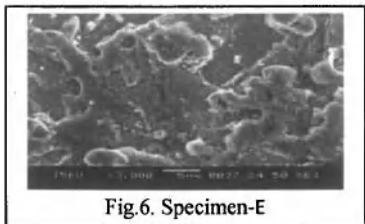
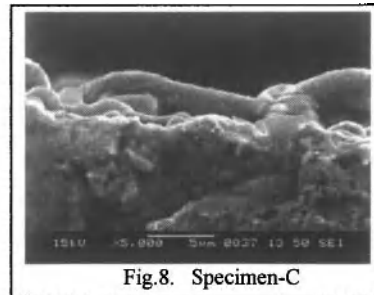
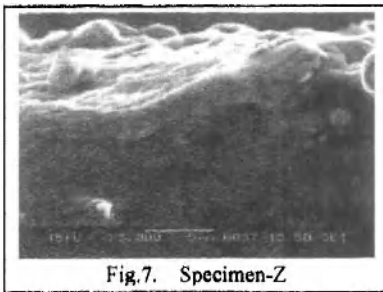


Fig.6. Specimen-E

Table-VI Specimen-E		
Droplets Size	Circular in $\mu\text{m}$	Elongated in $\mu\text{m}$
Minimum	02	03
Maximum	06	15

### White Layer Thickness

The term 'white layer' is originated from the fact that these surfaces appear white under an optical microscope or featureless in a scanning electron microscope (SEM). Thus, in literature, the term white layer is used as a generic phrase referring to very hard surface layers formed in ferrous materials under a variety of conditions, which appear white under the microscope. The earliest mention of the presence of hard white layer on surface was in the year 1912 by Stead, who observed white etching layers on the surface of used steel wire ropes. He interpreted this as the formation of martensite as a result of frictional heating in service followed by quenching due to colder sub layers[3]. White layers in their different forms are as a result of factors attributed to the material removal process, such as thermal, mechanical or chemical unit events. These can be directly related to such factors as strain rate, heating rate, cooling rate and local environmental operating conditions. The typical depth of a white layer zone is approximately 10  $\mu\text{m}$  however, the depth can vary depending on the thermal, mechanical or chemical properties present. Below the white layer, there is a relatively shallow transition into the bulk material which is largely unaffected thermally by the machining process. The mechanical properties of the bulk should be similar to that of the original workpiece material. While machining a workpiece with W-EDM, a multilayered heat affected zone is formed at the surface of workpiece. The upper layer of this zone is the white layer, which has a different microstructure and metallographic characteristics than the base material. Kruth reported a light zone on the machined surface consisting of several cracks. The cracks were mostly perpendicular to the surface of the sample, running across the total depth of the white layer and only seldom continued to the layers underneath[3.6]. Fig.7 -10 shows the photographs of white layer formed on test pieces after W-EDM. The 'white layer' thickness observed is an average of readings measured at various places on different cross-sections of the specimen concerned. The data obtained for different test pieces is tabulated in Table VII and same is graphically presented in Fig11. It shows that in Z type test piece the white layer thickness observed is the highest where as in case of C type it is minimum. Thus it shows that softer the material higher is the thickness and vice-versa. Though the machining parameters such as cutting temperature, depth of cut, cooling media contribute a lot in formation of white layer but still hardening and tempering also affects its formation.



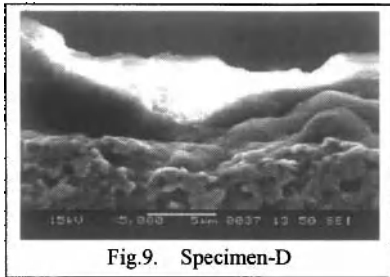


Fig.9. Specimen-D

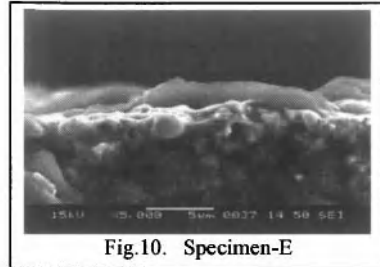


Fig.10. Specimen-E

Table VII. White Layer Thickness

Sr.No	Test piece type	Thickness in mm		Thickness in $\mu\text{m}$
		Readings in mm	Avg. mm	
01	Z	09,10,07,07,05	7.6	5.8
02	C	07,08,05,08,06	6.8	5.2
03	D	07,09,05,07,08	7.2	5.5
04	E	05,10,08,06,06	7.0	5.3

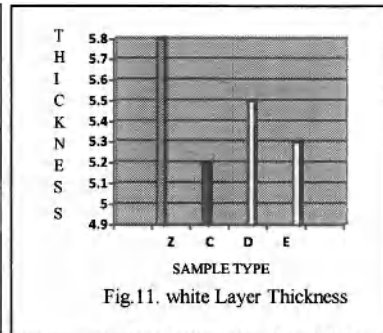


Fig.11. white Layer Thickness

### Conclusions

In order to examine the effects of heat treatment on the surface machined by W-EDM, specimen test pieces of die steel AISI D2 were prepared by hardening and tempering in different ways and then machined. To summarize the main features of the present experimental work, the following conclusions can be drawn:

1. Because of heat treatment, hardness increases with hardening and single tempering. At the same time it slightly goes on decreasing with double and triple tempering. Specimen C gives higher hardness than others (type D-H).
2. As seen from the Table II, there is small variation in surface roughness in all the specimens heat treated in different ways. The surface roughness mainly depends on machining parameters. Even after keeping machining parameters constant during this study, specimen type C gave smoother surface compared to others.
3. The topographical image shows that the surface texture is composed of a random array of overlapping craters or cusps after machining. These are formed due to the rapid heating and cooling during WEDM. Though, the machining parameters are more responsible for its formation, specimen type C shows circular and elongated droplets of minimum size where as type E shows elongated droplets of maximum size.

4. After examining the cross section of machined surface, the four zones were identified in which outermost surface is debris or recast layer and next layer is white layer. Below the white layer is an area which was heated and cooled more slowly. This created an annealed area, softer than the parent material. Finally parent material is present. The thickness of the heat affected zone or white layer on the surface is measured and tabulated in Table VII and found that the average minimum thickness is observed in case of C type specimen.

#### References

1. K.K.Choi, W.J.Nam and Y.S.Lee, "Effects of heat treatment on the surface of a die steel STD 11 machined by W-EDM", *Journal of materials processing Technology*, 201 (2008), 580-584.
2. Ahmet Hascalyk, Ulas Catdas, "Experimental study of wire electrical discharge machining of AISI D5 tool steel", *Journal of materials processing Technology*, 148 (2004), 362-367.
3. S.S. Boshkeh and P.T.Mativenga, "White layer formation in hard turning of H13 tool steel at high cutting speed using CBN tooling", *International Journal of Machine Tools and Manufacture*, 46 (2006), 225-233.
4. J.C.Rebelo, A. Moarao Dias, D. Kremer and J.L.Lebrun, "Influence of EDM pulse energy on the surface integrity of martensitic steels", *Journal of materials processing Technology*, 84 ( 1998), 90-96.
5. M. Yu. Akhmedpashev, "A study of Heat treated carburized alloyed steels for blanking dies", *Journal of Material Science and Heat Treatment* , 49 (2007), 11-12.
6. Y.S.Liao, J.T. Huang and Y.H. Chen, "A study to achieve a fine surface finish in W-EDM", *Journal of Material Processing Technology*, 149 (2004), 165-171.
7. Ashan Ali Khan, Munira Bt. Mohd Ali and Norhashimah Bt. Mohd Shaffiar, "Relationship of Surface Roughness with Current and Voltage during W-EDM", *Journal of Applied Sciences*, 6(10) (2006), 2317-2320.
8. M.A.E.R. Merdan, and R.D. Amell, "The surface integrity of a die steel after electro discharge machining, 2. Residual stress distribution", *Surface Engineering*, 7(2) (1997), 154-158.
9. C.A. Huang, C.C. Hsu and H.H. Kuo, "The surface characteristics of P/M high-speed steel (ASP 23) multi-cut with wire electrical discharge machine (WEDM)", *Journal of Material Processing Technology*, 140 (2003) 298-302.

## HOT DEFORMATION STUDY BY PROCESSING MAPS OF N CONTAINING MICROALLOYED STEEL

M. Dikovits<sup>1</sup>, C. Poletti<sup>1</sup>, F. Warchomicka<sup>2</sup>, G.P. Chaudhari<sup>3</sup>, V. Pancholi<sup>3</sup>

<sup>1</sup>IWS - Institute for Materials Science and Welding, Graz University of Technology  
Kopernikusgasse 24, A-8010 Graz, Austria

<sup>2</sup>IMST – Institute of Materials Science and Technology, Vienna University of Technology  
Karlsplatz 13/E308, A-1040 Vienna, Austria

<sup>3</sup>IITR – Department of Metallurgical and Materials Engineering, Indian Institute of Technology  
Roorkee, Roorkee 247 667 (UA) India

Keywords: Hot deformation, Processing maps, Microalloyed steel

### Abstract

The hot formability of a microalloyed steel with 0.16 wt-%C modified with N is studied by using processing maps. Compression tests of cylindrical samples are carried out using a Gleeble<sup>®</sup>3800 simulator in the range of temperature between 750 – 1000°C and strain rates between 0.01 – 100 s<sup>-1</sup>. For this alloy, an A<sub>r3</sub>-temperature about 740°C is determined by means of dilatometry. Processing maps are calculated using the modified dynamic material model developed by Murty and Rao for different logarithmic strains. For the instability map, the parameter  $\kappa_j$  developed by the authors in previous works is used and compared with other instability values. Softening in the flow curves provoked by induced ferrite during deformation at low temperatures and low strain rates is reflected in the  $\eta$ -value. Light optical microscopy (LOM) and electron back scattered diffraction (EBSD) measurements are used to study the microstructure of the hot deformed samples to determine the deformation mechanisms active and to verify the processing maps.

### Introduction

Processing maps offer a good possibility to optimize thermomechanical process parameters and to avoid defects in the products. Prasad et al. [1] developed the processing maps using the dynamic material model (DMM) and Murty & Rao [2] modified it. Processing maps consist of two superimposed maps: the dissipation efficiency and the instability map. The processing maps can be used to detect areas with a good hot formability, which are normally related to restoration of the material by dynamic recovery/recrystallization. For a high dissipation efficiency value and no instabilities, a good hot formability is predicted. In the DMM no storage of energy takes place and so the material is considered essentially dissipative, this is only true for high temperatures and high strain rates [1]. If the power of dissipation  $P$  can be separated into two phenomena

$$P_{T,\dot{\epsilon}} = \sigma \dot{\epsilon} = G + J = \int_0^{\dot{\epsilon}} \sigma d\dot{\epsilon} + \int_0^{\sigma} \dot{\epsilon} d\sigma \quad (1)$$

where  $G$  is related to the thermal transport within the sample and  $J$  to the microstructural changes during deformation [3]. The efficiency of power ( $\eta$ ) is defined as:

$$\eta = \frac{J}{J_{max}} = \frac{2J}{P} \quad (2)$$

The  $\eta$  value determined by Murty and Rao [4] is calculated using the following equations

$$G = \int_0^{\dot{\epsilon}} \sigma d\dot{\epsilon} = \int_0^{\dot{\epsilon}_{min}} \sigma d\dot{\epsilon} + \int_{\dot{\epsilon}_{min}}^{\dot{\epsilon}} \sigma d\dot{\epsilon} = \left[ \frac{\sigma \dot{\epsilon}}{m+1} \right]_{\dot{\epsilon}=0}^{\dot{\epsilon}_{min}} + \int_{\dot{\epsilon}_{min}}^{\dot{\epsilon}} \sigma d\dot{\epsilon} \quad (3)$$

$$\eta = \frac{2J}{P} = \frac{2(P-G)}{P} = 2 \left( \frac{1 - \left( \int_0^{\dot{\epsilon}} \sigma d\dot{\epsilon} \right)}{\sigma \dot{\epsilon}} \right) \quad (4)$$

where  $m$  is the strain rate sensitivity and it is defined as [2]:

$$m = \frac{\partial \log \sigma}{\partial \log \dot{\epsilon}} \quad (5)$$

On the other hand, flow instability occurs when,

$$\frac{dD}{d\dot{\epsilon}} < \frac{D}{\dot{\epsilon}} \quad (6)$$

where  $D$  is the dissipation function. If  $D = P$  instabilities occur when [5]:

$$\frac{dP}{d\dot{\epsilon}} < \frac{P}{\dot{\epsilon}} \Rightarrow \dot{\epsilon} \frac{\partial \sigma}{\partial \dot{\epsilon}} + \sigma < P \Rightarrow m < 0 \quad (7)$$

In the case of  $D = J$ , Murty and Rao predict flow instabilities when  $\kappa < 0$  [6]:

$$\kappa = \frac{2m}{\eta} - 1 \quad (8)$$

To avoid the use of  $m$  in the calculation of  $\kappa$ , flow instability is predicted when  $\kappa_j$  is negative [7]:

$$\kappa_j = 1 - \frac{\partial \log(J)}{\partial \log(\dot{\epsilon})} \quad (9)$$

At high temperatures the deformation in low alloyed steel takes place in the austenite phase. The process of dynamic recovery in austenite is low because of the low stacking fault energy of the fcc phase, so dynamic recrystallization occurs [8]. This work is focused on the deformation behaviour of a microalloyed steel modified with N at different temperatures above  $A_{r3}$  during compression tests by processing maps and microstructure observation.

## Experimental

### Material

The main alloying elements of the N containing microalloyed steel can be seen in Table I [9]. The  $A_{r3}$  temperature for this alloy is around 740°C which is determined by means of dilatometry at 1 K/s.

Table I. Chemical composition in wt-% of the main elements

C	Mn	V	N	Ti	Si	Nb	Al
0.155	1.460	0.051	0.0108	0.002	0.020	0.002	0.026

### Compression Tests

Compression tests were performed using a Gleeble®3800 simulator. Cylindrical specimens of 15 mm length and 10 mm diameter were deformed at temperatures between 750°C – 1000°C and strain rates from 0.01 – 100 s<sup>-1</sup> up to 0.7 of global true strain. The temperature during the experiment was controlled with a K - thermocouple welded in the middle of the sample. A nickel based lubricant and a tantalum foil were used to reduce the temperature gradient and the friction between the sample and the anvils. The samples were heated at 5 K/s up to 1000°C, held for 2 minutes and then cooled down to the deformation temperature with a cooling rate of 1 K/s. The samples were in situ water quenched immediately after the deformation with a cooling rate of about 360 K/s.

### Metallography

Before and after the deformation the samples were cut along the deformation axes, embedded and polished. Light optical microscopy (LOM) and EBSD measurements were done to get information about the microstructure before and after deformation. The samples were etched with Nital (3%) for light optical microscope. The EBSD measurements were carried out with the samples tilted 70°, an accelerating voltage of 25 kV and a spot size of ~6 nm. An increment step of 0.1 µm was used and the confidence index (CI) average values of each measurement (raw data) were higher than 0.55.

## Results And Discussion

### Flow Behaviour

The flow curves at three different temperatures at 750°C, 900°C and 1000°C are shown in Figure 1. A ringing effect is observed for deformations at 100 s<sup>-1</sup> of strain rate due to vibrations in the system whose affect the signal of the load cell [10]. This signal can be misunderstand as typical

oscillations of dynamic recrystallization [8]. The flow curves at low strain rates ( $0.01 - 0.1 \text{ s}^{-1}$ ) exhibit softening independent on the temperature. At  $1 - 10 \text{ s}^{-1}$  steady state is observed.

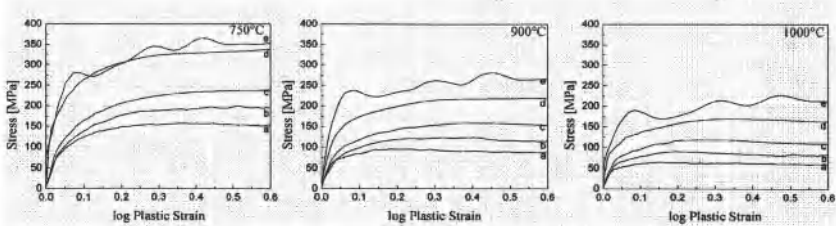


Figure 1. Flow curves at  $750^{\circ}\text{C}$ ,  $900^{\circ}\text{C}$  and  $1000^{\circ}\text{C}$  for different strain rates.  
 $a = 0.01 \text{ s}^{-1}$ ,  $b = 0.1 \text{ s}^{-1}$ ,  $c = 1 \text{ s}^{-1}$ ,  $d = 10 \text{ s}^{-1}$ ,  $e = 100 \text{ s}^{-1}$

### Microstructure

Microstructure Before Hot Deformation. The microstructure of a sample heat treated at  $1000^{\circ}\text{C}$  and water quenched afterwards is shown in Figure 2. The micrograph shows a lamellar structure and a little amount of ferrite on the grain boundaries.

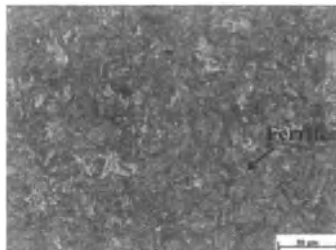


Figure 2. Microstructure evolution after heat treatment at  $1000^{\circ}\text{C}$  for 2 min, a heating rate of  $5 \text{ K/s}$  and water quenching

Microstructure After Hot Deformation. Figure 3 shows the microstructure evolution of deformed samples up to a true strain of 0.7 for different parameters. An increment of the ferrite amount when increasing the strain rate, could be determined in the not fully austenitized microstructure. An influence of the strain rate on the grain size was distinguished with a decrement of the grain size when increasing the strain rate for temperatures higher than  $900^{\circ}\text{C}$ . In Figure 4 a) at low temperatures ( $750^{\circ}\text{C}$ ) a small grain size (compared to the same strain rate at higher temperatures) as well as a high amount of ferrite could be detected for the smallest strain rate of  $0.01 \text{ s}^{-1}$ . No indication of defects like pores were identified in the samples.

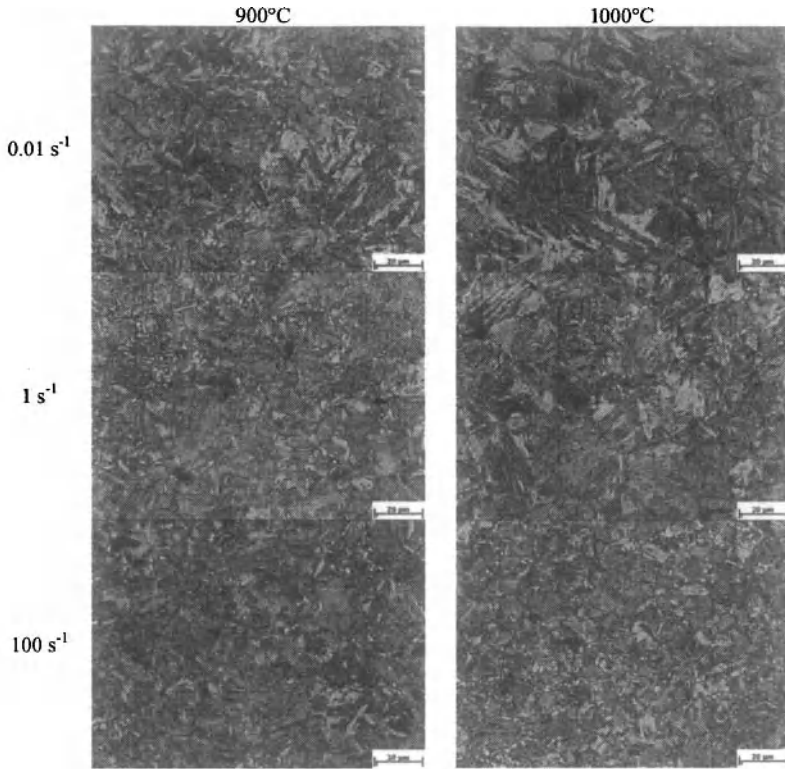


Figure 3. Microstructure evolution of water quenched samples after compression at 900°C and 1000°C for 0.01 s<sup>-1</sup>, 1 s<sup>-1</sup> and 100 s<sup>-1</sup>; compression axis is vertical.

**EBSD – Measurement.** In Figure 4 b) and c) two inverse pole figure maps are shown for 750°C and 1000°C for a strain rate of  $0.01 \text{ s}^{-1}$ . The grains of the low temperature deformed sample show a globular structure with a big amount of ferrite, while the sample deformed at high temperature shows a lamellar microstructure with a few globular grains of ferrite.

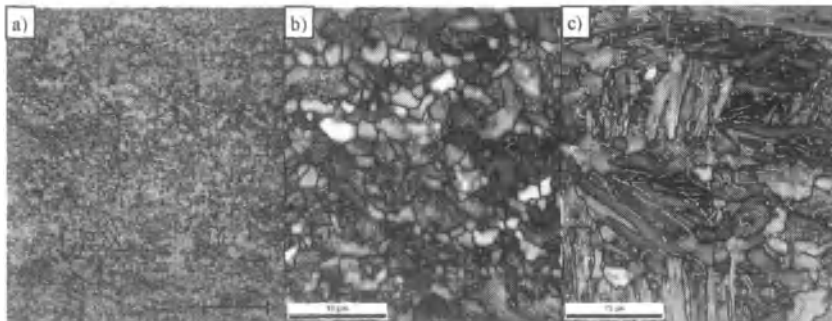


Figure 4. a) LOM of a water quenched sample deformed at  $750^\circ\text{C}$  for  $0.01 \text{ s}^{-1}$ ; b) and c) EBSD Inverse Pole Figure Map of samples deformed at  $750^\circ\text{C}$  (b) and  $1000^\circ\text{C}$  (c) for a strain rate of  $0.01 \text{ s}^{-1}$ . Grain boundaries (black) are defined from  $15 - 180^\circ$  and subgrain boundaries (white) from  $3 - 15^\circ$ . Compression axis is vertical.

### Processing Maps

The processing maps were implemented using OriginPro 8 Software. For calculating them, the flow data was used as described in [4]. The flow data at all strains were used to build the models. In Figure 5 processing maps are calculated using the model of Murty and Rao and are shown for a strain of 0.3 and 0.6. Additionally, the strain rate sensitivity is compared. The isolines represent the value of  $m$  or  $\eta$ , and the dashed zones predict instability by  $\kappa < 0$  and  $\kappa_f < 0$ .

The  $m$  values are positive in the whole tested range, and increase by increasing the temperature. In both ranges: temperature below  $875^\circ\text{C}$  and strain rates below  $0.1 \text{ s}^{-1}$ , and temperature above  $875^\circ\text{C}$  for all strain rates, the  $m$  values increase with the strain. A similar tendency shows the  $\eta$  value with the strain. In the low temperature range,  $\eta$  values are large at moderate strain rates, and very low at low and high strain rates. At moderate to high strain rates, the highest  $\eta$  values can be recognized at temperatures above  $850^\circ\text{C}$ .

The different criteria to predict instability result in different values. No instability occurs for the model of  $D = P$  ( $m < 0$ , left column in Figure 5), while the model of Murty and Rao predict instabilities almost in the whole area. The model of  $\kappa_f$  is negative at moderate strain rates and temperatures above  $950^\circ\text{C}$ . Stabilities are then only predicted at low temperatures and low or high strain rates, and the range at low strain rates disappears with increasing strain.

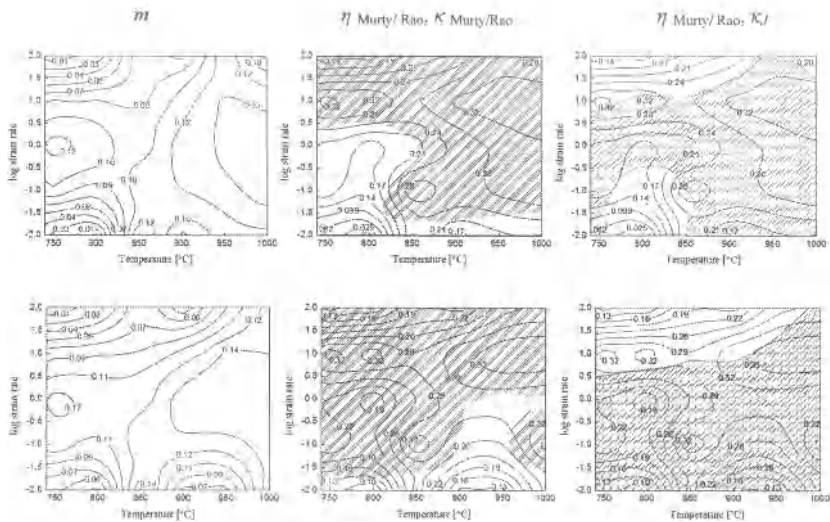


Figure 5. Processing maps, as a function of the temperature and the log strain rate for 0.3 (first row) and 0.6 (second row) of strain.  $\kappa < 0$  (dashed zones)

A summary of the results for the investigated microalloyed steel is given in Table II.

Table II. Comparison of the domains in the processing maps with the flow behaviour

Strain rates [ $s^{-1}$ ]	T [°C]	$\eta$ Murty/Rao	$\kappa$ Murty/Rao	$\kappa_J$	Flow behaviour
0.01 – 0.1	< 850°C	Lowest $\eta$ value.	No instability for 0.01/s. Instability for 0.1/s (strain 0.6) and no instability at strain 0.3.	Stability.	Softening.
	> 850°C	Moderate $\eta$ value.	No instability for 0.01/s. Instability for 0.1/s (strain 0.3) and no instability at strain 0.6.	Instability.	Softening.
0.1 – 10	< 850°C	Moderate $\eta$ value.	Strain 0.3: stability. Strain 0.6: Instability	Instability.	Steady state.
	> 850°C	Highest $\eta$ value increasing with strain.	Strain 0.3: Instability. Strain 0.6: lower strain rates and high temperatures: stability, others: instability.	Instability.	Softening.
10 – 100	< 850°C	Moderate $\eta$ value.	Instability.	Stability.	Steady state.
	> 850°C	High $\eta$ value.	Instability.	Stability.	Steady state.

## Conclusions

Strengthening at low strains, as seen in Figure 1, is due to increment of dislocations density. At a particular strain, for low strain rates softening is seen at low temperatures and if this is compared with the processing maps it is the area with the lowest  $\eta$  value. In this area a big amount of ferrite is formed, which is deformed by dynamic recovery. At high temperatures for low strain rates, moderate  $\eta$  values are dominate in the area. The grains are coarser than at lower temperatures and only a few percentage of ferrite is present. For high temperatures and moderate strain rates, high  $\eta$  values can be seen, while at very high strain rates the value decreases again. The dependence of the grain size with the temperature and the strain rate, and the moderate  $\eta$  values above the 850°C can be related to dynamic recrystallization of austenite. The microstructure shows smaller austenite grains than for samples deformed at lower temperatures and higher strain rates. Two effects should be added to the high temperatures range, which retard recrystallization and result in low  $\eta$  value:

- Due to the incomplete austenitization, ferrite still transforms into austenite by diffusion. This effect is observed at low strain rates which takes place during long times
- Very large strain rates do not promote recrystallization and flow instabilities take place

Damage has not been identified in any analysed sample. The instabilities at high strain rates are related to adiabatic flow, where the increment of temperature was measured about 30°C.

## Acknowledgements

The authors would like to thank FWF (Austrian Science Fund) for funding project number [P22238-N22], Voestalpine Stahl GmbH for the provision of the material, to USTEM (Vienna University of Technology) for the provision of the FIB-SEM EBSD facilities and the OeAD (Austrian Agency for International Cooperation in Education and Research) for funding the project WTZ Indien 2011-12.

## References

- [1] Y.V.R.K. Prasad and H.L. Gegel, "Modeling of Dynamic Material Behaviour in Hot Deformation: Forging of Ti-6264", Metallurgical Transactions A, 15A (1984), 1883-1892.
- [2] S.V.S. Narayana Murty and B. Nageswara Rao, "Ziegler's criterion on the instability regions in processing maps", Journal of Materials Science Letters, 17 (1998), 1203-1205.
- [3] Y.V.R.K. Prasad, "Author's Reply: Dynamic Materials Model: Basis and Principles", Metallurgical and Materials Transactions A, 27A (1996), 235-236.
- [4] C. Poletti, H. Dieringa and F. Warchomicka, "Local deformation and processing maps of as-cast AZ31 alloy", Materials Science and Engineering A, A516 (2009), 138-147.
- [5] S.V.S. Narayana Murty and B. Nageswara Rao, "On the dynamic material model for the hot deformation of materials", Journal of Materials Science Letters, 18 (1999), 1757-1758.
- [6] S.V.S. Narayana Murty and B. Nageswara Rao, "On the hot working characteristics of 2014 Al-20vol% Al<sub>2</sub>O<sub>3</sub> metal matrix composite", Journal of Materials Processing Technology, 166 (2005), 279-285.
- [7] C. Poletti et al., "Hot Deformation Behaviour of Low Alloy Steel", Steel research International, 82 (2011), 710-718.
- [8] F.J. Humphreys and M. Hatherly, Recrystallization and Related Annealing Phenomena (1996).
- [9] B. Skandera, „Development of V-based microalloyed high strength hot strip for production with reduced rolling forces" (Internal Intermediate report, TU Wien, February 2003).
- [10] Dynamic Systems Inc., „Elimination of Load Cell Ringing during High Speed Deformation by Mathematical Treatment" (Application note, New York, 2001).

## **INFLUENCE OF ANNEALING TREATMENT ON MICROSTRUCTURE AND MECHANICAL PROPERTIES OF COLD-ROLLED SHEET OF FE-36NI INVAR ALLOY**

Xiang Jiang, Lijuan Li\*, Xin Xia, Junjun Huang, Qijie Zhai

Modern Shanghai Key Laboratory of Metallurgy & Materials Processing, Shanghai University,  
149 Yanchang Road, Shanghai 200072, China, E-mail: [neullj@163.com](mailto:neullj@163.com)

Keywords: Cold-rolled Invar Alloy, Annealing Treatment, Microstructure, Fracture Morphology, Mechanical Properties

### **Abstract**

Some experiments with different temperatures (1173, 1223, and 1273K) and different annealing times (3, 4, 5, 6min) were carried out on cold-rolled plate of Fe-36Ni invar alloy. The microstructure and the mechanical properties were observed and tested respectively, and the fracture morphology was observed by SEM. The results show that with increasing of the temperature and the annealing time, the austenite grains gradually grow up accompanied by a small amount of annealing twin crystals, meanwhile, its plasticity and toughness are improved, and it is typical ductile fracture under the condition of tensile failure. After annealed at 1223K, the invar alloy has better comprehensive properties than that at the other annealing temperatures, and the grains size is more uniform. Furthermore, when the annealing time is 4min, the invar alloy has the best comprehensive properties.

### **Introduction**

As we known, most metals and alloys expand with increasing temperature. More than one hundred years ago (in 1897), Guillaume observed that Fe-Ni alloy with face-centered cubic (fcc) crystal structure, consisting of 36%Ni, showing a very small thermal expansion coefficient below the ferro-to-paramagnetic transition, the thermal expansion coefficient around room temperature ( $<2 \times 10^{-6} \text{K}^{-1}$  compared to most metallic materials which have a thermal expansion coefficient of  $10\text{-}20 \times 10^{-6} \text{K}^{-1}$ ) [1, 2]. Since then, the subject has attracted many researchers, and various alloys with low thermal expansion coefficients have been developed. These alloys, generally known as “invar alloys”, are in demand where dimensional changes due to variation in temperature must be minimized and where high stability is required [3, 4].

In view of low thermal expansion and good dimensional stability, these alloys are increasingly becoming important for several applications, such as precision measurement instruments, shadow masks, computer terminals, fire safety cutoffs, core wires of long distance power cables, advanced electronic components, and so on [5-8]. Therefore, market demand of invar alloy is very large. But the product quality of 4J36 invar alloy produced by most domestic manufacturer is not stable, which leads to bad plasticity, low strength and other defects. So annealing treatment is a very important process in production procedure of 4J36 invar alloy, because it can directly affect the final product quality. This article focuses on the effect of annealing treatment on the microstructure and mechanical properties of cold-rolled plate of 4J36 invar alloy, and supplies the reference data for rolling process of 4J36 cold-rolled strip in industry.

## Experimental Procedure

The experiment material is cold-rolled sheet of 4J36 invar alloy, and its thickness is 2mm. The chemical composition of this material is listed in Table 1.

Table 1. Chemical composition of the tested 4J36 invar alloy (wt%)

C %	Mn %	S %	P %	Si %	Cr %	Ni %	Fe %
0.018	0.30	0.001	0.009	0.23	0.06	36.25	balance

All the samples were obtained by wire-cut, and the diameter of metallographic specimens is 10mm. Fig.1 shows the geometry and dimension of tensile samples [9], in order to ensure the reliability of the testing results, three pieces of tensile samples were cut for the same heating treatment parameter.

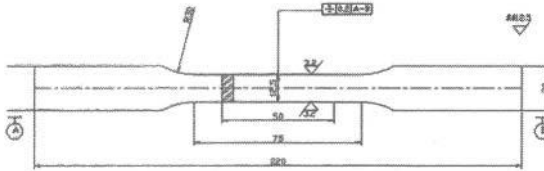


Fig.1. Geometry and dimension of the tensile specimens at room temperature

Then these samples were subjected to the following heat treatments in the box-type resistance furnace: Annealing treated at 1173, 1223 and 1273K for 3, 4, 5 and 6 min, respectively, followed by air cooling. The metallographic specimens were prepared by mechanical polishing followed with chemical etching in a mixture of 4g CuSO<sub>4</sub>, 20ml HCl, 12ml H<sub>2</sub>SO<sub>4</sub>, and 25ml H<sub>2</sub>O, then use metallographic microscope of Nikon LV150 to get the optical microscopy. Tensile test was carried out on electronic universal testing machine CMT5305, and three pieces of samples treated with the same process parameter were tested, and then removed the data of the sample which was broken abnormally. And the fracture morphology was observed by Hitachi SU1510 SEM (scanning electron microscopy). The hardness (HRB) was measured on a Brinell, Rockwell and Vickers tester at load of 100kgf, and each specimen was tested five times and then gets the average value of the data in reason.

## Results and Discussion

### Metallographic Structure

From the phase diagram of Fe-Ni binary alloy (as shown in Figure 2.) [10], there is a  $\alpha+\gamma$  two phases equilibrium structure when the Fe-Ni binary alloy of Ni content 28%-44% (wt%) slowly cools down, but obtains face-centered cubic  $\gamma$  solid solution after rapid cooling. And when Ni content is approximately 36%, 4J36 alloy is of a single  $\gamma$ -phase state without phase transition above 430°C, and  $\gamma$  austenitic structure is very stable.

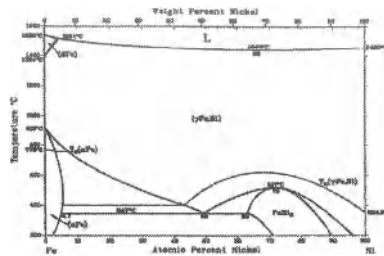


Fig.2. The Fe-Ni binary alloy phase diagram

Metallographs of all the specimens are shown in Fig.3-5. Fig.3 shows that it is a typical rolling structure with single-phase austenite in the original sample (rolling direction parallel to the horizontal plane), and the austenitic crystal grains deformed along the rolling direction can be observed obviously. From Fig.4-5, it is found that they are still single-phase austenite microstructures after annealing treatment, and the austenitic grains of all the samples gradually grow up accompanied by a small amount of annealing twin crystals with the increasing of the temperature and the annealing time, but the grains size is more uniform. The reason why annealing twins occur is that  $\gamma$  austenite has lower fault energy when new grain interface moves forward due to the stacking fault caused by some reasons, such as heat stress, etc [11].

Besides, from Fig.4 (a), it is found that after 1173K for 3min, the recrystallization process has been completed, and the grain size is small. At 1223K, annealing times have little effect on the grain size. However, at 1173K and 1273K, with the increasing of annealing time, the grain sizes increase. In addition, the occurrence of twin crystal is found in almost all the samples, and with the increasing of the temperature and the annealing time, the proportion of twin crystal structure increases, and in some grains, the twin crystals grow across the whole grain. And at 1273K for 6min, the grain size is larger than that in the sample after any other process.

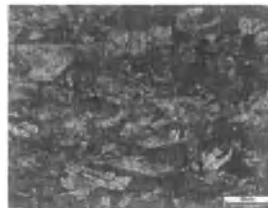


Fig.3. Metallographic structure of cold-rolled sample

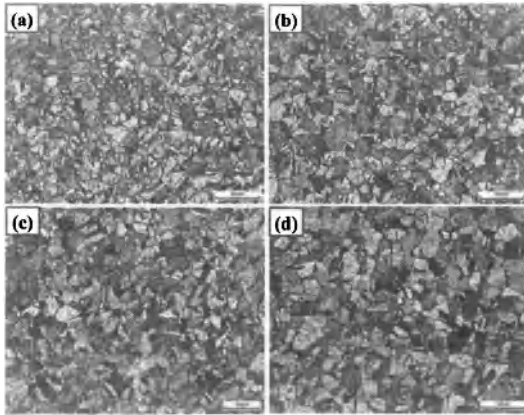


Fig.4. Metallographic structure of samples heated at 1173K, (a) 3 min; (b) 4 min; (c) 5 min; (d) 6 min.

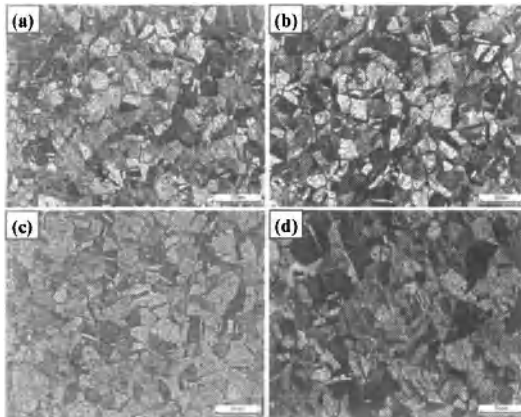


Fig.5. Metallographic structure of samples heated at 1273K, (a) 3 min; (b) 4 min; (c) 5 min; (d) 6 min.

#### The Effect of Annealing Treatment on Mechanical Properties

As the mechanical properties of the plate play an important role in rolling process in industry, the mechanical properties of all the samples are tested. Tensile strength of original sample of 4J36 invar alloy is 723.7MPa, and elongation is 6.4%, and hardness (HRB) is 94.2, respectively. After

deep cold deformation, the grains are elongated and the dislocation density is enhanced leading to the increase of alloy's lattice distortion, therefore the strength and the hardness is very high. In order to satisfy the production following rolling process, we carried on heat treatment to enhance alloy's comprehensive mechanical properties. Fig.6-8 show the effect of annealing time on strength, hardness and elongation at different temperatures.

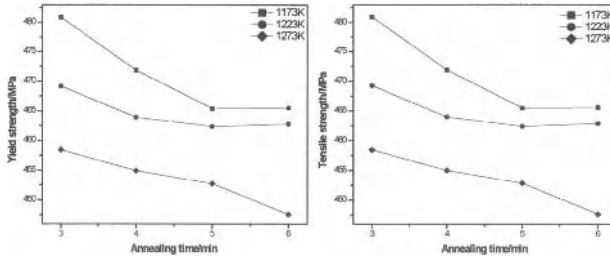


Fig.6. Curves of yield strength and tensile strength changed with different temperatures and annealing times

Fig.6 shows that with the increasing of heating temperature and annealing time, the yield strength and tensile strength of 4J36 invar alloy sharply decline and have little difference among them. And when the annealing time is less than 5min, strength of 4J36 alloy declines, furthermore in details; the higher the temperature is, the more obviously the strength decreases. While when the annealing time is more than 5min, the strength decreases to a minimum value, and at 1173K and 1223K, the strength of 4J36 alloy will not change any more.

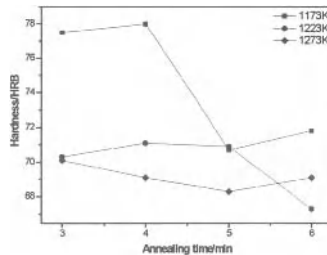


Fig.7. Curves of hardness changed with different temperatures and annealing times

As shown in Fig.7, the hardness of 4J36 invar alloy drops sharply with the increasing of heating temperature and annealing time compared with the original sample. However, the hardness of 4J36 alloy treated at 1173K is always higher than those that treated at 1223K and 1273K. At 1223K and 1273K, the minimum hardness values are 67.3 and 68.3 respectively which reduce by

28.6% and 27.5% compared with the original sample. The hardness of 4J36 alloy treated at these two temperatures changes little, because their structures become more stable. When the heating temperature is 1223K, the grain size is very uniform seen from metallographic structure, so the hardness has little difference. But at 1273K, the grain size is very big and the twin crystal grows across the whole grain, which results in the decline of hardness.

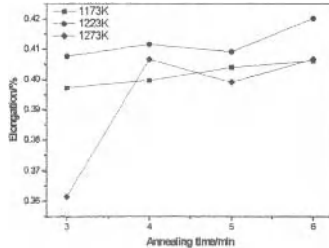


Fig. 8. Curves of elongation changed with different temperatures and annealing times

From Fig. 8, it is found that the annealing treatment can significantly improve the elongation of 4J36 cold-rolled sheet. As a whole, although the elongation improves along with the increasing of annealing times, the elongation of 4J36 invar alloy treated at 1173K and 1223K is more stable than at 1273K, and the elongation of 4J36 alloy treated at 1223K is always higher than those that treated at 1173K and 1273K along with the increasing of annealing time. When the heating temperature is 1223K with the increasing of annealing time, the elongation is getting up to the maximum value 42.0% which is 5 times more than that in original sample.

### Fracture Morphology

Observed from the macroscopic fracture of the sample, no obvious necking near the tensile fracture is seen before and after failure, which showing that the samples happened uniform deformation along the longitudinal direction in the process of tensile deformation, while the contraction of the thwart direction was less. The microscopic fracture morphology of 4J36 invar alloy was observed by SEM which is shown in Fig. 9. It is found that there are many different sizes of dimples in the fracture morphology showing in fig. 9 (b) and (c), while the dimples are fewer and the deformation range near the fracture is very small in Fig. 9 (a). All these results indicate that annealing treatment can significantly improve the ability of plastic deformation of 4J36 cold-rolled alloy. In general, the bigger the depth of dimple is, the better the ability of plastic deformation is [12]. After comparative analysis, the quantity and depth of the dimple of fracture change little, while the elongation changed with different temperatures and annealing times as shown in Fig. 8, and the increasing of heating temperature has little influence on the ability of plastic deformation.

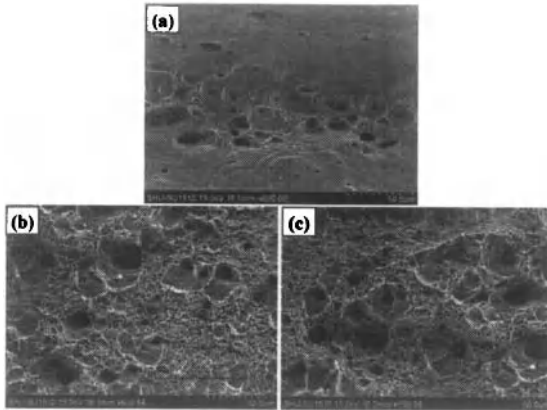


Fig.9. The fracture morphology of samples after different heat treatment  
(a) Original sample; (b) Heated at 1173K, 6min; (c) Heated at 1273K, 6min.

From analysis above, heating temperature and annealing time can directly influence the strength, hardness and plasticity of 4J36 cold-rolled plate. But changes of these properties, will affect the quality of shadow masks, precision instruments and other industrial products manufactured by 4J36 invar alloy. The annealing temperature is too high or the annealing time is too long, it is easy to cause the extension of the product not uniform, and will result in adhesion after annealing, while the annealing temperature is too low or the annealing time is too short, it is easy to make the product out of shape when deformed. Thus, choosing the appropriate heating temperature and annealing time is critical in the heat treatment process of 4J36 invar alloy. Considering the requirements in industry and the experiment results, it is found that 1223K, 4min is appropriate to the rolling process of 4J36 cold-rolled sheet.

### Conclusions

- 1) 4J36 invar alloy is still single-phase austenite microstructure after annealing treatment, and the austenitic equiaxial grains of all the samples gradually grow up accompanied by a small amount of annealing twin crystals along with the increasing of the temperature and the annealing time, and it is typical ductile fracture under the condition of tensile failure.
- 2) The yield strength and tensile strength of 4J36 alloy decline with increasing of heating temperature and annealing time, the higher the temperature is and the longer the annealing time is, the more obviously the strength decreases, and the more sharply the hardness drops.
- 3) As a whole, the elongation improves along with the increasing of annealing time, and the elongation of 4J36 alloy treated at 1223K is always higher than those that treated at 1173K and 1273K, the elongation is getting up to the maximum value 42.0% when the annealing is 6min

which is 5 times more than that in original sample.

4) Considering the requirements in industry and the experiment result, it is found that 1223K, 4min is appropriate to the rolling process of 4J36 cold-rolled sheet.

#### Acknowledgement

This work was financially supported by National Natural Science Foundation (Granted No. 50804028). SEM test was carried out at Instrumental Analysis & Research Center, Shanghai University. The authors also appreciate the Center.

#### References

- [1] L.L. Harner, "Invar at 100 years," *Advanced Materials and Processes*, 151 (5) (1997), 31-34.
- [2] H. Flor, H.J. Guhladt and Ch. Schwink, "Plastic deformation of Fe-Ni invar alloys," *Acta Metallurgica*, 28 (12) (1980), 1611-1619.
- [3] D.D. Johnson, W.A. Shelton, "The Invar Effect: A Centennial Symposium," ed. J. Wittenauer (Warrendale, PA: The Minerals, Metals and Materials Society, 1997), 6374.
- [4] M. Shiga, "Invar alloys," *Current Opinion in Solid State & Material Science*, 1 (3) (1996), 340-348.
- [5] K. Fukamichi, H. Saito, "On new nonferromagnetic B.C.C. Cr-Fe-Mn Invar alloys," *Physica Status Solidi A*, 10 (2) (1972), 129-131.
- [6] A. Ampere et al., "Mechanical and bending characteristics of invar sheets," *Department of Mechanical Engineering and Mechanics*, 17 (2) (1996), 89-96.
- [7] K. Hamada et al., "Effect of processes of drawing on tensional property of high-tensile strength Invar alloy wire," *Wire J. Int.*, 21 (4) (1988), 84.
- [8] I. Michihiko et al., "Development of an Invar (Fe-36Ni) shadow mask for color cathode ray tubes," *IEEE Trans. Electron Devices*, 35 (10) (1988), 1721-1729.
- [9] H.L. Tu, Y. Gan, *Physicochemistry Testing of Metal Materials* (Beijing, BJ: Chemical Industry Press, 2008).
- [10] J.Q. Yu et al., *Atlas of Binary Alloy phase diagram* (Shanghai, SH: Shanghai Science and Technology Press, 1987), 368-369.
- [11] W.X. Song, *Metals Handbook* (Beijing, BJ: Metallurgical Industry Press, 1989), 212-214.
- [12] Y. Zhou, G.H. Wu, *Analysis Methods in Materials Science* (Harbin, HRB: Harbin Industry University Press, 2007), 214.

## **MECHANICAL PROPERTIES OF FRICTION STIR WELDED INCONEL 600/SS 400 LAP JOINTS**

K.H. Song<sup>1</sup>, W.Y. Kim<sup>1</sup>, K. Nakata<sup>2</sup>

<sup>1</sup>KITECH (Korea Institute of Industrial Technology); 7-47, Songdo-Dong, Yeonsu-gu, Incheon, 406-840, Korea

<sup>2</sup>JWRI (Joining and Welding Research Institute); Osaka University, 11-1 Mihogaoka, Ibaraki, Osaka 567-0047, Japan

Keywords: Friction stir welding, Lap joints, Microstructures, Mechanical properties

### **Abstract**

The present study was carried out to evaluate the mechanical properties of friction stir welded Inconel 600/SS 400 lap joints. In this process, friction stir welding (FSW) was performed at a tool rotation speed of 200 rpm and welding speed of 100 mm/min, and argon gas was utilized to prevent surface oxidation during the welding. Application of FSW notably decreases the grain size of Inconel 600 alloy from 20  $\mu\text{m}$  in the base material to 8  $\mu\text{m}$  in the stir zone. However, the grain size of SS 400 in the weld zone was slightly coarsened, when compared to the base material. Also, the hooking in the advancing side and the intermetallic compounds (M7C3) in the weld interface between Inconel 600 and SS 400 were well formed. These intermetallic compounds and hooking were effective to increase in mechanical properties such as tensile and peel strengths.

### **Introduction**

Friction stir welding (FSW), applicable welding process at solid state, has several advantages in defect suppression such as blow hole, segregation and cracking which mainly occurs in fusion welding [1, 2]. Notable grain refinement in the stir zone due to FSW can expect the outstanding increase in mechanical properties of the welds. In constructing the chemical and power plants, Ni base superalloys have been used in many parts, moreover, fusion welding as construct method, such as gas tungsten arc welding, electron beam welding and laser welding, has been mainly used [3-5]. However, fusion welding has a limit in an increase in chemical and mechanical properties in the welds. Lately, Ni base superalloys to which FSW applied have been reported with notable enhancement in mechanical properties, which resulted from refined grains in the welds [6-10]. These researches showed the possibility in applying the FSW, directly.

On the other hands, welding between the dissimilar materials can be used in many ways. FSW as a welding method between dissimilar materials is promising to be a new welding process, and many researches on dissimilar materials (Al/Mg, Al/Steel and Al/Cu) has been reported [11-13]. However, the research on Ni base superalloy and Steel has not been reported thus far. Therefore, this study was carried out to evaluate the microstructures and mechanical properties of lap jointed Inconel 600 and SS 400.

### **Experimental Procedures**

The materials used in this study were Inconel 600 and SS 400. To carry out the FSW, samples were prepared by 200 mm  $\times$  70 mm  $\times$  1 mm (Inconel 600, the upper side) and 200 mm  $\times$  75 mm

× 10 mm (SS 400, the lower side) sheets in size. FSW was conducted using WC-Co tool with 15 mm shoulder in diameter, and 6 mm probe in diameter and 1 mm in length. To obtain a sound welds, the tool was tilted at 3° forward from the vertical, and argon gas was utilized to prevent the surface oxidation during the welding. FSW was performed at a tool rotation speed of 200 rpm, a tool down-force of 22.5 kN and a traveling speed of 100 mm/min. In addition, the two types of welds, in which Inconel 600 alloy is located at advancing side and retreating side, were fabricated by FSW, respectively.

In order to observe the macrostructures and microstructures on the welds, 10 ml HClO<sub>4</sub> and 90 ml CH<sub>3</sub>OH solution was prepared, and samples were electro etched on surface after polished with abrasive paper. Also, to evaluate the microstructure of the welds, scanning electron microscope (SEM) and energy dispersive spectroscopy (EDS) analysis were employed. Evaluation on grain shape, size and grain misorientation of the welds was carried out through electron backscattering diffraction (EBSD) technique. Furthermore, to evaluate the dispersed intermetallic compounds and MC carbides in the lap joint interface, transmission electron microscopy (TEM) analysis was employed. TEM observations were performed at an acceleration voltage of 200 kV. For the evaluation of mechanical properties, Vickers microhardness, tensile and peel test were employed. Vickers hardness was carried out on the cross section of the weld zone with a load of 9.8 N and a dwell time of 15 s. In case of tensile test, two types of tensile test specimens, in which Inconel 600 is located at advancing side and retreating side, were used to evaluate the transverse tensile strength of friction stir lap joints, respectively, as shown in Fig. 1. Two types of peel strength also carried out by similar methods which were applied at tensile tests.

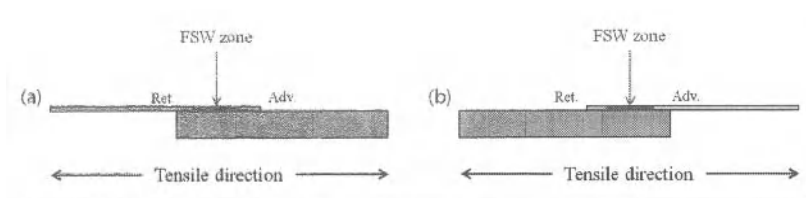


Figure 1. Tensile tested specimens in this study. (a) specimen in which Inconel 600 is located at retreating side and (b) specimen in which Inconel 600 is located at advancing side.

### Results and Discussion

Macrostructure and microstructures of friction stir welded zone are shown in Fig. 2. Cross sectioned macrostructure showed a good weld without defects such as void and cracks well formed at lap joint interface, as shown in Fig. 2(a). Microstructures on lap jointed interface (lowercase letters from b to d in Fig. 2(a)) were observed by SEM. At b and c, jointed interfaces exhibited a good weld interfaces without any weld defect, as shown in Figs. 2(b) and (c), however, a hook was formed at advancing side, along the interface of Inconel 600 alloy from SS 400, as shown in Fig. 2(d).

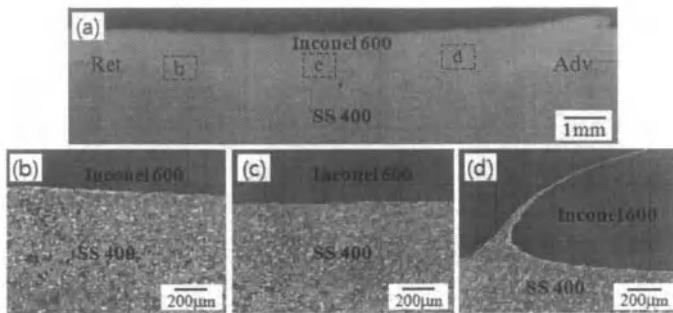


Figure 2. (a) Macro and (b-d) microstructures of jointed materials acquired by SEM. Ret. A and Adv. in figure (a) indicate retreating side and advancing side, respectively. Lowercase letters of b, c and d indicate the lap joint interfaces, and it was magnified at figures (b), (c) and (d), respectively.

Grain boundary maps of Inconel 600 part are shown in Fig. 3. At base material, the grain size in average was approximately 20  $\mu\text{m}$ , and the low angle boundaries in the grain interiors was not observed, as shown in Fig. 3(a). Stir zone consists of significantly refined grains than those of base material, showing the average grain size of 8.5  $\mu\text{m}$ . There is not also observed the low angle boundaries in the grain interiors, as shown in Fig. 3(b). EDS analysis on the hook formed at advancing side of Inconel 600 was carried out, and its results are shown in Fig. 4. Ni and Cr elements in the Inconel 600 area were mainly detected. However, Fe element was strongly detected at the hook area. Therefore, these results show that the hook at the advancing side was formed by SS 400.

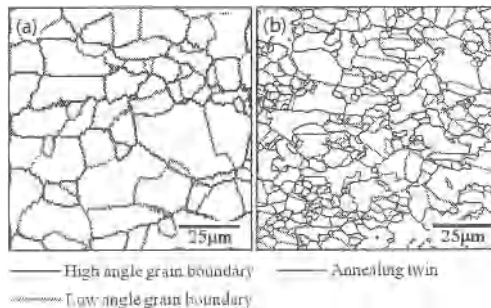


Figure 3. Grain boundary maps of friction stir welded Inconel 600 acquired by EBSD. (a) base material and (b) stir zone.

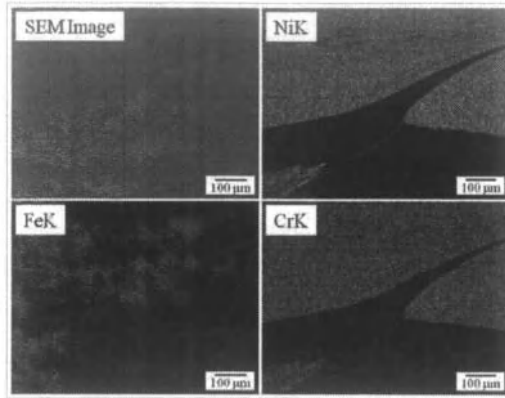


Figure 4. SEM image and EDS results of the hook formed at joint interface between Inconel 600 and SS 400.

Results of TEM analysis on the joint interface of Inconel 600 and SS 400 are shown in Fig. 5. Grains with size from 200 to 500 nm in Inconel 600 alloy were distributed, as shown in Fig. 5(a). Also, MC carbides in the microstructure of Inconel 600 area were partially dispersed with size of 50 nm, which were identified by  $M_7C_3$  carbides, as shown in Fig. 5(b). However, the intermetallic layer at the joint interface of Inconel 600 and SS 400 was not observed.

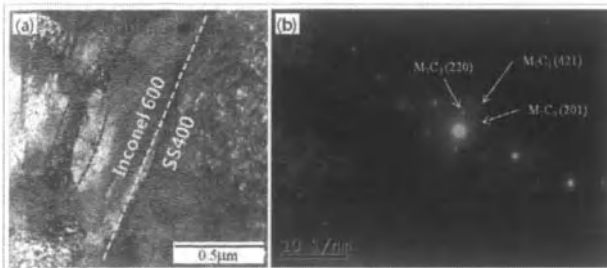


Figure 5. (a) TEM bright field image and (b) selected area diffraction pattern observed at joint interface of Inconel 600 and SS 400.

Microhardness distributions of friction stir lap jointed Inconel 600 and SS 400 are shown in Fig. 6. The base material of Inconel 600 showed the Vickers microhardness values of 200 – 210 Hv, as shown in Fig. 6(a). Application of FSW led to an increase in microhardness, as a result, the microhardness of the stir zone exhibited from 235 to 265 Hv, significantly increased values than those of base material, as shown in Fig. 6(a). Contrarily, SS 400 area below jointed interface showed the decreased microhardness values than those of base material. As a result, the base material and jointed zone below the interface exhibited 190 – 230 and 160 – 190 Hv, respectively, as shown in Fig. 6(b).

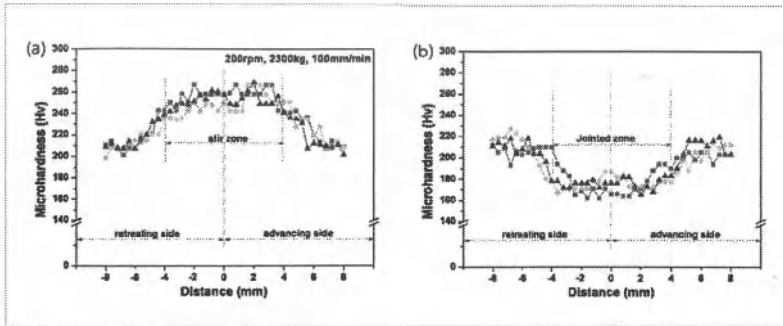


Figure 6. Vickers micro hardness distributions of friction stir welded materials. (a) Inconel 600 and (b) SS 400 areas.

Tensile and peel properties of lap joints are shown in Fig. 7. At base material, yield and tensile strengths were 319 and 656 MPa, with elongation of 51%. Friction stir welded joints showed slightly higher values, as a result, yield and tensile strengths of specimen, in which Inconel 600 alloy is located at advancing side, exhibited 328 and 663 MPa with elongation of 50%, as shown in Fig. 7(a). Specimen welded at retreating side (Inconel 600) showed 346 and 685 MPa in yield and tensile strength, respectively, while elongation was 49%. Results of peel test on friction stir lap joints are shown in Fig. 7(b). Peel strength of the joints exhibited 0.128 and 0.44 kN/mm in adv. and ret. specimens, respectively, significantly higher strength at ret. specimen.

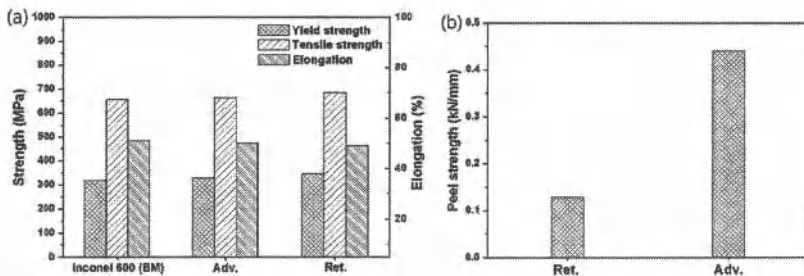


Figure 7. Tensile and peel properties of friction stir welded lap joints.

The material used in this study was Inconel 600 alloy which has low stacking fault energy of FCC metals [14]. In general, these materials can be easily led to the dynamic recrystallization, compared to the material with high stacking fault energy such as Al alloys, while it is difficult to rearrange the dislocation by the dynamic recovery [15, 16]. In other words, the materials with low stacking fault energy can make recrystallization nuclei more easily, compared to the materials with high stacking fault energy. Also, accompanying the higher dislocation density by severe deformation during the FSW can notably promote the recrystallization nuclei in density. Therefore, the recrystallization nuclei can be coincidentally created at the grains and grain boundaries which have a higher density at dislocations. As a result, grain refinement can be obtained by the FSW, as shown in Fig. 3.

Vickers microhardness values of Inconel 600 alloy were significantly increased by FSW. This can be also explained in terms of the smaller grain size in the stir zone than those of the base material by FSW. In microhardness, the base material was ranged between 190 Hv and 215 Hv, however, the stir zone was ranged from 235 Hv to 269 Hv, increased over 20% in frequency when compared to the base material, as shown in Fig. 6(a). These increases in microhardness were caused by the reduced grain size in the stir zone, when compared to the base material. However, microhardness value in SS 400 was decreased in the just below joint interface, as shown in Fig. 6(b), which could be affected by the phase transformation due to the friction heat in the joint interface. Generally, the grain size is affected to the mechanical properties such as hardness and strength, therefore, this work showed clearly the effect of the grain refinement.

The tool probe used in this study was a length of 1 mm, resulted in no penetration in the stir zone of SS 400 side, and joint interfaces between Inconel 600 and SS 400 showed the sound interface without any voids and cracks. Generally, FSW is accompanied with a high tool down force and heat in material, therefore, the interface of materials can be imposed the high pressure and heat, which results in mechanical bonding between the materials [17]. At lap joining, the formation of intermetallic compounds layer in the joint interface led to the deterioration in mechanical properties due to its brittleness [11, 12]. However, in this study, the intermetallic compounds layer in the joint interface was not formed, and just MC carbides like a M7C3 were partially formed at Inconel 600 side, as shown in Fig. 5. Therefore, the absent of intermetallic compounds layer and the strong mechanical bonding due to FSW in this study could lead to an increase in tensile properties, as shown in Fig. 7(a).

The hook formed at advancing side, along the Inconel 600 alloy at joint interface, was effective to enhance the peel strength. Especially, the specimen, in which Inconel 600 alloy is located at advancing side, showed the higher peel strength than that of the specimen located at retreating side, as shown in Fig. 7(b). The hook formed in this study has the shape which tilted to advancing side, as shown in Fig. 4, along the Inconel 600 alloy from SS 400, which results in more high strength of advancing sided specimen due to the higher peel resistance in advancing side. Therefore, the peel strength of adv. specimen in this study could be shown higher value than that of ret. specimen.

### Conclusions

Friction stir lap joints on Inconel 600 and SS 400 can be successfully obtained without weld defects such as voids and cracks. Application of FSW led to the notable grain refinement in the stir zone of Inconel 600, accompanying with dynamic recrystallization, which resulted in an increase in mechanical properties of Inconel 600. Lap joints showed a mechanically jointed sound weld interface, and MC carbides were formed at Inconel 600 area in the interface, however, intermetallic compounds layer in the welds was not formed. Also, the formation of hook in advancing side, along the Inconel 600 alloy from SS 400, was effective to develop the mechanical properties. Particularly, Lap joint, in which Inconel 600 is located at advancing side, showed notably higher peel strength. Therefore, the application of FSW in lap joint between Inconel 600 and SS 400 can develop the mechanical properties, effectively.

## References

- [1] R.S. Mishra, and Z.Y. Ma, "Friction stir welding and processing." *Materials Science & Engineering R*, 50 (2005) 1-78.
- [2] R.S. Mishra, and M.W. Mahoney, *Friction Stir Welding and Processing* (ASM Int., 2007).
- [3] O.A. Ojo, N.L Richards, and M.C. Chaturvedi, "Contribution of constitutional liquation of gamma prime precipitate to weld HAZ cracking of cast Inconel 738 superalloy." *Scripta Materialia*, 50 (2004) 641-646.
- [4] C.A. Huang et al., "A study of the galvanic corrosion behavior of Inconel 718 after electron beam welding." *Materials Chemistry and Physics*, 104 (2007) 293-300.
- [5] J.D. Kim, C.J. Kim, and C.M. Chung, "Repair welding of etched tubular components of nuclear power plant by Nd:YAG laser." *Journal of Materials Processing Technology*, 114 (2001) 51-56.
- [6] K.H. Song, H. Fujii, and K. Nakata, "Effect of welding speed on microstructural and mechanical properties of friction stir welded Inconel 600." *Materials & Design*, 30 (2009) 3972-3978.
- [7] K.H. Song, T. Tsumura, and K. Nakata, "Development of microstructure and mechanical properties in laser-FSW hybrid welded Inconel 600." *Materials Transactions*, 50 (2009) 1832-1837.
- [8] K.H. Song, and K. Nakata, "Mechanical properties of friction stir welded Inconel 625 alloy." *Materials Transactions*, 50 (2009) 2498-2501.
- [9] K.H. Song, and K. Nakata, "Effect of precipitation on post heat treated Inconel 625 alloy after friction stir welding." *Materials & Design*, 31 (2010) 2942-2947.
- [10] K.H. Song, and K. Nakata, "Microstructural and mechanical properties of friction stir welded and post heat treated Inconel 718 alloy." *Journal of Alloys and Compounds*, 505 (2010) 144-150.
- [11] Y.C. Chen, and K. Nakata, "Friction stir lap joining aluminum and magnesium alloys." *Scripta Materialia*, 58 (2008) 433-436.
- [12] Y.C. Chen et al., "Interface microstructure study of friction stir lap joint of AC4C cast aluminum alloy and zinc coated steel." *Materials Chemistry and Physics*, 111 (2008) 375-380.
- [13] A. Abdollah-Zadeh, T. Saeid, and B. Sazgari, "Microstructural and mechanical properties of friction stir welded aluminum/copper lap joints." *Journal of Alloys and Compounds*, 460 (2008) 535-538.
- [14] P. Lin et al., "Influence of grain boundary character distribution on sensitization and intergranular corrosion of alloy 600." *Scripta Metallurgica et Materialia*, 33 (1995) 1387-1392.
- [15] F.J. Humphreys, and M. Hatherly, 2nd ed., *Recrystallization and Related Annealing Phenomena* (U.K., Elsevier Science Ltd, 2004) .

[16] R.E. Reed-Hill, and R. Abbaschian, 3rd ed., *Physical Metallurgy Principles* (Boston, PWS Publishing Company, 1994), 106.

[17] Y.C. Chen, and K. Nakata, "Effect of tool geometry on microstructure and mechanical properties of friction stir lap welded magnesium alloy and steel." *Materials & Design*, 30 (2009) 3913-3919.

# AUTHOR INDEX

## Characterization of Minerals, Metals, and Materials

### A

Abreu, A. ....	403
Acchar, W. ....	163, 169
Ahmad-Bitar, R. ....	319
Ahmadzadegan, A. ....	349
Aktas, B. ....	269
Anopuo, O. ....	27
Asghar, M. ....	327

### B

Başargan, T. ....	239
Bahadir, A. ....	131
Bai, C. ....	139, 421
Barbosa de Souza Martins, L. ....	381
Barcelos, F. ....	163
Barreto, L. ....	169
Barreto Bevitoni, A. ....	395
Barriuso, S. ....	443
Batson, R. ....	19
Bleck, W. ....	177
Brynjulfson, T. ....	147
Bunin, I. ....	89

### C

Camposo-Pereira, A. ....	357
Carneiro Garcia Rosa, N. ....	381
Carreon, H. ....	443
Chanturiya, V. ....	89
Chaudhari, G. ....	503
Chavarriaga, E. ....	155
Chen, J. ....	115, 311
Chinellato, A. ....	373, 403
Chopde, I. ....	495
Cortes, V. ....	49
Cosin, S. ....	259
Costa, A. ....	169

### D

Dai, L. ....	115
Das, D. ....	303
da Silva Crespo, A. ....	365
del Mastro, N. ....	403
DeMarco, J. ....	451
de Paula Barbosa, A. ....	365
Dhobe, M. ....	495
Dikovits, M. ....	503

Doyle, F. ....	99
----------------	----

### E

Erdem, E. ....	99
Erden, I. ....	131
Ergun, C. ....	131
Espinosa, D. ....	221

### F

Fang, H. ....	211
Faria, R. ....	259
Fischer, M. ....	177
Flender, R. ....	11
Flores, J. ....	203
Flores, M. ....	203
Frommert, M. ....	11

### G

Garcia-Caballero, F. ....	443
Gogte, C. ....	495
González-Carrasco, J. ....	443
Gordon, A. ....	451
Gu, R. ....	193
Gunes, G. ....	131

### H

Hara, Y. ....	79
Hashida, T. ....	487
He, X. ....	229
Hernandez, J. ....	203
Hilerio, I. ....	49
Hinze, B. ....	185
Huang, D. ....	311
Huang, J. ....	511
Huang, X. ....	123
Hwang, J. ....	211, 285

### I

Ikhmayies, S. ....	293, 319
Iqbal, K. ....	327

## J

James, A.....	303
Jansen, H.....	435
Jaramillo, L.....	155
Jayaraman, T.....	303
Jha, A.....	79
Jiang, X.....	511
Junca, E.....	221

## K

Karl, J.....	451
Kesselheim, B.....	435
Khabarova, I.....	89
Kim, H.....	61
Kim, W.....	61, 519
Koporulina, E.....	89
Kovalev, A.....	89
Kremer, U.....	435
Kumar, A.....	277

## L

Leão Amaral da Silva, I.....	395
Ledford, K.....	69
Li, D.....	139
Li, J.....	43
Li, L.....	511
Liang, W.....	115
Lieblich, M.....	443
Lin, J.....	311
Lin, M.....	311
Lin, S.....	69
Lin, T.....	311
Liu, H.....	131
Liu, X.....	139
Lopez-Hirata, V.....	487
Lu, L.....	211
Lutomski, P.....	177
Lv, X.....	123, 139

## M

Maich, A.....	99
Maier, P.....	27
Mallesham, B.....	303
Mallick, A.....	277
Maqsood, A.....	327
Matson, D.....	193
Medina, D.....	49
Monden, K.....	479
Monteiro, S.....	341
Moral, Ç.....	239

Moura, E.....	373, 403
Moura, T.....	169
Mujahid, M.....	327
Muñoz, J.....	49
Muylaert Margem, F.....	357, 365, 381, 395

## N

Nadler, J.....	69
Nakata, K.....	519
Nasun-Saygili, G.....	239
Nath, M.....	277
Neves Monteiro, S.....	357, 365, 381, 395
Nogueira, B.....	373

## O

Oliveira, J.....	221
Ortiz, A.....	373

## P

Pan, C.....	139
Pan, F.....	421
Pancholi, V.....	503
Parveen, A.....	373
Patiffo, F.....	203
Peng, J.....	115
Peng, Z.....	285
Penttilä, S.....	43
Pereira, A.....	403
Pereira, L.....	163
Pereira-Inácio, W.....	357
Pérez, M.....	203
Picanço Oliveira, M.....	365
Poletti, C.....	503

## R

Rangari, V.....	373
Rastegar, V.....	3
Reip, C.....	11
Restrepo, O.....	155
Reyes, I.....	203
Riad, M.....	251
Rivera, I.....	203
Roesler, J.....	185

## S

Saigal, A.....	193, 349
Salinas, E.....	203

Salman, S. ....	269
San Marchi, C. ....	193
Santafé-Júnior, H. ....	341
Saucedo-Muñoz, M. ....	487
Schemmel, T. ....	435
Sharma, K. ....	387
Shoukry, S. ....	251
Simonassi, N. ....	341
Sohn, Y. ....	451
Son, H. ....	61
Song, C. ....	35
Song, K. ....	61, 519
Sopeletto Carreiro, R. ....	395
Soria, A. ....	403
Souza, V. ....	259
Sripathy, M. ....	387
Stieben, A. ....	177
Suely Silva Santos, N. ....	365
Sun, X. ....	285

## T

Tangstad, M. ....	147
Tekeli, S. ....	269
Tenório, J. ....	221
Tober, G. ....	27
Toledo, R. ....	259
Trápala, N. ....	203
Tsai, J. ....	311

## V

Vargas, H. ....	259
-----------------	-----

## W

Warchomicka, F. ....	503
Webster, T. ....	131
Wei, Z. ....	115
Weng, Z. ....	115
William, G. ....	251
Wu, L. ....	413

## X

Xia, W. ....	35
Xia, X. ....	511
Xuc, G. ....	211

## Y

Yang, R. ....	35
---------------	----

Yao, G. ....	413
Ye, Q. ....	115

## Z

Zhai, Q. ....	35, 511
Zhang, B. ....	427
Zhang, J. ....	19, 421, 427
Zhang, M. ....	107
Zhang, R. ....	123
Zhang, Z. ....	285
Zheng, W. ....	43
Zhou, M. ....	123
Zhu, H. ....	115
Zhu, S. ....	229
Zimmerman, M. ....	349

# SUBJECT INDEX

## Characterization of Minerals, Metals, and Materials

**2**  
 2024 Aluminum Alloy ..... 413

**3**  
 3d Metallography ..... 177

**A**  
 Abrasive Wear ..... 49  
 Absorber Material ..... 185  
 Accelerated Aging ..... 311  
 Agglomerates ..... 147  
 Alumina ..... 163  
 Aluminium ..... 435  
 Annealing ..... 327  
 Annealing Treatment ..... 511  
 Aqueous Synthesis ..... 99  
 Attapulgite ..... 169  
 Austenitic Stainless Steels ..... 487

**B**  
 Banana Fiber ..... 381  
 BF Slag ..... 211  
 Biocompatibility ..... 131  
 Biomaterials ..... 443  
 Boron ..... 239  
 Bridge Deck Cracking ..... 251  
 Buriti Fiber ..... 365

**C**  
 Cadmium Compounds ..... 319  
 Carbide ..... 35  
 Carbon Fiber ..... 413  
 CdS/CdTe Solar Cells ..... 293, 319  
 Cellular Ceramic ..... 163  
 Cement Clinker ..... 229  
 Cementitious Material ..... 229  
 Ceramic ..... 259  
 Ceramic Pigments ..... 155  
 Characterization ..... 107  
 Characterization Materials ..... 155  
 Characterizations ..... 327  
 Chemical Methods ..... 155  
 Chromite ..... 139  
 Clay ..... 169  
 CoFe Alloy ..... 79  
 Coir Fiber ..... 341

Cold Working of Steel ..... 19  
 Cold-Rolled Invar Alloy ..... 511  
 Colemanite ..... 239  
 Color Metallography ..... 3  
 Compacted Graphite Cast Iron ..... 3  
 Complex Hot Forming ..... 27  
 Composite ..... 373, 403  
 Composites ..... 413  
 Concrete Setting Time ..... 251  
 Concrete Stability And Expansion ..... 211  
 Concrete Without Cement ..... 211  
 Copper ..... 69  
 Corrosion ..... 43  
 Creep Life Assessment ..... 479  
 Cross-Roll Rolling ..... 61  
 Crushing Behavior ..... 387  
 CSP ..... 11  
 Cubic Zirconia ..... 269  
 Curing Fresh Concrete ..... 251  
 Cycled Fluidized Bed Ash (CFBA) ..... 229

**D**  
 Deformation ..... 421  
 Dendrites Arm Spacing ..... 3  
 Density Elastic Modulus ..... 357  
 Density/Diameter Correlation ..... 365  
 Diameter Correlation ..... 357  
 Die Swell ..... 349  
 Dielectric Constant ..... 115  
 Direct Reduced Iron ..... 115  
 Doping ..... 131  
 DSC ..... 381  
 DTG ..... 381

**E**  
 EBSD ..... 11  
 Elastic Modulus ..... 395  
 Electric Breakdown Channels ..... 89, 89  
 Electric Field ..... 285  
 Electric Resistivity ..... 139  
 Electrode Potential ..... 89  
 Electron Back-Scattered Diffraction ..... 61  
 Electron-Beam Irradiation ..... 403  
 Extrusion ..... 349

**F**  
 Fatigue Testing ..... 193  
 Fe-Mn-C ..... 35

Fiber Diameter Effect.....	395
Fiber/Matrix Interaction.....	341
Finite Element.....	349
Fluxes.....	147
Foam.....	387
Fracture Morphology.....	511
Fracture Toughness.....	487
Free CaO.....	229
Free Lime.....	211
Friction Stir Welding.....	519

## G

Gamma Irradiation.....	403
Grain Refinement.....	61
Granulated Slag.....	211
Grit Blasting.....	443

## H

Hardness.....	495
Heat Treatment.....	495
Heterojunctions.....	293
High-Power Nanosecond Pulses.....	89
Hot Deformation.....	503
Hot Rolling.....	27, 427
Hot Rolling Simulation.....	451
Hydrogen Storage.....	277, 285
Hydroxyapatite.....	239
Hydroxylapatite.....	131

## I

II-VI Semiconductors.....	293
Illumination Effect.....	311
Image Stacks.....	177
Imaginary Initial Strain Rate.....	479
Iron Ore.....	107, 123
Iron Ore Fine.....	115
Iron Oxide.....	99

## L

La <sub>2</sub> O <sub>3</sub> .....	269
La <sub>2</sub> Zr <sub>2</sub> O <sub>7</sub> .....	269
Lap Joints.....	519
LCP.....	349
Lead Solder.....	479
Lead-Free Solder.....	479
Light Optical Microscopy.....	177

## M

Magnesium Alloy.....	421
Manganese.....	147
Mass Transfers.....	49
Mechanical Characterization.....	451
Mechanical Properties.....	61, 163, 511, 519
Metal-Matrix Composites.....	451
Metal-Organic Compounds.....	277
Mg Alloy.....	427
Micro- And Nanophases.....	89
Micro-Alloyed Steels.....	11
Microalloyed Steel.....	503
Microreactor.....	99
Microstructural Investigation.....	269
Microstructure.....	11, 69, 169, 421, 511
Microstructures.....	519
Microwave Fields.....	115
Mineralogical.....	107
Mineralogical Characterization.....	221
Mining Wastes.....	203
Morphological Properties.....	373
Multilayer.....	327
Multiple Regression Analysis.....	19

## N

Nanobond.....	435
Nanocrystallites.....	293
Nanoparticle Synthesis.....	99
Near-Rapid Solidification.....	35
Ni-20Cr Alloy.....	61
Nickel Oxide.....	285
No Cement Castables.....	435
Noise Reduction.....	185

## P

Particle Size.....	139
Perovskite.....	303
Phosphorus.....	107
Photothermal Techniques.....	259
Physical Properties of Steel.....	19
Piassava Fibers.....	373
Piezoelectric Charge Coefficient.....	303
Pollutant Gas.....	259
Polyester Composites.....	341
Polyurethane.....	387
Pore Size.....	185
Porosity.....	185
Process Chemistry.....	79
Processing.....	69
Processing Maps.....	503
Properties.....	169
Pyrochlore.....	303

## Q

Quick Drying ..... 435

## R

Ramie Fiber..... 395  
Reduction ..... 79, 147  
Refractory ..... 435  
Relaxor Ferroelectrics ..... 303  
Residual Stresses..... 443  
Reusing of Wastes..... 203  
RF Magnetron Sputtering..... 327  
Rheology..... 349  
Roughness..... 123

## S

SCW..... 43  
SEM..... 373  
SEM-EDX and XRD..... 79  
Serial Sectioning..... 177  
Sinter..... 147  
Sintering..... 269  
Sisal Fibers..... 357  
Small-Punch Test..... 487  
Smelting..... 147  
SO<sub>2</sub>..... 79  
Solution..... 427  
Sorption..... 89  
Sorption Study..... 277  
Soundness..... 229  
Specific Surface Area..... 123  
Spinel Structure..... 155  
Spray Pyrolysis..... 319  
Stacking Fault..... 35  
Steel Slag..... 211  
Steel Tube Production..... 19  
Strain-Dependent Modeling..... 451  
Sugarcane Bagasse Fiber..... 403  
Sulfide Mineral..... 89  
Sulfur..... 107  
Surface Modification..... 43  
Surface Roughness..... 495

## T

Temperature Rise..... 193  
Temperature-Dependent Modeling..... 451  
Temperature-Rising Characteristics..... 115  
Tensile Mechanical Properties..... 427  
Testing Traction..... 365  
TGA..... 381  
Thermal Decomposition..... 99, 381

Thermal Properties..... 259, 373  
Thermal Wick..... 69  
Thermo-Mechanical Properties..... 403  
Thermoelectric Measurements..... 443  
Thermography..... 193  
Thermogravimetric Analysis..... 341  
Thick Plates..... 27  
Thin Films..... 293  
Tile Production..... 203  
Toughness..... 11  
Trace Elements..... 107  
Transparent Conducting Oxides..... 319  
Tribofinishing..... 49

## W

W-EDM..... 495  
Waste Steel..... 221  
Water Evolution..... 381  
Wear..... 49  
Weibull Analysis..... 357, 365, 395  
White Layer..... 495

## X

X-Ray Diffraction..... 277